# DYNAMICAL SYSTEMS

## Mathematical and Numerical Approaches

Editors
J. AWREJCEWICZ
M. KAŹMIERCZAK
J. MROZOWSKI
P. OLEJNIK

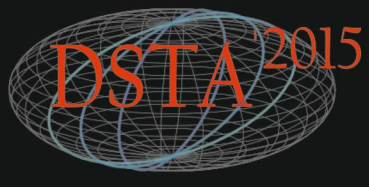

# DYNAMICAL SYSTEMS

## Mathematical and Numerical Approaches

Editors

JAN AWREJCEWICZ, MAREK KAŹMIERCZAK
JERZY MROZOWSKI, PAWEŁ OLEJNIK

© Department of Automation, Biomechanics and Mechatronics
ISBN 978-83-7283-706-6
10.34658/9788372837066
https://doi.org/10.34658/9788372837066

Cover design: Marek Kaźmierczak
Technical editor: Marek Kaźmierczak

Printed by:
ARSA Druk i Reklama
90-270 Łódź, ul. Piotrkowska 4
tel./fax (042) 633 02 52
marta@arsa.net.pl
www.arsa.net.pl

# PREFACE

This is the thirteen time when the conference “Dynamical Systems: Theory and Applications” gathers a numerous group of outstanding scientists and engineers, who deal with widely understood problems of dynamics met in daily life.

Organization of the conference would not have been possible without a great effort of the staff of the Department of Automation, Biomechanics and Mechatronics, as well as Committee of Mechanics of the Polish Academy of Sciences. The financial support has been given by the Polish Academy of Sciences.

It is a great pleasure that our invitation has been accepted by recording in the history of our conference number of people, including good colleagues and friends as well as a large group of researchers and scientists, who decided to participate in the conference for the first time. With proud and satisfaction we welcomed over **180** persons from **29** countries all over the world. They decided to share the results of their research and many years experiences in a discipline of dynamical systems by submitting many very interesting papers.

This year, the DSTA Conference Proceedings were split into three volumes entitled “Dynamical Systems” with respective subtitles: *Mathematical and numerical approaches*; *Mechatronics and life sciences* and vol. 3 *Control and stability*. Additionally there will be also published two volumes of Springer Proceedings in Mathematics and Statistics entitled “*Dynamical Systems. Modelling”* and *“Dynamical Systems. Theoretical and Experimental Analysis”.*

These books include the invited papers and regular papers dealing with the following topics:

- control in dynamical systems,
- stability of dynamical systems,
- asymptotic methods in nonlinear dynamics,
- mathematical approaches to dynamical systems,
- dynamics in life sciences and bioengineering,
- engineering systems and differential equations,
- original numerical methods of vibration analysis,
- bifurcations and chaos in dynamical systems,
- vibrations of lumped and continuous systems,
- non-smooth systems,
- other problems.

Proceedings of the 13th Conference „Dynamical Systems - Theory and Applications" summarize **164** and the Springer Proceedings summarize **60** best papers of university teachers and students, researchers and engineers from whole the world. The papers were chosen by the International Scientific Committee from **315** papers submitted to the conference. The reader thus obtains an overview of the recent developments of dynamical systems and can study the most progressive tendencies in this field of science.

Our previous experience shows that an extensive thematic scope comprising dynamical systems stimulates a wide exchange of opinions among researchers dealing with different branches of dynamics. We think that vivid discussions will influence positively the creativity and will result in effective solutions of many problems of dynamical systems in mechanics and physics, both in terms of theory and applications.

We do hope that DSTA 2015 will contribute to the same extent as all the previous conferences to establishing new and tightening the already existing relations and scientific and technological co-operation between both Polish and foreign institutions.

On behalf of both
Scientific and Organizing Committees

Chairman
Professor Jan Awrejcewicz

**CONTENTS**

**Iwona Adamiec-Wójcik, Jan Awrejcewicz, Witold Grzegożek, Stanisław Wojciech**
*Dynamics of articulated vehicles by means of multibody methods* ..... 11

**Iwona Adamiec-Wójcik, Łukasz Drąg, Stanisław Wojciech**
*Validation of the rigid finite element method used for modelling of lines and risers* ..... 21

**Fusun Alisverisci**
*Nonlinear normal modes for vibrational conveyers with crank-and-rod exciters* ..... 31

**Igor V. Andrianov, Jan Awrejcewicz, Alexander A. Diskovsky**
*Strain analysis and structural optimization of functionally graded rod with small concentration of inclusions* ..... 41

**Jan Awrejcewicz, Lidiya Kurpa, Tatiana Shmatko**
*Vibration of functionally-graded shallow shells with complex shape* ..... 57

**Marek Barski, Adam Stawiarski, Piotr Pająk**
*Numerical study of. the optimal position of Lamb wave actuator for detection of fatigue damages in an isotropic plate with a circular hole* ..... 69

**Hüseyin Bayıroğlu**
*Nonlinear normal modes for unbalanced mass of vertical conveyer-elevator* ..... 81

**Carsten Behn, Nikolai Bolotnik, Igor Zeidis, Klaus Zimmermann**
*Mechanics of terrestrial locomotion systems in application to mobile robots* ..... 91

**Valter Böhm, Tobias Kaufhold, Igor Zeidis, Klaus Zimmermann**
*Dynamic analysis of the rolling locomotion of mobile robots based on ensegrity structures with two curved compressed components* ..... 105

**Andrzej Buchacz**
*Characteristics of model freight wagon subsystems of transverse vibrating complex mechanical system determined by approximate method and their correction* ..... 117

**Rafał Burdzik**
*Application of original method of vibration analysis for investigation on passenger car suspension as nonlinear dynamical system* ..... 127

**Rafał Burdzik, Łukasz Konieczny,**
**Jan Warczek, Witold Cioch**
*Adaptation of linear decimation procedures for identification of haracteristics components of non-stationary vibration signals in car's suspension* ..... 139

**Dengqing Cao, Huatao Chen,**
**Jingfei Jiang**
*Kernel and Kernel section for a nonlinear thermo-elastic beam subjected to time-varying external excitations* ..... 149

**Adrian Chmielewski, Robert Gumiński,**
**Jędrzej Mączak**
*3 DOF dynamic model of the piston-crankshaft system of the Stirling engine* ..... 159

**Berenice Damasceno, Luciano Barbanti**
*Some remarks about unanswered questions regarding spring-pot processes* ..... 171

**Barry Gallacher, Zhongxu Hu,**
**Stephen Bowles**
*Full control and compensation scheme for a rate integrating MEMS gyroscope* ..... 177

**Adam Gałęzia, Robert Gumiński,**
**Marcin Jasiński, Jędrzej Mączak**
*Use of energy operators in condition monitoring of gearboxes* ..... 189

**Adam Gałęzia, Stanisław Radkowski**
*Teager-Kaiser energetic plane – novel tool for condition monitoring of machines* ..... 199

**Piotr Gierlak, Andrzej Burghardt, Dariusz Szybicki,**
**Marcin Szuster, Magdalena Muszyńska**
*The manipulator tool fault diagnostics based on vibration analysis* ..... 211

**Szymon Gontarz, Robert Gumiński**
*The use of magnetic phenomena and Bayesian updating in the risk assessment of structural damage* ..... 223

**Grzegorz Górski, Grzegorz Litak,**
**Romuald Mosdorf, Andrzej Rysak**
*Two-phase flow patterns identification based on recurrence statistics of a pressure drop* ..... 235

**Ahmed Haris, Eliot Motato, Stephanos Theodossiades, Alex Vakakis,**
**Lawrence A. Bergman, Donald M. McFarland, Ben Struvé**
*Targeted energy transfer in automotive powertrains* ..... 245

**Andrzej Harlecki, Andrzej Urbaś**
*Dynamics simulations of spatial linkages using the LuGre friction model* ..... 255

**Elżbieta Kasperska, Andrzej Kasperski,**
**Tomasz Bajon, Rafał Marjasz**
*Modeling and simulation of ecosystems on the base of 'prey-predator' model of system dynamics type - sensitivity analysis, calibration and gaming* ..... 267

**Matthias Klaerner, Mario Wuehrl,**
**Steffen Marburg, Lothar Kroll**
*Efficient FEA simulation of structure borne sound radiation* ..... 279

**Liubov Klimina, Marat Dosaev, Yury Selyutskiy,**
**Shih-Shin Hwang, Kao-Huei Lin**
*Asymptotic analysis of the model of a wind-powered vehicle moving against the flow* ..... 291

**Robert Kostek**
*Eighth-order direct numerical methods for second-order ordinary differential equations* ..... 301

**Robert Kostek**
*Tenth-order direct numerical methods for second-order ordinary differential equations* ..... 313

**Tomáš Lack, Juraj Gerlici,**
**Josef Soukup**
*Modified strip method utilization for wheel/rail contact stress assessment* ..... 325

**Maciej Major, Izabela Major**
*Numerical modelling of wave phenomena in the Zahorski material using ADINA software* ..... 339

**Damian Mazur, Marek Rudy**
*Natural frequency analysis of home wind turbines with vertical axes* ..... 351

**Arkadiusz Mężyk, Wojciech Klein,**
**Mariusz Pawlak, Jan Kania**
*Numerical simulation of vibration control system designed for Continuous Miner machines* ..... 363

**Maciej Mikulski, Sławomir Wierzbicki**
*Numerical investigation of the impact of gas composition on the combustion process in a dual-fuel compression-ignition engine* ..... 371

**Maciej Mikulski, Sławomir Wierzbicki,**
**Andrzej Piętak**
*Validation of a zero-dimensional, 2-phase combustion model for dual-fuel compression ignition engine simulation* ..... 383

**Andrzej Nowak, Paweł Nowak,**
**Jan Awrejcewicz**
*Influence of position of an anvil beam on vibrations of collecting electrodes* ..... 391

**Tomasz Pałczyński**
*1D model of the pulsating flows in pipes dynamics using the MOC* ..... 403

**Anthony Rosato, Denis Blackmor**e
*Advances in dynamical simulation and analysis of granular flow* ..... 413

**Anton Sauter, Christoph Will,**
**Joachim Steigenberger, Carsten Behn**
*Artificial tactile sensors with pre-curvature for object scanning* ..... 425

**Wojciech Sawczuk, Grzegorz M. Szymański**
*Application of analysis of resonance vibration for the diagnosis of a pair of friction of the railway disc brake* ..... 437

**Maxim V. Shamolin**
*On lower- and multi-dimensional pendulum in a nonconservative force fields* ..... 449

**Tiago Silva, Nuno Maia**
*Error localization in the finite element modelling of structures* ..... 461

**Josef Soukup, Jan Skočilas,**
**Blanka Skočilasová**
*Experimental determination of eigenfrequency and stiffness of suspension of elastically embedded body – vehicle application* ..... 475

**Adam Stawiarski, Marek Barski,**
**Piotr Pająk**
*Fatigue crack identification by dynamic analysis of elastic wave propagation* ..... 489

**Anna Szcześniak, Adam Stolarski**
*Analysis of critical damping in dynamic relaxation method for reinforced concrete structural elements* ..... 501

**Michał Szewc, Igor Wojtunik,**
**Grzegorz Kudra, Jan Awrejcewicz**
*Dynamics simulations of a rigid body lying on a vibrating table with the use of special approximations of the resulting contact forces* ..... 513

**Eliza Tkacz, Zbigniew Kozanecki,**
**Dorota Kozanecka, Jakub Łagodziński**
*Model of the gas journal bearing dynamics with a flexibly supported foil* ..... 523

**Eliza Tkacz, Zbigniew Kozanecki,**
**Dorota Kozanecka, Jakub Łagodziński**
*Theoretical analysis of the foil bearings dynamic characteristics* ..... 533

**Stefania Tomasiello, Jan Awrejcewicz**
*Simulating the damped vibrations of a fractional oscillator with fuzzy initial conditions* ..... 543

**Andrzej Urbaś**
*Application of the rigid finite element method in the dynamics of grab cranes* ..... 555

**Viktorija Volkova**
*Qualitative theory and identification of non-linear dissipative systems*..... 567

**Grzegorz Wasilewski, Grzegorz Kudra, Jan Awrejcewicz, Maciej Kaźmierczak, Mateusz Tyborowski, Marek Kaźmierczak**
*Experimental and numerical investigations of a pendulum driven by a low-powered DC motor*..... 579

**Igor Wojtunik, Michał Szewc, Grzegorz Kudra, Jan Awrejcewicz**
*On the clutch dynamics with the approximations of resulting contact forces*..... 591

**Janusz Wójcik, Barbara Gambin**
*Numerical analysis of reflection and transmission phenomena of nonlinear ultrasound wave*..... 603

# Dynamics of articulated vehicles by means of multibody methods (MAT143-15)

Iwona Adamiec-Wójcik, Jan Awrejcewicz, Witold Grzegożek, Stanisław Wojciech

*Abstract:* The paper presents modelling of an articulated vehicle by means of joint coordinates, which enable us to describe the motion of the system with a minimal number of generalised coordinates. We consider a model of a semi-trailer formulated using joint coordinates and homogenous transformations. Such an approach enables us to treat the vehicle as a kinematic chain consisting of three single units with an even number of wheels. This means that a single unit vehicle has a structure of an open kinematic chain in a tree form. The contact of wheels with the road is modelled by the Dugoff-Uffelman model. The model is validated by comparing the simulation results with those obtained from experimental measurements. Friction in the fifth wheel is one of the important parameters influencing the motion of a tractor with a semi-trailer. The model presented enables us to analyse different models of friction in the fifth wheel. The influence of those friction models on the results is presented and discussed.

## 1. Introduction

When articulated vehicles are modelled, they are usually treated as a system of single vehicle units connected in various ways [1-3]. The division of a vehicle into several elements (rigid and/or flexible) is a natural way of dealing with such a complex multibody system. The motion of rigid elements is described by six generalized coordinates ; these elements are then connected by means of either constraint equations or spring-damping elements. When the equations of motion are integrated, not only the generalized coordinates and velocities but also reactions and moments of reactions in joints are calculated. The mass matrix of the system is in a block-diagonal form, which shortens numerical calculation time. However, the number of generalized coordinates is large, which slightly reduces the advantages of the method when constraint equations need to be stabilized. Such an approach is used in commercial software packages for simulation of vehicle dynamics (DADS, DYTRAN). On the other hand there are methods using joint coordinates in which the dynamics of a system is described by a minimal number of generalized coordinates. The disadvantage of such an approach is a full mass matrix and the lack of direct calculations of reactions in joints.

Friction occurring in couplings of any multibody system influences its motion. There is also a large number of papers in which different models of friction are discussed; however, the examples are usually limited to mechanisms with one or very few degrees of freedom [4,5]. Dynamic models of

articulated vehicles, even when some simplifications are assumed, usually have several numbers of degrees of freedom. Thus consideration of friction is especially difficult. Friction is usually taken into account in models of contact of the tires with the road [6,7]. Friction in couplings of units is considered less often [8].

This paper is concerned with phenomena accompanying friction in rotary couplings in articulated vehicles such as semi-trailers. Knowledge of the influence of friction in the couplings on the motion of the vehicles is important when the stability of the vehicles is examined. Simplified models are formulated using the joint coordinates for simulation of motion of vehicles. In order to derive the equations of motion, homogenous transformations are used, while the Newton-Euler algorithm for an inverse dynamic problem is applied to calculate the reaction at couplings. This enable us to analyze the influence of different models of friction in the coupling on the motion of the vehicle. The models elaborated have been validated by comparing the simulation results with those obtained from experimental measurements. The results of numerical simulations for different friction models are also presented and the conclusions about the influence of friction on the motion are formulated.

## 2. Model of articulated vehicles

The model of any articulated vehicle can be formulated using homogenous transformations and joint coordinates by combining models of single units. Dynamic analysis requires a physical model which takes into consideration components of a vehicle such as a vehicle body, suspensions, wheels and a steering system. For the purpose of this paper a model of a semi-trailer is composed of models of three single units. A simplified model of a single unit consists of an uneven number of rigid bodies, one of which represents a vehicle body. Motion of the rigid body (single unit) is be described by one to six degrees of freedom describing the motion of the unit with respect to the preceding unit. Other elements represent wheels, while the flexibility of suspensions is reduced to the contact point between the tire and the road. The motion of a vehicle is performed on a planar, horizontal and undeformable road surface. The steering is reflected by additional functions describing the change in time of the steering angle of the wheels.

The equations of motion are derived using the Lagrange equations. All external forces and moments acting on the vehicle unit are included by means of the generalized forces. The following forces are taken into account: air resistance, drive, braking and aligning torques as well as forces describing the contact between the wheel and the road surface. The latter are derived using the Dugoff-Uffelmann model.

The model of a tractor with semi-trailer consists of three units which are treated as rigid bodies (Fig.1). The motion of each unit is described using its own generalised coordinates and the generalised coordinates of the preceding links in the kinematic chain.

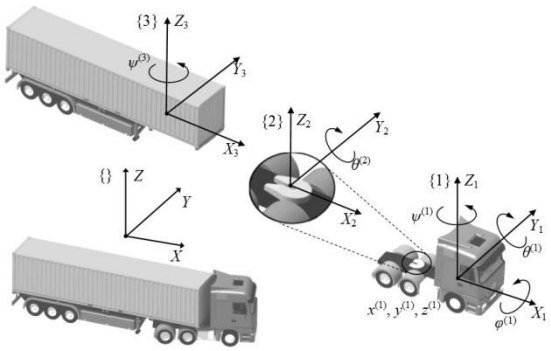


**Figure 1.** Tractor with semi-trailer as a system of three units

The generalised coordinates describing the motion of each link are the components of the following vectors:

1) tractor

$$\mathbf{q}^{(1)} = \tilde{\mathbf{q}}^{(1)} = \left[ x^{(1)} \quad y^{(1)} \quad z^{(1)} \quad \psi^{(1)} \quad \theta^{(1)} \quad \varphi^{(1)} \quad \varphi_1^{(1)} \quad \varphi_2^{(1)} \quad \varphi_3^{(1)} \quad \varphi_4^{(1)} \right]^T \tag{1.1}$$

2) fifth wheel

$$\mathbf{q}^{(2)} = \left[ \mathbf{q}^{(1)^T} \quad \tilde{\mathbf{q}}^{(2)^T} \right]^T = \left[ \mathbf{q}^{(1)^T} \quad \tilde{\mathbf{q}}^{(2)^T} \right]^T, \tilde{\mathbf{q}}^{(2)} = \left[ \theta^{(2)} \right] \tag{1.2}$$

3) semi-trailer

$$\mathbf{q}^{(3)} = \left[ \mathbf{q}^{(2)^T} \quad \tilde{\mathbf{q}}^{(3)^T} \right]^T, \tilde{\mathbf{q}}^{(3)} = \left[ \psi^{(3)} \quad \varphi_1^{(3)} \quad \varphi_2^{(3)} \quad \varphi_3^{(3)} \quad \varphi_4^{(3)} \quad \varphi_5^{(3)} \quad \varphi_6^{(3)} \right]^T \tag{1.3}$$

The equations of motion of the whole vehicle can be written in the compact form:

$$\mathbf{A}\ddot{\mathbf{q}} = \mathbf{f} \tag{2}$$

The number of equations of motion is

$$n = \tilde{n}^{(1)} + \tilde{n}^{(2)} + \tilde{n}^{(3)} + n_{w1} + n_{w2} + n_{w3} = 6 + 1 + 1 + 4 + 0 + 6 = 18$$

Integration of equations of motion (2) requires initial conditions to be determined, so an appropriate quasi–static problem has to be solved, which can be done in the way presented in [9].

## 2.1. Coulomb model of friction in the coupling

Modelling of articulated vehicles becomes more complex when friction in connections is taken into consideration. The model of the coupling between units *m* and *m*-1 is assumed as in Fig.2.

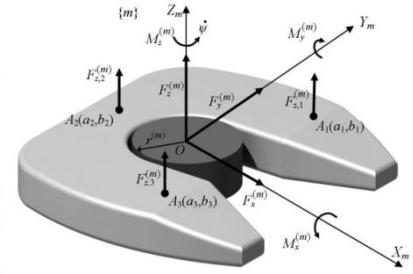


**Figure 2.** Connection of link *m*-1 and *m* with dry friction

Let $\mathbf{F}^{(m)} = \left[F_x^{(m)},\ F_y^{(m)},\ F_z^{(m)},\ 0\right]^T$ and $\mathbf{M}^{(m)} = \left[M_x^{(m)},\ M_y^{(m)},\ M_z^{(m)},\ 0\right]^T$ be respectively the force and the moment about point *O* with which the link *m*-1 acts on link *m*. Following the convention used in robotics, it is assumed that force $\mathbf{F}^{(m)}$ and moment $\mathbf{M}^{(m)}$ are defined with respect to system $\{m\}$ and are balanced by inertial forces and moments of body *m* and external forces and moments acting on this body.

Let us assume that force $\mathbf{F}^{(m)}$ and components $M_x^{(m)}$ and $M_y^{(m)}$ are known and moment $M_z^{(m)} = M_F$ is the moment of kinetic friction in the connection $(\dot{\psi}^{(m)} \neq 0)$. Then an additional moment:

$$M_{z,k}^{(m)} = -\operatorname{sgn}\dot{\psi}^{(m)} M_F \tag{3}$$

will act on link *m*. It is obvious that the value of moment $M_F$ depends on $F_x^{(m)}, F_y^{(m)}, F_z^{(m)}$ as well as on $M_x^{(m)}$ and $M_y^{(m)}$. The friction moment on force $\mathbf{F}^{(m)}$ and components $M_x^{(m)}$ and $M_y^{(m)}$ of moment $\mathbf{M}^{(m)}$ can be calculated according to the following formula:

$$\begin{aligned} M_F = {} & \mu \cdot r^{(m)} \sqrt{(F_x^{(m)})^2 + (F_y^{(m)})^2} \\ & + \mu \left| F_{z,1}^{(m)} \right| \sqrt{(a_1)^2 + (b_1)^2} + \mu \left| F_{z,2}^{(m)} \right| \sqrt{(a_2)^2 + (b_2)^2} + \mu \left| F_{z,3}^{(m)} \right| \sqrt{(a_3)^2 + (b_3)^2} \end{aligned} \tag{4}$$

where $F_{z,1}^{(m)}, F_{z,2}^{(m)}, F_{z,3}^{(m)}$ are calculated as in [9], $a_i, b_i$ are coordinates of points $A_i$ in local coordinate system $\{m\}$. If in this formula $\mu$ is replaced by $\mu_k$ (coefficient of kinetic friction), the moment of friction in the case of kinetic friction can be calculated from (3) after substituting (4). When $\mu = \mu_s$

(coefficient of static friction), formula (4) gives the maximal value of the friction moment which can be transferred by the connection.

In order to use formula (4), the phase of friction in the connection and values of forces $F_x^{(m)}, F_y^{(m)}, F_z^{(m)}$ and moments $M_x^{(m)}, M_y^{(m)}$ have to be determined. This problem is also addressed in other research concerned with dry friction, for example [10].

Let us introduce the following index defining the phase of friction in the connection:

$$i_m = \begin{cases} 0 & \text{if} \quad \dot{\psi}^{(m)} = 0 \ - \text{static friction} \\ 1 & \text{if} \quad \dot{\psi}^{(m)} \neq 0 \ - \text{kinetic friction} \end{cases} \tag{5}$$

During motion, index $i_m$ changes in the following way:

If $i_m = 0$: $M_z^{(m)}$ is an additional unknown and the additional constraint equation is formulated:

$$\dot{\psi}^{(m)} = 0 \tag{6.1}$$

Transition into the kinetic friction phase ( $i_m = 1$ ) takes place when the following relation is fulfilled:

$$\left| M_z^{(m)} \right| \geq M_F \tag{6.2}$$

where $M_F$ is defined in (4) assuming $\mu = \mu_s$.

If $i_m = 1$: The moment of friction can be calculated according to formulae (3) and (4). The change in the state of motion in the connection is expected when velocity $\dot{\psi}_m$ changes its sign. Moment $M_{z,k}^{(m)}$ has to be taken into account in the equations of motion of the vehicle. For the semi-trailer the relative motion of unit *m* with respect to unit *m*-1 is defined by angle $\psi^{(3)}$ (*m*=3). The above model of friction is called a Coulomb model with stiction and it is used for comparative analysis as the reference ('C').

In robotics calculation of force $\mathbf{F}^{(m)}$ and moment $\mathbf{M}^{(m)}$ in the coupling is carried out by means of the Newton-Euler procedure for solving inverse dynamics [11]. However, it is impossible to use this approach directly in the case of articulated vehicles because of the specific tree structure of articulated vehicles and the way of assigning the coordinate systems. Detailed description of this algorithm is presented in [9].

## 3. Other models of friction

There are many different models of friction used in simulations of dynamics of multibody systems. Since friction is a complex phenomenon, the analysis of its influence on the motion of systems is very often limited to simple mechanisms with only a few degrees of freedom. Articulated vehicles are examples of multibody systems with several degrees of freedom and therefore consideration of friction is a difficult task. The most popular model of friction assumes two phases of relative motion

in the coupling, so called stick-slip motion, and it is described in section 2.1 as a Coulomb model with stiction. Due to the discontinuity of the friction force at zero relative velocity, this model causes computational problems, so that some researchers consider continuous functions in the vicinity of zero. For the comparative analysis we consider some other models of kinetic friction described below.

'P' – model with continuous function of the third order:

It is assumed that the moment of friction is calculated as follows:

$$M_{z,k}^{(m)} = \begin{cases} \operatorname{sgn}\dot{\psi}^{(m)} M_F & \text{if} \quad \left|\dot{\psi}^{(m)}\right| > \Delta\dot{\psi}^{(m)} \\ \operatorname{sgn}\dot{\psi}^{(m)} M_F \; p_3\left(M_F, \dot{\psi}^{(m)}\right) & \text{if} \quad \left|\dot{\psi}^{(m)}\right| \le \Delta\dot{\psi}^{(m)} \end{cases} \tag{7.1}$$

where $p_3\left(M_F, \dot{\psi}^{(m)}\right)$ is a polynomial of the third degree calculated according to the formula:

$$p_3 = \operatorname{sgn}\dot{\psi}^{(m)} \left( \left( \frac{\dot{\psi}^{(m)}}{\Delta\dot{\psi}^{(m)}} \right)^3 - 3\left( \frac{\dot{\psi}^{(m)}}{\Delta\dot{\psi}^{(m)}} \right)^2 + 3\left| \frac{\dot{\psi}^{(m)}}{\Delta\dot{\psi}^{(m)}} \right| \right) M_F \tag{7.2}$$

'A' – Awrejcewicz model [12]:

The moment of kinetic friction $M_{z,k}^{(m)}$ can be calculated according to the following formula:

$$M_{z,k}^{(m)} = \begin{cases} \operatorname{sgn}\dot{\psi}^{(m)} M_F & : \left|\dot{\psi}^{(m)}\right| > \Delta\dot{\psi}^{(m)} \\ \operatorname{sgn} M_z^{(m)} M_F & : \left|\dot{\psi}^{(m)}\right| \le \Delta\dot{\psi}^{(m)} \wedge \left|M_z^{(m)}\right| > M_F \wedge \operatorname{sgn}\left(\dot{\psi}^{(m)} M_z^{(m)}\right) \ge 0 \\ (2A-1)\operatorname{sgn}\dot{\psi}^{(m)} M_F & : \left|\dot{\psi}^{(m)}\right| \le \Delta\dot{\psi}^{(m)} \wedge \left|M_z^{(m)}\right| > M_F \wedge \operatorname{sgn}\left(\dot{\psi}^{(m)} M_z^{(m)}\right) < 0 \\ A(-M_z^{(m)} + \operatorname{sgn}\dot{\psi}^{(m)} M_F) + M_z^{(m)} & : \left|\dot{\psi}^{(m)}\right| \le \Delta\dot{\psi}^{(m)} \wedge \left|M_z^{(m)}\right| \le M_F \end{cases} \tag{8}$$

where $A = \left( \frac{\dot{\psi}^{(m)}}{\Delta\dot{\psi}^{(m)}} \right)^2 \left( 3 - 2\left| \frac{\dot{\psi}^{(m)}}{\Delta\dot{\psi}^{(m)}} \right| \right)$, $M_z^{(m)}$ is the moment calculated from the Newton-Euler procedure.

'T' – Threlfall model [13]:

$$M_{z,k}^{(m)} = \begin{cases} \operatorname{sgn}\dot{\psi}^{(m)} M_F & \text{if} \quad \left|\dot{\psi}^{(m)}\right| > \Delta\dot{\psi}^{(m)} \\ \operatorname{sgn}\dot{\psi}^{(m)} M_F \left( 1 - e^{\frac{3\left|\dot{\psi}^{(m)}\right|}{\Delta\dot{\psi}^{(m)}}} \right) & \text{if} \quad \left|\dot{\psi}^{(m)}\right| \le \Delta\dot{\psi}^{(m)} \end{cases} \tag{9}$$

All the above models depend on arbitrary parameter $\Delta\dot{\psi}^{(m)}$ which is a velocity tolerance.

## 4. Numerical simulations

The model of a semi-trailer presented in section 2 was validated by comparing the computer simulation results with the experimental measurements carried out in [9].

In order to examine the influence of the assumed friction model and friction coefficients on the dynamics of the semitrailer, several numerical experiments were carried out, assuming an idealized steering angle of front wheels of the tractor in such a way that the mass center of the tractor moves 8.5m in a lateral direction when there is no friction in the coupling analyzed (Fig.3).

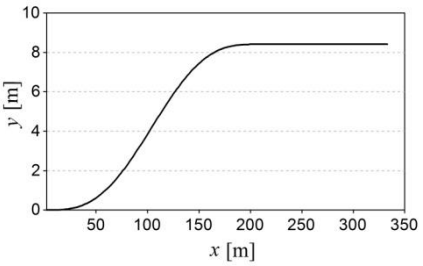


**Figure 3.** Trajectory of the mass center of the tractor without friction in the coupling

Having performed some numerical simulations, it is assumed that the velocity tolerance is $\Delta\dot{\psi}^{(m)} = 0.001$. The comparison of the trajectory of the tractor calculated for different models with different values of friction coefficient is presented in Fig.4.

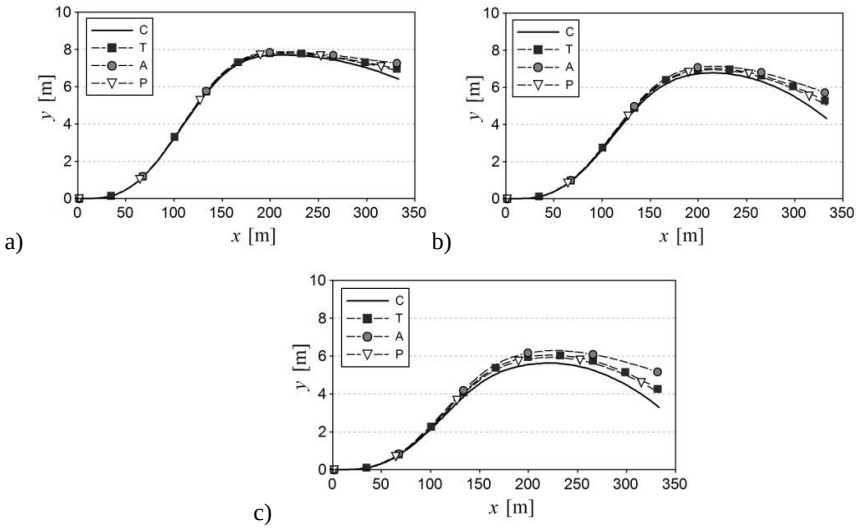


**Figure 4.** Trajectory of the tractor for different values of the friction coefficient
a) $\mu = 0.1$ b) $\mu = 0.2$ c) $\mu = 0.3$

The results show that the choice of the friction model influences the resulting trajectory of the tractor. The larger the friction coefficient, the larger is the difference in the trajectory. The moment of friction calculated using the Newton-Euler algorithm for different friction coefficients is presented in Fig.5.

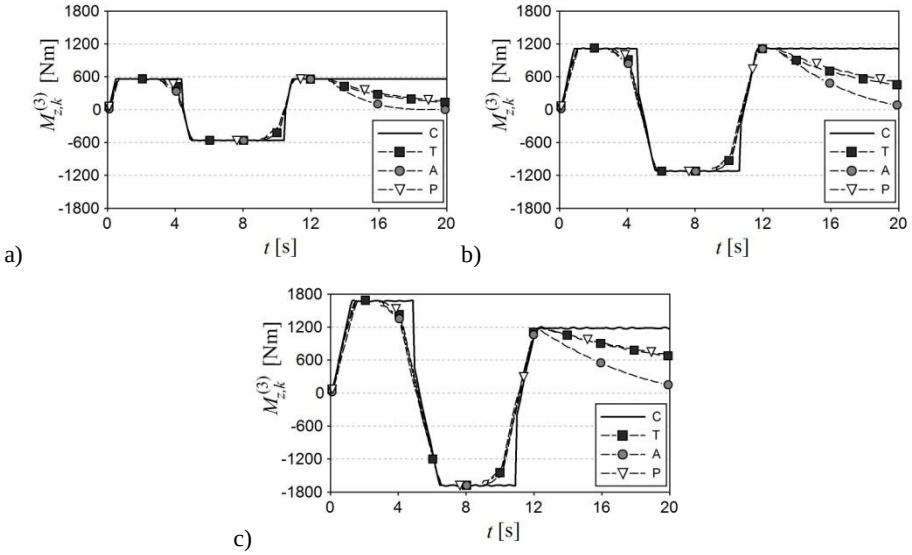


**Figure 5.** Friction torque in the fifth wheel a) $\mu = 0.1$, b) $\mu = 0.2$, c) $\mu = 0.3$

The larger the friction coefficient, the smaller are the differences between model T and P. The friction force depends on the friction coefficient, but each model depends on it in a different way.

Since friction is considered in the coupling, the next figures present both the relative rotation and the relative angular velocity in the fifth wheel for different friction models and friction coefficients.

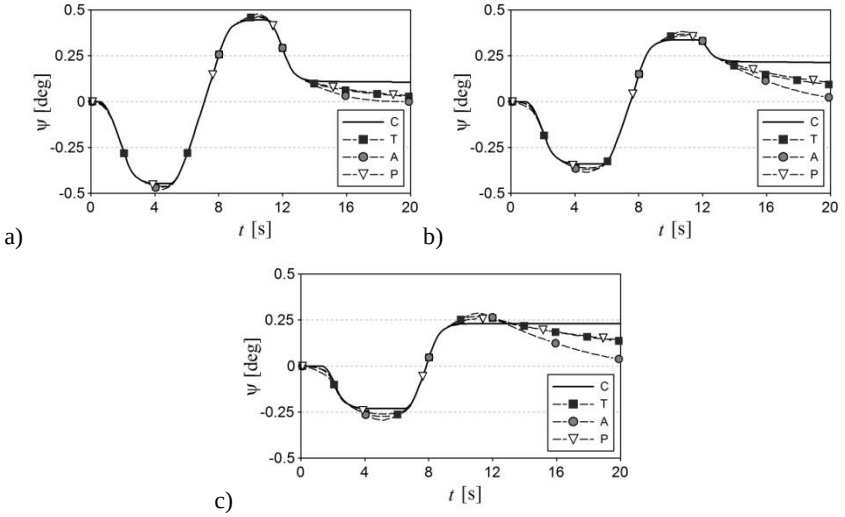


**Figure 6.** The relative rotation of the fifth wheel for different values of the friction coefficient a) $\mu = 0.1$, b) $\mu = 0.2$, c) $\mu = 0.3$

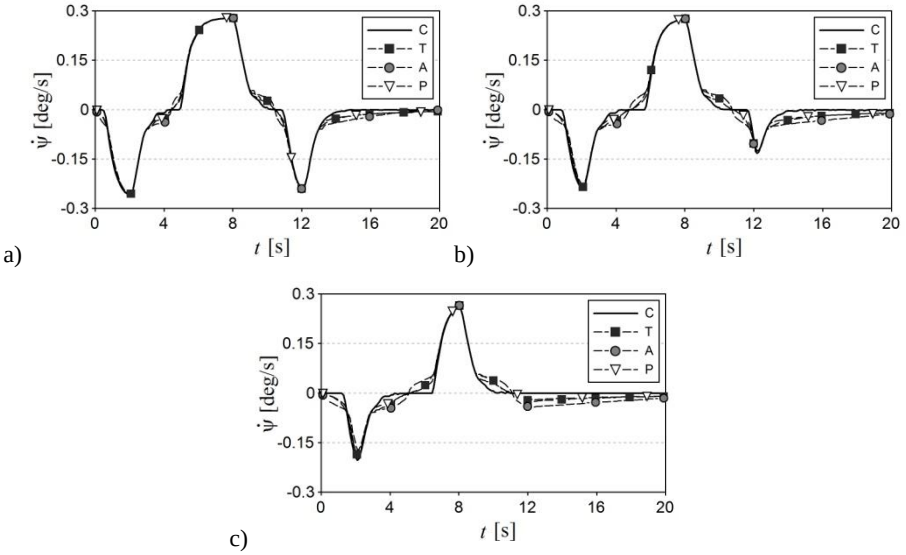


**Figure 7.** The relative velocity in the fifth wheel for different values of the friction coefficient a) $\mu = 0.01$, b) $\mu = 0.02$, c) $\mu = 0.03$

## 5. Conclusions

The paper presents a validated model of an articulated vehicle formulated using multibody methods, with homogenous transformations and joint coordinates. The analysis presented is concerned with the influence of friction in the coupling between the tractor and the semitrailer. In order to calculate the forces and moments acting in the fifth wheel, the Newton-Euler algorithm for solving an inverse dynamic problem is used. The Coulomb model of friction with two phases of relative motion is described and used as a background for comparative analysis of different models of friction in which discontinuity at zero velocity is replaced by continuous functions. It is shown that the larger the coefficient of friction, the larger is the influence of the choice of the friction model on the results of simulations of motion. Owing to the development of active safety systems in vehicles, the mathematical model of a vehicle implemented in these systems is very important. In articulated lorries the joint systems are essential when vehicle motion in extreme conditions is considered. One of the tasks of active safety systems is to prevent these vehicles knifing during some maneuvers, for example during braking. The analysis of the accepted friction model in the fifth wheel carried out in this article points to its influence on the trajectory and relative rotation of the tractor and trailer during motion. These differences are particularly noticeable in friction torque values and relative rotation angles during the last phase of the maneuver. Our analysis reveals the necessity of experimental research to make the proper choice of the friction model in the fifth wheel.

**References**


[1] Bolzern P., DeSantis R.M., Locatelli A. An input-output linearization approach to the control of an n-body articulated vehicle. *Journal of Dynamic Systems, Measurement, and Control*. 123, (2001) 309-316.

[2] Wu D-H. A theoretical study of the yaw/roll motions of a multiple steering articulated vehicle. *Journal of Mechanical Engineering*. 215, (2001) 1257-1265.

[3] Cheng C., Cebon D. Parameter and state estimation for articulated heavy vehicles. *Vehicle System Dynamics: International Journal of Vehicle Mechanics and Mobility*, 49, 1-2 (2011) 399-418.

[4] Andersson S., Söderberg A., Björklund S. Friction models for sliding dry, boundary and mixed lubricated contacts, *Tribology International*, 40, 4, (2007) 580-587.

[5] Marques F., Flores P., Lankarani H.M. On the frictional contacts in multibody system dynamics. *Proceedings of ECCOMAS Thematic Conference on Multibody Dynamics*, Barcelona, 2015.

[6] Muller S., Uchanski M., Hedrick K. Estimation of the Maximum Tire-Road Friction Coefficient. *Journal of Dynamic Systems, Measurement, and Control*, 125 (2003) 607-617.

[7] Kaneko T., Kageyama I. A study on the braking stability of articulated heavy vehicles. *JSAE Review* 24 (2003) 157–164.

[8] Arczewski K., Frączek J. Friction models and stress recovery methods in vehicle dynamics modelling, *Multibody System Dynamics* 14, (2005) 205-224.

[9] Grzegożek W., Adamiec-Wójcik I., Wojciech S. *Komputerowe modelowanie pojazdów* (*Computer modelling of vehicles*). Wydawnictwo Politechniki Krakowskiej, Kraków, 2003.

[10] Wojciech S. Dynamic analysis of manipulators with consideration of dry friction. *Computers & Structures*, 6 (1995) 1045-1050.

[11] Craig J.J. *Introduction to robotics.* Addison-Wesley, Massachusetts, 1988.

[12] Awrejcewicz J., Grzelczyk D., Pyryev Y. A novel dry friction modeling and its impact on differentia equations computation and Lyapunov exponents estimation. *Journal of Voibroengineering*, 10 (2008) 475-482.

[13] Trelfall D.C. The inclusion of Coulomb friction in mechanisms programs with particular reference to DRAM au programme DRAM. *Mechanism and Machine Theory*, 13 (1978) 475-483.



Iwona Adamiec-Wójcik, Professor: University of Bielsko-Biała/Faculty of Management and Transport, ul.Willowa 2, 43-309 Bielsko-Biała, Poland (*i.adamiec@ath.bielsko.pl*). The author gave a presentation of this paper during one of the conference sessions.

Jan Awrejcewicz, Professor: Lodz University of Technology/Faculty of Mechanical Engineering ul.Stefanowskiego 1/15, 90-924 Łódź, Poland (*awrejcew@p.lodz.pl*)

Witold Grzegożek, Professor: Cracow University of Technology/Faculty of Mechanical Engineering, al. Jana Pawła II 37, 31-864 Kraków, Poland (*witek@mech.pk.edu.pl*).

Stanisław Wojciech, Professor: University of Bielsko-Biała/Faculty of Management and Transport, ul.Willowa 2, 43-309 Bielsko-Biała, Poland (*swojciech@ath.bielsko.pl*).

# Validation of the rigid finite element method used for modelling of lines and risers (NUM144-15)

Iwona Adamiec-Wójcik, Łukasz Drąg, Stanisław Wojciech

*Abstract:* The rigid finite element method is numerically effective especially for modeling of slender systems such as lines and risers used in offshore engineering. The basic advantage of the method is a simple physical interpretation. A flexible link is divided into rigid segments which represent mass features of the link and spring-damping elements responsible for its flexible and damping features. The essential aspect of the method is the possibility of accounting for large deflections of links. Recently, the authors have been dealing with new formulations of the method which enable numerical efficiency to be increased. The formulation elaborated allows elimination of large values of stiffness coefficients: shear, longitudinal and torsional (dependent on permissibility of the system analyzed). The paper presents results of validation of the models and computer programs used in dynamic analysis of lines and risers. The validation is concerned with: deflections of the catenary line; frequencies of free vibrations of a vertical riser additionally loaded with tension; vibrations of a vertical riser with the upper end moving periodically. The comparisons with the results presented by others indicate the correctness of the models obtained by means of the rigid finite element method even when the influence of the water environment (drag forces, hydrodynamic resistance or added mass and currents) is considered.

## 1. Introduction

Considerable deformation and change of shape is one of the inherent features of slender links, and additional difficulty in modeling dynamics is when they are coupled with a moving base. Such systems are used in offshore engineering where there is a coupling between the dynamics of a vessel and attached risers, mooring lines and cables. Modeling of slender elements requires not only bending and longitudinal flexibilities but also large deflections to be considered. Moreover, in the sea environment uplift pressure, drag force, added mass water and, in the case of risers, internal flow of hydrocarbons (petroleum and gas) have to be taken into account. An extensive discussion on the state of the art in modeling and on problems in total dynamic analysis of offshore systems is presented by Chakrabarti [1]. Patel [2] reports many different methods used in modeling of such systems; however, the most popular are the lumped mass [3,4] and finite element methods [5-7]. Many commercial packages both of general use (Abaqus) or specialized for offshore engineering (Riffex, Orcaflex or Offpipe) are based on those methods. Another similar approach is used in the method called the Flexible Segment Model (FSM) presented in [8]. Nevertheless, new methods of modeling slender

systems used in offshore engineering are still being sought [9-11]. This paper presents one of such methods, which is a modified formulation of the rigid finite element method.

Applications of the rigid finite element method (RFEM) in its classical formulation, when the elements have 6 degrees of freedom [12]. This paper presents a continuation of research [13,14] in which two different formulations of the rigid finite element method are used for analysis of both bending and longitudinal flexibilities of slender links. This paper presents the formulation in absolute coordinates, which is supplemented with relations describing the influence of hydrodynamic forces. Additionally, a special algorithm for calculating natural frequencies and modes of free vibrations is described. Exemplary numerical simulations demonstrate the validation of the method in the analysis of statics, dynamics and natural vibrations.

## 2. Model of a riser

The Rigid Finite Element Method (RFEM) is used in order to formulate the model of a riser. Detailed derivation of equations of motion is presented in [13]. A flexible link is divided into rigid elements reflecting mass features of the link connected by means of dimensionless spring-damping elements reflecting bending ⊗ and longitudinal ⊠ flexibilities (Fig.1).

The vector of generalized coordinates takes the following form:

$$\mathbf{q}_i = \begin{bmatrix} x_i & y_i & \Delta_i & \varphi_i \end{bmatrix}^T . \tag{1}$$

where: $x_i, y_i$ are coordinates of point $A_i$, $\Delta_i$ is the elongation of sde ⊠, $\varphi_i$ is the declination angle of rfe *i* towards the axis x of the global coordinate system.

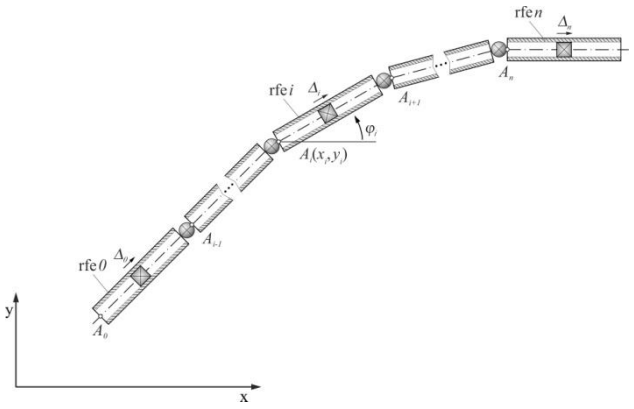


**Figure 1.** System of rigid finite elements

In the paper the hydrodynamic forces are taken into account according to Morison's law. Having omitted the detailed derivations [13], the equations of motion describing the dynamics of the system can be written in the form:

$$\mathbf{M}\ddot{\mathbf{q}} - \mathbf{D}\mathbf{R} = \mathbf{F} \tag{2.1}$$

$$\mathbf{D}^T\ddot{\mathbf{q}} = \mathbf{G} \tag{2.2}$$

where $\mathbf{q} = \left[\mathbf{q}_0^T \quad \mathbf{q}_1^T \quad \ldots \quad \mathbf{q}_n^T\right]^T$ is the vector of generalized coordinates of the system with 4($n$+1) elements, $\mathbf{R} = \left[\mathbf{R}_0^T \quad \mathbf{R}_1^T \quad \ldots \quad \mathbf{R}_n^T\right]^T$ is the vector of constraint reactions with 2($n$+1) elements, $\mathbf{M} = \mathbf{M}(\mathbf{q}) = diag(\mathbf{M}_0, \mathbf{M}_1, ..., \mathbf{M}_i, ..., \mathbf{M}_n)$ is the mass matrix with variable elements together with the mass of added water, and $\mathbf{D} = \mathbf{D}(\mathbf{q})$, $\mathbf{F} = \mathbf{F}(t, \mathbf{q}, \dot{\mathbf{q}})$, $\mathbf{G} = \mathbf{G}(t, \mathbf{q}, \dot{\mathbf{q}})^T$, and $x_A(t), y_A(t)$ are known functions defining the motion of point $A_0$.

Since matrix **M** has a block diagonal form, it is easy to calculate the inverse matrix $\mathbf{M}^{-1}$. The following can be obtained from (2.1)

$$\ddot{\mathbf{q}} = \mathbf{M}^{-1}(\mathbf{F} + \mathbf{D}\mathbf{R}) = \mathbf{f}(t, \mathbf{q}) \tag{3}$$

where **R** is calculated by solving the system of linear algebraic equations:

$$\left(\mathbf{D}^T\mathbf{M}^{-1}\mathbf{D}\right)\mathbf{R} = \left(\mathbf{G} - \mathbf{D}^T\mathbf{M}^{-1}\right)\mathbf{F} \tag{4}$$

## 3. Algorithm for calculations of natural frequencies

The equations for calculations of free vibrations of a slender link can be obtained from equations (3). The methodology applied for calculations of natural frequencies is similar to that presented in [15]. This enables us to use the equations of motion derived without the necessity of applying a special approach for the calculations of free vibrations by linearization of equations (3) and (4). Let us assume:

$$\mathbf{q} = \mathbf{q}_0 + \Delta\mathbf{q} \tag{5.1}$$

$$\ddot{\mathbf{q}} = \ddot{\mathbf{q}}_0 + \Delta\ddot{\mathbf{q}} \tag{5.2}$$

Linearization of the right side of equation (3) yields:

$$\ddot{\mathbf{q}}_0 + \Delta\ddot{\mathbf{q}} = \mathbf{f}(\mathbf{q}_0) + \frac{\partial \mathbf{f}}{\partial \mathbf{q}}\Delta\mathbf{q} \tag{6}$$

and thus:

$$\Delta\ddot{\mathbf{q}} = \frac{\partial \mathbf{f}}{\partial \mathbf{q}} \Delta\mathbf{q} = \mathbf{C}\Delta\mathbf{q} \tag{7}$$

where $\mathbf{C} = \frac{\partial \mathbf{f}}{\partial \mathbf{q}}$ is the gradient matrix.

Having assumed that:

$$\Delta\mathbf{q} = \Delta\bar{\mathbf{q}} \sin \omega t \tag{8}$$

the eigenvalue problem is obtained:

$$\det(-\mathbf{C} - \omega^2 \mathbf{I}) = 0 \tag{9}$$

Matrix **C** has been calculated using five points finite difference formulae. Deformations of the riser caused by its mass, buoyancy forces, mass of added water and fluid inside the riser are taken into account.

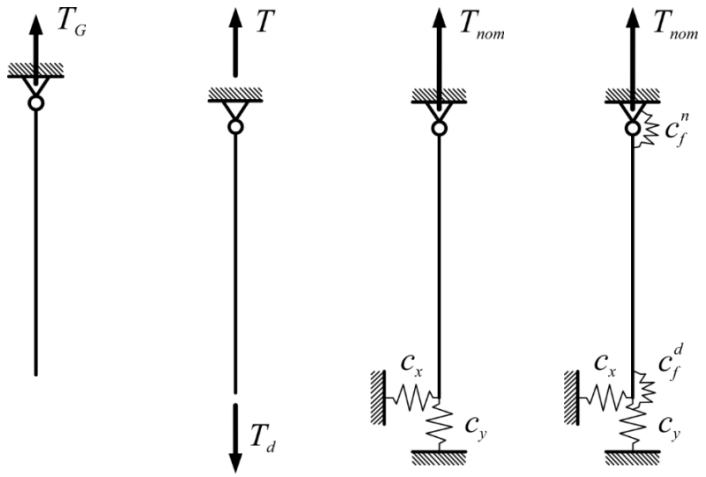


a) b) c) d)

**Figure 2.** Scheme for consideration of tension in modelling the riser

When vibrations of the tensioned riser are analyzed, two statics problems are solved in order to calculate initial deflection of the riser:

1. Calculation of elongation deformation of the riser caused by the weight of the riser and internal fluid (Fig.5a);

2. The bottom end of the riser is loaded with tension $T_d$ until $T_G + T_d \geq T_{nom}$ (Fig.2b).

When tension of the riser achieved the nominal value $T = T_{nom}$, the bottom end of the riser was fixed by means of springs (Fig.2c) with large stiffness ($c_x = c_y = 10^{12}$ N/m). In order to model clamped conditions, additional rotational springs with stiffness $c_\varphi^0, c_\varphi^n$, which prevent rfes 0 and *n* from rotating, were introduced into the model (Fig.2d). Having finished calculation for statics the gradient matrix is calculated from equation (10) for the riser - presented either in Fig.2c or Fig.2d.

## 4. Numerical simulations

### 4.1. Catenary line

In the offshore industry catenary equations are often used for approximation of the shape of deep water risers or mooring lines. Thus, it is interesting to compare the results of the method presented with the analytical solution of a catenary line. The analytical equations used for the calculations of *x, y* coordinates and force *T* in the cables are as in [3].

The calculations were carried out for the rope with length $L = 300$ *m*, cross-section $A = 0{,}07^2/4$ m$^2$, Young modulus $E = 10^{11}$ N/m$^2$, density $\rho = 6{,}5 \cdot 10^3$ kg/m$^3$ and load with forces: $H = 20000$ N, $V = 50000$ N (Fig. 6). The comparison of the curves $y(x)$ obtained for the analytical solution and the method presented assuming $n = 15$ elements is shown in Fig. 3. As can be seen, the proposed method correctly reflects the shape of the rope.

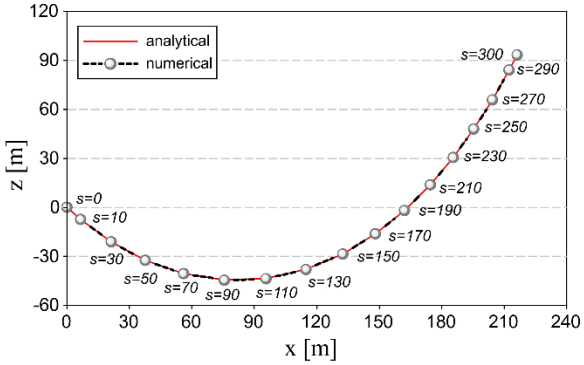


**Figure 3.** Comparison of the results

The maximum differences in displacements in $x, y$ directions do not exceed 0.5% and the largest errors are obtained at points where there is the largest curvature.

### 4.2. Vibrations and free vibrations

The models presented were successfully applied in dynamic analysis of slender systems with large amplitude vibrations. In order to check the correctness of the models, the results obtained were compared with those calculated using Abaqus. The analysis of vibrations of a long hanging rope which was forced to move by applying two forces at its free end is presented in [13]. Very good compatibility of results was observed. It is important to note that calculations with Abaqus last about 50 minutes but only 5 minutes using the authors' program.

Using the procedure presented above analysis of free vibrations has been carried out for two different supports of the riser, and the results are compared with those presented in the literature. The first riser analyzed is that described in [5], and Table 1 presents the data assumed.

Table 1. Parameters of the riser

| Parameter | Denotation | Value | Unit |
|---|---|---|---|
| Length of the riser | $L$ | 300 | m |
| Outer diameter | $D_{Out}$ | 0.26 | m |
| Inner diameter | $D_{Inn}$ | 0.20 | m |
| Young modulus | E | $2.07 \cdot 10^{11}$ | $N/m^2$ |
| Density of the riser | $\rho_r$ | 7850 | $kg/m^3$ |
| Density of water | $\rho_w$ | 1025 | $kg/m^3$ |
| Density of internal fluid | $\rho_f$ | 998 | $kg/m^3$ |
| Coefficient | $C_M$ | 2.0 | |

Two different boundary conditions are considered: both ends of the riser are hinged (H-H) and both clamped (C-C). The number of rfes into which the riser was divided changed from 10 to 160, and this influence on the calculation of the first, third and fifth natural frequency is shown in Fig.4.

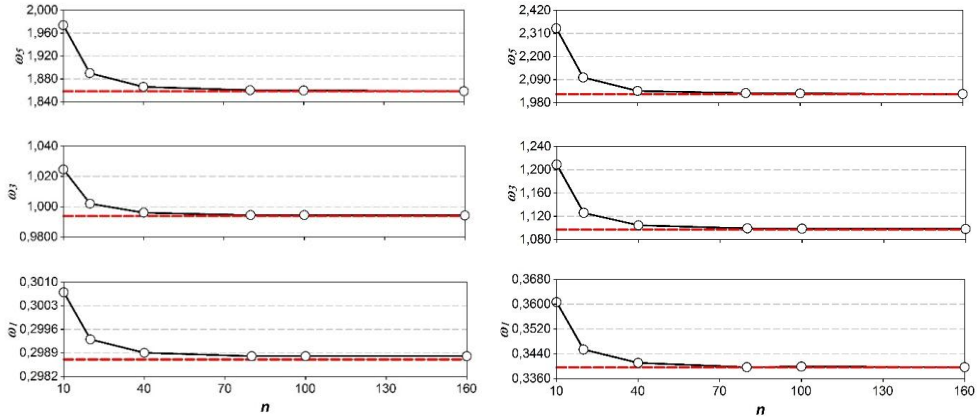


**Figure 4.** The influence of the number of rfes on free vibrations of the H-H and C-C riser

It can be seen that even for $n$=40 the error is less than 0.1% . For further calculations we assumed that the riser is divided into 80 elements.

Results of calculations for tension $T_{nom} = 476198$N and two different boundary conditions are presented in Table 2.

Table 2. The influence of the number of rfes on free vibrations of the riser with different boundary conditions

| n | 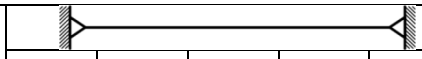 | | | | | 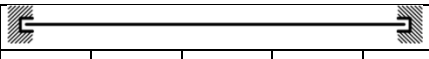 | | | | |
|---|---|---|---|---|---|---|---|---|---|---|
| | $\omega_1$ | $\omega_2$ | $\omega_3$ | $\omega_4$ | $\omega_5$ | $\omega_1$ | $\omega_2$ | $\omega_3$ | $\omega_4$ | $\omega_5$ |
| [*] | 0.2987 | 0.6284 | 0.9937 | 1.4018 | 1.8578 | 0.3395 | 0.7025 | 1.0970 | 1.5337 | 2.0196 |
| 10 | 0.3007 | 0.6389 | 1.0245 | 1.4681 | 1.9735 | 0.3607 | 0.7574 | 1.2088 | 1.7324 | 2.3346 |
| 20 | 0.2993 | 0.6312 | 1.0018 | 1.4193 | 1.8900 | 0.3453 | 0.7170 | 1.1255 | 1.5834 | 2.0997 |
| 40 | 0.2989 | 0.6292 | 0.9958 | 1.4063 | 1.8660 | 0.3410 | 0.7063 | 1.1044 | 1.5464 | 2.0347 |
| 80 | 0.2988 | 0.6287 | 0.9943 | 1.4031 | 1.8600 | 0.3396 | 0.7035 | 1.0989 | 1.5370 | 2.0247 |
| 100 | 0.2988 | 0.6286 | 0.9942 | 1.4027 | 1.8593 | 0.3398 | 0.7032 | 1.0983 | 1.5359 | 2.0229 |
| 160 | 0.2988 | 0.6285 | 0.9940 | 1.4022 | 1.8585 | 0.3396 | 0.7028 | 1.0976 | 1.5346 | 2.0209 |

For both types of boundary conditions very good compatibility of results has been achieved.

### 4.3. Vibrations of a vertical riser with an oscillating upper end

In order to examine the influence of tension on natural frequencies, another riser is analysed [16,17]. Analysis is carried out for a riser presented in Fig.5, which was used for experimental measurements with data described in Table 3. Some comparison of the results obtained with those presented in [16] is described in [13]. Here the comparison is carried out for the points and tension examined in [17].

Table 3. Parameters of the riser from the experiment

| Parameter | Notation | Value | Unit |
|---|---|---|---|
| Length | $L$ | 6.5 | [m] |
| Length of the elements | $L_{rfe}$ | 0.325 | [m] |
| Inner diameter | $D_{in}$ | 0.0127 | [m] |
| Outer diameter | $D_{out}$ | 0.0225 | [m] |
| Average density in air | $\rho$ | 1476.4 | [kg/m$^3$] |
| Young modulus | $E$ | $3.489 \cdot 10^6$ | [N/m$^{2]}$ |
| Bottom weight in air | $W$ | 3.974 | [N] |
| Density of water | $\rho_w$ | 1025 | [kg/m$^3$] |
| Drag coefficient | $D_v'$ | 1.55 | - |
| Inertial coefficient | $C_M$ | 2.0 | - |
| Frictional coefficient | $C_f$ | 0.016 | - |

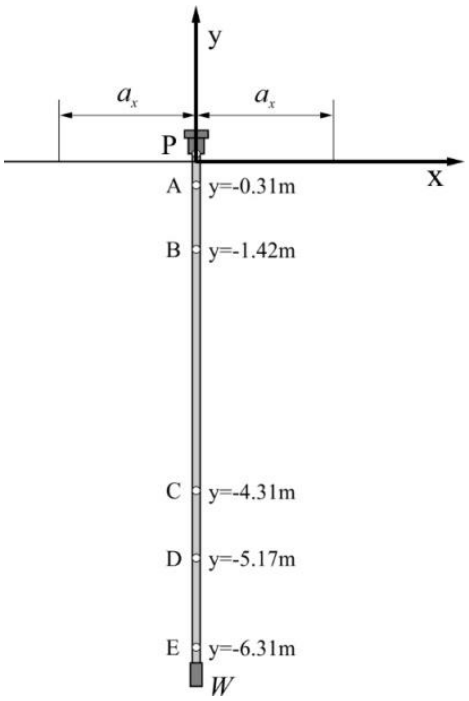


**Figure 5.** Experimental set-up

Point *P* undergoes an oscillatory motion described as follows:

$$x_P = a_x(t)\sin\left(\frac{2\pi}{T}t\right) \tag{10}$$

where: $a_x(t) = \begin{cases} a_{\max}\dfrac{t}{t_b} & \text{for} \quad t \le t_b \\ a_{\max} & \text{for} \quad t > t_b \end{cases}$, $a_{max}$ = 0.2 m, $T$ is the period assumed as 2s in [16] and 5s in [17], $t_b - n_b \cdot T$ ($n_b$ = 5, 10).

Figure 6 shows the comparison of vibrations calculated at points D, B and P when $a_{max}$ = 0.2 and $T$ = 5 s [17].

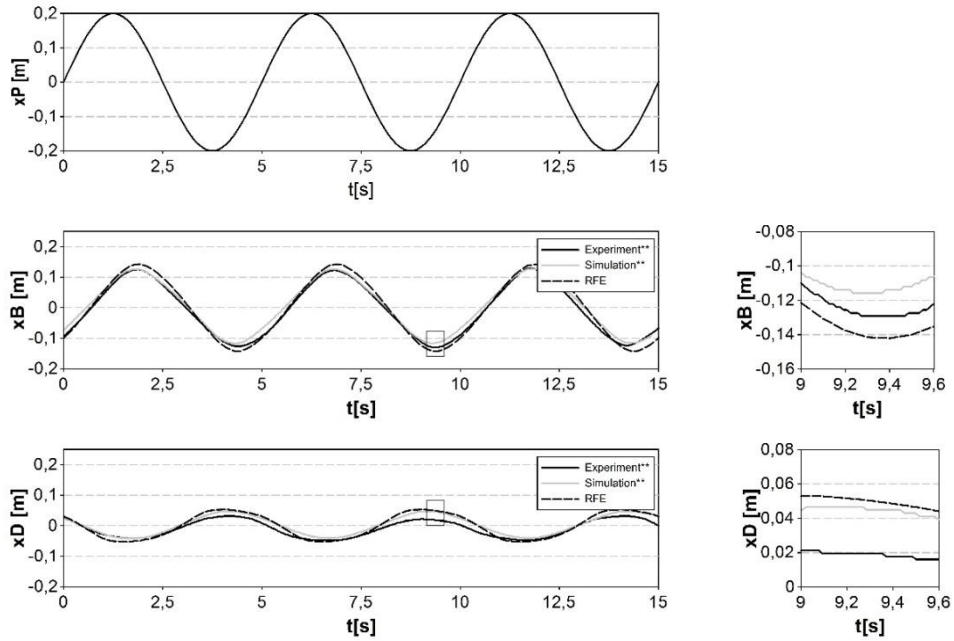


**Figure 6.** Vibrations in x direction for $a_{max}$ = 0.2 and $T$ = 5 s

It can be seen that in both cases a very good compatibility of results is obtained.

## 5. Final remarks

The paper presents an application of the modification of the rigid finite element method to modeling of dynamics of risers. It is shown that the formulation using absolute coordinates gives reliable results both in static and dynamic analysis. The static analysis deals with a catenary line while free vibrations are calculated for the dynamic analysis. The results obtained using the modified rigid finite element method are compared with those presented by other authors and obtained using commercial software.

## References

[1] Chakrabarti, S. Challenges for a total system analysis on deepwater floating systems, *The Open Mechanics Journal*, 2 (2008), 28-46.

[2] Patel, M.H., Seyed, F.B. Review of flexible riser modelling analysis techniques, *Engineering Structures* 17, 4 (1995), 293-304.

[3] Raman-Nair, W., Baddour. R. Three-dimensional dynamics of a flexible marine riser undergoing large elastic deformations, *Multibody System Dynamics* 10, (2003), 393-423.

[4] Liping, S., Bo, Q. Global analysis of a flexible riser, *Journal of Marine Science and Application* 10 (2011), 478-484.

[5] Kaewunruen, S., Chiravatchradej, J., Chucheepsakul, S. Nonlinear free vibrations of marine risers/pipes transporting fluid, *Ocean Engineering*, 32 (2005), 417-440.

[6] Park, H-I., Jung, D-H. A finite element method for dynamic analysis of long slender marine structures under combined parametric and forcing excitations, *Ocean Engineering* 29 (2002), 1313-1325.

[7] Chai, Y.T., Varyani, K.S. An absolute coordinate formulation for three-dimensional flexible pipe analysis, *Ocean Engineering* 33 (2006), 23-58.

[8] Xu, X., Wang, S.: A flexible-segment-model-based dynamics calculation method for free hanging marine risers in re-entry, *China Ocean Engineering* 26 (2012), 139-152.

[9] Jensen, G.A., Säfström, N., Nguyen, T.D., Fossen, T.F. A nonlinear PDE formulation for offshore vessel pipeline installation, *Ocean Engineering* 37 (2000), 365-377.

[10] Niedzwecki, J.M., Liegre, P.-Y.F. System identification of distributed-parameter marine riser models, *Ocean Engineering* 33 (2003), pp.1387-1415.

[11] Chen, H., Xu, S., Guo, H. Nonlinear analysis of flexible and steel catenary risers with internal flow and seabed interaction effects, *Journal of Marine Science and Application* 10 (2011), 156-162.

[12] Wittbrodt, E., Adamiec-Wójcik, I., Wojciech S. *Dynamics of flexible multibody systems: rigid finite element method*, Springer, Berlin, 2006.

[13] Adamiec-Wójcik, I., Brzozowska, L., Drąg, Ł. An analysis of dynamics of risers during vessel motion by means of the rigid finite element method, *Ocean Engineering* 106 (2015), 102-114.

[14] Adamiec-Wójcik, I., Awrejcewicz J., Brzozowska, L., Drąg Ł. Modeling of ropes with consideration of large deformations by means of the rigid finite element method, *Applied Non-linear Dynamical Systems, Springer Proceedings in Mathematics & Statistics* 93, (2014), 115-137.

[15] Ghadimi, R. A simple and efficient algorithm for the static and dynamic analysis of flexible marine risers, *Computers and Structures* 29 (4), (1988), 541-555.

[16] Senga, H., Koterayama, W. Development of a Calculation Method for Vortex Induced Vibration of a Long Riser Oscillating at its Upper End, *Engineering Sciences Reports* 27 (3), Kyushu University, (2005), 335-341.

[17] Xu, X., Yao, B., Ren P. Dynamics calculation for underwater moving slender bodies based on flexible segment model, *Ocean Engineering* 57 (2013), 111-127.

Iwona Adamiec-Wójcik, Professor: University of Bielsko-Biała, Faculty of Managenment and Transport, Willowa 2, 43-309 Bielsko-Biala, Poland, (i.adamiec@ath.bielsko.pl)

Jan Awrejcewicz, Professor: Lodz University of Technology, Departament of Automation and Biomechanics Stefanowskiego 1/15, 90-924 Łódź, Poland, (awrejcew@p.lodz.pl)

Łukasz Drąg, PhD: University of Bielsko-Biała, Faculty of Managenment and Transport, Willowa 2, 43-309 Bielsko-Biala, Poland, (ldrag@ath.bielsko.pl). The author gave a presentation of this paper during one of the conference sessions.

Stanisław Wojciech, Professor: University of Bielsko-Biala, Faculty of Managenment and Transport, Willowa 2, 43-309 Bielsko-Biala, Poland, (swojciech@ath.bielsko.pl)

# Nonlinear normal modes for vibrational conveyers with crank-and-rod exciters (NUM081-15)

G. Füsun Alışverişçi

*Abstract:* Vibrations are used iIn industrial applications for conveying materials. In this study nonlinear normal modes for vibrational conveyers with crank-and-rod exciters have been analysed. The conveyers have a trough supported on elastic stands (which are rigidly fastened to the trough) and a supporting frame. The trough is oscillated by a common crank drive. This vibration causes the load to move forward and upward. The movement is strictly related to the vibrational parameters. Modes of coupled and localized vibration are selected. In this work the stability and bifurcation analysis are numerically calculated and the results of numerical simulation are plotted.

## 1. Introduction

Nonlinear normal vibrations modes (NNMS) are a generalization of the normal vibrations in linear systems. In the normal vibration mode, a finite degree-of-freedom (DOF) system vibrates like a single-DOF conservative one. If the damping is large or represented by nonlinear functions then the response of the system may depend not only on the displacement, but also on velocities as shown by Rosenberg and Vakakis [1, 2, 5]. In the case of a nonlinear autonomous coupled self-exited system, the method of nonlinear normal modes was proposed by Shaw and Pierre [3]. The vibrating system consists of a cubic non-ideal excite analyzed [8]. In this paper, we characterize the dynamic behavior of vibrational conveyers with crank-end-rod exciters. We use nonlinear normal modes but before we use bifurcation analysis to obtain chaos, instability, and so on. We use the invariant manifold approach for NNMs technic. Such a manifold is invariant under the flow (i.e., orbits that start out in the manifold remain in it for all time), which extends the invariance property of LNMs to nonlinear systems. In order to parametrize the manifold, a single pair of states variables (i.e., both the displacement and the velocity) are chosen as master coordinates, the remaining variables being functionally related to the chosen pair. Therefore the system behaves likes a nonlinear single-DOF system on the manifold [4].

## 2. Governing Equations:

The equation of motion may be obtained by using Lagrange's equations

$$\frac{d}{dt}(\frac{\partial T}{\partial \dot{q}_i}) - \frac{\partial T}{\partial q_i} + \frac{\partial U}{\partial q_i} = Q_i \tag{1}$$

Here, $T$ is the kinetic energy $U$ is the potential energy, $Q$ is the generalized force. They are given by

$$T = \frac{1}{2}m\dot{x}^2 + \frac{1}{2}m\dot{z}^2 + \frac{1}{2}J\dot{\theta}^2 \tag{2}$$

$$U = \frac{1}{2}(k_1L_1^2 + k_2L_2^2)\sin^2\theta + \frac{1}{2}(k_1 + k_2)x^2 + (k_2L_2 - k_1L_1)z\sin\theta + \frac{1}{2}(k_1 + k_2)z^2 \tag{3}$$

$$Q_x = \left\{M\cos\left[\beta - \arcsin(\frac{r\sin(t\omega)}{L})\right]\sin\left[t\omega + \arcsin(\frac{r\sin(t\omega)}{L})\right]\right\}/r \tag{4}$$

$$Q_z = \left\{M\sin\left[\beta - \arcsin(\frac{r\sin(t\omega)}{L})\right]\sin\left[t\omega + \arcsin(\frac{r\sin(t\omega)}{L})\right]\right\}/r \tag{5}$$

$$Q_\theta = \left\{M\,L_1\sin\left[\beta - \arcsin(\frac{r\sin(t\omega)}{L})\right]\sin\left[t\omega + \arcsin(\frac{r\sin(t\omega)}{L})\right]\right\}/r \tag{6}$$

where, the constants $k_1$ and $k_2$ are the elastic coefficients of the springs, $g$ is acceleration due to gravity, $m$ is the mass of the system (see Figs.1 and 2), $r$ is the crank length, $\theta$ is the angle of the rotation of the system, $J$ is the Inertial moment of the system about mass center , $x$ and $z$ are the position of mass center of the system, $M$ is the applied moment of the crank shaft, $\omega$ is the excitation frequency, and $q_i$ is the generalized coordinates. Lagrange's equation of motion for the coordinates $q_1 = x$, $q_2 = z$ and $q_3 = \theta$ can be written as

$$(k1 + k2)x + m\ddot{x} = \left\{M\cos\left[\beta - \arcsin(\frac{r\sin(t\omega)}{L})\right]\sin\left[t\omega + \arcsin(\frac{r\sin(t\omega)}{L})\right]\right\}/r \tag{7}$$

$$\begin{aligned}&(-k_1L_1 + k_2L_2)\sin\theta + (k_1 + k_2)z + m\ddot{z} = \\ &\qquad\left\{M\sin\left[\beta - \arcsin(\frac{r\sin(t\omega)}{L})\right]\sin\left[t\omega + \arcsin(\frac{r\sin(t\omega)}{L})\right]\right\}/r\end{aligned} \tag{8}$$

$$\begin{aligned}&\cos\theta\left((k_1L_1^2 + k_2L_2^2)\sin\theta + (-k_1L_1 + k_2L_2)z\right) + J\ddot{\theta} = \\ &\qquad Q_\theta = \left\{M\,L_1\sin\left[\beta - \arcsin(\frac{r\sin(t\omega)}{L})\right]\sin\left[t\omega + \arcsin(\frac{r\sin(t\omega)}{L})\right]\right\}/r\end{aligned} \tag{9}$$

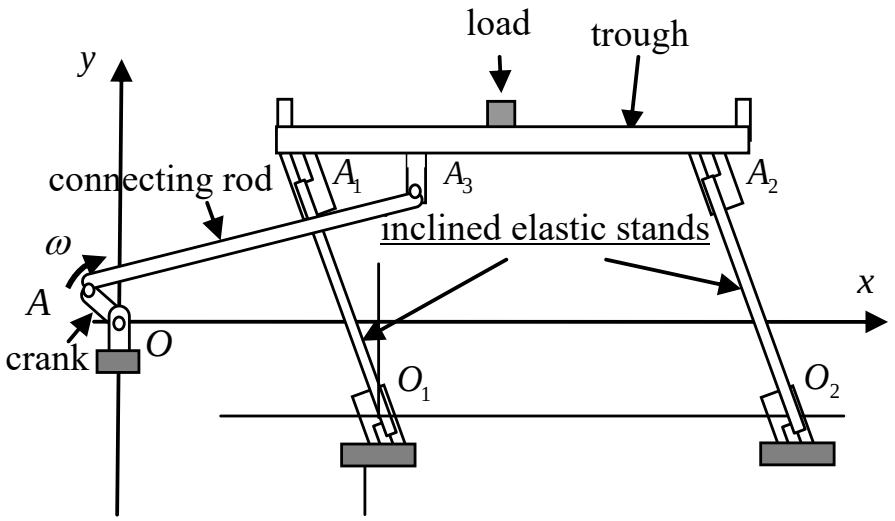


**Figure 1.** Vibrational Conveyers with Crank-and-Rod Exciters.

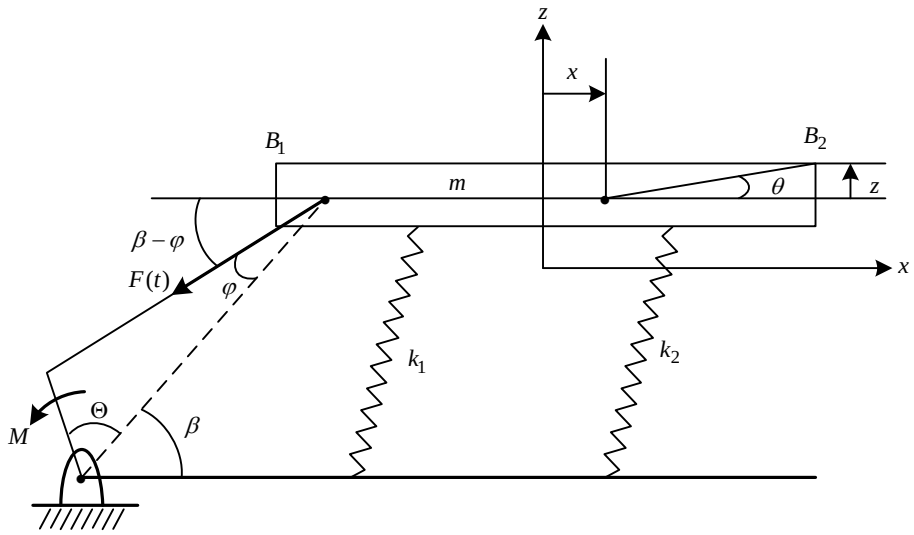


**Figure 2.** Vibrating model of system.

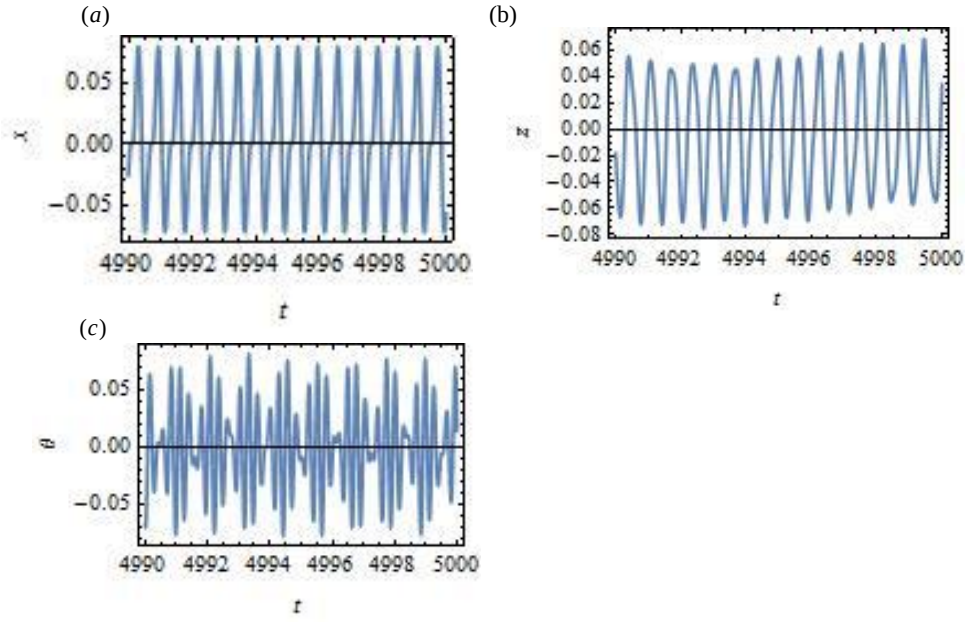


**Figure 3.** Time histories in physical coordinates for system, a) horizontal displacement b) vertical displacement c) angular displacement.

Figure 3 is obtained by using (Eq. 7), (Eq. 8) and (Eq. 9). This figure shows time histories in physical coordinates $(x,t)$ and $(\theta,t)$ for non ideal system. The time histories of $x$ and $\theta$ generated for initial conditions $x(0)=0$, $\dot{x}(0)=0$, $z(0)=0.05m$, $\dot{x}(0)=0$, $\theta(0)=0.01rad.$, $\dot{\theta}(0)=0$ are presented in Fig. 3(a),(b) and (c). The bifurcation diagram of the physical coordinate $x,z,\theta$ versus excitation frequency is presented in Fig. 4(a), (b), (c) respectively. The phenomenon of internal chaos appearance is clearly visible near the principal parametric resonance around the first and second natural frequency for approximately 10 in Fig. 4(a), (b) and third natural frequency for approximately 25.6 In Fig. 4(c) .

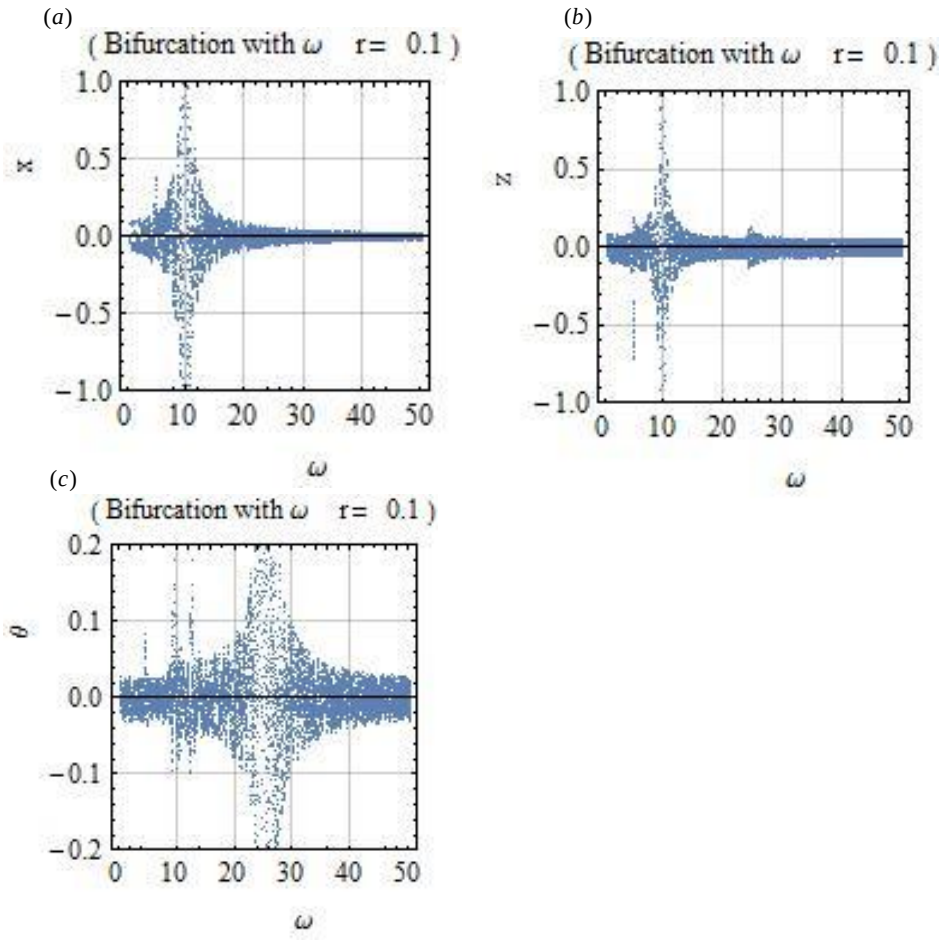


**Figure 4.** Bifurcation diagram.

$$(k1+k2)x + m\ddot{x} = 0 \tag{10}$$

$$(-k_1L_1 + k_2L_2)\sin\theta + (k_1 + k_2)z + m\ddot{z} = 0 \tag{11}$$

$$\cos\theta\left(\left(k_1L_1^2 + k_2L_2^2\right)\sin\theta + \left(-k_1L_1 + k_2L_2\right)z\right) + J\ddot{\theta} = 0 \tag{12}$$

(13)

where

$$m = m_0 + m_1,\ k = k_1 + k_2,\ J_1 = J + l_3^2 m_0\ ,\ q_1 = k_1\, l_1 - k_2\, l_2,\ q_2 = k_1\, l_1^2 + k_2\, l_2^2,\ q_3 = l_3\, m_0 \tag{14}$$

Assuming that $\theta$ is small ( $\cos\theta \approx 1$, $\sin\theta = \theta$ ) than we get a linear conservative system and natural frequencies as follows.

$$(k_1 + k_2)x + m\,\ddot{x} = 0 \tag{15}$$

$$(-k_1 L_1 + k_2 L_2)\theta + (k_1 + k_2)z + m\,\ddot{z} = 0 \tag{16}$$

$$+J\ddot{\theta} + (-k_1 L_1 + k_2 L_2)z + \left(k_1 L_1^2 + k_2 L_2^2\right)\theta = 0 \tag{17}$$

$$m_m = \begin{pmatrix} m & 0 & 0 \\ 0 & m & 0 \\ 0 & 0 & J \end{pmatrix}, \quad k_m = \begin{pmatrix} k_1 + k_2 & 0 & 0 \\ 0 & k_1 + k_2 & -k_1 L_1 + k_2 L_1 \\ 0 & -k_1 L_1 + k_2 L_1 & k_1 L_1^2 + k_2 L_1^2 \end{pmatrix} \tag{18}$$

where $m_m$ is the mass matrix and $k_m$ is the stiffness matrix. The frequency equation is

$$frequencyEq = \det[k_m - \lambda\, m_m] = \det\begin{pmatrix} k_1 + k_2 - m\,\lambda & 0 & 0 \\ 0 & k_1 + k_2 - m\,\lambda & -k_1 L_1 + k_2 L_2 \\ 0 & -k_1 L_1 + k_2 L_2 & k_1 L_1^2 + k_2 L_2^2 - J\,\lambda \end{pmatrix} \tag{19}$$

where $\lambda = \omega^2$ ,

$$\begin{aligned} frequencyEq = {} & -J\,m^2\lambda^3 + 2J\,m\,\lambda^2 k_1 - J\,\lambda\,k_1^2 + 2J\,m\,\lambda^2 k_2 - 2J\,\lambda\,k_1 k_2 - J\,\lambda\,k_2^2 + m^2\lambda^2 k_1 L_1^2 \\ & - m\,\lambda\,k_1^2\,L_1^2 + m^2\lambda^2 k_2 L_1^2 - 6m\,\lambda\,k_1 k_2 L_1^2 + 4k_1^2\,k_2 L_1^2 - m\,\lambda\,k_2^2 L_1^2 + 4k_1 k_2^2 L_1^2 \end{aligned} \tag{20}$$

$$\lambda_1 = \frac{k_1 + k_2}{m} \tag{21}$$

$$\lambda_{2,3} = \frac{J\,k_1 + J\,k_2 + m k_1 L_1^2 + m k_2 L_1^2 \pm \sqrt{-16J\,m\,k_1 k_2 L_1^2 + \left(-J\,k_1 - J\,k_2 - m k_1 L_1^2 - m k_2 L_1^2\right)^2}}{2J\,m} \tag{22}$$

**Table 1.** Numerical analysis of the system is performed according to the following data.

| $k_1$ $N/m$ | $k_2$ $N/m$ | $r$ $m$ | $L$ $m$ | $L_1$ $m$ | $L_2$ $m$ | $M$ $kg.r$ | $m$ $kg$ | $J$ $kg.m^2$ | $g$ $m/s$ | $\omega$ $rad/s$ | $\beta$ $rad$ |
|---|---|---|---|---|---|---|---|---|---|---|---|
| 5000 | 5000 | 0.1 | 1 | 2 | 3 | 100 | 100 | 100 | 9.81 | 20 | $\pi/6$ |

$\lambda_1 = 100, \quad \omega_1 = 10\,rad/s$ , $\lambda_2 = 95.491, \quad \omega_2 = 9.77\,rad/s$ , $\lambda_3 = 654.51, \quad \omega_3 = 25.58\,rad/s$

## 3. Nonlinear normal modes

For the nonlinear normal modes formulations the set of equations (10), (11), and (12) is rewritten in the form [6], [7] ;

$z = x_1 \qquad \theta = x_2$

$$\dot{x}_1 = y_1 \qquad \dot{y}_1 = f_1(x_1, y_1, x_2, y_2) \tag{23}$$

$$\dot{x}_2 = y_2 \qquad \dot{y}_2 = f_2(x_1, y_1, x_2, y_2) \tag{24}$$

The master coordinates can be chosen as:

$$x_1 = u \qquad y_1 = v \tag{25}$$

The slaved coordinates can be expressed as :

$$x_2 = X_2(u, v) \qquad y_2 = Y_2(u, v) \tag{26}$$

The functions $X_2(u, v)$ , $Y_2(u, v)$ are constraint equations and they represent the so called model surfaces. It the invariant manifold technique can be used to eliminate the time dependence.

$$Y_2(u, v) = \frac{\partial X_2(u, v)}{\partial u} v + \frac{\partial X_2(u, v)}{\partial v} f_1(u, v, X_2(u, v), Y_2(u, v)) \tag{27}$$

$$f_2(u, v, X_2(u, v), Y_2(u, v)) = \frac{\partial Y_2(u, v)}{\partial u} v + \frac{\partial Y_2(u, v)}{\partial v} f_1(u, v, X_2(u, v), Y_2(u, v)) \tag{28}$$

A local solution can be approximated using polynomial expansion of $X_1$ and $X_2$ in terms of u and v.

$$X_2 = a_1 u + a_2 v + a_3 u^2 + a_4 u v + a_5 v^2 + a_6 u^3 + a_7 u^2 v + a_8 u v^2 + a_9 v^3 \tag{29}$$

$$Y_2 = b_1 u + b_2 v + b_3 u^2 + b_4 u v + b_5 v^2 + b_6 u^3 + b_7 u^2 v + b_8 u v^2 + b_9 v^3 \tag{30}$$

$$\begin{aligned} \dot{X}_2 = {} & a_1 u' + a_2 v' + 2a_3 u u' + a_4 u v' + a_4 u' v + 2a_5 v v' + 3a_6 u^2 u' + 2a_7 u u' v + a_7 u^2 v' + \\ & a_8 u' v^2 + 2a_8 u v v' + 3a_9 v^2 v' \end{aligned} \tag{31}$$

$$\begin{aligned} \dot{Y}_2 = {} & b_1 u' + b_2 v' + 2b_3 u u' + b_4 u v' + b_4 u' v + 2b_5 v v' + 3b_6 u^2 u' + 2b_7 u u' v + b_7 u^2 v' + \\ & b_8 u' v^2 + 2b_8 u v v' + 3b_9 v^2 v' \end{aligned} \tag{32}$$

Considering the above expressions, and the last two equations of (Eq.23), (Eq.24), going back to the original notation, we can get:

$$\begin{aligned} y_2 = {} & a_1 y_1 + a_2 f_1 + 2a_3 x_1 y_1 + a_4 x_1 f_1 + a_4 y_1^2 + 2a_5 y_1 f_1 + 3a_6 x_1^2 y_1 + 2a_7 x_1 y_1^2 + \\ & a_7 x_1^2 f_1 + a_8 y_1^3 + 2a_8 x_1 y_1 f_1 + 3a_9 y_1^2 f_1 + \ldots \end{aligned} \tag{33}$$

$$\begin{aligned} f_2 = {} & b_1 y_1 + b_2 f_1 + 2b_3 x_1 y_1 + b_4 x_1 f_1 + b_4 y_1^2 + 2b_5 y_1 f_1 + 3b_6 x_1^2 y_1 + 2b_7 x_1 y_1^2 + \\ & b_7 x_1^2 f_1 + b_8 y_1^3 + 2b_8 x_1 y_1 f_1 + 3b_9 y_1^2 f_1 + \ldots \end{aligned} \tag{34}$$

Next (Eq.29), (Eq.30), (Eq.31) and (Eq.32) can be introduced into the functions $f_1(x_1, y_1, x_2, y_2) = f_1(u, v, X_2(u, v), Y_2(u, v))$ ,

$f_2(x_1, y_1, x_2, y_2) = f_2(u, v, X_2(u, v), Y_2(u, v))$ in (Eq.35), (Eq. 36). From (Eq.26), we obtain

$$y_2 - \dot{x}_2 = 0 \qquad f_2(x_1, y_1, x_2, y_2) - \dot{y}_2 = 0 \tag{35}$$

Thus, grouping the terms of (Eq.35) in a proper order with respect to the master coordinates, we receive a set of two equations composed of the terms: $u, v, u^2, uv, v^2, u^3, u^2v, uv^2, v^3$. Terms of higher order are truncated from the expansions. We get a set of eighteenth algebraic nonlinear equations with eighteen unknown parameters $a_1,...,a_9, b_1,...,b_9$.

After application of the decoupling procedure, we get a differential equation for the two non-linear oscillators:

mod 1

$$\ddot{u}_1 + 95.4915\, u_1 = 0.00951\, u_1^3 - 0.0001432\, u_1\, \dot{u}_1^2 - 4.7685\, u_1^3\, \dot{u}_1^2 \tag{36}$$

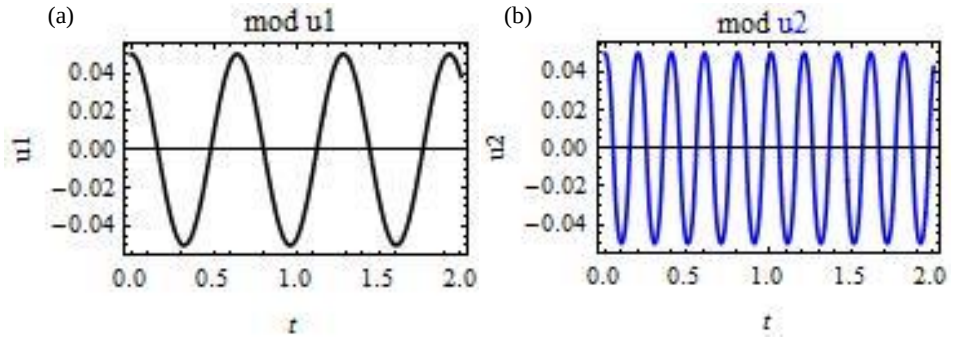


**Figure 5.** Time histories in normal coordinates, a) mod1 b) mod2

mod 2

$$\ddot{u}_2 + 654.5085\, u_2 = 23895.445\, u_2^3 - 787.218\, u_2\, \dot{u}_2^2 + 48410.711\, u_2^3\, \dot{u}_2^2 \tag{37}$$

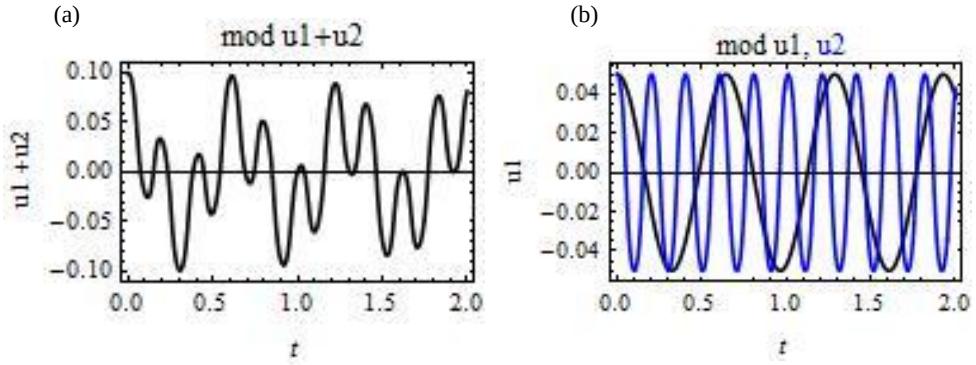


**Figure 6.** Time histories in normal coordinates a) mod 1+mod 2 b) comparison u1 and u2

Two extracted normal modes $u_1$ and $u_2$ are presented in Figure 5 and Figure 6. One can remark that the motions are very well separated.

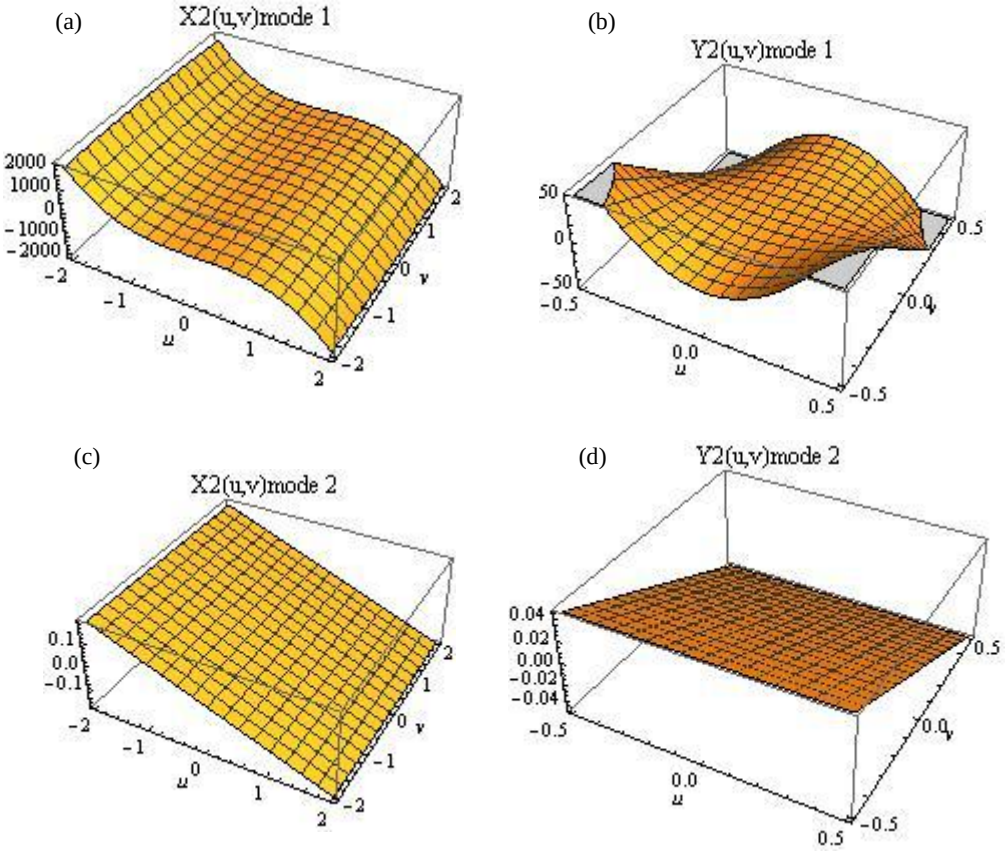


**Figure 7.** Nonlinear modal surfaces (a), (b) mod 1, (c), (d) mod 2.

The slave coordinates $x_2$, $y_2$ are related with the master ones *u*, *v* by the model functions $X_2(u,v)$, $Y_2(u,v)$. These model surfaces for the first and secon modes, respectevely, are presented in Fig. 7.

As a results from the above Fig. 7(a) the nonnlinear model surfaces for angular displacement of the system strongly depend on the vertical displacement From Fig. 7(b) the nonnlinear model surfaces for the angular velocity of the system strongly depend both on the vertical displacement and on the vertical velocity. Fig. 7(c) the nonnlinear model surfaces for angular displacement of the system Linearly depend on the displacement but in Fig. 7(d) the nonnlinear model surfaces for angular velocity of the system Linearly depend on the vertical velocity

## 4. Conclusions

The analysis presented in the paper concerns the dynamic behavior of the suspension structures of a non-ideal torsional machine. Initially NNMs were defined as periodic solutions of the underlying conservative system; continuation algorithms were recently exploited to compute them. We use nonlinear normal modes but before we use bifurcation analysis to obtain chaos. The NNMs are applied to decouple the motions of the system.

A width of synchronization regions, near the principal parametric resonance fits well to the regions found by numerical simulations, presented in the bifurcation diagrams. The nonnlinear model surfaces for angular velocity of the system strongly depend both on the vertical displacement and on the vertical velocity.

## References


[1] Rosenberg, R.M. Normal modes of non-linear dual-mode systems, *Journal of Applied Mechanics*, Ser. E, 27, 2, (1960), pp. 263-268.

[2] Vakakis, A.F. Non-linear normal modes (NNMs) and their applications in vibrations theory: an overview,Mechanical systems and signal and processing,11,1,3-22, 1997.

[3] Shaw S.W.,Pierre C., Normal modes for non-linear vibratory system, Journal of sound and vibrations, 164, 1, 85-124,1993.

[4] Kerschen G., Peeters M., Golinval J.C., Vakakis, A.F. Nonlinear normal modes, part I: Useful framework for the structural dynamicst, Mechanical Systems and Signal Processing, 23, 170-194, 2009.

[5] Vakakis, A.F. et al. Nonlinear Targeted Energy Transfer in Mechanical System and Structures Systems, *Springer*, New York, 2008.

[6] Warminsky, J., Nonlinear normal modes of a self-excited system driven by parametric and external excitations**,** *Nonlinear Dyn 61DOI 10.1007/s11071-010-9679-5*, (2010), pp 677.

[7] Warminsky, J. Nonlinear Normal Modes of Coupled Self-Excited Oscillators In Regular And Chaotic Vibration Regimes, *Journal Of Theoretical And Applied Mechanics 46, 3*, Warsaw (2008), pp. 693-714.

[8] Alisverisci, G.F., "The Nonlinear Analysis of Vibrational Conveyers with Non-Ideal Crank-and-Rod Exciters", Dynamics and Control of Technical Systems, Volume 706 of Applied Mechanics and Materials, ISSN print 1660-9336, ISSN cd 1660-9336, ISSN web 1662-7482, pp 44,: 2015.



G. Füsun Alışverişçi, Associate Professor: Yıldız Technical University, 34349 Istanbul, Turkey, (gfusun@yahoo.com.tr).

# Strain analysis and structural optimization of functionally graded rod with small concentration of inclusions (MAT303-15)

Igor V. Andrianov, Jan Awrejcewicz, Alexander A. Diskovsky

Abstract. The homogenization procedure is applied to strain analysis and optimal design of a Functionally Graded (FG) rod in the case when the inclusion size is essentially less than a distance between them. The method is illustrated using an example of the rod longitudinal strain. We considered separately the cases of FG inclusion sizes and FG steps between inclusions. Two particular problems of optimal design are discussed in some details.

## 1. Introduction

A fundamental approach allows deducing the macro-scale laws and the constitutive relation by properly homogenization over the micro-scale is known as the homogenization method [1-9]. This method also used to modeling and simulating mechanical behavior of FG Materials (FGM) and FG Structures (FGS) [10-15]. FGMs are composites consisting of two different materials with a gradient composition. For homogenization method coefficients of regular composites state equations are usually [1-4] approximated by the first terms of their Fourier series (Fig. 1).

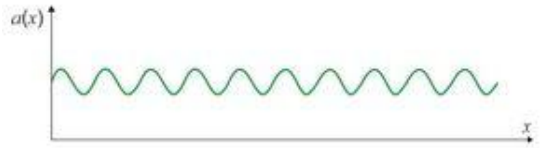


**Figure 1.** Example of equation coefficient for regular composites.

Similarly [10-15] can be approximated the coefficients of FGSs state equations with FG inclusion sizes **(**Fig. 2) and FG step between the inclusions (Fig. 3).

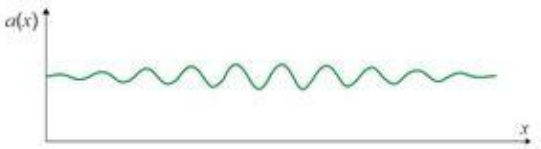


**Figure 2.** Example of equations coefficient for composite with FG inclusion sizes.

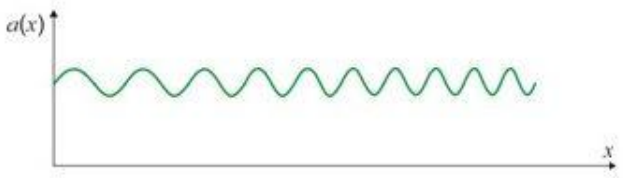


**Figure 3.** Example of equation coefficient for composite with FG steps between inclusions.

However, the truncated Fourier parts even for a small number of terms relatively good approximate the coefficients of the state equations for large concentration of inclusions (fibers, cells, etc.), when the distance between inclusions have been the same order as their typical size. For small concentration, when the distance between inclusions is essentially larger than their size, the state equations coefficients are approximated by impulsive periodic function (see, for instance, Fig. 4). In this case usual homogenization procedure may meet some problems to be directly applied.

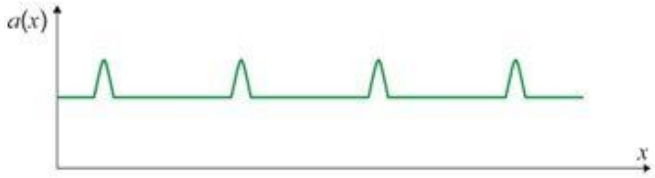


**Figure 4.** Example of coefficient for composites with small inclusion concentration.

Therefore, for a small concentration of inclusions it is recommended to use the further presented variant of homogenization method, where used small size of the inclusions with respect to the distance between them for asymptotic procedure. Modifications of this approach for FGS with small inclusion concentrations are proposed.

The applied method is illustrated using a relatively simple problem, i.e. a rod with a longitudinal strain. Rod diameter is taken commensurable with inclusions dimension.

**2. FG inclusion sizes**

FG properties can be achieved, for instance, with respect to different inclusion sizes. Let us analyse an influence of different sizes of inclusions on the longitudinal rod stiffness, keeping constant the distance between inclusions (Fig. 5). We define changes of the inclusion dimensions by a function $V = V(x)$.

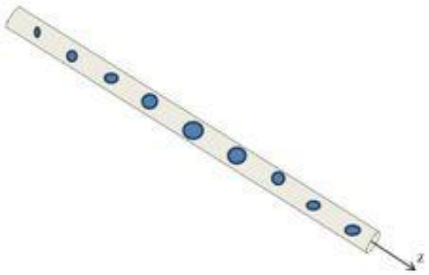

**Figure 5.** Rod with FG inclusions.

We approximate inclusions (Fig. 5) by concentrated elastic elements (Fig. 6), where stiffness $k_1(z)$ characterizes the inclusions influence. Observe that for composites with regular structure in the analogous models of two-component rod are applied (see [16-18]).

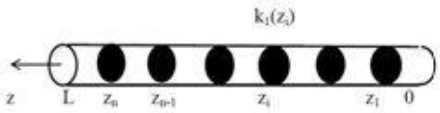


**Figure 6.** Two-component rod with concentrated elastic elements.

Obviously, a number of inclusions n is large, and hence the distance $l = z_i - z_{i-1}$ between them is much less than the rod length $L$, $l<<L$. Therefore, in order to investigate the longitudinal deformation of the two components rod (Fig. 6), one may apply the following variant of the homogenization procedure.

Equilibrium equation of the rod part between the inclusions has the following form

$$\frac{d^2u}{dx^2} = q, \tag{1}$$

where $x = z/l$; $u = v/l$; $v$ is the longitudinal displacement; $q = \frac{p(x)}{lk_0}$; $p(x)$ is the applied load; $k_0=E_0F$; $E_0$ is the Young modulus matrix; $F$ is the cross-sections area.

Compatibility conditions regarding the $i$-th elastic cross-sections are as follow

$$(u)^- = (u)^+; \quad \left(\frac{du}{dx}\right)^- - \left(\frac{du}{dx}\right)^+ = ku, \tag{2}$$

where $(...)^- = \lim_{x=i-0}(...)$; $(...)^+ = \lim_{x=i+0}(...)$; $k = \frac{lk_1(x)}{k_0}$.

## 3. Homogenization procedure

Owing to the multiscale homogenization approach, let us introduce the fast variable $\xi$

$$\xi = x / \varepsilon, \tag{3}$$

where $\varepsilon=1/n<<1$.

We treat the variables $x$ and $\xi$ as independent ones, and the differential operator occurred in (1), (2) has the following form

$$\frac{d}{dx} = \frac{\partial}{\partial x} + \varepsilon^{-1}\frac{\partial}{\partial \xi}. \tag{4}$$

Displacement $u$ can be presented in the following form

$$u = u_0(x) + \varepsilon^2 u_1(x,\xi) + \varepsilon^3 u_2(x,\xi) + ..., \tag{5}$$

where $u_s$ ($s$=1,2,...) is periodic with respect to $\xi$.

Substituting formulas (4), (5) into equation (1) and condition (2), and carrying out the splitting with respect to $\varepsilon$, the following equations are obtained

$$\frac{\partial^2 u_1}{\partial \xi^2} + \frac{\partial^2 u_1}{\partial x^2} = q, \tag{6}$$

$$(u_1)_{\xi=0} = (u_1)_{\xi=n}, \tag{7}$$

$$\left(\frac{\partial u_1}{\partial \xi}\right)_{\xi=0} - \left(\frac{\partial u_1}{\partial \xi}\right)_{\xi=n} = \varepsilon^{-1} k u_0. \tag{8}$$

We assumed $\varepsilon^{-1}k \sim 1$ while deriving formula (8).

Integrating (6) with regard to $\xi$ and defining the integration constant via condition (7), we get

$$\frac{\partial u_1}{\partial \xi} = \left(q - \frac{d^2 u_0}{dx^2}\right)\left(\xi - \frac{n}{2}\right). \tag{9}$$

Substituting formula (9) into condition (8), the following homogenized equation describing the longitudinal displacement of the two-component rod is obtained

$$\frac{d^2 u_0}{dx^2} + k(x) u_0 = q. \tag{10}$$

Micromechanical effects are described by functions $u_s$ ($s$=1,2,...).

## 4. Inverse problem

The main advantage of the proposed approach is that it allows efficiently solving the problems of optimization, i.e. problems devoted to determination of optimal characteristics of the internal material structure protecting the given structure properties. In the studied case of the FG amplitudes, the target characteristic is the function $V=V(x)$ governing a rule of the inclusion dimensions change.

As an example we consider the problem of determination of the function $V(x)$ protecting the larger longitudinal stiffness for a given load $q(x)$. It is convenient to take rather the function $k(x)$ as the control function instead of the function $V(x)$.

Without lose of generality let us take the boundary conditions in the following form

$$u_0(0) = 0, \quad \frac{du_0}{dx}_{x=n} = 0. \tag{11}$$

In order to measure the rod stiffness properties we take energy of the elastic deformations and use zero order approximation of the displacement (10). Then, we define a minimum of the following functional

$$I = \int_0^n q u_0 dx \to \min_k. \tag{12}$$

One can introduce the following isoperimetric condition which guarantees a constant total inclusion volume

$$\sum_{i=1}^{n} k(x_i) = C - const. \tag{13}$$

Condition (13) can be transformed to the isoperimetric form owing to application of an Euler-Maclaurin formula [19]

$$\sum_{i=1}^{n} k(x_i) = \int_0^L k(x)dx + \frac{1}{2}(k(0) + k(L)) - \frac{1}{12}(k'(0) + k'(L)) + \frac{1}{720}(k''(0) + k''(L)) - \ldots.$$

For large number of inclusions $n \gg 1$ and smooth function $k'(x) \sim 1,$ we can neglect non-integral terms

$$\int_0^n k(x)dx = c. \tag{14}$$

In practice, the inclusion sizes meet the technological constrains. Hence, next constraint for the target function is required

$$k_{\min} \le k(x) \le k_{\max}. \tag{15}$$

Constraint (15) is satisfied through introduction of the following new control function $\theta$ (x) [20]:

$$k = \alpha + \gamma \sin\theta, \tag{16}$$

where: $\alpha = 0.5(k_{\min} + k_{\max})$, $\gamma = 0.5(k_{\min} + k_{\max})$.

Obtaining of the function $\theta(x)$ requires solution to the following inverse problem (10)-(16):

$$I = \int_0^n q u_0 dx \to \min_\theta, \tag{17}$$

$$I_1 = \gamma \int_0^n \sin\theta dx = c, \tag{18}$$

$$\frac{d^2 u_0}{dx^2} + (\alpha + \gamma \sin\theta) u_0 = q, \tag{19}$$

$$u_0(0) = 0, \qquad \left(\frac{du_0}{dx}\right)_{x=n} = 0. \tag{20}$$

Defining first variations of integrals (17), (18), and a variation equation corresponding to (19) with the boundary conditions (20), one obtains

$$\delta I = \int_0^n q \delta u_0 dx, \qquad \delta I_1 = \gamma \int_0^n \cos\theta \delta\theta dx, \tag{21}$$

$$\frac{d^2 \delta u_0}{dx^2} + (\alpha + \gamma \sin\theta)\delta u_0 + \gamma \cos\theta u_0 \delta\theta = 0, \tag{22}$$

$$\delta u_0(0) = 0, \qquad \left(\frac{d\delta u_0}{dx}\right)_{x=n} = 0. \tag{23}$$

The variation of Lagrange functional follows

$$\delta I + \lambda \delta I_1 + \int_0^n \tilde{v}\left(\frac{d^2 \delta u_0}{dx^2} + (\alpha + \gamma \sin\theta)\delta u_0 + \gamma \cos\theta u_0 \delta\theta\right) dx = 0, \tag{24}$$

where $\lambda$ denotes the Lagrange multiplier, and $\tilde{v}$ is the conjugated variable.

Conjugated variable $\tilde{v}$ being defined through the condition minimizing functional (17) should not contain the variation $\delta w_0$ . For this purpose, we integrate by parts the first term of the integrand two times taking into account conditions (23). Non-integral terms are equal zero if the following boundary conditions are applied to the conjugated variable

$$\tilde{v}(0) = 0, \qquad \left(\frac{d\tilde{v}}{dx}\right)_{x=n} = 0. \tag{25}$$

Finally, equation (24) takes the following form

$$\int_0^n \left( \left( \frac{d^2\tilde{v}}{dx^2} + (\alpha + \gamma \sin\theta)v + q \right) \delta u_0 + \gamma \cos\theta (\tilde{v}u_0 + \lambda)\delta\theta \right) dx = 0. \tag{26}$$

In order to keep variation $\delta J$ independent on $\delta u_0$, the following equation should be satisfied

$$\frac{d^2\tilde{v}}{dx^2} + (\alpha + \gamma \sin\theta)\tilde{v} + q = 0, \tag{27}$$

and the following optimality condition takes place

$$\cos\theta(\tilde{v}u_0 + \lambda) = 0. \tag{28}$$

Comparison of the boundary condition (22), (23) and (25), (27) yields

$$\tilde{v} = -u_0. \tag{29}$$

Taking into account equation (29), optimality condition is result to the following form

$$\cos\theta(u_0^2 - \lambda) = 0. \tag{30}$$

As it has been pointed out in references [10-15], the occurrence of singular points belongs to typical problems, while solving the problems of optimization of FGS. If one is looking for the control function $\theta(x)$ as continuous one, then it is impossible to satisfy the boundary condition (20) for $x = 0.$ Therefore, we assume the control function $\theta(x)$ in the form of piece-wise continuous function, which in the $(0, x_1)$ satisfies the following condition

$$\cos\theta = 0, \tag{31}$$

and on $(x_1, L)$ we have

$$u_0^2 - \lambda = 0. \tag{32}$$

One gets a co-ordinate of the point $x_1$ from continuity condition in this point of both the function $u_0$ and its derivative $u_{0x}$ (these conditions are yielded by the external Weierstrass-Erdmann relations [21]):

$$\lim_{x \to x_1 - 0} u_0 = \lim_{x \to x_1 + 0} u_0, \qquad \lim_{x \to x_1 - 0} \frac{du_0}{dx} = \lim_{x \to x_1 + 0} \frac{du_0}{dx}. \tag{33}$$

The conditions (33), taking into account relations (31), take the following form

$$u_{01}(x_1) = \pm\sqrt{\lambda}, \tag{34}$$

$$\left( \frac{du_{01}}{dx} \right)_{x = x_1} = 0, \tag{35}$$

where $u_{01}$ denotes displacement in the interval $(0, x_1)$. Relations (16), (19), (31) allow to derive the following equation

$$\frac{d^2 u_{01}}{dx^2} + k_{\min} u_{01} = q, \tag{36}$$

with BCs (11), (35). Assuming that $u_{01}$ is known, conditions (34) allow describing $x_1$ via $\lambda$. Substituting conditions (32) into equation (19), we find a formula for $\sin\theta$ in the interval $(x_1, L)$. Then, taking into account formula (18), the following optimal control function is defined

$$k = \begin{cases} k_{\min}, & x \in (0, x_1), \\ \pm \dfrac{q}{\sqrt{\lambda}}, & x \in (x_1, L). \end{cases} \tag{37}$$

The Lagrange constant $\lambda$ is found from an isoperimetric condition (14), which takes the following form

$$\int_{x_1}^{n} q dx = \pm\sqrt{\lambda}(c - k_{\min} x_1). \tag{38}$$

**5. Example of amplitude optimization**

In order to illustrate the proposed method, we consider the problems (10)-(15) for linearly distributed load, i.e.

$$q = \rho x, \qquad \rho = const. \tag{39}$$

Assume that the minimal size of inclusions is equal to zero, i.e.

$$k_{\min} = 0. \tag{40}$$

Formulas (39), (40), taking into account the boundary conditions (36), (11), (35), yield

$$u_{01} = \rho\left(\frac{x^3}{6} - \frac{x_1^2}{2}x\right). \tag{41}$$

Equation (34) gives

$$\sqrt{\lambda} = \frac{\rho}{3}x_1^3. \tag{42}$$

Formula (38) taking into account (39), (40), (42), implies the following equation to find $x_1$:

$$2cx_1^3 + 3x_1^3 - 3L^2 = 0. \tag{43}$$

Observe, that equation (43) does not include an intensity of the load $\rho$, i.e., the variable $x_1$ depends only on the applied load character, which is typical for the linear statement formulation. We take the following parameters in order to carry out the numerical computations

$$n = 100, \qquad c = 10^2 \cdots 10^3. \tag{44}$$

It should be emphasized that for the chosen parameters equation (43) uniquely defines $x_1$, since among any three roots of the equation, only one is positive.

The function $x_1$ versus $c$ is reported in Figure 7.

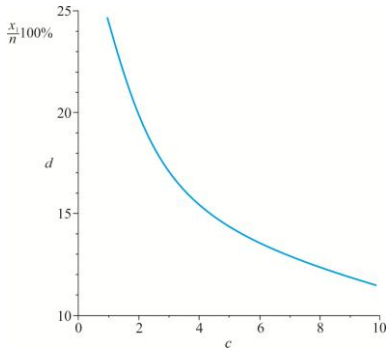

**Figure 7.** The function $x_1$ versus $c$ ($x_1$ denotes a boundary area without inclusions).

Finally, (37) yields the optimal control function

$$k = \begin{cases} 0, & x \in (0, x_1), \\ \dfrac{3\rho x}{x_1^3}, & x \in (x_1, n). \end{cases} \tag{45}$$

Let us estimate the efficiency of the proposed optimization. For this purpose we compare the extension of the rod for the optimal stiffness distribution for the equivalent cross-section (45) and extension of the rod of the regular form. Extension $\Delta_0$ of the optimal rod can be found from equations (32), (42)

$$\Delta_0 = \frac{\rho x_1^3}{3}. \tag{46}$$

Extensions of the regular form rod $\Delta$ can be found from the boundary value problem (10), (11), (39) for $\bar{k} = c / n$

$$\Delta = \frac{\rho n^3}{c}\left(1 - \frac{\tan\sqrt{c}}{\sqrt{c}}\right). \tag{47}$$

With a help of relations (46), (47) we find the relative decrease of the rod extension due to optimal distribution of the inclusions volume

$$\delta = \frac{\Delta - \Delta_0}{\Delta} 100\%. \tag{48}$$

For the considered parameters (44) the relative decrease of the extension $\delta$ is of amount 50%, i.e. for $c = 10^2$, $\delta = 46.6\%$; $c = 5 \cdot 10^2$, $\delta = 49.1\%$; $c = 10^3$, $\delta = 49.7\%$.

**6. FG steps between inclusions**

Now we are aimed to analyse an influence of FG steps between equal inclusions. Consider the basic two-component rod (Fig. 6) with equal elastic inclusions, $k = const$. Assuming a fixed number of inclusions $n$ and $L = n$, we have $l = 1$. Now we change the distance $l$. In order to describe the rule of the step changes, and following reference [15], we apply a steps function $f(x)$, such that

$$f(x_i) = i, \tag{49}$$

where $x_i$ is a co-ordinate of the *i*-th inclusion.

Properties of the steps function protecting the constant number of inclusions can be defined via Fig. 8, which can be treated as a nomogram to define co-ordinates of the inclusions versus function steps.

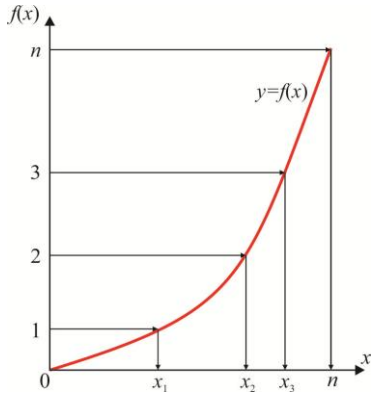


**Figure 8.** **N**omogram to define co-ordinates of the *i*-th elastic inclusions $x_i$ for a given steps function $f(x)$.

Figure 8 implies that in order to protect constant number of inclusions, the function $f(x)$ should have the following properties

$$f(0)=0, \quad f(n)=n, \quad f'(x)\geq 0. \tag{50}$$

Relation $\Delta f \approx f'(x)\Delta x$ yields approximation to the steps between inclusions. For the given step of the basic rod (Fig. 6) $\Delta f = 1$, the non-constant step of the FG rod $\Delta x = s$ takes the following form

$$s \approx \frac{1}{f'(x)}. \tag{51}$$

**7. Direct problem for FG steps**

Proceeding in the similar way to that used for the FG inclusion sizes, we now consider the inclusions thickness approaching to zero, and the equations governing the rod deformation with the FG steps takes the following form

$$\frac{d^2u}{dx^2} + k\sum_{i=1}^{n}\delta(f(x_i)-i)u = q, \tag{52}$$

where $\delta(x)$ denotes the Dirac delta function.

We introduce the following variable $\eta = f(x)$ $(x = f^{-1}(\eta))$. Therefore, equation (52) is recast to the following form

$$\frac{d}{d\eta}\left(\frac{du}{\varphi d\eta}\right) + k\sum_{i=1}^{n}\delta(\eta - i)\varphi u = Q, \tag{53}$$

where: $\varphi = \frac{d(f^{-1})}{d\eta}$, $Q = \varphi q$.

Equation (53) presents an equation with periodically discontinuous coefficients, and we may apply a homogenization procedure. Equation of equilibrium between inclusions (1) and compatibility conditions (2) for the considered FG steps take the following form

$$\frac{d}{d\eta}\left(\frac{du}{\varphi d\eta}\right) = Q, \tag{54}$$

$$(u)_{\eta=i-0} = (u)_{\eta=i+0}, \qquad \left(\frac{du}{\varphi d\eta}\right)_{\eta=i-0} - \left(\frac{du}{\varphi d\eta}\right)_{\eta=i+0} = ku. \tag{55}$$

After introduction of the fast variable $\xi = \eta / \varepsilon$ and applying asymptotic series development regarding displacements

$$u = u_0(\eta) + \varepsilon^2 u_1(\eta, \xi) + \varepsilon^3 u_2(\eta, \xi) + ..., \tag{56}$$

relations (54), (55) yield the following homogenization equations for $u_0$:

$$\frac{d}{d\eta}\left(\frac{du_0}{\varphi d\eta}\right) + ku_0 = Q \tag{57}$$

and the equation for the correction term $u_1$:

$$\frac{\partial u_1}{\partial \xi} = \varphi\left(Q - \frac{d}{d\eta}\left(\frac{du_0}{\varphi d\eta}\right)\right)\left(\xi - \frac{n}{2}\right). \tag{58}$$

If in the homogenization equation (57) we return to the original variable, we get

$$\frac{d^2 u_0}{dx^2} + kf'(x)u_0 = q. \tag{59}$$

It should be emphasized that the obtained homogenized equation (59) represents all physical aspect of the problem. The non-differentiable term occurring in the left hand side of this equation presents an "additional stiffness" governed by inclusions and continuously distributed along the rod length. In the case of FGS, this distribution is not uniform. In the case of FG steps, more dense localization of inclusions involves larger contribution of the "additional stiffness". Mathematically, this property is described by the derivative of the steps function $f'(x)$ in equation (59).

**8. Inverse problem for FG steps**

Consider the inverse problem for equation (59) with the boundary conditions (11), take the following control function

$$\psi = kf'(x). \tag{60}$$

Minimizing functional *I* represents the energy of elastic deformation

$$I = \int_0^n u_0 q dx \to \min_{\psi}. \tag{61}$$

Condition of keeping constant the number of inclusions (50) yields the isoperimetric form for the control function

$$\int_0^n \psi dx = kn. \tag{62}$$

We apply also the technological bounds for $\psi$, analogous to (15), which will be satisfied automatically after introduction of the control function (16). One may easily convince that the considered inverse problem for the FG rod (59)-(62) coincides with the analogous problem (10)-(16). In what follows we illustrate how to find solution to the considered problem.

**9. Example of steps optimization**

We consider optimization of the steps for the rod (39). Similarly to condition (40), the following formula holds

$$\psi_{\min} = 0. \tag{63}$$

It means, that inclusions do not appear in the interval $(0, x_1)$. The illustrated requirement (63) yields the particular case considered in section 5 (for $k = \psi$). After defining the control function due to formula (45), the function $f(x)$ defining the optimal coordinated of the inclusion constant is estimated with a help of the second condition of (50). We get finally

$$f(x)=\begin{cases}0, & x\in(0,x_1),\\ \dfrac{3\rho(x^2-n^2)}{2x_1^3k}+n, & x\in(x_1,n).\end{cases} \tag{64}$$

The function $f(x)$ for $\rho=100,\ k=10,\ n=100$ is shown in Figure 9.

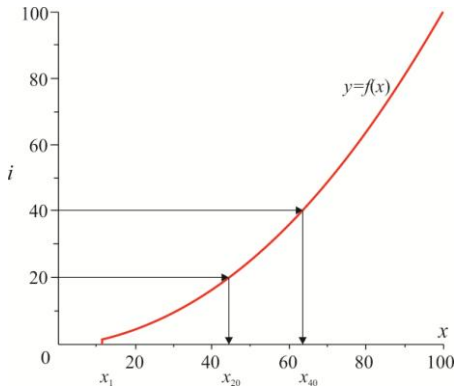


**Figure 9.** **N**omogram for determination of the optimal coordinates of inclusions protecting the larger longitudinal rod stiffness for the linearly distributed load.

Substituting equation (49) into (64) yield optimal coordinates of the inclusions:

$$x_i=\sqrt{n^2-\frac{2x_1^3k(n-i)}{3\rho}}, \tag{65}$$

where: $i=1...100,$ and $x_1$ is defined by equation (43).

In Figure 10 the a window enlargement of the nomogram part (Fig. 9) is shown for two first inclusions.

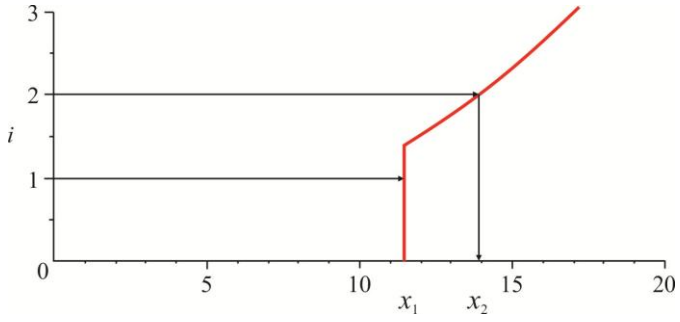


**Figure 10.** Scheme for determination of the coordinate of two first inclusions $x_1$ and $x_2$.

The first inclusion coordinate ( $x_1 = 11.45$ ) is found from equation (43), whereas the second inclusions coordinate $x_2 = 13.88$ is given by formula (65).

**Concluding remarks**

Introduction the step function (49) allowed solving problems of computations and optimal design of FGS with a FG inclusion dimensions and FG steps between inclusions using the unique approach. Both considered problems occurred identical from the mathematical points of view, whereas the difference between them consists in the meaning of coefficients in the state equations and control functions.

While optimization the FGS with FG inclusion sizes and FG steps between inclusions it is recommended to search the control function on a set of piece-wise continuous functions. The optimization process is realized with a help of two mechanisms. First, we define boundary area where inclusions do not occur. Second, in the case of FG inclusion sizes we interlace inclusion dimensions to fit a rule of the external load distribution. The reported optimization mechanisms, being obvious from physical point of view, have found a mathematical foundation in our work. It is expected that the proposed method will be also sufficient during computations and optimal design of more complex heterogeneous structures governed by the differential equations of higher order.

A second direction of the proposed method development is the FGS, where FG inclusion sizes and FG steps between inclusions appear simultaneously.

**Acknowledgments**

This work has been supported by the Polish National Science Centre, MAESTRO 2, No. 2012/04/A/ST8/00738.

**References**

[1] Bensoussan, A., Lions, J.-L., Papanicolaou, G.: Asymptotic Analysis for Periodic Structures. North-Holland: Amsterdam (1978).

[2] Sanchez-Palencia, E.: Non-Homogeneous Media and Vibration Theory. Springer-Verlag: Berlin (1980).

[3] Bakhvalov, N.S., Panasenko, G.P.: Averaging Processes in Periodic Media. Mathematical Problems in Mechanics of Composite Materials. Kluwer: Dordrecht (1989).

[4] Panasenko, G.P.: Multi-Scale Modeling for Structures and Composites. Springer-Verlag: Berlin (2005).

[5] Babushka, I.: The computation aspects of the homogenization problem. Lect. Notes Math. 704, 309-316 (1979)

[6] Andrianov, I.V., Awrejcewicz, J., Manevitch, L.I.: Asymptotical Mechanics of Thin-Walled Structures: A Handbook. Springer-Verlag: Berlin, Heidelberg (2004).

[7] Kolpakov, A.G.: Stressed Composite Structures: Homogenized Models for Thin-Walled Nonhomogeneous Structures with Initial Stresses. Springer-Verlag: Berlin, New York (2004).

[8] Manevitch, L.I., Andrianov, I.V., Oshmyan, V.G.: Mechanics of Periodically Heterogeneous Structures. Springer-Verlag: Berlin, Heidelberg, New York (2002).

[9] Movchan, A.B., Movchan, N.V., Poulton, C.G.: Asymptotic Models of Fields in Dilute and Densely Packed Composites. Imperial College Press: London (2002).

[10] Andrianov, I.V., Awrejcewicz, J., Diskovsky, A.A.: Homogenization of the irregular cell-types constructions. In: Awrejcewicz, J., Sendkowski, D., Mrozowski, J. (Eds) Proc. 8th Conf. Dyn. Syst. - Theory & Appl., Lodz, 2, pp. 871-876 (2005).

[11] Andrianov, I.V., Awrejcewicz, J., Diskovsky, A.A.: Homogenization of quasiperiodic structures. Trans. ASME J. Vibr. Acoust. 128(4), 532-534 (2006).

[12] Andrianov, I., Awrejcewicz, J., Diskovsky, A.: Asymptotic investigation of corrugated elements with quasi-periodic structures. In: Awrejcewicz, J., Kaźmierczak, M., Olejnik, P., Mrozowski, J. (Eds) Proc. 10-th Conf. Dyn. Syst. – Theory & Appl., Lodz, 2, pp. 523-532 (2009).

[13] Andrianov, I., Awrejcewicz, J., Diskovsky, A. Design of the non-homogeneous quasi-regular structures. In: Bolshakov, V.I., Weichert, D. (eds) Advanced Problems in Mechanics of Heterogeneous Media and Thin-walled Structures. ENEM, Dnipropetrovs'k, pp. 7–18 (2010).

[14] Andrianov, I., Awrejcewicz, J., Diskovsky, A.: Homogenization of the functionally-graded materials. In: Awrejcewicz, J., Kaźmierczak, M., Olejnik, P., Mrozowski, J. (Eds) Proc. 11-th Conf. Dyn. Syst. – Theory Appl., Lodz, 2, pp. 55-62 (2011).

[15] Andrianov, I.V., Awrejcewicz, J., Diskovsky, A.A.: Sensitivity analysis in design of constructions made of functionally-graded materials. Proc. Inst. Mech. Eng. Part C: J. Mech. Eng. Sc. 227(1), 19-28 (2013).

[16] Andrianov, I.V., Danishevs'kyy, V.V., Topol, H., Weichert, D.: Homogenization of a 1D nonlinear dynamical problem for periodic composites. ZAMM 91(6), 523-534 (2011).

[17] Goland, M., Reissner, E.: The stresses in cemented joints. J. Appl. Mech. 11, A17–A27 (1944).

[18] Geymonat, G., Krasucki, F., Lenci, S.: Mathematical analysis of a bonded joint with a soft thin adhesive. Math. Mech. Solids 201–225 (1999).

[19] Hamming, R.W.: Numerical Methods for Scientists and Engineers. McGraw Hill: New York (1962).

[20] Banichuk, N.V.: Introduction to Optimization of Structures. Springer-Verlag: New York (1990).

[21] Masur, E.F.: Singular problems of optimal design. In: Haug, E.J., Cea, J. (Eds) Optimization of Distributed Parameter Structures, pp. 200-218. Sijthoff-Noordhoff: Iowa, Alphen Aan den Rijn (1980).

Igor V. Andrianov, Professor, Institut für Allgemeine Mechanik, RWTH Aachen University, Templergraben 64, D-52056, Aachen, Germany (igor_andrianov@hotmail.com)

Jan Awrejcewicz, Professor, Department of Automation, Biomechanics and Mechatronics, Lodz University of Technology, 1/15 Stefanowski St., 90-924, Lodz and Department of Vehicles, Warsaw University of Technology, 84 Narbuta Str., 02-524 Warsaw, Poland (awrejcew@p.lodz.pl)

Alexander A. Diskovsky, Professor, National Metallurgical Academy of Ukraine, Department of Higher Mathematics, Gagarina 23, UA-49005, Dnepropetrovsk, Ukraine (alex_diskovskiy@ukr.net)

# Numerical study of the optimal position of a Lamb wave actuator for detection of fatigue damage in an isotropic plate with a circular hole (NUM065-15)

Marek Barski, Adam Stawiarski, Piotr Pająk

*Abstract:* A rectangular plate with a circular cutout located in the geometrical center of the plate is subjected to cyclic tension. Generally, this type of the load causes formation of fatigue damage in the vicinity of the hole. This paper is devoted to the problem of damage detection and evaluation with the use of Lamb waves. The propagation of the waves in the vicinity of the hole is simulated with the use of the finite element method. The most effective position of the actuator is looked for. The position of an actuator as well as the appropriate algorithm of signal processing should make it possible to detect the existence of damage and also to provide information about the length of a fatigue crack. It enables engineers to estimate the actual length of the lifetime of the considered structure. Four different positions of the actuator have been analyzed.

## 1. Introduction

Nowadays the problem of detection of various defects in engineering structures is becoming very important. For this purpose, advanced systems known as the SHM (Structural Health Monitoring), are designed. According to Rytter [1], we can distinguish four levels of the SHM systems:

- level 1: detection of damage,
- level 2: detection and localization of damage,
- level 3: detection, localization and evaluation (type, size, orientation, etc.) of damage,
- level 4: estimation of lifetime of structure with detected damage.

Additionally, together with discovering smart materials (shape memory alloys), another level of the SHM systems should be taken into consideration. This level is strictly connected with the possibility of self-repairing of the structure, where the damage has been detected (Park et al. [2]). However, the majority of works are devoted to the SHM systems of the 1 and 2 levels. It seems that designing the SHM systems of the 3 level is very difficult.

Nowadays, in modern SHM systems, propagation of elastic waves is very frequently used to detect various defects in solid structures. Depending on the properties of the medium in which the wave propagates we can distinguish different types of waves. The comprehensive description of those waves can be found in numerous monographs, for example: [3], [4], [5]. It is worth noting here that in

practical applications two types of elastic waves are mainly used. They are Lamb waves [6] and Rayleigh waves [7]. The waves are most frequently generated by using piezoelectric transducers. Regardless of the type of the applied elastic waves, damage is detected and located by means of substantially two methods, i.e. *Pulse - Echo* and *Pitch - Catch* [8]. The *Pulse - Echo* method is based on recording the signal which is reflected from a flaw. Here the activator and sensors are placed on the same side of the investigated structure. In the *Pitch - Catch* configuration, the elastic waves travel across the investigated structure and they are then captured by a sensor at the other end of the wave path. If a defect is present in the object, the signal captured by the sensor will be changed and will be different from the signal received in the case of an intact structure. Moreover, using the array of sensors, it is not only possible to detect damage but also precisely locate and evaluate it.

The above-discussed methods are successfully applied in the case of rails [9], pipes and cylinders [10], [11] or thin-walled structures like, for example, elements of aircraft skin [12], [13]. The method based on the propagation of the elastic waves can also be applied in the case of composite materials in order to detect defects which are characteristic of this kind of materials, e.g. matrix cracking, delaminations or fiber debonding [14], [15]. They can also be used to evaluate mechanical properties (spring constants) of composite materials [16], thickness measurement [17] or phase velocity [18].

The work presented in this article is devoted to the problem of detecting and evaluating a fatigue crack which is localized in the vicinity of a hole. The existence of different perforations in the members of support structures is necessary due to, for example, fuel or hydraulic lines, rivet joints or simply reduction of the structure's weight. Moreover, all discontinuities of this kind cause stress concentration which, in consequence, can trigger the fatigue crack growth. It especially happens when the object is subjected to cyclic tension. In practice, the access to the places where the holes are present can be often very difficult or even impossible. Therefore, development of a special SHM system which is dedicated to this problem seems to be very important. However, this task is rather complicated mainly due to the reflection of the incident wave from the edges of the hole. The detection of the crack is rather easy, though. The main problem is connected with the effective evaluation of the crack length.

Only a few papers can be quoted where similar investigations have been carried out. Chang and Mal [19] studied scattering of Lamb waves in the vicinity of the rivet hole. They used a modified finite element method (global local FE). The theoretical results were compared with experimental ones and a broad agreement was observed between them. Fromme and Sayir [20] also analyzed scattering of the guided wave (anti-symmetric $A_0$ mode of the Lamb wave) in the vicinity of the rivet hole. They observed a significant reduction of the amplitude of the received signal in the case of the structure with a crack. They also conducted numerical simulations with the use of a different finite

method. The work by Hong et al. [22] has also been devoted to the problem of detection and localization of a fatigue crack on the edge of the hole.

In the above-mentioned papers, the experimental studies are generally compared with the numerical simulations. However, there are also available works in which a pure analytical approach is utilized. For example, the work by Grahn [21] deals with scattering of an incident plane $S_0$ Lamb wave in a plate with a circular hole. McKeon and Hinders [23] studied the Lamb waves scattering in the vicinity of the hole in an analytical manner.

The presented paper consists of 7 chapters. In the chapter 2 the definition of the investigated problem is discussed. Next (chapter 3 and 4) the proposed SHM system, based on the array of the piezoelectric transducers, is described. The analyzed SHM system is simulated with the aid of finite element method. The details of the numerical simulation are presented in the chapter 5. The obtained results are discussed in the chapter 6.

## 2. Analyzed structure

The analyzed structure is shown in Fig.1. It is a square plate with a circular hole placed in the geometric center of the structure. The length of the external edge is equal to $a_0$=250[mm] and the diameter of the cutout d=50[mm]. The structure is made of the aluminum alloy PA38 with the following mechanical properties: E=69.5[GPa], $\nu$=0.33, and the density $\rho$=2700[kg/m³]. It is assumed that the studied structure is subjected to uniform tension in the horizontal direction, which is symbolically shown in Fig. 1 (a horizontal arrow).

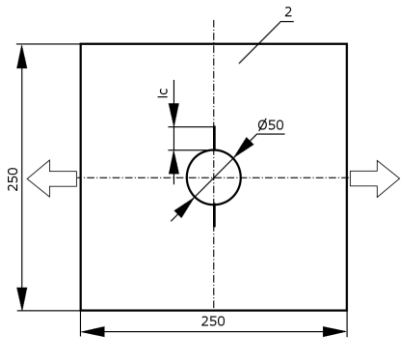


**Figure 1.** Investigated aluminum square plate with a circular hole $l_c$ denotes the crack length.

The applied load (uniform pressure or uniform displacement) causes stress concentration in the vicinity of the hole. The distribution of the circumferential stress component and the distribution of the stress equivalent are shown respectively in Fig. 2. These figures are obtained as a result of a basic finite element analysis. Both vertical edges have been uniformly stretched, where $\Delta u$=0.01[mm]. The

maximum value of the circumferential stress component (tension) is about three times greater in comparison with the absolute value of the minimal stress component (compression). Moreover, the circumferential stress component is dominant. It is confirmed by the fact that the maximum equivalent stress is identical with the maximum circumferential stress component. In the case of a cyclic load, in the areas where the circumferential stresses achieve their maximum, a fatigue crack can be initiated. After damage initialization, the crack will grow strictly in the vertical direction. It is shown in Fig. 1. Therefore, the main aim of this work is to design the SHM system of the 3-th level. The proposed SHM system should not only detect the crack at an early stage of its creation but it also should enable the estimation of the actual length of the crack. This is necessary in order to determine the safe lifetime of the structure.

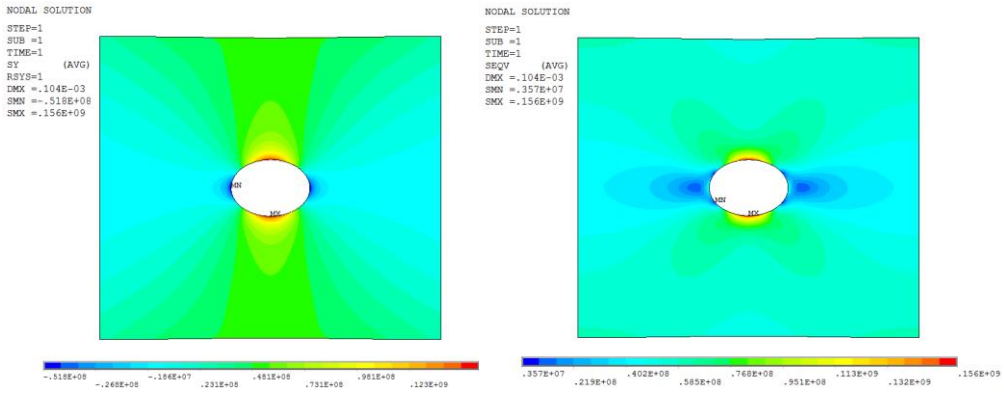


**Figure 2.** Circumferential component of stress and stress equivalent in a uniformly stretched square plate with a hole.

## 3. The designed SHM system

The proposed SHM system utilizes Lamb waves that propagate through plates. It is based on the comparison of the signal received in the case of the intact structure with the signal from the structure that contains damage. This kind of an approach is called a *Pitch - Catch* method. An appropriate signal is generated by a single piezoelectric activator and next the incident wave is received by the array of piezoelectric sensors. The localization of the sensors is constant and it is shown in Fig. 3. One sensor, S1, is placed directly on the edge of the cutout. If the crack is very small (an initial stage of the crack growth), this sensor should immediately indicate the presence of a flaw. To estimate the actual length of the crack, 14 sensors are installed in the vicinity of the hole, i.e. sensors S2 - S15. The distance between these sensors is constant and equal to $l_s$=5[mm]. The exact localizations of the mentioned piezoelectric elements are depicted in Fig. 3. The detailed description how to evaluate the

crack length taking into account the information obtained from the sensors is discussed in the next chapter.

The effectiveness and sensitivity of the developed SHM system depend on the optimal position of the actuator. In Fig.3, there are presented possible localizations of the actuators, namely: a) the A1 actuator is placed at the point where the edge of the hole is intersected by the line which starts from the geometrical center of the hole and is oriented at an angle of 45° with respect to the horizontal direction, b) the A2 actuator is also located on the edge of the hole at the point where the horizontal line intersects the edge of the cutout, c) the A3 actuator is shifted to the left with respect to the A2 sensor, d) the A4 actuator is placed at some distance from the hole.

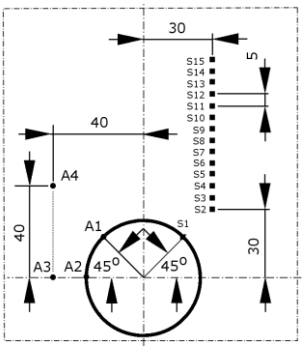


**Figure 3.** Localization of sensors and activators.

In cases a) and b), the incident wave propagates along the edge of the cutout and any additional effects connected with the reflection are avoided. However, in cases c) and d) the incident wave at first is reflected from the free edge of the hole and then is received by the sensors. This fact can make the process of damage detection more difficult. It has to be noted that in the real structure the crack grows on both sides of the hole in the vertical direction. Therefore, an identical set of sensors has to be installed in a symmetric manner with respect to the horizontal axis of the symmetry of the hole. Moreover, taking under consideration the symmetry of the investigated structure, in cases a) and d) it is also necessary to use a pair of activators which should be activated sequentially in order to test the bottom and top surroundings of the hole.

## 4. The applied method for fatigue damage detection

The proposed SHM system is based on the comparison of the actually received signal by the sensor with the signal obtained in the case of the intact or reference structure. The situation when these signals are different can be caused by the presence of a flaw in the inspected plate. In order to estimate the magnitude of the change in the picked up signal, the linear correlation coefficient is introduced:

$$\lambda^*_{fg} = \frac{\sum_{i=1}^{N}\left[\left(f_i - \mu_f\right)\left(g_i - \mu_g\right)\right]}{\sqrt{\sum_{i=1}^{N}\left(f_i - \mu_f\right)^2}\sqrt{\sum_{i=1}^{N}\left(g_i - \mu_g\right)^2}} \tag{1}$$

where N is a number of discrete values describing the compared signals; $f_i$, $g_i$ denote the value of the reference and actual signals; and $\mu_f$, $\mu_g$ are the average values computed for the signals f and g. Generally, the values of $\lambda^*_{fg}$ belong to the range [1, –1]. However, for identical signals, the coefficient $\lambda^*_{fg}=1$. Further, the results obtained from the set of sensors should be normalized. Another disadvantage of this approach is that the coefficient $\lambda^*_{fg}$ is very sensitive in the case when the actual signal is shifted in phase. On the other hand, the value of the $\lambda^*_{fg}$ is quite insensitive to the reduction of the amplitude of the actual signal in comparison with the reference signal (without a change in phase). This fact could make the process of damage identification very difficult.

In the next step, the appropriate damage index DI has to be defined. Generally, this parameter should consist of two terms. The first term describes the qualitative or quantitative difference between the actual and reference signals. The second term defines the propagation path of the Lamb wave and assigns the computed value of the DI. In a two-dimensional case, the DI can be defined as follows:

$$DI(x,y) = \left(1-\lambda_{fg}\right)\left(\frac{\beta - R(x,y,x_a,y_a,x_s,y_s)}{\beta - 1}\right) \tag{2}$$

$$R(x,y,x_a,y_a,x_s,y_s) = \begin{cases} R_c(x,y,x_a,y_a,x_s,y_s), & R_c(x,y,x_a,y_a,x_s,y_s) < \beta \\ \beta, & R_c(x,y,x_a,y_a,x_s,y_s) \geq \beta \end{cases} \tag{3}$$

$$R_c(x,y,x_a,y_a,x_s,y_s) = \frac{\sqrt{(x-x_a)^2+(y-y_a)^2}+\sqrt{(x-x_s)^2+(y-y_s)^2}}{\sqrt{(x_a-x_s)^2+(y_a-y_s)^2}} \tag{4}$$

where $\lambda_{fg}$ is the normalized correlation factor; $x_a$, $y_a$ are the coordinates of the activator; $x_s$, $y_s$ are the coordinates of the sensor; and β is a parameter which determines the width of the propagation path. It is convenient to mark each propagation path as follows: A1- S1, A1 - S2, etc. Moreover, in cases a), b) and c), the line which links the position of the activator and the sensor goes through the cutout. Thus, in these cases, the coordinates of the activator are changed. Now, it is the point where the line passing through the sensor is tangent to the edge of the hole. The modified propagation path is shown in Fig. 4.

Having prepared the damage indexes for all possible propagation paths, the resultant value is evaluated according to the following formula:

$$DI^{RES}(x,y) = \sum_{k=1}^{M} DI(x,y)^{A_m - S_k} \tag{5}$$

where the superscript m denotes the considered case, i.e. a), b), c) or d). Finally, the additional path $L^{ADD}$ is introduced. This path begins at the point which belongs to the edge of the hole and where the appearance of the crack is most likely. This path is oriented strictly in the vertical direction. This is the expected direction of the damage evolution. Additionally, it is assumed that the value of the DI=1. In order to estimate the crack length $L^{CRK}$, the following computation has to be carried out:

$$L^{CRK} = DI^{RES}(x,y) \cap L^{ADD} \tag{6}$$

Further, it is convenient to introduce a threshold value α. If the value of the parameter $L^{CRK}$ is greater than α, the $L^{CRK}$=1, otherwise $L^{CRK}$=0. The last substitution allows precise estimation of the crack length. The main idea of the described algorithm for the discussed cases is depicted in Fig. 4.

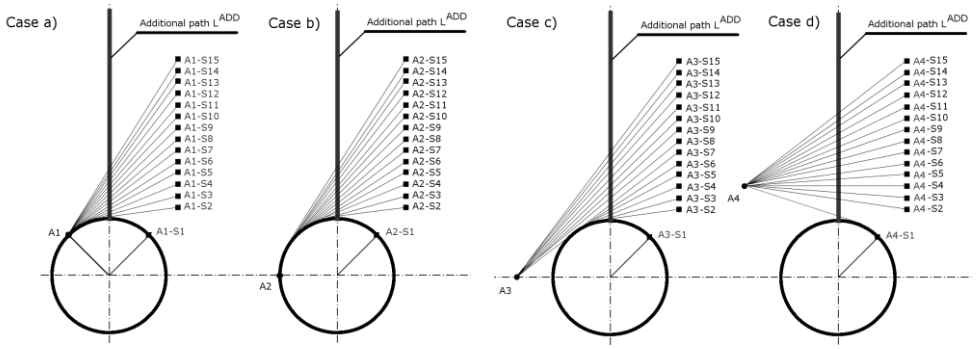


**Figure 4.** The propagation paths and the additional path (expected crack direction)

## 5. Finite element model

The mesh size strongly depends on the excited signal and the length of the propagating wave. Due to the assumed level of simplicity of the numerical simulation, it is assumed that the wave is excited by the point force (normal to the surface of the plate) acting in the selected node. Therefore, it can be considered that only the antisymmetric mode $S_0$ of the Lamb wave is excited. The input signal is described by the following equation:

$$F(t) = \begin{cases} \frac{1}{2} F_0 \left[ 1 - \cos\left( \frac{2\pi f_0 t}{n_0} \right) \right] \cos(2\pi f_0 t), & t \le \frac{n_0}{f_0} \\ 0, & t > \frac{n_0}{f_0} \end{cases} \tag{7}$$

where $F_0$=1[N] is the amplitude of the applied force, $f_0$=250[kHz] is the frequency, and $n_0$=5 is the number of wave packages. The wave speed in the studied plate can be estimated as follows:

$$v_{wave} = \sqrt{\frac{E}{\rho}} \tag{8}$$

Now it can be calculated that the wave length λ=20.294[mm]. It is worth stressing here that the chosen frequency $f_0$ of the excited signal causes the wave length λ to be much shorter than the shortest distance between the activator and the sensor. It is very convenient when the picked up signal has to be interpreted as the incident or reflected wave.

It is well known that in order to obtain reasonable results of the FE simulation there should be more than about 10 nodes per wave length. Therefore, it is assumed that the approximate element size $l_e \approx 2$[mm] is a parameter of the automatic mesh generator. The simulations are carried out with the use of the commercial FE system ANSYS 12.1. The analyzed plate is considered as a shell structure. Thus, the standard SHELL281 element is applied. This element has a quadratic shape function (higher order element) and in each node has 6 degrees of freedom: 3 transitional and 3 rotational ones. The element stiffness matrix is defined according to the first order shear deformation theory. The generated mesh consists of square-shape elements. Generally, the mesh is regular. However, in the vicinity of the cutout the mesh is irregular. In Fig.5 a part of the FE mesh in the vicinity of the hole is shown. The mesh consists of 16852 shell elements.

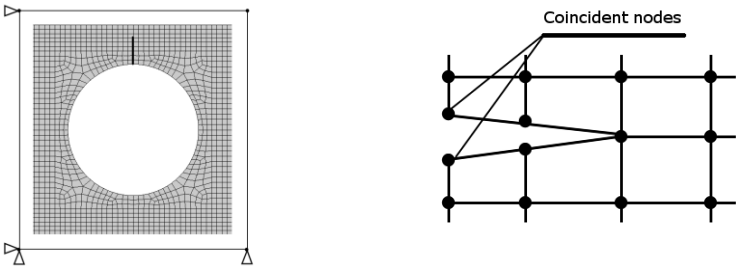


**Figure 5.** Part of the finite element mesh and the way of crack modelling by the coincident nodes.

The crack is modelled by the introduction of the coincident nodes. In other words, the nodes which belong to the crack are duplicated and their positions overlap each other. The idea of this approach is presented in Fig. 5. The plate is supported in the corners, as shown in Fig. 5, which makes the rigid motion of the structure impossible. Additionally, in all four corners, the possibility of motion in the direction perpendicular to the surface of the plate is also constrained.

## 6. Results and discussion

A comparison of the received signals recorded by sensors S2, S5, S8, and S11 for intact and damaged structures is shown in Fig. 6. The numerical simulation is carried out in case a), where the assumed crack length is equal to $l_c$=10[mm] (Fig.4a). In other studied cases, the results of the numerical

simulation are similar. It is worth stressing that the presence of the crack causes mainly the reduction of the amplitude of the received signal. Moreover, the signal obtained for the damaged structure is shifted in phase in comparison with the intact structure. The change of the phase is significant in the cases when the propagation path goes through the crack. For other propagation paths, the reduction of the amplitude is mainly observed. The use of Fourier's transformation (not presented in this paper) shows that the frequencies of the analyzed signals are almost identical. In other words, the existence of the damage does not change the frequency of the applied signal. It should also be stressed that the main disadvantage of the linear correlation coefficient (1) is that it is very sensitive to the change of the phase in contrast to the reduction of the amplitude. Therefore, the comparison of the signals recorded for the intact and damaged structures may not be quite effective.

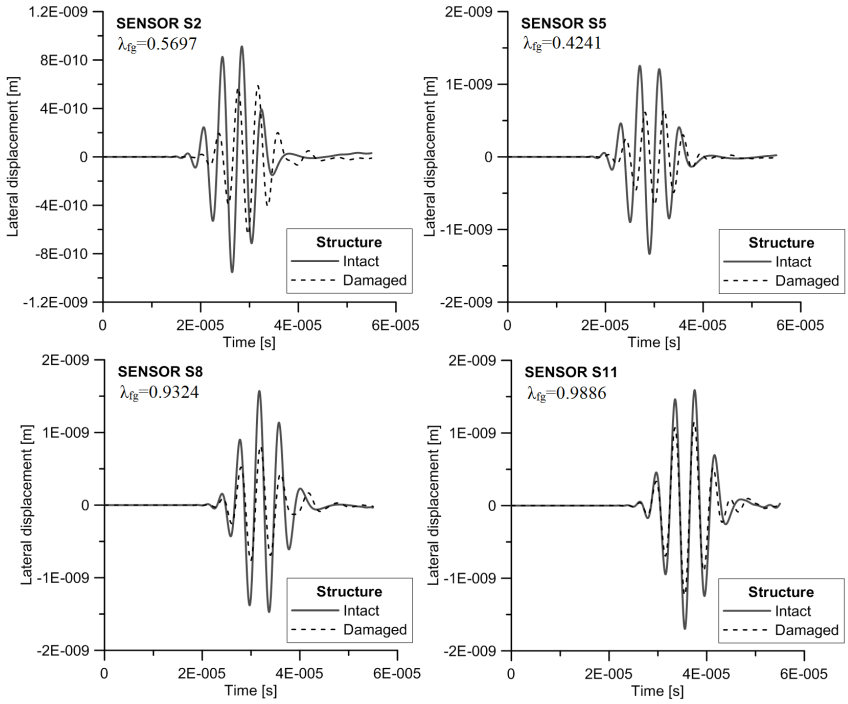


**Figure 6.** Registered signals for intact and damaged structures, sensors S2, S5, S8, S11.

Fig. 6 also presents normalized values of the linear correlation coefficient. In this particular case the obtained values of $\lambda_{fg}$ differ significantly for sensors S2 - S7. However, the values of $\lambda_{fg}$, computed for sensors S8 - S15 are close to unity $\lambda_{fg} \approx 1$. Thus, this fact could be used to evaluate the actual length of the crack. Then, the question where the most effective position of the actuator is arises. In order to find the answer to this question, four different locations of the actuator are studied, as it is presented in Fig. 4. The results obtained with the use of the algorithm discussed in Chapter 4 of this paper are

presented in Fig. 7. The normalized values of the relationship (6) along the additional path $L^{ADD}$ are also shown in Fig.7. The origin of the global coordinate system is in the geometrical center of the studied plate. The intersection point of the edge of the hole and the additional path $L^{ADD}$ has a vertical coordinate y=0.025[m]. For example, the crack tip of the length $l_c$=5[mm] has the vertical coordinate 0.03[m]. The discussed graphs also present the optimal values of the threshold α in particular cases.

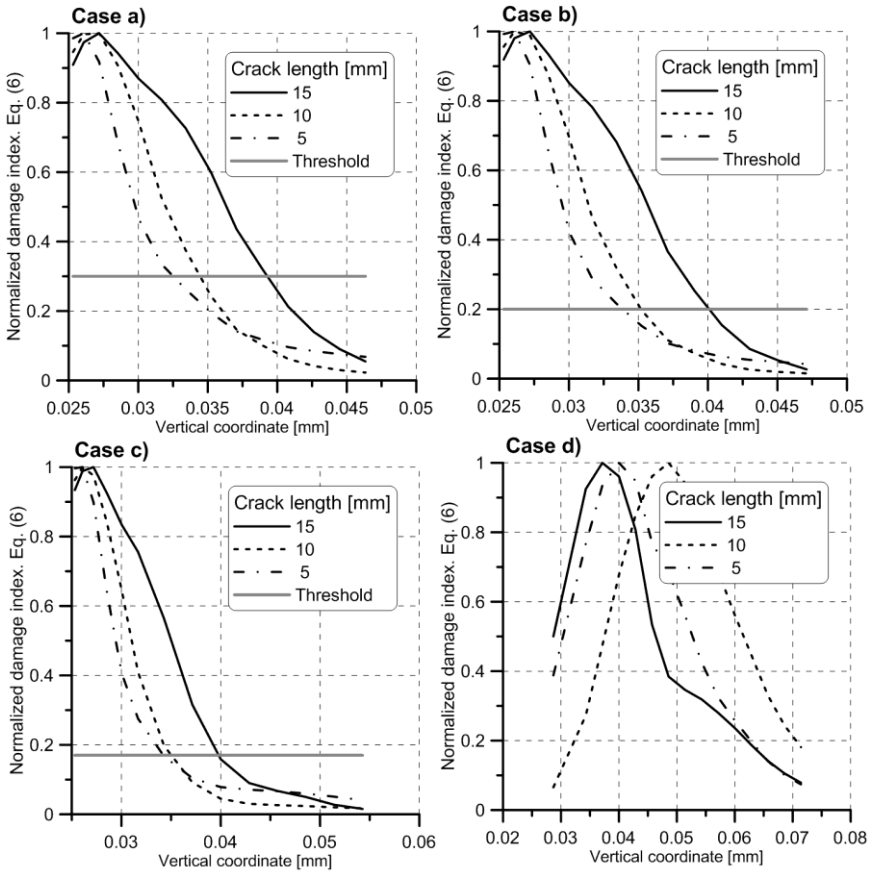


**Figure 7.** Registered signals for intact and damaged structures, sensors S2, S5, S8, S11.

It seems that in case a) the obtained results are most reasonable. For the threshold α=0.3, the length of the longer crack ($l_c$=10[mm], 15[mm]) is precisely estimated. However, in the case of the smaller crack $l_c$ < 5[mm], the length of the crack is overestimated. In case b), although the value of the threshold is different, i.e. α=0.2, the overestimation of the length of the small crack is more significant. The same effect can be observed in case c), where α=0.17. In contrast to the previous results, the curves which can be observed in case d) seem to be useless. Therefore, it is impossible to estimate the length of the crack taking into account the results obtained in case d).

It seems that the major improvement of the efficiency of the proposed method can be achieved by the changing of the method of signal analysis for the intact plate and the plate with crack. The value of the proposed linear correlation factor varies significantly due to shift in phase of the received signals. In the other hand the linear correlation factor is insensitive on the reduction of the amplitude as in the case of the plate with crack. Thus, according to the authors experience, it is necessary to find the method of the signal analysis, which is equally sensitive on the shift in phase as well as amplitude reduction of the received signals.

## 7. Conclusion

The authors of the paper look for the most effective position of the actuator. Four different positions are studied. The most reasonable estimation of the crack length is obtained when the actuators are placed on the edge of the circular hole - cases a) and b). If the actuators are installed at some distance from the edge, the estimation of the damage size is inaccurate or even impossible. The main disadvantage of the studied approach is connected with the use of the linear correlation coefficient, which is very sensitive to the change of the phase of the compared signals. The reduction of the amplitude does not cause significant variations of the linear correlation coefficient. It is very important since both effects are observed in performed numerical simulations.

## References


[1] Rytter, A., *Vibration based inspection of civil engineering structures*, Ph.D. Dissertation, Department of Building Technology and Structural Engineering/ Aalborg University, Denmark, 1993.

[2] Park, G., Muntges, D. E., Inman, D. J., Self-Monitoring and Self-Healing Jointed Structures, Damage Assessment of Structures, *Key Engineering Materials* 204-205, (2001), 75-84.

[3] Achenbach, J.D., *Wave propagation in elastic solids*, North-Holland Publ. Co., New York, 1984.

[4] Rose, J. L., *Ultrasonic waves in solid media*, Cambridge University Press, 1999.

[5] Viktorov, A., *Rayleigh and Lamb waves - physical theory and applications*, Plenum Press, New York, 1967.

[6] Lamb, H., On waves in an elastic plate, *Proceedings of the Royal Society, A Mathematical, Physical and Engineering Sciences* 93, (1917), 114-128.

[7] Lord Rayleigh, On Waves Propagated along the Plane Surface of an Elastic Solid, *Proceedings of the London Mathematical Society* s1-17 (1), (1885), 4-11.

[8] Su, Z., Ye L., *Identification of damage using Lamb waves*, Springer, 2009.

[9] Rose, J. L., Avioli M. J., *Elastic waves analysis for broken rail detection*, 15th World Conference on Non-Destructive Testing, Rome, (2000).

[10] Haig, A. G., Mudge, P., Balachandran W., *Advanced transducer development for long range ultrasonic inspection systems*, Proceedings of the 4th International Conference on Emerging Technologies in Non-Destructive Testing, (2008), 79 - 82.

[11] Li, J., Rose J. L., Excitation and propagation of non-axisymmetric guided waves in a hollow cylinder, *Journal of Acoustical Society of America* 109, (2001), 457 - 464.

[12] Diamanti, K., Soutis, C., Structural health monitoring techniques for aircraft composite structures, *Progress in Aerospace Sciences* 46(8), (2010), 342 - 352.

[13] Hedl, R., Finda, J., Parthasarathy, G., *Advanced approach for multi-site damage monitoring on aircraft fuselage panel using sparse PZT actuator/sensor arrays*, Structural Health Monitoring 2011: Condition Based Maintenance and Intelligent Structure - Proceedings of the 8th International Workshop on Structural Health Monitoring vol. 1., 2011, 643 - 650.

[14] Saravanos, D. A., Heyliger, P. R., Coupled layerwise analysis of composite beams with embedded piezoelectric sensors and actuartors, *Journal of Intelligent Material Systems and Structures* 6, (1995), 350 - 362.

[15] Saravanos, D. A., Birman, V., Hopkins, D. A., *Detection of delamination in composite beams using piezoelectric sensors*, Proceedings of the 35th Structures, Structural Dynamics and Materials Conference of the AIAA, 1994.

[16] Wu, T.T., Liu, Y. H., On the measurement of anisotropic elastic constants of fiber-reinforced composite plate using ultrasonic bulk wave and laser generated Lamb wave, *Ultrasonics* 37(6), (1999), 405 - 412.

[17] Moreno, E., Acevedo P., Thickness measurement in composite materials using Lamb waves, *Ultrasonics* 35, (1998), 581 - 586.

[18] Grondel, S., Assad, J., Delebarre, C., Blanquet, P., Moulin E., The propagation of lamb waves in multilayered plates: phase velocity measurement, *Measurement Science and Technology* 10(5), (1999), 348-353.

[19] Chang, Z., Mal A., Scattering of Lamb waves from a rivet hole with edge cracks, *Mechanics of Materials* 31, (1999), 197 - 204.

[20] Fromme, P., Sayir, M. B., Detection of cracks at rivet holes using guided waves, *Ultrasonics* 40, (2002), 199 - 203.

[21] Grahn T., Lamb wave scattering from a circular partly through-thickness hole in a plate, *Wave Motion* 37, (2003), 63 - 80.

[22] Hong, M., Su, Z., Lu, Y., Sohn H., Qing X., Locating fatigue damage using temporal signal features of nonlinear Lamb waves, *Mechanical Systems and Signal Processing* 60 - 61, (2015), 182 - 197.

[23] McKeon, J. C. P., Hinders, M. K., Lamb wave scattering from a through hole, *Journal of Sound and Vibration* 224(5), (1999), 843 - 862.

Marek Barski, PhD: Cracow University of Technology /Faculty of Mechanical Engineering /Institute of Machine Design, al. Jana Pawła II 37, 31-864 Kraków, Poland (*mbar@mech.pk.edu.pl*). The author gave a presentation of this paper during one of the conference sessions.

Adam Stawiarski, Ph.D.: Cracow University of Technology /Faculty of Mechanical Engineering /Institute of Machine Design, al. Jana Pawła II 37, 31-864 Kraków, Poland (*asta@mech.pk.edu.pl*).

Piotr Pająk M.Sc. (Ph.D. student): Cracow University of Technology /Faculty of Mechanical Engineering /Institute of Machine Design, al. Jana Pawła II 37, 31-864 Kraków, Poland (*ppajak@mech.pk.edu.pl*).

# Nonlinear normal modes for unbalanced mass of vertical conveyer-elevator (NUM069-15)

Hüseyin Bayıroğlu

*Abstract:* In the area of mechanics and electronics, the behaviors of the mechanical systems under periodic loadings have been examined by many researchers. Vertical conveyers are effective examples observing various kinds of parameters of this problem. The elevator has a cylindrical casing, a helical open trough or closed pipe is attached at the outside or at the inside of the vertical tubular casing, along which the load can be transported from the bottom upwards. A vibration-exciting drive is mounted at the top or bottom of the casing to impart to the latter directed vibrations along and around the vertical axis, which cause the load to move upwards along the helix. In this work, nonlinear normal modes and stability analysis has been shown graphically in Mathematica software.

## 1. Introduction

The vibrating model of the conveyer excited by the rotation of four equal unbalanced masses is shown in Figure 1. We consider mathematical model with spring of cubic nonlinearity and linear damping.

A practical difficulty with unbalanced mass exciters, observed as early as 1904 by A Sommerfeld, is that local instabilities may occur in operating speed of such devices. Presented an overview of the main properties of nonideal vibrating systems by Balthazar, et al. [1,2].

Linear or non-Linear excited vibrations have been examined by many authors in the current literature, as an example, the physical model of the ideal vibrating system consists of linear spring and sinusoidal excitation (ideal source) [3] and the physical model of the vibrating system consists of a cubic non-linear spring and non-ideal exciters [4].

Nonlinear normal vibrations modes (NNMS) are a generalization of the normal vibrations in linear systems. In the normal vibration mode, a finite degree-of-freedom system vibrates like a single-degree-of-freedom conservative one. The damping is large or represented by nonlinear functions then the response of the system may depend not only on the displacement but also on velocities Rosenberg and Vakakis [5,6,7,9,10]. In the case of a nonlinear autonomous coupled self-exited system, the method of nonlinear normal modes proposed by Shaw and Pierre [8]. In this paper, we characterized the dynamic behavior of a non-ideal torsional machine suspension structure. We use nonlinear normal modes but before a nonideal analysis to obtain chaos, instability, and so on. We use the invariant

manifold approach for NNMs technic. Such a manifold is invariant under the flow (i.e., orbits that start out in the manifold remain in it for all time), which extends the invariance property of LNMs to nonlinear systems. In order to parametrize the manifold, a single pair of states variables (i.e., both the displacement and the velocity ) are chosen as master coordinates, the remaining variables being functionally related to the chosen pair. Therefore the system behaves likes a nonlinear single-dof system on the manifold [11,12].

## 2. Governing Equations:

The equation of motion may be obtained by using Lagrange's equations

$$\frac{d}{dt}(\frac{\partial T}{\partial \dot{q}_i}) - \frac{\partial T}{\partial q_i} + \frac{\partial U}{\partial q_i} = Q_i \tag{1}$$

Here, $T$ is the kinetic energy $U$ is the potential energy, Q is the generalized force, they are given by

$$T = \frac{1}{2} m \dot{z}^2 + \frac{1}{2} J \dot{\theta}^2 \tag{2}$$

$$U = k_1 \left( Lz^2 + R^2 + 2L * z + z^2 - 2R\cos(\theta) R_1 + R_1^2 \right) + \frac{1}{2} \left( -2gmz + k_2 \left( Lz^2 + R^2 + 2Lzz + z^2 - 2R\cos(\theta) R_1 + R_1^2 \right)^2 \right) \tag{3}$$

$$Q_z = \sum M_z \tag{4}$$

$$Q_\theta = \sum M_\theta \tag{5}$$

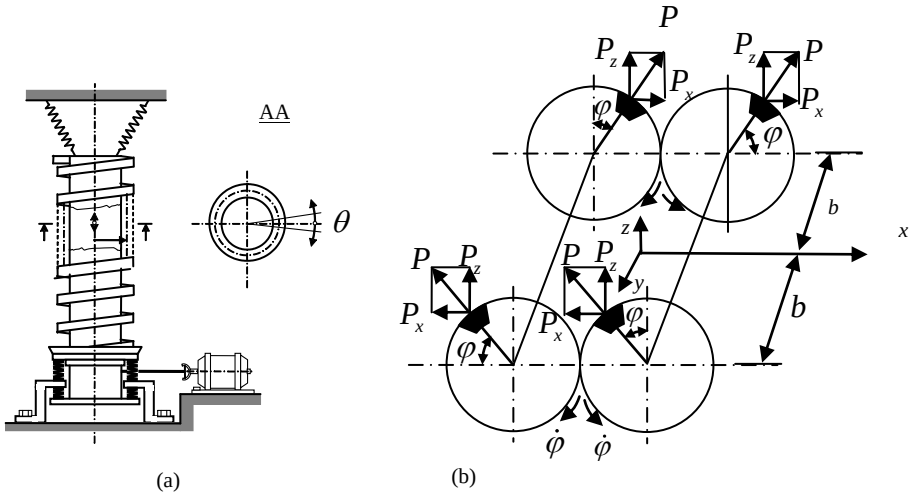


(a) (b)

**Figure 1.** (a) Vertical shaking conveyer, (b) Four unbalanced mass.

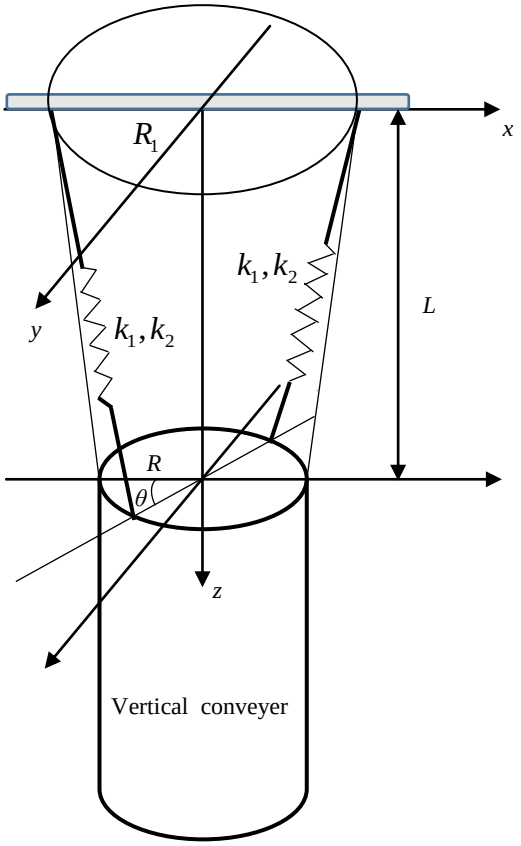


**Figure 2.** Vertical shaking conveyer for analysis nonlinear normal modes.

Where, the constants $k_1$ and $k_2$ are the elastic linear and non-linear coefficients of the springs respectivle, $g$ is acceleration due to gravity, $m$ is the mass of the conveyer and $J$ is the inertial moment of the conveyer about vertical $z$ axes (see Figure 2) , $R$ is the radius of the conveyer cylinder $\varphi$ is the angle of the rotation of the shaft carrying unbalanced mass, $\theta$ is the angle of the rotation of the conveyer cylinder about $z$ axes, $\sum P_z$ is the total forces of these 4 unbalanced masses, $\sum M_z$ is the total moment about the axes of the conveyer of these forces.

These four disks should be rotate synchronously in order to make same angle between the unbalanced masses on the crossing disks in (Figure 1b). This situation is provided by the gears. The force due to the inertia of the unbalanced masses applied to the system is written as

$$P = m_0 r_0 \Omega^2 \tag{6}$$

Where $m_0$, $r_0$, $\Omega$ are the unbalanced mass, radius of the unbalanced mass and angular frequency of the unbalanced mass respectively, and $b$ is the distance of these four disks from the z axes,

The total generalized forces of these 4 unbalanced masses are computed as,

$$Q_z = 2m_0 r_0 \Omega^2 (\cos\Omega t + \sin\Omega t) \tag{7}$$

$$Q_\theta = 2m_0 r_0 b \Omega^2 (\cos\Omega t + \sin\Omega t) \tag{8}$$

$q_i$ is the generalized coordinates. Lagrange's equation of motion for the coordinates $q_1 = z$, $q_2 = \theta$ can be written as

$$-gm - 4Lk_2R_1R\cos\theta + 2L[k_1 + k_2(Lz^2 + R^2 + R_1^2)] + 2z[k_1 + z(3Lz + z)k_2 - 2k_2R_1R\cos\theta + k_2(3Lz^2 + R^2 + R_1^2)] + m\ddot{z} = 2m_0 r_0 \Omega^2 (\cos\Omega t + \sin\Omega t) \tag{9}$$

$$2R_1R[k_1 + k_2(2L + z)z - 2k_2R_1R\cos\theta + k_2(Lz^2 + R^2 + R_1^2)]\sin\theta + J\ddot{\theta} = 2m_0 r_0 b \Omega^2 (\cos\Omega t + \sin\Omega t) \tag{10}$$

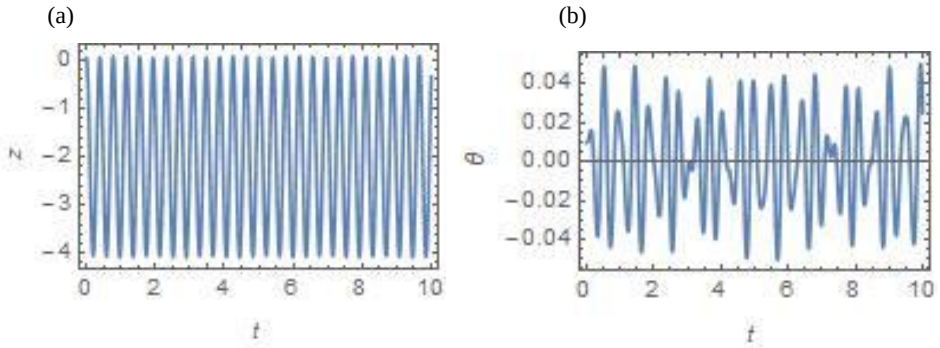


Time histories in physical coordinates for conveyer, a) vertical displacement b) angular displacement.

Figure 3 is obtained by using (Eq. 9), (Eq.10). This figure shows time histories in physical coordinates $(z,t)$ and $(\theta,t)$ for this conveyer. Time histories of $x$ and $\theta$ generated for initial conditions $z(0) = 0.05m$, $\dot{z}(0) = 0$, $\theta(0) = 0.01rad.$, $\dot{\theta}(0) = 0$ are presented in Figure 3(a) and (b).

Figure 4 shows a representetive bifurcation diagram which is obtained by solving numericaly from (Eq.9), (Eq.10).

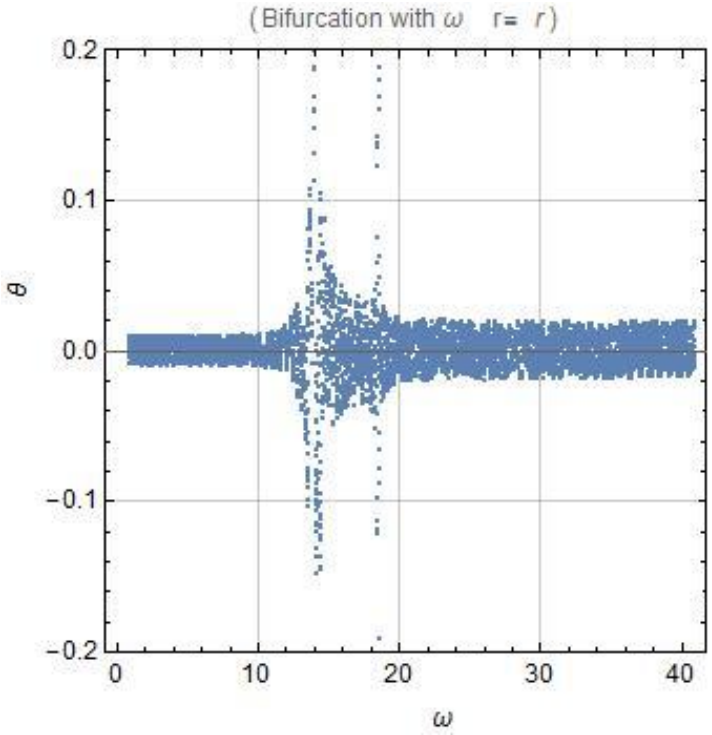


**Figure 3.** Bifurcation diagram for conveyer vibration.

If $\sin\theta$ and $\cos\theta$ are expanding Taylor series and getting 3 terms in equations (9),(10) we get,

$$-2(L+z)k_1 - 2(L+z)k_2[L^2+R^2+2L\,z+z^2+R_1R(-2+\theta^2)+R_1^2] - m(g+\ddot{z}) = 0 \tag{11}$$

$$\begin{aligned}&\frac{1}{3}\{-R\theta(-6+\theta^2)k_1R_1 - R\theta k_2R_1[-6R^2-6z^2+R^2\theta^2+Lz^2(-6+\theta^2)+\\&2L\,z(-6+\theta^2)+4R_1R(3-2\theta^2)+R_1^2(-6+\theta^2)]+3J\ddot{\theta}\} = 0\end{aligned} \tag{12}$$

Assuming that nonlinear terms are zero, we get a linear conservative system and natural frequencies as follows.

$$-gm - 2Lk_1 - 2Lk_2[L^2+(R-R_1)^2] - 2[k_1+k_2(3L^2+(R-R_1)^2)]z - m\ddot{z} = 0 \tag{13}$$

$$2R_1R\{k_1+k_2[L^2+(R-R_1)^2]\}\theta + J\ddot{\theta} = 0 \tag{14}$$

$$\lambda_1 = \frac{2\left(k_1+k_2\left(3L^2+(R-R_1)^2\right)\right)}{m}, \quad \lambda_2 = \frac{2R\left(k_1+k_2\left(L^2+(R-R_1)^2\right)\right)R_1}{J} \tag{15}$$

$$\omega_1 = \sqrt{\lambda_1}\ , \quad \omega_2 = \sqrt{\lambda_2} \tag{16}$$

Where $\omega_1$ and $\omega_2$ conservative linearized system.

**Table 1.**

| $k_1$ $N/m$ | $k_2$ $N/m$ | $R_1$ $m$ | $R$ $m$ | $L$ $m$ | m | $\omega$ $rad/s$ | $J$ $kg.m^2$ | $g$ m/ $s$ | $\omega_1$ $rad/s$ | $\omega_2$ $rad/s$ |
|---|---|---|---|---|---|---|---|---|---|---|
| 10000 | 1000 | 0.8 | 0.5 | 2 | 10 | 10 | 2 | 9.81 | 15.01 | 21.02 |

Table 1. Shows numerical values for Figures (3)-(7).

## 3. Nonlinear normal modes

For the nonlinear normal modes formulations the set of equations (eq.9), (eq.10) is rewritten in the form [11, 12],

$$\dot{x}_1 = y_1 \qquad \dot{y}_1 = f_1(x_1, y_1, x_2, y_2) \tag{17}$$

$$\dot{x}_2 = y_2 \qquad \dot{y}_2 = f_2(x_1, y_1, x_2, y_2) \tag{18}$$

It can be chosen master coordinates as

$$x_1 = u \qquad y_1 = v \tag{19}$$

İt can be expressed slaved coordinates as

$$x_2 = X_2(u,v) \qquad y_2 = Y_2(u,v) \tag{20}$$

The functions $X_2(u,v)$, $Y_2(u,v)$ are constraint equations and they represent, the so called, model surfaces. It can be used the invariant manifold technique to eliminate time dependence.

$$Y_2(u,v) = \frac{\partial X_2(u,v)}{\partial u} v + \frac{\partial X_2(u,v)}{\partial v} f_1(u,v,X_2(u,v),Y_2(u,v)) \tag{21}$$

$$f_2(u,v,X_2(u,v),Y_2(u,v)) = \frac{\partial Y_2(u,v)}{\partial u} v + \frac{\partial Y_2(u,v)}{\partial v} f_1(u,v,X_2(u,v),Y_2(u,v)) \tag{22}$$

It can be approximated a local solution using polynomial expansion of $X_1$ and $X_2$ in term of u and v.

$$X_2 = a_1 u + a_2 v + a_3 u^2 + a_4 uv + a_5 v^2 + a_6 u^3 + a_7 u^2 v + a_8 uv^2 + a_9 v^3 \tag{23}$$

$$Y_2 = b_1 u + b_2 v + b_3 u^2 + b_4 uv + b_5 v^2 + b_6 u^3 + b_7 u^2 v + b_8 uv^2 + b_9 v^3 \tag{24}$$

$$\begin{aligned} \dot{X}_2 = {} & a_1 u' + a_2 v' + 2a_3 uu' + a_4 uv' + a_4 u'v + 2a_5 vv' + 3a_6 u^2 u' + 2a_7 uu'v + a_7 u^2 v' + \\ & a_8 u'v^2 + 2a_8 uvv' + 3a_9 v^2 v' \end{aligned} \tag{25}$$

$$\dot{Y}_2 = b_1u' + b_2v' + 2b_3uu' + b_4uv' + b_4u'v + 2b_5vv' + 3b_6u^2u' + 2b_7uu'v + b_7u^2v' + b_8u'v^2 + 2b_8uvv' + 3b_9v^2v' \quad (26)$$

Considering the above expressions, the last equations of (Eq.17), (Eq18) and going back to the original notation it can be get

$$y_2 = a_1y_1 + a_2f_1 + 2a_3x_1y_1 + a_4x_1f_1 + a_4y_1^2 + 2a_5y_1f_1 + 3a_6x_1^2y_1 + 2a_7x_1y_1^2 + a_7x_1^2f_1 + a_8y_1^3 + 2a_8x_1y_1f_1 + 3a_9y_1^2f_1 + \ldots \quad (27)$$

$$f_2 = b_1y_1 + b_2f_1 + 2b_3x_1y_1 + b_4x_1f_1 + b_4y_1^2 + 2b_5y_1f_1 + 3b_6x_1^2y_1 + 2b_7x_1y_1^2 + b_7x_1^2f_1 + b_8y_1^3 + 2b_8x_1y_1f_1 + 3b_9y_1^2f_1 + \ldots \quad (28)$$

then it can be substitute (Eq. 23), (Eq. 24), (Eq. 25) and (Eq. 26) into functions $f_1(x_1,y_1,x_2,y_2) = f_1(u,v,X_2(u,v),Y_2(u,v))$, $f_2(x_1,y_1,x_2,y_2) = f_2(u,v,X_2(u,v),Y_2(u,v))$ in (Eq.28), (Eq. 28). From (Eq.18), we obtain

$$y_2 - \dot{x}_2 = 0 \qquad f_2(x_1,y_1,x_2,y_2) - \dot{y}_2 = 0 \quad (29)$$

Thus, grouping the terms of (Eq.29) in a proper order with respect to the master coordinates, we receive a set of two equations composed of the terms: $u, v, u^2, uv, v^2, u^3, u^2v, uv^2, v^3$. Terms of higher order are truncated from the expansions. We get a set of eighteenth algebraic nonlinear equations with eighteen unknown parameters $a_1,\ldots,a_9$, $b_1,\ldots,b_9$.

After application of the decoupling procedure, we get a differential equation for the two non-linear oscillators:

mod 1

$$\ddot{u}_1 + 225.44u_1 - 31.2191u_1^3 - .001008u_1\dot{u}_1^2 + 0.0006u_1^2\dot{u}_1^2 + 0.0016835u_1^3\dot{u}_1^2 = 0 \quad (30)$$

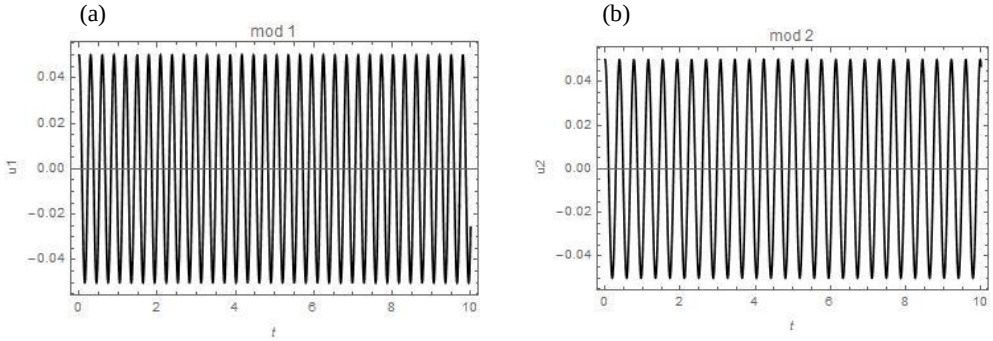


**Figure 4.** Time histories in normal coordinates, a) mod1 b) mod2

mod 2

$$\ddot{u}_2 + 441.8u_2 + 120u_2^2 + 20u_2^3 + 573.4 = 0 \tag{31}$$

Two extracted normal modes $u_1$ and $u_2$ are presented in Figure 4. The motion is very well separated.

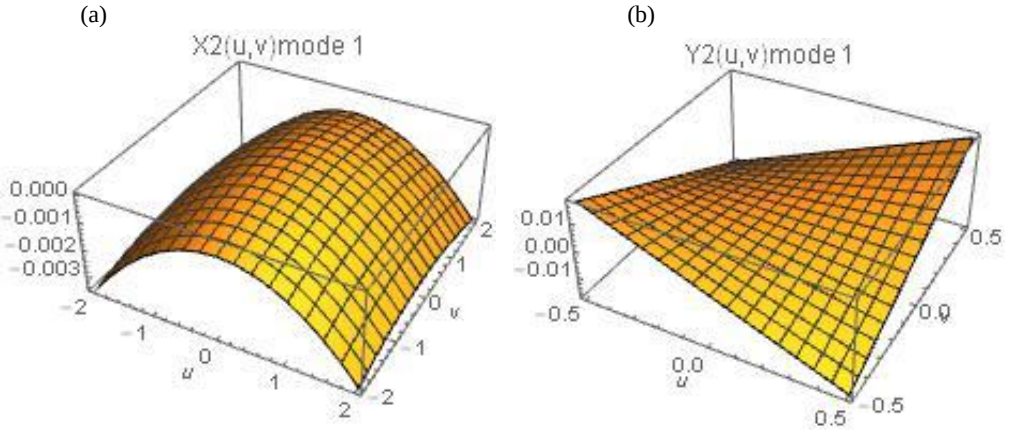


**Figure 5.** Nonlinear modal surfaces X2(u,v) and Y2(u,v) for mod1

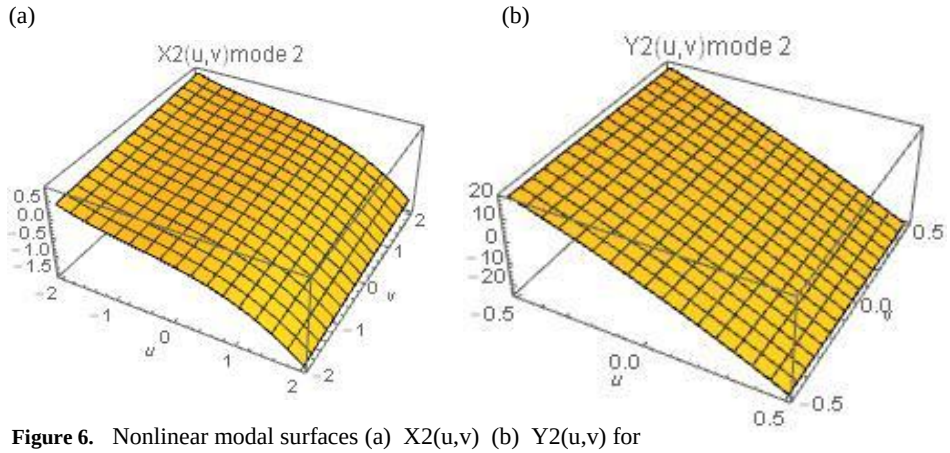


**Figure 6.** Nonlinear modal surfaces (a) X2(u,v) (b) Y2(u,v) for

The slave coordinates $x_2$ , $y_2$ are related with the master ones *u*, *v* by the model functions $X_2(u,v)$ , $Y_2(u,v)$ . These model surfaces for the first and secon modes, respectevly, are presented in Figure 5 and Figure 6. As a results from the above Figure (5), the nonnlinear model surfaces of the system strongly depend on the displacement and velocity for mod 1 but Figure 6(b), the nonnlinear model surfaces for system strongly depend on the displacement for mod 2.

## 4. Conclusions

The analysis presented in the paper concerns dynamic behavior of a non-ideal torsional machine suspension structure. Initially NNMs were defined as periodic solutions of the underlying conservative system, and continuation algorithms were recently exploited to compute them. We use nonlinear normal modes but before a non-ideal analysis to obtain chaos, instability, and so on. The NNMs are applied to decouple motion of the system.

A width of synchronization regions, near the principal parametric resonance fits very well to the regions found by numerical simulations, presented in the bifurcation, the nonnlinear model surfaces for the system mod1 strongly depend both on the displacement and velocity.

## References


[1] Balthazar, J.M., Brasıl, R. M. L. R. F., Weber, H. I., Fenili, A., Belato, D., Felix, J.L.P., Garzelli, F.J. A Review of New Vibration Issues due to Non-Ideal Energy Sources, CRC Press, LLC, (2004).

[2] Balthazar, J.M.,Mook, D.T., Brasıl, R. M. L. R. F., Weber, H. I., Fenili, A., Belato, D., Felix, F.J. An Overview on Non-Ideal Vibration, Mechanica, 38: 613-621, (2003).

[3] Spivakovsky, A.O.,Dyachkov, V.K. Conveying Machines, Mir Publichers Moscow, Volume 2 (1985).

[4] Bayıroğlu, H. Nonlinear analysis of unbalanced mass of vertical conveyer with Non-ideal Exciters, Applied Mechanics and Materials Vol 706 pp 35-43,2015.

[5] Rosenberg, R.M. Normal modes of non-linear dual-mode systems, *Journal of Applied Mechanics*, Ser. E, 27, 2, (1960), pp. 263-268.

[6] Rosenberg, R.M. Normal modes of non-linear dual-mode systems, *Journal of Applied Mechanics*, Ser. E, 27, 2, (1960), pp. 263-268.

[7] Vakakis, A.F. Non-linear normal modes (NNMs) and their applications in vibrations theory: an overview,Mechanical systems and signal and processing,11,1,3-22, 1997.

[8] Shaw S.W.,Pierre C., Normal modes for non-linear vibratory system, Journal of sound and vibrations, 164, 1, 85-124,1993.

[9] Kerschen G., Peeters M., Golinval J.C., Vakakis, A.F. Nonlinear normal modes, part I: Useful framework for the structural dynamicst, Mechanical Systems and Signal Processing, 23, 170-194, 2009.

[10] Vakakis, A.F. et al. Nonlinear Targeted Energy Transfer in Mechanical System and Structures Systems, *Springer*, New York, 2008.

[11] Warminsky, J. _Nonlinear normal modes of a self-excited system driven by parametric and external excitations**,** *Nonlinear Dyn 61DOI 10.1007/s11071-010-9679-5*, (2010), pp 677.

[12] Warminsky, J. Nonlinear Normal Modes of Coupled Self-Excited Oscillators In Regular And Chaotic Vibration Regimes, *Journal Of Theoretical And Applied Mechanics 46, 3*, Warsaw (2008), pp. 693-714.

Hüseyin Bayıroğlu, Assistant Professor: Yıldız Technical University, Yıldız Technical University ,34349, Istanbul, Turkey ( hbayir@yildiz.edu.tr) .

# Mechanics of terrestrial locomotion systems in application to mobile robots
## (MAT270-15)

Carsten Behn, Nikolai Bolotnik, Igor Zeidis, Klaus Zimmermann

*Abstract:* Locomotion has always exuded immense fascination. Matching nature's feats of efficiency, flexibility and speed has posed a challenge to engineers for centuries. Beside walking motion, which is still a major area of research (e.g., in humanoid robots), actually, increasing interest amongst the researchers is devoted to the concept of legless motion, as demonstrated by snakes and worms. Worm-like locomotion systems will prove an efficient form of locomotion in application to inspection of pipes or for rescue missions. In this paper, a number of issues related to the dynamics and control of artificial limbless locomotion systems are discussed. Simplest models of a limbless locomotor are two-body or three-body systems that move along a horizontal straight line. One class of systems is driven by harmonically varying forces acting between these bodies. Mechanisms of another type consist of a body with movable internal masses. The inertial masses interact with the body by means of forces generated and controlled by drives. The aim of these investigations is to answer the question whether the motion of a locomotion system with known resistance laws is possible in principle, and if so, what control algorithms for a given configuration can realize this locomotion. Based on the results, new operating principles for the locomotion are developed. The formulation of optimal gaits for these new principles is given. The working principles and control algorithms are tested using several prototypes of worm-like locomotion systems.

### 1. Introduction

Recent developments in mobile robotics show that, especially in medicine, for inspection technology and for urban search and rescue scenarios, locomotion systems are needed, which can move through narrow tubular and complex environments, i.e., blood vessels, pipelines and ruins. For such applications the systems should be characterized by a relatively small size and weight, as well as by the possibility to move autonomously. To realize such artificial locomotion systems, the research focus in mobile robotics has been shifted more and more towards limbless and compliant locomotion systems that are inspired by snakes, worms and similar biological objects [19,22,29]. Thus, this paper relates to the mechanics and control of worm-like locomotion systems [15,28,32]. A key issue of mechanics of limbless locomotion is the identification of conditions of the physical interaction between the locomotion system and the environment, subject to which the system can move progressively in the environment. If

the motion is possible, then the next question is finding out what gaits (i.e., specific control algorithms for the internal shape variables [24]) lead to an optimal locomotion, e.g. a motion with a maximal velocity of the center of mass.

Worm-like locomotion systems designed as a chain of links connected by powered prismatic and/or revolute joints are investigated in several publications [9, 31, 35]. The papers [31, 36] deal with the analysis of the rectilinear motion along a rough plane of chains of bodies (*discrete mass points*) interconnected by elastic elements in the case where the normal pressure does not change and the system is driven by harmonically varying forces acting between the bodies. The asymmetry in the force of friction is provided by the dependence of the coefficient of friction on the direction of the velocity of the systems components. This can be provided, for example, by covering the contact surfaces of the robot with scaly or pinned plates with an appropriate orientation of scales. Focusing on the aim of autonomous locomotion, the studies [30] and [33] present the idea of making an elastic element using smart materials (a magneto-sensitive elastomer [1]). The harmonically varying force is created through a controllable magnetic field. In [13, 14, 23], for a particular model, it was shown that a one-dimensional *distributed-mass locomotor* can move progressively in a viscous medium with linear rheology. The motion was excited by a periodic extension-contraction deformation wave travelling through the worm's body.

Mechanisms of another type consist of a body with movable internal masses [7, 8, 11, 16, 17, 26, 34]. The inertial masses interact with the body by means of internal forces generated and controlled by drives. When the control force is applied to an internal mass, the reaction force is applied to the body and changes its velocity, which affects the resistance force exerted on the body by the environment. The investigations in [8] deal with the motion of a single body with an unbalanced vibration exciter along a straight line on a rough horizontal plane. A difference in the coefficients of forward and backward friction was not assumed. The dynamic asymmetry was provided by the phase shift between the horizontal and vertical components of the driving force produced by the exciter. A mobile system that consists of two identical modules connected by a spring was considered in [34]. Each module contains an unbalanced vibration exciter. The exciters rotate with the same frequency in one direction but have a phase shift. It was shown, that when the excitation frequency passes through the resonance with the natural frequency of the system, the direction of the motion changes.

The issue of the optimal control of the motion of a body with movable internal masses was considered in [7, 10, 11, 18]. Adaptive control problems of finite degree of freedom worm-like locomotion systems which contact the ground with Coulomb dry friction are discussed in [2,3,5,6]. Gaits based on kinematic equations are tracked by means of adaptive controllers. In [20] an extended admissible control for a two piece worm with an asymmetric dry friction

model is presented. Control problems in connection with the realization of artificial worm prototypes are discussed in [12, 21, 25].

## 2. Mechanical model of the worm-like locomotion system and methods of investigation

The basic model for the investigations in the following sections is a chain of three identical bodies (particles) moving along a straight line on a rough horizontal plane (see figure 1). We number the particles by 1, 2, and 3 consecutively from the left to the right end of the chain. Let $x_1$, $x_2$, and $x_3$ denote the coordinates of the respective particles measured along the line of motion of the chain from a fixed point 0. The motion is excited and controlled by changing the distances $l_i(t)$ between the particles.

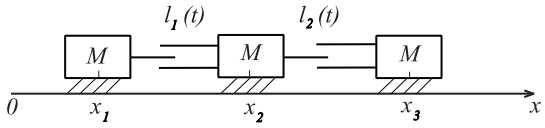


**Figure 1.** Three-body system with prismatic joints.

The medium acts on the $i$th particle with the force $F(\dot{x}_i)$, depending on the velocity $\dot{x}_i$ of this particle relative to the environment that is assumed to be unmoved in an inertial reference frame. The force $F$ is the force of friction between the particle and the medium.

By *viscous friction* we understand the resistance characterized by a continuously, monotonically decreasing function $F(\dot{x}_i)$, vanishing at $\dot{x}_i = 0$. A typical example of the viscous friction is the power-law friction characterized by

$$F(\dot{x}_i) = \begin{cases} \mu_-|\dot{x}_i|^\alpha & \text{if } \dot{x}_i \le 0, \\ -\mu_+|\dot{x}_i|^\alpha & \text{if } \dot{x}_i > 0, \end{cases} \tag{1}$$

where $\mu_-$ and $\mu_+$ are positive coefficients of friction resisting the leftward ($\dot{x} < 0$) and rightward ($\dot{x} > 0$) motion, respectively, and $\alpha > 0$ is the power exponent of the resistance law.

By *dry friction* we understand the resistance characterized by the law:

$$F(\dot{x}_i) = \begin{cases} k_-N, & \text{if } \dot{x}_i < 0 \text{ or } \dot{x}_i = 0, \text{ and } \Phi < -k_-N \\ -\Phi, & \text{if } \dot{x}_i = 0 \text{ and } -k_-N \le \Phi \le k_+N \\ -k_+N, & \text{if } \dot{x}_i > 0 \text{ or } \dot{x}_i = 0, \text{ and } \Phi > k_+N, \end{cases} \tag{2}$$

where $k_-$ and $k_+$ are the coefficients of dry friction at the leftward ($\dot{x} < 0$) and rightward ($\dot{x} > 0$) motion, respectively, $N$ is the force of normal pressure (in the case under consideration,

$N = mg$, where $g$ is the acceleration due to gravity), and $\Phi$ is the resultant of the forces, other than frictional ones, applied to the particle. The friction characterized by this law is sometimes called *Coulomb's anisotropic friction*. The classical Coulomb law is a particular case of equation (2) for $k_- = k_+$.

The motion of the chain is excited and controlled by changing the relative positions of the adjacent particles characterized by the differences

$$l_1 = x_2 - x_1, \quad l_2 = x_3 - x_2. \tag{3}$$

In what follows, the quantities $l_1$ and $l_2$ are assumed to be specified and prescribed as functions of time, which makes the system under consideration a single-degree-of-freedom system. We assume that the change in the relative positions of the particles in the chain is produced by forces of interaction between the particles, which are internal forces for the entire system. The only external forces acting on the system are the forces of friction. In what follows, we will be interested in the motion of the center of mass of the chain, which characterizes the motion of the system "as a whole". The absolute coordinate $X$ of the center of mass of the chain and its velocity $V$ are defined by

$$X = \frac{1}{3}\left(x_1 + x_2 + x_3\right), \quad V = \dot{X}. \tag{4}$$

The motion of the center of mass is governed by the equation

$$3M\dot{V} = F(\dot{x}_1) + F(\dot{x}_2) + F(\dot{x}_3), \tag{5}$$

where $M$ is the mass of each particle of the chain. Using equations (3) and (4), the coordinates $x_i$ of the particles can be expressed in terms of $X$ and $l_j$:

$$x_1 = X - \frac{2}{3}l_1 - \frac{1}{3}l_2, \quad x_2 = X + \frac{1}{3}l_1 - \frac{1}{3}l_2, \quad x_3 = X + \frac{1}{3}l_1 + \frac{2}{3}l_2. \tag{6}$$

Substituting these relations into (5) results the equation

$$3M\dot{V} = F\left(V - \frac{2}{3}\dot{l}_1 - \frac{1}{3}\dot{l}_2\right) + F\left(V + \frac{1}{3}\dot{l}_1 - \frac{1}{3}\dot{l}_2\right) + F\left(V + \frac{1}{3}\dot{l}_1 + \frac{1}{3}\dot{l}_2\right). \tag{7}$$

Introducing the dimensionless variables

$$t^* = \frac{t}{T}, \quad l_1^* = \frac{l_1}{L}, \quad l_2^* = \frac{l_2}{L}, \quad V^* = \frac{VT}{L}, \quad F^* = \frac{F}{F_0}, \tag{8}$$

where $T$ is the period of the functions $l_i(t)$, $L$ is a length characteristic of the change in the distances between the particles, and $F_0$ is a quantity that has a dimension of force and

characterizes the magnitude of the friction force. For the dry friction law of equation (2), it is reasonable to take $F_0 = \max(k_- N,\, k_+ N)$.

In what follows, we deal only with the dimensionless form of (7) and omit the asterisks identifying the dimensionless variables. The nondimensionalized equation (7) can be represented as

$$\begin{aligned} &\dot{V} = \varepsilon G(V,t), \\ &G(V,t) = \frac{1}{3}\left[F\left(V - \frac{2}{3}u_1(t) - \frac{1}{3}u_2(t)\right) + F\left(V + \frac{1}{3}u_1(t) - \frac{1}{3}u_2(t)\right)\right. \\ &\qquad \left. + F\left(V + \frac{1}{3}u_1(t) + \frac{2}{3}u_2(t)\right)\right], \end{aligned} \tag{9}$$

where

$$\varepsilon = \frac{F_0 T^2}{ML}, \quad u_i(t) = \dot{l}_i(t), \quad i = 1,\, 2. \tag{10}$$

If we assume the functions $l_i(t)$ are periodic (with period 1), the functions $u_i(t)$ are also periodic (with the same period) and have zero averages, i.e.,

$$\int_0^1 u_i(t)dt = 0, \quad i = 1,\, 2. \tag{11}$$

### 3. Undulatory excitation of motion

We consider the motion excited by a periodic change in the relative position of adjacent particles according to the law

$$l_i(t) = a\left(t + (i-1)\,\tau\right), \quad i = 1,\, 2, \tag{12}$$

where $a(z)$ is a periodic function and $\tau$ is a parameter of dimension of time. Equation (3) implies that the function $l_i(t)$ defines the motion of particle $i+1$ relative to particle $i$. We say that particles $i$ and $i+1$ form the $i$th pair of adjacent particles of the chain. From (12), it follows that the relative motion of particles in the $i$th pair repeats the relative motion of particles in the $(i+1)$st pair with a time shift of $\tau$. Expression (12) can be reduced to the relation

$$l_i(t) = f\left(i + \frac{t}{\tau}\right), \quad \text{where } f(z) = a\left(\tau\,(z-1)\right), \tag{13}$$

which describes a deformation wave running forward (for $\tau < 0$) or backward (for $\tau > 0$) through the chain with a velocity of $1/|\tau|$. For that reason, we call the excitation mode

defined by equation (12) and the corresponding motion of the chain the undulatory excitation and the undulatory motion, respectively.

For the three-body system subject to the undulatory excitation, $u_2(t) = u_1(t+\tau)$, and equation (2) becomes

$$\begin{aligned} &\dot{V} = \varepsilon G(V,t), \\ &G(V,t) = \frac{1}{3}\left[F\left(V - \frac{2}{3}u_1(t) - \frac{1}{3}u_1(t+\tau)\right) + F\left(V + \frac{1}{3}u_1(t) - \frac{1}{3}u_1(t+\tau)\right)\right. \\ &\qquad \left. + F\left(V + \frac{1}{3}u_1(t) + \frac{2}{3}u_1(t+\tau)\right)\right] \end{aligned} \tag{14}$$

If both distances $l_1(t)$ and $l_2(t)$ change synchronously, i.e., $\tau = 0$, and the function $F$ is odd, then $G(V,t) = F(V)/3$ and $F(0) = 0$. Hence, $V(t) \equiv 0$ is a solution of (14), and, due to the uniqueness theorem, the system cannot start moving from a state of rest. This implies, in particular, that locomotion of the system, the distances between the bodies of which change synchronously, is impossible for the case of isotropic friction ($\mu_- = \mu_+$ in equation (1) or $k_- = k_+$ in equation (2)).

## 4. Behavior of the system for the case of dry friction

We restrict the investigations to the case where the interaction between the bodies of the chain and the environment is characterized by the dry-friction law (2). Let the excitation law be specified by the functions $l_1(t)$ and $l_2(t)$ that are composed of parabolic segments and have continuous derivatives $u_1(t)$ and $u_2(t)$ defined by

$$\dot{l}_1(t) = u_1(t) = \begin{cases} 0, & 0 \le t \le \dfrac{1}{3}, \\ 2\,(3\,t-1), & \dfrac{1}{3} < t \le \dfrac{1}{2}, \\ -2\,(3\,t-2), & \dfrac{1}{2} < t \le \dfrac{5}{6}, \\ 6\,(t-1), & \dfrac{5}{6} < t \le 1\,. \end{cases} \qquad \dot{l}_2(t) = u_2(t) = \begin{cases} 6\,t, & 0 \le t \le \dfrac{1}{6}, \\ -2\,(3\,t-1), & \dfrac{1}{6} < t \le \dfrac{1}{2}, \\ 2\,(3\,t-2), & \dfrac{1}{2} < t \le \dfrac{2}{3}, \\ 0, & \dfrac{2}{3} < t \le 1. \end{cases} \tag{15}$$

The functions $u_1(t)$ and $u_2(t)$ are plotted in figure 2 by the solid and dashed curves, respectively. They are equal to zero on an interval of length 1/3 and are shifted in time by this quantity relative to one another. For this excitation mode, the parameter $\tau$ occurring in equation (12) is equal to 1/3.

We assume that the parameter $\varepsilon$ is small ($\varepsilon \ll 1$) and average the right-hand side of

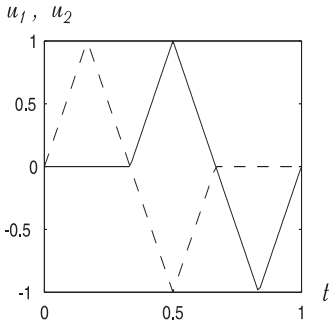


**Figure 2.** The function $u_1(t)$ (sol. line), $u_2(t)$ (dott. line).

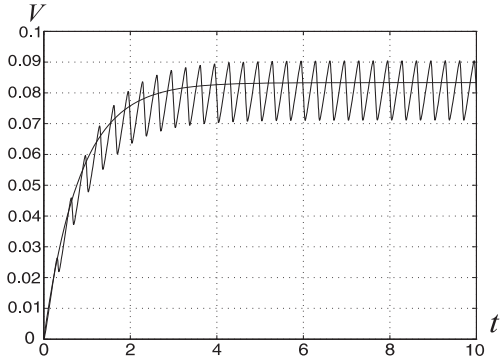


**Figure 3.** Solutions of the exact and the averaged equations for dry friction.

equation (9) with respect to the explicit time to obtain the time-invariant averaged equation

$$\frac{dV}{dt} = \frac{\varepsilon}{3} \begin{cases} 3\,, & V \le -\frac{2}{3}\,, \\ 2-\mu-\frac{3}{2}V\,(1+\mu), & -\frac{2}{3} < V \le 0\,, \\ 2-\mu-6\,V\,(1+\mu)\,, & 0 < V \le \frac{1}{3}\,, \\ -3\,\mu\,, & V > \frac{1}{3}\,, \end{cases} \tag{16}$$

where $\mu = \frac{k_+}{k_-} \ge 0$.

We solve equation (16) with the initial condition $V(0)=0$. If $\mu = 2$ (the coefficient of friction resisting the forward motion is twice the coefficient of friction resisting the backward motion), the system remains at rest.

For $\mu < 2$, the chain of mass points moves rightward with the velocity

$$V = \frac{2-\mu}{6\,(1+\mu)}\left[1 - e^{-2\,\varepsilon\,(1+\mu)\,t}\right] \tag{17}$$

that tends to the steady-state value $V_s = \dfrac{2-\mu}{6\,(1+\mu)}$, as $t \to +\infty$. For the case of isotropic friction $\mu = 1$, we find $V_s = \frac{1}{12}$.

Thus, under this control algorithms, motion is possible in the case of isotropic friction as well as in the direction of the greater friction in the case of non-isotropic friction. If $\mu > 2$ the chain moves to the left with the velocity

$$V = \frac{2\,(2-\mu)}{3\,(1+\mu)}\left[1 - e^{-\frac{\varepsilon}{2}\,(1+\mu)\,t}\right] \tag{18}$$

and tends to stationary value $V_s = \dfrac{2\,(2-\mu)}{3\,(1+\mu)}$.

In figure 3 the results of the numerical integration of the exact and averaged equations in the case of symmetric friction ($\mu = 1$) and for parameter $\varepsilon = 0.3$ are shown.

## 5. Adaptive Control

From the point of view of practical realization, the question arises how to prescribe and realize the time-dependent link lengths $l_i(t)$ (or in a special case (12) and (13)). A solution is the consideration of actuators between consecutive mass points. In most cases, an actuator is treated massless, but otherwise it could be handled as one of the mass points. Often the internal dynamics of an actuator are not modeled, rather the output is connected with the input by means of working hypotheses: the actuator remains a black box. It becomes a (almost) white box if for its internal dynamics a (more or less crude) model is established which yields an output law. Its output are forces, torques, displacements, twists, respectively, which depend on time and may be connected with the actual state or the state history of the system, see [28].

Here, our starting-point is introducing a force actuator with a visco-elastic coupling, see figure 4 for a physical model. Under the assumption that all actuators have the same data,

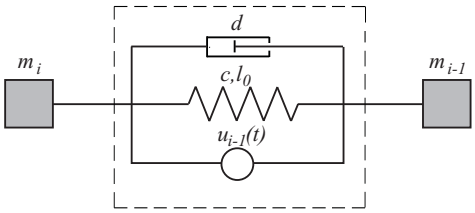


**Figure 4.** Actuator as a parallel arrangement of a linear-elastic spring with constant stiffness $c$ and original length $l_0$, a Stokes damping element with rate $d$, and time-dependent force $u_{i-1}(t)$.

the equations of motions are formulated by means of Newton's law for each of the mass points and are in the actual form (in dimensionless variables):

$$\begin{aligned} m\,\ddot{x}_3 = \;& -c\,(x_3 - x_2 - l_0) - d\,(\dot{x}_3 - \dot{x}_2) - u_2(t) + F(\dot{x}_3)\,, \\ m\,\ddot{x}_2 = \;& c\,(x_3 - x_2 - l_0) + d\,(\dot{x}_3 - \dot{x}_2) \\ & -c\,(x_2 - x_1 - l_0) - d\,(\dot{x}_2 - \dot{x}_1) + u_2(t) - u_1(t) + F(\dot{x}_2)\,, \\ m\,\ddot{x}_1 = \;& c\,(x_2 - x_1 - l_0) + d\,(\dot{x}_2 - \dot{x}_1) + u_1(t) + F(\dot{x}_1)\,. \end{aligned} \tag{19}$$

We point out, that this theory can be easily extended to an arbitrary, but fixed number of mass points, see [28].

At this stage, the $u_i$ are to be seen as prescribed functions of $t$ (offline-controls). If the

actuator data are known ($l_0$, $c$ and $d$) and $n = 2$ (two mass points), then an actuator input $u(t)$ can be calculated which controls the system in such a way as to track a preferred motion-pattern (constructed in kinematical theory).

But, as a rule, the actuator data are not known exactly – we have to deal with an uncertain system. Then, the $u_i$ are handled as depending on the state $(x, \dot{x})$, i.e., feedback, online-controls. Hence, an *adaptive control scheme* is now required that, despite of this drawback, achieves tracking at least approximately.

We have to design a controller which generates the necessary output forces on its own to track a prescribed (kinematical) gait[1]. We focus on an adaptive high-gain output feedback controller [2], not to identify the actuator data, rather to simply control the system in order to track a given gait that is to achieve a desired movement of the worm system. We do not focus on exact tracking, but on the $\lambda$-tracking control objective:

Precisely, given $\lambda > 0$, a control strategy $y \mapsto u$ is sought which, when applied to the worm system (19) achieves $\lambda$-tracking for every reference signal $y_{\text{ref}}(\cdot)$ (prescribed gait), i.e., the following:

(i) every solution of the closed-loop system is defined and bounded on $\mathbb{R}_{\geq 0}$, and

(ii) the output $y(\cdot)$ tracks $y_{\text{ref}}(\cdot)$ with asymptotic accuracy quantified by $\lambda > 0$ in the sense that $\max\Big\{0, \big\|y(t) - y_{\text{ref}}(t)\big\| - \lambda\Big\} \to 0$ as $t \to +\infty$.

The following controller realizes our goal, [6]:

$$\begin{array}{rcl} e(t) & := & y(t) - y_{\text{ref}}(t)\,, \\ u(t) & = & -\gamma\left(k(t)e(t) + \frac{d}{dt}\big(k(t)e(t)\big)\right), \\ \dot{k}(t) & = & \max\Big\{0, \big\|e(t)\big\| - \lambda\Big\}^2\,, \end{array} \tag{20}$$

with any $k(0) \in \mathbb{R}$, $\lambda > 0$, $y_{\text{ref}}(\cdot) \in \mathcal{R}$ (a Sobolev-Space), $(u(t)\,, e(t)) \in \mathbb{R}^2$ and $k(t) \in \mathbb{R}$. The adaptor in (20) makes $k(t)$ monotonically increase as long as the tracking error is not permanently below the prescribed admissible tolerance (dead zone behavior).

In application to our worm system, we take as outputs the actual lengths of the links $y_1(t) := x_2(t) - x_1(t)$ and $y_2(t) := x_3(t) - x_2(t)$. The reference signal is

$$\begin{array}{rcl} y_{\text{ref}\,2}(t) & = & l_2(t) := l_0 + a\,l_0\ (1 - \cos(\pi\,t))\ h(0, 2, t)\,, \\ y_{\text{ref}\,1}(t) & = & l_1(t) := l_2(t + \frac{1}{3}) - l_0\,, \end{array} \tag{21}$$

and its $T = 3$-periodic continuation to $\mathbb{R}^+$, where $h(t_1, t_2, \cdot)$ is the Heaviside function [32]. The cycle of resting mass points should be $\{2 \to 3 \to 1\}$.

[1]The set of all prescribed time-dependent link length functions is called a "gait".

We choose the following data for all simulations in this paper – worm system: $m = 1$, $c = 10$, $d = 5$; environment (Coulomb friction): $k_- N = 15$ and $k_+ N = 3$ (anisotropic) in (2) (stiction not taken into account); reference gait: (21) with $l_0 = 2$, $a = 0.2$; controller: $k(0) = 0$, $\lambda = 0.2$, $\gamma = 100$. For numerical reasons, we use the smooth approximation of the Heaviside function using $\tanh(10^6\, x)$.

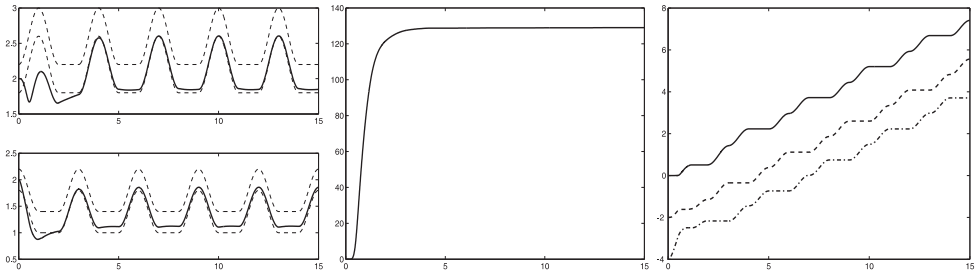

**Figure 5.** Simulation results – left: tubes around the gait (dashed) and outputs (solid), middle: gain parameter, and right: worm motion, all vs. time $t$.

Figure 5 show that the adaptive controller works successfully and effectively. From now on, several improvements concerning the adaptive structure of the controller are done in [4]. Moreover, we focus on special gaits from the kinematic theory which prescribe a pre-defined order of resting mass points during motion in [27], and not prior heuristic gaits. After analyzing these gaits, we perform some gait transitions in [5] to achieve an optimal locomotion pattern in an uncertain environment, i.e., a hilly landscape. General results can be found in [28].

## 6. Conclusions and Outlook

In the case of small friction conditions for the locomotion of worm-like locomotion systems with the help of an average method are derived. The results of the investigation concerning the central question, when motion is possible and when not, are given in figure 6.

Adaptive control is promising in application to worm-like robotic locomotion systems to achieve an optimal locomotion pattern of an uncertain system. Improved adaptive controllers are useful and should be developed further. They shall serve for tracking under friction which randomly changes online, possibly combined with appropriate change of gaits ("gear shift"). Prototypes of described systems are created and the experimental results with these systems coincide with the qualitative predictions of the theory.

Future work will be focused on new models of interaction of the locomotor with the environment, e.g. considering other forms of friction. In particular, for worm-like locomotion

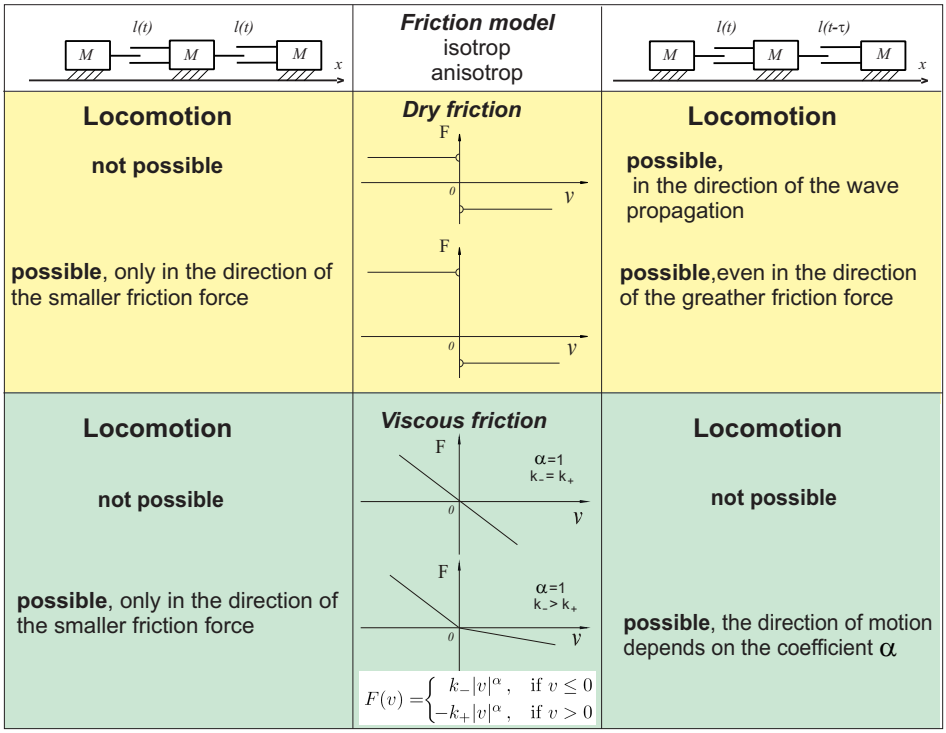


**Figure 6.** Résumé of the locomotion possibilities.

system modelled as a continuous system the coefficient of friction is constant for a mass element, whereas in an other model, this coefficient is constant for a length element.


### Acknowledgments

This research was partially financed by the German Research Society (DFG) (projects ZI 540/12-1, ZI 540/19-1 and SFB 622) and the Russian Foundation for Basic Research (project 14-01-00061 and 15-51-12381). The authors thank V. Boehm, H.-P. Walkling and T. Kaestner for the innovative design and the practical realisation of the prototypes. We are grateful to Prof. J. Steigenberger for his permanent interest in our work and his helpful suggestions.


### References


[1] Alonso, V. I. *Constitutive Models of Rubber VIII.* CRC Press, Cambridge, MA, 2013.

[2] Behn, C. Adaptive control of straight worms without derivative measurement. *Multibody Systems Dynamics 26*, 3 (2011), 213–243.

[3] Behn, C. Adaptive control of singularly perturbed worm-like locomotion systems. *Differential Equations and Dynamical Systems 21*, 1-2 (2013), 59–69.

[4] Behn, C., and Loepelmann, P. Adaptive vs. fuzzy control of uncertain mechanical systems. *International Journal of Applied Mechanics 4*, 2 (2012).

[5] Behn, C., and Schwebke, S. Gear shift patterns in uncertain terrestrial locomotion systems. In *Applied Non-Linear Dynamical Systems, Springer Proceedings in Mathematics and Statistics Vol. 93* (2014), J. Awrejcewicz, Ed., Springer International Publishing Switzerland, pp. 37–48.

[6] Behn, C., and Zimmermann, K. Adaptive $\lambda$-tracking for locomotion systems. *Robotics and Autonomous Systems 54* (2006), 529–545.

[7] Bolotnik, N. N., and Figurina, T. Y. Optimal control of the rectilinear motion of a rigid body on a rough plane by means of the motion of two internal masses. *Journal of Applied Mathematics and Mechanics 72*, 2 (2008), 126–135.

[8] Bolotnik, N. N., Zeidis, I., Zimmermann, K., and Yatsun, S. F. Dynamics of controlled motion of vibration-driven systems. *Journal of Computer and Systems Sciences International 45*, 5 (2006), 831–840.

[9] Chernousko, F. L. The optimum rectilinear motion of a two-mass system. *Journal of Applied Mathematics and Mechanics 66*, 1 (2002), 1–7.

[10] Chernousko, F. L. Analysis and optimization of the motion of a body controlled by means of a movable mass. *Journal of Applied Mathematics and Mechanics 70*, 6 (2006), 819–842.

[11] Chernousko, F. L. On the optimal motion of a body with an internal mass in a resistive medium. *Journal of Vibration and Control 14*, 1–2 (2008), 197–208.

[12] Daltorio, K. A., Boxerbaum, A. S., Horchler, A. D., Shaw, K. M., Chiel, H. J., and Quinn, R. D. Efficient worm-like locomotion: slip and control of soft-bodied peristaltic robots. *Bioinspiration and Biomimetics 3*, 8 (2013), 251–272.

[13] DeSimone, A., Guarnieri, F., Noselli, G., and Tatone, A. Crawlers in viscous environments: Linear vs nonlinear rheology. *International Journal of Non-Linear Mechanics 56* (2013), 142–147.

[14] DeSimone, A., and Tatone, A. Crawling mobility through the analysis of model locomotors: Two case studies. *Eur. J. Phys. E 35*, 85 (2012), 2–8.

[15] Fang, H. B., Li, S., Wang, K. W., and Xu, J. A comprehensive study on the locomotion characteristics of a metameric earthworm-like robot-part a: Modeling and gait generation. *Multibody System Dynamics 34* (2014), 391–413.

[16] Fang, H. B., and Xu, J. Dynamic analysis and optimization of a three-phase control mode of a mobile system with an internal mass. *Journal of Vibration and Control 17*, 1 (2011), 19–26.

[17] Fang, H. B., Xu, J., and Huang, Y. Optimal motion of vibration-driven systems in a resistant medium induced by internal acceleration-controlled masses. In *7th European Nonlinear Dynamics Conference ENOC 2011, 24-29 July 2011, Rome, Italy* (2011). 6p.

[18] Figurina, T. Y. Optimal control of the motion of a two-body system along a straight line. *Journal of computer and systems sciences international 46*, 2 (2007), 227–233.

[19] Hu, D. L., Nirodya, J., Scotta, T., and Shelleya, M. J. The mechanics of slithering locomotion. *Proc. Natl. Acad. Sci. USA 2009 106* (2009), 10081–10085.

[20] Hyun, N. P., and Verriest, E. Optimal periodic locomotion for a two piece worm with an asymmetric dry friction model. In *21st International Symposium on Mathematical Theory of Networks and Systems July 7-11, 2014. Groningen, The Netherlands* (2014), Groningen : University of Groningen, pp. 1109–1115.

[21] Kano, T., Kobayashi, R., and Ishiguro, A. Decentralized control scheme for adaptive earthworm locomotion using continuum-model-based analysis. *Advanced Robotics* (2014), 197–202.

[22] Lipson, H. Soft robotics challenges and opportunities. In *Workshop Digest of the International Workshop on Soft Robotics and Morphological Computation 2013, Ascona, Switzerland July 14-19, 2013.* p. K-4.

[23] Noselli, G., Tatone, A., and DeSimone, A. Discrete one-dimensional crawlers on viscous substrates: Achievable net displacements and their energy cost. *Mechanics Research Communications 58* (2014), 73–81.

[24] Ostrowski, J., Burdick, J., Lewis, A. D., and Murray, R. M. The mechanics of undulatory locomotion: The mixed kinematic and dynamic case. In *Proceedings of the 1995 IEEE International Conference on Robotics and Automation* (1995), vol. 2, pp. 1945–1951.

[25] Seok, S., Onal, C. D., Wood, R., Rus, D., and Kim, S. Peristaltic locomotion with antagonistic actuators in soft robotics. In *Proceedings of IEEE International Conference on Robotics and Automation (ICRA)* (2010), pp. 1228 – 1233.

[26] Sorokin, K. S. Motion of a mechanism along a rough inclined plane using the motion of internal oscillating masses. *Journal of Computer and Systems Sciences International 48*, 6 (2009), 993–1001.

[27] Steigenberger, J., and Behn, C. Gait generation considering dynamics for artificial segmented worms. *Robotics and Autonomous Systems 59* (2011), 555–562.

[28] Steigenberger, J., and Behn, C. *Worm-like locomotion systems: an intermediate theoretical approach.* Oldenbourg, Muenchen, 2012.

[29] Verl, A., Albu-Schffer, A., Brock, O., and Raatz, A. *Soft Robotics-Transferring Theory to Application.* Springer-Verlag, Berlin, Heidelberg, 2015. 10.1007/978-3-662-44506-8.

[30] Zimmermann, K., and Zeidis, I. Mathematical models and prototypes of worm-like motion systems using magnetic materials. In *Proceedings of Romansy 2004 : the 15th CISM-IFToMM Symposium on Robot Design, Dynamics and Control, June 14-18, 2004, Montreal, Canada* (2004), Springer, 6p.

[31] Zimmermann, K., and Zeidis, I. Worm-like locomotion as a problem of nonlinear dynamics. *Journal of Theoretical and Applied Mechanics 45*, 1 (2007), 179–187.

[32] Zimmermann, K., Zeidis, I., and Behn, C. *Mechanics of terrestrial locomotion with a focus on nonpedal motion systems.* Springer, Heidelberg, 2009.

[33] Zimmermann, K., Zeidis, I., Boehm, V., Kaufhold, T., Volkova, T., Waske, A., Krautz, M., Schroedner, M., Popp, J., Kaestner, M., and Spieler, C. Mechanics of actuators based on magnetic hybrid materials with application for robotics, fluid control and sensor technology. *Scientific Journal of IFToMM Problems in Mechanics 54*, 4 (2014), 23–41.

[34] Zimmermann, K., Zeidis, I., Bolotnik, N., and Pivovarov, M. Dynamics of a two-module vibration-driven system moving along a rough horizontal plane. *Multibody System Dynamics 22*, 1 (2009), 199–219.

[35] Zimmermann, K., Zeidis, I., and Pivovarov, M. Dynamics of two interconnected mass points in a resistive medium. *Differential Equations and Dynamical Systems 21*, 1,2 (2013), 21–28.

[36] Zimmermann, K., Zeidis, I., Pivovarov, M., and Abaza, K. Forced nonlinear oscillator with nonsymmetric dry friction. *Archive of Applied Mechanics 77*, 5 (2006), 353–362.

Carsten Behn, PD Dr.-Ing. habil. Dipl.-Math.: TU Ilmenau, Department of Mechanical Engineering, Max-Planck-Ring 12, D-98693 Ilmenau, Germany (*carsten.behn@tu-ilmenau.de*).

Nikolai N. Bolotnik, Prof. Dr.: Institute for Problems in Mechanics of the Russian Academy of Sciences, 101 bld. 1 Vernadskii Ave, Moscow 119526, Russia (*bolotnik@ipmnet.ru*).

Igor Zeidis, Dr.: TU Ilmenau, Department of Mechanical Engineering, Max-Planck-Ring 12, D-98693 Ilmenau,Germany (*igor.zeidis@tu-ilmenau.de*).

Klaus Zimmermann, Prof. Dr.-Ing. habil.: TU Ilmenau, Department of Mechanical Engineering, Max-Planck-Ring 12, D-98693 Ilmenau, Germany (*klaus.zimmermann@tu-ilmenau.de*).
The author gave a keynote presentation of this paper during the conference sessions.

# Dynamic analysis of the rolling locomotion of mobile robots based on tensegrity structures with two curved compressed components (ENG030-15)

Valter Böhm, Tobias Kaufhold, Igor Zeidis, Klaus Zimmermann

*Abstract:* The use of mechanically compliant tensegrity structures in mobile robots is an attractive research topic, due to the possibility to adjust their mechanical properties reversibly during locomotion. In this paper rolling locomotion of mobile robots, based on a simple tensegrity structure, consisting of two rigid disconnected compressed curved members connected to a continuous net of eight prestressed tensional members with pronounced elasticity, is discussed. The locomotion is induced by the movement of two internal masses. To study the system behavior, after kinematic considerations the nonlinear equations of motion are derived and transient dynamic analyses are performed. The dependency of the movement behavior on the prestress and actuation parameters are discussed focused on systems with minimal control effort.

## 1. Introduction

The use of mechanically prestressed compliant structures in mobile robotics is a recently discussed topic. One specific class of these structures builds tensegrity structures, consisting of a set of rigid disconnected compressed components connected to a continuous net of prestressed tensional components. Robots based on these structures are deployable, lightweight, have a simple system design, very high strength to weight ratio, and shock absorbing capabilities [1-3]. An overview of actual developments and development directions can be found in [4-8]. A recent development direction is the realization of rolling mobile robots based on these structures [9-11]. Known systems use conventional tensegrity structures, based on straight components. Rolling is realized by body deformation, due to periodically changing the length of selected tensioned or compressed components. The application of curved components in tensegrity structures indicates their potential ability for the use in rolling mobile robots. In the present work, we focus on the dynamic properties of a simple rolling mobile robot, based on a spatial non-conventional tensegrity structure with two curved compressed components. In section 2 the structure, the assumptions, and the type of actuation of the system are discussed. After consideration on the system's kinematics in section 3, with the help of a simple equivalent mechanical model, basic dynamic properties of the system are presented in section 4.

## 2. Structural properties, assumptions, and type of actuation

The considered tensegrity structure, based on [12], consists of two equal curved components (j=0,1) with constant radius of curvature R and length Rπ (figure 1 a). The curved (compressed) components are indirectly interconnected through eight (tensioned) springs. Each end point of one strut is connected with both end points of the other strut (four springs of type 1 between 00-10, 00-11, 01-10, and 01-11, initial length $L_{01}$, spring constant $k_1$). Furthermore, the points 02 at $\varphi_0=0$ and 12 at $\varphi_1=0$ are connected with the end points of the other compressed component (4 springs of type 2 between 02-10, 02-11, 12-00, and 12-01, initial length $L_{02}$, spring constant $k_2$). The structure is in the symmetrical configuration (curved component 0 with the points 00, 01 and 02 in the $x_0$-$y_0$ plane, curved component 1 with the connecting points 10, 11 and 12 in the $y_0$-$z_0$ plane; with equal deformed spring lengths for both spring types $L_1$ and $L_2$, where $L_1 \neq L_2$), depicted in figure 1 a, in stable equilibrium. The shape of the structure in this configuration is defined by the spring parameters and can be expressed only by the parameters d (distance between the arc centre points) and R. Considering the equilibrium, the location vectors of the spring attachment points to the struts and the parameter d can be found analytically:

$$\vec{r}_{ji} = R \cdot \{(1-j)(1-i/2)(1-3i), (j-1/2)\left(i(i-1) - d/R\right), j(1-i/2)(1-3i)\}^T;\ j=0,1;\ i=0,1,2$$
$$\frac{d/R}{1-d/R} = \frac{k_2(1-L_{02}/L_2)}{k_1(1-L_{01}/L_1)} \qquad (1)$$

The locomotion system based on the introduced structure is capable for uniaxial rolling and also for movement in plane with combined tip over and rolling [13-14] (see figure 1 e). The movement of the system is induced by internal mass displacement. Two equal internal masses can be moved along the lines connecting the end points of the curved struts with two linear stepping motors (figure 1 d).

The rolling movement consists of several basic movement sequences. During a sequence the robot has at two points contact to the ground: a non-changing endpoint of a strut, and a continuously changing second point on the other curved strut. At the end of each moving sequence the continuously changing second contact point reaches an end point and then changes to a non-changing contact point. At the subsequent rolling sequence the process repeats with a change between the curved components, with respect to which a rolling movement occurs.

In the theoretical considerations following assumptions are used:

- The internally moved masses are considered as mass points ($A_0$ and $A_1$, where $m_{A0}=m_{A1}=m$), masses and mass moments of inertia of other system parts are neglected. The time dependent position $a_j(t)$ of mass point $A_j$ is given with the relative distance from the end point j1 of component j.

- The prestress of the system is assumed as high. Elastic deformation of the system, due to gravitational and dynamic forces, is neglected.
- The gravity vector is perpendicular to the plane ($\vec{g} = -g \cdot \vec{e}_z = -9810\,\mathrm{mm/s^2} \cdot \vec{e}_z$).

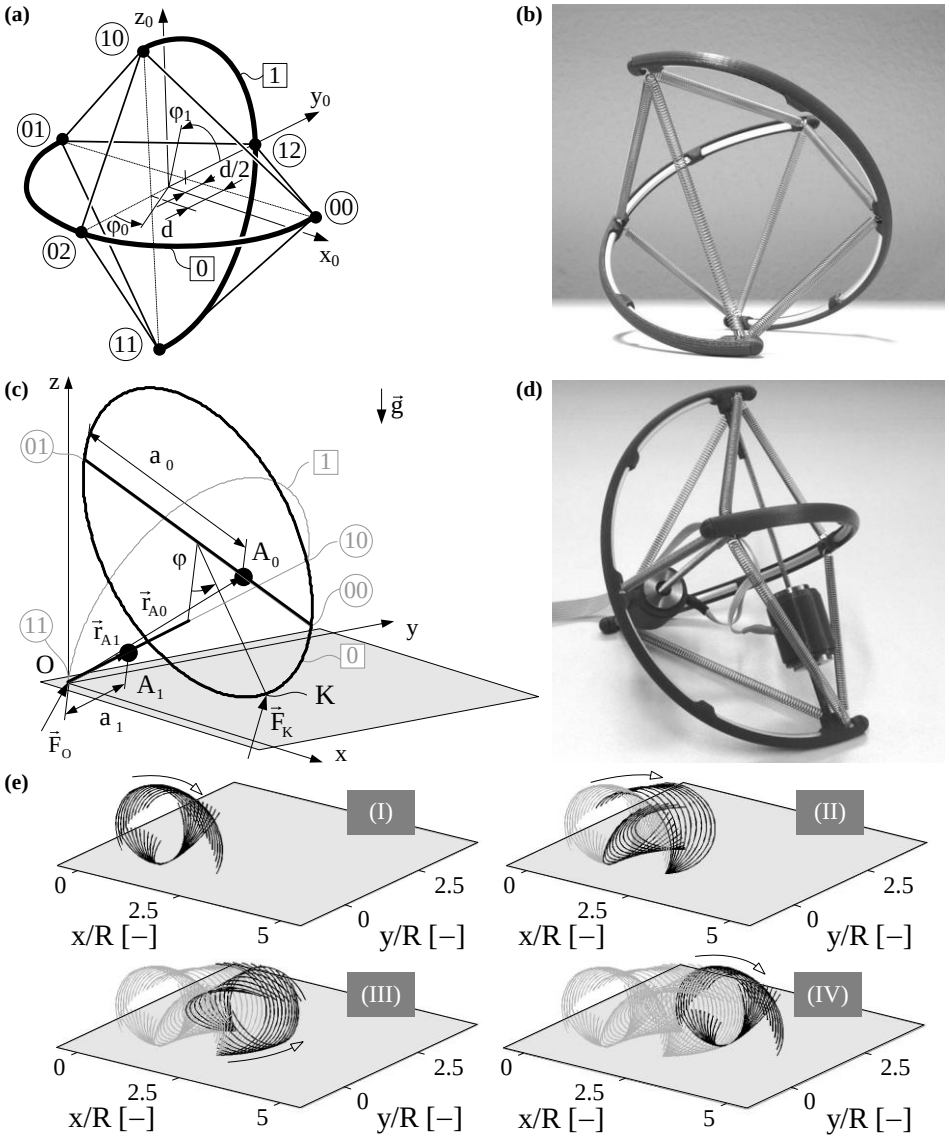


**Figure 1.** Mechanical model (a) of the tensegrity structure (b), and mechanical model (c) of the considered corresponding locomotion system (d), and a possible locomotion sequence (e) ((I)→(IV); (I),(IV): tip over; (II),(III): rolling - basic movement sequence, displaying of only the curved compressed components).

## 3. Kinematics of the system

We consider rolling motion of a rigid circular disc (radius R) on a plane ground surface (x-y plane) without slipping to describe the system's kinematics for a basic movement sequence (figure 2). On the disc (centre: point C) a rigid rod with end points O, N is eccentrically connected normal to the disc plane (connection point N), without relative movement capability between disc and rod. The free end of the rod (point O) is rotatable supported in the origin of the inertial coordinate system.

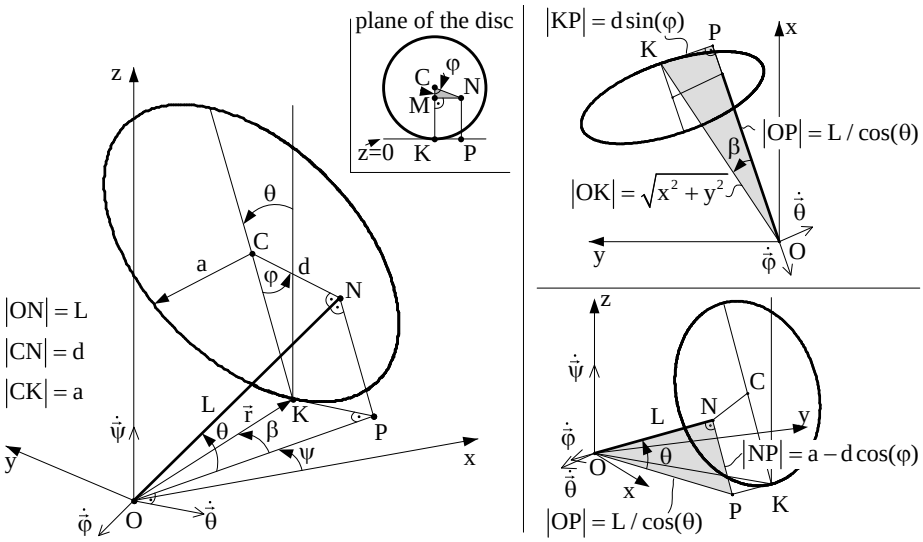


**Figure 2.** The considered mechanical model with geometric parameters in different views (important geometric relationships are marked with gray right-angled triangles; $0 \le d < a$).

The position of the contact point K ( $\vec{r}=\overrightarrow{OK}=x\vec{e}_x+y\vec{e}_y$) between disc and ground is to be determined in dependence on the rotation angle φ. The coordinates of the position vector $\vec{r}$ are

$$x = r\cos(\psi+\beta) \quad ; \quad y = r\sin(\psi+\beta) \tag{2}$$

where $r=|\vec{r}|=(x^2+y^2)^{0.5}$. The goal is to determine the coordinates of the position vector as a function of φ. Therefore, the relationship between the angles ψ+β and φ is to be determined. Using the geometrical relationships (see figure 2)

$$x^2 + y^2 = L/\cos^2\theta + d^2\sin\varphi\,, \quad a - d\cos\varphi = L\tan\theta \tag{3}$$

following relationship between x, y, and the rotation angle φ can be found:

$$x^2+y^2 = L^2+a^2+d^2-2ad\cos\varphi \tag{4}$$

In accordance with (2) the coordinates of the velocity vector $\dot{\vec{r}} = \dot{x}\vec{e}_x + \dot{y}\vec{e}_y$ are

$$\dot{x} = \dot{r}\cos(\psi+\beta) - r\sin(\psi+\beta)(\dot{\psi}+\dot{\beta}), \quad \dot{y} = \dot{r}\sin(\psi+\beta)+r\cos(\psi+\beta)(\dot{\psi}+\dot{\beta}) \tag{5}$$

These coordinates can also be expressed with the help of the classical condition for rolling without slipping

$$\dot{x} = -a\dot{\varphi}\sin\psi, \quad \dot{y} = a\dot{\varphi}\cos\psi \tag{6}$$

From (5) and (6) follows

$$\dot{r}\cos(\psi+\beta) - r\sin(\psi+\beta)(\dot{\psi}+\dot{\beta}) = -a\dot{\varphi}\sin\psi, \quad \dot{r}\sin(\psi+\beta)+r\cos(\psi+\beta)(\dot{\psi}+\dot{\beta}) = a\dot{\varphi}\cos\psi \tag{7}$$

The transformation of equations (7) leads to

$$r(\dot{\psi}+\dot{\beta}) = a\dot{\varphi}\left(\sin\psi\sin(\psi+\beta)+\cos\psi\cos(\psi+\beta)\right) = a\dot{\varphi}\cos\beta \tag{8}$$

With regarding the geometric relationships $\cos^{-1}\theta=(L^2+(a-d\cos\varphi)^2)^{0.5}/L$ and $\cos\beta=L/(r\cos\theta)$ (see gray triangles in figure 2) from (8) follows the direct relationship between the angles $(\psi+\beta)$ and $\varphi$:

$$\dot{\psi}+\dot{\beta} = \dot{\varphi}a(L^2+(a-d\cos\varphi)^2)^{0.5}(L^2+a^2+d^2-2ad\cos\varphi)^{-1} \tag{9}$$

$$\psi+\beta = \int_0^{\varphi} a(L^2+(a-d\cos\xi)^2)^{0.5}(L^2+a^2+d^2-2ad\cos\xi)^{-1}\,d\xi \tag{10}$$

In summary, the coordinates x, y, and the angles $\Theta$ and $\Psi$ in dependence on the rotation angle $\varphi$ are

$$x = (L^2+a^2+d^2-2ad\cos\varphi)^{0.5}\cos\left(\int_0^{\varphi}\frac{a(L^2+(a-d\cos\xi)^2)^{0.5}}{L^2+a^2+d^2-2ad\cos\xi}\,d\xi\right) \tag{11}$$

$$y = (L^2+a^2+d^2-2ad\cos\varphi)^{0.5}\sin\left(\int_0^{\varphi}\frac{a(L^2+(a-d\cos\xi)^2)^{0.5}}{L^2+a^2+d^2-2ad\cos\xi}\,d\xi\right) \tag{12}$$

$$\theta = \tan^{-1}\left((a-d\cos(\varphi))/L\right) \tag{13}$$

$$\psi = -\tan^{-1}\left(d\sin(\varphi)/(L/\cos(\theta))\right)+\int_0^{\varphi}\frac{a(L^2+(a-d\cos\xi)^2)^{0.5}}{L^2+a^2+d^2-2ad\cos\xi}\,d\xi \tag{14}$$

For the considered tensegrity system, the disc and the rod are both replaced with semicircular arcs ($\varphi_j=-\pi/2\ldots\pi/2$, a=L=R). With the help of the above kinematic considerations it can be seen, that the geometric parameter d (see figure 1) plays an essential role with respect to the rolling locomotion of the system (figure 3). The maximum covered travel distance within a basic movement sequence can be achieved if $d\rightarrow R$.

During locomotion, rolling on both curved components takes place successively alternating (see figure 4 for the case of eight basic movement sequences (I→VIII)). With repeating these eight movement sequences uniaxial locomotion of the system in the positive y-direction can be realized. The change of the directions of rotation for both curved components leads to locomotion in the opposite direction.

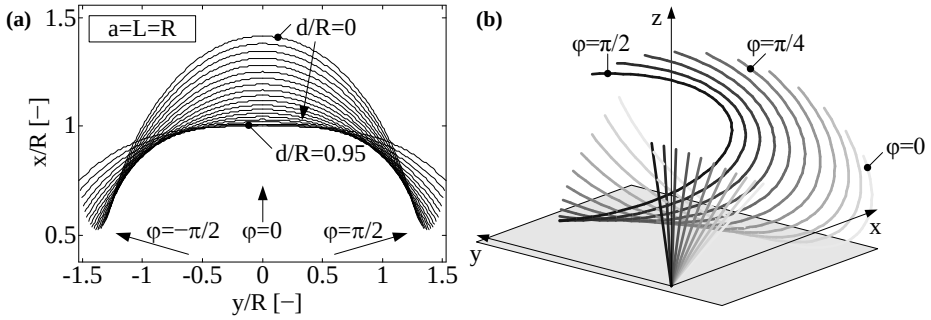


**Figure 3.** Path of the contact point K on the ground in dependence of d (a=L=R) for two basic movement sequences (φ=−π/2…π/2) (a); rotation of the system (b) (basic movement sequence: φ=0→π/2, white→black, d/R=0.5).

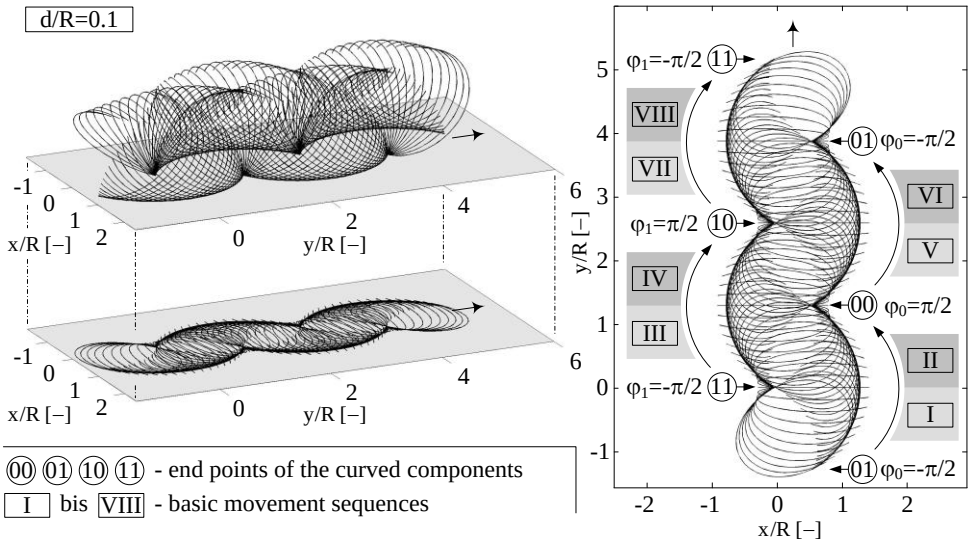


**Figure 4.** Rolling locomotion of the system in the positive y-direction for eight basic movement sequences (I→VIII), (d/R=0.1, displaying of only the curved compressed components).

## 4. Dynamic system behavior for the basic movement sequence

The actuation of the system is carried out with changing the relative mass point positions $a_j(t)$ (see figure 1 c). The goal is to determine the time-dependent position of the system φ(t) for the basic movement sequence in dependence of the actuation parameters, characterized with $a_j(t)$. The description of the motion of the system is carried out with respect to the inertial x-y-z coordinate system. The system is considered as a system of mass points. The assumptions in section 2 are still valid.

### 4.1. Equation of motion

The angular velocity and acceleration of the system can be expressed with

$$\vec{\omega} = \dot{\vec{\varphi}} + \dot{\vec{\psi}} + \dot{\vec{\theta}} = \dot{\varphi} \cdot \vec{C}_{d1}(\varphi) \tag{15}$$

$$\dot{\vec{\omega}} = \ddot{\varphi} \cdot \vec{C}_{d1}(\varphi) + \dot{\varphi}^2 \cdot \vec{C}_{d2}(\varphi) \tag{16}$$

where

$$\vec{C}_{d1}(\varphi) = \left\{ -\cos(\theta)\cos(\psi) + \frac{d\sin(\varphi)\sin(\psi)}{L((\tan(\theta))^2+1)}, -\cos(\theta)\sin(\psi) - \frac{d\sin(\varphi)\cos(\psi)}{L((\tan(\theta))^2+1)}, 0 \right\}^T,$$

$$\vec{C}_{d2}(\varphi) = \dot{\vec{C}}_{d1}(\varphi) \cdot \dot{\varphi}^{-1}.$$

The position and velocity vectors of the mass points of the system are:

$$\left(\vec{r}_{Aj}\right)^T = \left\{ L \cdot (1-j) + j \cdot a_j \, , (1-j) \cdot (a_j - a) \, , (1-j) \cdot d \right\} \cdot \left[T(\varphi)\right] = \left(\vec{r}_{Aj,init}\right) \cdot \left[T(\varphi)\right] \tag{17}$$

$$\left(\dot{\vec{r}}_{Aj}\right)^T = \dot{\varphi} \cdot \left(\vec{r}^{\,*}_{Aj}\right)^T + \left(\dot{\vec{r}}^{\,*}_{Aj,init}\right)^T \tag{18}$$

where

$$\left[T(\varphi)\right] = \begin{bmatrix} 1 & 0 & 0 \\ 0 & \cos(\varphi) & -\sin(\varphi) \\ 0 & \sin(\varphi) & \cos(\varphi) \end{bmatrix} \cdot \begin{bmatrix} \cos(\theta) & 0 & \sin(\theta) \\ 0 & 1 & 0 \\ -\sin(\theta) & 0 & \cos(\theta) \end{bmatrix} \cdot \begin{bmatrix} \cos(\psi) & \sin(\psi) & 0 \\ -\sin(\psi) & \cos(\psi) & 0 \\ 0 & 0 & 1 \end{bmatrix},$$

$$\left(\vec{r}^{\,*}_{Aj}\right)^T = \left(\vec{r}_{Aj,init}\right) \cdot \dot{\varphi}^{-1} \cdot \left(\left[T(\varphi)\right]\right)^{\cdot}, \; \left(\dot{\vec{r}}^{\,*}_{Aj,init}\right)^T = \left(\dot{\vec{r}}_{Aj,init}\right) \cdot \left[T(\varphi)\right].$$

The angular momentum and the moment of forces with respect to the origin O of the inertial coordinate system are (see figure 1 c)

$$\vec{M}_O = m \cdot \sum_{j=0}^{1} \left(\vec{r}_{Aj} \times \vec{g}\right) + \vec{r}_K \times \vec{F}_K \, , \qquad \vec{D}_O = m \cdot \sum_{j=0}^{1} \left(\vec{r}_{Aj} \times \left(\vec{\omega} \times \vec{r}_{Aj}\right)\right) \tag{19}$$

where $\vec{F}_K$ is the contact force vector and $\vec{r}_K$ the position vector with respect to the point K. Using the principle of angular momentum the equation of motion of the model takes the form

$$\dot{\vec{D}}_O - \vec{M}_O = m \cdot \sum_{j=0}^{1} \left( \dot{\vec{r}}_{Aj} \times \left(\vec{\omega} \times \vec{r}_{Aj}\right) + \vec{r}_{Aj} \times \left(\dot{\vec{\omega}} \times \vec{r}_{Aj}\right) + \vec{r}_{Aj} \times \left(\vec{\omega} \times \dot{\vec{r}}_{Aj}\right) - \vec{r}_{Aj} \times \vec{g} \right) - \vec{r}_K \times \vec{F}_K = \vec{0} \tag{20}$$

Under the assumptions mentioned above, equation (20) can be rewritten as

$$\ddot{\varphi} + \dot{\varphi}^2 \cdot C_{dI}(\varphi) + \dot{\varphi} \cdot C_{dII}(\varphi) + C_{dIII}(\varphi) = 0 \tag{21}$$

where

$$C_{dI}(\varphi) = \frac{C_{d5}C_{d2x} + C_{d6}C_{d2y} + C_{d7}}{C_{d5}C_{d1x} + C_{d6}C_{d1y}}, \; C_{dII}(\varphi) = \frac{C_{d8}}{C_{d5}C_{d1x} + C_{d6}C_{d1y}}, \quad C_{dIII}(\varphi) = \frac{C_{d9}}{C_{d5}C_{d1x} + C_{d6}C_{d1y}}$$

with

$$C_{d5} = \left(r_{A0y}^2 + r_{A0z}^2 + r_{A1y}^2 + r_{A1z}^2\right) - \frac{r_{Ky}}{r_{Kx}} \cdot \left(r_{A0x} r_{A0y} + r_{A1x} r_{A1y}\right)$$

$$C_{d6} = \frac{r_{Ky}}{r_{Kx}} \left(r_{A0x}^2 + r_{A0z}^2 + r_{A1x}^2 + r_{A1z}^2\right) - \left(r_{A0x} r_{A0y} + r_{A1x} r_{A1y}\right)$$

$$C_{d7} = \left(\sum_{j=0}^{1} \left(\vec{r}_{Aj}^{\,*} \times \left(\vec{C}_{d1} \times \vec{r}_{Aj}\right) + \vec{r}_{Aj} \times \left(\vec{C}_{d1} \times \vec{r}_{Aj}^{\,*}\right)\right)\right) \cdot \left(\vec{e}_x + \frac{r_{Ky}}{r_{Kx}} \cdot \vec{e}_y\right)$$

$$C_{d8} = \left(\sum_{j=0}^{1} \left(\dot{\vec{r}}_{Aj,init}^{\,*} \times \left(\vec{C}_{d1} \times \vec{r}_{Aj}\right) + \vec{r}_{Aj} \times \left(\vec{C}_{d1} \times \dot{\vec{r}}_{Aj,init}^{\,*}\right)\right)\right) \cdot \left(\vec{e}_x + \frac{r_{Ky}}{r_{Kx}} \cdot \vec{e}_y\right)$$

$$C_{d9} = -\left(\sum_{j=0}^{1} \left(\vec{r}_{Aj} \times \vec{g}\right)\right) \cdot \left(\vec{e}_x + \frac{r_{Ky}}{r_{Kx}} \cdot \vec{e}_y\right)$$

In the real case, during or after shifting of the mass points $A_0$, $A_1$ a damped oscillation of the system with respect to the contact point O is to be expected. For simplifying reasons, this behavior can be approximated considering Stokes friction, with the friction coefficient $k_{Sto}$:

$$\ddot{\varphi} + \dot{\varphi}^2 \cdot C_{dI}(\varphi) + \dot{\varphi} \cdot \left(C_{dII}(\varphi) + k_{Sto}\right) + C_{dIII}(\varphi) = 0 \tag{22}$$

### 4.2. Simulations

In the simulations following position changes of the system are considered: $\varphi=0 \rightarrow \pm\pi/2$ (initial conditions: $\varphi(t=0)=0$, $\dot{\varphi}(t=0)=0$) and $\varphi=\pm\pi/2 \rightarrow 0$ (initial conditions: $\varphi(t=0)=\pm\pi/2$, $\dot{\varphi}(t=0)=0$). Model parameters are: a=L=R=80 mm, m=25g, d/R=0.7. Actuation parameters are the start and end times ($t_{j,start}$, $t_{j,end}$) of the actuation and the associated relative positions ($a_{j,start}$, $a_{j,end}$) of the mass points:

$$a_j(t) = \begin{cases} a_{j,start} & \text{if} \quad t < t_{j,start} \\ a_{j,start} + \left(a_{j,end} - a_{j,start}\right) \cdot \left(t - t_{j,start}\right) / \left(t_{j,end} - t_{j,start}\right) & \text{if} \quad t_{j,start} \le t \le t_{j,end} \\ a_{j,end} & \text{if} \quad t > t_{j,end} \end{cases} \tag{23}$$

Based on the simulations by varying the actuation parameters and the damping coefficient following results were found:

- The change in the equilibrium position of the system from $\varphi=0$ to $\varphi=\pm\pi/2$ (basic sequence of movement) can be effected with the actuation of only one mass point (result 1).
- For specific cases, different equilibrium positions of the system can be achieved after the actuation, if the speed of actuation of the mass points is changed (in the case that several equilibrium positions of the system at given relative positions of the mass points after their actuation exist) (result 2)

- For specific cases, different equilibrium positions of the system can be achieved after the actuation, if the order of the actuated mass points is changed (in the case that several equilibrium positions of the system at given relative positions of the mass points after their actuation exist) (result 3)
- The vibration behavior of the system is essentially influenced by the speed of actuation of the mass points. Thus, an effective control algorithm can be determined to minimize the decay of oscillation of the system, so that the speed of the rolling movement of the system can be maximized (result 4).

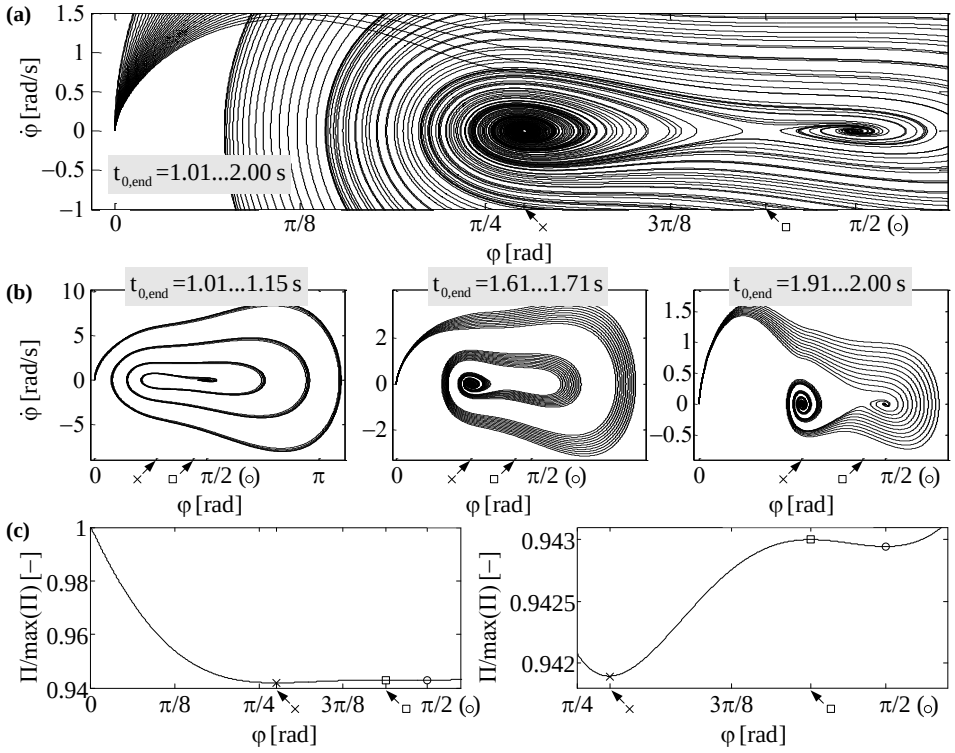


**Figure 5.** Example 1 – influence of the speed of actuation of mass point $A_0$ on the system's equilibrium position after the actuation. Phase portraits for the considered speeds of actuation (a) and detailed views for selected subsets (b); normalized potential energy of the system for $a_0$=1.21R, $a_1$=0.79R in dependence of φ (c); ($k_{Sto}$=0.5 Ns/mm, markers: x – φ=0.8689, □ – φ=1.3813, o – φ=π/2).

Regarding result 1 we consider the case in which only mass point $A_0$ is moved (from $a_{0,start}$=1R to $a_{0,end}$=1.21R). The relative position of mass point $A_1$ is constant: $a_{1,start}$=$a_{1,end}$=0.79R. With respect to the initial conditions and selected initial positions of the mass points, the system is at the beginning of

the actuation in stable equilibrium (φ=0). The dynamic system behavior is shown in figure 5 under varying the speed of movement of the mass point $A_0$, controlled by the parameter $t_{0,end}$=1.01…2 s in 0.01 s steps ($t_{0,start}$=1 s). The results show that multiple ranges of the speed of actuation for mass point $A_0$ exist, for which at the end of the movement sequence the stable equilibrium position of the system at φ=π/2 can be realized (e.g. for $t_{0,end}$=1.01…1.15 s). Thus, the actuation of only one mass point with an appropriately selected speed is sufficient to realize a basic movement sequence of the system. As the results further show, the system's equilibrium position at the end of movement varies in dependence of the speed of actuation, in accordance with result 2. Two stable equilibrium positions of the system are possible for the parameters $a_{0,end}$=1.21R, $a_{1,end}$=0.79R: at φ=0.8689 and φ=π/2 (see markers x and o in figure 5).

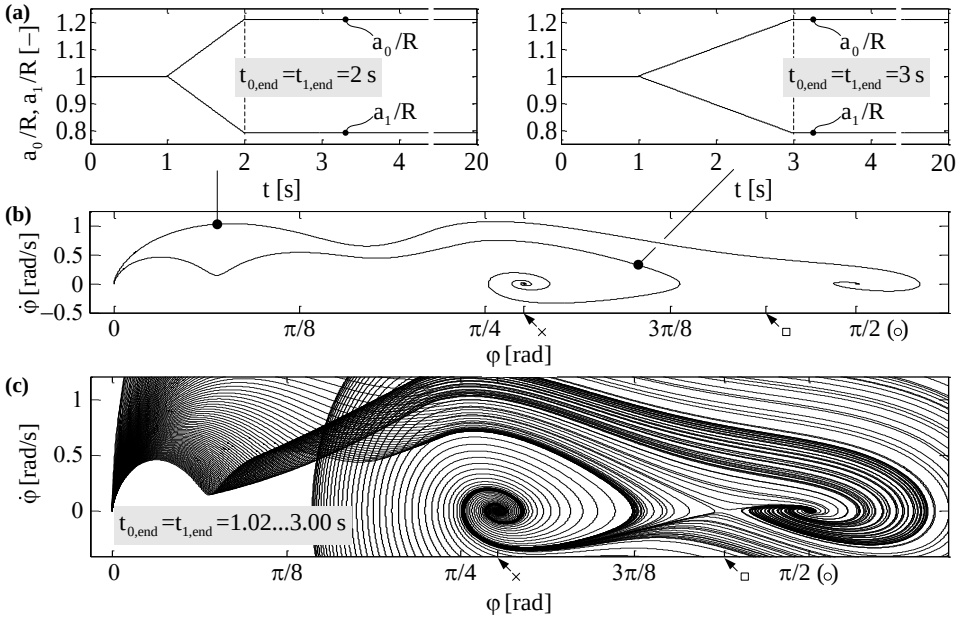


**Figure 6.** Example 2 – influence of the speed of actuation on the system's equilibrium position after the actuation. Detailed view of two selected sets of actuation parameters over time (a) and corresponding phase portraits (b); phase portraits for the considered speeds of actuation (c) ($k_{Sto}$=1 Ns/mm, markers: x – φ=0.8689, □ – φ=1.3813, o – φ=π/2, see figure 5 bottom).

Regarding result 2 a second case is considered in which both mass points are simultaneous actuated (from $a_{0,start}$=$a_{1,start}$=R to $a_{0,end}$=1.21R, $a_{1,end}$=0.79R), with equal speeds of actuation. With respect to the initial conditions and selected initial positions of the mass points the system is at the beginning of the actuation in stable equilibrium (φ=0). Selected results for different speeds of actuation

($t_{0,end}$= $t_{1,end}$=1.02…3 s, step size: 0.02 s, $t_{0,start}$=$t_{1,start}$=1 s) are depicted in figure 6. After the actuation, the equilibrium position of the system depends also in this case on the applied actuation parameters. Regarding result 3 an example is depicted in figure 7. As the results show, different equilibrium positions of the system after the actuation can be realized in dependence of the order of the actuated mass points ($A_0 \rightarrow A_1$: $\varphi=\pi/2$, $A_1 \rightarrow A_0$: $\varphi=0.8689$).

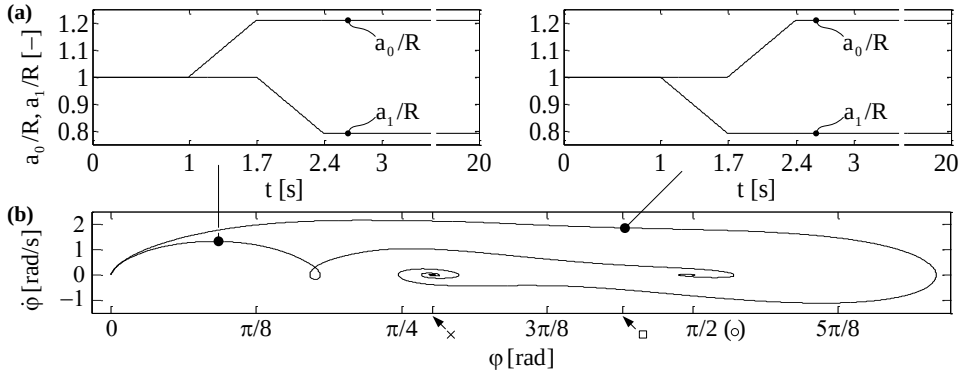


**Figure 7.** Example 3 – influence of the order of the mass point actuation on the system's equilibrium position after the actuation. Two selected sets of actuation parameters over time (a) (left: $A_0 \rightarrow A_1$, right: $A_0 \rightarrow A_1$) and corresponding phase portraits (b) ($k_{Sto}$=1 Ns/mm, markers: x – $\varphi=0.8689$, □ – $\varphi=1.3813$, o – $\varphi=\pi/2$, see figure 5 bottom).

The considered examples show that the motion of the system is essentially dependent on the type of actuation. Accordingly, the decay time of the oscillation (see result 4) and the maximum oscillation amplitude is decisively influenced by actuation parameters. Due to the oscillation amplitudes the use of curved components with $\max(|\varphi_j|) > \pi/2$ is required instead of semicircular arcs.

## 5. Conclusions

In this paper basic dynamic properties of a rolling mobile robot, based on a non-conventional tensegrity structure is presented. The actuation of the robot is realized with internal movement of two masses. It was shown, that rolling locomotion can easily realized with tensegrity structures consisting of curved compressed components. Furthermore, the influence of mechanical parameters of the components and actuation parameters on the movement behavior is discussed.


## Acknowledgments

This work is supported by the Deutsche Forschungsgemeinschaft (DFG project BO4114/2-1).

**References**


[1] Paul C., et al.: Gait production in a tensegrity based robot. Proc. of ICAR '05, 12th Int. Conf. on Advanced Robotics, Seattle, 2005, pp. 216–222.

[2] Rieffel J.A., et al.: Morphological communication: exploiting coupled dynamics in a complex mechanical structure to achieve locomotion. *J. Roy. Soc. Interf.*, 7, 2010, pp. 613–621.

[3] Koizumi Y., et al.: Rolling tensegrity driven by pneumatic soft actuators. Proc. of IEEE Int. Conf. on Robotics and Automation, Saint Paul, 2012, pp. 1988–1993.

[4] Mirats Tur J.M., et al.: Tensegrity frameworks: Dynamic analysis review and open problems. *Int. Journal of Mechanism and Machine Theory*, 44(1), 2009, pp. 1–18.

[5] Skelton R.E., et al.: *Tensegrity Systems*. Dordrecht, Springer, 2009.

[6] Khazanov, M., et al.: Evolution of Locomotion on a Physical Tensegrity Robot. Proc. of the 14th Int. Conf. on the Synthesis and Simulation of Living Syst., New York, 2014, pp. 232-238.

[7] Caluwaerts, K., et al.: Design and control of compliant tensegrity robots through simulation and hardware validation. *J. Roy. Soc. Interf.*, 11, 2014, 20140520.

[8] Böhm, V., et al.: An approach to the dynamics and control of a planar tensegrity structure with application in locomotion systems. *Int. Journal of Dynamics and Control*, 3(1), 2015, pp. 41-49.

[9] Kim, K., et al.: Rapid Prototyping Design and Control of Tensegrity Soft Robot for Locomotion. Proc. of IEEE Int. Conf. on Robotics and Biomimetics, Bali, 2014, pp. 7-14.

[10] Luo, A., et al.: Structure of the ball tensegrity robot. Proc. of IEEE Int. Conf. on Robotics and Biomimetics, Bali, 2014, pp.1781-1786.

[11] Sabelhaus, A.P., et al.: System design and locomotion of SUPERball, an untethered tensegrity robot. Proc. of IEEE Int. Conf. on Robotics and Automation, Seattle, 2015, pp. 2867-2873.

[12] Barber, G.T.: Structures composed of compression and tensile members. United States Patent, US 6868640 B2, 2005.

[13] Böhm, V., et al.: An approach to compliant locomotion systems based on tensegrity structures. Proc. of 56rd IWK – Internationales Wissenschaftliches Kolloquium, Ilmenau, 2011.

[14] Böhm, V., et al.: An approach to locomotion systems based on 3D tensegrity structures with a minimal number of struts. Proc. of 7th German Conf. on Robotics, München, 2012, pp. 150-155.



Valter Böhm, Ph.D.: Ilmenau University of Technology, PF 10 05 65, D-98684 Ilmenau, Germany, (*valter.boehm@tu-ilmenau.de*). The author gave a presentation of this paper during one of the conference sessions.

Tobias Kaufhold, M.Sc. (Ph.D. student): Ilmenau University of Technology, PF 10 05 65, D-98684 Ilmenau, Germany (*tobias.kaufhold@tu-ilmenau.de*).

Igor Zeidis, Ph.D.: Ilmenau University of Technology, PF 10 05 65, D-98684 Ilmenau, Germany (*igor.zeidis@tu-ilmenau.de*).

Klaus Zimmermann, Professor: Ilmenau University of Technology, PF 10 05 65, D-98684 Ilmenau, Germany (*klaus.zimmermann@tu-ilmenau.de*).

# Characteristics of model freight wagon subsystems of transverse vibrating complex mechanical system determined by approximate method and their correction (NUM213-15)

Andrzej Buchacz

*Abstract:* The main subject of deliberation was to determine the dynamical flexibilities of the freight wagon subsystems within transverse vibrating complex mechanical system with constant cross section using the exact and approximate method. The characteristic of the subsystems using the exact and approximate method has been determined according to accepted frequencies and the coefficient correction. The frequencies where chosen from the spectrum in which the synthesis of complex systems will be conducted. It is very important that the difference of flexibility values in the spectrum was minimal. The coefficient of the correction has been determined according to the flexibility values of chosen points and it is equal to quotient of flexibility calculated using the exact method across the flexibility delivered by using the approximate method. The coefficient of the correction is the zero-dimensional quantity. After determination of the correction coefficient the medium value has been calculated, which has been afterwards considered in correlation of dynamic characteristics. The problems presented in this paper are the necessary condition to the synthesis of transverse vibrating complex mechanical systems with assume frequency spectrum.

## 1. Introduction

The problems of modelling by the graphs, hypergraphs*** and analysis of vibrating beam systems, discrete and discrete-continuous mechanical systems by means the structural numbers methods has been made in the Gliwice research Centre (e.g. [3-5,20]). The problems of analysis and synthesis of electrical systems were presented in monograph [1]. Selected class of synthesis continuous, discrete - continuous discrete mechanical systems and active mechanical systems concerning the frequency spectrum has been made [3-9]. Other problems have been modeled by different category graphs and next they were examined and analyzed by classical and unclassical methods in (e.g.[17-20]). The continuous-discrete transverse [10,11] and torsionally vibrating mechatronic systems were analyzed for example in [12,13]. The approximate-Galerkin's method of analysis has been used to obtain the frequency-modal characteristics. To comparison of obtaining dynamical characteristics – dynamical flexibilities only for mechanical torsionally vibrating bar and transverse vibrating beam, as a parts of complex mechatronic systems, exact method and Galerkin's method were used [10-16].

In this paper frequency–modal analysis for the mechanical system, that means flexibly vibrating beam have been presented.

## 2. Dynamic characteristics of vibration simple beam as the subsystem of complex transverse vibrating mechanical system

### 2.1. Frequency – modal analysis

The beam with the constant cross section excited with harmonic force in form $F(t) = F_0 \cos \omega t$ is considered (see figure 1).

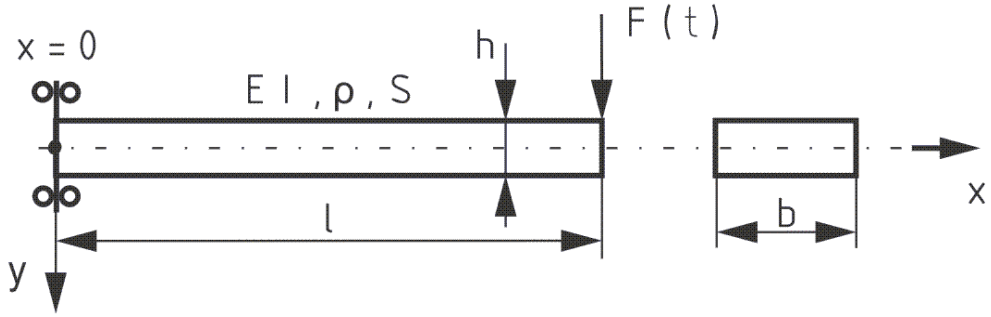


**Figure 1.** The beam with sliding and free boundary conditions

The equation of motion of the beam without excitation takes form

$$EI\frac{\partial^4 y(x,t)}{\partial x^4} + \rho S\frac{\partial^2 y(x,t)}{\partial t^2} = 0, \tag{1}$$

where: $y(x,t)$ - deflection at the time moment $t$ of the lining beam section within the distance $x$ from the beginning of the system, $E$ - Young modulus, $\rho$ - mass density of material of the beam, $I$ -polar inertia moment of the beam cross section, $S$ – area of the beam cross section.

The boundary conditions on the beam ends, but without excitation are following

$$\frac{\partial y(0,t)}{\partial x} = 0, \frac{\partial^3 y(0,t)}{\partial x^3} = 0, \frac{\partial^2 y(l,t)}{\partial x^2} = 0, \frac{\partial^3 y(l,t)}{\partial x^3} = 0, \tag{2}$$

where: $l$- length of the beam.

Using the Fourier's method, the equations (1) and (2) are following

$$X^{(\mathrm{IV})}(x) - k^4 X(x) = 0, \tag{3}$$

$$X'(0) = 0,\ X'''(0) = 0,\ X''(l) = 0,\ X'''(l) = 0. \tag{4}$$

The general solution of (3) has the form

$$X(x) = A\sin kx + B\cos kx + C\sinh kx + D\cosh kx. \tag{5}$$

After substitution following derivatives of (5) into (4) was received

$$\begin{cases} A + C = 0, \\ -A + C = 0, \\ -A\sin kl - B\cos kl + C\cosh kl + D\sinh kl = 0, \\ -A\cos kl + B\sin kl + C\cosh kl + D\sinh kl = 0. \end{cases} \tag{6}$$

Characteristic determinant of (6) equals zero, when

$$-\mathrm{tg}z = \tanh z, \quad z = kl. \tag{7}$$

Own values of (7) are presented in table 1.

Own values of characteristic - equation (7) Table 1

| $n$ | 0 | 1 | 2 | 3 | $n$ >3 |
|---|---|---|---|---|---|
| $z_n$ | 0 | 2.365 | 5.4978 | 8.6394 | $\frac{4n-1}{4}\pi$ |

From (7) $A$=$C$=0 and own function of beam after transformation is following

$$X_n(x) = B_n\left[\cos\frac{z_n}{l}x + \frac{\cos z_n}{\cosh z_n}\cosh\frac{z_n}{l}x\right], \quad n = 0,1,2,\ldots . \tag{8}$$

### 2.2. Dynamical flexibility - the exact method

The deflection $y(x,t)$ is the harmonic function, because excitation is harmonic function as well, that means

$$y(x,t) = X(x)\cos\omega t = \left(A\sin kx + B\cos kx + C\sinh kx + D\cosh kx\right)\cos\omega t\ . \tag{9}$$

The boundary conditions for the beam (see figure 1) are following

$$\frac{\partial y(0,t)}{\partial x} = 0,\ \frac{\partial^3 y(0,t)}{\partial x^3} = 0,\ \frac{\partial^2 y(l,t)}{\partial x^2} = 0,\ EI\ \frac{\partial^3 y(l,t)}{\partial x^3} = -F(t). \tag{10}$$

After calculating suitable derivatives of (9) as well and substituting into (10) the set of equations, after transformations, is following

$$\begin{cases} A + C = 0, \\ -A + C = 0, \\ -A\sin kl - B\cos kl + C\cosh kl + D\sinh kl = 0, \\ -A\cos kl + B\sin kl + C\cosh kl + D\sinh kl = \dfrac{F_0}{EIk^3}. \end{cases} \tag{11}$$

From (11) the constants $A$, $B$, $C$, $D$ are equal

$$\begin{cases} A = 0, \\ C = 0, \\ B = \dfrac{F_0 \cosh kl}{EIk^3\left(\sin kl \cosh kl - \sinh kl \cos kl\right)}, \\ D = \dfrac{F_0 \cos kl}{2EIk^3\left(\sin kl \cosh kl - \sinh kl \cos kl\right)}. \end{cases} \tag{12}$$

Substituting (12) into (5) is received

$$X(x) = \frac{F_0\left(\cos kx \cosh kl + \cos kl \cosh kx\right)}{EIk^3\left(\sin kl \cosh kl - \sinh kl \cos kl\right)}. \tag{13}$$

Next after substituting (13) into (9) deflection of beam takes form

$$y(x,t) = \frac{\cos kx \cosh kl + \cos kl \cosh kx}{EIk^3\left(\sin kl \cosh kl - \sinh kl \cos kl\right)} F_0 \cos \omega t. \tag{14}$$

The dynamic flexibility according to definition is equal

$$y(x,t) = Y_{xl} F_0 \cos \omega t, \tag{15}$$

and from (15)

$$Y_{xl} = \frac{\cos kx \cosh kl + \cos kl \cosh kx}{EIk^3\left(\sin kl \cosh kl - \sinh kl \cos kl\right)}. \tag{16}$$

When $x=l$ (see figure 1), then absolute value of dynamical flexibility is following

$$Y = \left|Y_{ll}\right| = \left|\frac{2 \cos kl \cosh kl}{EIk^3\left(\sin kl \cosh kl - \sinh kl \cos kl\right)}\right|, \tag{17}$$

were: $k = \sqrt[4]{\omega^2 \dfrac{\rho S}{EI}}$.

The transient of absolute value of (17) is drawn in Figure 2.

### 2.3. Dynamical flexibility - the Galerkin's method

The equation of excited vibration beam can described as

$$EI \frac{\partial^4 y(x,t)}{\partial x^4} + \rho S \frac{\partial^2 y(x,t)}{\partial t^2} = F_0 \cos \omega t. \tag{18}$$

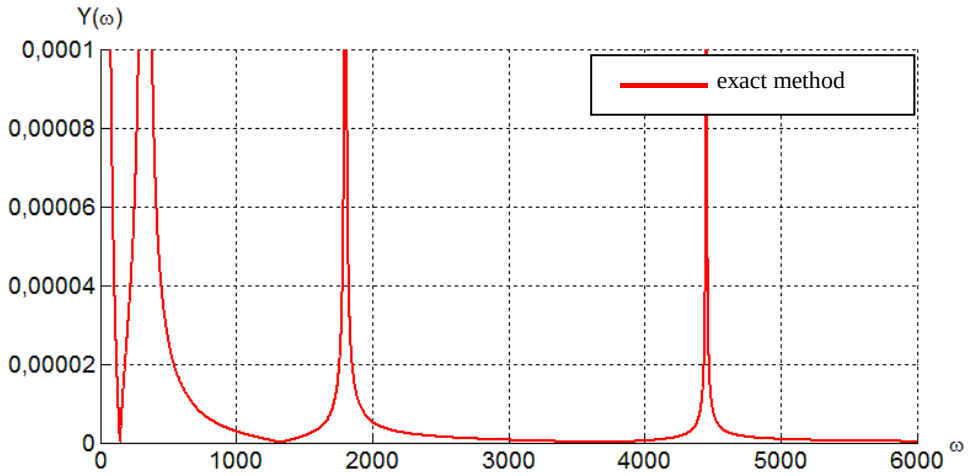


**Figure 2.** The dynamic flexibility of beam obtained by exact method

The solution of equation (18) by means of approximate-Galerkin's method is given as

$$y(x,t)=\sum_{n=1}^{\infty}y_n(x,t)=\sum_{n=1}^{\infty}A_n\cos kx\cos\omega t. \tag{19}$$

Determining derivatives of (19) and substituting them into (18) after transformations the amplitude $A_n$ has the form of

$$A_n=\frac{F_0}{EIk^4-\rho S\omega^2}. \tag{20}$$

The dynamic flexibility for $x=l$, after putting (20) into (19) – after transformations as well – gests shape of

$$Y_{ll}^{(n)}=\frac{1}{EIk^4-\rho S\omega^2}. \tag{21}$$

In global case the dynamic characteristic – flexibility at the ride end of beam (see figure 1) equals

$$Y(\omega)=\left|\sum_{n=1}^{\infty}Y_{ll}^{(n)}\right|=\left|\sum_{n=1}^{\infty}\frac{1}{EIk^4-\rho S\omega^2}\right|. \tag{22}$$

The plot of (22) for sum $k$=0,1,2,3 is shown in Fig. 3.

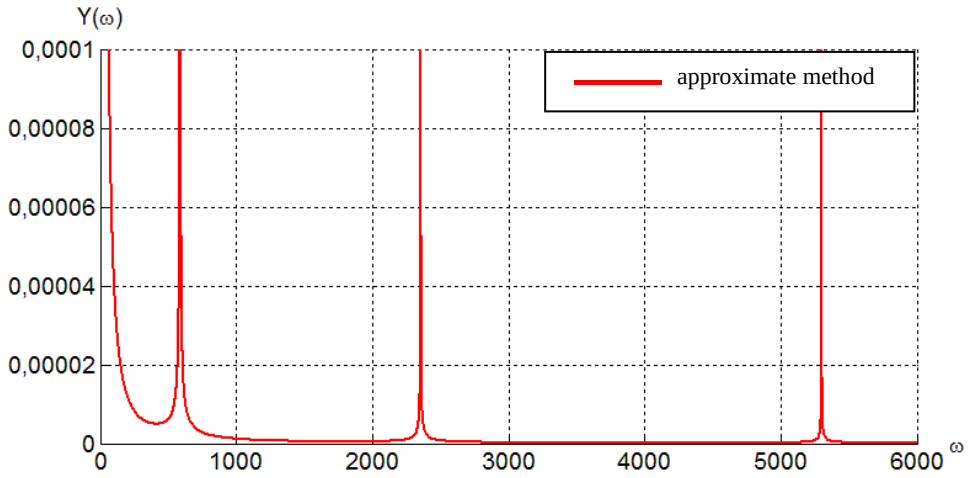


**Figure 3.** The dynamic flexibility of beam obtained by Galerkin's method

### 2.4. Corrections of dynamical characteristics obtained by Galerkin's method

**The characteristics obtained different methods and the same – different own values (see figures 2 and 3. The differences are shown in table 2.**

Natural frequency Table 2

| $n$ | Exact method $\omega_e \left[\frac{rad}{s}\right]$ | Approximate method $\omega_a \left[\frac{rad}{s}\right]$ | $\lvert\Delta\omega\rvert$ | Error $p[\%]$ |
|---|---|---|---|---|
| 0 | 0 | 0 | 0 | 0 |
| 1 | 333,833 | 589,073 | 255,240 | 76,457 |
| 2 | 1804,037 | 2356,294 | 552,256 | 30,612 |
| 3 | 4454,868 | 5301,661 | 846,793 | 19,008 |
| $>3$ | $\omega_e = \left(\frac{4n-1}{4l}\pi\right)^2 \sqrt{\frac{EI}{\rho S}}$ | $\omega_e = \left(\frac{n\pi}{l}\right)^2 \sqrt{\frac{EI}{\rho S}}$ | $\lvert\Delta\omega_n\rvert$ | $p_n$ |

In figure 4 the transients of flexibilities obtained by exact and Galerkin's method are presented.

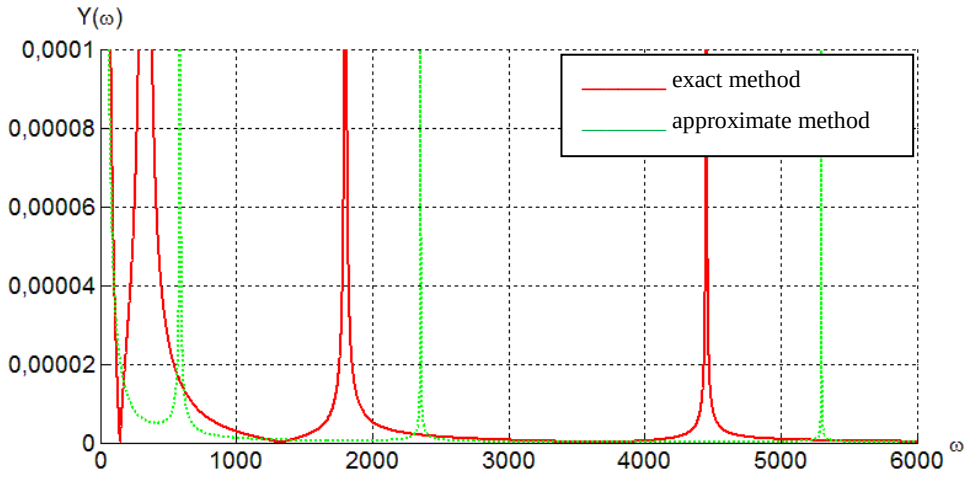


**Figure 4.** The dynamic flexibilities – comparision of the exact and approxiomate method

The range of flexibility in first compartment of frequency, that is from first pole to first zero, has meaning, in problem of synthesis of complex mechanical and the same of the mechatronic ones (see figure 5).

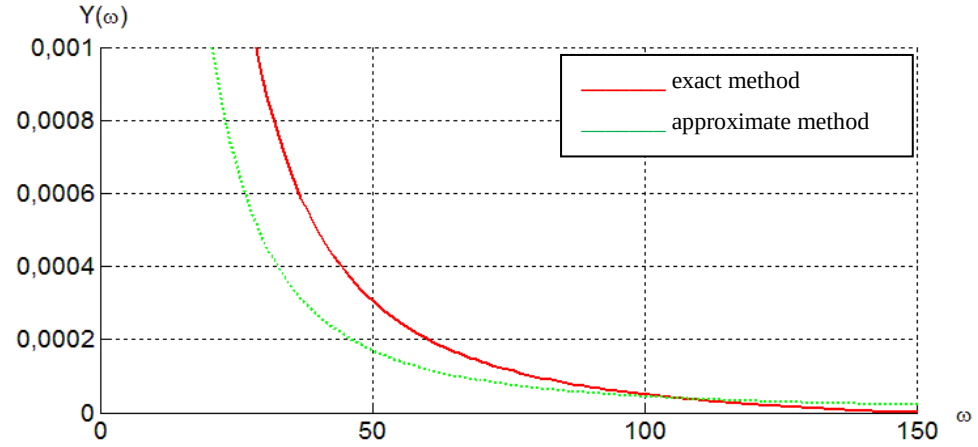


**Figure 5.** The dynamic flexibilities evolution around zeros and first of frequency

Analyzing the flexibility charts of considered beam it has been nominated that there is a mistake in approximate method, that is why it is necessary to make the correction of the results obtained by approximate method. The dependence on the correction coefficient is following

$$\lambda = \frac{Y_e}{Y_a} \tag{23}$$

and presented in table 3.

The difference of dependence value Table 3

| Frequency $\omega\left[\frac{rad}{s}\right]$ | Exact method $Y_e(\omega)\left[\frac{1}{N}\right]$ | Approximate method $Y_a(\omega)\left[\frac{1}{N}\right]$ | Correction coefficient $\lambda[\ ]$ |
|---|---|---|---|
| 20 | 231,7674*10$^{-5}$ | 117,6074*10$^{-5}$ | 1,97 |
| 40 | 52,5476*10$^{-5}$ | 28,0140*10$^{-5}$ | 1,87 |
| 60 | 21,0930*10$^{-5}$ | 12,3155*10$^{-5}$ | 1,70 |
| 80 | 10,2350*10$^{-5}$ | 6,9288*10$^{-5}$ | 1,46 |
| 100 | 5,1855*10$^{-5}$ | 4,4619*10$^{-5}$ | 1,14 |
| | | Medium value | 1,86 |

In the table 3 the flexibilities of the beam determined by exact and Galerkin's method with chosen points were included. The correction coefficient was calculated in order to (23) and it is the unmeasured value.

After determining the correction coefficient the medium value which has been considered in dependence on dynamic flexibility was calculated. Medium value of correction coefficient was introduced to the dependence in approximate method. After substituting the correction coefficient to the dependence on considered beam flexibility was written as

$$Y_{ll}^{(n)} = \frac{\lambda}{EIk^4 - \rho S\omega^2}. \tag{24}$$

The transients of flexibilities after correction of flexibility obtained by approximate method is shown in figure 6.

**3. Last remarks**

On the base of the obtained formulas, which were determined by the exact and approximate method, it is possible to make the analysis of the considered vibrating system by only Galerkin's method. In case of others boundary conditions of mechanical or mechatronic systems and other kinds of their vibrations it is necessary to achieve of offered other researches review in this paper. The problems will be presented in future works, because necessary conditions to synthesis of transverse vibrating mechanical or/and complex mechatronic systems must be obtained.

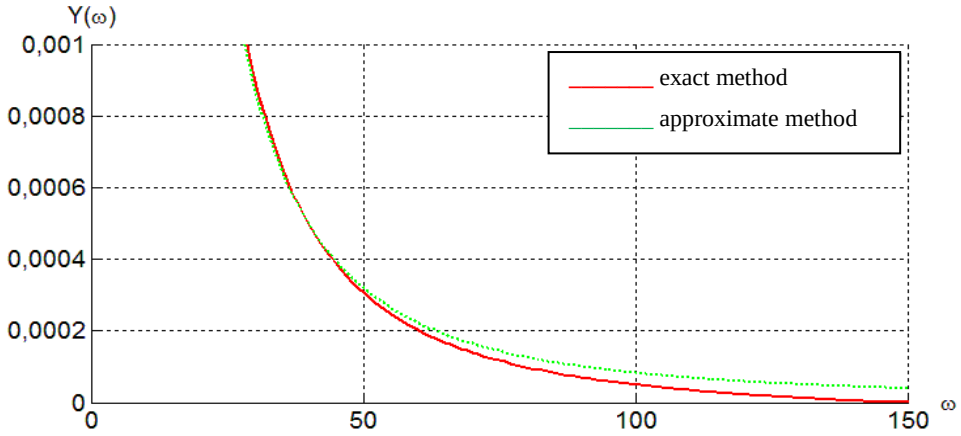


**Figure 6.** The dynamic flexibilities evolution around zeros and first of frequency after correction of approximate method

**Acknowledgement**

This work has been conducted as a part of research project PBS2/A6/17/2013 supported by the National Centre for Research and Development in 2013-2016.

**References**

[1] Bellert, S., Woźniacki, H. *The analysis and synthesis of electrical systems by means of the method of structural numbers* [in Polish]. WNT, Warszawa, 1968.

[2] Berge, C.: *Graphs and hypergraphs.* American Elsevier Publishing Co., Inc., New York/ North Holland Publishing Co., Amsterdam-London, 1973.

[3] Białas, K., Buchacz, A., Dzitkowski, T.: *Synthesis of active mechanical systems with dumping in view of polar graphs and structural numbers* [in Polish]. Monograph No. 230. Silesian University of Technology Press, Gliwice 2009.

[4] Buchacz, A *The synthesis of vibrating bar-systems represented by graphs and structural numbers* [in Polish]. ZN Politechniki Śląskiej, Mechanika, z.104, Gliwice 1991.

[5] Buchacz, A. *Modelling, synthesis and analysis of bar systems characterized by a cascade structure represented by graphs*. Mech. Mach. Theory, **30**, 7,, Pergamon (1995). 969-986

[6] Buchacz, A., Dymarek, A., Dzitkowski, T. *Design and Investigation of Sensitivity of Continuous and Discrete-Continuous Mechanical Systems with Assumed Frequency Spectrum by Means Graphs and Structural Numbers* [in Polish]. Monografia nr 88. Wydawnictwo Politechniki Śląskiej, Gliwice 2005.

[7] Buchacz, A. *The Expansion of the Synthesized Structures of Mechanical Discrete Systems Represented by Polar Graphs*. Journal of Materials Processing Technology. Vol. 164-165, Complete Elsevier, (2005), 1277-1280.

[8] Buchacz, A., Żurek, K. *Reverse Task of Dynamice of Active Mechanical Systems by Means the Graphs and Structural Numbers Methods* [in Polish]. Monografia nr 81. Wydawnictwo Politechniki Śląskiej, Gliwice 2005.

[9] Buchacz, A. *Modelling, Synthesis, Modification, Sensitivity and Analysis of Mechanic and Mechatronic Systems*. Journal of Achievements in Materials and Manufacturing Engineering, International OCOSCO World Press,Vol. 24, Issue 1, September (2007), 198-207.

[10] Buchacz, A. *Dynamical flexibility of discrete-continuous vibrating mechatronic system*. Journal of Achievements in Materials and Manufacturing Engineering, International OCOSCO World Press 28, 2, January (2008), 159-166.

[11] Buchacz, A. *Characteristics of discrete-continuous flexibly vibrating mechatronic system.* Journal of Achievements in Materials and Manufacturing Engineering, International OCOSCO World Press 28, 1, May (2008) 43-46.

[12] Buchacz, A. and Wróbel A. *Computer aided analysis of piezoelectric plates.* Solid State Phenomena - Mechatronic Systems and Materials: Mechatronic Systems and Robotics, Volume 164 (2010), 239-242.

[13] Buchacz, A. *The Supply of Formal Notions to Synthesis of The Vibrating Discrete-Continuous Mechatronic Systems.* Journal of Achievements in Materials and Manufacturing Engineering, International OCOSCO World Press, Vol. 44, Issue 2, February (2011), 168-178.

[14] Callahan, J. and Baruh H. *Vibration Monitoring of Cylindrical Shells Using Piezoelectric Sensors*. Finite Elements in Analysis and Design 23 (1996), 303-318.

[15] Kurnik W. *Damping of Mechanical Vibrations Utilizing Shunted Piezoelements*. Machine Dynamics Problems 2004, Vol. 28, No 4, 15-26.

[16] 10Lu, P, K. H. Lee, K.H., S. P. Lim, S.P. *Dynamical Analysis of a Cylindrical Piezoelectric Transducer*. Journal of Sound and Vibration (2003) 259(2), 427-443.

[17] Sękala, A., Świder, J. *Hybrid Graphs in Modelling and Analysis of Discrete–Continuous Mechanical Systems*. Journal of Materials Processing Technology, Vol. 164-165, Complete Elsevier (2005), 1436-1443.

[18] Świder, J., Michalski, P., Wszołek, G. *Physical and geometrical data acquiring system for vibration analysis software.* Journal of Materials Processing Technology, Vol. 164-165, Complete Elsevier (2005), 1444-1451.

[19] Świder, J., Wszołek, G. *Analysis of Complex Mechanical Systems Based on the Block Diagrams and The Matrix Hybrid Graphs Method*. Journal of Materials Processing Technology 157-158, Complete, Elsevier (2004), pp. 250-255.

[20] Wojnarowski, J., Buchacz, A. *Use of hypergraphs and complete structural numbers in the analysis of vibrating beam systems with non-linearly changing cross-sections*. VIBRATION ENGINEERING, **3**, 4, Hemisphere Publishing Corp., (1989), 593-598.

Andrzej Buchacz, Professor: Silesian University of Technology/ Faculty of Mechanical Engineering/ Institute of Engineering Processes Automation and Integrated Manufacturing Systems, Konarskiego 18A, 44-100 Gliwice, Poland (*andrzej.buchacz@polsl.pl*).

# Application of original method of vibration analysis for investigation on passenger car suspension as nonlinear dynamical system (NUM272-15)

Rafał Burdzik

*Abstract:* Each vehicle should be considered as nonlinear complex dynamical system. Due to dynamics requirements and vibration exposure of passenger cars one of the most important system is suspension. The main elements of the suspension are shock absorbers and spring and tire. These elements determine damping and stiffness properties. For modern cars, where the customer and safety requirements are much more restrictive, the characteristics of these elements are nonlinear and more often adjustable for driving condition. Thus all suspension should be considered as strongly nonlinear system. The paper presents application of original methods of vibration analysis for investigation on passenger car suspension. The research was conducted on real car. During the experiments the vibration were measured in chosen localization on suspension elements. The scope of the research contained investigations on influence of damping and stiffness properties on vibration transferred from forced wheel into car (in the result on passenger). The signals of vibration of such nonlinear system are non-stationary thus TFR methods are recommended for the analysis. The author presents original numerical method of resonance vibration analysis.

## 1. Introduction

The range of impacts vibrations exert on a vehicle driver is very broad, starting from the feeling of discomfort to safety hazards caused by vibrations at resonant frequencies of specific organs, thus affecting the driver's responses. Ride quality and comfort increasingly begins refer to vibration and noise in terms of sensation or feel of the passengers [1,2]. Lower range of vibration frequencies mostly are correlated to vibration comfort and higher (more than 80 Hz) to noise [3]. Vibration and noise are perceived differently by humans, so there is a need to adopt methods that help quantify and control them [4-6]. Each vehicle should be considered as nonlinear complex dynamical system. Due to dynamics requirements and vibration exposure of passenger cars one of the most important system is suspension.

The current state of art presents many different approaches and methods for vibration signal processing. The vibration has to be considered in terms of amplitude, time and frequency. The evaluation of impact of chosen factors on vibration occurring in motor vehicles requires wide scope

of amplitude, time and frequency characteristics analysis [7]. The properties of human vibration perception require observation of distribution of vibration in time and frequency domains. Thus it is very helpful to identify structure of the vibration as correlated time-frequency distribution. Such an approach enables the analysis of exposure to vibration. This presentation of vibration's structure enables identification of time of exposure to chosen vibration dynamics. This approach allows precise evaluation of exposure to vibration correlated to natural vibration of human organs. In the scope of engineering applications the presented approach allows designing and developing of elements and systems dedicated to absorb or isolate of vibration in chosen frequency bands. Studies presented in [8] focused on the dynamics of a passive car suspension, the nonlinear characteristics of tyres and the effect of shimming in vehicle wheels. However, due to various nonlinearities in the vehicle dynamics, the chaotic behaviour may produce noise like responses [9]. Authors of [10] have studied the vibrations of a quarter-car model with a softening stiffness of the Duffing type, focusing on the potential for chaotic behaviour. They examined the global homoclinic bifurcations that appear as instabilities at the boundaries of the basins of attraction, and the cross-sections of stable and unstable manifolds, by the perturbation approach using Melnikov theory. A critical amplitude was found for which the system can exhibit chaotic vibrations. The paper [11] presents a nonlinear decoupling approach based on the Modified Generalized Frequency Response Functions and the nonlinear feature of phase in variance, for the pure nonlinearity input nonlinear system. When nonlinearity is introduced into linear system, nonlinear behaviour is the rule in the dynamic behaviour of the physical system [12].

One may think of numerous systems and components of a vehicle which purpose is to absorb vibrations or minimise their impact. A vehicle suspension system, which consists of damping, springing and steering elements, are responsible to a considerable extent for damping of vibrations generated by road irregularities [13-15]. Rubber components which provide mounting to such systems as engine, gearbox or exhaust system also bear a fair share of responsibility for absorption of the vibrations generated by these assemblies. The purpose of every shock absorbing system and element is to minimise the impact exerted by vibrations on other systems as well as on the persons inside the vehicle. Oscillatory waves propagate and influence people via the vehicle structure, i.e. the frame or the body. Vehicle vibrations are classified into two general types of the rigid body vibration of sprung and unsprung mass and stiffness vibration. Stiffness vibration is determined by mass, stiffness and damping forces which are contained in suspension component parts..

## 2. Research methodology

One of the main sources of vehicle vibration is vertical movement of the wheel. It is caused by driving on road roughness. The excitation can be considered as time functions of the wheel strokes. It

causes force transfer and dynamics response to the vehicle construction. The analysis of the mechanical system dynamics requires conducting research with vibration excitation system. It enables forcing of the tested system with the excitation programmed for the chosen frequency bands. One of the assumptions of the research method was guarantee of the force excitation recurrence with possibilities of changing of the technical parameters of the researched vehicle.

The goal of the investigation was evaluation of developed method of vibration analysis for investigation on passenger car suspension as nonlinear dynamical system. It was assumed that this method has to be sensitive on changes of dynamical system properties. Thus research comprised a series of active diagnostic experiments conducted in passenger cars. A car prepared to the tests, with the suspension components mounted having their technical condition known was subject to oscillatory input functions. For that purpose, a station enabling kinematic vibration excitation was used, making it possible to programme the dynamic frequency structure of input functions. The input frequency range envisaged comprised resonance frequency bands of both sprung and unsprung masses.

Each time the test was conducted, a wheel of one vehicle axle was subject to the input function. For the sake of analysis of the suspension system damping parameters, vertical vibrations of excitation platform, unsprung elements (suspension arm) and the vehicle body (upper shock absorber mounting) were recorded coaxially. The scheme of the experimental research has been depicted in Figure 1.

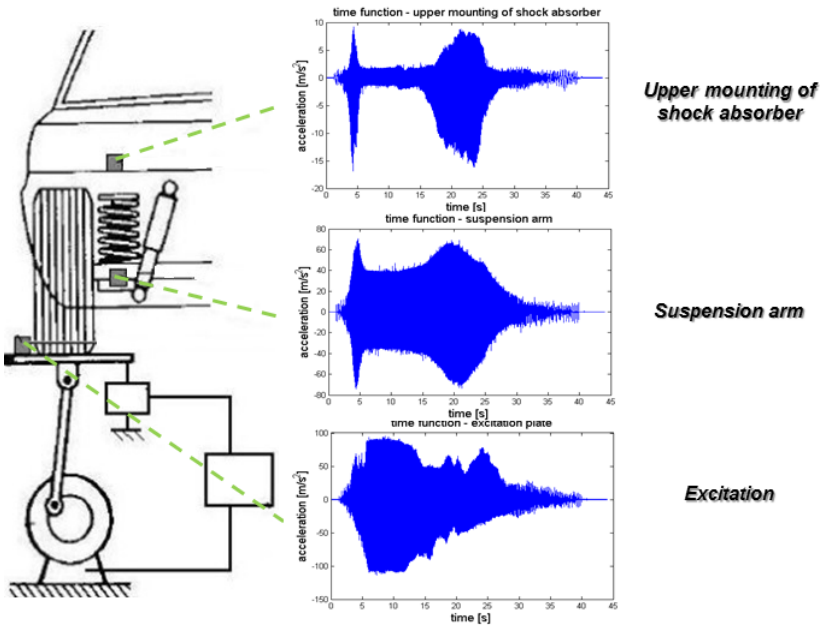


**Figure 1.** Scheme of the experimental research.

One of the most important components of the vehicle suspension is shock absorber. It is responsible for damping of the vibration transferred from wheel into car body. Thus for the purpose of investigation on the influence of changes in the technical condition of suspension elements on the vibration distribution in a vehicle the damping properties of the shock absorber were chosen as determinant of technical condition of suspension. The damping properties of the shock absorber are described as force vs. velocity characteristics. One of the most common reason of decrease of damping properties during operating of vehicle is leak of shock absorber fluid. The influence of the volume of the shock absorber fluid on damping characteristic has been depicted in Figure 2. It is very significant how the damping force changed under different fluid volume. When consider novel suspensions with active vibration control such kind of characteristics are not enough to represent damping properties [16].

The paper presents results occurring during research vehicle with shock absorber with damping characteristic presented as force vs. velocity functions depicted in Figure 2.

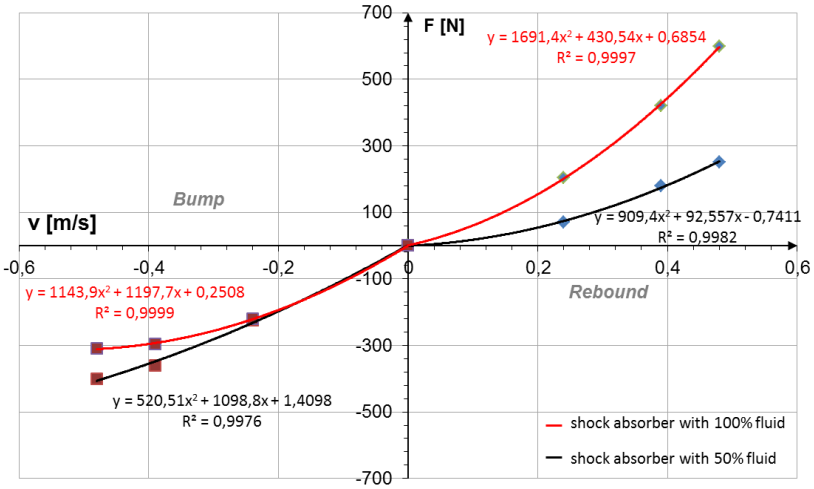


**Figure 2.** Force vs. velocity characteristics of the investigated shock absorbers.

## 3. Research results

The vibration occurring during research are results of forces acting on wheel by the exciter machine. The signals have non-stationary properties (fig. 3). Thus the analysis of the signal or evaluation of human vibration exposure based on global estimators is difficult. Distribution of the vibration in defined frequency bands enables observing of vibration exposition in time function.

Depending on the characteristics of the vibration signal or even its period's different mathematical transformations can be made. It enables elaborating of dedicated signal processing method for research on vibration in many terms. The evaluation of impact of chosen factors on

vibration occurring in motor vehicles requires wide scope of amplitude, time and frequency characteristics analysis.

The analysis spectrum is very difficult because frequency components are blurry (fig. 3). For the constant frequency the signal is stationary and frequency component are strongly isolated. As the applications of frequency analysis in automotive industry are typically automotive fatigue research relied on power spectral densities (PSDs) to represent stochastic dynamic behaviours [17,18]. Due to limitation in evaluation based on the one-dimension (frequency) analysis, it has been proved that tests and analytical tools are not always successful in producing failures observed in the field. The Ford Corporation found that a module could pass the qualification test but fail in the field [19]. Thus the research was conducted on develop new approach for multidimensional analysis of vibration in vehicle research.

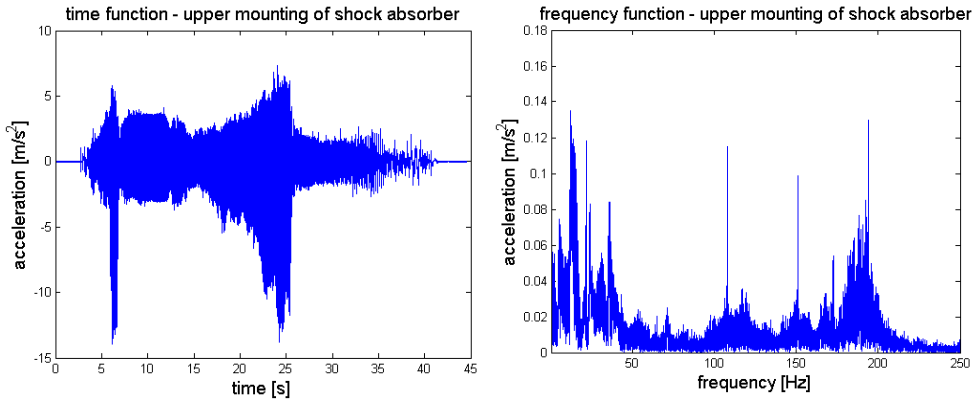


**Figure 3.** Non-stationary signal of vibration of upper mounting of shock absorber on car body.

The time-frequency representations of the structure of the vibration enable selective evaluation of distribution of vibration. For the purpose of analysis of the influence of the technical condition of suspension elements on the vibration propagation it is useful to identify the components of the signal which are best representation of those influences. Thus the symptoms of the technical conditions or value of the operating parameters can be determined.

For the research results analysis on influence of suspension's technical condition on structure of occurring vibration the STFT of the signals were calculated. The reason of choosing the STFT was time consumption of the analysis process, because utility and applicability requirements. The distribution in time of vibration energy for next frequencies can be observed. The STFT transformation of vibration registered during research on vehicle with build in shock absorbers with 100% and 50% of liquid volume are shown in figures below. It shows that for the shock absorber with 50% of liquid the vibration energy become more centred and occurred in non-stationary parts of the signal.

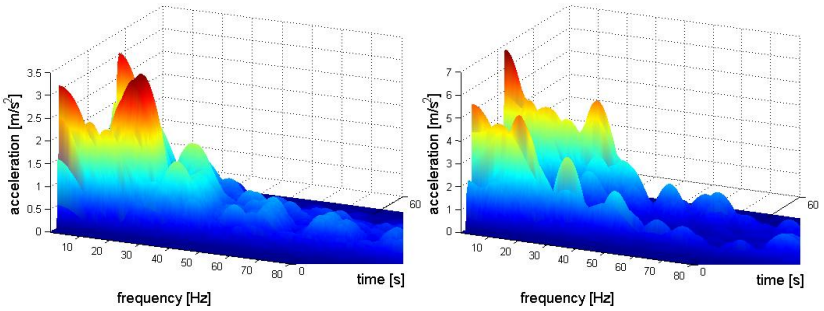


**Figure 4.** Non-stationary signal of vibration of upper mounting of shock absorber on car body (shock absorber with: left - 100%, right - 50% of liquid volume).

### 3.1 Distribution of the vibration of defined frequency bands

Depending on purpose of vibration research different approaches are present. The properties of human vibration perception require observation of distribution of vibration in time and frequency domains for the analysis of vibration phenomena. Thus it is very helpful to identify structure of the vibration as correlated time-frequency distribution. Such an approach enables the analysis of exposure to vibration. This presentation of vibration's structure enables identification of time of exposure to chosen vibration dynamics. This approach allows precise evaluation of exposure to vibration correlated to natural vibration of human organs. The paper presents investigations conducted to develop novel method of signal processing, which can be used for research on exposure to vibration transferred into the passenger car occupants.

The paper addresses results of analysis of application of one of the TFR techniques to the identification of structure of vibration to identify impact damping properties on exposure to vibration. The possibilities of identification of characteristics components of vibration structure and sensitivity on the changes in mechanical system parameters have been investigated on the results of the research on influence of technical condition of suspension of the vehicle. The influence of the damping of shock absorber can be observed in vibration's structure, as an increase of the vibration energy. The time-frequency distribution of the vibration allows localization of window with highest increase of energy generated during passing by resonance frequency of unsprung masses in the time period of coasting of exciter machine. Basing on the analysis of the spectrum and TFR results the main frequency bands were chosen for further observation. The obtained representation of the vibration as structure of STFT transformation allow to determine time function of separate frequency bands which represents the isolated vibration dynamics phenomena, expressed as:

$$S_f = \sum_{f=a}^{b} \sum_{i=0}^{\infty} S(\omega_f, t_i) \tag{1}$$

where:

$f$ – frequency band from $a$ to $b$,
$t$ – time,
$S(\omega_f,t_i)$ – Short-Time Fourier Transformation of the signal.

This function allows separation of the chosen dynamics structure of the vibration and analysis of energy changes by the time realization in isolated frequency bands.

This method of identification of vibration dynamics allows observing time of increase of vibration activity of the vehicle and influence of the damping properties on time function of the chosen frequency bands of the signal. Results analysis of vibration structure occurred during research on different damping properties of shock absorbers it was assumed that the most sensitivity frequency components are ca. 12 Hz, 21.5 Hz and 64.5 Hz. There were set as centres of the analysed frequency bands range ca. 2 Hz each. Figures below present time distribution of the vibration in those frequencies.

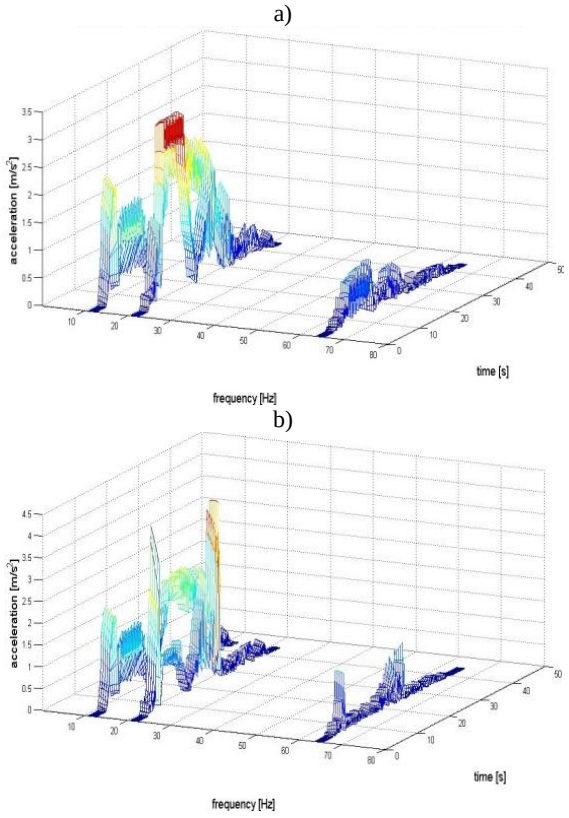


**Figure 5.** Time distribution of the vibration of upper mounting of shock absorber for chosen frequency bands (shock absorber with: a) - 100%, b) - 50% of liquid volume).

### 3.2 Function of exposure time to the vibration of defined frequency bands

The procedure as regulated by the international ISO 2631-1 standard [20] prescribes the vibration total value of weighted root mean square accelerations as a reference quantity for the assessment of vibration effects on the comfort. Many more estimators for the assessment of vibration effects on the comfort have been presented in [1,21,22], especially for the child seat [23].

Considering the variability of the time and frequency distribution of the vibration even in selected analysed bands, the time function was developed as vibration exposure estimator. It is calculated of average value of frequency bands vibration in time domain, expressed as:

$$S_{avr} = \sum_{i=0}^{\infty}\left(\frac{1}{(b-a)/d}\sum_{f=a}^{b} S(\omega_f, t_i)\right) \tag{2}$$

where:

*a*- lover edge of the passband,
*b*– upper edge of the passband,
*d*– STFT frequency resolution (integer rounded value),
*(b-a)/d* – returns number of samples in frequency bands.

Figures below present process of the determination of the average value of frequency bands vibration 11 – 13 Hz, in time domain.

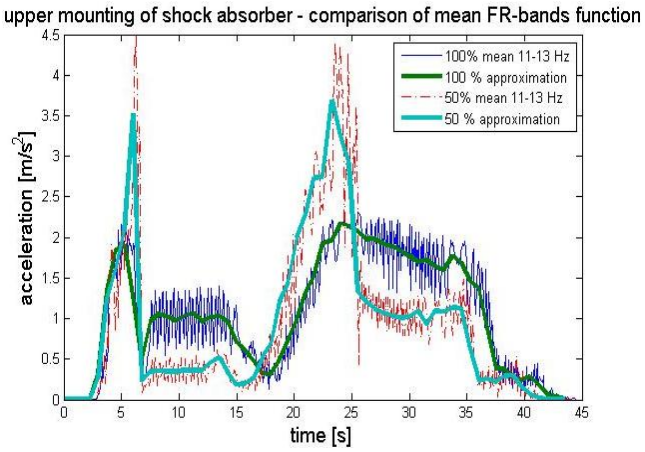


**Figure 6.** The process of the determination of the average value of frequency bands vibration (11 – 13 Hz) in time domain.

Figures below present the comparison of time function of average vibration in chosen frequency bands for the vehicle with build in shock absorber with 100% and 50% of liquid volume. The paper presents result obtained for the following frequencies bands: 11-13 Hz (fig. 6), 20.5-22.5 Hz and 63.5-65.5 Hz (fig. 7).

a)

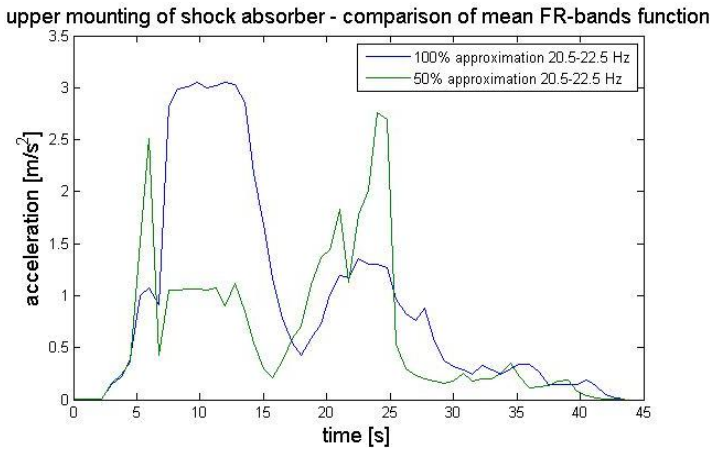


b)

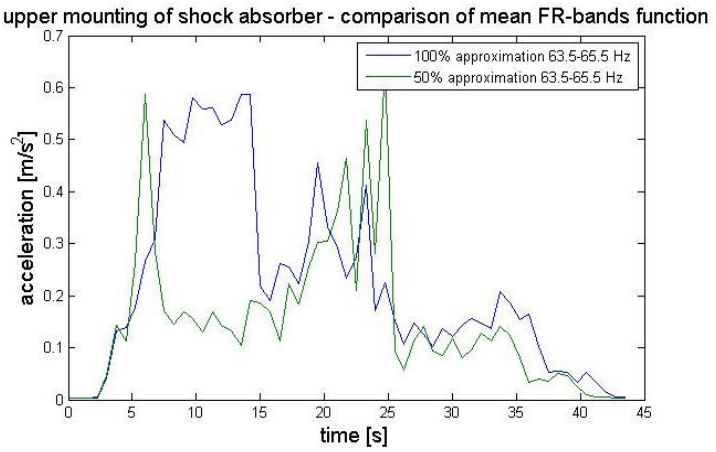


**Figure 7.** Time function of average vibration in frequency bands: a) 20.5-22.5 Hz, b)- 63.5-65.5 Hz: upper mounting of shock absorber (shock absorber with: blue- 100%, green- 50% of liquid volume).

Previous section presents the application of STFT 3-D time-frequency distributions for proper observation of the vibration structure. The obtained representation of the vibration allows determining time function of separate frequency bands represents the isolated vibration dynamics phenomena. The changes of the vibration energy in chosen frequency bands can be observed by the time function of average vibration in chosen frequency bands. The results of comparison of the vibration of the vehicle with build in shock absorber with 100% and 50% of liquid volume show the influence of damping properties on chosen frequency bands.

## 4. Conclusions

For the vibration perception properties as type of vibration we can consider the value, dynamics and exposure time of chosen frequency components of the vibration. The possibilities of simultaneous observation of distribution of signal in time and frequency domains are reached by the time-frequency representation (TFR) of the signal.

Such a wide range of experimental studies and analyses enables accurate assessment of the human exposure to vibrations in vehicles based on multidimensional analysis of the vibration exposure time for successive frequency bands. It may also initiate a new approach to experimental modelling and identification of the oscillatory wave propagation in a vehicle structure.

The research methodology proposed and a dedicated analysis of results enables comparison of the vibration dynamics between specific frequency bands. These measures demonstrated a considerable susceptibility to changes in the technical condition of shock absorber with regard to the assessment of human exposure to vibrations.

The analysis of the results shows increase of the vibration energy for the vehicle with shock absorber with 50% of liquid volume but for determined time realization. For the rest of the time of excitation the vibration are even lower, especially during constant excitation (ca. between 9-14 seconds). The maximums values of the functions are in ca. 5th and 25th seconds of the excitation. It is the effect of time of passing thru unsprung masses resonance, ca. 12 Hz.

Very important conclusion is that function proposed of exposure time to the vibration of defined frequency bands is sensitivity for vibration of the suspension element and car body. The car body vibrations are transfer from vehicle via feet to the humans in mean of transport. Thus formulated and developed function may be useful for exposure to vibration evaluation or monitoring.

In the scope of engineering applications the presented approach allows designing and developing of elements and systems dedicated to absorb or isolate of vibration in chosen frequency bands.

## References

[1] Burdzik, R. *Identification of sources, propagation and structure of vibrations affecting men in means of transport based on the example of automotive vehicles*. JVE International Ltd., Kaunas, 2014.

[2] Burdzik, R. Identification of structure and directional distribution of vibration transferred to car-body from road roughness. *Journal of Vibroengineering*, 16(1) (2014) 324-333.

[3] Pawełczyk, M. Acoustics and vibration as fascinating challenges to specialists in automatic control and signal processing. *International Journal of Acoustics and Vibrations*, 11(3) (2006) 118-119.

[4] Wszołek, T., and Kłaczyński, M. Automatic detection of long-term audible noise indices from corona phenomena on UHV AC power lines. *Acta Physica Polonica A*, 125 (4A) (2014) A93-A98.

[5] Kłaczyński, M. and Wszołek, T. Artificial intelligence and learning systems methods in supporting long-term acoustic climate monitoring. *Acta Physica Polonica A*, 123 (6) (2013) 1024-1028.

[6] Klaczynski, M. Vibroacoustic methods in diagnosis of selected laryngeal diseases. *Journal of Vibroengineering*, 17 (4) (2015) 2089-2098.

[7] Dabrowski, Z. and Zawisza, M. Investigations of the Vibroacoustic Signals Sensitivity to Mechanical Defects not Recognised by the OBD System in Diesel Engines. *Solid State Phenomena*, 180 (2012) 194-199.

[8] Szabelski, K. The vibrations of self-excited system with parametric excitation and non-symmetric elasticity characteristics. *J Theor Appl Mech*, 29 (1991) 57–81.

[9] Li, S. and Yang, S. and Guo, W. Investigation on chaotic motion in histeretic non-linear suspension system with multi-frequency excitations. *Mech Res Commun*, 31 (2004) 229–36.

[10] Litak, G. et al. Chaotic vibration of a quarter-car model excited by the road surface profile. *Communications in Nonlinear Science and Numerical Simulation*, 13 (2008) 1373–1383.

[11] Xiao, B. et al. Decoupling analysis on nonlinear system based on the modified generalized frequency response functions. *Mechanical Systems and Signal Processing*, 42 (2014) 283-299.

[12] Kerschen, G. and Worden, K. and Vakakis, A.F. et al. Past, present and future of nonlinear system identification in structural dynamics. *Mechanical Systems and Signal Processing*, 20 (2006) 505–592.

[13] Borowiec, M. and Hunicz, J. and Sen, A. and Litak, G. and Koszalka, G. and Niewczas, A. Vibration of a vehicle excited by real road profiles. *Forschung im Ingenieurwessen*, 74 (2010) 99–109.

[14] Burdzik, R. Research on structure and directional distribution of vibration generated by engine in the location where vibrations penetrate the human organism. *Diagnostyka*, 14(2) (2013) 57-61.

[15] Burdzik, R. and Konieczny, Ł. Research on structure, propagation and exposure to general vibration in passenger car for different damping parameters. *Journal of Vibroengineering*, 15 (4) (2013) 1680-1688.

[16] Praus, A. and Powałka, B. and Marchelek, K. et al. Active vibration control in milling flexible workpieces. *Journal of Vibration and Control*, 19 (7) (2013) 1103-1120.

[17] Bonte, M.H.A. and De Boer, A. and Liebregts, R. Prediction of mechanical fatigue caused by multiple random excitations. *Proceedings of the ISMA Conference*, (2004) 697–708.

[18] Bonte, M.H.A. and De Boer, A. and Liebregts, R. Determining the von Mises stress power spectral density for frequency domain fatigue analysis including out-of-phase stress components. *Journal of Sound and Vibration*, 302 (1-2) (2007) 379–386.

[19] Thomas, D.A. and Avers, K. and Pecht, M. The "trouble not identified" phenomenon in automotive electronics. *Microelectronics Reliability*, 42 (4-5) (2002) 641–651.

[20] ISO 2631. Mechanical vibration and shock-evaluation of human exposure to whole-body vibration, second ed. *ISO – International Organization for Standardization*, 1997.

[21] Griffin, M. Discomfort from feeling vehicle vibration. *Vehicle System Dynamics*, 45 (7-8) (2007) 679-698.

[22] Griffin, M. *Handbook of Human Vibration*. New York: Academic Press Ltd, 1990.

[23] Wicher, J. and Więckowski, D. Influence of vibrations of the child seat on the comfort of child's ride in a car. *Eksploatacja i Niezawodnosc – Maintenance and Reliability*, 1 (77) (2010) 77-93.

1) Rafał Burdzik, Ph.D. D.Sc. Assistant Professor: Silesian University of Technology, Faculty of Transport, Krasińskiego 8, 40-019 Katowice, Poland (rafal.burdzik@polsl.pl), the author presented this work at the conference.

# Adaptation of linear decimation procedures for identification of characteristics components of non-stationary vibration signals in car's suspension (NUM277-15)

Rafał Burdzik, Łukasz Konieczny, Jan Warczek, Witold Cioch

*Abstract:* During modelling, designing and producing of car's suspension a lot of requirements have to be fulfilled. Most of them are determined by the safety and comfort of passengers. When consider car as multi-DOF dynamical system the meaning of suspension become even more important. Due to its functions as: isolation and damping of vibration, assurance of constant contact of wheel to road. Many of the important information of the vibration phenomena and dynamical system properties refer to frequency domain. Regardless of the vibration test it is essential to correctly identify the frequency components of vibration signals. Given the unsteady nature of the vibrations resulting from the nonlinear characteristics of suspension elements of the vehicle and the random nature of the dynamic interactions, determining the frequency characteristics is a complicated issue. For the non-stationary signals the time-frequency transformation methods are recommended. These transformation algorithms are time consuming during signal processing. Thus the novel method, developed in AGH University of Science and Technology, for transfer non-stationary signals into pseudo-stationary signals has been tested on vibration registered on real car's suspension system. The paper presents the results of research which aimed to examine the possibility of adapting the linear decimation procedure for the identification of characteristics components of non-stationary vibration signals of a car.

## 1. Introduction

Vibration is the mechanical phenomena caused by machines in operation. Generally the vibration is undesirable, wasting energy and creating unwanted effects. The vehicle vibrations are one of the most important unwanted effects. It causes decrease of safety and comfort factors and increase of fuel consumption [1-5]. Taking into account the problem of rough surface road profiles and its influence on vehicle unwanted vibrations due to kinematic excitations and other dynamical forces occurring during drive the scope of subjects of research among automotive manufacturers and research groups, whose objective is to minimize vibration effects on the driver and passengers is still growing [6]. Traffic induced vibrations are a common source of environmental nuisance as they may cause malfunctioning of sensitive equipment, discomfort to people and damage to buildings and engineering structures [7,8]. Like most vibration problems, road and rail traffic vibrations can be characterized by

a source-path-receiver scenario. Vehicle contact with irregularities of the road and rail surface induce dynamic loads, that generate stress waves, which propagate in the soil, eventually reaching the foundations of adjacent buildings and causing them to vibrate. Road traffic vibrations are caused by heavy vehicles such as buses and trucks. Passenger cars and light trucks rarely induce vibrations that are perceptive in buildings. Road traffic tends to produce vibrations in the range from 5 to 25 Hz. Rail traffic vibrations are produced in a similar way by vehicle contact with irregularities in the rail surface. The produced vibrations in this case are in the range from 60 to 100 Hz, according with [9,10]. The problem of vibration caused by underground traffic is discussed in [11,12]. Other aspects of the vibration analysis of bridges under moving vehicles and trains can be found in [13]. The environmental problems of vibrations, caused by train/traffic, construction activities and factory operation, and other man-made sources are investigated in [14]. It can be observed than for the widely named transport vibration the information about frequency distribution is very important.

During the last few years, the interaction problem between moving vehicles and buildings and structures has drawn much attention. For the analysis of vibration of solid structure, as bridge for example, interesting approach has been presented in [15,16], where authors developed the fundamental concept of power-flow analysis to investigate the steady-state responses of vibration isolation systems [17]. Authors of papers [18,19] extended this approach to coupled structural systems comprising various subsystems. For identify the dominant vibration frequencies the concept of mobility and power-flow analysis in the frequency domain have been used. This concept assumed considering the vehicle, track and bridge subsystems as a coupled system. The general vehicle–track–bridge system consists of multi-rigid-bodies for the vehicles; infinite Euler beams representing the rails; two-or three-dimensional finite elements of the concrete bridges and spring-dashpot pairs to model the wheel–rail contacts, the vehicle suspensions, the rail pads and the bridge bearings. Unlike most commonly used power-flow analysis methods, the spring-dashpot pairs in the coupled system are not treated as subsystems but as unknown since the force-method based equilibrium equations. The dynamic interaction forces between various subsystems are obtained first by solving the equations. The mobility of point, defined as subsystem, and the power flow scan then be calculated and used to analyse the dominant vibration frequencies [17].

## 2. Linear Decimation Procedure (LDP) for the rotary-machine

Linear Decimation Procedure involves the dynamic signal resampling in accordance with rotation speed variations. It assumes the linear approximation of cycle variations curbed with values representing its beginning $\Theta_p$ and end $\Theta_k$. Fig. 1 presents process of obtaining secondary signal vector after LDP from primary vector.

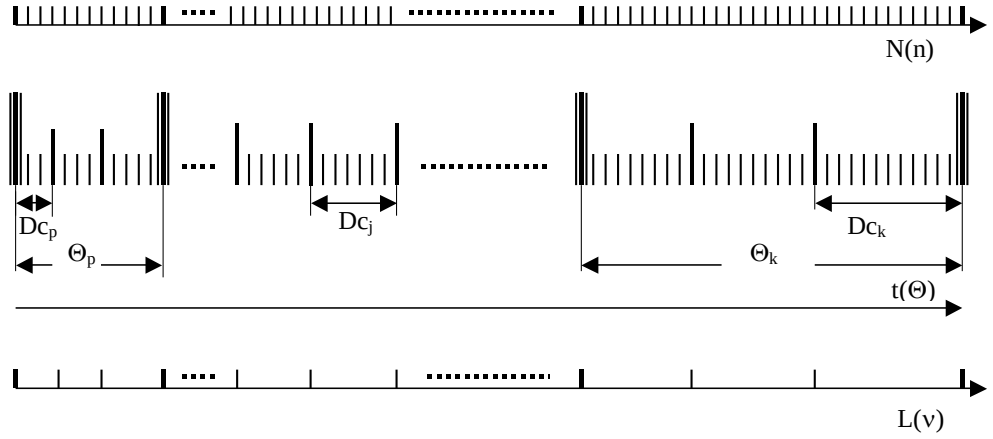


**Figure 1.** Linear Decimation Procedure – resampling method: Θ- cycle time, t(Θ)- observation time, N(n)- primary sample-cluster in the observation window, L(ν)- secondary sample-cluster in the observation window (after LDP), $Dc_p$ - initial decimation coefficient, $Dc_k$ - final decimation coefficient [20].

The key element of LDP is to define decimation coefficient $Dc_K$. This coefficient characterizes the increment of signal resampling. It varies according to increase or decrease of the rotation speed that means with the cycle variations. By adapting the final decimation coefficient we determine its variations in accordance with linear signal trend. The selection of the final decimation coefficient enables to reduce the signal to the stationary form in the observation window for the last cycle which is very convenient in real-time analysis. By the applying the selected final decimation coefficient value and the linear approximation of cycle variations the formula can be determined for the value of decimation coefficient of n-sample. The formula is shown below:

$$Dc_n = Dc_k \frac{N_{\Theta p}}{N_{\Theta k}} + \frac{n}{n_{Dk}}(Dc_k - Dc_p) \tag{1}$$

As the result of calculation with this formula, the secondary vector of the signal representing the constant sample-per-cycle number.

$$w(\nu_k) = u(n_{Dk} + Dc_n) = u(n) \tag{2}$$

where:

**u**(n) – primary vector

**w**(*ν*)– secondary vector (after resampling)

As result of LDP and resampling the signal gets the form similar to the stationary-signal form thus enhancing the spectral selectivity. As for rotary machines at the stage of run-up, particularly machines of dynamic changes of rotation speed, preserving linearity did not significantly improve spectral selectivity, especially in high-frequency band. This prompted developing modified algorithm of the method enabling adjustment to cycle change in short time-periods of an observation window. The new method of analysing signals in narrow time-periods was referred to as Short-time Procedure of Linear Decimation STPLD (Fig. 2).

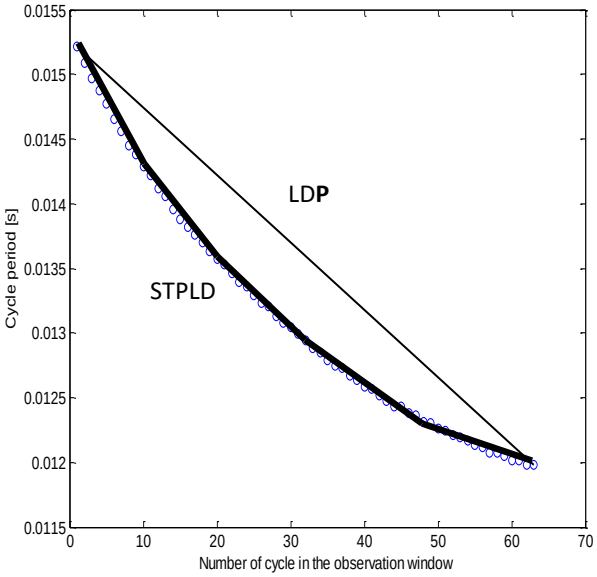


**Figure 2.** Approximation of cycle change in observation window with STPLD [20].

## 3. Adaptation of LDP for vibration signals in car's suspension

LDP or STPLD are dedicated for diagnosing of rotary machine, where information about cycles are easy to get [21]. When consider car as multi-DOF dynamical system and vibrations resulting from the nonlinear characteristics of suspension elements application of LDP seems to be impossible. Authors put a lot of effort to adapt LDP for such non-stationary signals as vibration in car's suspension. It was developed new algorithm to identify cycles without reference signal. The methodology was tested on results of research of vibration of passenger car forced to vibration by the special kinematic excitation machine. The signals were registered in chosen location of the suspension. The result obtained are signals with splot of stationary and non-stationary vibrations (Fig. 3). Analysis of frequency distribution based on FFT is very difficult. It is impossible to identify main frequency components other than correlated to stationary cycle of signal (ca. 21.5 Hz) (Fig. 4).

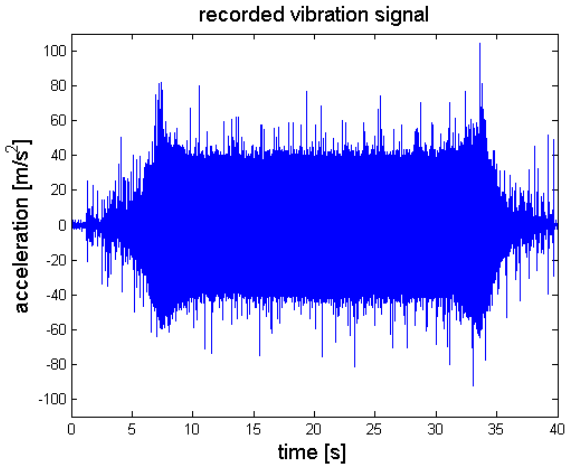


**Figure 3.** Waveform of recorded vibration signal.

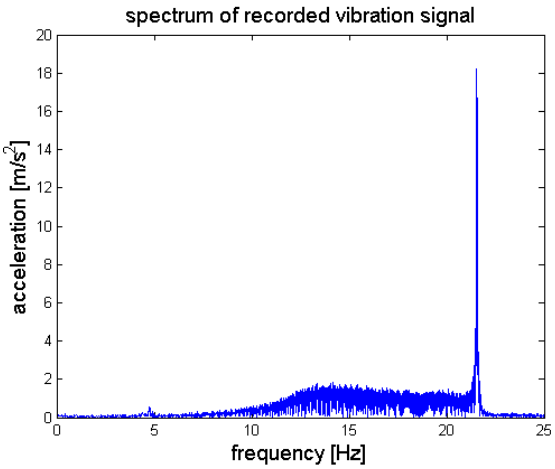


**Figure 4.** Spectrum of recorded signal.

The author developed the algorithm of the signal distribution by the stationary and non-stationary conditions. The mathematical algorithm prepared and programmed enables analysis and separation of the vibration signals in accordance with the stationary and non-stationary states. It is based on core of the frequency comparison to localize the signal with constant frequency as the main condition for stationary signal. Simultaneous the changes of the mean values of the signal in processed window are compared. Those operations allow dividing of the signal for windows with stationary and non-stationary part of the recorded signal (Fig. 5).

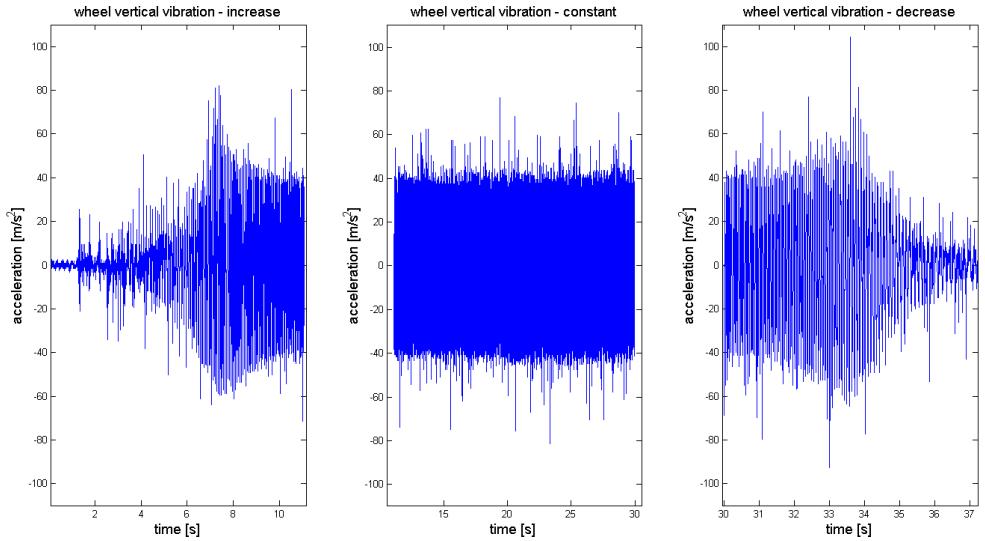


**Figure 5.** Signal divided due to stationary and non-stationary cycles.

It enables to analyse separately signal but the identification of dominant frequency components is still difficult (Fig. 6) because spectrums are affected by blurring. Of course for such divided signal we can use different signal processing methods, such as multidimensional transformations. But the purpose of this investigation was to identify characteristics components of non-stationary vibration signals based on LDP.

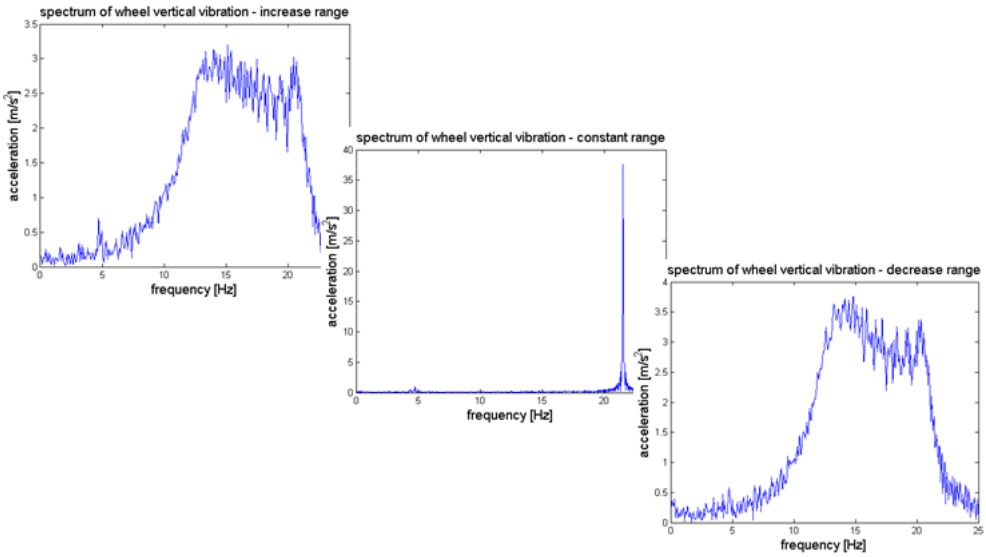


**Figure 6.** Spectrums of the divided signal.

Thus the adaptation of LDP for transfer non-stationary signals into pseudo-stationary signals has been tested. Fig. 7 presents amplitude spectrum after applying LDP with final decimation coefficient $D_{ck}$=10, spectrum band width is 25 Hz. It features the significant improvement of spectrum quality in sprung masses resonance band. It is clearly visible frequency components correlated to sprung masses resonance as higher amplitudes peaks in the frequency range of ca. 5 Hz. The isolated after applying LDP frequency component have been indicated in Figure 7. The vibration control in automotive vehicles is focused on safety and comfort. Due to this issue the amplitudes of vibration in unsprung masses frequency bands should by analysed in term of safety and sprung masses frequency bands in term of comfort. Thus damping and stiffness elements of car suspension are optimised by the characteristics focused on vibration transferred, especially for those resonances bands. Thus the signal processing methods allowing for identification of frequency components are recommended.

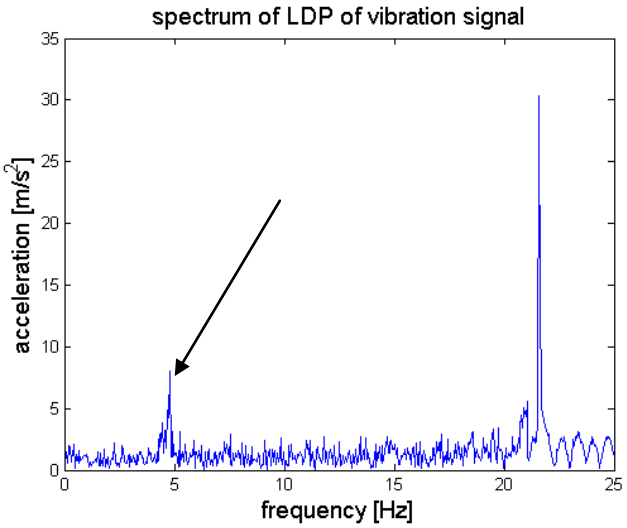


**Figure 7.** Amplitude spectrum after applying LDP.

For the better illustration of improvement selectivity of the signal after applying LDP frequency components distribution in time have been calculated. The signal was transferred into spectrogram computes as short-time Fourier transform of a signal. Result of transformation contains an estimate of the short-term, time-localized frequency content of signal. Signal is divided into segments equal to defined value and a Hamming window is used with 80% overlap between segments. For time-frequency distribution of signal the power spectral density (PSD) of each segment is calculated. It contains the two-sided modified periodogram estimate of the PSD of each segment. The comparison of spectrograms and PSD distribution of each segment for registered signal and after applying LDP have been presented in Figs. 8 and 9. It shows that sprung masses frequency (ca. 5 Hz) is barely visible in original signal because it is blurry by frequencies correlated with increase of frequency of

excitation machine (Fig. 8). After applying LDP the sprung masses resonance frequency has been identified. Fig. 9 presents clearly visible amplitude of PSD for ca. 5 Hz frequency and it is active during whole time of the registered signal.

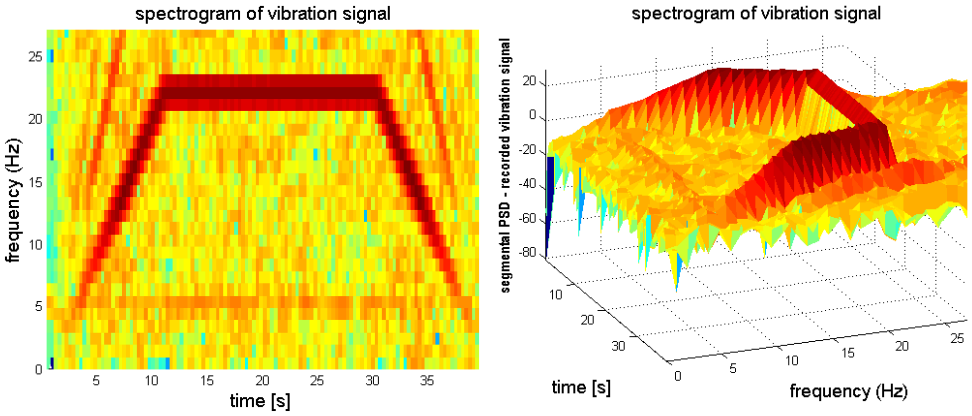


**Figure 8.** Spectrogram of the original registered signal.

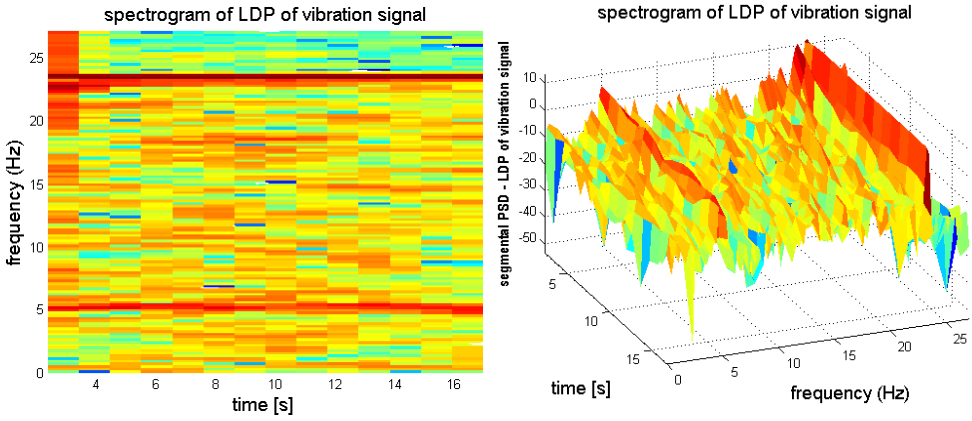


**Figure 9.** Spectrogram of signal after applying LDP.

## 4. Conclusions

Major function of car's suspension is isolation of vibration transfer into car-body. Thus it is important to evaluate suspension properties due to vibration tests. Regardless of the vibration test it is essential to correctly identify the frequency components of vibration signals. Given the unsteady nature of the vibrations resulting from the nonlinear characteristics of suspension elements of the vehicle and the random nature of the dynamic interactions, determining the frequency characteristics is a complicated issue. The paper presents the results of investigation which aimed to examine the possibility of

adapting the linear decimation procedure for the identification of characteristics components of non-stationary vibration signals of a car's suspension.

For the sake of analysis of vehicle vibration it is important to observe the magnitude of vibration for resonances bands of sprung and unsprung masses. Adaptation of LDP allows identifying amplitude of vibration for sprung masses frequency band. These components of vibration are extremely important for driving comfort and whole-body vibration exposure. Unfortunately, distinct stripe selectivity in the frequency band of unsprung masses resonance was not achieved. According to paper [20] the reason of such situation can be approximation by a linear function in the observation window, which is suitable only for signals with linear cycle-change trend.

Thus proposed method of car's suspension vibration signal processing has to be extend for other tools. For example methods of TFR (time-frequency representation) can be very useful for observation of the vibration and evaluation if we didn't lose any important information after applying LDP.

**References**


[1] Burdzik, R. *Identification of sources, propagation and structure of vibrations affecting men in means of transport based on the example of automotive vehicles*. JVE International Ltd., Kaunas, 2014.

[2] Burdzik, R. Identification of structure and directional distribution of vibration transferred to car-body from road roughness. *Journal of Vibroengineering*, 16(1) (2014), 324-333.

[3] Burdzik, R., and Gardulski. J. Frequency analysis decimation vibration signals of passenger car's suspensions. *Transport Problems*, 2 (2007), 23-29.

[4] Klaczynski, M. Vibroacoustic methods in diagnosis of selected laryngeal diseases. *Journal of Vibroengineering*, 17 (4) (2015), 2089-2098.

[5] Dabrowski, Z. and Zawisza, M. Investigations of the Vibroacoustic Signals Sensitivity to Mechanical Defects not Recognised by the OBD System in Diesel Engines. *Solid State Phenomena*, 180 (2012), 194-199.

[6] G. Litak et al. Chaotic vibration of a quarter-car model excited by the road surface profile. *Communications in Nonlinear Science and Numerical Simulation*, 13 (2008) 1373–1383.

[7] Adamczyk, J., and Kowal, J., and Wszołek, W., and Wszołek, T. The impact of road traffic on a TV studio. *Proceedings of the Tenth International Congress on Sound and Vibration*, (2003), 4807-4814.

[8] Clemente, P., and Rinaldis D. Protection of a monumental building against traffic-induced vibrations. *Soil Dynamics and Earthquake Engineering*, 17 (1998), 289–296.

[9] Popescu, Th.D. Analysis of traffic-induced vibrations by blind source separation with application in building monitoring. *Mathematics and Computers in Simulation*, 80 (2010), 2374–2385.

[10] Hunaidi, O., and Rainer, J.H., and Pernica, G. Measurement and analysis of traffic-induced vibrations. *Proceedings of the 2nd International Symposium on Transport Noise and Vibrations*, (1994), 103–108.

[11] Hung, H.H., and Yang, Y.B. A review of researches on ground-borne vibrations with emphasis on those induced by trains. *Proc. Natl. Sci. Counc.*, 25 (2001), 1–16.

[12] Yang, Y.B., and Hung, H.H. Soil vibrations caused by underground moving trains using the 2.5D finite/infinite element approach. *J. Geotech. Geoenviron. Eng. ASCE*, 134 (2008), 1633–1644.

[13] Au, F.T.K., and Cheng, Y.S., and Cheung, Y.K. Vibration analysis of bridges under moving vehicles and train: an overview. *Progress in Structural Engineering and Materials*, 3, (2006), 299–304.

[14] Takemiya, H. (Ed.) Environmental vibrations: prediction monitoring and evaluation. *Proceedings and Monographs in Engineering, Water and Earth Sciences*, (2005).

[15] Goyder, H., and White, R. Vibration power flow from machines into built-up structures. *Journal of Sound and Vibration*, 68 (1980), 59–117.

[16] Pinnington, R.J. and White, R. Power flow through machine isolators to resonant and non-resonant beam. *Journal of Sound and Vibration* 75 (1981), 179–197.

[17] Li, Q. and Wu, D.J. Analysis of the dominant vibration frequencies of rail bridges for structure-borne noise using a power flow method. *Journal of Sound and Vibration*, 332 (2013), 4153–4163.

[18] Xiong, Y.P. and Xing, J.T. and Price, W.G. Power flow analysis of complex coupled systems by progressive approaches. *Journal of Sound and Vibration*, 239 (2001), 275–295.

[19] Choi, W.J. and Xiong, Y.P. and Shenoi, R.A. Power flow analysis for a floating sandwich raft isolation system using a higher-order theory. *Journal of Sound and Vibration* 319 (2009), 228–246.

[20] Krzyworzeka, P., and Cioch, W., and Jamro, E. Hardware abilities of Linear Decimation Procedure in practical applications. *Polish Cimac*, (2007), 115-122.

[21] Dabrowski, D., and Cioch, Analysis of Signals Pre-processing Algorithm in Case of Hardware and Software Implementation on Diagnostic Programmable Device PUD-2. *Acta Physica Polonica A*, 123 (6) (2013), 1020-1023.

1) Rafał Burdzik, Ph.D. D.Sc. Assistant Professor: Silesian University of Technology, Faculty of Transport, Krasińskiego 8, 40-019 Katowice, Poland (rafal.burdzik@polsl.pl), the author presented this work at the conference.

2) Łukasz Konieczny, Ph.D.: Silesian University of Technology, Faculty of Transport, Krasińskiego 8, 40-019 Katowice, Poland (lukasz.konieczny@polsl.pl).

3) Jan Warczek, Ph.D.: Silesian University of Technology, Faculty of Transport, Krasińskiego 8, 40-019 Katowice, Poland (jan.warczek@polsl.pl).

4) Witold Cioch, Ph.D.: AGH University of Science and Technology, Faculty of Mechanical Engineering and Robotics, al. Mickiewicza 30, 30-059 Cracow, POLAND (cioch@agh.edu.pl).

# Kernel and Kernel sections for a nonlinear thermo-elastic beam subjected to time-varying external excitations (MAT190-15)

Dengqing Cao, Huatao Chen, Jingfei Jiang

*Abstract:* This paper concerns with the long-time dynamical behavior of a thermo-elastic beam subjected to time-varying external excitations and time-varying nonlinear feedback forces. Taking into account the interaction between temperature and deformation, the vibration of thermo-elastic beam can be described by a coupled partial differential equation which can generate a Process. According to the priori estimation of energy function for the beam, it can be proved that the Process has Kernel and Kernel sections.

## 1. Introduction

Let $D = [0, 1]$ be a bounded domain in $\mathbb{R}$, $\Gamma$ represents the boundary of $D$, $\Delta$ denotes the Laplace operator, $\nabla$ is the Hamilton operator. Consider the governing equation for a thermo-elastic beam

$$u_{tt} - \alpha\Delta u_t + \Delta^2 u + \gamma\Delta\theta + \left[f_1 - \beta\int_0^1 |\nabla u|^2\, dx\right]\Delta u - g(t,u) = f(t,x). \tag{1a}$$

$$k\theta_t - \eta\Delta\theta - \gamma\Delta u_t = 0, \tag{1b}$$

where $u(t,x)$ is the lateral displacement of beam, $\theta(t,x)$ denotes the temperature. The boundary condition of the beam is assumed to be

$$x \in \Gamma : u = \frac{\partial u}{\partial n} = 0 \tag{1c}$$

$$x \in \Gamma : \theta = 0; \tag{1d}$$

where $n$ is the outer normal vector. The parameters $\alpha$ and $\eta$ which denote the damping coefficient of the system and thermal capacity respectively are positive constants, $\beta > 0$ is a constant. $f_1$ is the longitudinal force, $f(t,x)$ represents the time-varying external excitations, $g(t,u)$ is the feedback force. For the physical description of System (1a)-(1d), one can refer to the literature [6, 7]and the references therein.

Studying the existence of attractor is an useful way to capture the long-time behavior of dynamical system [5]. Under some conditions, System (1a)-(1d) generate a Nonautonomous dynamical system (NDS) or a Process [17]. There are several type of attractors for NDS or Process, one of them is called as Kernel and Kernel sections proposed by Chepyzhov and

Visik [3], which are natural generalizations of maximal invariant set for NDS or Process. Many authors have studied NDS or Process associated with mathematical physics problems by the methods in [3]. Various and wonderful phenomenon about long-time behavior are obtained. such as those in [10–12]and the references therein.

Without the effect of temperature ($\gamma = 0$), then Equation (1a) becomes the Euler-Bernoulli beam model which is very famous in nonlinear elastic dynamics. There are a lot of investigations about the kind of beam, for practical aspect, one can see [6, 7]. The reader also can refer to [8, 9, 13] for the mathematical analysis, such as existence and uniqueness of solution, stability, and so on. With respect to the long time behavior of Euler-Bernoulli beam, there exist meaningful results in [13] and the references therein. It is mentioned that, according the traditional approach based on splitting method , the existence of Kernel and Kernel sections for Euler-Bernoulli beam rely on the strong damping, i.e., the damping is in the form of $\alpha\Delta u_t$. With the technique proposed in [14], the damping can be reduce to weakly form $\alpha u_t$. But in the thermo-elastic case, Our results shows that the strongly damping of the beam is necessary for the existence of uniform attracting set. Furthermore, in the case of equation (1b) $k = 0$, the structural damping of the beam itself can be neglected. In this case, the damping term $\gamma\Delta\theta$ can be written as $-\gamma^2\eta^{-1}\Delta u_t$. This means that, although we neglect the structural damping of beam itself, there also exists strongly damping caused by thermal effect. For the thermo-elastic beam, there also exists many results, for the existence and uniqueness of solution, one can see [19] and the references therein. With regard to the stability, one can refer to [13, 16]. Giorgi et al. [15] have studied the long-time behavior for autonomous thermo-elastic beams.

This paper concerns with the long-time dynamical behavior of a nonlinear nonautonomous thermo-elastic beam which take into account the interaction between temperature and deformation. According to the priori estimation of energy function for the beam and the nonautonomous version of Theorem 2 in [18], we prove that the Process associated with System (1a)-(1d) has Kernel and Kernel sections. The rest of this paper is organized as follows. In Section 2, some notations and preparation results are given. It is shown that the system (1a)-(1d) can generate Process; Section 3 is devoted to the existence of random attractors for the Process.

## 2. Existence and uniqueness of solutions

Let $H^s(D)$ denotes the $L^2-$ based Sobolev space of order $s$ and $H_0^s$ is the closure of $C_0^\infty(D)$ in $H^s(D)$. The following notation are also emphasized

$$\|u\| \equiv \|u\|_{L^2(D)}, \|u\|_s \equiv \|u\|_{H_0^s(D)},$$
$$(u,v) \equiv (u,v)_{L^2(D)}, ((u,v)) = (u,v)_{H_0^2(D)}.$$

Let $E = H_0^2(D) \times L^2(D) \times L^2(D)$ equiped with inner product $(y_1, y_2)_E = ((y_1, y_1)) + (y_2, y_2) + (y_3, y_3),\ \forall (y_1, y_2) \in E$ and norm $\|y\|_E = (y, y)_E^{\frac{1}{2}}$. For other situations, $\|\cdot\|_Y$ represent the norm relevant to Banach space $Y$.

It is well known that $\Delta^2 : H_0^2(D) \bigcap L^2(D) \to L^2(D)$ and $-\Delta : H_0^1(D) \bigcap L^2(D) \to L^2(D)$ are two self-adjoint,positive, linear operators. Their eigenvalues $\{\lambda_i\}_{i\in\mathbb{N}}$ and $\{\overline{\lambda}_i\}_{i\in\mathbb{N}}$ satisfy $0 < \lambda_1 \le \lambda_2 \le \cdots$, and $0 < \overline{\lambda}_1 \le \overline{\lambda}_2 \le \cdots$, and $\lambda_m \to \infty, \overline{\lambda}_m \to \infty$ as $m \to +\infty$, respectively. Throughout this paper, the following embedding inequalities are frequently used

$$\|u\|_1^2 \ge \overline{\lambda}_1 \|u\|^2, \quad \forall u \in H_0^1(D) \tag{2a}$$

and

$$\|u\|_2^2 \ge \lambda_1 \|u\|^2, \quad \forall u \in H_0^2(D). \tag{2b}$$

The letter $c$ and $c_i$ $(i = 1, 2, 3, \cdots,)$ are positive constants.

Let $(X, d)$ be complete metric space (with the metric $d$) and $\{U(t,\tau)\}_{t\ge s}, t, s \in \mathbb{R}$ be a family mappings satisfying:
(i) $U(\tau,\tau) = id$;
(ii) $U(t,\tau) = U(t,s) \circ U(s,\tau)$;
(iii) $u \mapsto U(t,\tau)u$ is continuous.

Then $\{U(t,\tau)\}_{t\ge s}, t, s \in \mathbb{R}$ is called a Process which was introduced by Dafermos [17]. In the following, we use $\{U(t,\tau)\}$ instead of $\{U(t,\tau)\}_{t\ge s}, t, s \in \mathbb{R}$. A function $u(s), s \in \mathbb{R}$ is said to be a complete trajactory of Process $\{U(t,\tau)\}$ if

$$U(t,\tau)u(\tau) = u(t), \quad t \ge \tau, t, \tau \in \mathbb{R} \tag{3}$$

A complete trajactory $u(s), s \in \mathbb{R}$ of a Process $\{U(t,\tau)\}$ is bounded if the set $\{u(s)|s \in \mathbb{R}\}$ is bounded in the norm of $X$, for more detail about Process and its trajactory, the reader can refer to [17].

**Definition 2.1.** *[3] The Kernel $K$ of a Process $\{U(t,\tau)\}$ consists of all bounded complete trajactory of $\{U(t,\tau)\}$:*

$$K = \{u(\cdot)|u(\cdot) \text{ satisfies (3) and } \|u(s)\|_X \le C_u, \forall s \in \mathbb{R}\}$$

**Definition 2.2.** *[3] The Kernel section $K(s) \subset E$ of a Kernel $K$ at time $s \in \mathbb{R}$ is defined by*

$$K(s) = \{u(s) | u(\cdot) \in K\} \tag{4}$$

**Proposition 2.3.** *[3] Let $K$ be the kernel of a Process $\{U(t,\tau)\}$, Then*

$$U(t,\tau)K(\tau) = K(t), \quad t \geq \tau, t, \tau \in \mathbb{R} \tag{5}$$

Next, we turn to the criteria for the existence of Kernel and Kernel sections of a Process. A set $P \subset X$ is said to be a uniformly attracting set of Process $\{U(t,\tau)\}$ if for any bounded set $B \subset X$,

$$\lim_{T\to\infty} \sup_{\tau\in\mathbb{R}} dist(U(T+\tau,\tau)B, P) = 0 \tag{6}$$

where dist denotes the Hausdorff semidistance:

$$dist(A,B) = \sup_{x\in A} \inf_{y\in B} d(x,y), \quad A, B \subset X$$

A Process is uniformly asymptotically compact, if it possesses a compact uniformly attracting set. The next Theorem contains the conditions under which the Process has Kernel and Kernel sections

**Theorem 2.4.** *[3] Let $\{U(t,\tau)\}$ is a uniformly asymptotically compact Process acting on $E$, with a compact uniformly attracting set $P \subset E$. Each mapping $U(t,\tau) : E \to E$ is continuous. Then the Kernel of Process $U(t,\tau)$ is non-empty, the Kernel sections $K(\tau)$ is compact and given by*

$$K(\tau) = \bigcap_{s>0} \overline{\bigcup_{T>s} U(\tau, \tau - T)P}$$

The following arguments are very important to obtain the main results. Suppose $v$ is the solution of the following problem

$$\begin{cases} \Delta^2 v = \lfloor u, u \rfloor \\ x \in \Gamma : v = \frac{\partial v}{n} = 0. \end{cases} \tag{7}$$

where $\lfloor v, u \rfloor = \Delta v \Delta u, x \in D$, Then we can get the similar "sharp regularity" estimations in [14] which play a key roll in our analysis. Let $u_t = \overline{w}$, then System (1a)-(1b) is equivalent to the following initial value problem

$$\begin{cases} u_t = \overline{w} \\ \overline{w}_t = -\Delta^2 u + \alpha\overline{w} - \gamma\Delta\theta + \lfloor v, u \rfloor - f_1\Delta u - g(t,u) + f(t,x) \\ \theta_t = \frac{\eta}{k}\Delta\theta + \frac{\gamma}{k}\Delta\overline{w} \\ t = \tau : u = u_{0,\tau}, \overline{w} = u_{1,\tau}, \theta = \theta_\tau \end{cases} \tag{8}$$

with the boundary value (1c)-(1d). Let $w = u_t + \varepsilon u$, where $\varepsilon = \frac{(\lambda_1\alpha+\overline{\lambda}_1 f_1)\beta}{4\beta+2(\alpha\eta+\alpha\gamma)\alpha+\frac{\gamma\alpha}{k\lambda_1}}$, We obtain the following system from System (8).

$$\begin{cases} u_t = w - \varepsilon u \\ w_t = (-\Delta^2 - (\varepsilon\alpha + f_1)\Delta - \varepsilon^2)u + (\varepsilon + \alpha\Delta)w - \gamma\Delta\theta \\ \qquad\qquad - \lfloor v, u \rfloor - g(t,u) + f(t,x) \\ \theta_t = -\frac{\gamma\varepsilon}{k}\Delta u + \frac{\gamma}{k}\Delta w + \frac{\eta}{k}\Delta\theta \\ t = \tau : u = u_{0,\tau}, w = u_{1,\tau} + \varepsilon u_{0,\tau}, \theta = \theta_\tau \end{cases} \tag{9}$$

Let $Y = (u, w, \theta)^T$, and

$$L = \begin{pmatrix} -\varepsilon I & I & 0 \\ -\Delta^2 - ((\varepsilon\alpha + f_1)\Delta + \varepsilon^2)I & \varepsilon + \alpha\Delta & -\gamma\Delta \\ -\frac{\gamma\varepsilon}{k}\Delta & \frac{\gamma}{k}\Delta & \frac{\eta}{k}\Delta \end{pmatrix},$$

$$F(t,Y) = \begin{pmatrix} 0 \\ \lfloor v, u \rfloor - g(t,u) + f(t,x) \\ 0 \end{pmatrix}.$$

Then, the System (9) can be written as the following abstract evolution equation

$$\frac{dY}{dt} = LY + F(t,Y) \tag{10}$$

Assume that feedback force $g(t,u)$ and external excitation $f(t,x)$ satisfy

(H1) Growth condition: $C_0$ is a positive constant,

$$|g(t,s)| \le C_0(1 + |s|^p), p \ge 1 \quad \forall t \in \mathbb{R}.$$

(H2) $f(t,x) \in L^2(\mathbb{R}, L^2(D)), \|f(t,x)\|_{L^2(\mathbb{R},L^2(D))} \le M$.

It follows from [2] that $L$ is the infinitesimal generator of a $C_0-$ semigroup $e^{Lt}$ on $E$. According to the "sharp regularity" about $\lfloor\cdot,\cdot\rfloor$ in [14]and the assumptions (H1)-(H2), it can be obtained that $F(t,Y)$ is local Lipschitz continuous. Then we have the following theorem which concerns with the existence and uniqueness of solution for System (9)

**Theorem 2.5.** *For any $T > 0$, Under the conditions (H1) and (H2), for any bounded initial value $Y_\tau \in E$, there exists a unique mild solution for System (9), $Y(t, Y_\tau)$ that satisfies*

$$Y(t, Y_\tau) = e^{L(t-\tau)}Y_\tau + \int_\tau^t e^{L(t-s)}F(s, Y(s))ds$$

*and $Y(t,\tau) \in C([\tau, \tau+T), E)$. Moreover $Y(t,\tau)$ is is jointly continuous with respect to $t$ and $Y_\tau$.*

By theorem (2.5), we can assert that the System (9) generates a Process $\overline{U}(t,\tau) : E \to E$. Let $U(t,\tau) = \Sigma_\varepsilon(t)\overline{U}(t,\tau)\Sigma_\varepsilon(\tau)$ where $\sigma_\varepsilon(\cdot) : (u_1(\cdot), u_2(\cdot)) \to (u_1(\cdot), u_2(\cdot) + \varepsilon u_1(\cdot))$, then $\{U(t,\tau)\}$ is a Process associated with System (8). In this article, we will prove the existence of non-empty compact kernel sections for the process $\{U(t,\tau)\}$.

## 3. Kernel and Kernel sections

In this section, the Main results about the existence of Kernel and Kernel sections for $\{U(t,\tau)\}$ are given. Firstly, we present a lemma which plays an important role in this article.

**Lemma 3.1.** *For any $Y = (u, w, \theta) \in E$, we have*

$$(LY, Y)_E \leq -\frac{\varepsilon}{2}\|Y\| - \frac{c}{2}\|w\|_2 \tag{11}$$

*where $k$ is a positive constant.*

*Proof.* Taking the inner product $(\cdot,\cdot)_E$ of $LY$ with $Y$, we have

$$\begin{aligned}
(LY, Y)_E &= (w - \varepsilon u, u)_2 \\
&\quad +((-\Delta^2 - (\varepsilon\alpha + f_1)\Delta - \varepsilon^2)u + (\varepsilon + \alpha\Delta)w - \gamma\Delta\theta, w) \\
&\quad +(-\frac{\gamma\varepsilon}{k}\Delta u + \frac{\gamma}{k}\Delta w + \frac{\eta}{k}\Delta\theta, \theta) \\
&= (\Delta^2 w, u) - \varepsilon\|u\|_2 \\
&\quad -(\Delta^2 u, w) - (\varepsilon\alpha + f_1)\Delta - \varepsilon^2)u, w) + ((\varepsilon + \alpha\Delta)w, w) + \gamma(\nabla\theta, \nabla w) \\
&\quad +\frac{\gamma\varepsilon}{k}(\nabla u, \nabla\theta) - \frac{\gamma}{k}(\nabla w, \nabla\theta) - \frac{\eta}{k}\|\theta\|_1 \\
&\leq -\varepsilon\|u\|_2 + \varepsilon\|w\| - \alpha\lambda_1\|w\| - \frac{\eta}{k}\|\theta\|_1 \\
&\quad -(\Delta^2 u, w) - ((\varepsilon\alpha + f_1)\Delta - \varepsilon^2)u, w) + \gamma(\nabla\theta, \nabla w) \\
&\quad +\frac{\gamma\varepsilon}{k}(\nabla u, \nabla\theta) - \frac{\gamma}{k}(\nabla w, \nabla\theta) - \frac{\eta}{k}\|\theta\|_1
\end{aligned}$$

with the $\varepsilon = \frac{(\lambda_1\alpha + \overline{\lambda}_1 f_1)\beta}{4\beta + 2(\alpha\eta + \alpha\gamma)\alpha + \frac{\gamma\alpha}{k\lambda_1}}$ and the Cauchy-Schwartz inequality, the result of (11) can be easily obtained. □

The next lemma concerns with the uniformly attracting set of Process $U(t,\tau)$ in $E$.

**Lemma 3.2.** *There exists initial time independent constant $\overline{M}_0 > 0$ such that for any bounded set $B \subset E$, there exists $\overline{T}(B) > 0$ such that the solution of system (8) $\overline{Y}(t,\tau,Y(\tau)) = (u, \overline{w}, \theta)^T$ with $\overline{Y}(\tau) \in B$ satisfies*

$$\|Y\|_E \leq M_0, \quad t \geq \overline{T}(B) \geq \tau, \ \forall\tau \in \mathbb{R}. \tag{12}$$

*Proof.* Let $Y$ be a solution of the System (9) with the initial value $Y_{-\tau} = (u_0, u_1 + \varepsilon u_0, \theta_0)^T$. Taking the inner product $(\cdot,\cdot)_E$ of (9) with $Y$, we have

$$\begin{aligned} & \frac{1}{2}\frac{d}{dt}\left(\|u\|_2^2 + \|w\|^2 + \|\theta\|^2\right) \\ \leq\ & -\frac{\varepsilon}{2}\left(\|u\|_2^2 + \|w\|^2 + \|\theta\|^2\right) - \frac{k}{2}\|w\|_2 \\ & +\beta(\lfloor v, u\rfloor, w) - (g(t,u), w) + (f(t,x), w) \end{aligned} \tag{13}$$

It follows from (7) and Proposition 1.4.2 and Theorem 1.4.3 in [14] that

$$\beta(\lfloor v, u\rfloor, w) = -\frac{\beta}{4}\frac{d}{dt}\|v(u)\|^2 - \beta\varepsilon\|v(u)\|^2 \tag{14}$$

According to the condition (H1)-(H2), the following inequalities hold

$$(g(t,u), w) \leq \frac{\varepsilon}{4}\|u\|_2^2 + \frac{c}{4\varepsilon}\|w\|^2, \tag{15}$$

$$(f(t,x), w) \leq \frac{c}{4\varepsilon}\|w\|^2 + c_3\|f(t,x)\|^2. \tag{16}$$

Define

$$\mathcal{E}(u, w, \theta) = \|u\|^2 + \|w\|_2^2 + \|v(u)\|^2 + \|\theta\|^2.$$

Then, from the relations (13)-(16), we can obtain that

$$\frac{d}{dt}\mathcal{E}(u,\theta)(t) \leq \varepsilon_1\mathcal{E}(u,\theta)(t) + c_3\|f(t,x)\|^2. \tag{17}$$

Therefore,

$$\mathcal{E}(u,w,\theta)(t) \leq e^{\varepsilon_1(t-\tau)}\mathcal{E}(u,w,\theta)(\tau) + \int_\tau^t c_3 e^{\varepsilon_1(t-s)}\|f(s,x)\|^2 ds. \tag{18}$$

where $\varepsilon_1 > 0$. Thus, with the similar arguments in [4], the result of Lemma 3.2 can be got. □

From Lemma 3.2, the Process $\{U(t,\tau)\}$ has an uniformly attracting set. In the following, we prove that the attracting set is compact.

**Lemma 3.3.** *Assume $B$ is a bounded subset of $E$. Then for any $\varepsilon > 0$ there exists $T = T_B(\varepsilon)$ such that*

$$\limsup_{n\to\infty}\sup_{p\in\mathbb{N}}\|U(\tau+T,\tau)Y_{n+p} - U(\tau+T,\tau)Y_n\|_E \leq \varepsilon \tag{19}$$

*where $\{Y_n\}$ is a sequence in $B$ and $\{U(T+\tau,\tau)Y_n\}$ weakly star converges in $L^\infty(\tau,\infty;E)$).*

*Proof.* This is the nonautonomous version of Theorem 2 in [18]. Rely on Kuratowski $\alpha-$ measure of nocompactness, with the process in [1], the Lemma can be proved. □

According to the Lemma 3.3, with the analogical arguments, the compactness of attracting set can be obtained. Then, combine with Theorem 2.5, Lemma 3.1 and Lemma 3.2. the main result can be formulated.

**Theorem 3.4.** *The Process associated with* (1a)-(1d) *owns Kernel and Kernel sections in* $E$.

In conclusion, the long-time dynamical behavior of System (1a)-(1d) have been studied in this paper. We have proved that the system can generate a Process which owns Kernel and Kernel sections. The proof relay on the strongly damping $\alpha\Delta u_t$ and the uniform bounded with respect to time of nonlinear feedback force. if the two condition are not satisfied, the pullback attractors is a good way to capture the long-time behavior of the System (1a)-(1d). From the view of qualitative, the dimension of Kernel and Kernel section of pullback attractor is also an important problem. The numerical result that based on the Approximate Inertial Manifolds for System (1a)-(1d) is also important and meaningful in the practical aspect. The authors will pursue this line of research in the near future.

**Acknowledgment**

This research was supported by NSFC (NO.91216106 and NO.11472089).

**References**

[1] Sun C, Cao D, Duan J. Non-autonomous dynamics of wave equations with nonlinear damping and critical nonlinearity. Nonlinearity, 2006, 19(11): 2645.

[2] Lions J L. Quelques méthodes de résolution des problèmes aux limites non linéaires,Dunod, Paris, 1969.

[3] Chepyzhov V, Vishik M. A Hausdorff dimension estimate for kernel sections of non-autonomous evolution equations. Indiana University Mathematics Journal, 1993, 42(3): 1057.

[4] Fan X, Zhou S. Kernel sections for non-autonomous strongly damped wave equations of non-degenerate Kirchhoff-type. Applied mathematics and computation, 2004, 158(1): 253-266.

[5] Crauel H, Kloeden P E. Nonautonomous and Random Attractors. Jahresbericht der Deutschen Mathematiker-Vereinigung, 2015, 117(3): 173-206.

[6] Shen H S. A two-step perturbation method in nonlinear analysis of beams, plates and shells. John Wiley & Sons, 2013.

[7] Han S M, Benaroya H, Wei T. Dynamics of transversely vibrating beams using four engineering theories. Journal of sound and vibration, 1999, 225(5): 935-988.

[8] Brzeniak Z, Maslowski B, Seidler J. Stochastic nonlinear beam equations. Probability theory and related fields, 2005, 132(1): 119-149.

[9] Patcheu S K. On a global solution and asymptotic behaviour for the generalized damped extensible beam equation. Journal of Differential Equations, 1997, 135(2): 299-314.

[10] Caraballo T, Lukaszewicz G, Real J. Pullback attractors for asymptotically compact non-autonomous dynamical systems. Nonlinear Analysis: Theory, Methods & Applications, 2006, 64(3): 484-498.

[11] Caraballo T, Langa J A, Valero J. The dimension of attractors of nonautonomous partial differential equations. The ANZIAM Journal, 2003, 45(02): 207-222.

[12] Carvalho A, Langa J A, Robinson J. Attractors for infinite-dimensional non-autonomous dynamical systems. Berlin-Heidenburg: Springer Science & Business Media, 2012.

[13] Fitzgibbon W E. Global existence and boundedness of solutions to the extensible beam equation. SIAM Journal on Mathematical Analysis, 1982, 13(5): 739-745.

[14] Chueshov I, Lasiecka I. Von Karman Evolution Equations: Well-posedness and Long Time Dynamics. Springer Science & Business Media, 2010.

[15] Giorgi C, Naso M G, Pata V, et al. Global attractors for the extensible thermoelastic beam system. Journal of Differential Equations, 2009, 246(9): 3496-3517.

[16] Leiva H, Sivoli Z. Existence, stability and smoothness of a bounded solution for nonlinear time-varying thermoelastic plate equations. Journal of mathematical analysis and applications, 2003, 285(1): 191-211.

[17] Dafermos C M. Semiflows associated with compact and uniform processes. Theory of Computing Systems, 1974, 8(2): 142-149.

[18] Khanmamedov A K. Global attractors for von Karman equations with nonlinear interior dissipation. Journal of Mathematical Analysis and Applications, 2006, 318(1): 92-101.

[19] Hansen S W, Zhang B Y. Boundary control of a linear thermoelastic beam. Journal of Mathematical Analysis and Applications, 1997, 210(1): 182-205.

Dengqing Cao, M.Sc. (Ph.D. student): Harbin Institute of Technology/School of Astronautics/Division of Dynamics and Control, XiDaZhi street No.92, P.O. Box 137, 150001, Harbin, China (*htchencn@aliyun.com*). The author gave a presentation of this paper during one of the conference sessions.

Dengqing Cao, Ph.D.(Professor): Harbin Institute of Technology/School of Astronautics/Division of Dynamics and Control, XiDaZhi street No.92, P.O. Box 137, 150001, Harbin, China (*dqcao@hit.edu.cn*).

, Jingfei Jiang: M.Sc.(Ph.D. student), Harbin Institute of Technology/School of Astronautics/Division of Dynamics and Control (*XiDaZhi street No.92, P.O. Box 137, 150001, Harbin, China*). jjf860623@yeah.net

# 3 DOF dynamic model of the piston-crankshaft system of the Stirling engine (ENG290-15)

Adrian Chmielewski, Robert Gumiński, Jędrzej Mączak

*Abstract:* In the paper, a dynamic model of the piston-crankshaft system of the Stirling engine, with three degrees of freedom, is presented. In the model, similarly to the real object, the torque excitation due to the working gas pressure was considered. The working gas pressure was modelled using the thermodynamic submodel in which the working volume was divided into partial volumes and thus analysed. While creating the model, the piston crankshaft model based on the physical model of the real object with static mass reduction was developed. Then the model was expanded to include a section describing the changes in pressure in the cylinder. Based on the developed equations of motion, the influence of selected model parameters on the behaviour of the simulation model was analysed. In the paper, the results of the performed simulations, among others waveforms of displacement, velocity and acceleration of pistons, as well as waveforms of angular displacement, velocity and acceleration of crankshaft were presented. The results carry information about the dynamic behaviour of the simulated real object, which works at the given thermodynamic parameters of working gas.

## 1. Introduction

The view of 2030 [1] assumes new purposes for the member states of the European Union, connected with respect for energy. These purposes include: increasing power efficiency to 27%, growth of the RES [2] participation in the energy market to 27%, and reduction of $CO_2$ emissions to nearly 40%. Improvement of energy efficiency is perceived as dependent on development of distributed generation sources [3-6], which, when dispersed change the form of the waste heat energy into electric energy, or generate electric energy (RES) in close proximity to the place of its consumption. In many sources of distributed generation [3-6], changing form of chemical energy (e.g.: fuel energy – internal combustion engines or energy of working element, for example Stirling engines [7-16]) into mechanical energy takes place with the use of working mechanisms.

The most frequently used transmission mechanism in engine construction practice is the piston-crankshaft assembly [17-19]. In this work, the geometric, analytical, and simulation models of the crankshaft assembly with three degrees of freedom have been presented. As was mentioned before in the context of ever growing interest in distributed cogeneration systems and distributed micro cogeneration [3], which comprises Stirling engines [7-16], the need arises of optimisation (improving efficiency) and rationalisation of waste heat management. Thus, it is worthwhile preparing the tasks

regarding optimisation of the Stirling engine work parameters [20-23]. The presented dynamic model of the Stirling engine will be used for this purpose. The prepared model of the piston-crankshaft assembly will be extended in the future with the subsequent constituent parts, among others: a quasi-adiabatic model of heat exchange [24] and geometric parameters optimisation model [18, 21-22, 26] during operation of the heat cycle with the purpose of a faithful description of processes taking place in a real-life engine.

Depending on input parameters, a multi-layer neural network [26] or Fuzzy Logic [27] will assure the adaptiveness of the model's work. Such an approach will allow for investigating the influence of the chosen work parameters and their optimisation in order to obtain the maximal efficiency and use this knowledge on the real-life object.

It should be mentioned, that similar works were conducted by the authors [10, 12, 17-19]. In work [10], a dynamic model of the Stirling engine has been presented, the key element of which was a crankshaft assembly. A model of changing dynamics of the piston-crankshaft assembly was connected with a thermodynamic second-order model, which takes into account energy and heat losses taking place in the engine [10].

## 2. Modelling the dynamics of the piston-crankshaft assembly

### 2.1. Analytical and geometric models of the piston-crankshaft assembly

The presented model concerns the piston-crankshaft assembly used in, among others, Stirling engines. Geometry of the presented piston-crankshaft assembly is different from geometry of the piston-crankshaft assembly of the combustion engine by the fact of the cranks in the combustion engine's layout being offset by 180°, whereas in the discussed system the offset between cranks of the hot and cold cylinders amounts to 90°. Figure 1 shows the geometric model, which assumes static reduction of the connecting rod masses. Similar assumptions were made in works [16, 17]. The analysed physical model has three degrees of freedom. The flywheel is connected with the shaft by means of the elastic element of the $k_1$ rigidity (section: flywheel – the first piston). On the farther section between the first and the second piston, the shaft has rigidity $k_2$.

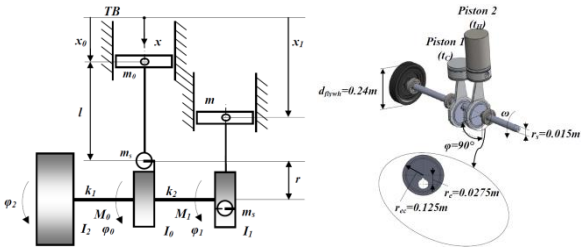


**Figure 1.** Model of a piston-crankshaft assembly.

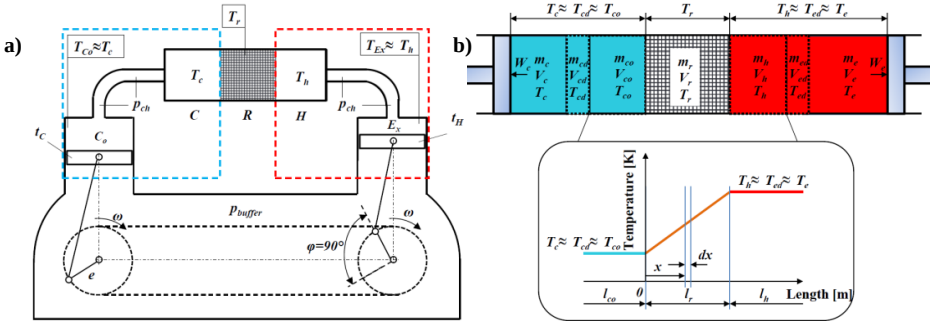


**Figure 2.** Diagram of a real-life Stirling engine a), illustration of temperature change in working chamber b).

Figure 2a shows the diagram of the Alpha-type Stirling engine. Angular shift between the piston working in the compression space and the piston working in the expansion space amounts to 90°. Figure 2b illustrates temperature change in the working space. It was assumed that the temperature of the lower heat source is approximately equal to the temperature in the compression space, in the dead space above the piston, and in the cooler space, which means that $T_c \approx T_{cd} \approx T_{co}$. Similar simplification was adopted for the upper heat source. It was assumed that the temperatures in the expansion space $V_e$, in the dead space above the piston $V_{ed}$ working in the expansion space and in the heater space $V_h$ are more or less the same, which means that $T_h \approx T_{ed} \approx T_e$. It is a known fact that temperature $T_r$ on the $l_r$ regenerator ranges between the temperature of the lower $T_c$ and upper $T_h$ heat source (it is a linear relationship in approximation). In order to determine the temperature on the regenerator, relationships from (14) to (16) have been used. The crank of piston 1 (Figure 1) is shifted against the crank of piston 2 by the angle of 90°. Figure 2 shows the diagram of the crankshaft mechanism with the angles marked, which will serve the purpose of determining equations of motion.

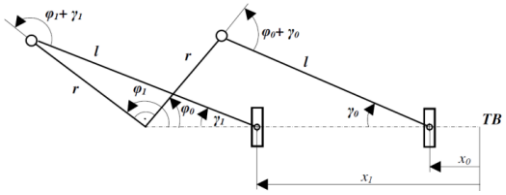


**Figure 3.** Diagram illustrating geometry of the considered piston-crankshaft assembly.

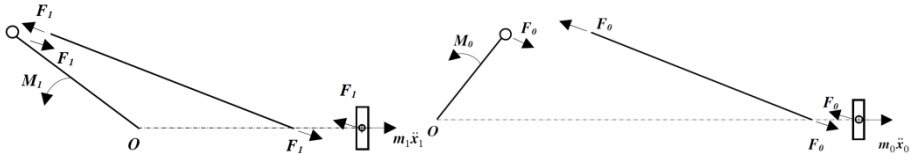


**Figure 4.** Diagram showing the distribution of forces in the considered system

On the basis of analysis of Figures 1, 3 and 4 the equation of moments can be written for the crank 2 inertia:

$$I_1\ddot{\varphi}_1 = M_1 - F_1 r \sin(\varphi_1 + \gamma_1 + 90°) - k_1(\varphi_1 - \varphi_0) \tag{1}$$

The crank 1 motion can be described with similar equation:

$$I_0\ddot{\varphi}_0 = M_0 - F_0 r \sin(\varphi_0 + \gamma_0) - k_2(\varphi_0 - \varphi_2) + k_1(\varphi_1 - \varphi_0) \tag{2}$$

The sum of moments for the flywheel (Figure 1) equals to:

$$I_2\ddot{\varphi}_2 = k_2(\varphi_0 - \varphi_2) \tag{3}$$

The sum of projections of the forces on the x-axis for piston 2 (on the basis of Figure 4) amounts to:

$$F_1 \cos\gamma_1 - m_1\ddot{x}_1 = 0 \tag{4}$$

The sum of projections of the forces on the x-axis for piston 1 (on the basis of Figure 4) amounts to:

$$F_0 \cos\gamma_0 - m_0\ddot{x}_0 = 0 \tag{5}$$

From the trigonometric dependencies (the theorem of sinuses) the relations can be determined (relations between $\gamma_0$ and $\varphi_0$ and also $\gamma_1$ and $\varphi_1$. The detailed derivation path for these dependencies was shown in work [19].

The last unknown for determining the forces $F_0$ and $F_1$ from the equations (4) and (5) are the linear accelerations $\ddot{x}_0$ and $\ddot{x}_1$. In order to define the sought unknown on the basis of analysis of the kinematic relationships shown in Figure 2, employing the theorem of sinuses allows for eliminating the angle $\gamma_0$, then:

$$x_0(\varphi_0) = r\left\{(1-\cos\varphi_0) + \frac{l}{r}\left(1 - \sqrt{1 - \frac{r^2}{l^2}\sin^2\varphi_0}\right)\right\} \tag{6}$$

Expanding the root from (6) into a power series, which was limited to the first two terms, the final relationship for $x_0$ can be formulated:

$$x_0(\varphi_0) = r\left\{(1-\cos\varphi_0) + \frac{\lambda}{4}(1-\cos 2\varphi_0)\right\} \tag{7}$$

As a result of differentiating the equation (7), a relationship describing linear velocity and linear acceleration for piston 1 ($t_C$) is obtained. The detailed derivation of the relationship of the piston 1 velocity and acceleration was presented in work [19].

As follows from the analysis of Figure 1 and 2, the linear displacement for piston 2 ($t_H$) is offset against piston 1 ($t_C$) by the value corresponding to the difference of crank angles amounting to *90°*, which can be described by the following:

$$x_1(\varphi_1 + 90°) = r\left[\left(1 - \cos(\varphi_1 + 90°)\right) + \frac{\lambda}{4}\left(1 - \cos(2\varphi_1 + 180°)\right)\right] \tag{8}$$

Using the trigonometric relationships (reduction formulae), the expression (8) was reduced to the form of:

$$x_1 = r\left\{\left(1+\sin\left(\varphi_1\right)\right)+\frac{\lambda}{4}\left(1+\cos\left(2\varphi_1\right)\right)\right\} \tag{9}$$

As a result of differentiating the equation (9) the relationship is obtained, describing linear velocity and linear acceleration for piston 2. The detailed derivation of these relationships was presented in work [19].

The moment acting on piston 1 ($t_C$) can be described with the equation, which takes into consideration the change of pressure in a cylinder, acting on the bottom; this can be written as follows:

$$M_0 = pA_C e \tag{10}$$

The moment acting on piston 2 ($t_H$) can be described with the equation, which takes into consideration the change of pressure in a cylinder, acting on the bottom; this can be written as follows:

$$M_1 = pA_H e \tag{11}$$

In this work, it has been assumed that $M_0$=$M_1$ as far as value is concerned.

Pressure $p$ in the working space is a mean pressure which can be determined on the basis of the known total mass of the gas in the working space. The total mass of gas in the working space is a sum of masses in individual working spaces, which can be described by a relationship:

$$m_{tot} = m_c + m_{cd} + m_{co} + m_r + m_h + m_{ed} + m_e \tag{12}$$

On the basis of the Clapeyron equation $pV$=$mRT$ for individual working spaces, the relationship describing the working gas mass in the working space can be written, taking into account the thermodynamic parameters of the gas in each of the spaces, with the assumption that the mean pressure in the working chamber is constant:

$$m_{tot} = \frac{p}{R}\left(\frac{V_c}{T_c}+\frac{V_{cd}}{T_{cd}}+\frac{V_{co}}{T_{co}}+\frac{V_r}{T_r}+\frac{V_h}{T_h}+\frac{V_{ed}}{T_{ed}}+\frac{V_e}{T_e}\right) \tag{13}$$

In the relationship (13) the temperature on the regenerator's element $T_r$ changes along its length, which can be written as follows:

$$T_r(x) = (T_h - T_c)x/l_r + T_c \tag{14}$$

Analysing Figure 2 leads to conclusion that if the relationship (14) describing temperature change is inserted in the Clapeyron equation, we receive [20]:

$$m_r = \frac{A_r l_r}{R}\int_0^{l_r} p\frac{1}{(T_h - T_c)x + T_c l_r}dx = p\frac{V_r}{R(T_h - T_c)}\ln\frac{T_h}{T_c} \tag{15}$$

As a consequence, the temperature on the regenerator can be determined, and it amounts to:

$$T_r = \frac{T_h - T_c}{\ln\frac{T_h}{T_c}} \tag{16}$$

As a consequence, the relationship describing pressure change in the working space can be formulated:

$$p = \frac{m_{tot}R}{\left(\left(V_c/T_c\right)+\left(V_{cd}/T_{cd}\right)+\left(V_{co}/T_{co}\right)+\left(V_r/T_r\right)+\left(V_h/T_h\right)+\left(V_{ed}/T_{ed}\right)+\left(V_e/T_e\right)\right)} \tag{17}$$

The volume change $V_{Co}$ in the compression space using the relationship describing $x_0$ (7) can be written in the following way:

$$V_{Co} = x_0(\varphi_0)A_{Co} \tag{18}$$

The change of volume $V_{Ex}$ in teh compression space using the relationship describing $x_1$ (9) can be written as follows:

$$V_{Ex} = x_1(\varphi_0)A_{Ex} \tag{19}$$

The total dead volume present in the considered system can be written as follows:

$$V_{dead} = V_c + V_{cd} + V_r + V_h + V_{ed} \tag{20}$$

The total change of volume in the working space can be written as follows:

$$V_{all} = V_{dead} + V_c + V_e \tag{21}$$

### 2.2. Simulation model of the system

On the basis of the given relationships (1-21) a simulation model of the piston-crankshaft assembly with three degrees of freedom was built, shown in this sub-chapter in Figure 4. The model was created with the help of the Matlab&Simulink programme.

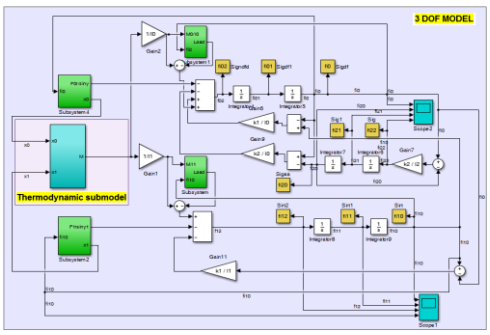


**Figure 5.** Simulation model of the piston-crankshaft assembly with three degrees of freedom (designed with Matlab&Simulink)

In the presented model, an external load was introduced in the form of a load torque, accounting for 0–100% of moments $M_0$ and $M_1$. When the system reaches the constant rotational velocity, it is loaded with the predetermined value of a load torque.

**Table 1.** Model's input data

| ***Parameter*** | ***Parameter value*** | ***Parameter*** | ***Parameter value*** |
|---|---|---|---|
| Individual gas constant for nitrogen | $R_{N2}$=296*J/kgK* | Crankshaft radius | $r_s$=0.015m |
| Temperature in compression space | $T_c$=300*K* | Crankshaft mass | $m_s$=3.45kg |
| Temperature in expansion space | $T_{Ex}$=910*K* | Crank radius | $r_{ec}$=0.125m |
| Total mass of working gas in working space | $m_{tot}$=0.0055*kg* | Crankshaft rigidity | $k_1 \approx k_2$=7200*Nm/rad* |
| Volume of space $V_{cd}$ (above piston $t_C$) | $V_{cd}$=0.000075$m^3$ | Piston diameter | *D*=0.11*m* |
| Volume of cooler space $V_c$ | $V_c$=0.00055$m^3$ | Regenerator length | $l_r$=0.055*m* |
| Volume of space $V_{ed}$ (above piston $t_H$) | $V_{ed}$=0.000085$m^3$ | Crankshaft length | $D_{shaft}$=0.8*m* |
| Volume of heater space $V_h$ | $V_h$=0.0004$m^3$ | Piston stroke s=2r | *s*=0.055*m* |
| Volume of regenerator space $V_r$ | $V_r$=0.00035$m^3$ | Length of connecting rod | *l*=0.207*m* |
| Reduced moment of crankshaft inertia for piston 1 ($t_C$) | $I_0$=0.0107$kgm^2$ | Mass of connecting rod | $m_c$=0.5*kg* |
| Reduced moment of crankshaft inertia for piston 2 ($t_H$) | $I_1$=0.0124$kgm^2$ | Mass of piston 1 | $m_0$=0.7*kg* |
| Moment of flywheel inertia | $I_2$=0.0235$kgm^2$ | Mass of piston 2 | $m_1$=0.9*kg* |
| Crankshaft length | $l_s$=*0.8m* | Crankshaft rigidity | $k_1 \approx k_2$=*7200Nm/rad* |

Table 1 shows input parameters for the simulation model (Fig. 4) based on the real Stirling engine.

### 2.3. Simulation results

Figure 6 shows closed-loop flow charts of pressure changes (Fig. 6a) and an open-loop flow chart (Fig. 6b) and flow charts of volume changes of the working space of the cold piston ($t_C$), hot piston ($t_h$) and the sum of their total volume ($V_{all}$) (Fig. 6c) in the course of the working cycle. Similar results with change of pressure were obtained from the tests, which was presented in work [7]. It is worthwhile drawing attention to the system's dynamics after simulation time *0ing .5s*, where the piston-crankshaft system starts to accelerate (increasing density of pressure flow charts Fig. 6b, and volume flow charts Fig. 6c), after 0.25 seconds on the pressure curve there are constant amplitude values obtained (0.16MPa) of pressure changes, the character of which is sinusoidal (od 0.275 do 0.435 MPa, compression ratio does not exceed 1.6).

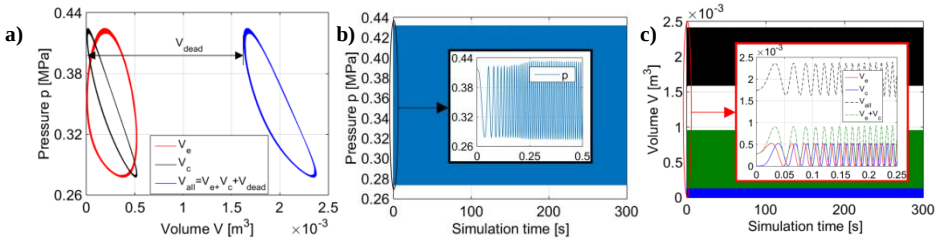


**Figure 6.** Closed-loop flow charts of pressure a), open-loop pressure flow chart b) and flow charts of volume changes c).

Figure 7 illustrates the curves of displacements $x_0$ and $x_1$, linear velocity values $v_0$ and $v_1$ and of linear accelerations $a_0$ and $a_1$ respectively for piston 1 ($t_C$) and piston 2 ($t_H$) (Fig.2). The change of rotational velocity is accompanied by the increase in frequency, which illustrates the growing density of displacements, velocity, and accelerations. After approximately 0.5s the system achieves the constant amplitude of velocity (Fig. 7b) and acceleration (Fig.7c). Similar results were obtained in work [19], in which the moment of extortion was over 30-fold lower, and the start-up of the system lasted nearly 18 seconds.

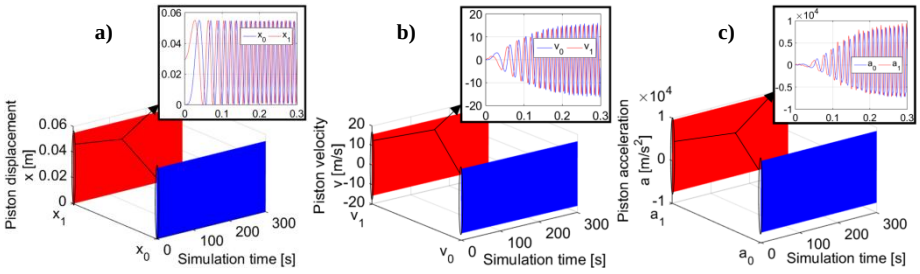


**Figure 7.** Flow charts of linear displacements a), Flow charts of linear velocities b) Flow charts of linear accelerations c) for piston 1 ($t_C$) and 2 ($t_H$).

Figure 8a) shows the flow charts of angular displacements respectively for: the flywheel ($\varphi_2$), crank 1 ($\varphi_1$) and crank 2 ($\varphi_0$). Figure 8b) presents the flow charts of angular velocities, which have similar character of changes (after 0.5s of simulation) rotational velocity reaches values of: $\omega_0$=615.2rad/s, $\omega_1$=578.7rad/s, $\omega_2$=583.7rad/s. Figure 8c presents the flow charts of angular accelerations for the flywheel ($\varepsilon_2$), the second crank ($\varepsilon_1$), as well as for the first crank ($\varepsilon_0$). The analysis of Figure 1 results in the statement that the biggest angular accelerations take place for the first crank ($\varepsilon_0$)- piston 1 ($t_C$) in Figure 1. Bigger angular aceleration (existing for $\varepsilon_0$) is caused by the sum of existing moments $M_1$ and $M_0$, which influence the system. The flywheel has the smallest acceleration, which is caused by the big moment of inertia of the flywheel.

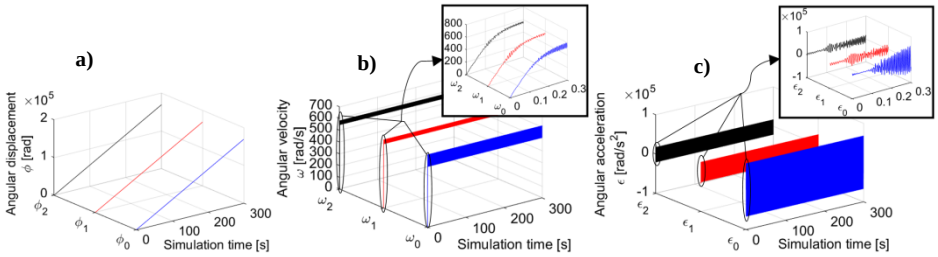


**Figure 8.** Flow charts of angular displacements a), Flow charts of angular velocities b) Flow charts of angular accelerations c).

The presented model allows for testing the influence of loading the assembly with the preset torque after the rotational velocity was determined by the system. Figure 10 shows the influence of loading the piston-crankshaft assembly with the preset torque equal to, respectively: 25, 50, and 75% of the maximal torque.

The increasing load of the piston-crankshaft assembly is accompanied by the decreasing angular velocity of the system (Fig. 9b) with over 600 rad/s for the non-loaded system, to nearly 350rad/s for 75% load. The increasing load is also accompanied by slower increase of angular displacement (Fig. 9a) and smaller values of angular accelerations (Fig. 9c).

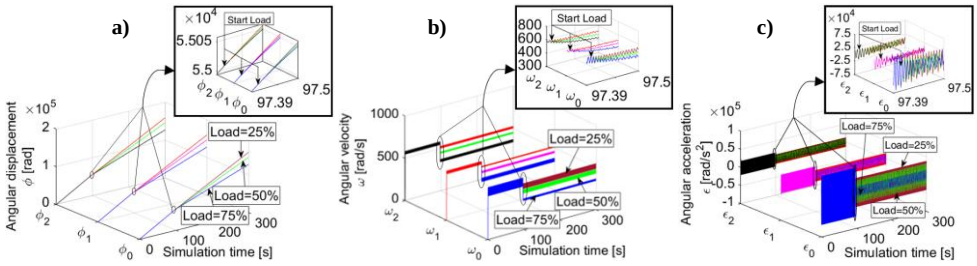


**Figure 9.** Flow charts of influence of load change on: angular displacements a), angular velocities b), angular accelerations c).

The next, very important parameter influencing the behaviour and dynamics of the piston-crankshaft assembly is rigidity of the crankshaft, the change of which, for the values of 0.5k=3200*Nm/rad*, 2k=14600*Nm/rad* and 4k=28800Nm/rad, is shown in Figure 10. With the changing rigidity of the crankshaft, the torsional angles change too, which is accompanied by the changes in oscillation of the angular velocity of the system (Fig. 10b), as well as the changes in angular displacement (Fig. 10a), and oscillations of angular accelerations (Fig. 10c). The most noticeable influence of the change in rigidity 0.5k=3600*Nm/rad* took place for crank 2 (piston 1 ($t_C$)- Fig. 1), the amplitude of oscillation with the determined angular velocity amounted to over 120 rad/s. In work [10] the authors presented a combination of a piston-crankshaft assembly model of the Stirling engine with a thermodynamic model. The subject of the authors' analysis was also the piston-crankshaft assembly behaviour with

the changing moments of flywheel inertia and system's load torques, which were similar to those presented in this work.

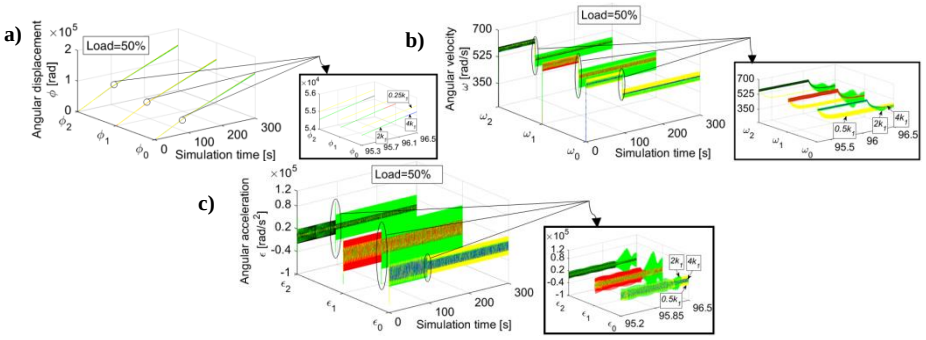


**Figure 10.** Flow charts of influence of change in crankshaft rigidity on: angular displacements a), angular velocities b), angular accelerations c).

From a practical point of view and from the user standpoint, it is essential to choose an adequate mass, and in consequence, the right inertia of the flywheel.

Figure 11 illustrates the influence of the changing flywheel inertia on the change in displacements (Fig. 11a), velocities (Fig. 11b), and angular accelerations (Fig. 11c) of the considered piston-crankshaft assembly. With the increasing moment of inertia of the flywheel (of the flywheel mass), the time extends, after which the system reaches the defined rotational velocity (Fig. 11b), the time of the system's start-up gets longer, for 50-fold increased moment of inertia of the flywheel $50I_2$, the start-up time gets extended from 0.3s to nearly 10s (Fig.11). It should also be emphasised, that the increased flywheel moment of inertia is accompanied by greater oscillations of angular accelerations (Fig. 11c).

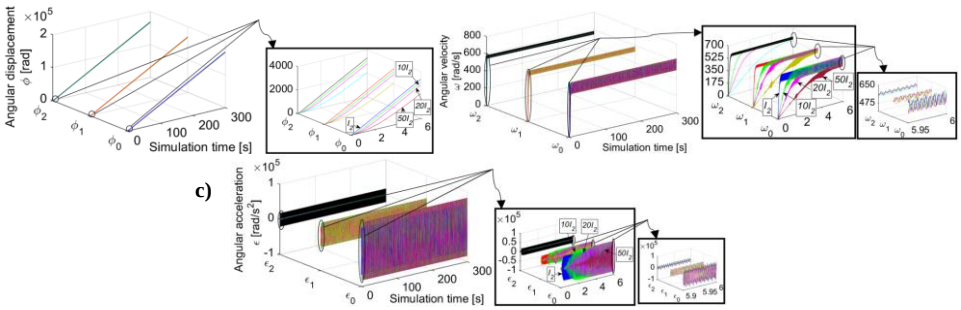


**Figure 11.** Flow charts of influence of change in flywheel moment of inertia on: angular displacements a), angular velocities b), angular accelerations c).

## 3. Conclusions

In this work, the analytical and simulation models have been presented, and the chosen results of the simulation of the piston-crankshaft assembly with three degrees of freedom have been discussed. The flow charts of displacements, velocities, piston accelerations, and flow charts of angular displacement, angular velocity, and angular acceleration of the crankshaft have been presented. The influence of the flywheel moment of inertia, load torque and also of the crankshaft rigidity on the behaviour of the piston-crankshaft assembly during start-up have also been presented.

On the basis of the performed simulations a conclusion can be drawn that the increasing moment of inertia of the flywheel causes a slower start-up of the system (with 50-fold increase of the moment of inertia of the flywheel the start-up time gets extended over 30-fold, which is also accompanied by greater oscillations of the rotational velocity amplitude). This demonstrates the twisting of the shaft during operation. In works [10, 19], where the influence of the flywheel moment of inertia and load torque were presented, results similar to this work were obtained.

In this work, the influence of change in rigidity of the crankshaft (the state before loading the system and after applying the preset value of torque) on the behaviour of the considered system has been presented. After twofold (0.5k=3600*Nm/rad*) decrease in rigidity, a significant rise in oscillation of rotational velocity has been obtained – the highest amplitude of angular velocity amounted to over 120rad/s in the place of piston 1($t_C$) mounting. This was caused by the twisting moment from the flywheel and from piston 2 acting on the section of the crankshaft where piston 1 was mounted. It should be emphasised that with the growing rigidity, the oscillations of rotational velocity decreased, after loading the system with 75% value of the torque excitation, the oscillation amplitudes of the angular velocity dropped, the greatest decrease took place with the rigidity 4k=28800*Nm/rad*, for piston 2 ($t_H$) the amplitude change from 65 to 23*rad/s* took place.

### References


[1] EUCO 169/14 Conclusions – 23/24 October 2014 {http://www.consilium.europa.eu/ –accessed 25.08.2015}.

[2] Bolük G., Mert M. Fossil & renewable energy consumption, GHGs (greenhouse gases) and economic growth: Evidence from a panel of EU (European Union) countries. Energy, Vol. 74, pp. 439–446, 2014.

[3] Chmielewski A., Gumiński R., Radkowski S., Szulim P. Aspekty wsparcia i rozwoju mikrokogeneracji rozproszonej na terenie Polski, Rynek Energii, 2014, nr 5 (114), pp. 94–101. [In Polish]

[4] Directive 2004/8/EC of the European Parliament and of the council of 11 February 2004 on the promotion of cogeneration based on a useful heat demand in the internal energy market and amending Directive 92/42/EC.

[5] Milewski J., Wołowicz M., Bernat R., Szabłowski Ł., Lewandowski J.. Variant analysis of the structure and parameters of SOFC hybrid systems, Applied Mechanics and Materials Vol. 437 (2013) pp 306-312, doi:10.4028/www.scientific.net/AMM.437.306.

[6] Milewski J., Szabłowski Ł., Kuta J.. Control strategy for an Internal Combustion engine fuelled by Natural Gas operating in Distributed Generation. Energy Procedia, Vol 14, 2012, pp. 1478-1483, doi:10.1016/j.egypro.2011.12.1120.

[7] Chmielewski A., Gumiński R., Lubikowski K., Mączak J., Szulim P. Badania układu mikrokogeneracyjnego z silnikiem Stirlinga. Część I. (Research on the micro cogeneration system with Stirling engine. Part I). Rynek Energii 2015; 119(4): 42-48. [In Polish]

[8] Chmielewski A., Gumiński R., Radkowski S., Szulim P. Experimental research and application possibilities of microcogeneration system with Stirling engine. Journal of Power Technologies 2015; 95 (Polish Energy Mix): 14-22.

[9] Li, T., Tang, D., W., Li, Z., Du, J., Zhou, T., Jia, Y. Development and test of a Stirling engine driven by waste gases for the micro–CHP system. Applied Thermal Engineering Vol. 33–34, pp. 119–123, 2012.

[10] Cheng, C., H., Yang, H. S., Jhou, B. Y., Chen, Y. C., Wang, Y. J. Dynamic simulation of thermal–lag Stirling engines. Applied Energy Vol. 108, pp. 466–476, 2013.

[11] Cheng, C., H., Yang, H., S., Keong, L. Theoretical and experimental study of a 300W beta–type Stirling engine. Energy,Vol. 59, pp. 590–599, 2013.

[12] R. A. Margarita, M. Santillán On the dynamical vs. thermodynamical performance of a β-type Stirling engine Physica A, Vol. 409 pp. 162–174, 2014.

[13] Xiao, G., Chen, C., Shi, B., Cen, K., Ni, M. Experimental study on heat transfer of oscillating flow of a tubular Stirling engine heater. International Journal of Heat and Mass Transfer, Vol. 71, pp. 1–7, 2014.

[14] L.S. Scollo, P.E.Valdez, S.R. Santamarina, M.R. Chini, J.H. Baron "Twin cylinder alpha stirling engine combined model and prototype redesign," International Journal of Hydrogen Energy, Vol. 38, pp. 1988–1996, 2013.

[15] C.H. Cheng, Y.J. Yu. Dynamic simulation of a beta-type Stirling engine with cam-drive mechanism via the combination of the thermodynamic and dynamic models," Renewable Energy, Vol. 36, pp. 714-725, 2011.

[16] C.H. Cheng, Y.J. Yu. Combining dynamic and thermodynamic models for dynamic simulation of a beta-type Stirling engine with rhombic-drive mechanism," Renewable Energy, Vol. 37, pp.161-173, 2012.

[17] Jankowski, A., Jeż, M., Świder, A. Investigation of non–linear dynamics of crankshaft assembly. Journal of Kones, Vol. 5,No 1–2, pp. 217–227, 2000.

[18] Jeż, M., Świder, A. Analiza drgań nieliniowych jednocylindrowego silnika tłokowego. Journal of Kones, Vol 8, No 3–4, pp. 98–105, 2001. (In polish).

[19] Chmielewski A., Gumiński R., Radkowski S. Chosen properties of a dynamic model of crankshaft assembly with three degrees of freedom. 20th International Conference On Methods and Models in Automation and Robotics (MMAR), IEEE, pp. 1038-1043, 2015. ISBN: 978-1-4799-8700.

[20] Urieli I., Berchowitz D.M. Stirling cycle engine analysis. Adam Hilger Ltd. Bristol 1984.

[21] Shoureshi R. Analysis and design of Stirling Engines for Waste-Heat Recovery. Massachusetts Institute of Technology, June 1981.

[22] Timoumi Y., Tlili I., Nasrallah S. B. Design and performance optimization of GPU-3 Stirling engines. Energy 2008; 33: 1100–1114.

[23] Sala F., Invernizzi C., Garcia D., Gonzalez M.A., Prieto J.I. Preliminary design criteria of Stirling engines taking into account real gas effects. Applied Thermal Engineering 2015; 89: 978–989.

[24] Babaelahi M., Sayyaadi H. A new thermal model based on polytropic numerical simulation of Stirling engines. Applied Energy 2015; 141: 143–159.

[25] Paul C. J., Engeda A. Modeling a complete Stirling engine. Energy 2015; 80: 85–97.

[26] Ahmadi M. H., Ahmadi M. A., Sadatsakkak S. A., Feidt M. Connectionist intelligent model estimates output power and torque of stirling engine. Renewable and Sustainable Energy Reviews 2015; 50: 871–883.

[27] Alcan P., Balin A., Baslıgil H. Fuzzy multicriteria selection among cogeneration systems: A real case application. Energy and Buildings 2013;67: 624–634.

Adrian Chmielewski, M.Sc. (Ph.D. student): Warsaw University of Technology, Faculty of Automotive and Construction Machinery Engineering, Institute of Vehicles, Narbutta 84, 02–524 Warsaw, Poland (*a.chmielewski@mechatronika.net.pl*).

Robert Gumiński, Ph.D.: Warsaw University of Technology, Faculty of Automotive and Construction Machinery Engineering, Institute of Vehicles, Narbutta 84, 02–524 Warsaw, Poland (*rgumin@simr.pw.edu.pl*).

Jędrzej Mączak, Ph.D. D.Sc. (Assistant Professor): Warsaw University of Technology, Faculty of Automotive and Construction Machinery Engineering, Institute of Vehicles, Narbutta 84, 02–524 Warsaw, Poland (*jma@mechatronika.net.pl*).

# Full control and compensation scheme for a rate integrating MEMS gyroscope (ENG267-15)

Barry Gallacher, Zhongxu Hu and Stephen Bowles

*Abstract:* The major difficulties in the control of a vibratory MEMS gyroscope operating in the rate integrating mode are the frequency mismatch and damping imperfection between the two preferred degenerate vibration modes. Frequency mistuning not only leads to quadrature error, it also affects the orbit phase locking that is critical in controlling the excitation frequency. For high Q MEMS vibratory gyroscopes, damping imperfections are not critical in rate mode. Their influence on mistuning, quadrature error and zero-rate output may even be hard to recognize. However, in rate integration mode, damping imperfections are the major cause of angle drift. Electrostatic mode tuning and velocity feedback control are common methods employed in MEMS gyroscopes to minimize the influences of these imperfections, where it is often difficult to arrange enough electrodes for applying parametric drive as in the HRG. This paper presents the control implementation applied to a ring type MEMS vibratory gyroscope operating in rate integrating mode, which shows maximum angle drift rate reduced to 2.5 degrees/second. This result was achieved by, first of all, employing an automatic high precision electrostatic frequency matching process that is able to minimize frequency mismatch to the order of a few mHz. This enables the orbit phase to be locked at 90 degrees, with a high accuracy of less than 0.1 degrees phase deviation. Then a quadrature nulling control effectively suppresses the Quadrature motion while two term velocity feedback corrects for damping asymmetry.

## 1. Description of the MEMS ring gyroscope

The most common high performance vibratory gyroscopes make use of the property of modal degeneracy associated with axisymmetric structures. Examples include the hemispherical shell, ring and cylinder gyroscopes. Gyroscopes may be classified into two distinct classes. The most common type is the Rate gyroscope. In this type of gyroscope, which is prevalent in MEMS technology, the vibration is maintained along a particular direction and may be decomposed into two orthogonal contributions represented by a pair of degenerate normal modes. Structural imperfections break the ideal symmetry causing a frequency split and the modes cease being degenerate. Rate gyros measure the angular velocity thus angle information requires numerical integration. In the other class known as Rate Integrating the vibration pattern is free to precess in response to an applied angular velocity. Rate Integrating gyros provide a direct measure of the angle with no need to integrate. In addition, the bandwidth and dynamic range of the Rate Integrating gyro is infinite in the linearized mechanical model. However, the allowed tolerances on structural imperfections for the Rate Integrating gyro are

typically two orders of magnitude lower than that of the same device operating in Rate mode [1]. This makes the control problem for the Rate Integrating gyro substantially more complex [2-5].

A prerequisite to operating in rate integration mode is to minimise the frequency split between the normal modes. A systematic procedure to perform this task is described in detail in [6]. A brief description is provided here. The gyroscopic is first operated in rate mode whereby an artificial Coriolis force is generated electrostatically. It is shown in [1-4] that all structural imperfections manifest as either a response in quadrature to the Coriolis response or as a cross-coupling between the two otherwise degenerate modes. In the rate gyroscope it is convenient to reference the two modes of vibration with respect to a fixed coordinate system related to the drive electrodes. In this coordinate system structural imperfections from mass and stiffness manifest as cross-coupling and frequency separation. The systematic approach has been fully automated and commences by electrostatically reducing the cross-coupling between the two modes referenced with respect to axes aligned with the drive electrode. Note that in the rate gyroscope, one mode is forced externally at resonance. Excitation of the other mode is through Coriolis coupling or coupling due to off axis structural imperfections. In the absence of any applied Coriolis force, real or artificial, any response of the non-forced mode must be due to cross-coupling. Electrostatic reduction of this contribution may then be performed. With the cross-coupling from structural imperfections removed, the remaining direct imperfection terms may be addressed.

Figure 1 show the MEMS ring gyroscope. The gyroscopic element is manufactured by Silicon Sensing from single crystalline silicon of orientation <111>. This orientation exhibits approximately isotropic elastic properties making it preserve the modal degeneracy. Furthermore, the material has a high intrinsic Q-factor which is a desirable attribute for resonant sensors in general. There are eight section electrodes which provide electrostatic actuation (SD and PD) and sensing (PPO and SPO) of the in-plane flexural motion of the ring. Electrostatic modification of the stiffness matrix is performed using the four groups of four tuning electrodes labelled as PCW, PACW, SCW and SACW. The axis $q_1$ corresponds to a fixed reference that bisects a drive electrode. The axis $x_1$ is rotated relative to $q_1$ by the angle $\theta_p$ and corresponds to one of the normal mode axes.

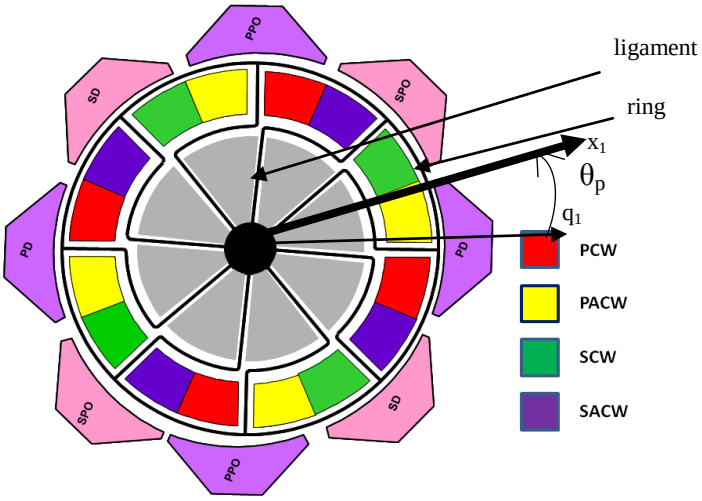


**Figure 1.** Schematic of the micro-ring vibrating gyroscope.

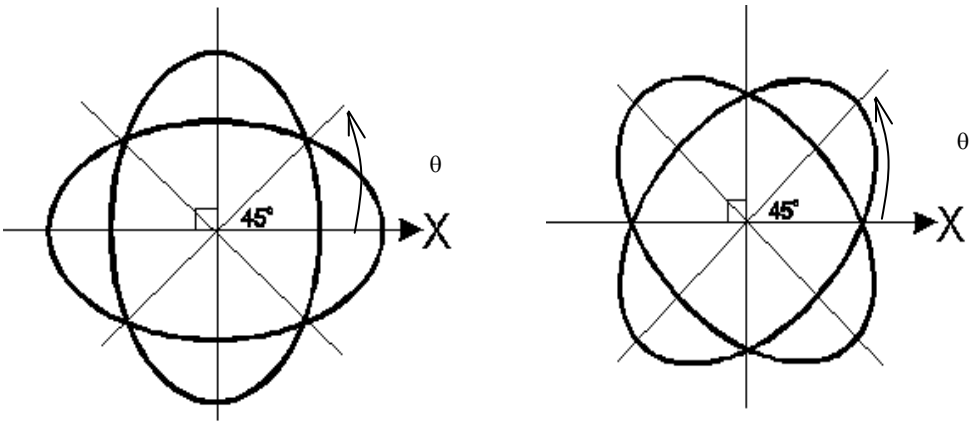


(a) (b)

**Figure 2.** Radial displacement of the flexural modes of the ring for n=2. (a) Primary mode, (b) Secondary mode.

## 2. Equations of motion

As described in the introduction, a prerequisite to operating in rate integration mode is to minimise the frequency split between the normal modes. The key effect of the tuning is to minimize the structural cross coupling. As a result the cross-coupling is small. Performing the coordinate transformation from the electrode coordinate system to the normal mode coordinate system, shown in figure 1, using the orthogonal transformation matrix $[X] = \begin{bmatrix} 1 & -\epsilon\tilde{\eta} \\ \epsilon\tilde{\eta} & 1 \end{bmatrix}$ where $\eta = \tan^{-1}\theta_p$ , $\eta = \epsilon\tilde{\eta}$ gives the coupled equations of motion for the two normal modes.

$$\underline{\ddot{x}} + 2\epsilon[C+G]\underline{\dot{x}} + [D]\underline{x} = \epsilon\begin{bmatrix} 1 & -\epsilon\tilde{\eta} \\ \epsilon\tilde{\eta} & 1 \end{bmatrix}\underline{F} \quad (1)$$

$$[C] = v_o\omega_0\begin{bmatrix} 1+\gamma_1 & \gamma_2 \\ \gamma_2 & 1-\gamma_1 \end{bmatrix}, [D] = {\omega_0}^2\begin{bmatrix} 1+\epsilon\xi & 0 \\ 0 & 1+\epsilon\xi \end{bmatrix}, [G] = \phi\begin{bmatrix} 0 & -1 \\ 1 & 0 \end{bmatrix}$$

Figure 2 shows the radial component of the *n*=2 in-plane flexural modes which have been used as generalized coordinates in the equations of motion.

In obtaining equation (1) note that the Q-factor is typically of the order of $10^4$ thus the damping ratio <<1 has be written in terms of the small parameter $\varepsilon$. The small parameter $\varepsilon$ has subsequently been used to express the structural imperfections, angular rate and control force. The vector $\underline{x}$ is the normal mode displacement and *F* is the force applied from the drive electrodes expressed relative to the electrode axes. Furthermore, it should be reiterated that angular acceleration terms (such as those arising from centripetal acceleration) have been neglected in this analysis due to their small magnitude. The eigenvectors of the dynamical matrix can be used to diagonalize both the mass and stiffness matrices. Thus the structural imperfections arising from anisoinetia and anisoelasticity have been conveniently described by the imperfection term $\xi$ within matrix *D* of equation (1). The forcing vector is transformed and cross-coupling from mass and stiffness imperfections in the electrode coordinate system manifest as cross-coupling forcing terms. The damping matrix *C* is not diagonalized and has direct and cross terms $v_o\gamma_1$ and $v_o\gamma_2$, respectively. The unperturbed modal damping is represented by $v_o$. The damping imperfections are defined as $\gamma_1$and $\gamma_2$. The angular rate is applied about the polar axis of the ring and the Bryan factor has been incorporated into the definition of $\phi$. The gyroscopic matrix *G* is skew symmetric. It is obvious that cross-terms in the damping matrix *C* can result in similar dynamic behaviour to that produced as a result of Coriolis coupling.

A two time scale perturbation solution to the equation (1) is sought. This has the advantage of separating the slow time evolution or envelope dynamics from the fast time dynamics associated with the modal vibration. Using $\varepsilon$ as the small parameter and defining the slow and fast time scales $\bar{t} = \epsilon t$ , $\hat{t} = t$ a solution may be obtained of the form

$$x(\hat{t}, \bar{t}) = x_{(0)}(\hat{t}, \bar{t}) + x_{(1)}(\hat{t}, \bar{t}) + O(\epsilon).$$

Removal of the secular terms and transforming to elliptical orbital parameters [2] yields the slow-time equations describing the evolution of the elliptical trajectory. The transformation to elliptical parameters provides an insight into the control problem. The major and minor axes of the ellipse are shown in figure 3 and are *a* and *b*, respectively

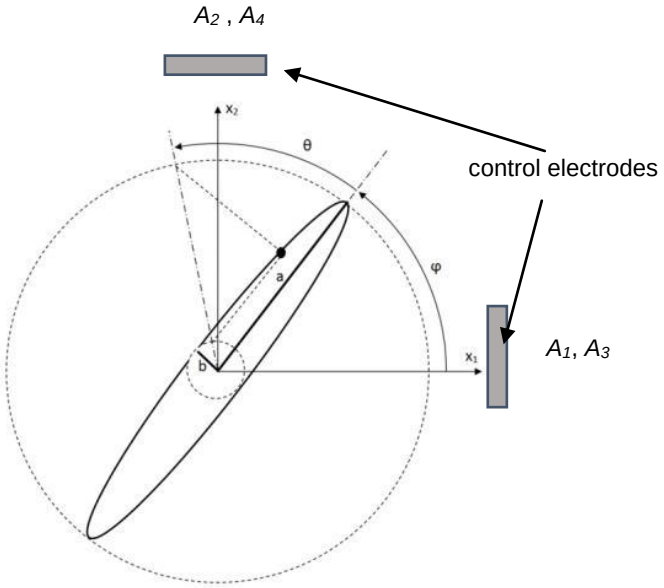


**Figure 3.** The orbital elliptic parameters used to describe gyroscope vibration

For the perfect ring, free of imperfections *b*=0 and the major axes will rotate in response to an applied angular velocity $\phi$ . The angle that the ellipse makes with the reference axis is represented by $\varphi$, while $\theta$ is known as the orbital phase and represents the position of an arbitrary point on the parameter of the ellipse. Note that $\theta = \omega_0 t + \Phi_0$. Using the coordinate transformation

$x_1$=$a$cos$\theta$cos$\varphi$− $b$sin$\theta$sin$\varphi$, $x_2$=$a$cos$\theta$sin$\varphi$+ $b$sin$\theta$cos$\varphi$ and the assumption that $a \gg b$ yields the orbital elliptical equations of motion

$$\dot{a}+a\omega_0\upsilon_0(1+\epsilon\widetilde{\gamma_1}\cos2\varphi+\epsilon\widetilde{\gamma_2}\sin2\varphi)+0.5b\omega_0\xi\sin2\varphi-F_1=0 \quad (2)$$

$$\dot{b}-0.5a\omega_0\xi\sin2\varphi+b\omega_0\upsilon_0(1-\epsilon\widetilde{\gamma_1}\cos2\varphi-\epsilon\widetilde{\gamma_2}\sin2\varphi)-F_2=0 \quad (3)$$

$$\dot{\varphi}-\omega_0\upsilon_0(\epsilon\widetilde{\gamma_1}\sin2\varphi-\epsilon\widetilde{\gamma_2}\cos2\varphi)+ba(\Phi_o+0.5\omega_0\xi\cos2\varphi)+\phi+F_3=0 \quad (4)$$

$$\Phi_o-0.5\omega_0\xi\cos2\varphi+b\{\phi+\dot{\varphi}+\omega_0\upsilon_0(\epsilon\widetilde{\gamma_1}\sin2\varphi-\epsilon\widetilde{\gamma_2}\cos2\varphi)\}-F_4=0 \quad (5)$$

The damping imperfections $\gamma_j$ are small and have been written in terms of small parameter ε as $\epsilon\widetilde{\gamma_j}$.

The control forces $F_j$ j=1..4 described by equation (6) are generated electrostatically and are in general not independent. The forcing generated by two electrodes orientated such their angular separation $\pi/2n$ in physical space ($\pi/2$ in mode space as shown in figure 3) results in force contributions affecting the major and minor axes of the ellipse as well as the precession. The control problem is to permit independent adjustment of the major axis, the minor axis whilst simultaneously nulling the contributions to angle or rate error.

$$\begin{aligned}
F_1&= A_1\sin\sigma_1\cos\varphi+A_2\sin\sigma_2\sin\varphi+A_3\sin\sigma_3\cos\varphi+A_4\sin\sigma_4\sin\varphi\\
F_2&= A_1\cos\sigma_1\sin\varphi-A_2\cos\sigma_2\cos\varphi+A_3\cos\sigma_3\sin\varphi-A_4\cos\sigma_4\cos\varphi\\
F_3&= A_1\sin\sigma_1\sin\varphi-A_2\sin\sigma_2\cos\varphi+A_3\sin\sigma_3\sin\varphi-A_4\sin\sigma_4\cos\varphi\\
F_4&= A_1\cos\sigma_1\cos\varphi+A_2\cos\sigma_2\sin\varphi+A_3\cos\sigma_3\cos\varphi+A_4\cos\sigma_4\sin\varphi
\end{aligned} \quad (6)$$

with

$$\sigma_j=\Phi_{Dj}+\lambda t+\Phi_{oj} \quad (7)$$

$$j=1,2,3,4.$$

In the control force expression $A_j$ is the forcing magnitude and $\Phi_{Dj}$ the phase of the forcing applied to the electrode. The term $\Phi_{oj}$ is the phase angle measured with respect to a reference waveform. The excitation frequency of the control forces is $\omega=\omega_o+\epsilon\lambda$. Recall that the unperturbed mode frequency is defined by $\omega_o$. The control amplitudes $A_j$ are functions of voltage and enable velocity or displacement feedback as well as conventional electrostatic control.

## 3. Independent control

The control forces $F_j$ $j$=1, 2, 3, 4 generated by the two electrodes are in general not independent. Recall that the damping imperfection $\epsilon\widetilde{\gamma_j}$ $j$=1, 2 make contributions of O($\epsilon$) in the envelop equations

of the ellipse, as described by equations (2-5). The control strategy is to first make $F_3$= 0 + O($\epsilon$) where O($\epsilon$)= $\omega_0 v_0(\epsilon\widetilde{\gamma_1}\sin 2\varphi - \epsilon\widetilde{\gamma_2}\cos 2\varphi)$ is the contribution from the damping imperfections, whilst controlling the major and minor axes of the ellipse using $F_1$ and $F_2$. The contribution O($\epsilon$) from damping can then be addressed using an additional control force $\epsilon\widetilde{F_3}$= $\omega_0 v_0(\epsilon\widetilde{\gamma_1}\sin 2\varphi - \epsilon\widetilde{\gamma_2}\cos 2\varphi)$. It is not possible with this electrode configuration to satisfy the condition $F_3$= 0 + O($\epsilon$) and $F_4$=0 whilst ensuring $F_1 \neq 0$ and $F_2 \neq 0$. In this case the control force $F_4$ will perturb the orbital phase as shown in equation (5). However, providing the phase lock can be achieved then the effect of this can be ignored.

The condition $F_3$= 0+ O($\epsilon$) yields the force expressions

$$F_1 = \left(A_2 sin(\sigma_2) + A_4 sin(\sigma_4)\right)\frac{1}{sin(\varphi)} \tag{8}$$

$$F_2 = \left(\frac{A_2 sin(\sigma_2 - \sigma_1)}{sin(\sigma_1)} + \frac{A_4 sin(\sigma_4 - \sigma_3)}{sin(\sigma_3)}\right) cos(\varphi) \tag{9}$$

Independent control is made possible if the phases satisfy the

$$sin(\sigma_2 - \sigma_1) = 0$$

$$sin(\sigma_4 - \sigma_3) = \pm 1 \tag{10}$$

$$sin(\sigma_2) = \pm 1$$

$$sin(\sigma_4) = 0$$

The phases can be set to $\sigma_1 = \sigma_2 = \sigma_3 = \pm\frac{\pi}{2}$ and $\sigma_4 = 0$ . This corresponds to velocity feedback for the *j*=1, 2 force component to sustain the major axis *a* of the ellipse. Nulling of the minor axis *b* or quadrature is performed using a superposition of velocity and displacement feedback corresponding to force components *j*=3, 4, respectively. The force expressions for the ellipse control are then given by

$$F_1 = A_2\frac{1}{sin(\varphi)} \tag{11}$$

$$F_2 = A_4 cos(\varphi) \tag{12}$$

Control of the major and minor axes of the ellipse is achieved through the independent amplitudes $A_2$ and $A_4$.

## 4. Contributions to rate error

Equation (4) describes the slow-time evolution of the precession φ of the ellipse and deserves special attention. In the absence of any damping, structural imperfections, phase error and control

action the precession rate and the input angular velocity are related by $\dot{\varphi}+\phi=0$. This is the ideal case. The imperfection constitute errors to the angular velocity and make different sized contributions.

The mass and stiffness imperfections result in the term $ba\omega_0\xi\cos 2\varphi$. This contribution must be minimised first. To minimise this contribution the mistuning between the normal mode frequencies described by $\xi$ is reduced using a two stage mode tuning scheme. This greatly simplifies the control problem first yielding a slowly evolving ellipse and rendering parasitic control forces due to misalignment between the normal mode axes and the electrode axes as higher order contributions. Then control force $F_2$ is applied to the ellipse through the amplitude $A_4$ in order to minimise the minor axis of the ellipse $b$. Thus $b\xi \rightarrow 0$.

The damping imperfections make the smallest contribution to the precession. A separate velocity based feedback control force is generated to minimise this contribution after the other control loops are in operation.

## 5. Systematic reduction of the normal mode frequency split

A prerequisite to operating in rate integration mode is to minimise the frequency split $\xi$ between the normal modes. The experimental setup and tuning results are shown in figures 4 to 6. Typically the modal mistuning can be automatically reduced from 2 Hz to 2 mHz. The resonant frequency of the gyro is approximately 14 kHz. The tuning is therefore approximately 1:$10^7$.

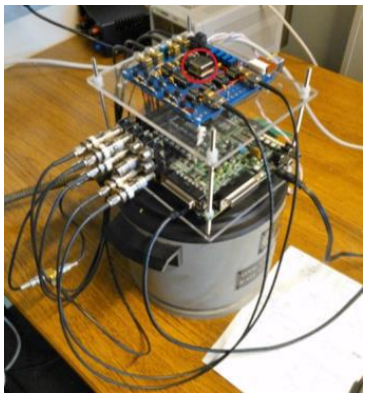

**Figure 4.** The gyroscope (circled in red) mounted on a PCB, DSP board and CUPE rate table

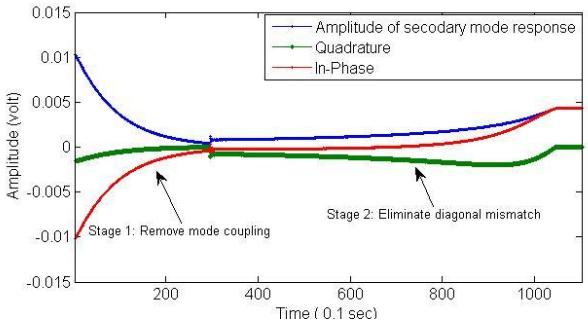


**Figure 5.** The automatic tuning process

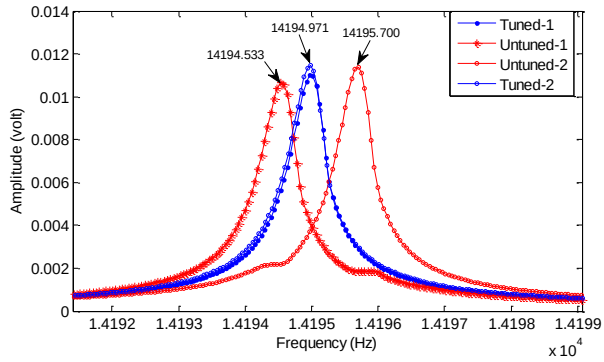


**Figure 6.** Frequency responses of the two modes with both diagonal and off-diagonal imperfections

## 6. Experimental results of the rate integrating gyro control

The first objective for the rate integrating controller is to minimize the minor axis (referred to as quad) of the ellipse *b*. This is performed using the control force $F_2$ described by equation (12). Figure (7) shows that without the controller the minor axis of the ellipse evolves with the precession angle with an amplitude of 0.9 mV peak to peak. With the minor axis controller engaged the peak to peak variation reduces to less than 10 μV, as shown in figure (8). The minor axis has been reduced by a factor of 100 using the controller. The major axis of the ellipse *a* is sustained using the control force $F_1$ described by equation (11). The sustaining of the major axis is shown in figure (8). Note that the major axis is now a factor of 1000 larger than the minor axis making the ellipse approach a straight line. With the major and minor axes under control the remaining error contribution is due to the damping imperfection term $\omega_0 v_0(\epsilon\widetilde{\gamma_1}\sin 2\varphi - \epsilon\widetilde{\gamma_2}\cos 2\varphi)$ in equation (4). The effect of this contribution can be clearly seen in the plot of the precession rate as a function of time for a constant rate input, as shown in figure (9).

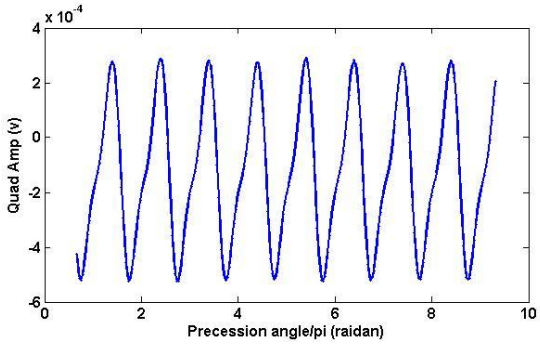


**Figure 7.** Without quad nulling, quadrature amplitude evolves during precession.

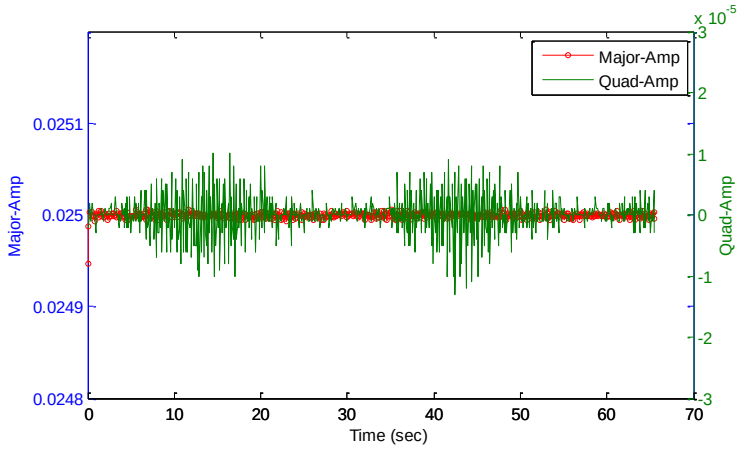


**Figure 8.** Major axis sustain and quad nulling performance.

The drift due to damping imperfections can be minimized using a the control force $\epsilon\widetilde{F_3}$= $\omega_0 v_0(\epsilon\widetilde{\gamma_1}\sin 2\varphi - \epsilon\widetilde{\gamma_2}\cos 2\varphi)$. Velocity feedback is used to provide this control force. The results of this damping correction are shown figure (10). The modulation amplitude of the drift rate due to damping imperfections has been reduced by a factor of 5.

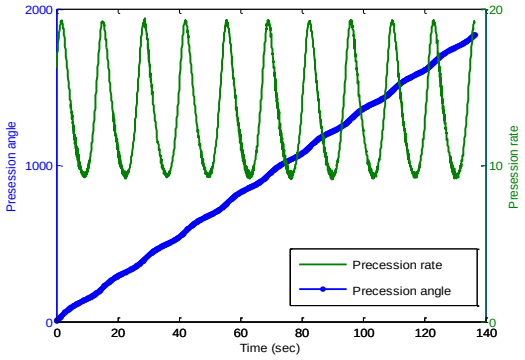


**Figure 9.** Effect of damping imperfections on drift rate.

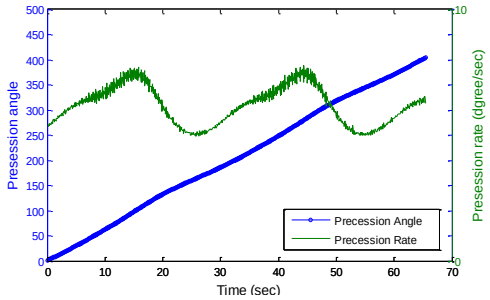


**Figure 10**. Compensation of damping imperfections.

## 7. Conclusions

The implementation of feedback control and damping imperfection compensation based on a DSP platform is described in this paper. The motion equation transformed into the elliptical orbital system indicates that the minor axis of the ellipse (known as quadrature error) is caused by mass and stiffness imperfections in the normal modes and also energy dissipation due to the average of the modal damping. Angle drift is mainly caused by damping imperfections. An important distinction between the rate and rate integrating gyro is that the effect of the structural imperfections in the rate integrating gyro depends on the precession angle, rather than constant as in rate mode.

By using electrostatic mode tuning in the calibration stage, mass and stiffness imperfections are reduced by a factor of 1000 prior to operating in rate integrating mode. This has significantly relaxed the control problem of suppressing the minor axis of the ellipse (quad). The minor axis amplitude is suppressed to less than one thousandth of the major axis during fast precession.

Amplitude of vibration in the major axis is readily sustained by velocity feedback control in the presence of damping variation during precession. The modulation pattern of the control gain is used to estimate the amount of damping imperfection and its distribution. Their values are then put in the feedback control to reduce angle drift. Experimental results validate the compensation method.

**Acknowledgments**

The authors wish to acknowledge the support from K Townsend, C Gregory and A Kazer of UTAS (Plymouth, UK) to this research project in terms of the provision of hardware, developing the algorithms and interpretation of the experimental results.

**References**

[1] Gallacher, B.J. Principles of a micro-rate integrating ring gyroscope. *IEEE Trans. Aerosp. Electron. Sys.*, 48 (2002), 658-672.

[2] Friedland, B and Hutton, M.F. Theory and error analysis of vibrating member gyroscope. *IEEE Trans. Autom. Control.*, 23, 4 (1978), 545–556.

[3] Lynch, D.D. Vibratory gyro analysis by the method of averaging. in *Proc. 2nd Int. Conf. Gyroscopic Technol. Navigat.*, St. Petersburg, FL, USA, (1995), 18–26.

[4] Zhuravlev, V.P. Drift of an Imperfect Hemispherical Resonator Gyro. *Mechanics of solids*, 39 (2004), 15-18.

[5] Lynch, D.D. MRIG Frequency Mismatch and Quadrature Control. *International Symposium on Inertial Sensors and Systems Proceedings*, (2014), 21-24.

[6] Hu, Z.X., Gallacher, B.J., Burdess, J.S., Bowles, S.R. A systematic approach for precision electrostatic mode tuning of a MEMS gyroscope. *Journal of Micromechanics and Microengineering*, *24*, 12 (2014).

[7] Zhang F., Keikha, E., Shahsavari B., and Horowitz R. Adaptive Mismatch Compensation for Vibratory Gyroscopes. *International Symposium on Inertial Sensors and Systems Proceedings*, (2014), 67-70.

[8] Gregory, J.A., Cho, J., and Najafi, K. Novel Mismatch Compensation Methods for Rating Integrating Gyroscopes, *Proceedings of IEEE/ION PLANS*, (2012), 252-258.

Barry J Gallacher, Reader of Engineering Dynamics: Newcastle University and School of Mechanical and Systems Engineering, Stephenson Building, NE1 7RU Newcastle, UK (*b.j.gallacher@ncl.ac.uk*). The author gave a presentation of this paper during one of the conference sessions.

Zhongxu Hu, Senior Research Associate: Newcastle University and School of Mechanical and Systems Engineering, Stephenson Building, NE1 7RU Newcastle, UK (zhongxu.hu@newcastle.ac.uk).

Stephen R Bowles, Ph.D: Newcastle University and School of Mechanical and Systems Engineering, Stephenson Building, NE1 7RU Newcastle, UK (stevebowles89@gmail.com).

# Use of energy operators in condition monitoring of gearboxes (NUM287-15)

Adam Gałęzia, Robert Gumiński, Marcin Jasiński, Jędrzej Mączak

*Abstract:* In the paper the possibility of detection of early stages of local faults in gears using energy operators is analyzed. Such faults, during operation of gearbox, are causing disturbances in the teeth contacts resulting in creation of local and transient anomalies in a vibration signal. Analysis performed on the diagnostic signal are focused on, as early as possible, detection of such anomalies but also on assess localization of defects and remaining useful life of gears. Presented in the paper methods of signal analysis allow detection of local nonstationarities in the time-domain vibration signal. It is assumed that such transient events are linked to the fatigue tooth damages such as pitting and tooth base fracture. Described methods use energetic operators for obtaining diagnostically useful information.

## 1. Introduction

Constant development of machines is forced by increasing ecological, economical and safety demands. Fulfilling them is related with creation of new technical solutions and designs, use of new materials [1], such as e.g.: sustainable composite materials, implementation of new monitoring techniques and maintenance strategies. Awareness of footprint of human activities related with technological progress puts constant pressure on taking care for environment and socio-economical costs of machine failures and making every effort to develop new and reliable techniques for determination of technical condition of machines and structures. Those techniques are developed in many fields and directions and can be related with: development and use of signal processing techniques [2, 3, 5], research and application of structures with embedded sensors [16] or distributed monitoring systems [7], use of different physical phenomena for detection of early stages of failures [8] or implementation of Proactive Maintenance Strategy [18, 19].

Reliability of machines and industrial facilities often depend on reliability of basic elements such as bearings, shafts or gearboxes. Their failure can caused high, direct and indirect, financial losses, pollution of natural environment, lost of life and health of people.

Detection of early stages of failure is important because it gives ability to monitor development of failure and undertake actions reducing financial losses caused by unexpected shutdown (e.g. plan of repairs) or threat of catastrophe (e.g. destruction of machine) [19]. In vibroacoustic condition monitoring of machines it is assumed that changes of technical condition of machine, resulting from

arise and development of failure will cause changes in amplitude and frequency structure of signal generated by working machine [17].

Detection of early stages of local failures in gears is important due to wide area of their application, e.g. in machines, power transmission systems of wind turbines, helicopters or trains. Basic degradation mechanisms of gears are: pitting and tooth base fracture. Pitting is a slowly developing failure usually not causing catastrophic failure of machine, while fatigue brake of tooth can develop very fast and is difficult for detection in its early stage. Both failures result in disturbance of the teeth contacts introducing transient anomalies in vibration signal recorded for diagnostic purposes [19]. The major disadvantage of commonly used diagnostic methods is the use of integral transformations of the signal (e.g. Fourier transform) that are averaging results [21]. Presented methods of signal analysis, based on the energetic operator, allows for detection of local and transient nonstationarities in the time-domain vibration signal. They are directly linked to the fatigue tooth damages such as pitting and tooth base fracture as well as manufacturing errors (e.g. imbalance or misalignment of shafts) in gearbox. These methods use differential parameters of the acceleration signal calculated for the consecutive meshes that are based on instantaneous power of the signal and Teager-Kaiser energy operator. This solution additionally allows predicting the remaining useful life of gears by detection of trends in local disturbances of the meshing process for particular tooth pairs during the normal exploitation of the gearbox [13,15].

## 2. Detection of local disturbances in the signal based on changes of its instantaneous power

In the electric circuits instantaneous power of the signal could be described as:

$$p(t) = \frac{|v(t)|^2}{R} \quad \text{or} \quad p(t) = Ri^2(t) \tag{1}$$

where $v(t)$ and $i(t)$ denotes voltage and current that are changing in time and $R$ is the resistance of the circuit. Normalizing the above equation (Eq. 1) by applying unitary value of resistance allows obtaining instantaneous power of the signal as its squared envelope [2]:

$$p(t) = |s(t)|^2 \tag{2}$$

In case of the signal that was digitally sampled with sample step of $\mathrm{d}t$, momentary changes of the energy in the period of $\mathrm{d}t$ equals its instantaneous power. Additionally, usage of the squared envelope improves the signal to noise ratio (SNR) [9].

Envelope of the signal could be calculated as a modulus of the analytic signal:

$$\tilde{x}(t) = x(t) + j\mathrm{H}[x(t)] \tag{3}$$

obtained by taking the real signal $x(t)$ and adding the imaginary part created as its Hilbert transform [6, 20]:

$$A(t) = \left|\tilde{x}(t)\right| = \sqrt{x^2(t) + \mathrm{H}^2[x(t)]} \tag{4}$$

Envelope analysis could be used for detection of local disturbances in the gearbox signal (e.g. acceleration of the gearbox case) caused by the fatigue damages of teeth. In the work [12] a methodology of diagnosis of such defects based on the segmentation of the signal was presented. It was later improved as described in works [13-15]. The method involves comparing each of successive segments of the instantaneous power waveform of the recorded and synchronously averaged acceleration signal. The length of segments is related to the transverse radial pitch. Beginnings of consecutive segments are defined based on the geometry of gears. The method requires simultaneous recording of a trigger signal on the gear shaft along with the acceleration signal so the shifts of beginnings of tooth contacts resulting from the manufacturing inaccuracies, bending of teeth etc. are reflected in the resulting parameter. Envelope of the signal in contrary to the signal itself is of a low frequency nature, insensitive to the phase shifts. It allows obtaining better comparison results of the consecutive segments compared to the unprocessed signal containing high frequency components. Taking into consideration squared value of envelope this additionally increases sensitivity of the method for the small changes in the signal. Developed diagnostic parameter based on the comparison of instantaneous power of the signal for its consecutive, related to each other segments, called Envelope Contact Factor (ECF) is a new time signal, variable in time, calculated as a point-by-point difference of the squared envelope waveforms for the segments related to the consecutive tooth pair contacts [15].

$$ECF(t) = \left|A^2(i,t) - A^2(i-1,t)\right| \tag{5}$$

where $i-1$ and $i$ are numbers of the compared signal segments related to the contacts of the consecutive tooth pairs. Time symbol $t$ in equation (Eq. 5) should be treated conventionally. For the sampled signal it means consecutive samples of both signal segments.

ECF is an energy parameter enhancing changes in the consecutive tooth contacts caused by the differences in the meshing force resulting from the pitch errors, differences in the meshing stiffness and all the inaccuracies in manufacturing of shafts and gears of the gearbox. Changes in the contacts of the tooth pairs result in a growth of the teeth dynamic load and increase of stress in the tooth base.

The higher the calculated values o ECF, the bigger load acts on given pair of teeth and the greater the likelihood that damage (if in the future any) will take place on this pair.

ECF, as a differential parameter, is insensitive to slow or monotonic changes taking place in the signal. This is why it is well suited for detection of the signals containing changes of the impulse type that are common in case of pitting and fractures at the tooth base. Its calculation is very fast as it could be performed by cyclic shift (of the size of single segment) of the signal data buffer corresponding to the single shaft rotation and subtracting both buffers. In this case Eq. 5 will take the form:

$$ECF(t) = \left| A^2(t-\tau) - A^2(t) \right| \tag{6}$$

where $\tau$ is the shift of one segment corresponding to the transverse pitch.

This method of calculation means that user do not have to divide the signal into the segments. It is important however that the length of the signal sample corresponding to the averaged single shaft rotation was divisible by the number of teeth of the gear on this shaft. This means that the length of each signal segments corresponding to the transverse pitch would be the same.

As the ECF is a continuous time signal it could be analyzed with the use of any methods used in signal analysis e.g. statistical, tabulation etc. This allows for the compression of the information particularly useful in case of autonomous real time diagnostic systems.

## 3. Teager-Kaiser Energy Operator (TKO)

Teager-Kaiser Energy Operator (TKO) was first proposed by Teager [22], but the method of its calculation for digital signals and analysis of its properties for the first time gave Kaiser [10]. TKO is a nonlinear operator that for continuous signals has the following form:

$$\psi[x(t)] = \dot{x}^2(t) - x(t)\ddot{x}(t) \tag{7}$$

It allows for estimation of the instantaneous energy of the signal, so called Teager energy and can be used in the process of signal demodulation [4, 11] instead of classical method with use of Hilbert transform.

In case of the harmonic oscillator without damping, the total energy of the system is proportional to the product of squared amplitude and squared frequency of oscillations:

$$E \propto \omega^2 A^2 \tag{8}$$

For the harmonic motion

$$x(t) = A\cos(\omega t + \varphi) \tag{9}$$

equation (Eq. 7) calculating Teager Energy of the signal reduce to the form

$$\psi[x(t)] = A^2\omega^2 \tag{10}$$

Comparison of (Eq. 8) and (Eq. 10) shows similarity of these two approaches. As could be seen Teager-Kaiser Energy Operator allows estimation of the energy of the signal. In general case the result of the operator is a function that varies in time.

For the discrete signals, sampled with the sampling frequency much higher than the highest frequency components in the signal, equation (Eq. 7) takes the form:

$$\psi[x_n] = x_n^2 - x_{n-1}x_{n+1} \tag{11}$$

where $n$ denotes samples of discrete time domain signal.

One might note the simplicity of calculations. It requires multiplying the signal by itself and multiplying the signal by the signal shifted in time, which is very easy to obtain in digital systems. This form is also very convenient for use in real-time diagnostic systems and systems working on-line since it requires only a simultaneous access to the three most recent signal samples. One should note also the similarity of the operator (Eq. 11) to the square of the amplitude of the signal.

The resulting form of the operator is unfortunately sensitive to noise in the signal. It can be shown [10] that adding a Gaussian random noise signal with zero mean and variance $\sigma^2$ cause increase of the expected value of the operator by the variance of the noise. This effect could be minimized using averaging of the resulting TKEO signals.

## 4. Comparison of the instantaneous power of the signal and TKO operator

To compare the two energetic operators (instantaneous power of the signal and TKO operator) the diagnostic experiment on a back-to-back tester used for accelerated fatigue examining of gears (Figure 1) has been conducted. During the experiment that lasted 72 minutes, housing vibrations and synchronizing pulses from the induction sensor placed on the pinion shaft were recorded. The examined gear pair was equipped with spur gears, with a 4 mm module, having 27 teeth in the pinion and 35 teeth in the gear. During the accelerated test the gears were loaded with a torque of ca. 1300 Nm. Gears were not specially prepared for the experiment, i.e. no artificial defects like notch, cut or crack were introduced. The experiment was conducted until full breaking of a single pinion tooth. The signal recording and on line analysis of the acquired signal samples was performed continuously (without breaks) in 6 second data blocks with use of National Instruments equipment consisting of NI-PXI 8186 measuring computer equipped with NI-PXI 4472B DSA measuring card. Sampling frequency was selected to 25,6 kHz and rotational frequency of the pinion shaft set to ~25 Hz. The recording and analyzing system was controlled by the LabVIEW program. Upon

completing the experiment it was discovered that the pinion tooth no. 11 (fourth tooth, counting from the synchronizing pulse) became completely fractured.

Figure 2 shows the comparison of the instantaneous power and Teager-Kaiser Energy Operator calculated for the acceleration signal synchronously averaged for the single rotation of the pinion shaft. Signal averaging was performed for the signal segments of the length of single shaft rotation obtained during registration of the 6 second length data blocks. Taking into the account the rotational speed of the pinion shaft the number of averages was around of 150. Before averaging each rotation was resampled so to obtain the same length of each segment.

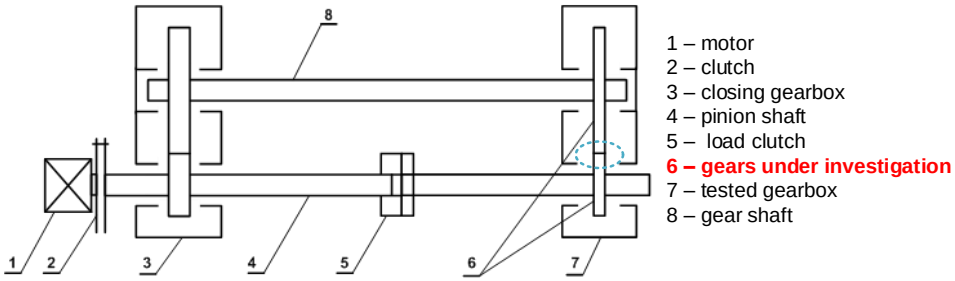


**Figure 1.** Back-to-back tester used during the experiments

Presented results were obtained after 60, 65 and 68 minutes from the beginning of the experiment that lasted 72 minutes. Instantaneous power was calculated as a squared envelope of the signal (Eq. 4) and the Teager-Kaiser Energy Operator according to the Eq. 11. Local changes in the signal marked with ellipse indicate the emerging local fault that was linked to the emerging crack at the pinion tooth base. In each case, one can note the similarity of the instantaneous power (squared envelope) waveform and TKO operator. In fact, the differences concern only the scale, which is confirmed by Eq. 8 and Eq. 10. As shown in Figure 2 changes in meshing stiffness arising due to the increasing crack in the tooth base are visible in instantaneous power and TKO waveforms as a small disturbance of the instantaneous amplitude of the power signal. At the same time this small changes does not change the overall RMS level of the signals nor its peak amplitude.

Because the result of acting of the Teager-Kaiser Energy Operator on signal is a time waveform, we can analyze it using methods previously described for the analysis of the signal envelope. In particular the ECF coefficient, which proved to be particularly sensitive to local disturbances of the signal. The enlarged portion of the waveform of a new indicator called ECF (TKO) around the damaged area for the last 20 minutes of the experiment is shown in Figure 3.

Looking at this graph, we can see that the growing trend of the ECF (TKO) indicator for the teeth no. 4 to 7 appears for about 15 minutes before completely breaking out of the tooth. Even better results could be obtained if we compare maximal values of this coefficient for the consecutive

segments of the length of the transverse pitch that equals to the teeth contacts (Figure 4). Moreover this allows for compression of information needed to be stored in the diagnostic system. The compressed information from all the experiment was stored in the array of a size "27 segments" x "710 Measurements" (total of 19170 elements). For long-term monitoring, a two dimensional cyclic buffer may also be used for capturing trends in the predetermined time. In addition, the rate of ECF featured as a relative parameter comparing consecutive contacts is little sensitive to long-term changes in signal amplitude due to for example changes in the load of the machine.

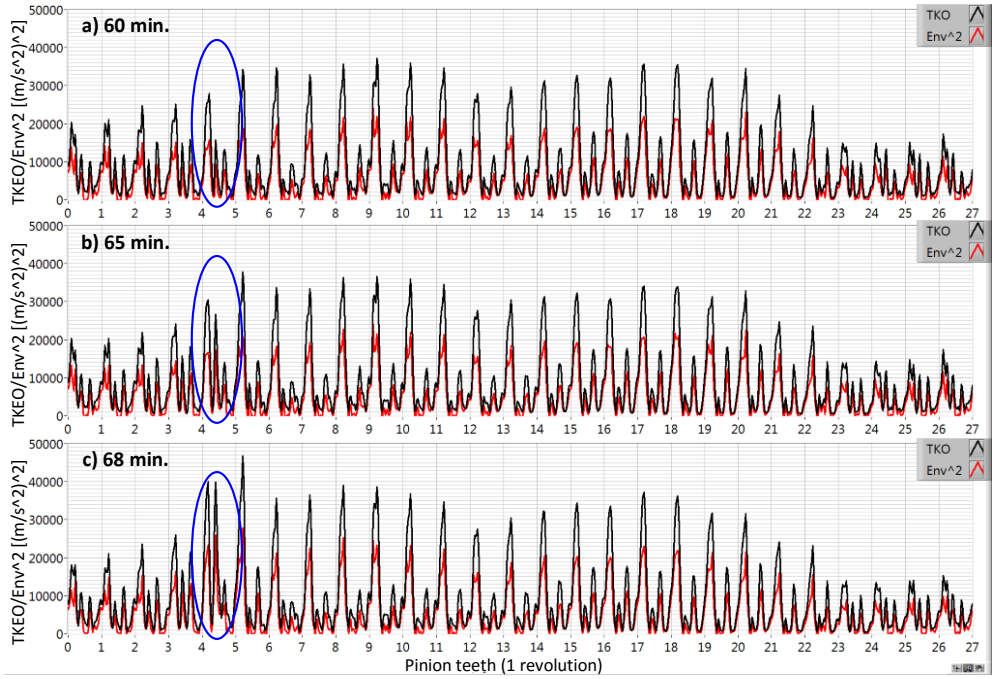


**Figure 2.** Changes of instantaneous power and TKEO for the end part of the experiment after: a) 60 min., b) 65 min. and c) 68 min. of the experiment.

The principal advantage of the envelope indicator contact factor ECF is the simplicity of its calculation, while exceptional sensitivity to local disturbances in the signal. It can be used to diagnose any type of equipment in which the cyclic phenomena are repeated regularly over a longer period of time, for example for diagnostic hydraulic pumps, fans, compressors, pumps, etc. In the case of multi piston pumps ECF indicator is capable of detecting damage to the pistons of the pump based on the analysis of momentary fluctuations of fluid pressure in successive segments of the signal. All these features make the ECF useful tool in autonomous unmanned systems diagnosing the work of various types of rotating equipment.

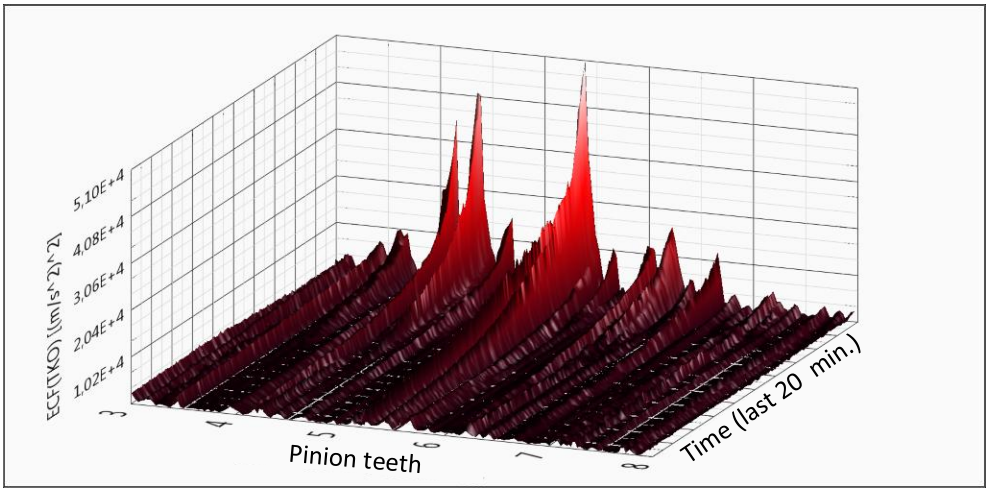


**Figure 3.** ECF of Teager-Kaiser Energy Operator for the last 20 min. of the experiment shown for the selected part of the rotation (pinion teeth 3-8).

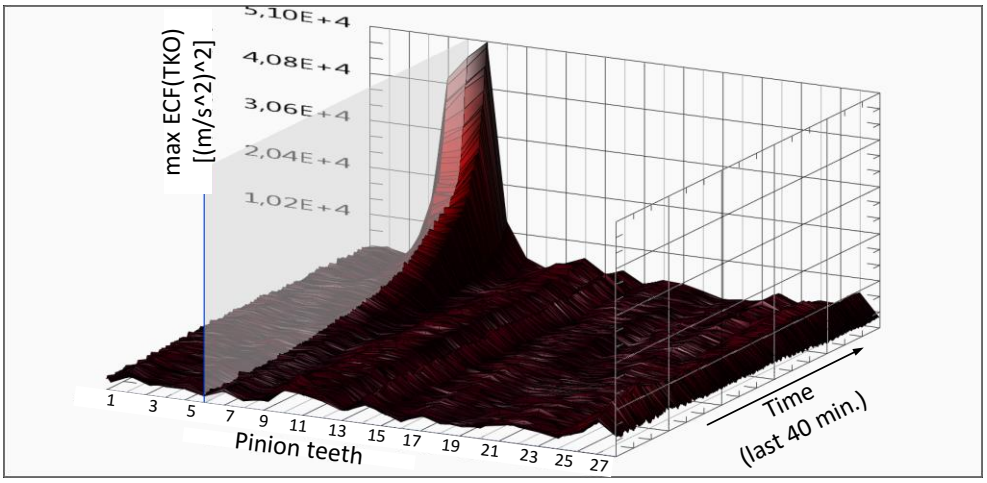


**Figure 4.** Maximal values of the ECF (TKO) coefficient for the last 40 min. of the experiment.

A certain problem arouse with calculating the signal envelope, as a module of the analytical signal (eq. 4). This is due to the necessity of calculating the Hilbert transform, which is an operation usually performed by direct and inverse Fourier transform. In the case of stand-alone diagnostic systems with limited hardware resources, especially with limited computing power, this operation may be an additional load on the system. In this case usage of Teager-Kaiser Energy Operator simplifies the calculations freeing valuable resources of the controller.

## 5. Conclusions

All the described methods are based on analysis of the time-domain signals. Contrary to the integral methods based on spectral analysis these methods allow not only for precise localization of local gear defects like pitting and fatigue fracture at the tooth base linking them to the particular pinion or gear teeth but also for quantification of the size of the fault. The common feature of developed methods is a segmentation according to the kinematic of the machine of resampled and averaged acceleration signal so the results can be related to the accuracy of the cooperation (meshing) of the individual teeth of the pinion (or wheel).

All presented methods are relatively simple algorithmically, easy to implement in diagnostic systems equipment, especially one working online. They do not require large computational power or high-capacity memory. Additionally they could be used in the procedure of gear manufacturing quality assessment.

## References


[1] Burdzik, R., Folega, P., Lazarz, B., Stanik, Z., Warczek, J., 2012, Analysis of the impact of surface layer parameters on wear intensity of friction pairs, Archives of Metallurgy and Materials, Volume: 57, Issue: 4, Pages: 987-993.

[2] Combet, F., Gelman, L., 2009, Optimal filtering of gear signals for early damage detection based on the spectral kurtosis, Mechanical Systems and Signal Processing, 23(3), 652–668.

[3] Delvecchio S., 2012, On the Use of Wavelet Transform for Practical Condition Monitoring Issues, In: Advances in Wavelet Theory and Their Applications in Engineering, Physics and Technology, Baleanu D. (Ed.), InTech.

[4] Dimitriadis, D., Potamianos, A., Maragos, P., 2009, A Comparison of the squared energy and Teager-Kaiser Operators for short-term energy estimation in additive noise, IEEE Transactions on Signal Processing, 57(7), 2569–2581.

[5] Dybala J., 2013, Vibrodiagnostics of gearboxes using NBV-based classifier: A pattern recognition approach, Mechanical Systems and Signal Processing, 38(1), 5-22.

[6] Feldman, M., 2011, Hilbert transform in vibration analysis, Mechanical Systems and Signal Processing, 25(3), 735–802

[7] Galezia A., Gontarz S., Jasinski M., Maczak J., Radkowski S., Senko J., 2012, Distributed system for monitoring of the large scale infrastructure structures based on analysis of changes of its static and dynamic properties, Key Engineering Materials, 518, 106–118.

[8] Gontarz S., Radkowski S., 2012, Impact of different factors on relationship between stress and eigenmagnetic field in steel specimen. IEEE Transactions on Magnetics, 48(3), 1143-1154.

[9] Ho, D., Randall, R.B., 2000, Optimization of bearing diagnostic techniques using simulated and actual bearing fault signals, Mechanical Systems and Signal Processing, 14(5), 763–788.

[10] Kaiser, J.F., 1990, On a simple algorithm to calculate the energy of a signal, Acoustics, Speech, and Signal Processing, ICASSP-90, 381–384.

[11] Kvedalen, E., 2003, Signal processing using the Teager energy operator and other nonlinear operators, MSc Thesis, University of Oslo Department of Informatics.

[12] Maczak, J., Radkowski, S., 2002, Use of envelope contact factor in fatigue crack diagnosis of helical gears, Machine Dynamics Problems, 26(2/3), 115–122.

[13] Maczak, J., 2009, Evolution of the instantaneous distribution of energy density on a local meshing plane as the measure of gear failures, In Proceedings of the 8th International Conference on Reliability, Maintainability and Safety, 8th International Conference on Reliability, Maintainability and Safety (ICRMS 2009), Chengdu, China, 951–957.

[14] Maczak, J., 2005, A method of detection of local disturbances in dynamic response of diagnosed machine element, In Proceedings of the International Conference on Condition Monitoring 2005. International Conference on Condition Monitoring 2005, King's College Cambridge.

[15] Maczak J., 2013, Local meshing plane analysis as a source of information about the gear quality, Mechanical Systems and Signal Processing, 38(1), 154–164.

[16] Orlowska A., Kolakowski P., Holnicki-Szulc J., 2011, Detecting delamination zones in composites by embedded electrical grid and thermographic methods, Smart Materials and Structures, 20(10).

[17] Radkowski S., 2008, Non-linearity and intermodulation phenomena tracking as a method for detecting early stages of gear failures. Insight - Non-Destructive Testing and Condition Monitoring, 50(8), 419-422.

[18] Radkowski S., Guminski R., 2010, Impact of vibroacoustic diagnostics on certainty of reliability assessment, Engineering Asset Lifecycle Management, 16, 574-582.

[19] Radkowski S., Jasinski M., 2013, Use of Condition Monitoring in the Proactive Maintenance Strategy, in Engineering Asset Management - Systems, Professional Practices and Certification, P. W. Tse, J. Mathew, K. Wong, R. Lam, and C. N. Ko, Eds. Cham: Springer International Publishing, 2015, pp. 601–610.

[20] Randall, R.B., 1987, Frequency analysis, 3rd edition, Copenhagen, Denmark, Bruel & Kjaer.

[21] Randall, R.B., 2011, Vibration-based condition monitoring: industrial, aerospace, and automotive applications. Chichester, West Sussex, U.K. ; Hoboken, N.J: Wiley.

[22] Teager, H.M., 1980, Some observations on oral flow during phonation, IEEE Trans. Acoustics, Speech and Signal Process, 28(5), 599–601.

Adam Gałęzia, Ph.D.: Warsaw University of Technology/Institute of Vehicles, Narbutta 84, 02-524 Warszawa, Poland (*agalezia@simr.pw.edu.pl*). The author gave a presentation of this paper during one of the conference sessions.

Robert Gumiński, Ph.D.: Warsaw University of Technology/Institute of Vehicles, Narbutta 84, 02-524 Warszawa, Poland (*rgumin@simr.pw.edu.pl*).

Marcin Jasiński, Ph.D.: Warsaw University of Technology/Institute of Vehicles, Narbutta 84, 02-524 Warszawa, Poland (*jachuu@simr.pw.edu.pl*).

Jędrzej Mączak, Ph.D., D.Sc.: Warsaw University of Technology/Institute of Vehicles, Narbutta 84, 02-524 Warszawa, Poland (jma@*simr.pw.edu.pl*).

# Teager-Kaiser energetic plane – novel tool for condition monitoring of machines (NUM284-15)

Adam Gałęzia, Stanisław Radkowski

*Abstract:* The paper presents concept of Teager-Kaiser energetic plane created on axis of Teager-Kaiser energy and axis of velocity of change of Teager-Kaiser energy of examined signal. Representation of examined signal on the energetic plane has form of energetic trajectory. It illustrates simultaneously changes of instantaneous values of the Teager-Kaiser energy of the signal and velocity of change of the energy. In the paper the authors first presents basic information on Teager-Kaiser energy operator which is used for calculation of the Teager-Kaiser energy of examined signal. Next discussion on methods for calculation of the velocity of change of Teager-Kaiser energy of signal is presented. In the following part of the paper examples of the energetic trajectories of simulated signals are presented. The paper is finished with discussion on possibilities of application of the Teager-Kaiser energetic plane in task of condition monitoring of rotation machinery.

## 1. Introduction

Possible high costs, for environment and people, of failures of machines and structures constantly force research and development of reliable techniques of determination of condition of technical systems. In general, these research activities are related to the use of new techniques of signal processing [1-3], the application of new measurement strategies [4, 5] such as sensors embedded in structure [6], different physical phenomena for detection of early stages of failures [7-10].

It is known that the emergence and development of failure in machine component result in the change of energetic structure of vibro-acoustic signal generated during operation [3, 7, 9]. In particular, it can be related to the change of amplitude and frequency structure of vibration signal [9,11]. All condition monitoring methods aim at, as early as possible, the detection of failure symptoms. The detection of such low-energy symptoms allows to identify an early phase of failure and to monitor its further development leading to the selection of the optimal maintenance strategy and, as a result, to obtaining measurable savings.

Fatigue break of tooth, next to pitting, is one of the basic mechanisms of damaging of toothed wheels [12, 13]. Detection of early symptoms of such failure from vibro-acoustic signal requires use the of signal processing and analysis techniques which allow to reveal diagnostically useful information. Nowadays, one can choose among wide range of signal analysis methods. The most

popular are: methods based on analysis of average measures of signals e.g.: RMS, kurtosis [14]; methods based on analysis of modulation phenomena [15-17]; methods based on spectrum analysis [18], time-frequency and wavelet methods [19-23]. However, main disadvantage of all methods mentioned above is the use of integration operators in search process of diagnostic information which cause averaging of signals and possible lost of information on early symptoms of failures. Due to this fact, research is carried out aiming in development of methods sensible to transient disturbance in diagnostic signal. In group of such methods one can find for example method based on: analysis of envelope contact factor [3] or analysis of Teager-Kaiser energy of signal [24, 25].

The paper presents concept of Teager-Kaiser energetic plane which uses Teager-Kaiser energy of examined signal and velocity of its change. Representation of examined signal on the energetic plane has the form of energetic trajectory. It illustrates simultaneously changes of instantaneous values of the Teager-Kaiser energy and the velocity of change of the Teager-Kaiser energy. Presented in the paper concept of Teager-Kaiser energetic plane is a novel method allowing detecting in signal changes related with diagnostic symptoms.

The paper is organized as follows: in first section present brief information on Teager-Kaiser energy, next section introduce concept of Teager-Kaiser energetic plane and describe how it is created, in section 3 the authors present examples of energetic trajectories of different signals and influence of signals parameters change on shape of the trajectory.

## 2. Teager-Kaiser energy – brief information

Teager-Kaiser energy $E_{TK}(t)$ of examined time signal is a waveform obtained as a result of acting of Teager-Kaiser energy operator (TKEO) $\Psi(x(t))$ on the signal $x(t)$. TKEO is differential operator first introduced in [24]. The operator was described and its properties were analyzed in many publications [25-28]. For continuous time signals, the operator is defined as:

$$\Psi(x(t)) = \dot{x}^2(t) - x(t)\ddot{x}(t) \tag{1}$$

while for discrete signals it has form:

$$\Psi_d(x_n) = x_n{}^2 - x_{n-1}x_{n+1} \tag{2}$$

In literature there are examples of successful applications of TKEO in condition monitoring of gears and bearings [29-31].

As it is presented in [26] and recalled below (3) the instantaneous value of Teager-Kaiser energy of examined signal is a function of instantaneous value of signals amplitude and frequency. Due to this fact, it can be used for detection of transient events changing the amplitude of frequency structure of diagnostic signal. Such a change can be c a result of an emerging failure.

For simple harmonic time signal $x(t) = A\cos(\omega t)$, with amplitude $A$ and frequency $\omega$, using (2) one can calculate Teager-Kaiser energy in the following way:

$$\begin{aligned} E_{TK}(t) &= \Psi(x(t)) = (-A\omega\sin(\omega t))^2 - A\cos(\omega t)(-\omega^2 A\cos(\omega t)) \\ E_{TK}(t) &= \omega^2 A^2(\sin^2(\omega t) + \cos^2(\omega t)) \\ E_{TK}(t) &= \Psi(x(t)) = A^2\omega^2 \end{aligned} \tag{3}$$

In the case of a simple harmonic signal Teager-Kaiser energy has constant value due to constant amplitude and frequency. However, in signal duration, even a small and transient variation of the value of the amplitude or frequency will cause corresponding change in $E_{TK}(t)$ waveform.

It must be remembered that in the classical approach the energy of signal has unit equal to square of signals unit. However in the case of the $E_{TK}(t)$ unit of energy will be equal to square of signals unit divided by [$s^2$]. If an examined signal is the signal of acceleration expressed in [$m/s^2$] then $E_{TK}(t)$ will be expressed in [$m^2/s^6$].

## 3. Teager-Kaiser energetic plane

Analysis of Teager-Kaiser energy of vibroacoustic diagnostic signal allows to obtain information on failures arising in machine components under monitoring. However, in authors' opinion it important also to analyse velocity of change of Teager-Kaiser energy to determine the significance of observed phenomena.

Concept underlying the creation of Teager-Kaiser energetic plane is to allow simultaneous observation of Teager-Kaiser energy $E_{TK}(t)$ and velocity of its change $\dot{E}_{TK}(t)$. The coordinates of the energetic plane are: the energy of signal and the velocity of change of energy of signal, both calculated using the Teager-Kaiser energy operator (1 or 2). As the result of calculation of $E_{TK}(t)$ and $\dot{E}_{TK}(t)$, the signal is presented on the energetic plane $E_{TK} - \dot{E}_{TK}$, if form of energetic trajectory, also called Teager-Kaiser energetic trajectory.

One might sense some similarity between the concept of Teager-Kaiser energetic plane and the phase plane [32], however it must be pointed out that the representation of a signal in the form of the energetic trajectory on $E_{TK} - \dot{E}_{TK}$ plane is a significantly different approach to signal analysis.

In following part of the paper, the time index $(t)$ in $E_{TK}(t)$ and $\dot{E}_{TK}(t)$ will be dropped for clarity reasons and due to the fact that in most cases when $E_{TK}$ and $\dot{E}_{TK}$ are referred to, they are related to discrete time signals.

### 3.1. Calculation of the Teager-Kaiser energetic plane

The application of condition monitoring system on a machine requires the use of sensors and suitable digital tools for recording of signals. As a result one deals with discrete-time domain signals.

The equation (2) allows the calculation of the energy $E_{TK}$ (in reality estimate of the energy) of discrete-time signal. Due to its simplicity and form it allows for fast (with delay of 1 sample) calculation of $E_{TK}$ waveform and can be easily implemented in computing environment. In [25] authors, using Lie bracket nomenclature, presented higher order differential energy operators. Among others, reader will find third-order equation differential energy operator which allows calculation of an energy velocity of continuous-time signal $x(t)$. This third-order operator is presented in the form of:

$$\Upsilon_3(x(t)) = \dot{x}(t)\ddot{x}(t) - x(t)x^{(3)}(t) \tag{4}$$

In later part of [25] authors present version of third-order equation differential energy operator for discrete-time signals. It is given in the form easy for numerical implementation:

$$\Upsilon_{3d}(x_n) = x_n x_{n+1} - x_{n-1}x_{n+2} \tag{5}$$

However, analysis of results, obtained using equation (5), reveal incorrect values and erroneous shape of expected waveform. Therefore, for the calculation of $\dot{E}_{TK}$ it is necessary to use another method.

There exists a variety of numerical methods, for the calculation of derivative of signal. They vary in terms of speed and accuracy of results as well as difficulty in numerical implementation. The most popular derivation method is based on the definition of derivative of function $f(x)$ (6):

$$\frac{df(x)}{dx} = f'(x_0) = \lim_{\Delta x \to 0} \frac{f(x_0 + \Delta x) - f(x_0)}{\Delta x} \tag{6}$$

where: $x_0$ - point in which derivative is calculated, $\Delta x$ - positive or negative increment.

Values of the first derivative of function $f(x)$, determined in any arbitrary point $x_i$ from set of discrete values of variable $x$, can be approximated using difference quotient defined as: left-sided approximation, right-sided approximation or double-sided approximation. Main advantage of numerical methods mentioned above is simplicity and calculation speed. In the case of left- and right-sided approximations to calculate value no. $k$ of derivative the value of signal no. $k+1$ must be known. This allows to calculate values of derivative with delay of one simple. In the case of double-sided approximation more samples of signal must be known and the length of result, the derivative of signal, will be shorter than the length of signal for 2 samples. In MATLAB environment, to calculate signal derivative, implemented function *diff* can be used, giving result identical with the result

obtained when using left-sided approximation. For more accurate results one can use central numerical differential formula of order four. However this solution requires the knowledge of a bigger number of signal samples and result will be shorter for 4 samples from signal. Another method to calculate derivative of signal is to differentiate interpolating polynomial. This method assumes interpolation of signal $f(x)$ with linear combination of set polynomials and calculation of derivative of interpolating polynomial. Signals derivative can also be performed using properties of Fourier transform according to the following diagram.

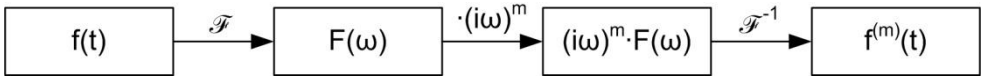


**Figure 1.** Derivative calculation diagram using Fourier transform.

As presented in [33, 34] this method can be used for the calculation of derivatives of integral and fractional orders. Main disadvantage of this method, resulting in decrease of speed and accuracy, is related to the finite duration of signal, potential aliasing effects and requirement regarding signal duration being the integral multiple of harmonic components.

Detail analysis, taking into account calculating speed and accuracy, of the methods mentioned above are presented in [35]. Concluding, left-sided approximation, in the form of function *diff*, implemented in MATLAB, gave suitable enough results to calculate the velocity of change of Teager-Kaiser energy - $\dot{E}_{TK}$.

Having determined the Teager-Kaiser energy $E_{TK}$ of signal as well the velocity of change of the energy $\dot{E}_{TK}$, signal can be visualized at the energetic plane $E_{TK} - \dot{E}_{TK}$ in the form of the energetic trajectory.

### 3.2. Examples of the energetic trajectories of signals

The energetic trajectory presents simultaneous changes of instantaneous values of the Teager-Kaiser energy of the signal and velocity of change of the Teager-Kaiser energy. Due to sensitivity of Teager-Kaiser energy of signal to transient events, the trajectory allows for easy observation of change of parameters of signal components such as the change of modulation depth $M$.

Below, the authors present the energetic trajectories of simulated signals: harmonic signal, signal with amplitude modulation (AM), signal with frequency modulation (FM), signal with amplitude and frequency modulation (AMFM). Because trajectories of simulated signals are presented on figures below no units are presented.

Harmonic signal was modeled as:

$$x(t) = A\cos(2\pi ft + \phi) \tag{7}$$

where: $A$ – carrier amplitude equal 2, $f$ – carrier frequency equal 500 Hz, $\phi$ – initial phase equal 0. The energy $E_{TK}$ of signal (7) is constant due to constant value of amplitude and frequency of signal. Its representation on $E_{TK} - \dot{E}_{TK}$ plane is single point. On figure 2 this point is the center of a gray circle used only as indicator.

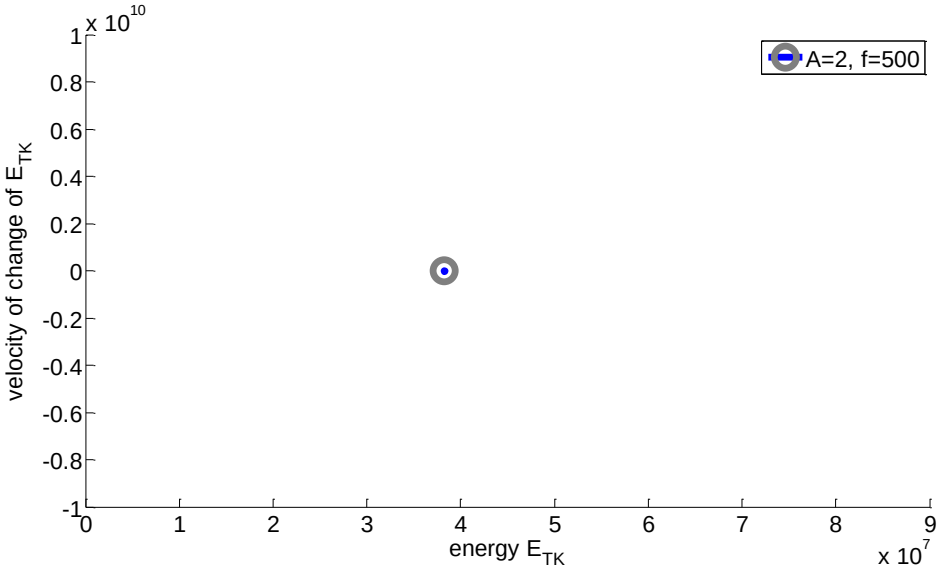


**Figure 2.** Graphic representation of harmonic signal on energetic plane.

Signal with modulation of amplitude was modeled as:

$$x_{AM}(t) = A*(1+M*\cos(2\pi f_{AM}t))*\cos(2\pi ft+\phi)) \tag{8}$$

where: $A$ – carrier amplitude equal 2, $f$ – carrier frequency equal 500 Hz, $\phi$ – initial phase equal 0, $M$ – modulation depth, for reason of example equal: 0,05 or 0,1 or 0,5, $f_{AM}$ – modulation frequency equal 25 Hz.

Figure 3 presents example of trajectories of AM signals differing only with value of modulation depth $M$. Reader might notice that for increasing values of $M$, the shape and magnitude of energetic trajectory change. A technical condition manifesting itself with the change of amplitude modulation will influence the shape of signals representation on the energetic plane. The shapes of observed trajectories are related to the variation of instantaneous amplitude of a signal. The magnitude of trajectory is related to the magnitude of $M$ and $f_{AM}$.

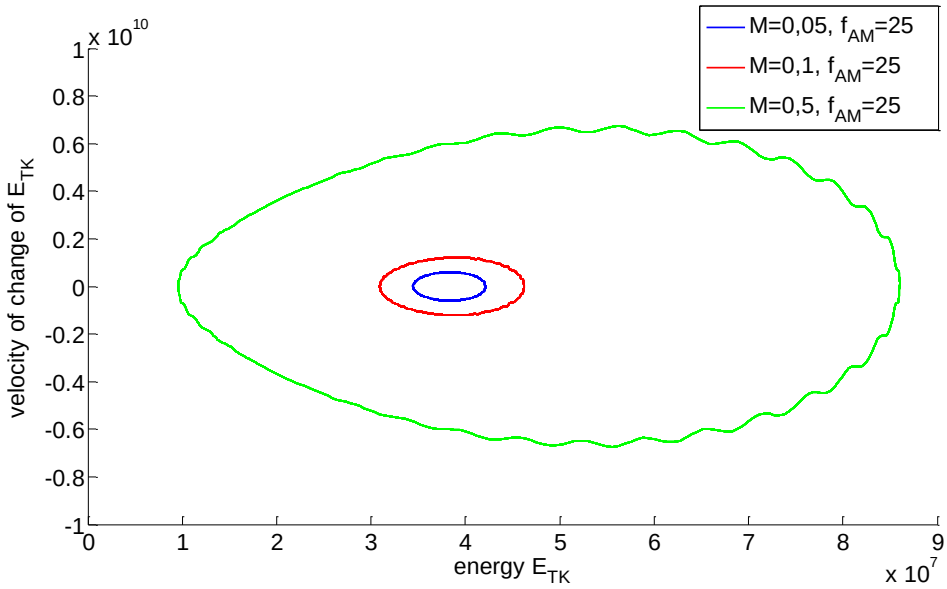


**Figure 3.** Energetic trajectories of AM signals differing with value of modulation depth $M$ .

Operation abnormality of machine component often manifest as change of modulation index in signal [36]. To demonstrate the influence of modulation index value on the representation of FM signal on energetic plane, the following model of FM signal was used:

$$x_{FM}(t) = A\cos(2\pi ft + m*\cos(2\pi f_{FM}t)) + \phi) \tag{9}$$

where: $A$ – carrier amplitude equal 2, $f$ – carrier frequency equal 500 Hz, $\phi$ – initial phase equal 0, $m$ – modulation index, for reason of example equal: 0,5 or 1 or 2, $f_{FM}$ – modulation frequency equal 25 Hz.

The figure below presents the example of trajectories of FM signals varying from each other only with the value of modulation index $m$. It is visible that the modulation index value influences mainly the magnitude of the trajectory. The shape of the trajectory is related to $f_{FM}$. It is well seen that energetic trajectory of FM signal differs significantly from the energetic trajectory of AM signal: the magnitude of the trajectory is related to the energy of modulation phenomena while shape is strictly related to the type of modulation. In the case of a signal with AM modulation the shape of energetic trajectory is elliptic and rather smooth while energetic trajectory of a signal with FM modulation is strongly ripple.

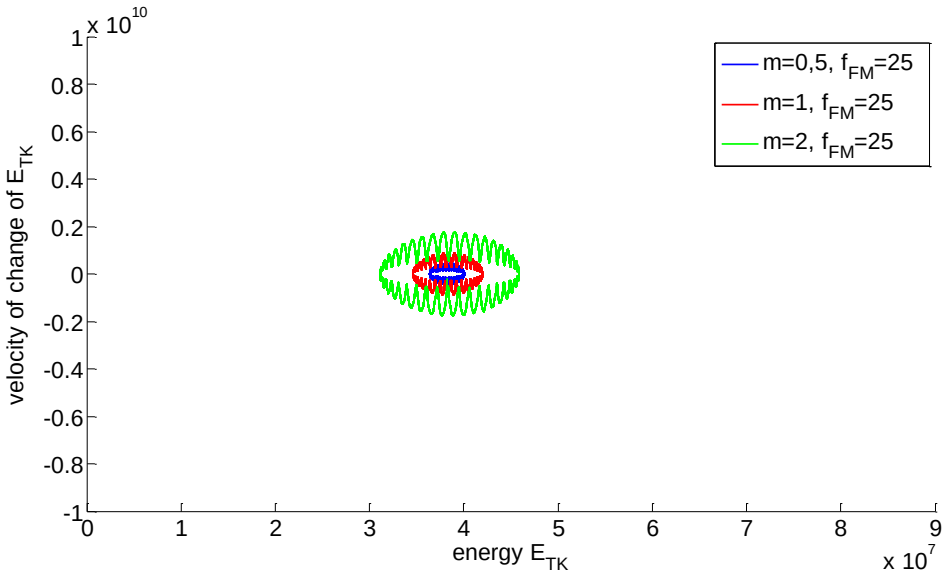


**Figure 4.** Energetic trajectories of FM signals differing with value of modulation index $m$.

Usually, failures arising in such components like bearings or gears result with appearance of phenomena modulating simultaneously amplitude and frequency of generated vibration [36]. Signal with amplitude and frequency modulation was modeled as:

$$x_{AMFM}(t) = A*(1+M*\cos(2\pi f_{AM}t))*\cos(2\pi ft + m*\cos(2\pi f_{FM}t)) + \phi) \tag{10}$$

where: $A$ – carrier amplitude equal 2, $f$ – carrier frequency equal 500 Hz, $\phi$ – initial phase equal 0, $M$ – modulation depth, for reason of example equal: 0,05 or 0,1 or 0,5, $f_{AM}$ – modulation frequency equal 25 Hz, $m$ – modulation index, for reason of example equal: 0,5 or 1 or 2, $f_{FM}$ – modulation frequency equal 25 Hz.

It is well visible that the change of modulation parameters $M$ and $m$ influences the shape and the magnitude of the energetic trajectory of the analyzed signal. The shape of trajectory of a AMFM signal is superposition of the shapes characteristic for the modulation components. It should be noted that phase relationship between AM and FM modulations will influence, to some extent, the shape of the trajectory. The center of gravity (calculated as a two dimensional mean) of presented trajectories shifts towards higher energy values for increasing values of modulation parameters $M$ and $m$.

Table 1 presents values of exemplary statistical parameters of energetic trajectories of signals described in the paper. The presented parameters are: location of the center of gravity, maximum value of $E_{TK}$ and $\dot{E}_{TK}$, range of values along $E_{TK}$ and $\dot{E}_{TK}$ axes. For presented cases, location of

gravity center of trajectory of AMFM signal with $M = 0{,}5$ and $m = 2$ along $E_{TK}$ axis is 13% higher than gravity center of trajectory of harmonic signal being carrier signal. It is related to the limited duration of signal and influence of modulations.

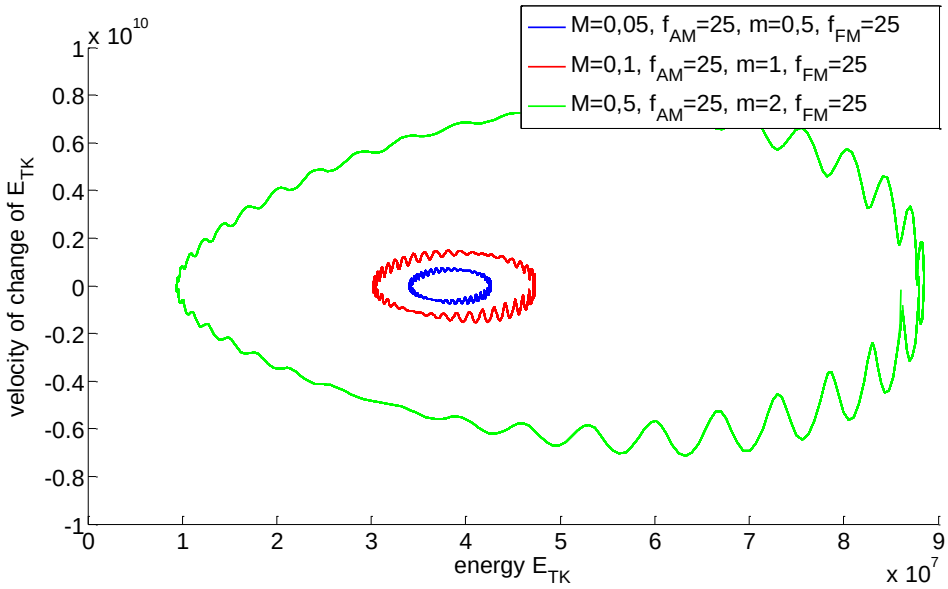


**Figure 5.** Energetic trajectories of AMFM signals differing with value of: $M$ and $m$.

**Table 1.** Values of exemplary statistical parameters of energetic trajectories

| type of signal (value of modulation parameters) | parameter | | | | | |
|---|---|---|---|---|---|---|
| | maximum value (multiplyer *1e7) | | value range (multiplyer *1e7) | | gravity center (multiplyer *1e7) | |
| | $E_{TK}$ | $\dot{E}_{TK}$ | $E_{TK}$ | $\dot{E}_{TK}$ | $E_{TK}$ | $\dot{E}_{TK}$ |
| harmonic | 38.197 | 0.0000 | 0 | 0 | 38.197 | 0 |
| AM (M=0,05) | 42.116 | 60.219 | 0.76 | 120.44 | 38.244 | 0 |
| AM (M=0,1) | 46.228 | 121.29 | 1.53 | 242.58 | 38.388 | 0 |
| AM (M=0,5) | 86.009 | 673.22 | 7.65 | 1346.4 | 42.981 | 0 |
| FM (m=0,5) | 4.006 | 44.24 | 0.369 | 96.099 | 38.207 | 0 |
| FM (m=1) | 4.197 | 87.96 | 0.738 | 175.92 | 38.237 | 0 |
| FM (m=2) | 4.589 | 177.35 | 1.476 | 354.7 | 38.356 | 0 |
| AMFM (M=0,05; m=0,5) | 4.26 | 74,01 | 0.85 | 149.02 | 38.254 | 0 |
| AMFM (M=0,1; m=1) | 4.73 | 149.29 | 1.71 | 303.43 | 38.428 | 0 |
| AMFM (M=0,5; m=2) | 8.85 | 766.39 | 7.91 | 1481.8 | 43.151 | 0 |

## 4. Summary

In the paper concept of the energetic plane and the energetic trajectories of the signals with modulation are presented. The energetic trajectory, being representation of a signal on $E_{TK} - \dot{E}_{TK}$ plane, has characteristic shape resulting from the type of the modulation existing in a signal. Also, it is sensitive to small and transient changes appearing in a signal which might not be detected using e.g. the methods based on the spectrum analysis. Arise of a failure resulting in change of amplitude-frequency structure of a signal will influence the magnitude and the shape of the energetic trajectory allowing for detection of its early stage. Future publications will present application of the Teager-Kaiser energetic plane in task of detection of anomalies in diagnostic signals as failure symptoms.

## References


[1] Dybała J. Vibrodiagnostics of gearboxes using NBV-based classifier: A pattern recognition approach. *Mech. Syst. Signal Process.* (2012), http://dx.doi.org/10.1016/j.ymssp.2012.08.021

[2] Delvecchio S. *On the Use of Wavelet Transform for Practical Condition Monitoring Issues*, (w: Baleanu D. (Ed.), Advances in Wavelet Theory and Their Applications in Engineering. Physics and Technology, InTech), 2012, DOI: 10.5772/35964

[3] Mączak J. Local meshing plane analysis as a source of information about the gear quality. *Mech. Syst. Signal Process.* (2012), http://dx.doi.org/10.1016/j.ymssp.2012.09.012

[4] Radkowski S., Guminski R, E*nergy of vibroacoustic signal as parameter of logistics model of the tooth's crack developmen*, 11th ASME Biennial Conference on Engineering Systems Design and Analysis, PROCEEDINGS OF THE ASME 11TH BIENNIAL CONFERENCE ON ENGINEERING SYSTEMS DESIGN AND ANALYSIS, 2012, VOL 1 pages: 271-272

[5] Radkowski S., Jasinski M. *Use of Condition Monitoring in the Proactive Maintenance Strategy*. Edited by: Tse, PW; Mathew, J; Wong, K; et al. Conference: 8th World Congress on Engineering Asset Management (WCEAM), Hong Kong, PEOPLES R CHINA, OCT 30-NOV 01, 2013. Book Series: Lecture Notes in Mechanical Engineering, 2015, pages: 601-610.

[6] Orlowska A., Kolakowski P., Holnicki-Szulc J. Detecting delamination zones in composites by embedded electrical grid and thermographic methods. *Smart Materials and Structures* vol. 20, no. 10. (2011), DOI: 10.1088/0964-1726/20/10/105009

[7] Gałęzia A. Utilization of components of signals from high frequency range in condition monitoring of bearings. *Diagnostyka*, nr. 3 (55), (2010) pages 35-44.

[8] Gontarz S., Szulim P., Seńko J., Dybała J. Use of magnetic monitoring of vehicles for proactive strategy development. *Transportation Research Part C: Emerging Technologies* 52, (2015) pages: 102-115

[9] Radkowski S., Gumiński R.: Impact of vibroacoustic diagnostics on certainty of reliability assessment. *Engineering Asset Lifecycle Management*, Part 16, pages. 574-582, (2010) DOI: 10.1007/978-0-85729-320-6_66

[10] Gontarz S., Mączak J., Szulim P. Online Monitoring of Steel Constructions Using Passive Methods, in: *Engineering Asset Management - Systems, Professional Practices and Certification*, editors: Tse P. W., Mathew J., Wong K., Lam R., Ko C. N., Springer International Publishing, 2015, pages 625–635.

[11] Cempel C., Żółtowski B. *Inżynieria Diagnostyki Maszyn*. PTDT/ITE, 2004.

[12] Radkowski S. *Non-linearity and intermodulation phenomena tracking as a method for detecting early stages of gear failures.* INSIGHT, Vol. 50, Issue 8, (2008) pages.: 419-422, DOI: 10.1784/insi.2008.50.8.419

[13] Randall B.: Vibration-based Condition Monitoring: Industrial, Aerospace and Automotive Applications, John Wiley & Sons, (2011).

[14] ISO 10816-Part 1, *Mechanical vibration - Evaluation of machine vibration by measurements on non-rotating parts - Part 1: General guidelines*, International Organization for Standardization, Geneva, 1995.

[15] Randal R.B. A new method for modelling gear faults. *Journal of Mechanical Design*, Vol. 104, April, (1982), pages: 259-267

[16] McFadden P.D. Detecting Fatigue Cracks in Gears by Amplitude and Phase Demodulation of the Meshing Vibration. *Journal of Vibration, Acoustics Stress and Reliability in Design*, 108(2), (1986) pages: 165–170.

[17] McFadden P.D. Determining the location of a fatigue crack in a gear from the phase of the change in the meshing vibration. *Mechanical Systems and Signal Processing*, 2(4), (1988) pages: 403–409.

[18] Zakrajsek J.J. *A review of transmission diagnostics research at NASA* Lewis Research Center, Cleveland. Ontario: Lewis Research Center 1994

[19] Antoniadis I., Yiakopoulos C.T., Maczak J., Rodopoulos K. Multicomponent decomposition of a time-varying acoustic Doppler signal generated by a passing railway vehicle using Complex Shifted Morlet Wavelets, *Transportation Research Part C Emerging Technologies* 07/2014; (2014) pages: 34–51.

[20] Barczewski R. *Diagnostycznie zorientowane metody krótkoczasowego przetwarzania sygnałów wibroakustycznych, rozprawa habilitacyjna*, Wydawnictwo Politechniki Poznańskiej, 2013, oai:www.wbc.poznan.pl:316720

[21] Łazarz B., Madej H., Wilk A., Figlus T., Wojnar G. *Diagnozowanie złożonych przypadków uszkodzeń przekładni zębatych*, Katowice; Radom: Wydawnictwo Instytutu Technologii Eksploatacji - Państwowego Instytutu Badawczego, 2006.

[22] Halim E.B., Shah S., Zuo M.J. *Fault detection of gearbox from vibration signals using time-frequency domain averaging*. Proc. of the 2006 American Control Conference. Minneapolis, Minnesota, USA, (2006) pages: 4430–4435.

[23] Pryor A., Lewicki D.G., Mosher M. *The Application of Time-Frequency Methods to HUMS*. in American Helicopter Society's 57th Annual Forum. Washington D.C. (2001) (http://citeseerx.ist.psu.edu/viewdoc/summary?doi=10.1.1.15.8641 access: 2014-09-06).

[24] Kaiser J.F. On a Simple Algorithm to Calculate the 'Energy' of a Signal, *Proceedings of IEEE International Conference on Acoustics, Speech, and Signal Processing*, Albuquerque, NM, Apr. 1990, (1990), pages: 381-384

[25] Maragos P. Potamianos A., Higher order differential energy operators, *IEEE Signal Processing Letters*, vol. 2, No. 8. (1995)

[26] Kaiser J. F. On Teager's Energy Algorithm and its generalization to continuous signals" a simple algorithm to calculate the 'energy' of a signal, *Proc IEEE Digital Signal Processing Workshop*, New Paltz, NY, Septemer 1990, (1990).

[27] Kvedalen E. *Signal processing using the Teager Energy Operator and other nonlinear operators*, Master of Science Thesis, University of Oslo, Department of Informatics, (2003).

[28] Maragos P., Kaiser J. F. Quatieri T. F. On amplitude and Frequency Demodulation Using Energy Operators, *IEEE Transactions on Signal Processing*, vol. 41, (1992), pages. 1532-1550.

[29] Gałęzia A. Averaged signal measures of TKEO energy waveform in detection of tooth break in gearbox, *Measurement Automation and Monitoring*, vol. 60, no 1/2014, (2014), pages: 31–34

[30] Liang M., Soltani B. I. An energy operator approach to joint application of amplitude and frequency-demodulation for bearing fault detection, *Mechanical Systems and Signal Processing, Vol. 24*, (2010), pages: 1473–1494.

[31] Feng Z., Wang T., Zuo M. J., Chu F., Yan S. Teager Energy Spectrum for Fault Diagnosis of Rolling Element Bearings, *Journal of Physics: Conference Series 305, 9th International Conference on Damage Assessment of Structures (DAMAS)*, (2011).

[32] Batko W., Korbiel T., Pawlik P. Experimental analysis of the phase trajectory usefulness in diagnostics of rotating machines, *Problemy Eksploatacji - Maintenance Problems* nr 1 (2012), pages 7–15.

[33] Teder, L., Pappel, T. Detection of cavitation in pumps through higher order derivatives. *Proc. of the 4th Int. DAAAM Conf. "Industrial Engineering- Innovation as Competitive Edge for SME"*, 29-30 April 2004, Tallinn, (2004), pages 98 – 101

[34] Lahdelma S., Kotila V. Complex Derivative - A New Signal Processing Method, *Kunnossapito* Vol.19 No.4, (2005), pages 39-46

[35] Gałęzia, A. *Wykorzystanie sygnałów niestacjonarnych w detekcji wczesnych faz uszkodzeń układów napędowych pojazdów*, Ph.D. thesis, Warsaw University of Technology / the Faculty of Automotive and Construction Machinery Engineering, 2015, Supervisor: S. Radkowski.

[36] Forrester D. B. *Advanced Vibration Analysis Techniques for Fault Detection and Diagnosis in Geared Transmission Systems*, Ph.D. thesis, Swinburne University of Technology, (http://researchbank.swinburne.edu.au/vital/access/manager/Repository/swin:7437, access: 2013-08-12), 1996

Adam Gałęzia, M.Sc.: Warsaw University of Technology / Faculty of Automotive and Construction Machinery Engineering, Narbutta Str. 84, 02-524 Warszawa, POLAND (*agalezia@simr.pw.edu.pl*). The author presented this work at the conference.

Stanisław Radkowski, Professor: Warsaw University of Technology / Faculty of Automotive and Construction Machinery Engineering, Narbutta Str. 84, 02-524 Warszawa, POLAND (*ras@simr.pw.edu.pl*).

# The manipulator tool fault diagnostics based on vibration analysis (NUM067-15)

Piotr Gierlak, Andrzej Burghardt, Dariusz Szybicki, Marcin Szuster, Magdalena Muszyńska

*Abstract:* This article presents an analysis of the tool damage detection problem on the example of the IRB 140 manipulator. The robot is intended for the realisation of research work in the field of position-force control methods and applying them to the machining processes. The robot is equipped with a force control system and the drive intended for light precision machining, such as grinding, polishing, and chamfering. The tool, which in this study is a ceramic fiber brush, is mounted in the holder of the drive. Often it happens that the tool is unbalanced due to the damage of the fibers. This causes mechanical vibrations, which are one of the factors that negatively affect machining accuracy and roughness of the machined surface. The phenomenon of vibrations and parameters of the vibratory motion of the tool have been used as a carrier of information about the state of the tool. Due to the time saving requirements, it is desirable to carry out the current control of the tool. On the basis of the measurement data, obtained during tests of tools with varying degrees of damage, classifiers of the tool state were built. For this purpose, a system based on the dSPACE board, that enables vibration signal acquisition and processing them, was used. In this system, the neural network has been implemented, which is used for the classification of the tool state. In case of an alarm signal being generated by the system, the operation of the robot is stopped. The results of the experiments confirm that it is possible to build a classifier of the tool state with high effectiveness.

## 1. Introduction

The problem described in this article has its genesis in the robotisation of processes of machining aircraft engine components. The correct realisation of robotised machining process requires constancy in as large as possible number of parameters, among which great importance has the quality of the cutting tool. Due to the specificities of the task of grinding of aircraft engine components, a ceramic fiber brush (see figure 1a) was selected for this purpose. It is a tool for finishing operations eg. grinding or chamfering. This tool ensures high quality of surface, but it is very undurable and therefore quickly wears out and is often damaged (see figure 1b). Due to the relatively high rotational speed required by the mentioned machining process (up to 6 000 rpm), the tool must be precisely balanced. However, due to the damage of the fibers during machining it often occurs that the tool

becomes unbalanced. This causes mechanical vibrations of the tool, which are one of the factors that negatively affect machining accuracy and roughness of the machined surface.

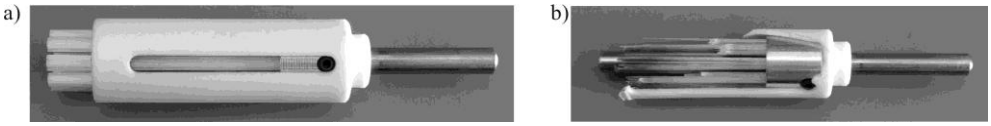


**Figure 1.** Ceramic fiber brush: a) unused, b) damaged fiber brush and protective sleeve.

In Table 1, six tool state cases, which were examined during the experiments, are presented: unused brush and unused protective sleeve (case 1), used brush and used protective sleeve (case 2), used brush ejected from the sleeve and used protective sleeve (case 3), damaged brush and damaged protective sleeve (case 4), used brush and damaged protective sleeve (case 5), damaged brush and used protective sleeve (case 6).

**Table 1.** The cases of tool state

| Case | State of the tool | View of the tool | Class |
|---|---|---|---|
| 1 | Unused brush and unused protective sleeve | | Class 1 - an acceptable condition of the tool |
| 2 | Used brush and used protective sleeve | | |
| 3 | Used brush (ejected from the sleeve) and used protective sleeve | | |
| 4 | Damaged brush and damaged protective sleeve | | Class 2 - an unacceptable condition of the tool |
| 5 | Used brush and damaged protective sleeve | 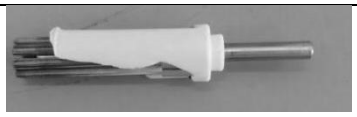 | |
| 6 | Damaged brush and used protective sleeve | | |

All of the presented cases fall into two classes: “class 1” means that thee tool is in an acceptable condition, “class 2” has the opposite meaning – such a tool must be changed. From the standpoint of engineering practice putting intermediate classes like "a little worn tool" or "heavily worn tool" is not useful. Due to the requirements of process automation, information about the state of the tool must be unambiguous. The two presented classes usually can be easily recognized by a human, but due to the time saving requirements and automation of the machining process, the tool condition must be determined without human intervention.

The paper presents a methodology of creating a tool state classifier that, based on the available measurement data, which will assign the current state of the tool to one of the two defined classes. The phenomenon of vibrations and parameters of the vibratory motion of the tool have been used as a carrier of information about the tool condition. This article falls within current research trends for tool condition monitoring [1, 2, 8, 9, 12, 13, 14].

## 2. The laboratory researches

The article presents an analysis of the tool damage detection problem on the example of the IRB 140 industrial robotic manipulator (see figure 2).

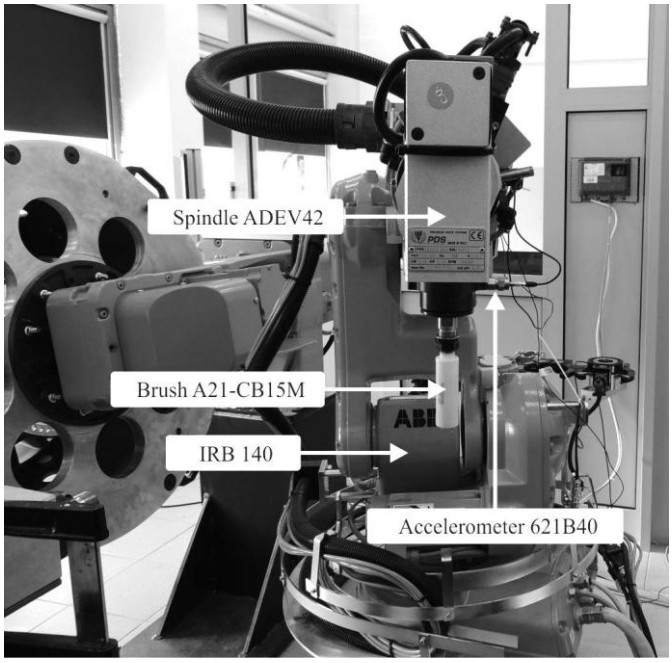


**Figure 2.** IRB 140 industrial robotic manipulator with equipment.

The robot is intended for the realisation of research work in the field of robotisation of the machining processes using position-force control methods. In addition to standard equipment, the robot is equipped with a Delta SI-330-30 force and moment sensor (made by ATI Industrial Automation) placed at the end-effector. Moreover, it is equipped with an ADEV42 electric spindle (made by Precision Drive Systems) with a 400W power and a rotational speed from 6000 to 24000 rpm. This is a drive intended for light to medium duty applications such as precision machining. The drive is controlled by an OMRON MX2 inverter. The cutting tool, which in this study is a ceramic fiber brush (A21-CB15M made by Xebec), is mounted in the holder of the drive.

For vibration measuring, the 621B40 industrial accelerometer (made by PCB Piezotronics) with a PCB 482C conditioning unit was used. The accelerometer was mounted on the spindle housing at the location of the lower bearing. The dSPACE 1104 digital signal processing (DSP) board was used for acquisition of the measured data.

### 2.1. The measuring experiment description

To obtain data for the construction of the tool condition classifier, numerous measuring experiments were performed. The vibrations of the spindle housing in the transverse direction to the axis of tool rotation were measured. The duration of a single measurement was T=8 s, and the sampling frequency $f_S$=8192 Hz. For each of the six cases presented in Table 1, 40 data strings were recorded, making a total of 240 data strings. Experiments were carried out at a rotational speed of the tool equal to 660 rpm (110 Hz). The selected measurement data for classes 1 and 2 are shown in figure 3.

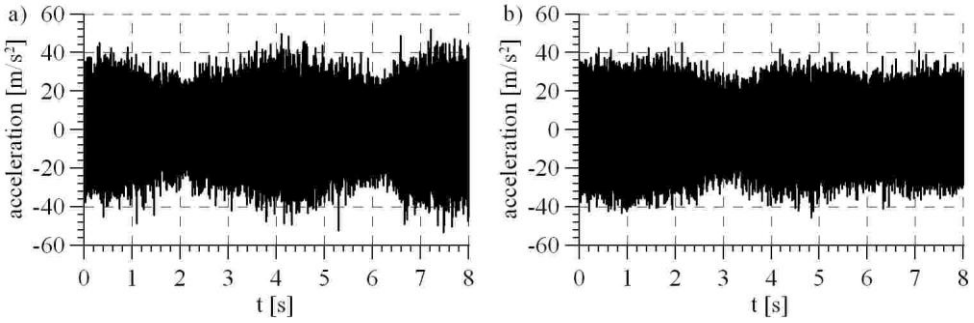


**Figure 3.** Selected data strings of measured acceleration of vibration: a) class 1 - case 3, b) class 2 - case 6.

Data strings presented in figure 3 a-c belong to the class 1, and data strings shown in figure 3 d-f belong to the class 2. A simple visual evaluation of the measured data does not allow for a clear differentiation of tool condition.

## 3. Post-processing of measurement data

The obtained data strings should be properly processed in order for it to be used to build the tool condition classifier. In this paper, the classifiers based on the features of vibration acceleration in the real variable (time) and complex variable (frequency) domains are considered.

### 3.1. Features in the discrete time domain

The result of acceleration measurement is the string of the acceleration value in discrete moments of time $a(T)$, where the discrete time domain is defined as: $T=k/f_S$, where $k=1,...N$ is a sample number in the data string, $N$=65536 is the total number of samples of the data string. It is convenient to use the notation $a(k)$, which is a discrete string of measurement data. For such data string some features are calculated. In the literature on tool condition monitoring [1, 8] most commonly used features describing the characteristics of the measurement signal *a(k)* in the discrete time domain are given. Features used in the current study are summarized in Table 2.

**Table 2.** Features in the time domain selected to the classification

| Feature of an acceleration $a(k)$ | Description of features |
|---|---|
| $F_{a,Min} = \min_k(a(k))$ | Minimum of $a(k)$. |
| $F_{a,Max} = \max_k(a(k))$ | Maximum of $a(k)$. |
| $F_{a,Mean} = \bar{a} = \frac{1}{N}\sum_{k=1}^{N} a(k)$ | The average of $a(k)$. |
| $F_{a,StDev} = \sigma = \sqrt{\frac{1}{N-1}\sum_{k=1}^{N}(a(k)-\bar{a})^2}$ | The standard deviation of $a(k)$. |
| $F_{a,Var} = \sigma^2 = \frac{1}{N-1}\sum_{k=1}^{N}(a(k)-\bar{a})^2$ | The variance of $a(k)$. |
| $F_{a,RMS} = \sqrt{\frac{1}{N}\sum_{k=1}^{N}\lvert a(k)\rvert^2}$ | Root mean square value of $a(k)$. |
| $F_{a,Mom3} = E(a-\bar{a})^3$ | The central moment of 3rd order of $a(k)$, where $E(.)$ is the expected value of $a$. |
| $F_{a,Skew} = \frac{E(a-\bar{a})^3}{\sigma^3}$ | The skewness of $a(k)$. |
| $F_{a,Kurt} = \frac{E(a-\bar{a})^4}{\sigma^4}$ | The kurtosis of $a(k)$. |

### 3.2. Features in the discrete frequency domain

For the discrete string $a(k)$ a discrete Fourier transform (DFT) according to the following formula is calculated

$$A(m) = \sum_{k=0}^{N-1} a(k) e^{-i2\pi m \frac{k}{N}}, \; m = 0,..., N-1, \tag{1}$$

$A(m)$ – $m^{\text{th}}$ output component of DFT, $N$ - number of samples of the input string and the number of frequency points in the output DFT. To compute DFT, the fast Fourier transform (FFT) algorithm implemented in the Matlab software was used. In figure 4 examples of an acceleration spectrum calculated by using FFT algorithm are shown. These spectra corresponds to the data strings shown in figure 3.

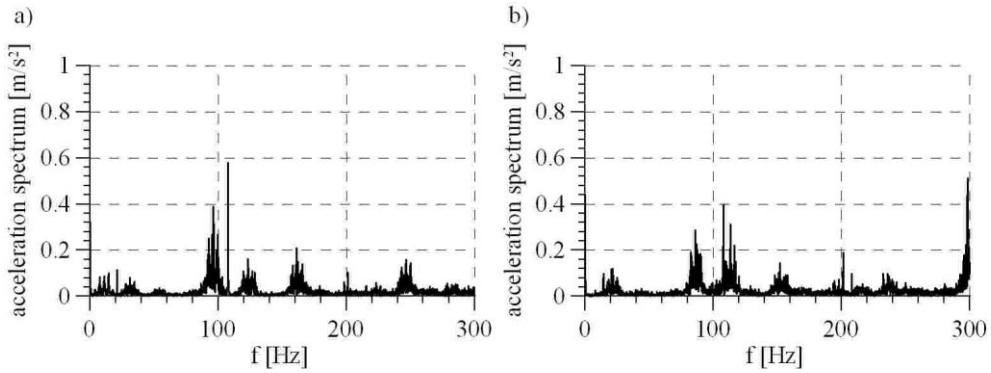


**Figure 4.** Examples of the spectrum of vibration acceleration: a) class 1 - case 3, b) class 2 - case 6.

The subject of analysis in the frequency domain will be fragments of the spectrum in the frequency bands corresponding to the environment of the main components and the first harmonic. Eq. 2 and is used to determine the mentioned bands. The environment of the main component is determined by the lower frequency $f(m1)$ and the upper frequency $f(m2)$, where

$$\begin{cases} m1 = round\left(\dfrac{f_t - \eta}{f_r}\right) \\ m2 = round\left(\dfrac{f_t + \eta}{f_r}\right) \end{cases} \tag{2}$$

and the environment of the first harmonic is determined by the lower frequency $f(2 \cdot m1)$ and the upper frequency $f(2 \cdot m2)$, where $f_t$ – frequency corresponding to the rotational speed of the tool, $\eta$ – positive constant experimentally selected as $\eta$=5 Hz, $f_r$ – frequency resolution defined as $f_r = f_S/N$. In our studies $f_t$=110 Hz, therefore $f(m1)$=104.8782 Hz, $f(m2)$=114.8785 Hz, $f(2 \cdot m1)$=209.8814 Hz,

$f(2 \cdot m2)$=229.8820 Hz. The selected features, that describe the vibration signals in the frequency domain are presented in the Table 3.

**Table 3.** Features in the frequency domain selected to the classification

| Feature of an acceleration spectrum $A(m)$ | Description of features |
|---|---|
| $F_{A,Max,i} = \max_{i \cdot m1 \le m \le i \cdot m2} (A(m))$ | Maximum in the neighborhood of the main component ($i$=1) or the first harmonic ($i$=2) in the spectrum of acceleration. |
| $F_{A,Mean,i} = \overline{A}_i = \frac{1}{(m2 - m1) \cdot i + 1} \sum_{m=i \cdot m1}^{i \cdot m2} A(m)$ | Average in the neighborhood of the main component ($i$=1) or the first harmonic ($i$=2) in the spectrum of acceleration. |
| $F_{A,StDev,i} = \sigma_{Ai} = \sqrt{\frac{1}{(m2 - m1) \cdot i} \sum_{m=i \cdot m1}^{i \cdot m2} \left(A(m) - \overline{A}\right)^2}$ | Standard deviation of the spectrum of acceleration in the neighborhood of the main component ($i$=1) or the first harmonic ($i$=2). |
| $F_{A,Var,i} = \sigma_{Ai}^2 = \frac{1}{(m2 - m1) \cdot i} \sum_{m=i \cdot m1}^{i \cdot m2} \left(A(m) - \overline{A}\right)^2$ | Variance of the spectrum of acceleration in the neighborhood of the main component ($i$=1) or the first harmonic ($i$=2). |
| $F_{A,RMS,i} = \sqrt{\frac{1}{(m2 - m1) \cdot i} \sum_{m=i \cdot m1}^{i \cdot m2} \left\|A(m)\right\|^2}$ | Root mean square value of the spectrum of acceleration in the neighborhood of the main component ($i$=1) or the first harmonic ($i$=2). |
| $F_{A,Mom3,i} = E\left(A_i - \overline{A}_i\right)^3$, $A_i = A(m)$, | The central moment of 3rd order of the spectrum of acceleration in the neighborhood of the main component ($i$=1) or the first harmonic ($i$=2), where $E(.)$ is the expected value of $A_i$, $A_i$=$A(m)$, where $m$=$i \cdot m1,\ldots,i \cdot m2$, $i$=1,2. |
| $F_{A,Skew,i} = \frac{E\left(A_i - \overline{A}_i\right)^3}{\sigma_{Ai}^3}$ | The skewness of the spectrum of acceleration in the neighborhood of the main component ($i$=1) or the first harmonic ($i$=2). |
| $F_{A,Kurt,i} = \frac{E\left(A_i - \overline{A}_i\right)^4}{\sigma_{Ai}^4}$ | The kurtosis of the spectrum of acceleration in the neighborhood of the main component ($i$=1) or the first harmonic ($i$=2). |

These features (9 in the time domain and 16 in the frequency domain) were calculated for the vibration acceleration of the previously obtained data strings. So each measuring data string obtained is represented in the form of a set of 25 features. Simultaneously, one of the two mentioned classes (1 - an acceptable condition of the tool, 2 - an unacceptable condition of the tool) was assigned to each set of features. In this way, a base of 240 sets of features used to build the classifier, was obtained. From this data base, ten learning sets and ten validation sets were created in order to apply the method of a 10-fold cross-validation of a classifier [10]. Learning sets contain 90 % of the features sets, and validation sets 10 % of them, wherein the validation sets are pairwise disjoint sets. Scheme of the measurement data post-processing is shown in figure 5.

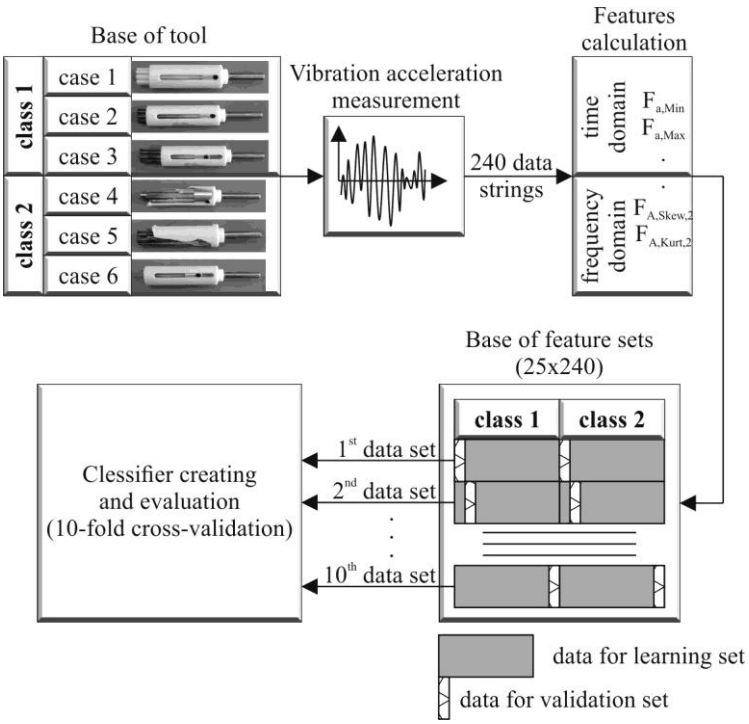


**Figure 5.** The scheme of measurement data post-processing method.

## 4. The tool condition classification

In order to pre-determine the most significant features of the signal, some of the most popular classifiers were used, i.e. decision trees (DTs) [4, 11]. They are implemented in a number of computational programs. In this researches, the method for creating and testing DTs implemented in the Matlab was used. For the construction of DTs the data sets discussed in the previous chapter were used. The 10-fold cross-validation method [10] was applied to the classification effectiveness

evaluation. From these analysis results, that most important features are (in the order of priority): $F_{A,StDev,1}$, $F_{A,RMS,2}$, $F_{a,Skew}$, $F_{A,Mean,2}$. Numerous combinations of features were investigated and found that an excessive amount of features cause the growth of the DT and adversely affect the effectiveness of the classification. With an increase in the number of features used for the classification of over four, classification effectiveness does not increase nor does it even decrease.

The second stage of the study was the use of neural networks (NNs) to classify the tool condition [3, 5]. Unlike a decision tree, the used NN classifiers belong to non-linear methods. Through this, nonlinear separation of classes is possible, which has an impact on the efficiency of classification. Using the "Neural Network Toolbox" library of the Matlab, a software tool to create and test NN classifiers, based on the feed-forward, artificial NN were built. NN classifiers were learnt according to the back-propagation error algorithm [7]. Software allows free choice of the main parameters of the NN such as: the number of inputs and outputs, the number of layers, the number of neurons in layers, the activation functions of neurons, learning parameters, etc. Using this software, different variants of the NN classifiers were tested by changing the number of layers in the range of 2-4 layers, and number of neurons in the range of 3-30 neurons in each hidden layer. In hidden layers, neurons with unipolar sigmoid activation functions were used while in the output layer linear neurons were applied. NN weights were learnt according to an algorithm based on the Levenberg-Marquardt optimization method. The NN classifiers creation and validation was performed with the use of the data prepared according to the scheme shown in figure 5, as for DTs. Similarly, for the classification effectiveness evaluation, the 10-fold cross-validation method was applied. Figure 6 shows the effectiveness of the NN classifiers, depending on the used features.

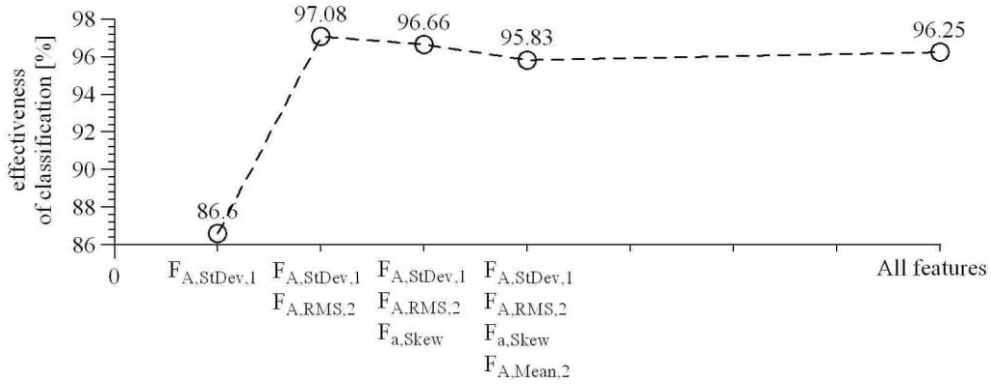


**Figure 6.** Effectiveness of NN classifiers.

Based on the analysis of effectiveness, the classifier based on features $F_{A,StDev,1}$ and $F_{A,RMS,2}$ was implemented on the robotic system. It takes the form of the two-layer NN with 18 neurons in each hidden layer.

## 5. Classifier implementation on robotic system

Developed NN classifier is implemented on the ds1104 DSP board. The algorithm of classification and decision making is built in the Simulink environment and then compiled. The algorithm saved in the corresponding code is loaded to the ds1104 DSP board's memory card and can be done in real-time. This card with the implemented classifier is the main element of the tool condition monitoring system (see figure 7).

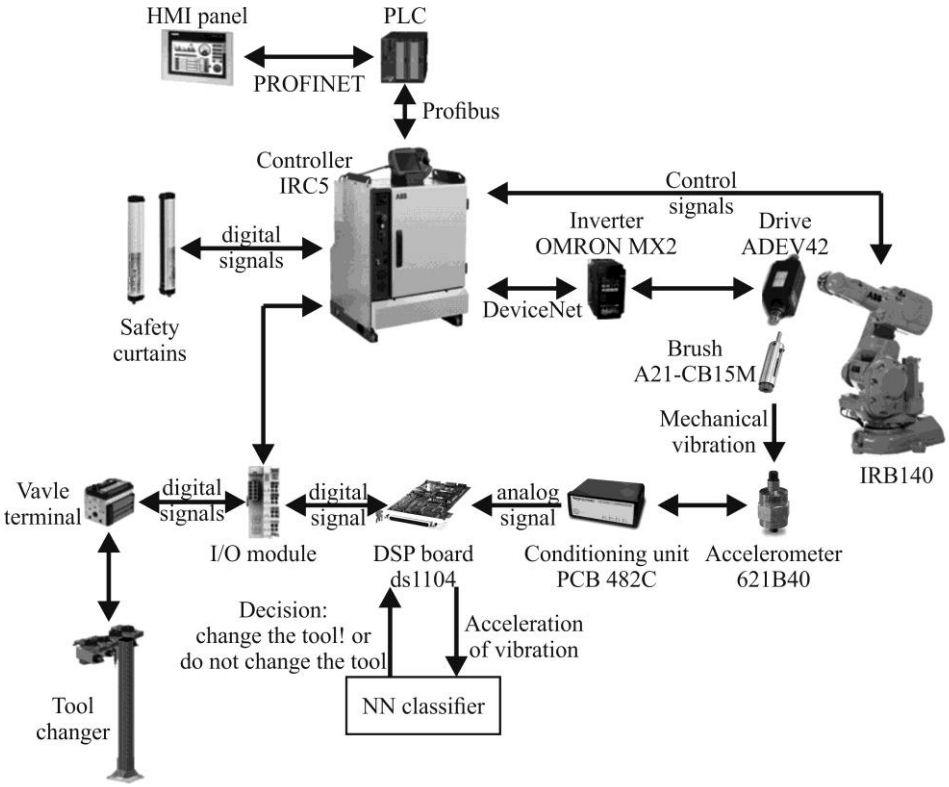


**Figure 7.** The scheme of the robotic system with implemented classifier of tool condition.

The DSP board is connected to the IRC5 controller by using an I/O module, which allows to start the procedure for tool condition control. The procedure begins with setting the robot's arm in a defined position. Simultaneously, the rotational speed of the tool is set to 660 rpm (110 Hz) by using an inverter. Then begins the recording of the vibration of the spindle and data processing. Calculated features are provided to the input of the NN, which generates information on the tool state. If the tool state is classified as unacceptable, the digital output of the DSP board is set to 1, otherwise it is set to 0. In order to increase the reliability of the system, the procedure is repeated. If the digital output of the DSP board for the first and the second time is set to 1, the procedure for changing the

tool is started. If the digital output for the first and the second time is set to 0, the tool remains unchanged. When the state of the digital output is different each time, the whole procedure is started again. For further ambiguity, the tool is changed, as this case is interpreted as “dangerous tool state”.

## 6. Conclusions

The paper presents a methodology for creating a system of the tool state diagnostics. The approach of using a DSP board has been used because of the ease of implementation of a classifier based on artificial intelligence methods. The use of a DSP board has additional advantages. The existing hardware infrastructure allows to build a classifier intended for other types of tools. It is also possible to implement the described system to another machining station. Each time, however, it is necessary to obtain a set of measurement data, and building a classifier dedicated to the problem being solved.

## References


[1] Abellan-Nebot, J.V., and Subirón, F.R. A review of machining monitoring systems based on artificial intelligence process models. *International Journal of Advanced Manufacturing Technology* 47 (2010), 237–257.

[2] Ambhorea, N., Kambleb, D., Chinchanikara, S., Wayala, V. Tool condition monitoring system: A review. *Materials Today: Proceedings* 2 ( 2015 ), 3419 – 3428.

[3] Dimla, Sr. D.E., Lister, P.M. On-line metal cutting tool condition monitoring II: tool-state classification using multi-layer perceptron neural networks. *International Journal of Machine Tools & Manufacture* 40 (2000), 769–781.

[4] Elangovan, M., Devasenapati, S.B., Sakthivel, N.R., Ramachandran, K.I. Evaluation of expert system for condition monitoring of a single point cutting tool using principle component analysis and decision tree algorithm. *Expert Systems with Applications* 38 (2011), 4450–4459.

[5] Elbestawi, M.A., Dumitrescu, M. Tool condition monitoring in machining - neural networks. *Information Technology for Balanced Manufacturing Systems* 220 (2006), 5-16.

[6] Gierlak, P., Szuster, M. The manipulator tool fault diagnostics based on vibration analysis in the frequency domain. *Applied Mechanics and Materials*, in print

[7] Hagan, M.T., Demuth, H.B., Beale, M.H. *Neural Network Design*, PWS Publishing, Boston, 1996.

[8] Jemielniak, K., Urbański, T., Kossakowska, J., Bombiński S. Tool condition monitoring based on numerous signal features. *International Journal of Advanced Manufacturing Technology* 59 (2012), 73–81.

[9] Liu, C., Wang, G.F., Li, Z.M. Incremental learning for online tool condition monitoring using Ellipsoid ARTMAP network model. *Applied Soft Computing* 35 (2015), 186–198.

[10] Picard, R.R., Cook, R.D. Cross-Validation of Regression Models. *Journal of the American Statistical Association* 79 (1984), 575-583.

[11] Saimurugan, M., Ramachandran, K.I., Sugumaran, V., Sakthivel, N.R. Multi component fault diagnosis of rotational mechanical system based on decision tree and support vector machine. *Expert Systems with Applications*, 38, 4 (2011), 3819-3826.

[12] Shen, C., Wang, G., Wang, S., Liu, G. The Imbalance Source of Spindle-Tool System and Influence to Machine Vibration Characteristics. *Digital Manufacturing and Automation (ICDMA)*, DOI 10.1109/ICDMA.2011.317 (2011), 1288-1291.

[13] Teti, R., Jemielniak, K., O'Donnell, G., Dornfeld, D. Advanced monitoring of machining operations. *CIRP Annals - Manufacturing Technology* 59 (2010), 717–739.

[14] Żabiński, T., Mączka, T., Kluska, J., Kusy, M., Gierlak, P., Hanus, R., Prucnal, S., Sęp, J. CNC Milling Tool Head Imbalance Prediction Using Computational Intelligence Methods. *Lecture Notes in Artificial Intelligence* 9119, Part I (2015), 503-514.

Piotr Gierlak, Ph.D.: Rzeszow University of Technology, Department of Applied Mechanics and Robotics, al. Powstańców Warszawy 12, 35-959 Rzeszów, Poland (*pgierlak@prz.edu.pl*). The author gave a presentation of this paper during one of the conference sessions.

Andrzej Burghardt, Ph.D. D.Sc. (Assistant Professor): Rzeszow University of Technology, Department of Applied Mechanics and Robotics, al. Powstańców Warszawy 12, 35-959 Rzeszów, Poland (*andrzejb@prz.edu.pl*).

Dariusz Szybicki, Ph.D.: Rzeszow University of Technology, Department of Applied Mechanics and Robotics, al. Powstańców Warszawy 12, 35-959 Rzeszów, Poland (*dszybicki@prz.edu.pl*).

Marcin Szuster, Ph.D.: Rzeszow University of Technology, Department of Applied Mechanics and Robotics, al. Powstańców Warszawy 12, 35-959 Rzeszów, Poland (*mszuster@prz.edu.pl*).

Magdalena Muszyńska, Ph.D.: Rzeszow University of Technology, Department of Applied Mechanics and Robotics, al. Powstańców Warszawy 12, 35-959 Rzeszów, Poland (*magdaw@prz.edu.pl*).

# The use of magnetic phenomena and Bayesian updating in the risk assessment of structural damage (MAT289-15)

Szymon Gontarz, Robert Gumiński

*Abstract:*Monitoring of civil engineering structures is an important issue due to a rapid development of the modern building techniques and growing fatigue wear during utilization of bridges, market halls etc. The complexity and diversity of civil engineering structures impose requirements on the diagnostic system, which are difficult to be satisfied. Many materials, that could cause real threat of the catastrophe caused by fatigue wear, exceeding stress limits or emerging of plastic deformation, have magnetic properties that could affect the local magnetic field.Therefore as a solution, a conception of monitoring system, based on passive magnetic field measurements is being developed. State of polarization of the magnetic structure (the distribution of magnetization) is carrier of diagnostic information about the level of effort and the progressive degradation of the material structure of the material. It is possible to obtain the diagnostic information through a remote, non-contact measurement of magnetic field near the test structure. Another part of the analysis is focused on the use of dynamic hysteresis model for diagnostics. With the help of hysteresis model it is chance to observe and identify changes which could be connected with technical state of research object. The proposed diagnostics can be used for any dynamic system where one can observe magneto-mechanical effects. The paper also describes possibility of use passive magnetic method in SHM as well as the directions of further scientific research.

## 1. Introduction

To-date innovative technical approach has involved use of advanced computer-assisted design and structure optimization systems. Widely-developed computer modeling accounted for complex loads in facilities as well as economic and ecological issues, and it was focused on minimizing the factors which could harm the environment in the course of construction of a technical facility. The approach fails to guarantee sufficient safety which is proven by the still happening unpredicted failures and catastrophes, such as: collapse of the roof of the International Trade Fair exhibition hall in Katowice during exhibition of homing pigeons on 26 January 2006. 65 people were killed and 170 were injured. Similar catastrophes also happened in Moscow in 2006 (collapse of trade fair building – 66 killed, 32 injured), in Gdańsk, where the roof of Leroy Merlin hypermarket collapsed in 2005, as well as in Paris (2004) and in Minorca (2006) where roofs of air terminals collapsed. There are also many examples of catastrophic events in the sea and rail transportation which could seriously affects not

only people directly connected with transportation system but also environment around. The reasons of such tragedies is usually loss of load-bearing properties by the structures due to various degradation processes or simply due to wear and tear of elements of technical facilities. In addition, there exists the risk of occurrence of unforeseen, complex operating conditions, which could bring about overload of a structure. This can happen in the case of occurrence of unexpected natural phenomena as well as due to influence of man or other technical objects.

Optimal way for risk of failure/damage assessment can be estimated at on the basis of the current technical condition of the analyzed object. Such a possibility is offered by the research presented in the paper which clearly leads to the development of diagnostic model for passive magnetic method of determining the state of stress and effort in a structure. Such approach is possible because materials which pose a real threat of failure or catastrophe in the infrastructural system, due to fatigue of a material, exceeding the permitted stress, or appearance of plastic deformations or micro-cracks, have magnetic properties themselves. Development of degradation and fatigue-related processes in such objects leads to qualitative and quantitative change of non-linear effects which are associated with magnetic properties of materials, both in the systems which are subject to dynamic loads as well as in the systems where static loads are dominant. These changes, when interacting with the Earth's magnetic field, offer a measurable image of behavior, which is visible as changes of distribution of the magnetic field around the objects which are subjected to diagnosis. The interaction between the external magnetic field and the material of which the elements of the operated technical object are made have enabled development of a group of magnetic methods which are part of technical diagnosis [1]. In opposite to active methods, techniques which exploit the Earth's natural field only are called passive [2-3]. Lack of the requirement to apply artificial sources of magnetic field offers the possibility of applying these technique not only for ad hoc analysis but also for continuous monitoring and it also offers the possibility of these methods being applied wherever it is not permitted to use artificial sources of magnetic field, e.g. due to safety reasons.

The paper will cover the problems of mathematical modeling and analytical/computational modeling of phenomena for the needs of diagnosis and detection of diagnostic information while referring to the passive magnetic method. Numerical modeling together with laboratory experiments and processing, which is agree with Bayesian updating, will indispensable to optimize the method of detecting the diagnostic information for a real-life technical object. The results proof that introducing dynamics to the system, there exist parameters which will have to be taken into account when analyzing the changes of own magnetic field of the examined object in the function of its effort, as well as when analyzing the global effort of the structure.

## 2. Application of Earth's magnetic field in diagnosing stress condition

Every "physical body" located within the magnetosphere has influence on the magnetic field in accordance with relevant mechanisms which are known in physics. The outcome of these changes is that these bodies (objects) can increase – in a varied degree – the density of the lines of magnetic field (they can increase the intensity of the field in themselves) or they can deflect the lines of the field away from the sample (they can decrease the intensity of the field in themselves).

Own magnetic field of object H, e.g. measured by a magnetometer, depends thus on the object's magnetization and distribution of this quantity in space. In addition, while bearing in mind the magneto-mechanical phenomena, it turns out that if the stress is changed in materials having magnetic properties, then the material is transformed into a different magnetic state. This phenomenon is described by the Villari effect, also called the magneto-elastic effect which is a reverse phenomenon to magnetostriction. It involves change of intensity of the magnetic field (or of magnetization) under the influence of mechanical stress applied to a material, and it includes transformation of the mechanical energy associated with deformation of the material into magnetic energy [4]. In general one can conclude that there is a quantitative change which describes relation between stress and degree of magnetization, and additionally there is a qualitative change of magnetic permeability which is associated with the fact of reaching the condition of plastic deformation [5-6]. This offers the possibility of obtaining new, extremely valuable diagnostic information on the degree of effort of the structure.

Taking into account magnetic properties of steel construction materials and values of the Earth's natural magnetic field, the resultant of volume magnetic susceptibility *Mvol* may be omitted. Therefore, the current degree of an object's (material) magnetization can be expressed as the resultant of reversible directional magnetization process and irreversible magnetization:

$$M(\sigma,t) = M_{dir}(\sigma,t) + M_{irr}(\sigma=0,t) \tag{1}$$

Hence, object's H own magnetic field measured by e.g. a magnetometer depends on the object's magnetization and its distribution in the space. Additionally, taking into account scientifically recognized magneto-mechanical phenomena [7], namely the Villary effect, the Matteuci effect, the Naganka-Honda effect or the phenomenon of austenite transforming into martensite in fatigue loads, it turns out that the change of stress degree in an object will be reflected by a corresponding change of magnetic field [8-9].

Generally it should be stated that there is a relation between stresses and the degree of magnetization that, after a comprehensive analysis, appears to be a highly complex one, but it definitely does depend on the type of material, temperature and stress degree. It is generally known that each 'physical body' in the area of magnetosphere influences Earth's magnetic field according to adequate mechanisms

known in physics. The critical problem is the fact that the magnetic state change of object is in accordance with certain characteristics specific to the material from which the object is made. The same level of magnetic can be invoked a variety of factors and does not necessarily imply that damage appears. There is therefore a high probability of misdiagnosis.

### 2.1. The use of diagnostic uncertainty in risk reduction

Reliability of the estimate of technical risk depends on a number of factors affecting the uncertainty of models describing the processes degradation and fatigue, uncertainty parameter and a quantitative assessment of the effect of propagation of uncertainty in the system. In many cases, the diagnostic observations can track the evolution of parameter values [10]. Issues of such use of diagnostic results of the experiments is particularly important that it was possible to reduce significant uncertainty.

In the scientific and technical community one can see increasing interest in the attempts of using the diagnosis methods for analyzing the degradation as well as for reliability of elements of critical technical systems estimation. Often it is the Bayes methods which serve as the basis for the adopted approach [11-12]. In Bayes methods, in contrast with the classical estimation theory, which assumes that the nature of parameters is determined, we assume certain, variously understood, randomness. This means the necessity for adopting the assumption of existence of a priori uncertainty as defined by a priori distribution of probability.

Bayes' papers elaborated on this understanding of probability, thus enabling estimation of conditional probability based on non-conditional probabilities. In addition the method enables qualification of the measure of subjective human experience or even individualized opinion about the obtained results of research and experiments. This approach involving the upgrade of estimated parameters of the probabilistic model can also be used in order to achieve better compliance of results of modeling and observation. In accordance with the above presented assumptions it is assumed that unknown or uncertain parameters of distribution are random variables.

Then, while assuming that we will be estimating the parameters of a priori distribution of parameter $a$ of the function of probability density $f(a)$ and that $D$ is an observation set enabling reduction of a priori uncertainty on the condition of the results of the observation being included, we should be able to conduct the estimation of a posteriori distribution parameters by means of the following formula:

$$f(a/D) = \frac{f(D/a)f(a)}{f(D)} \tag{2}$$

where:

$$f(D) = \int_{-\infty}^{\infty} f(D/a)f(a)da$$

Let us note that Bayes formula (2) can be simplified by accounting for proportionality of a posteriori and a priori distributions only :

$$f(a/D) = \frac{f(D/a)f(a)}{f(D)} \propto f(D/a)f(a) \tag{3}$$

In a similar way the probability density is proportional to the square root of Fisher's information matrix factor [13]:

$$f(a) \propto (\det \mathrm{I}(a))^{1/2} \tag{4}$$

where:

$\mathrm{I}(a) = -E\left[\frac{\partial^2 \ln f(D/a)}{\partial a^2}\right]$ - is calculated as the matrix of average second derivatives from the credibility function logarithm based on the results of the experiment.

Thus the presented method of using the risk analysis method, supported by diagnosis, in the process of making operational decisions refers on the one hand to the definition of risk and the associated estimation of probability of occurrence of undesirable incident as well as to estimation of the extent and value of loss accompanying such an incident. On the other hand it refers to the possibility of using the results of a diagnostic experiment in the task of reducing the uncertainty related to estimation of parameters of a posteriori distribution of intensity of defects. Use of Bayesian models enables direct application of the results of diagnostic observation in Bayesian estimation of a posteriori distribution as well as tackling the problem of selecting the a priori distribution. The use of diagnostic information enables one to solve the problem of determining the conditional probability distribution for the parameters of defect intensity while relying on the results of the diagnostic experiment.

## 3. A proposal of applying hysteresis model in passive magnetic method

The goal of the analysis proposed in the present section is to present the possibilities of applying hysteresis model for passive diagnostic method. Based on the research performed so far [5] one can propose a hypothesis saying that an adequate model of hysteresis will describe the change of the registered magnetic field's signal depending on the load and deformation of the construction's material as a dynamic system.

Magnetic materials that are frequently used in construction engineering are characterized by the process of hysteresis which describes the change of material's magnetization in the function of magnetic field influencing it (Fig.1). The following relationship entails different phenomena of physics, materials' parameters and numerically defined conditions of measurement. The parameters' values of hysteresis are in this case conditioned by the following factors: type of material, dimensions

of an object under examination, magnetic field's strength, deformations, stress degrees, temperature and fatigue cycle.

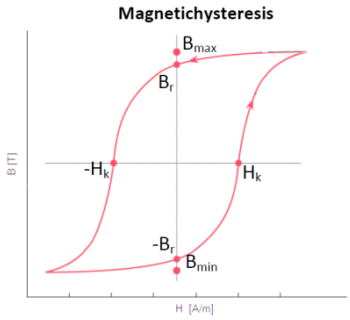


$$B = \mu(T, \sigma, \varepsilon, n_\sigma, A) \cdot H$$

**Figure 1.** Magnetic hysteresis

where:

$\mu$- depends on type of material, dimensions of an object under examination, magnetic field's strength, deformations, stress degrees, temperature, fatigue cycle.

We can see that the phenomenon of hysteresis depends on various factors proper for the problem analyzed. An adequate choice of these factors allows for defining new diagnostic parameters. The knowledge on the object and physical phenomena related to it along with the conditions in which the object is operated will support the process when introduced into an adequate model.

Hysteresis may be generalized to a system generating an input signal and a system causing the input transformation in such a way that it is possible to register hysteresis. The input signal is a signal of magnetic field strength. The output signal is the registered signal that has gone through the transformation system with given parameters. An adequate adjustment of the system transforming the signal and related with magnetic effects should provide access to information about the operation of the system generating the signal.

Analyzed phenomena that caused registered change of own magnetic field [5] are of a magneto-static nature. Theoretically this fact excludes the possibility of hysteresis because the prerequisite for its occurrence is an input signal of an dynamic character – like in case of typical magnetic hysteresis. However, the idea of the changes of an object's own magnetic field under the influence of magneto-elastic effects and in view of the possibilities to observe the hysteresis loops. The magnetic anomalies measured stand for the change of magnetic field's induction in the presence of the assumed constant external magnetic field *H=const*. This external field is identified with the Earth's magnetic field that – for the purposes of the present paper - may be regarded as constant, according to the results presented above. If we use an additional, already verified hypothesis saying that magnetic permeability of a given object's material depend on the degree of its stresses, we may draw the conclusion that the

shape of hysteresis will be obtained during cyclic changes of the examined object's loads. Introducing the cycle of dynamic loads as an input signal into a hypothetical model of hysteresis, we will get an output signal that represents forming of a hysteresis loop at the level of input/output (Fig. 2).

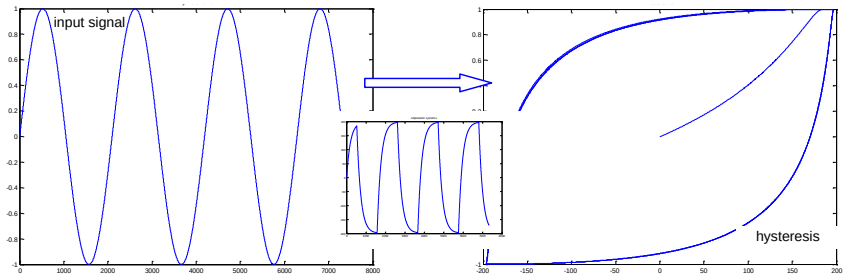


**Figure 2.** Example of hysteresis loop forming after dynamic input signal

It may be observed that after each full cycle of loading is completed a hysteresis loop appears. The introduction of dynamic load that will definitely be the case when real objects are analyzed, exposed the occurrence of hysteresis process. Based on the presented analysis it may be concluded that the characteristic behavior of a ferromagnetic material, namely its non-linear magnetization under the influence of external alternating magnetic field (classic magnetic hysteresis) may also occur in the presence of constant magnetic field (even a weak one). This is only possible under the condition of the change of ferromagnetic stress state. Created loop of hysteresis will be formed as a result of the system's properties with the assumption of a periodic input signal of $C^0$ class.

Currently we are observing a great progress in the development of non-linear models especially these ones characterizing hysteretic behaviours [14-15]. However, the presented proposals are rather complex and often require additional selection algorithms and optimisation of their parameters. As an alternative, we propose our original hysteresis model for the purposes of the issues discussed in the present paper – proposed model is detailed describe in [5]. The model is based on the transformation of the energy carried by the input signal. If the conditions concerning the input signal and resulting from the assumption of hysteresis are met then the model will generate hysteresis loop dependent on/independent from the frequency of the input signal and always dependent on the value of the input function. The model elaborated resulted to be able to perform hysteresis' characteristics modeling. These characteristics may be used for interpreting magneto-mechanical effects. The usefulness of such model will be verified during the experiment which describes next chapter.

## 4. Experimental Verification of Hysteresis

Development of a model, while using and modifying the general hysteresis model, requires an experiment which verifies the described theoretical considerations. An experiment was planned which

registered and analyzed the distributions of own magnetic fields of objects made of magnetic materials. Measurements concerned dynamic responses of the examined samples. The measured anomalies are intended to present change of magnetization which reflects the operation of major stresses, generated by the loads which were in turn caused by degradation or operation of a structure.

A measurement track, consisting of an APS536 FluxGate-type magnetometer (Fig. 3), a National Instruments data acquisition card and a measuring computer, was used to carry out the experiment. The examined objects were cylindrical samples made of a material with ferromagnetic properties, namely the C45 steel, which are visible on the photo (Fig. 3). The shape and the dimensions of the sample were designed from the point of view of using them in a machine with a specific type of a shoe and while accounting for the dynamic nature of the loads to which the sample was exposed. Load could be applied to the sample thanks to using a testing machine manufactured by MTS Systems Corporation - Material Testing System MTS 810 (Fig. 3).

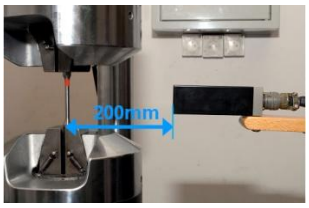


**Figure 3.** A view of the testing machine's shoe, the sample and the magnetometer

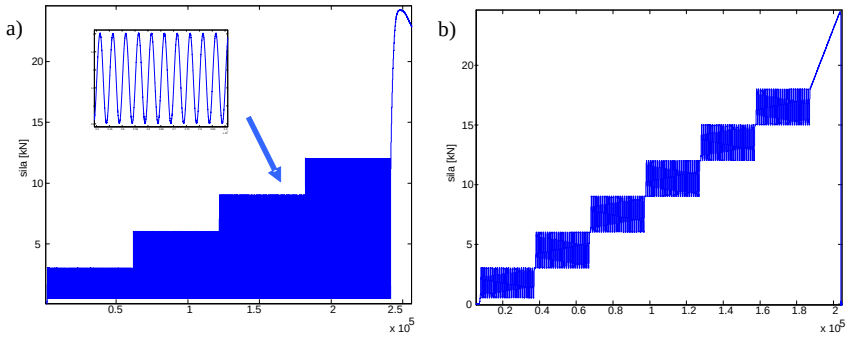


**Figure 4.** The cycle of applied loads

The program of the tests accounted for the impact that the sample's deformations had on the behavior of the sample's own magnetic field under regularly applied stress in the presence of the Earth's natural magneticfield H.

Implemented two types of excitations (loads) with their different values. Initial load was 0.5 kN, respectively, while the first type of extortion is a periodic (sinusoidal) with a constant change of force from the minimum value and increasing in increments of variance (Fig. 4a); the second is a periodic

(sinusoidal) force changes at constant amplitude variance and stepwise increasing the average (Fig.4b).

In order to verify the proposed models on the basis of experiments, graphs showing the dependence of the magnetic induction of the sample during loading were done. Figure 5 shows an example of the results of the tests carried out by the two loads scenarios.

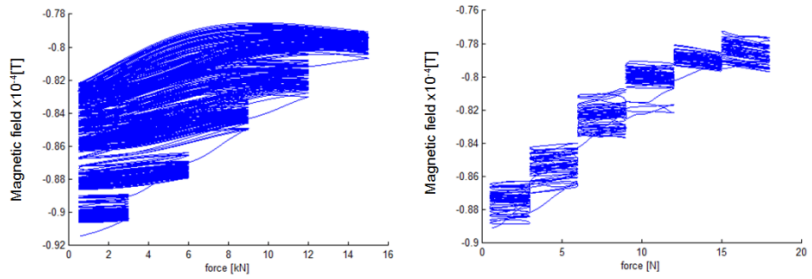


**Figure 5.** Change of induction of the magnetic field in the function of load of the samples during dynamic test

Analyzing presented waveforms, one can generally observe the rotation of the hysteresis loops and change in their surface area. To better illustrate the changes, we determined the surface area and as a measure of rotation slope of the straight line approximating the hysteresis loop was adopted. The results are shown in Figure 6a and b, and probability density functions considered measures displayed Figure 7a and 7b.

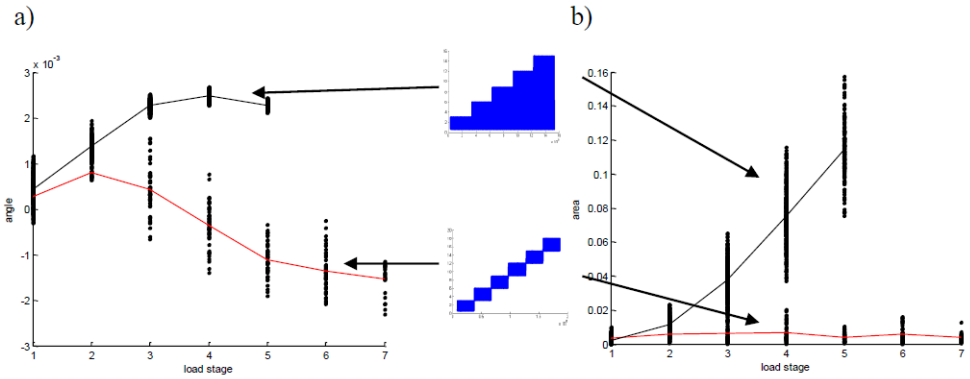


**Figure 6.** Changing the angle of rotation and the surface area of the hysteresis loops as a function of load

The analyzes carried out show the scatter of the results, but it is possible to observe a certain dependence. The thing to pay attention to the resulting differences in various scenarios loads. To express the parameter dependence in the form of the rotation angle hysteresis or its surface area of load it is necessary to use Bayesian probability. Examples of conditional probability density functions are shown in Figure 7 a, b.

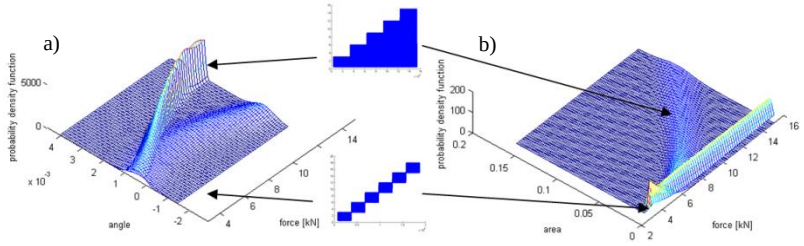


**Figure 7.** The dependence of the probability density function of the angle of rotation and the surface area of the hysteresis loop of the load

Worth emphasizing is that the reproducibility of the results achieved presented in the form of a probability density function of the proposed measures. Presented statistical functions despite some randomness confirm that the results are not a matter of chance, eg. the impact of uncontrollable factors. Obtained dispersion of diagnostic measures, angle and surface area are relatively large nevertheless allow differentiation occurring loading process, especially at the higher maximum strength. The ranges of variation of random variables presented measures for both loading schemes are clearly separated and consequently gives some diagnostic information. Problematic is the overlapping areas of the probability density function for small values of maximum force due to the smaller standard deviation of the amplitude strength. Information on how loading is desirable, however, with a low degree of effort of the structure, its absence or significant uncertainty poses no threat to the structure. Another issue is changing the standard deviation diagnostic measures. The preferred is decreasing standard deviation of the rotation angle hysteresis loop with the increase of the maximum load for the first load pattern (fixed value of minimum force and growing by leaps and bounds standard deviation). Unfavorable phenomenon, in terms of diagnostic use is increasing standard deviation of the surface area of the hysteresis loop (Fig.7b) for the first scheme load. This disadvantage little impact on diagnostic confidence due to the large differences in average values of the hysteresis loop field for both load patterns (especially for large values of maximum forces). Additionally, you should pay attention to the fact that both of the characteristics of significant diagnostic changes in hysteresis complement each other, if one measure has significant standard deviation can be supplemented by a second measure, which has a small dispersion and vice versa.

Waveforms obtained for enforce with fixed minimum value and increasing in increments of variance indicate a rotating loop in an elastic deformation, which corresponds to the range of loads to round 9 kN (Fig.6a). After exceeding the elastic limit there is no further increase in the angle of rotation, but followed by rapid increase in the surface area of the loop what did not take place before occurrence of plastic effects (Fig.6a) (or at least occurred on a smaller scale). As one can see the appearance of plastic deformation causes a change in the behavior of the hysteresis loops. It causes the need to use different models of hysteresis. In the first scenario in the range of elastic loads, a

model where a change in the amplitude of the input signal causes the rotation of the hysteresis loop should be used, while the elastic range is exceeded - model in which the surface area increases.

In the case of the second type of excitations, graphs indicate that, for the elastic rotation phenomenon does not occur (random changes occur only) (Fig. 6a) and the area of the loop increases (Fig.6b). After exceeding the elastic limit, substantial rotation of the loop (up to negative values). The observed changes do not allow for a single model of hysteresis for changes occurring throughout the range of loads (also in consideration of type of loads). In range of the elastic deformation, model uses surface area of hysteresis which increase with increasing amplitude of input signal should be used. However, after exceeding the elastic limit, magnetic field is changed, and there is a need to use the model of the hysteresis loop, which is rotated with increasing input signal amplitude.

In the context of the use of the presented results in order to improve the reliability of the diagnosis one must specify formulas conditional binding changes the symptom / diagnostic parameter of a specific type of load. These formulas make it possible to determine the corresponding conditional probabilities. Due to the nature of the research will be necessary reversal of the conditionality set of probabilities. On the basis of results of the analysis performed it can be concluded that the angle and area of the hysteresis loop are growing, where there are first load pattern. The second statement will be: value of the angle (directional factor) decreases and the value of the area will remain subject to the occurrence of a second load pattern. Determination of load pattern (i.e. determining whether a change in the maximum force is related to the change of the standard deviation at a constant minimum value, or the change in the mean while maintaining a standard deviation) is associated with a suitable model of hysteresis and, consequently, a significant reduction in uncertainty of the diagnosis. In fact, there may be changes being contemplated well as combinations of parameters does not allow for a clear inference using the rules above, therefore, it may be necessary to provide redundancy of the proposed systems diagnostics. This may result in the need to use other diagnostic methods.

## 5. Summary

Observed state of own magnetic field of samples is of magnetostatic (as well as the nature of the Villari phenomenon), but oscillating course of the input signal (eg. the force or elongation) introduced the necessary dynamics, by which existed sufficient conditions to form the shape of the hysteresis loop. It has been shown that such transformation creates a new potential for the identification of changes in signal parameters that correspond to specific physical phenomena. Analysis of the magnetic field, allows to define two diagnostic parameters characterizing the magneto-mechanical hysteresis (the shape parameter and surface hysteresis) and confirms the validity of the use of the model hysteresis. Introduced dynamics to the system resulted in the emergence of diagnostic information, which can only be interpreted properly provided taking into account the current system

behavior. For this purpose the effectiveness of the Bayesian approach revealed that pointed to the correct interpretation of results which is tantamount to enhance the certainty of diagnosis. The proposed diagnostic approach can provide sufficient information for managing the technical objects while accounting for technical risk whereas the presented status offers extensive application possibilities for the proposed passive method of assessing the condition of technical objects.

**Acknowledgments**

This work was supported by The National Centre of Research and Development (Poland) in frame of grants: DOB-BIO6/16/44/2014 and PBS1/B4/6/2012.

**References**

[1] Nowicki M., Szewczyk R., Ferromagnetic Objects Magnetovision Detection System.*Materials*, 6, 2013, 5593-5601.
[2] Lindgren M., Lepistö T., Relation between residual stress and Barkhausen noise in a duplex steel, *NDT & E International*,36(5), 2003, 279-288.
[3] Dubov A., 2004, Principal features of metal magnetic memory method and inspection tools as compared to known magnetic ndt methods, *Proceedings of the 16th Annual World Conference on Non-Destructive Testing, Montreal, Canada, 30 August–3 September*, 2004.
[4] GontarzS., Radkowski S., „Impact of Various Factors on Relationships Between Stress and Eigen Magnetic Field in a Steel Specimen", *Magn. IEEE Trans. On*, t. 48, nr 3, 2012, pp. 1143–1154.
[5] Gontarz S., Mączak J.,Szulim P., „Online Monitoring of Steel Constructions Using Passive Methods",*Engineering Asset Management - Systems, Professional Practices and Certification*, P. W. Tse, J. Mathew, K. Wong, R. Lam, i C. N. Ko, Red. Springer International Publishing, 2015, ss. 625–635.
[6] Gontarz S., Szulim P., Seńko J., Dybała J., „Use of magnetic monitoring of vehicles for proactive strategy development", *Transp. Res. Part C Emerg. Technol.*, t. 52, nr 0, 2015, pp. 102–115.
[7] Jiles, D.C., Theory of the magnetomechanical effect, *Journal Phys. D: Appl. Phys*., 28, 1995, 1537-1546.
[8] Sander D., Enders A., Kirschner J., Stress and magnetic properties of surfaces and ultrathin films, *J.Magn.Magn.Mater*. 200, 1999, 439-455.
[9] Xingliang J, Xingchao J, Deng Guoyong, Experiment on relationship between the magnetic gradient of low-carbon steel and its stress, *Journal of Magnetism and Magnetic Materials*, 321(21), 2009, 3600-3606.
[10] Galezia A., Averaged signal measures of TKEO energy waveform in detection of tooth break in gearbox, *Measurement Automation and Monitoring*, 60 (1), 2014, 31 – 34.
[11] J. Yang, H. F. Lam, and J. Hu, Ambient Vibration Test, Modal Identification and Structural Model Updating Following Bayesian Framework, *International Journal of Structural Stability and Dynamics*, October 2015, Vol. 15, No. 07.
[12] M. Askari, J. Li, and B. Samali, Application of Kalman Filtering Methods to Online Real-Time Structural Identification: A Comparison Study, *International Journal of Structural Stability and Dynamics*, doi: 10.1142/S0219455415500169.
[13] Jeffreys H. J., (1961), *Theory of Probability*, Oxford: Clarendon Press, 1961.
[14] Ikhouane F., Gomis-Bellmunt O., A limit cycle approach for the parametric identification of hysteretic systems. *Sys Control Lett*57, 2008, 663-669.
[15] Ahrens J., Tan X., Khalil H. K., Multirate sampled-data output feedback control of smart material actuated systems," *Proceedings of the American Control Conference*, New York, NY, 2007.

Robert Gumiński, Ph.D.: Warsaw University of Technology, Faculty of Automotive and Construction Machinery Engineering, Institute of Vehicles, Narbutta 84, 02–524 Warsaw, Poland (*rgumin@simr.pw.edu.pl*).
Szymon Gontarz, Ph.D.: Warsaw University of Technology, Faculty of Automotive and Construction Machinery Engineering, Institute of Vehicles, Narbutta 84, 02–524 Warsaw, Poland (*sgontarz@simr.pw.edu.pl*).

# Two-phase flow patterns identification based on recurrence statistics of a pressure drop
## (NUM260-15)

Grzegorz Górski, Grzegorz Litak, Romuald Mosdorf, Andrzej Rysak

*Abstract:* By changing air and water flow rates in the two-phase (air-water) flow through a minichannel we observed evolution air bubbles and slugs patterns. The identification of these spatio-temporal behaviour was done by a digital camera. Simultaneously, we provide the quantitative studies of these phenomena by using recurrences in the pressure time series response. To distinguish particular patterns we used recurrence plots and recurrence quantification analysis.

### 1. Introduction

Two-phase dynamics often appears in many technical applications. In the context of minichannel flow, the complex nature of this phenomenon was continuously studied in last 30 years [1, 3, 21, 23, 24]. The phase separation patterns were initially identified by Wang et al. [19]. The authors used the Hurst and Lyapunov exponents, and correlation dimension. In parallel, Jin et al. [9] applied the correlation dimension and Kolmogorov entropy, while Mosdorf et al. [17] discussed the results of various non-linear analyses of temperature and pressure fluctuations in microchannels. Gao et al. [6] characterized complex patterns arising from horizontal oil-water two-phase flows by network recurrence quantifiers. Additionally, Gorski at al. analysed a transition from slugs to bubbles and a self-aggregation phenomenon in similar systems [7, 8].

### 2. Experimental setup

The experiment involved analysis of data recorded for different flow patterns (water-air at $21^o$ C) in a 3mm diameter circular channel. Figure 1 shows the schematic design of the experimental stand is presented. Given to the size of the minichannel, it was necessary to use a special generator of mini bubbles (8 - Fig. 1a) to produce bubbly flow inside the channel. The proportional pressure regulator (Metal Work Regtronic with an accuracy of 1 kPa) was used to maintain the constant overpressure in the supply tank (10 - Fig. 1a) at 50 kPa. Flow patterns were recorded using the Phantom v. 1610 digital camera at 5000 fps (1280 $\times$ 64 pixels). The amount of air flowing through the minichannel was measured

by a laser-phototransistor sensor (3 - Fig. 1a). Data from the sensors was acquired by a acquisition system (Data translation 9804, an accuracy of 1 mV for voltages in the range of -10 V to 10 V), (11 - Figure 1a) at a sampling rate of 1 kHz. A schematic design of the laser-phototransistor sensor is shown in Fig. 1b.

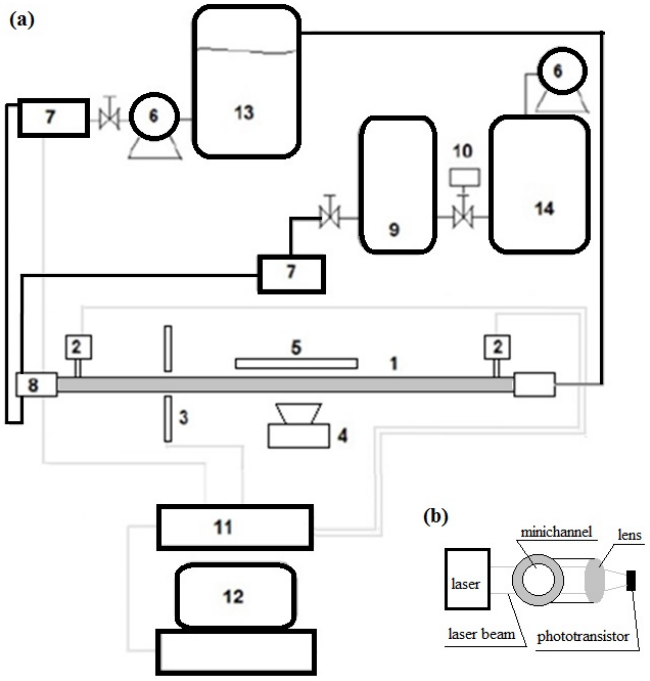


**Figure 1.** Schematic plot of the experimental stand. (a) Experimental setup: 1. minichannel with a diameter of 3mm, 2. pressure sensors (MPX12DP), 3. laser-phototransistor sensor. 4. Phantom v. 1610 camera, 5. lighting, 6. pumps (air or water), 7. flow meters. 8. mini bubbles generator, 9. air tank, 10. automatic valve to maintain a constant pressure in the tank 9, 11. data acquisition station (DT9800), 12. computer, 13. water tank, 14 air tank. The total length of the minichannel was 1m while the laser was located 10cm from the inlet end. (b) Laser-phototransistor sensor.

## 3. Results

### 3.1. Digital camera and pressure drop results

Figure 2 shows the digital camera photos on the air water flow with changing water and air rates. The mixture of air and water creates a flow with the nonuniform phase content. The air phase are visible as bubbles surrounded by water. As expected, the bubbles change the

size and the corresponding distribution depending on the assumed flow rates. It is clear that increasing the air contribution we form larger bubbles.

The corresponding pressure drops for selected cases are present in Fig. 3a-f. The related drops were measured between the sensor no. 2 in Fig. 1. Interestingly, the responses show some more (Fig. 3b,c,e) and less (Fig. 3a,d,f) periodic characters. In the next subsection we will apply the RP method to determine the periodic – nonperiodic transition (bifurcation).

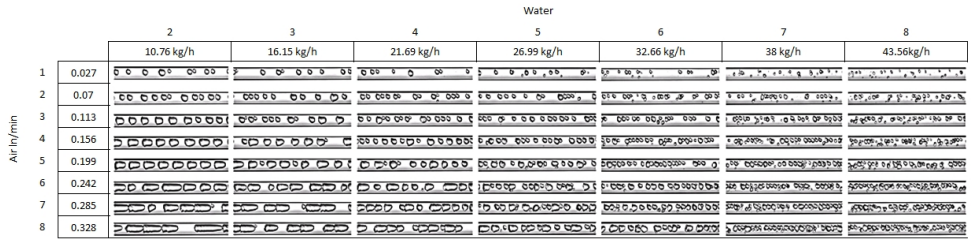


**Figure 2.** Digital camera photos for different air (columns), $q_a$, and water (rows), $q_w$ volume flow rates. This plots form of the matrix (1-8×2-8) with the horizontal and vertical elements.

### 3.2. Recurrence Plots and Recurrence Quantification Analysis

The dynamics of the underlying phenomena can be investigated by means of recurrences which are calculated for each visited state of the reconstructed trajectory. This method was developed by Eckmann [4] and extended by Webber [20], Casdagli [2] later by Marwan et al. [14, 16] and others. This approach can be used for both short deterministic and noise affected experimental data [12, 22].

Two points on a trajectory $x(t)$ are marked as neighbours if they are close enough to each other. This can be expressed by the distance matrix $R$ with its element $R^{\epsilon}_{ij}$ given by [4]:

$$R^{\epsilon}_{ij} = \Theta(\epsilon - ||\mathbf{x}_i - \mathbf{x}_j||), \tag{1}$$

where $\epsilon$ is the threshold value and $\Theta(x)$ denotes the Heaviside function. The number of recurrence points depends on both the underlying dynamics and also by the cosing the threshold value. A standard technique for approximations is that the threshold value should not be higher than a few percentage of the total number of points [16].

Following Takens [18] and basing on the laser light transmission $x$ time series, we define the following vectors $\mathbf{x}$ in the embedding space:

$$\begin{aligned}\mathbf{x}(t) &= (x(t), x(t - \delta i\Delta t), x(t - 2\delta i\Delta t),\\ &..., x(t - (m-1)\delta i\Delta t),\end{aligned} \tag{2}$$

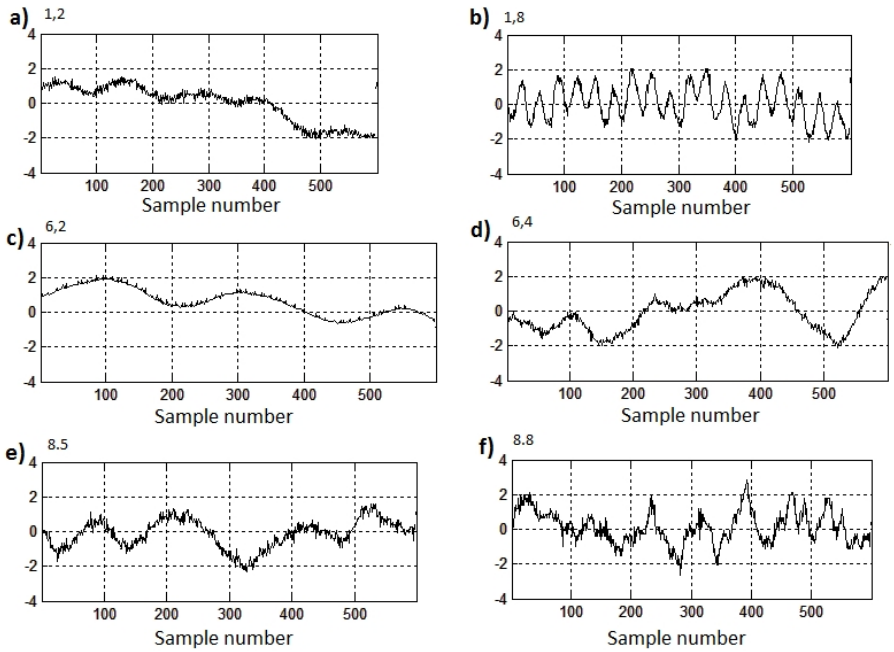


**Figure 3.** Pressure difference variability in the minichannel (estimated between sensors no. 2 in Fig. 1) for selected cases. The cases (a)-(f) have been chosen from the graphical matrix elements (1,2), (1,8) (6,2) (6,4), (8,5), and (8,8) respectively. In each case the laser intensity has been normalized by the standard deviation of $x$, $\sigma_x$ suitable for the next analysis.

where $\Delta t = 0.1$ ms is a sampling period while $\delta i$ is the time lag in the sampling interval units to be estimated and $m$ is the embedding system dimension. . The phase space reconstruction has been performed by using the standard methods of the first minimum of average mutual information and the nodal fraction of false neighbours [5, 10, 11]. The results for embedding parameters are presented in Fig. 4a-b. Here, we presented the results in the form of the matrix corresponding to the Fig. 2. The time delay $\delta i$ variate from-case-to-case with fairly large amount, however the dimension, $m \sim 4$, is more stable.

Furthermore, more detailed observations on Fig. 2 leads to the pattern classification based on the bubbles sizes (Fig. 4c). Note that the pattern have a descending diagonal character. We claim that the separation border lines are related to the pattern divergences. Figure 5 show the selected RPs (see cases presented in Fig. 3). Here, some periodicity (or are manifested in the cases Fig. 5b,e,f while the 5c,d seems to be nonstationary courses (the diagonal lines are effectively reduced beyond the area close to the main diagonal. Fig. 5a is

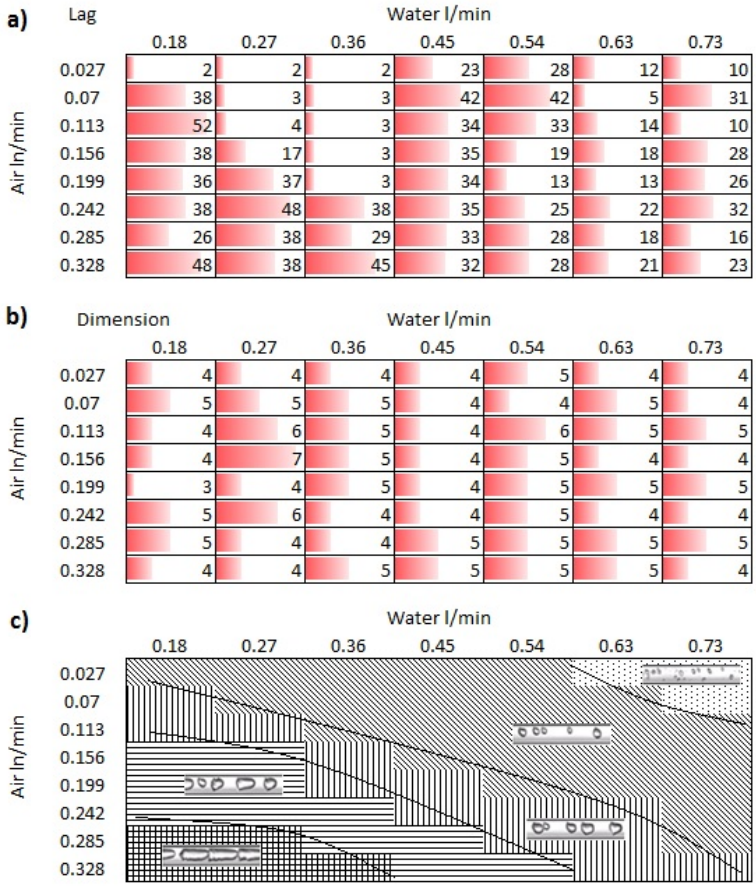


**Figure 4.** Embedding parameters for the all studied cases (see Fig. 2) The schematic table (a) shows the estimated time delays (time lags) $\delta i$ for the all cases (Fig.2), while the table (b) stands for the corresponding embedding dimension $m$. Pattern classification schema (c) made on the basis of visual observations (see Fig. 1).

different. The system shows considerably more distributed recurrences comparing to Figs. 5c,d. The main difference is in the properties of time series which can be embedded with fairly different embedding parameters (see the delay in Fig. 4a).

In the next step we quantify and compare the dynamics of a system with a systematic change of volume flow rates by using the Recurrence Quantification Analysis (RQA) for recurrence plots. This method was developed by Webber and Zbilut [20] and also Marwan et al. [14, 16]. Namely, the RQA analysis includes the recurrence rate variable, $RR$, which is

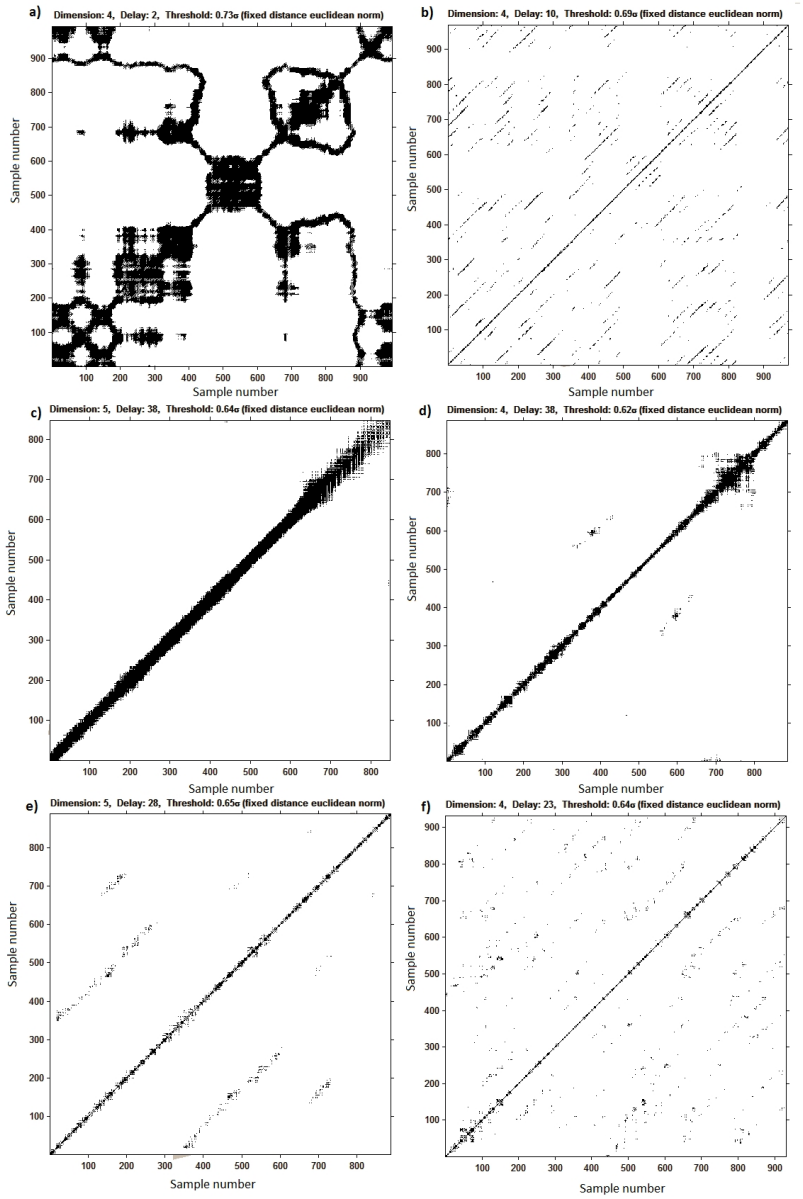


**Figure 5.** Recurrence plots for the cases presented in Fig. 3. The fixed distance Euclidean norm was used, while the threshold $\epsilon$ was chosen at the level of 30% of the maximal phase space diameter. The calculations were done using the Cross Recurrence Plot Toolbox [13].

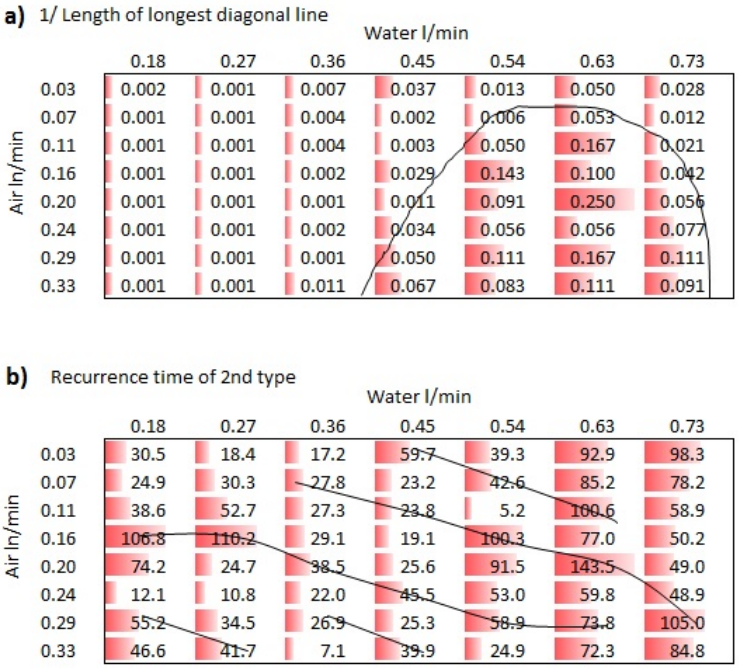


**Figure 6.** RQA results: inverse of the longest diagonal length, $1/L$ (a), The region inside the black line show the important contribution of distributed short lines. The recurrence time of the 2nd type, $T^{(2)}$ (b). The diagonal like lines shows connects maxima of $T^{(2)}$ where bubbles are exposed on transitions in the formed patterns. The calculations were done using the Cross Recurrence Plot Toolbox [13].

a measure of ability for the system to return to the neighbourhood of a previous state.

Among different measures there is maximal length $L$ (excluding the main diagonal). It refers to the predictability time of a dynamic system. On the other hand $1/L$ could indicate dynamical divergences and can indicate the chaotic dynamics [15]. The recurrence times of second type $T^{(2)}$ defines the average time distance between the beginning (vertically) subsequent recurrence structures in the RP. This can give an idea about the characteristic recurrence (period) in the system. Application of RQA would tell more about the bifurcations. Figure 6 shows $1/L$ (Fig. 6a) and $T^{(2)}$ (Fig. 6b). Interestingly, the shortest lines in RPs (larger $1/L$) are more visible as water and air volume flow rates ($q_w, q_a$) are increasing.

On the other hand, to reproduce the separation lines in terms of $T^{(2)}$, we estimated the corresponding maxima. Note that the corresponding sketched lines (Fig. 6a) are very similar to the visual observations (Fig. 4c).

## 4. Conclusions

The evolutions air bubbles and slugs patterns for different air and water flow rates were identified by using RP and RQA techniques. We observed the regions of parameters in terms of divergence and periodicity. Interestingly the regions were not defined for the localized points on the two dimensional map ($q_w$,$q_a$), but formed rather diagonal stripe structures. The above observations could be used to prepare the flow control strategy for technical systems which could rely on more predicable patterns.


## Acknowledgments

The research was funded by the National Science Centre, Poland with the number of decision: DEC-2013/09/B/ST8/02850.


## References


[1] Anjos, G., Borhani, N., Mangiavacchi, N., and Thome, J. 3d moving mesh finite element method for two-phase flows. *Journal of Computational Physics 270* (2014), 366–377.

[2] Casdagli, M. Recurrence plots revisited. *Physica D 108*, 1 (1997), 12–44.

[3] Chen, L., Tian, Y., and Karayiannis, T. The effect of tube diameter on vertical two-phase flow regimes in small tubes. *International Journal of Heat and Mass Transfer 49* (2006), 4220–4230.

[4] Eckmann, J.-P., Kamphorst, S., and Ruelle, D. Recurrence plots of dynamical systems. *Europhysics Letters 4* (1987), 973–977.

[5] Fraser, A., and Swinney, H. Independent coordinates for strange attractors from mutual information. *Physical Review A 33* (1986), 1134–1140.

[6] Gao, Z., Zhang, X., Jin, N., Marwan, N., and Kurths, J. Multivariate recurrence network analysis for characterizing horizontal oil-water two-phase flow. *Physical Review E 88* (2013), 032910.

[7] Gorski, G., Litak, G., Mosdorf, R., and Rysak, A. Two phase flow bifurcation due to turbulence: transition from slugs to bubbles. *European Physical Journal B 88* (2015), 239–244.

[8] Gorski, G., Litak, G., Mosdorf, R., and Rysak, A. Two phase flow bifurcation due to turbulence: transition from slugs to bubbles. *Zeitschrift für Naturforschung A 70*, 10 (2015), 843–849.

[9] Jin, N., Nie, X., Ren, Y., and Liu, X. Characterization of oil/water two-phase flow patterns based on nonlinear time series analysis. *Flow Measurement and Instrumentation 14* (2003), 169–175.

[10] Kantz H, S. T. *Non-linear Time Series Analysis*. Cambridge University Press, Cambridge, 1997.

[11] Kennel, M., Brown, R., and Abarbanel, H. Determining embedding dimension for phase-space reconstruction using a geometrical construction. *Physical Review A 45*, 6 (1992), 3403–3411.

[12] Litak, G., Wiercigroch, M., Horton, B., and Xu, X. Transient chaotic behaviour versus periodic motion of a parametric pendulum by recurrence plots. *Journal of Applied Mathematics and Mechanics 90*, 1 (2010), 33–41.

[13] Marwan, N. *Cross Recurrence Plot Toolbox for Matlab, Ver. 5.15, Release 28.10*. http://tocsy.pik-potsdam.de.

[14] Marwan, N. *Encounters with Neighbours: Current Development of Concepts Based on Recurrence Plots and their Applications*. PhD thesis, Universitaet Potsdam, 2003.

[15] Marwan, N., J., K., and S., F. Analysing spatially extended high-dimensional dynamics by recurrence plots. *Physics Letters A 379* (2015), 894900.

[16] Marwan, N., Romano, M., Thiel, M., and Kurths, J. Recurrence plots for the analysis of complex systems. *Physics Reports 438*, 5-6 (2007), 237–329.

[17] Mosdorf, R., Cheng, P., Wu, H., and Shoji, M. Non-linear analyses of flow boiling in microchannels. *International Journal of Heat and Mass Transfer 48*, 21-22 (2005), 4667–4683.

[18] Takens, F. *Detecting Strange Attractors in Turbulence Dynamical Systems and Turbulence*. Wareick 1980, Lecture Notes in Mathematics 898, Springer, Berlin, 1981.

[19] Wang, S., Mosdorf, R., and Shoji, M. Nonlinear analysis on fluctuation feature of two-phase flow through a t-junction. *International Journal of Heat and Mass Transfer 46* (2003), 1519–1528.

[20] Webber, Jr., C., and Zbilut, J. Dynamical assessment of physiological systems and states using recurrence plot startegies. *Journal of Applied Physiology 76* (1994), 965–973.

[21] Wongwises, S., and Pipathattakul, M. Flow pattern, pressure drop and fraction of two-phase gas-liquid flow in an inclined narrow annular channel. *Experimental Thermal and Fluid Science 30*, 4 (2006), 345–354.

[22] Yang, L., Ding, S., Litak, G., Song, E., and Ma, X. Identification and quantification analysis of nonlinear dynamics properties of combustion instability in a diesel engine. *Chaos 25*, 1 (2015), 013105.

[23] Zhao, L., and Rezkallah, K. Gas-liquid flow patterns at microgravity conditions. *International Journal of Multiphase Flow 19* (1993), 751–763.

[24] Zong, Y.-B., Jin, N., Wang, Z.-Y., Gao, Z.-K., and C., W. Nonlinear dynamic analysis of large diameter inclined oil-water two phase flow pattern. *International Journal of Multiphase Flow 36*, 3 (2010), 166–183.

Grzegorz Górski, Ph.D.: Faculty of Mechanical Engineering, Bialystok University of Technology, Wiejska 45 C, 15-351 Bialaystok, Poland (*grzesgor@o2.pl*).

Grzegorz Litak, Professor: Faculty of Mechanical Engineering, Lublin University of Technology, Nadbystrzycka 36, PL-20-618 Lublin, Poland (*g.litak@pollub.pl*). The author gave a presentation of this paper during one of the conference sessions.

Romuald Mosdorf, Professor: Faculty of Mechanical Engineering, Bialystok University of Technology, Wiejska 45 C, 15-351 Bialaystok, Poland (*mosdorf@gmail.com*).

Andrzej Rysak, Ph.D.: Faculty of Mechanical Engineering, Lublin University of Technology, Nadbystrzycka 36, PL-20-618 Lublin, Poland (*rysak.andrzej@gmail.com*).

# Targeted energy transfer in automotive powertrains
**(NUM050-15)**

Ahmed Haris, Eliot Motato, Stephanos Theodossiades, Alexander F. Vakakis,
Lawrence A. Bergman, D. Michael McFarland and Ben Struve

*Abstract:* Torsional oscillations generated by the internal combustion engine induce various NVH phenomena in the drivetrain system, one being transmission rattle. Palliatives devices such as the clutch predampers or dual mass flywheel have been used to mitigate these NVH phenomena. However, usually these devices are effective over a limited range of frequencies, and not so for broadband transient phenomenon, such as any impulsive actions. This paper considers the Targeted Energy Transfer (TET) method to mitigate torsional vibrations in automotive powertrains. TET is a concept which attempts to direct the mechanical (vibration) energy (in a nearly irreversible manner) from a source (primary system) to a strongly nonlinear attachment (Nonlinear Energy Sink – NES), where it is absorbed, redistributed and/or dissipated. In contrast to the classical powertrain palliative methods, NES should be capable of operating over a broader band of frequencies (with the additional aim of being lightweight and compact). Although the TET concept has been extensively studied for translational systems, there is a dearth of studies for rotational (torsional) ones. In the present work, preliminary parametric studies are performed on a reduced automotive powertrain model, incorporating a NES attachment. The NES parameters, including nonlinear stiffness, viscous linear damping and inertia are varied in order to determine NES effects on engine order (EO) vibration.

## 1. Introduction

Vehicle fuel consumption and emissions are the foremost powertrain development objectives. The EU automotive emissions regulation currently imposes a limit of 130 g/km for any manufacturer's fleet of vehicles. This limit is expected to be reduced to 95 g/km by 2020. To meet this stringent limit engine downsizing, light weight and compactness are seen to have the positive effect on fuel consumption and emissions. On the other hand, there is the trend to improve upon output power-to-weight ratio as desired by customer base, thus leading to increased powertrain NVH, mostly of torsional oscillations, owing to the inherent combustion signature and inertial imbalances of piston-connecting rod-crankshaft system [8]. Body boom, clutch judder, axle whine, driveline clonk and gearbox rattle are phenomena generated by the driveline oscillations across a broadband of NVH response, but all initiated by engine vibration or impulsive action.

Traditionally, vehicle manufacturers have implemented clutch predampers to control powertrain vibrations, but unacceptable oscillation levels still transmit through to the driveline system. The Dual Mass Flywheel (DMF) [1] and the DMF with centrifugal pendulum vibration absorbers (CPVA) [15] are additional palliatives used to minimize vibrations at specific

frequency ranges. Nevertheless, in modern engines, the vibration energy is distributed over a broad range of frequencies, reducing the effectiveness of the DMF and CPVA as passive vibration absorbers. This paper investigates the use of Targeted Energy Transfer (TET) as a way to attenuate broadband vibrations in powertrains.

TET is a concept where the vibration energy is directed from a source to a receiver in a uni-directional, nearly-irreversible manner [11]. From an engineering perspective, Gendelman et al. [2] and Vakakis et al. [12] have published studies of TET in two and three-degree-of-freedom (DOF) systems. The literature includes a plethora of publications dedicated to the understanding of TET ("energy pumping"). Vakakis et al. have studied the Non-linear Normal Modes (NNMs) [13] to classify the interaction of the Nonlinear Energy Sink (NES – non-linear attachment) with the modes of the primary linear system. Jiang et al. [4] studied the effect of NES on the steady-state dynamics of a weakly coupled system. Panagopoulos et al. [7] studied the transient resonance interactions of a finite number of linear oscillators coupled to a NES. Tsakirtzis et al. [10] studied TET transient resonance interactions. Kerschen et al. [5] conducted parametric studies to understand the dynamics of energy pumping. McFarland et al. [6] performed investigations in structures with grounded and ungrounded non-linear attachments. All the above studies have focused on translational systems, subjected to (mainly) impulsive inputs.

The first study on implementing a NES in torsional systems considers the application of a discrete torsional NES to stabilise a drill-string system [14]. Gendelman et al. [3] studied, numerically and experimentally, the dynamics of an eccentric rotational NES mounted inside a linear oscillator. Sigalov et al. [9] expanded the study of Gendelman et al. by analysing the resonance captures and the NNMs of the system. In all these works, impulsive excitation has been applied in the primary system. Nevertheless, transient excitations are a common input in the automotive powertrains.

This work proposes a methodology that uses the TET method (NES absorbers) to reduce the broadband vibrations generated in vehicle powertrains, subjected to transient excitations. The powertrain considered is a Front Wheel Drive (FWD) transaxle system coupled to a three cylinder engine. The NES parameters are numerically tuned to minimise the gearbox input shaft acceleration produced by the different engine order (EO) harmonics. The NES proposed is passive in nature and lightweight, and can be used in compact spaces. It is also able to operate over a broad range of frequencies.

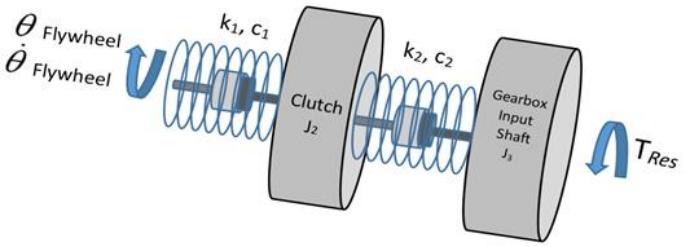


**Figure 1:** Schematic of the Reduced Powertrain Model

## 2. Powertrain Model Validation

A generic powertrain configuration comprises the engine, flywheel, clutch, gearbox, differential, transaxle half-shafts and tyres. Modelling the entire system can be computationally intensive, thus a simplified two DOF lumped parameter model (Figure 1) is used to introduce the proposed procedure. The reduced model includes the clutch assembly inertia ($J_2$) and the gearbox input shaft inertia ($J_3$). The effect of the other components located after the input shaft is represented by the resisting torque ($T_{Res}$) transferred to the gearbox input shaft. The resisting torque is modelled as a function of aerodynamic drag and tyre-road rolling resistance. The effect of engine torque on the clutch disc is represented by a torsional signal applied through a spring with stiffness $k_1$ and a damper with coefficient $c_1$. The applied torque is a function of the flywheel position and velocity.

Experimental data obtained from a vehicle equipped with a similar powertrain was used to validate the simplified numerical model. The 3-cylinder 1.0l engine produces 170 Nm peak torque. The vehicle uses a clutch torsional damper with a Single Mass Flywheel (SMF). The angular rotations of the shafts are measured using sensors located at the flywheel and gearbox input shaft for the vehicle operating at partial engine throttle (the engine was swept through the whole operating speed range with 25% throttle input).

The Continuous Wavelet Transform (CWT) was used for the analysis of the experimental, non-stationary angular velocities using AutoSignal commercial software. The CWT analysis highlights the 1.5, 3.0, 4.5 and 6.0 EO frequencies as expected. This particular engine has the 1.5 EO as dominant because combustion occurs three times over two crankshaft revolutions. The obtained frequency domain response is shown in Figure 2.

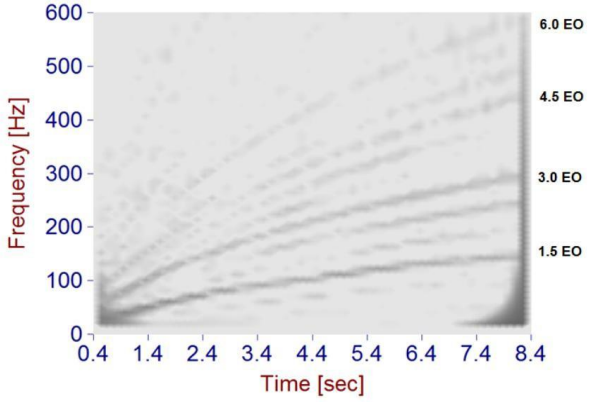


**Figure 2:** Experimental Input Shaft CWT in 1$^{st}$ gear with 25% open throttle

The equations of motion of the simplified model are:

$$\begin{bmatrix} J_2 & 0 \\ 0 & J_3 \end{bmatrix}\begin{bmatrix} \ddot{\theta}_2 \\ \ddot{\theta}_3 \end{bmatrix} + \begin{bmatrix} c_2 + c_1 & -c_2 \\ -c_2 & c_2 \end{bmatrix}\begin{bmatrix} \dot{\theta}_2 \\ \dot{\theta}_3 \end{bmatrix} + \begin{bmatrix} k_2 + k_1 & -k_2 \\ -k_2 & k_2 \end{bmatrix}\begin{bmatrix} \theta_2 \\ \theta_3 \end{bmatrix} = \begin{bmatrix} k_1\theta_1 + c_1\dot{\theta}_1 \\ -T_{Res} \end{bmatrix} \quad (1)$$

where $\dot{\theta}_1, \dot{\theta}_2, and\ \dot{\theta}_3$ are the angular velocities of the flywheel, clutch disc and gearbox input shaft, respectively. The parameter values of torsional linear stiffness $k_1$, $k_2$ and inertias $J_2$ and $J_3$ were provided by industrial partners.

**Table 1:** Model parameters

| Inertia [kgm$^2$] | Stiffness [Nm/rad] | Damping |
|---|---|---|
| $J_2$ = 0.001 | $k_1$ = 1000 | $\zeta_1$ = 0.8 |
| $J_3$= 0.003 | $k_2$ = 15000 | $\zeta_2$ = 0.5 |

The coefficients $c_1$ and $c_2$ were obtained using Caughey's method; $\varphi$ is the modal matrix obtained through solution of the generalised eigenvalue problem, thus:

$$[C] = \begin{bmatrix} J_2 & 0 \\ 0 & J_3 \end{bmatrix}\varphi\begin{bmatrix} \zeta_1 & 0 \\ 0 & \zeta_2 \end{bmatrix}\varphi^T\begin{bmatrix} J_2 & 0 \\ 0 & J_3 \end{bmatrix} \quad (2)$$

The damping ratios $\zeta_1$ and $\zeta_2$ corresponding to the 1$^{st}$ and 2$^{nd}$ natural frequencies of the system were fine tuned to obtain a near identical time and frequency domain response.

A Matlab/Simulink model, representing Eq. (1) is made, and the damping coefficients obtained through Eq. (2) are incorporated. Several combinations of damping ratios were evaluated with the objective of achieving a time and frequency response similar to the experimental data response, whilst

keeping $\zeta < 1$. The validation was conducted using the 1st gear engaged at 25% throttle manoeuvre. The damping ratios which resulted in a near identical system response were $\zeta_1 = 0.8$ and $\zeta_2 = 0.5$ with the corresponding natural frequencies being $f_1 = 62$ Hz, and $f_2 = 800$ Hz.

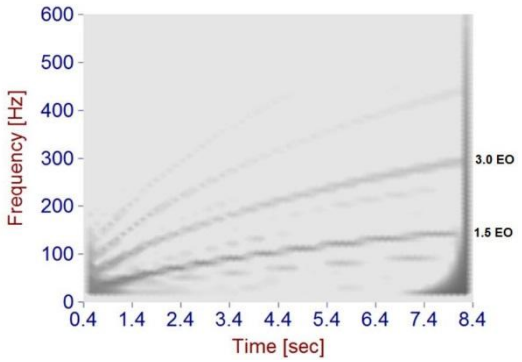


**Figure 3:** Simulated Input Shaft CWT response for 1st gear at 25% open throttle

CWT analysis was performed using the numerical data obtained. The results are shown in Figure 3. Indeed, the simulated CWT is similar to the corresponding experimental CWT displayed in Figure 2. A time domain plot of the gearbox input shaft angular velocity comparing the experimental and simulated responses is shown in Figure 4. The time domain CWT insets show very good correlation between the simulated and the experimental responses.

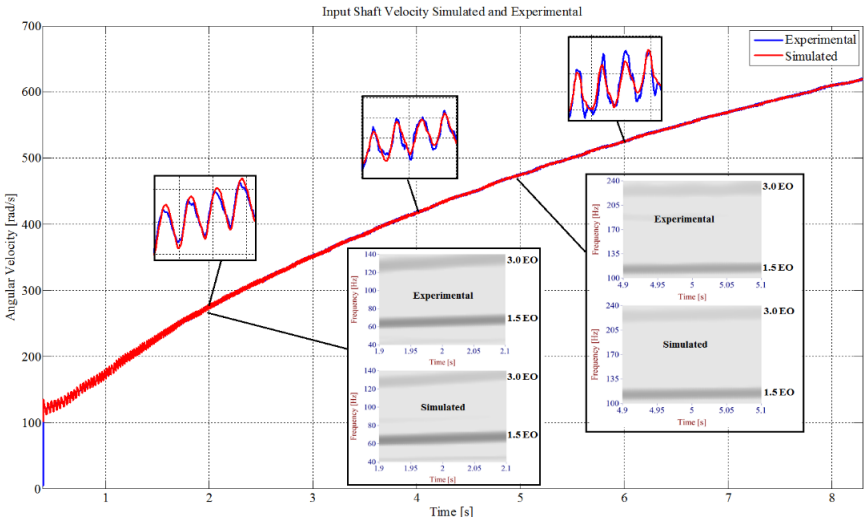


**Figure 4.** Simulated and experimental results comparison in frequency and time domains

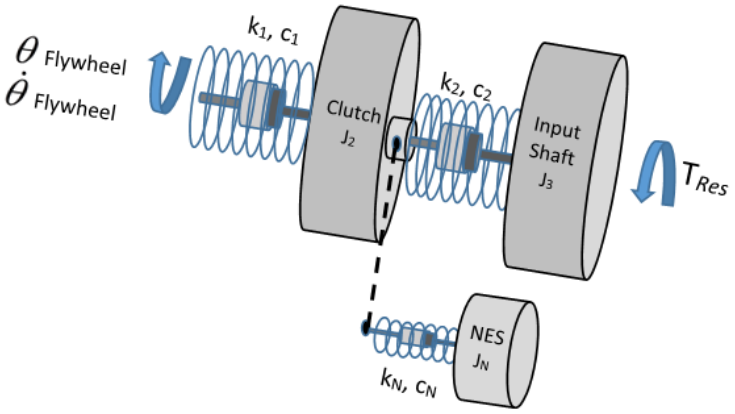


**Figure 5:** Powertrain model with NES attachment

## 3. Powertrain system with coupled NES attachment

The simplified powertrain model described in Eq. (1) was modified to incorporate a Non-linear Energy Sink (NES) with inertia $J_N$ as shown in Figure 5. The NES is coupled in parallel with the clutch disc through an essentially nonlinear torsional cubic spring with stiffness constant $k_N$ and a linear viscous damper with damping coefficient $c_N$. The NES is considered to be mounted on the spline coupling the clutch with the gearbox input shaft. The differential equations of motion describing the dynamics of the powertrain coupled with the NES are given by

$$\begin{bmatrix} J_2 & 0 & 0 \\ 0 & J_3 & 0 \\ 0 & 0 & J_N \end{bmatrix} \begin{bmatrix} \ddot{\theta}_2 \\ \ddot{\theta}_3 \\ \ddot{\theta}_N \end{bmatrix} + \begin{bmatrix} c_1 + c_2 + c_N & -c_2 & -c_N \\ -c_2 & c_2 & 0 \\ -c_N & 0 & c_N \end{bmatrix} \begin{bmatrix} \dot{\theta}_2 \\ \dot{\theta}_3 \\ \dot{\theta}_N \end{bmatrix} + \begin{bmatrix} k_2 + k_1 & -k_2 & 0 \\ k_2 & k_2 & 0 \\ 0 & 0 & 0 \end{bmatrix} \begin{bmatrix} \theta_2 \\ \theta_3 \\ \theta_N \end{bmatrix} = \begin{bmatrix} k_1\theta_1 + c_1\dot{\theta}_1 - k_N(\theta_2 - \theta_N)^3 \\ -T_{Res} \\ k_N(\theta_2 - \theta_N)^3 \end{bmatrix} \quad (3)$$

Since the 1.5 EO harmonic carries most of the vibration energy of the powertrain, the performance of the NES is measured based on the reduction of the amplitude of this harmonic. This is analysed by comparing the gearbox input shaft acceleration of the 1.5 EO when *(a)* the powertrain is operating with the NES *(active)* versus *(b)* the powertrain operating with the NES inertia simply added to the clutch inertia *(locked)*. The system response time histories are estimated from the dynamic model. The Matlab command *Pwelch* is then used to obtain the power spectral density (PSD) of the gearbox input shaft acceleration for *locked* and *active* systems using Welch's overlapped segment averaging estimator. To obtain the plot shown in Figure 6, the following method was used. The acceleration time histories for the gearbox input shaft were used as the input to the *Pwelch* command. The resultant PSD obtained contained all the engine harmonics with the units $rad^2/s^4/Hz$. Therefore, to obtain the 1.5 EO acceleration, the product of PSD x Frequency was square rooted i.e. $1.5\ EO = \sqrt{PSD \times Frequency}$, where frequency is the frequency of 1.5 EO harmonic.

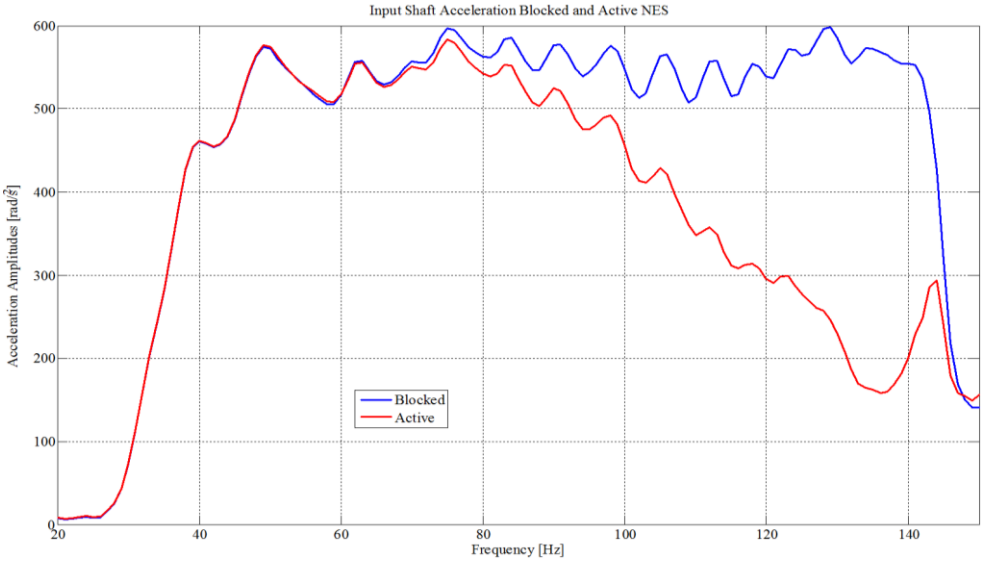


**Figure 6:** 1.5 EO acceleration amplitudes for active and locked NES

A series of simulations were performed for ranges of $k_N$, $J_N$ and $c_N$ using the numerical model. It is noted that significant acceleration reduction is achieved for $J_N$ = 11% of the gearbox input shaft inertia, $k_N$ = 2 x $10^6$ Nm/rad$^3$, and $c_N$ = 0.001 Nms/rad. The corresponding 1.5 EO acceleration amplitudes in the frequency domain for both systems (*active* and *locked* NES) are shown in Figure 6. The frequency range where substantial reduction in the 1.5 EO harmonic occurs is 80 - 150 Hz. It is also possible to observe a reduction in the amplitude of oscillations of the angular velocity (Figure 7) during the time (and corresponding frequency range) in the manoeuvre, where the NES operates effectively, absorbing the oscillations of the primary system. The amplitude of oscillations in the velocity is clearly linked to the magnitude of the 1.5 EO harmonics.

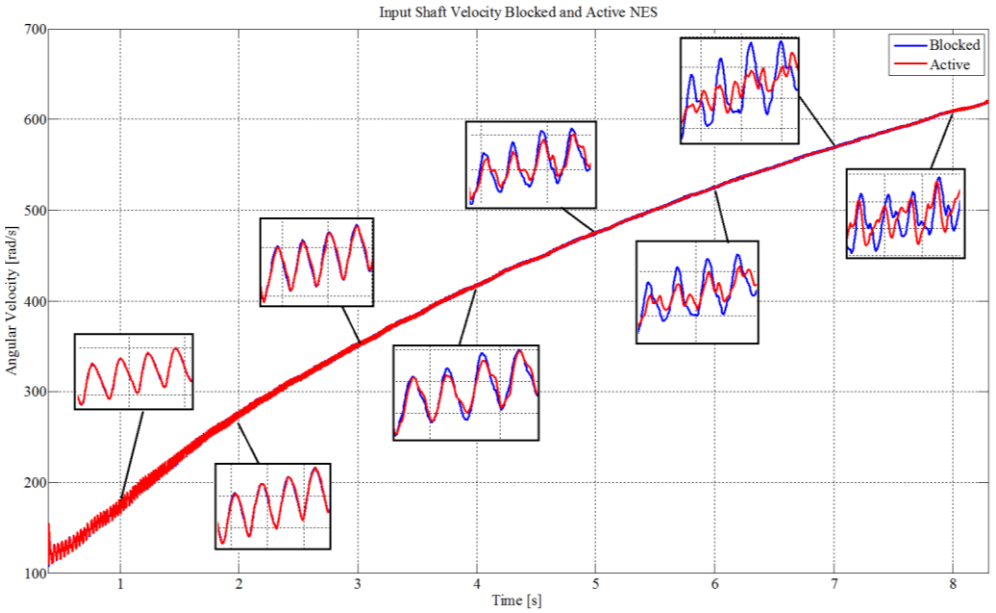


**Figure 7.** Input Shaft Angular velocity for systems with active and locked NES

## 4. Conclusion

This work studied the effect of implementing a NES vibration absorber to an automotive powertrain for passively absorbing torsional oscillations. From the results obtained it can be concluded that the NES induces an energy transfer mechanism, which redistributes the energy in the powertrain; as a result substantial reduction in vibrations is observed at the gearbox input shaft over a broad frequency range. Intensive simulations were conducted for different combinations of NES parameters to identify those that lead to reduction of the 1.5 EO harmonics of the gearbox input shaft. Furthermore, it appears that the range of NES operation is dependent on the input energy applied to the system, unlike the conventional palliatives which are tuned to specific engine frequencies.

## 5. Acknowledgments

The authors wish to express their gratitude to the EPSRC for the financial support extended to the **"Targeted energy transfer in powertrains to reduce vibration-induced energy losses"** Grant (EP/L019426/1), under which this research was carried out. Thanks are also due to Raicam Clutch and Ford Motor Company for their technical support.

## References

1. Drexl, H. J. Torsional dampers and alternative systems to reduce driveline vibrations. *SAE Technical Paper*. (1987), 1-11.

2. Gendelman, O., Manevitch, L. I., Vakakis, A. F., and M'Closkey, R. Energy Pumping in nonlinear oscillators: Part I – Dynamics of the underlying Hamiltonian systems. *Journal of Applied Mechanics*, 68 (2001), 34-41.
3. Gendelman, O. V., Sigalov, G., Manevitch, L. I., Mane, M., Vakakis, A. F., and Bergman, L. A. Dynamics of an eccentric rotational nonlinear energy sink. *Journal of Applied Mechanics*, 79 (2012).
4. Jiang, X., McFarland, D. Michael, Bergman, Lawrence. A., and Vakakis, Alexander F. Steady state passive nonlinear energy pumping in coupled oscillators: Theory and Experimental results. *Nonlinear Dynamics*, 33 (2003), 87-102.
5. Kerschen, G., Vakakis, Alexander F., Lee, Young S., McFarland, D. Michael, Kowtko, Jeffrey J., and Bergman, Lawrence A. Energy transfer in a system of two coupled oscillators with essential nonlinearity: 1:1 resonance manifold and transient bridging orbits. *Nonlinear Dynamics*, 42 (2005), 283-303.
6. McFarland, D. Michael, Kerschen, G., Kowtko, Jeffrey J., Lee, Young S., Bergman, Lawrence A., and Vakakis, Alexander F. Experimental investigation of targeted energy transfers in strongly and nonlinearly coupled oscillators. *Journal of Acoustical Society of America*, 118 (2005), 791-799.
7. Panagopoulos, Panagiotis N., Vakakis, Alexander F., and Tsakirtzis, S. Transient resonance interactions of finite linear chains with essentially nonlinear end attachments leading to passive energy pumping. *International Journal of Solid and Structures*, 41 (2004), 6505-6528.
8. Rahnejat, H. (1998). *Multi-body dynamics – Vehicles, Machines and Mechanisms*. Warrendale, Pa.: Society of Automotive Engineers, Inc.
9. Sigalov, G., Gendelman, O. V., Al-Shudeifat, M. A., Manevitch, L. I., Vakakis, A. F., and Bergman, L. A. Resonance captures and targeted energy transfers in an inertially-coupled rotational nonlinear energy sink. *Nonlinear Dynamics*, 69 (2012), 1693-1704.
10. Tsakirtzis, S., Kerschen, G., Panagopoulos, Panagiotis N., and Vakakis, Alexander F. Multi-frequency nonlinear energy transfer from linear oscillators to mdof essentially nonlinear attachments. *Journal of Sound and Vibration*, 285 (2005), 483-490.
11. Vakakis, A., Gendelman O. V., Bergman, L. A., McFarland, D. M., Kerschen, G., and Lee, Y. S. *Nonlinear Targeted Energy Transfer in Mechanical and Structural Systems*. Springer, 2008.
12. Vakakis, A. F., and Gendelman, O. V. Energy pumping in nonlinear mechanical oscillators: Part II – Resonance capture. *Journal of Applied Mechanics*, 68 (2001), 42-48.
13. Vakakis, A. F., Manevitch, L. I., Gendelman, O., and Bergman, L. Dynamics of linear discrete systems connected to local, essentially non-linear attachments. *Journal of Sound and Vibration*, 264 (2003), 559-577.
14. Viguie, R., Kerschen, G., Golinval, J.–C., McFarland, D. M., Bergman, L. A., Vakakis, A. F., Van de Wouw, N. Using passive nonlinear targeted energy transfer to stabilize drill-string systems. *Mechanical Systems and Signal Processing*, 23 (2009), 148-169.
15. Wedin, A., *Reduction of vibrations in engines using centrifugal pendulum vibration absorbers*. PhD thesis, Chalmers University of Technology, 2011.

Ahmed Haris, PhD student: Loughborough University, Wolfson School of Mechanical and Manufacturing Engineering. Loughborough. United Kingdom, LE11 3TU. *(a.haris@lboro.ac.uk).*
The author gave a presentation of this paper during one of the conference sessions

Eliot Motato. PhD. Research Associate: Loughborough University, Wolfson School of Mechanical and Manufacturing Engineering. Loughborough. United Kingdom, LE11 3TU. *(e.motato@lboro.ac.uk).*

Stephanos Theodossiades, Professor: Loughborough University, Wolfson School of Mechanical and Manufacturing Engineering. Loughborough. United Kingdom, LE11 3TU. *(s.theodossiades@lboro.ac.uk).*

Alex F. Vakakis, Professor: University of Illinois Urbana-Champaign, Department of Mechanical Science and Engineering. Urbana, IL 61801, USA *(avakakis@illinois.edu).*

Lawrence A. Bergman, Professor: University of Illinois Urbana-Champaign, Department of Aerospace Engineering, Urbana, IL 61801, USA *(lbergman@illinois.edu).*

D. Michael McFarland, Professor, University of Illinois Urbana-Champaign, Department of Aerospace Engineering, Urbana, IL 61801, USA *(dmmcf@illinois.edu).*

Ben Struve, M.Sc: Raicam Clutch, Driveline House, Leamington, CV31 3ER. *(b.struve@raicamclutch.com)*

.

# Dynamics simulations of spatial linkages using the LuGre friction model (MAT079-15)

Andrzej Harlecki, Andrzej Urbaś

*Abstract:* A method of dynamics analysis of a selected class of one-dof spatial linkages with one spherical joint in their structure was considered in the paper. These linkages contain neither redundant dof nor passive constraints. For the requirements of the method proposed here, the linkages are divided by using the cut-joint technique in the place of the spherical joint into two open-loop kinematic chains. The spherical joint is treated as ideal, while friction is present in the remaining kinds of connections of links, such as a revolute joint and a prismatic joint. The authors take into account both the pre-sliding displacements in the phases of static friction and the Stribeck effect in the phases of kinetic friction. The LuGre friction model, which is summarised by two first-order nonlinear differential equations, was used to model the friction. The first equation expresses the instantaneous friction coefficient as a function of the value of relative velocity in the joint considered and the average deflection of elastic bristles that are mentally taken into account in the joints modelled here. The second equation is an evolution equation for the average bristles' deflection. A spatial RUSP linkage was considered as an example of the analysis.

**Nomenclature**

$c$ – symbol of a chain

$(c, p)$ – symbol of link (joint) $p$ in chain $c$

$g$ – acceleration of gravity

$n_l^{(c)}$ – number of links in chain $c$

$l^{(c,p)}$ – length of link $p$ in chain $c$

$m^{(c,p)}$ – mass of link $p$ in chain $c$

$\tilde{\mathbf{r}}_{\alpha}^{(c,p)}\Big|_{\alpha\in\, C^{(c,p)},S}$ – vector of position of point $C^{(c,p)}$ or $S$ defined in the local coordinate system $\{c, p\}$ of link $(c, p)$

$\mathbf{H}^{(c,p)}$ – inertial matrix $4\times4$ of link $(c, p)$

$\tilde{\mathbf{T}}^{(c,p)}$ – transformation matrix $4\times4$ from local coordinate system $\{c, p\}$ of link $(c, p)$ to system $\{c, p-1\}$ of link $(c, p-1)$

$\mathbf{T}^{(c,p)}$ – transformation matrix $4\times4$ from local coordinate system $\{c,p\}$ of link $(c,p)$ to global reference system $\{1,0\}$

$$\mathbf{T}_i^{(c,p)}=\frac{\partial\mathbf{T}^{(c,p)}}{\partial q_i^{(c,p)}},\ \mathbf{T}_{i,j}^{(c,p)}=\frac{\partial^2\mathbf{T}^{(c,p)}}{\partial q_i^{(c,p)}\partial q_j^{(c,p)}}$$

dof – degree(s)-of-freedom

**Friction parameters**

$\mu_\alpha^{(c,p)}\big|_{\alpha\in A,B,C}$, $\mu^{(c,p)}$ – instantaneous friction coefficient in revolute joint $(c,p)$ and prismatic joint $(c,p)$, respectively

$\mu_{s,\alpha}^{(c,p)}\big|_{\alpha\in A,B,C}$, $\mu_s^{(c,p)}$ – static (limiting) friction coefficient (exactly – maximal value of the instantaneous friction coefficient)

$\mu_{k,\alpha}^{(c,p)}\big|_{\alpha\in A,B,C}$, $\mu_k^{(c,p)}$ – minimal value of the instantaneous friction coefficient

$\sigma_{0,\alpha}^{(c,p)}\big|_{\alpha\in A,B,C}$, $\sigma_0^{(c,p)}$ – stiffness coefficient of the bristles

$\sigma_{1,\alpha}^{(c,p)}\big|_{\alpha\in A,B,C}$, $\sigma_1^{(c,p)}$ – damping coefficient of the bristles

$\sigma_{2,\alpha}^{(c,p)}\big|_{\alpha\in A,B,C}$, $\sigma_2^{(c,p)}$ – viscous friction (damping) coefficient

$z_\alpha^{(c,p)}\big|_{\alpha\in A,B,C}$, $z^{(c,p)}$ – bristles' deflection

## 1. Introduction

This paper is devoted to a method of dynamics analysis of a selected class of spatial one-dof linkages containing one spherical joint in their structure. It was assumed that this spherical joint (providing three-dof) was treated as a frictionless joint, while friction could be taken into account in the remaining kinds of joints of the linkages (providing one-dof), i.e. in the revolute and prismatic joint. In the analysis, the authors took into account both the pre-sliding displacements [5], in phases of static friction occurring in these joints after reversals of relative velocities, and the Stribeck effect [13], in the phases of kinetic friction. In the method proposed here, linkages in the form of closed-loop kinematic chains are divided by using the cut-joint technique in the place of the spherical joint into two open-loop kinematic chains joined with the stationary base. Joint coordinates and homogeneous transformation matrices, defined according to the Denavit-Hartenberg notation [8], were used to describe the geometry of these chains. Equations of the chains' motion were derived using the formalism of Lagrange equations [11]. In order to determine unknown components of the joint forces

acting at the cut-joint, additional algebraic equations of geometrical constraints were introduced to complete the equations of motion. As a consequence, a set of differential-algebraic equations was obtained. In order to solve these equations, a procedure based on double differentiation of the constraints' equations in relation to time was applied. In the scope of the method presented here, models of a revolute joint and a prismatic joint were worked out. In order to determine the values of friction torque in a revolute joint and of friction force in a prismatic joint, in each integrating step of the equations of motion, the joint forces and joint torques acting at these joints were determined by using the recursive Newton-Euler algorithm [6].

## 2. Example of the analysis

The method described here was used to analyse a spatial one-dof RUSP linkage, as taken from paper [2], which includes revolute joint R, universal joint U (being a system of two revolute joints R), spherical joint S, and prismatic joint P. The driving link was loaded by the driving torque $\mathbf{t}_{dr}^{(1,1)}$ and the resistance torque $\mathbf{t}_{res}^{(1,1)}$ (Fig. 1a). In order to satisfy the requirements of the method presented here, the linkage was divided in the place of cut-joint S, and this resulted in obtaining two open-loop kinematic chains (Fig. 1b) joined with the stationary base: $1$ – formed by links $(1,1)$, $(1,2)$, $(1,3)$, and $2$ – formed only by link $(2,1)$.

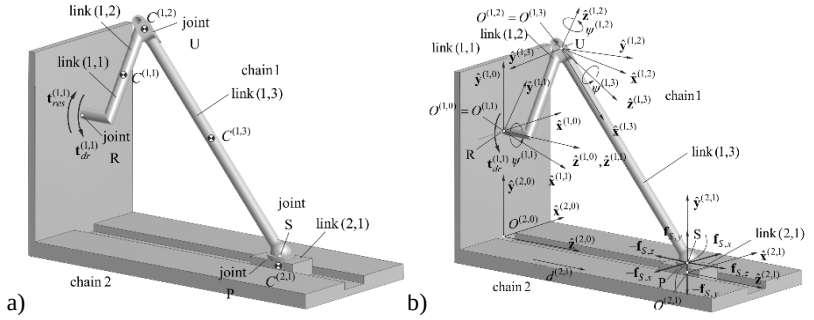


**Figure 1.** a) Spatial RUSP linkage, b) Joint forces acting at cut-joint S.

The motion of the chains was described by the joint (generalised) coordinates being the components of the vectors:

$$\mathbf{q}^{(c,n_l^{(c)})} = \left( q_j^{(c,n_l^{(c)})} \right)\Big|_{\substack{c=1, n_l^{(1)}=3,\ j=1,2,3 \\ c=2, n_l^{(2)}=1,\ j=1}} \tag{1}$$

So, for chain $1$: $\mathbf{q}^{(1,3)} = \left[ \psi^{(1,1)} \quad \psi^{(1,2)} \quad \psi^{(1,3)} \right]^T$, and for chain $2$: $\mathbf{q}^{(2,1)} = \left[ d^{(2,1)} \right]$.

The homogeneous transformation matrices from the local coordinate systems $\{c,p\}$ of links $(c,p)$ to the global reference system $\{1,0\}$ were determined according to the relationship:

$$\mathbf{T}^{(c,p)} = \mathbf{T}^{(c,p-1)}\tilde{\mathbf{T}}^{(c,p)}, \tag{2}$$

where $\mathbf{T}^{(c,0)} = \mathbf{I}$,

$$\tilde{\mathbf{T}}^{(1,1)} = \begin{bmatrix} \mathrm{c}\psi^{(1,1)} & -\mathrm{s}\psi^{(1,1)} & 0 & 0 \\ \mathrm{s}\psi^{(1,1)} & \mathrm{c}\psi^{(1,1)} & 0 & 0 \\ 0 & 0 & 1 & 0 \\ 0 & 0 & 0 & 1 \end{bmatrix}, \quad \tilde{\mathbf{T}}^{(1,2)} = \begin{bmatrix} \mathrm{c}\psi^{(1,2)} & -\mathrm{s}\psi^{(1,2)} & 0 & 0 \\ 0 & 0 & 1 & l^{(1,1)} \\ -\mathrm{s}\psi^{(1,2)} & -\mathrm{c}\psi^{(1,2)} & 0 & 0 \\ 0 & 0 & 0 & 1 \end{bmatrix},$$

$$\tilde{\mathbf{T}}^{(1,3)} = \begin{bmatrix} \mathrm{c}\psi^{(1,3)} & -\mathrm{s}\psi^{(1,3)} & 0 & 0 \\ 0 & 0 & 1 & 0 \\ -\mathrm{s}\psi^{(1,3)} & -\mathrm{c}\psi^{(1,3)} & 0 & 0 \\ 0 & 0 & 0 & 1 \end{bmatrix}, \quad \tilde{\mathbf{T}}^{(2,1)} = \begin{bmatrix} 1 & 0 & 0 & 0 \\ 0 & 1 & 0 & 0 \\ 0 & 0 & 1 & d^{(2,1)} \\ 0 & 0 & 0 & 1 \end{bmatrix},$$

$$\mathrm{c}\psi^{(\alpha,\beta)}\Big|_{\substack{\alpha\in\{1\}\\ \beta\in\{1,2,3\}}} = \cos\psi^{(\alpha,\beta)}\Big|_{\substack{\alpha\in\{1\}\\ \beta\in\{1,2,3\}}}, \ \mathrm{s}\psi^{(\alpha,\beta)}\Big|_{\substack{\alpha\in\{1\}\\ \beta\in\{1,2,3\}}} = \sin\psi^{(\alpha,\beta)}\Big|_{\substack{\alpha\in\{1\}\\ \beta\in\{1,2,3\}}}.$$

The joint forces $\mathbf{f}_{S,x}$, $\mathbf{f}_{S,y}$, $\mathbf{f}_{S,z}$ and $-\mathbf{f}_{S,x}$, $-\mathbf{f}_{S,y}$, $-\mathbf{f}_{S,z}$, acting on chains $1$ and $2$, respectively, in accordance with the versors' directions of the global reference system $\{1,0\}$, were applied at cut-joint S (precisely – at the centre of $S$ of this joint).

## 3. Equations of motion

The equations of motion of both open-loop kinematic chains can be presented in the following form:

$$\begin{bmatrix} \mathbf{A}^{(1,3)} & \mathbf{0} & -\mathbf{D}^{(1,3)} \\ \mathbf{0} & \mathbf{A}^{(2,1)} & \mathbf{D}^{(2,1)} \\ \mathbf{D}^{(1,3)^T} & -\mathbf{D}^{(2,1)^T} & \mathbf{0} \end{bmatrix} \begin{bmatrix} \ddot{\mathbf{q}}^{(1,3)} \\ \ddot{\mathbf{q}}^{(2,1)} \\ \mathbf{f}_S \end{bmatrix} = \begin{bmatrix} \mathbf{e}^{(1,3)} + \mathbf{t}_{dr}^{(1,3)} - \mathbf{t}_{res}^{(1,3)} - \mathbf{s}_f^{(1,3)} \\ \mathbf{e}^{(2,1)} - \mathbf{s}_f^{(2,1)} \\ \mathbf{c}^{(1,2)} \end{bmatrix}, \tag{3}$$

where: $\mathbf{A}^{(c,n_l^{(c)})} = \left( \mathbf{A}^{(c,n_l^{(c)})}{}_{i,j} \right)_{i,j=1,\ldots,n_l^{(c)}}$, $\mathbf{A}^{(c,n_l^{(c)})}{}_{i,j} = \sum_{p=\max i,j}^{n_l^{(c)}} \mathrm{tr}\ \mathbf{T}_i^{(c,p)}\mathbf{H}^{(c,p)}\mathbf{T}_j^{(c,p)^T}$,

$\mathbf{e}^{(c,n_l^{(c)})} = \left( \mathbf{e}^{(c,n_l^{(c)})}{}_k \right)_{k=1,\ldots,n_l^{(c)}}$, $\mathbf{e}^{(c,n_l^{(c)})}{}_k = \sum_{p=k}^{n_l^{(c)}} \left[ -h_k^{(c,p)} - g_k^{(c,p)} \right]$,

$$h_k^{(c,p)} = \sum_{i,j=1}^{p} \text{tr}\ \ \mathbf{T}_k^{(c,p)} \mathbf{H}^{(c,p)} \mathbf{T}_{i,j}^{(c,p)^T}\ \ \dot{q}_i^{(c,p)} \dot{q}_j^{(c,p)},\ \ g_k^{(c,p)} = m^{(c,p)} g\, \mathbf{j}_2 \mathbf{T}_k^{(c,p)} \tilde{\mathbf{r}}_{C^{(c,p)}}^{(c,p)},$$

$$\mathbf{t}_{dr}^{(1,3)} = \begin{bmatrix} t_{dr}^{(1,1)} & 0 & 0 \end{bmatrix},\ \mathbf{t}_{res}^{(1,3)} = \begin{bmatrix} t_{res}^{(1,1)} & 0 & 0 \end{bmatrix},$$

$$\mathbf{s}_f^{(1,3)} = \begin{bmatrix} t_f^{(1,1)} & t_f^{(1,2)} & t_f^{(1,3)} \end{bmatrix}^T,\ \mathbf{s}_f^{(2,1)} = \begin{bmatrix} f_f^{(2,1)} \end{bmatrix},\ \mathbf{f}_S = \begin{bmatrix} f_{S,x} & f_{S,y} & f_{S,z} \end{bmatrix}^T,$$

$$\mathbf{D}^{(c,n_l^{(c)})^T} = \mathbf{J} \begin{bmatrix} \mathbf{T}_1^{(c,n_l^{(c)})} \tilde{\mathbf{r}}_S^{(c,n_l^{(c)})} & \cdots & \mathbf{T}_{n_l^{(c)}}^{(c,n_l^{(c)})} \tilde{\mathbf{r}}_S^{(c,n_l^{(c)})} \end{bmatrix},$$

$$\mathbf{c}^{(1,2)} = \mathbf{J} \left[ \left( \sum_{i,j=1}^{n_l^{(2)}} \mathbf{T}_{i,j}^{(2,1)} \dot{q}_i^{(2,1)} \dot{q}_j^{(2,1)} \right) \tilde{\mathbf{r}}_S^{(2,1)} - \left( \sum_{i,j=1}^{n_l^{(1)}} \mathbf{T}_{i,j}^{(1,3)} \dot{q}_i^{(1,3)} \dot{q}_j^{(1,3)} \right) \tilde{\mathbf{r}}_S^{(1,3)} \right],\ \mathbf{J} = \left[ \begin{array}{cccc} 1 & 0 & 0 & 0 \\ \hline 0 & 1 & 0 & 0 \\ \hline 0 & 0 & 1 & 0 \end{array} \right] = \begin{bmatrix} \mathbf{j}_1 \\ \mathbf{j}_2 \\ \mathbf{j}_3 \end{bmatrix}.$$

In order to compute the values of kinetic friction torques in revolute joints and the kinetic friction force in the prismatic joint of the linkage, models of such kinds of joints were worked out (Figs. 2 and 3, respectively).

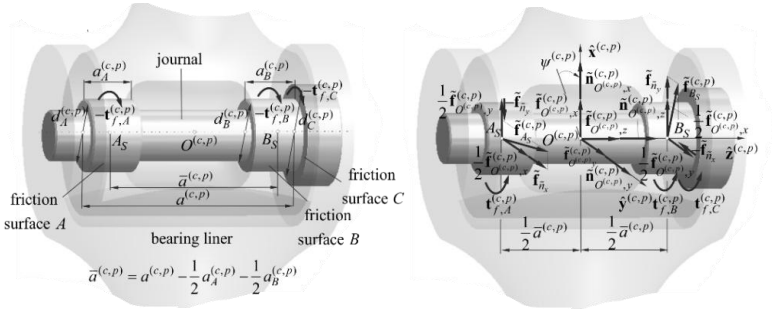


**Figure 2.** Model of a revolute joint.

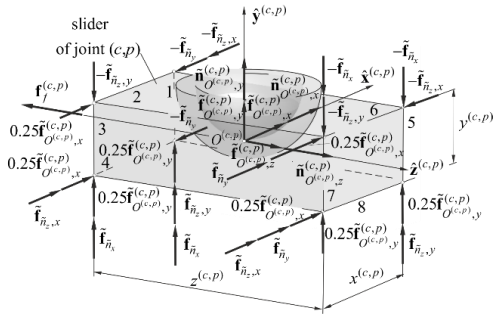


**Figure 3.** Model of a prismatic joint.

The values of the kinetic friction torques in the revolute joints $(c, p)$ were calculated as the following sum of values of kinetic friction torques acting on rotational surfaces *A* and *B* and face surface *C* of the journals (bearing liners):

$$t_f^{(c,p)} = t_{f,A}^{(c,p)} + t_{f,B}^{(c,p)} + t_{f,C}^{(c,p)}, \tag{4}$$

where $t_{f,A}^{(c,p)} = \frac{1}{2}\mu_A^{(c,p)} \tilde{f}_{A_S}^{(c,p)} d_A^{(c,p)}$, $t_{f,B}^{(c,p)} = \frac{1}{2}\mu_B^{(c,p)} \tilde{f}_{B_S}^{(c,p)} d_B^{(c,p)}$,

$t_{f,C}^{(c,p)} = \frac{1}{3}\mu_C^{(c,p)} \left| \tilde{f}_{O^{(c,p)},z}^{(c,p)} \right| \frac{d_C^{(c,p)^3} - d_A^{(c,p)^3}}{d_C^{(c,p)^2} - d_A^{(c,p)^2}}$ (this formula was taken from paper [12]),

$\tilde{f}_{A_S}^{(c,p)} = \sqrt{\left(\frac{1}{2}\tilde{f}_{O^{(c,p)},x}^{(c,p)} - \tilde{f}_{\tilde{n}_y}\right)^2 + \left(\frac{1}{2}\tilde{f}_{O^{(c,p)},y}^{(c,p)} + \tilde{f}_{\tilde{n}_x}\right)^2}$, $\tilde{f}_{B_S}^{(c,p)} = \sqrt{\left(\frac{1}{2}\tilde{f}_{O^{(c,p)},x}^{(c,p)} + \tilde{f}_{\tilde{n}_y}\right)^2 + \left(\frac{1}{2}\tilde{f}_{O^{(c,p)},y}^{(c,p)} - \tilde{f}_{\tilde{n}_x}\right)^2}$,

$\tilde{f}_{\tilde{n}_x} = \frac{\tilde{n}_{O^{(c,p)},x}^{(c,p)}}{\bar{a}^{(c,p)}}$, $\tilde{f}_{\tilde{n}_y} = \frac{\tilde{n}_{O^{(c,p)},y}^{(c,p)}}{\bar{a}^{(c,p)}}$ and $\tilde{f}_{O^{(c,p)},x}^{(c,p)}$, $\tilde{f}_{O^{(c,p)},y}^{(c,p)}$, $\tilde{f}_{O^{(c,p)},z}^{(c,p)}$, $\tilde{n}_{O^{(c,p)},x}^{(c,p)}$, $\tilde{n}_{O^{(c,p)},y}^{(c,p)}$ – components of joint force $\tilde{\mathbf{f}}_{O^{(c,p)}}^{(c,p)}$ and joint torque $\tilde{\mathbf{n}}_{O^{(c,p)}}^{(c,p)}$ at revolute joint $(c,p)$, respectively.

The value of the kinetic friction force acting on the slider of prismatic joint $(c,p)$ was calculated according to the following formula:

$$f_f^{(c,p)} = \mu^{(c,p)} \tilde{f}^{(c,p)}, \tag{5}$$

where: $\tilde{f}^{(c,p)} = \sum_{i=1}^{8} \tilde{f}_i^{(c,p)}$,

$\tilde{f}_i^{(c,p)}$ – values of normal reaction forces acting on the slider along its edges, and so

$\tilde{f}_1^{(c,p)} = \left|\frac{1}{4}\tilde{f}_{O^{(c,p)},y}^{(c,p)} + \tilde{f}_{\tilde{n}_x} + \tilde{f}_{\tilde{n}_z,y}\right|$, $\tilde{f}_2^{(c,p)} = \left|\frac{1}{4}\tilde{f}_{O^{(c,p)},x}^{(c,p)} - \tilde{f}_{\tilde{n}_y} - \tilde{f}_{\tilde{n}_z,x}\right|$,

$\tilde{f}_3^{(c,p)} = \left|\frac{1}{4}\tilde{f}_{O^{(c,p)},y}^{(c,p)} + \tilde{f}_{\tilde{n}_x} - \tilde{f}_{\tilde{n}_z,y}\right|$, $\tilde{f}_4^{(c,p)} = \left|\frac{1}{4}\tilde{f}_{O^{(c,p)},x}^{(c,p)} - \tilde{f}_{\tilde{n}_y} + \tilde{f}_{\tilde{n}_z,x}\right|$,

$\tilde{f}_5^{(c,p)} = \left|\frac{1}{4}\tilde{f}_{O^{(c,p)},y}^{(c,p)} - \tilde{f}_{\tilde{n}_x} + \tilde{f}_{\tilde{n}_z,y}\right|$, $\tilde{f}_6^{(c,p)} = \left|\frac{1}{4}\tilde{f}_{O^{(c,p)},x}^{(c,p)} + \tilde{f}_{\tilde{n}_y} - \tilde{f}_{\tilde{n}_z,x}\right|$,

$\tilde{f}_7^{(c,p)} = \left|\frac{1}{4}\tilde{f}_{O^{(c,p)},y}^{(c,p)} - \tilde{f}_{\tilde{n}_x} - \tilde{f}_{\tilde{n}_z,y}\right|$, $\tilde{f}_8^{(c,p)} = \left|\frac{1}{4}\tilde{f}_{O^{(c,p)},x}^{(c,p)} + \tilde{f}_{\tilde{n}_y} + \tilde{f}_{\tilde{n}_z,x}\right|$,

$\tilde{f}_{\tilde{n}_x} = \frac{1}{2}\frac{\tilde{n}_{O^{(c,p)},x}^{(c,p)}}{z^{(c,p)}}$, $\tilde{f}_{\tilde{n}_y} = \frac{1}{2}\frac{\tilde{n}_{O^{(c,p)},y}^{(c,p)}}{z^{(c,p)}}$, $\tilde{f}_{\tilde{n}_z,x} = \frac{1}{2}\frac{y^{(c,p)}}{x^{(c,p)^2} + y^{(c,p)^2}}\tilde{n}_{O^{(c,p)},z}^{(c,p)}$,

$\tilde{f}_{\tilde{n}_z,y} = \frac{1}{2}\frac{x^{(c,p)}}{x^{(c,p)^2} + y^{(c,p)^2}}\tilde{n}_{O^{(c,p)},z}^{(c,p)}$ and $\tilde{f}_{O^{(c,p)},x}^{(c,p)}$, $\tilde{f}_{O^{(c,p)},y}^{(c,p)}$, $\tilde{n}_{O^{(c,p)},x}^{(c,p)}$, $\tilde{n}_{O^{(c,p)},y}^{(c,p)}$, $\tilde{n}_{O^{(c,p)},z}^{(c,p)}$ – components of joint force $\tilde{\mathbf{f}}_{O^{(c,p)}}^{(c,p)}$ and joint torque $\tilde{\mathbf{n}}_{O^{(c,p)}}^{(c,p)}$ at prismatic joint $(c,p)$, respectively.

## 4. LuGre friction model

The LuGre model is a dynamic friction model that was developed by the authors of paper [4]. The value of relative velocity between the bodies in contact is the input and the value of the friction force/torque (instantaneous friction coefficient) is the output. It can also be seen as an extension of the Dahl friction model [7], which allows to model pre-sliding displacements and, as a result, rising friction forces/torques (instantaneous friction coefficients) in static friction phases. The LuGre friction model has become widespread because it incorporates many of the observed features of frictional behaviour. As compared to the Dahl model, this model can take into account the Stribeck effect [13], which exhibits a negative derivative with respect to slip velocity for small values of this velocity. This is one of the key features of friction that contributes to limit-cycles (often these are of a stick-slip character, i.e. motion alters between the zero value of velocity and the non-zero value). The surfaces of bodies are very irregular at the microscopic level; and two surfaces, therefore, make contact at various asperities. According to paper [9], the asperities' junctions of the facing surfaces behave like bristles in contact (Fig. 4a). In this figure, for simplicity's sake, the bristles on the stationary surface are shown as being rigid. The friction force contributed by each bristle is assumed to be proportional to the strain on this bristle. When a tangential force is applied to the sliding body, its bristles will deflect as springs (with a stiffness coefficient $\sigma_0$ and a damping coefficient $\sigma_1$). When the strain of any particular bristle exceeds a certain level, then the bond is broken and the bristles start to slip. The friction force between the two surfaces is assumed to be caused by a large number of bristles extending from each surface. Due to the irregular shape of the surfaces, contact phenomena are highly random. Therefore, the LuGre friction model is based on the average deflection $z$ of the bristles that make up the contact (Fig. 4b). The average bristles' deflection is determined by the slip velocity. As this velocity increases, the number of bristles in contact progressively decreases. Therefore, the value of the friction force between both bodies decreases along with an increasing slip velocity. This models the Stribeck effect.

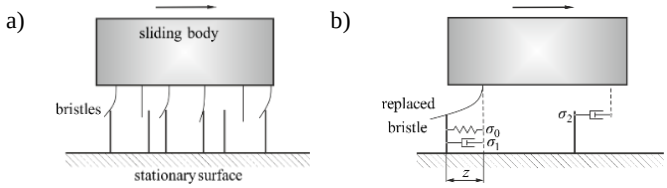


**Figure 4.** a) Bristle interpretation of friction, b) The LuGre model as an averaged description of the bristles' behaviour.

By averaging numerous individual interactions, the bulk phenomenon can be described by a simple model which has the form of two first-order nonlinear differential equations (the second equation for these is an evolution equation for the average bristle deflection):

$$\mu\Big|_{\substack{\mu=\mu_{\alpha}^{(c,p)}\Big|_{\alpha\in\{A,B,C\}} \\ \mu=\mu^{(c,p)}}} = \sigma_0 z + \sigma_1 \dot{z} + f\left(\dot{q}_j^{(c,n_l^{(c)})}\right)\Bigg|_{\substack{\sigma_i=\sigma_{i,\alpha}^{(c,p)}\Big|_{i\in\{0,1\}},\, z=z_{\alpha}^{(c,p)}\Big|_{\alpha\in\{A,B,C\}} \\ \sigma_i=\sigma_i^{(c,p)}\Big|_{i\in\{0,1\}},\, z=z^{(c,p)}}}, \tag{6.1}$$

$$\dot{z} = \dot{q}_j^{(c,n_l^{(c)})} - \frac{\sigma_0 \left|\dot{q}_j^{(c,n_l^{(c)})}\right|}{g\ \dot{q}_j^{(c,n_l^{(c)})}} z\ . \tag{6.2}$$

Function $f\left(\dot{q}_j^{(c,n_l^{(c)})}\right)$ represents viscous friction:

$$f\left(\dot{q}_j^{(c,n_l^{(c)})}\right) = \sigma_2\, \dot{q}_j^{(c,n_l^{(c)})}\Big|_{\substack{\sigma_2=\sigma_{2,\alpha}^{(c,p)}\Big|_{\alpha\in\{A,B,C\}} \\ \sigma_2=\sigma_2^{(c,p)}}}\ . \tag{7}$$

According to need, this function can also be assumed to be nonlinear.

Function $g\left(\dot{q}_j^{(c,n_l^{(c)})}\right)$ models the course of instantaneous friction coefficient $\mu$ in accordance with the generalised velocity $\dot{q}_j^{(c,n_l^{(c)})}$ (in other words – this function models the Stribeck effect). In this paper, the customarily used form of this function was assumed, i.e. as proposed by the authors of paper [3] and as presented in Fig. 5:

$$g\ \dot{q}_j^{(c,n_l^{(c)})} = \mu_k + \left(\mu_s - \mu_k\right) e^{-\left|\dot{q}_j^{(c,n_l^{(c)})}/\dot{q}_{s,j}^{(c,n_l^{(c)})}\right|^{\gamma}}\Bigg|_{\substack{\mu_s=\mu_{s,\alpha}^{(c,p)},\mu_k=\mu_{k,\alpha}^{(c,p)}\Big|_{\alpha\in\ A,B,C} \\ \mu_s=\mu_s^{(c,p)},\mu_k=\mu_k^{(c,p)}}}\ . \tag{8}$$

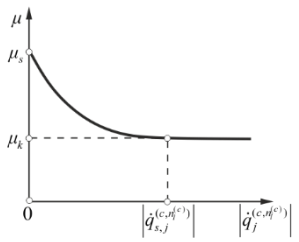


**Figure 5.** Stribeck curve.

It was assumed, according to paper [1], that the empirical parameter $\gamma = 2$ . According to the findings presented in this paper, other, i.e. either smaller or larger, values of this parameter can also be assumed.

## 5. Results of the calculations

The initial configuration of the linkage and its geometrical parameters are specified in Fig. 6, however, the parameters concerning friction modelling are presented in Tab. 1.

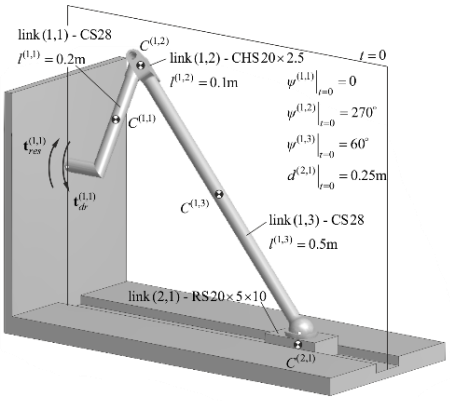


**Figure 6.** Initial configuration and geometrical parameters of the linkage.

**Table 1.** Friction parameters.

| joint $(c, p)$ | (1,1) | (1,2) | (1,3) | (2,1) |
|---|---|---|---|---|
| $\mu_{s,\alpha}^{(c,p)}\big\|_{\alpha\in A,B,C}$<br>$\mu_s^{(c,p)}$ | 0.2 | 0.2 | 0.2 | 0.2 |
| $\mu_{k,\alpha}^{(c,p)}\big\|_{\alpha\in A,B,C}$<br>$\mu_k^{(c,p)}$ | 0.1 | 0.1 | 0.1 | 0.1 |
| $\sigma_{0,\alpha}^{(c,p)}\big\|_{\alpha\in A,B,C}$ [Nmrad$^{-1}$]<br>$\sigma_0^{(c,p)}$[Nm$^{-1}$] | $10^2$ | $10^2$ | $10^2$ | $10^3$ |
| $\sigma_{1,\alpha}^{(c,p)}\big\|_{\alpha\in A,B,C}$ [Nmsrad$^{-1}$]<br>$\sigma_1^{(c,p)}$[Nsm$^{-1}$] | 0.5 | 0.5 | 0.5 | 5 |
| $\sigma_{2,\alpha}^{(c,p)}\big\|_{\alpha\in A,B,C}$ [Nmsrad$^{-1}$]<br>$\sigma_2^{(c,p)}$[Nsm$^{-1}$] | 0 | 0 | 0 | 0 |
| $\dot{\psi}_s^{(c,p)}\left[\text{rads}^{-1}\right]$<br>$\dot{d}_s^{(c,p)}$[ms$^{-1}$] | 1 | 1 | 1 | 0.1 |
| $\gamma$ | 2 | 2 | 2 | 2 |

The assumed courses of the value of the driving torque $t_{dr}^{(1,1)}$ and the resistance torque $t_{res}^{(1,1)}$ reduced to the axis of the joint connecting link $(1,1)$ with the stationary base are presented in Figs. 7a and 7b, respectively.

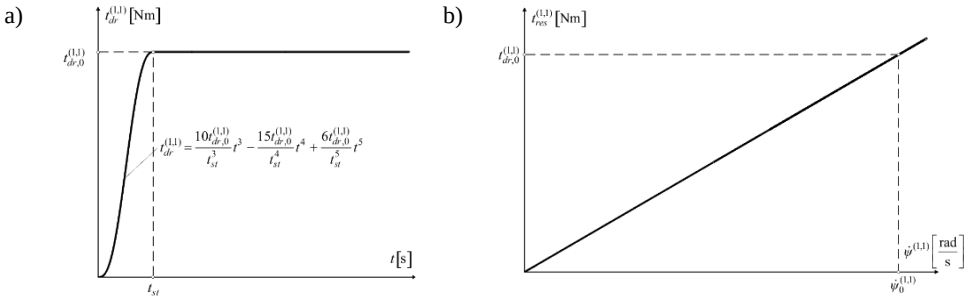


**Figure 7.** Course of: a) the driving torque, b) the resistance torque.

Examples of determined courses of instantaneous friction coefficients in particular joints of linkages, expressed as functions of generalised velocities, are presented in Fig. 8.

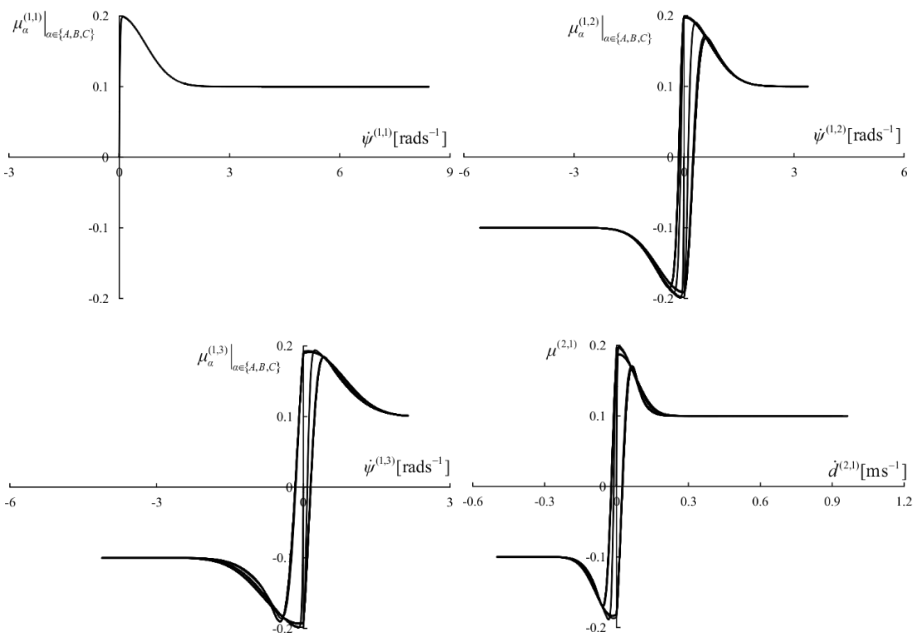


**Figure 8.** Courses of instantaneous friction coefficients in the joints of the linkage.

The parts referring to pre-sliding regimes and gross-sliding regimes can be detailed in each course. This second part has the form of the Stribeck curve. By analysing the plots we can observe that their parts, referring to the phases of accelerations, are slightly different from the parts determined for the

phases of decelerations. That is a consequence of the fact that the LuGre friction model also allows to consider the effect of frictional lag (frictional memory) both in the phases of kinetic and static friction (the courses determined take the form of loops of hysteresis) [10].

The courses of the components of joint forces acting at cut-joint S are presented in Fig. 9.

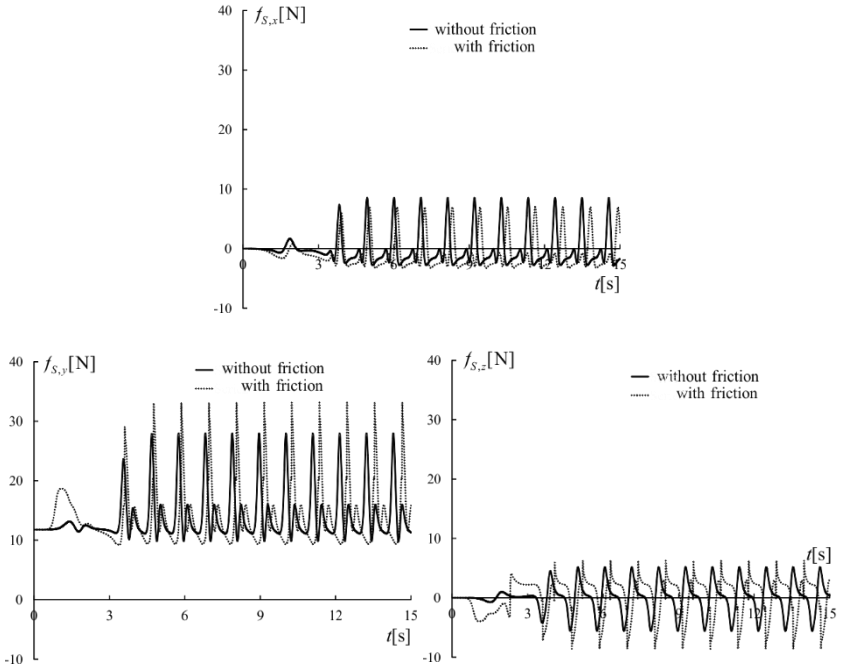


**Figure 9.** Courses of components of joint forces acting at cut-joint S.

As can be seen, friction in the joints caused a change of the components' courses of joint forces, thus resulting in their slight delay as compared with these forces' courses as determined by taking into account ideal joints. The friction also caused a noticeable increase of the components determined here.

## 6. Conclusions

Tribological investigations that have been conducted in that past few decades have proved that the phenomenon of friction shows a continuous nature. This means that the transition from static friction (apparent rest) phases to kinetic friction (gross-sliding) phases is smooth (unnoticeable). The advantage of the LuGre friction model is that both of these phases are described by the same simple mathematical model. As the courses of instantaneous friction coefficients presented here show, this model allows to take into account principle friction phenomena such as pre-sliding displacement, the Stribeck effect and also frictional lag. These phenomena are of interest in machine dynamics and in

control problems, and the LuGre friction model can be readily used in the simulation of mechanical systems, including primarily robots' manipulators and also spatial linkages.

**References**


[1] Armstrong-Hélouvry, B., *Control of machines with friction.* Kluwer Academic Publishers, Boston/Dordrecht/London, 1991.

[2] Bauchau, O.A., and Ju, C., Modelling friction phenomena in flexible multibody dynamics. *Computer Methods in Applied Mechanics and Engineering*, 195, (2006), 6909-6924.

[3] Bo, L.C., and Pavelescu D., The friction-speed relation and its influence on the critical velocity of stick-slip motion. *Wear*, 82, (1982), 277-289.

[4] Canudas de Wit, C., Olsson, H., Åström, K.J., and Lischinsky P., A new model for control of systems with friction. *IEEE Transactions on Automatic Control*, 40, 3, (1995).

[5] Courtney-Pratt, J.S., and Eisner E., The effect of a tangential force on the contact of metallic bodies. *Proc. R. Soc*., Ser. A, (1957), 529-550.

[6] Craig, J.J., *Introduction to robotics. Mechanics and control*. Addison-Wesley Publishing Company, Inc., 1989, 1986.

[7] Dahl, R., A solid friction model, Aerospace Corp. El Sequndo, CA, USA, Tech. Rep. TOR-0158(3107-18)-1, 1968.

[8] Denavit, J., and Hartenberg, R.S., A kinematic notation for lower-pair mechanisms based on matrices, *Journal of Applied Mechanics*, June, (1955).

[9] Haessig, D.A., and Friedland, B., On the modeling and simulation of friction, *Journal of Dynamical Systems, Measurements and Control Trans. of ASME*, 113, September, (1991).

[10] Hess, D.P., and Soom, A., Friction at a lubricated line contact operating at oscillating sliding velocities. *Journal of Tribology Trans. of ASME*, 112, (1990), 147-152.

[11] Jurevič, E.I. (ed.), *Dynamics of robot control*, Nauka, Moscow, 1984, (in Russian).

[12] Koževnikov, S.N., *Theory of mechanisms and machines*, Mašinostroenije, Moscow, 1969, (in Russian).

[13] Stribeck, R., Die wesentlichen Eigenschaften der Gleit- und Rollenlager, Zeitschrift des Vereines Deutscher Ingenieure, 46, 36, 1902.



Andrzej Harlecki, Prof.: University of Bielsko-Biala, Department of Mechanics, Bielsko-Biala, 43-309, Poland, (*aharlecki@ath.eu*). The author gave a presentation of this paper during one of the conference sessions.

Andrzej Urbaś, Ph.D.: University of Bielsko-Biala, Department of Mechanics, Bielsko-Biala, 43-309, Poland, (*aurbas@ath.eu*).

# Modeling and simulation of ecosystems on the base of "prey-predator" model of system dynamics type – sensitivity analysis, calibration and gaming (MAT046-15)

Elżbieta Kasperska, Andrzej Kasperski, Tomasz Bajon, Rafał Marjasz

*Abstract:* The aim of this paper is to present some new results of authors investigation in the area of modeling and simulation of ecosystems on the base of some SD type model. Authors decided to present the structure of the model Prey – Predator, and the results of simulation type sensitivity analysis and optimization, which are analyzed in the context of solving managerial problems of such ecosystems. We use the possibilities of visualization of simulation that are given by simulation language Vensim, and we try to apply so called calibration to detect the conditions, that stabilized that ecosystem and, what is quite new, build the simulation game on base of that model to examine different scenarios of the human intervention in that ecosystem. At the end some conclusions are formulated.

## 1. Introduction

Ecosystems are the complex, dynamical, nonlinear and multilevel systems that should be analyzed, modeled, and simulated by appropriate methods and tools. One of such method - System Dynamics [1-4,7-15] - was developed in the late 1950's and early 1960's at the Massachusetts Institute of Technology's Sloan School of Management by Jay W. Forrester. The approach can be applied to dynamics problems arising in complex social, managerial, economic or ecological systems. The main purpose of System Dynamics is to try to discover the structure that conditions the observed behavior of the system over time. System Dynamics try to pose dynamic hypotheses that endogenously describe the observed behavior of system.

The problem of managing of ecosystems is in the center of interest for observers of contemporary changes in the surrounding world. The methods of analysis and modeling of changes should be interdisciplinary, connecting such disciplines like ecology, economy, mathematics and informatics. Achievement of sustained development or opposing the effects of climate changing in nature or the disturbed relationships type: prey-predator, all of this requires from the decision makers the ability of prognostic looking into the future. The effects of the human activities are long-wave in time and space and sometimes unintuitive.

In the complex systems, like ecosystems, there are many feedbacks, thus the dynamic behavior is a result of co-operation of those positive and negative loops. Like we already said, System Dynamics

method is the appropriate tool for modeling and simulating such ecosystems. Many authors [1,5,6,16,17] have undertaken this problem, but in the literature of this field we have lack of the papers connecting the simulation with the optimization [10-13]. Such connection gives new opportunities for the analysis of decision making problems in ecosystems, and because of this we have undertaken this problem in our paper.

The object of experiments is described in the literature of this field [3]. The structure of Prey-Predator model in Vensim [18 - 19] convention is presented on figure 1.

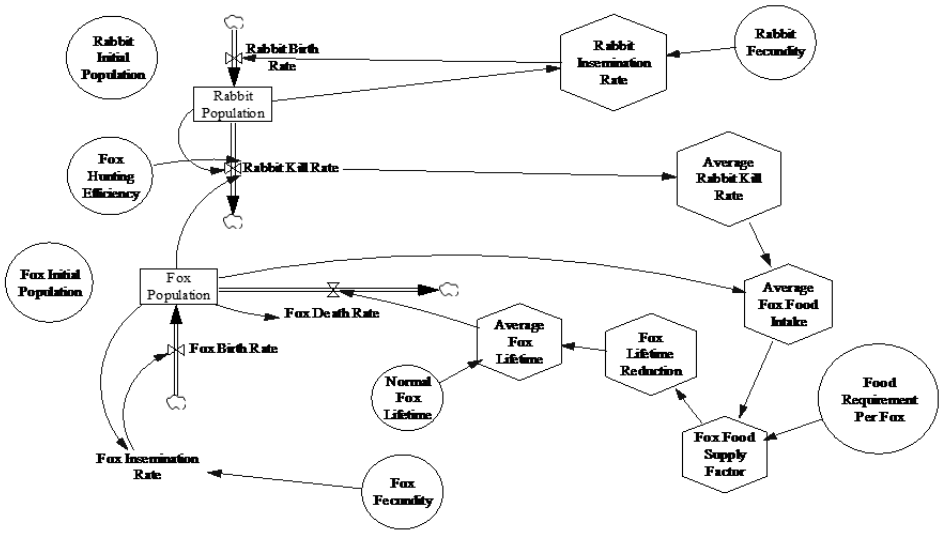


**Figure 1.** Structure of Predator – Prey Model in simulation Language Vensim (source: own idea on the base of Coyle 1996).

A list of model variables and equations is presented below:

$$Food\ Requirement\ Per\ Fox - FRPF = 5, \tag{1}$$

$$Fox\ \ Fecundity - FF = 0.05, \tag{2}$$

$$Fox\ \ Initial\ Population - FIP = 20, \tag{3}$$

$$Normal\ \ Fox\ \ Life - NFL = 120, \tag{4}$$

$$Average\ \ Fox\ Food\ Intake - AFFI(t) = ARKR(t)/FP\ (t), \tag{5}$$

$$Average\ \ Fox\ \ Lifetime - AFL(t) = NFL(t)*FLR\,(t), \tag{6}$$

$$Fox\ \ Birth\ \ Rate - \ FBR(t) = DELAY3(FIR(t),\ 7\ ), \tag{7}$$

$$Fox\ \ Death\ \ Rate - FDR(t) = FP(t)/(AFL\ (t)+1), \tag{8}$$

$$Fox\ Food\ \ Supply\ \ Factor - FFSF(t) = AFFI(t)/\ F\ RPF(t), \tag{9}$$

$$Fox\ Insemination\ Rate - FIR(t) = FF*FP(t), \tag{10}$$

$$Fox\ Lifetime\ Reduction - FLR(t) = WITH\ \ LOOKUP(FFS\ F(t)), \tag{11}$$

$$Fox\ Population - FP(t+dt) = FP(t)+dt*(FBR(t)-FDR\ (t)), \tag{12}$$

$$Rabbit\ Initial\ Population - RIP = 300, \tag{13}$$

$$Rabbit\ Insemination\ Rate - RIR(t) = RF*RP(t), \tag{14}$$

$$Rabbit\ Birth\ Rate - RBR(t) = DELAY3(RIR(t),\ 4), \tag{15}$$

$$Rabbit\ Population - RP(t+dt) = RP(t)+RBR(\ t)-RKR(t), \tag{16}$$

$$Rabbit\ Kill\ Rate - RKR(t) = FHE*RP(t)*FP(t), \tag{17}$$

$$Average\ \ Rabbit\ \ Kill\ Rate - ARKR(t+d\ t) = SMOOTH(RKR(t),\ 2), \tag{18}$$

$$Rabbit\ Fecundity - RF = 0.1, \tag{19}$$

$$Fox\ Hunting\ Efficiency\ - FHE = 0.005, \tag{20}$$

Like professor Coyle said: “the dynamics of the relationship between two populations of animals, one of which preys upon the other, is of great interest in ecological thinking and has been a fruitful area for analysis. One topic has been the academic need to understand why populations of animals undergo extreme fluctuations; another has been to suggest politics by which populations might be managed for economic reason or to preserve threatened species”. In the paper of professor Coyle [3], the mutual influences between populations of rabbits and foxes were modeled. Using the model of rabbits – foxes, we have conducted many types of experiments including sensitivity analysis, calibration, and gaming. Those features (included in Vensim) weren’t available for prof. Coyle in his times.

## 2. Experimental procedures

The SD models contain usually many parameters. It is interesting to examine the effect of their variation on simulation output. We select some parameters and assign maximum and minimum values along with a random distribution over which to vary them to see their impact on model behavior.

Vensim has a method of setting up such sensitivity simulation. Monte Carlo multivariate sensitivity works by sampling a set of numbers from within bounded domains. To perform one multivariate test, the distribution for each parameter specified is sampled, and the resulting values used in a simulation. When the number of simulation is set, for example, at 200, this process will be repeated 200 times.

In order to do sensitivity simulation you need to define what kind of probability distribution

values for each parameter will be drawn from. The simplest distribution is the Random Uniform Distribution, in which any number between the minimum and maximum values is equally likely to occur. The Random Uniform Distribution is suitable for most sensitivity testing and is selected by default. Another commonly used distribution is the Normal Distribution (or Bell Curve) in which value near the mean is more likely to occur that values far from the mean. Results of sensitivity testing can be displayed in different formats. Time graphs display behavior of a variable over a period of time and are displayed either in terms of confidence bounds or a separate values which combine to form an individual simulation traces.

The second type of experiments we performed, was so called calibration, which is a type of optimization. Optimization can be used to validate and estimate parameters(calibration), or to select among alternative policies(policy optimization).

In order to use optimization, you will need to define what is good and what is bad – it's called the payoff. The payoff is a measure, reported at the end of the simulation, stating numerically how good the simulation was. The payoff collapses your entire model, over the entire time it was simulated, into a single number. After defining the payoff, you need to select which constants will vary in order to maximize the payoff. Validation of a model relies in part on comparing the model behavior to time data string collected in the "real world". When a model is structurally completed and simulated properly, calibration of the model can proceed. Calibration involves finding the values of model constants that make the model generate behavior curves that best fit to real world data. It is possible to manually alter model constants, to try to achieve a better fit between the real world data and simulation output. For a complex model with many constants to optimize and many variables of data sets to fit, the process is very time consuming. Using optimization, Vensim will automatically vary the constants of your choice and look for the best fit between the simulation output and your real world data.

The third type of experiments we have performed was so called gaming. What are games in System Dynamics? Games are a way of actively engaging in process of a simulation. Games are examples of the "flight simulator" approach, where the user participate in the decisions that affect the simulation outcome for each step in time. A Vensim simulation model can be run as a game by stepping through time and making changes to gaming variables along the way. In contrast, a normal simulation model runs through the complete time span based on the initial setup of the model.

The base assumptions of our three types of experiments are as follow:

$$dt - simulation\ step\ (0.125[week]), \tag{21}$$

$$t_0 - simulation\ start\ time\ (0[week]), \tag{22}$$

$$t_H - simulation\ \ end\ \ time\ (300[\ week\ ]), \tag{23}$$

*Rabbits Initial Population – 300 [Rabbits],* (24)

*Fox Initial Population – 20 [Fox],* (25)

Like In the next section of this paper we present the results of some experiments types: sensitivity analysis, calibration and gaming.

## 3. Results

We performed several sensitivity analysis experiments and as a result we can see, that initial values of both population have great influences on the behavior of the model (see: figure 2, 3, 4, 5). The question is: how to stabilize the ecosystem? The model is "closed". The dynamics arise entirely from the structure, initial conditions and parameter values(usually including sharp non-linearities). How the system might be managed by the human intervention? For instance, foxes might have to be culled, and wild rabbits are the delicious food. We have performed some calibration type experiments, to solve the problem of choosing the initial values of populations.

The results are presented in table below.

**Table 1** Results of Calibration on Prey-Predator model (searching the condition for equilibrium state of the system)

| Assumptions for experiments | | | | | | | |
|---|---|---|---|---|---|---|---|
| Initial value of levels | | Conditions for calibration | | Initial values of levels | | Conditions for calibration | |
| Rabbits | Foxes | What variable must be fit?(Data sets) | Results from calibration (round to total rabbits) | Rabbits | Foxes | What variable must be fit? (Data sets) | Results from calibration (round to total foxes) |
| 300 | 20 | Fox population: 20 | Rabbit init. population: ≈411 [figure 6] [figure 7] [figure 8] | 300 | 20 | Rabbit population: 300 | Fox init. population: ≈15, Fox hunting efficiency: ≈0.00685 |
| 300 | 25 | Fox population: 25 | Rabbit init. population: ≈514, Fox hunting efficiency: ≈0.004 | 350 | 20 | Rabbit population: 350 | Fox init. population: ≈17, Fox hunting efficiency: ≈0.00587 |
| 300 | 30 | Fox population: 30 | Rabbit init. population: ≈617, Fox hunting efficiency: ≈0.003333 | 400 | 20 | Rabbit population: 400 | Fox init. population: ≈19, Fox hunting efficiency: ≈0.00516 |

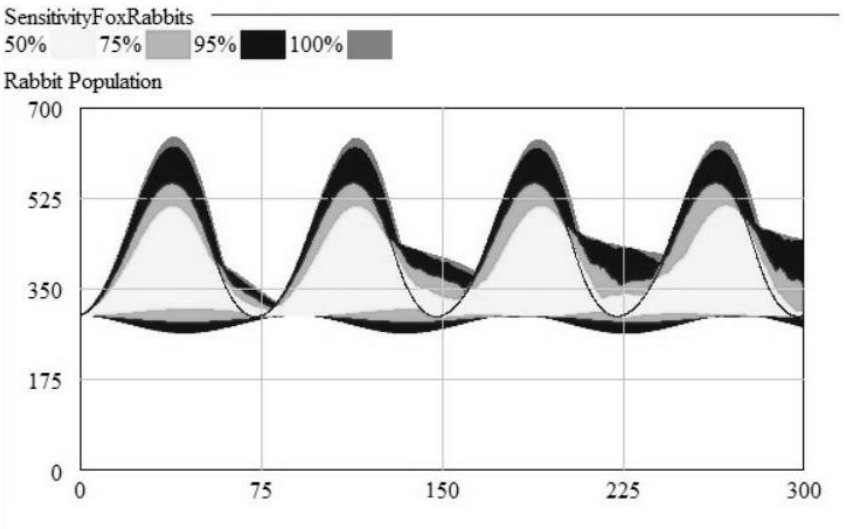


**Figure 2.** Confidence bounds of the variable Rabbit Population for Normal Fox Lifetime between 100 and 300 weeks.

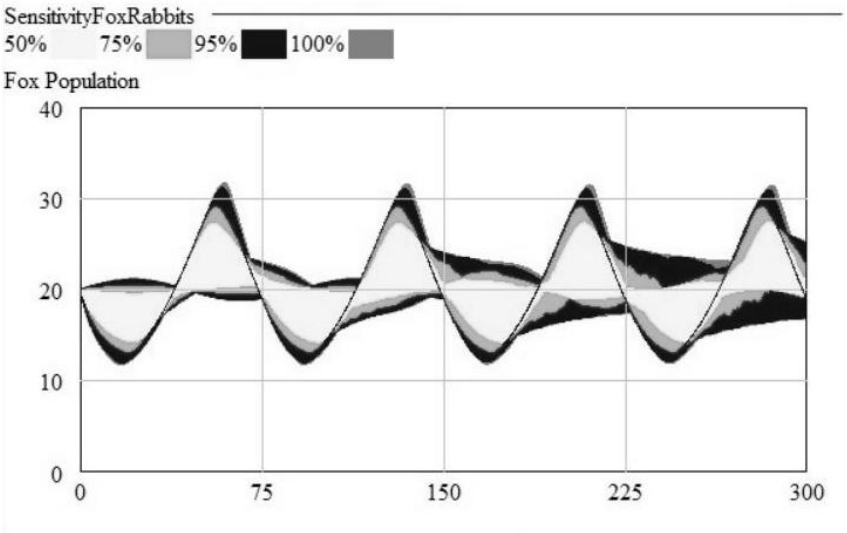


**Figure 3.** Confidence bounds of the variable Fox Population for Normal Fox Lifetime between 100 and 300 weeks.

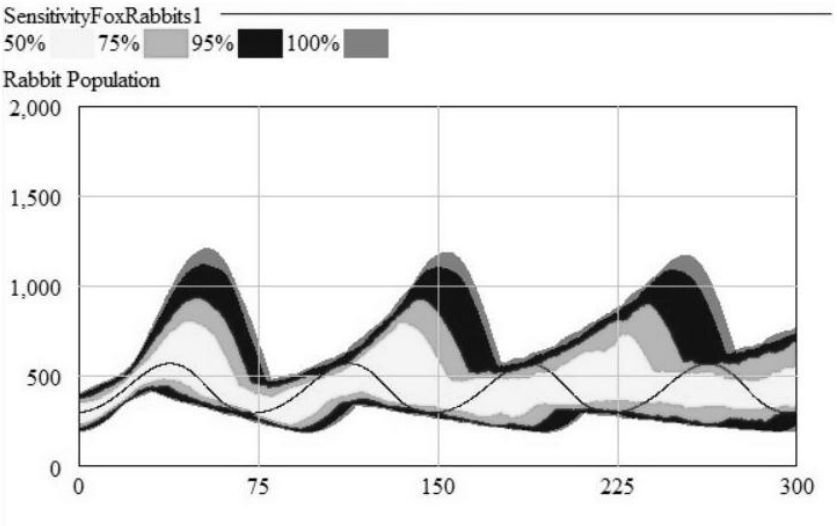


**Figure 4.** Confidence bounds of the variable Rabbit Population for: Rabbit Initial Population between 200 and 400 rabbits; Fox Initial Population between 15 and 25 foxes.

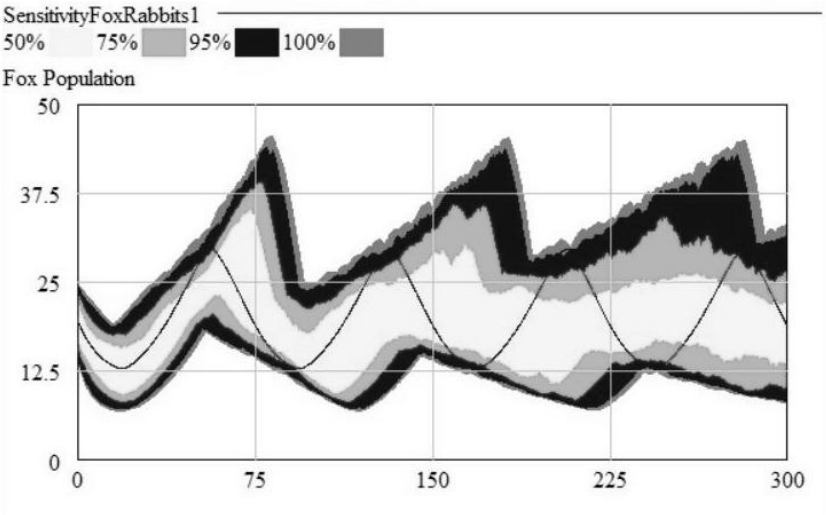


**Figure 5.** Confidence bounds of the variable Fox Population for: Rabbit Initial Population between 200 and 400 rabbits; Fox Initial Population between 15 and 25 foxes.

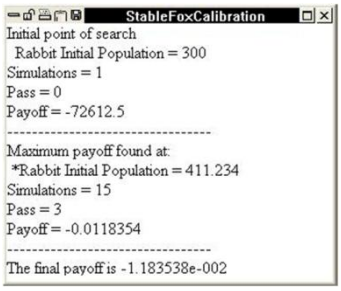


**Figure 6.** Example of calibration result shown in Vensim window (source: own results).

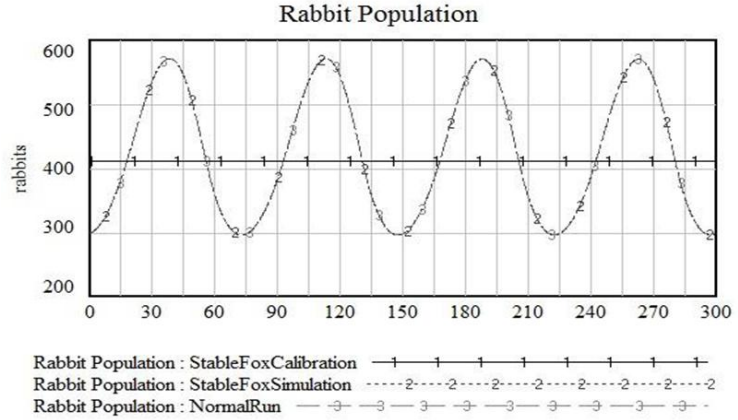


**Figure 7.** Graph illustrating the equilibrium for Rabbit Population achieved in calibration (source: own results).

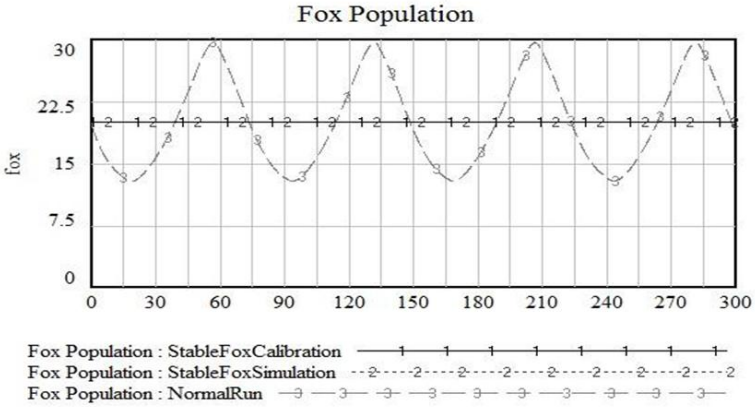


**Figure 8.** Graph illustrating the equilibrium for Fox Population achieved in calibration (source: own results).

### 3.1. Discussion of results

On model Prey-Predator we have performed three types of experiments. First we used so called sensitivity analysis. That experiment shows the sensitivity of the system to the changes in parameter values. Large scale models with non-linearities are very sensitive to changes in several parameters and are non sensitive for the rest of them. Searching this problem is very important, because it's an entrance for the process of optimization. In his book [3] prof. Coyle said that: "the purpose of the model is to represent the dynamics of predator/prey behavior and to study how those dynamics change with uncertainties in the data. When the system has been well understood, the purpose might develop into understanding how the system might be managed by human intervention." Of course in prof. Coyle's times it wasn't possible to use automatic search of sensitivities in data. Now with the use of language Vensim, we have unlimited possibilities of experimentation, and we performed few of them. They show that populations of fox and rabbits are characterized by sustained oscillations. It must be emphasized that the oscillations arise entirely from within the model and not due to outside influence. Prof. Coyle achieved by "trial and error" method the result that with 300 rabbits, there is no value of fox population, which stabilize the system. In our paper we presented results of so called calibration, and they shown that it is possible (see: table 2) to stabilize the system with small modification of data and the process of automatic calibration by Vensim.

In the context of the results of both type of experimentation: sensitivity analysis and calibration, it was very interesting and innovative to perform third type of experiments, so called – gaming. We examined different scenarios (see: game 1, game 2 in table 3) of the human intervention in that ecosystem or the intervention of nature. For example, we changed Rabbit birth rate (hypothetically) two times during the horizon of simulation, and we have the estimation how the system will behave after such scenario. It has practical implication, because in the real world the population of rabbits can die from disease such as myxomatosis, which is highly infectious and almost inevitably fatal for rabbits. Of course it has effects on the fox food supply. So these feedbacks can be examine by performing different games, with different scenarios. Problems similar to this arise in cases such as fishing policy. How many fish can safely be caught and what are the consequences for both fish and fisherman versus fishing industries subsides are obvious policy areas.

**Table 2** Results of Gaming on Prey-Predator Model (different human intervention and acting of nature)

| Assumptions for gaming | | | |
|---|---|---|---|
| Game 1 – Disease in rabbit birth population | | | |
| Initial value of levels | Gaming variables | | Dynamic behavior presented (on figures) |
| | Initial Value | Changing the value during time horizon | |
| Rabbit population: 300<br>Fox population: 20 | Rabbit birth rate: 30 | In time t=100 weeks<br>Rabbit birth rate: 10<br>In time t=200 weeks<br>Rabbit birth rate: 20 | Figure 9<br>Rabbit Population, Fox Population, Rabbit Birth Rate |
| Game 2 – Growth of fox population | | | |
| Initial value of levels | Gaming variables | | Dynamic behavior presented (on figures) |
| | Initial Value | Changing the value during time horizon | |
| Rabbit population 300<br>Fox population 20 | Fox Birth Rate: 1 | In time t=100 weeks<br>Fox Birth Rate: 2<br>In time t=200 weeks<br>Fox Birth Rate: 1.5 | Figure 10<br>Rabbit Population, Fox Population, Fox Birth Rate |

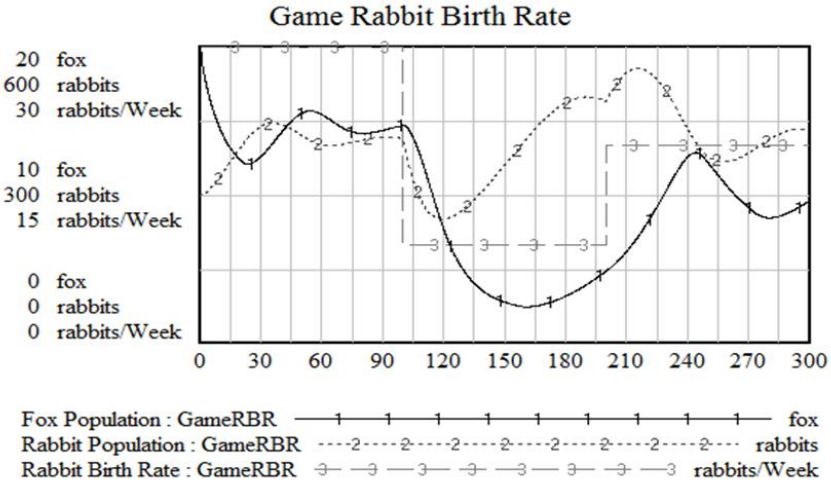


**Figure 9.** Graph for game 1 – disease in rabbit birth population (source: own results).

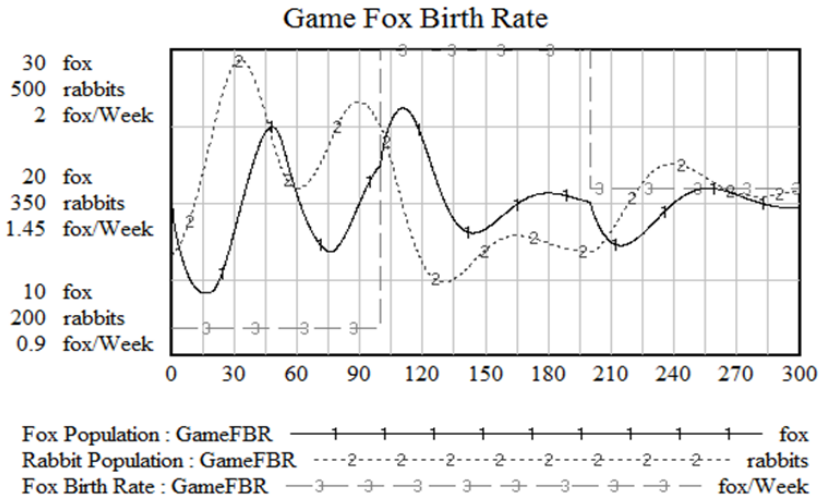


**Figure 10.** Graph for game 2 – growth of fox population (source: own results).

## 4. Conclusions

Firstly, we would like to draw a number of theoretical conclusions:

- System Dynamics method is appropriate for modeling and simulation of the ecosystems, specially prey-predator systems,
- Experimental procedures such as: sensitivity analysis, calibration and gaming, allow to search sensitive parameters, conditions that stabilize the system and examine different scenarios of the human intervention in that ecosystem (or "intervention" of nature).

Secondly, we would like to offer some practical conclusions:

- The simulation language Vensim is "friendly" and easily used tool for simulation and different type of research,
- Many "old" and widely known models never were investigated from perspectives that Vensim offers, so this is a promising field for researchers and practitioners as well.

## References

[1] Akhar M.K., Wibe J., Simonowic S.P., Mcbee J. Integrated assessment model society – climate – economy – energy system. *Environmental Modelling & Software* 49, (2013), p. 1-21.

[2] Bajon T, Analiza strategii policji i kierowców jako gra mieszana z użyciem systemu dynamicznego. *Systemy Wspomagania Organizacji*, Katowice, (2014), p. 9-24.

[3] Coyle R. G., *System Dynamics Modeling. A Practical Approach*, Chappman & Hall, London, 1996.

[4] Coyle R. G., Simulation by repeated optimization, J. Opt. R. S. 50, (1999), p. 429 – 438.

[5] Dacko M., System Dynamics in Modeling Sustainable Management of the Environment and its Resources, *Polish Journal of Environmental Study*, Vol.19, No 4, (2010), p. 699 – 706.

[6] Fiddman T. S., Exploring policy options with a behavioral climate-economy model. *System Dynamics* Review 18. (2002), p. 243-267.

[7] Garcia J. M. *Theory and practical exercises of System Dynamics*, JMG, Barcelona, 2006.

[8] Kasperska E., *Metodologia budowy i wykorzystania modeli ewolucyjnych w aspekcie uczenia się w organizacji społeczno – gospodarczej*. Wydawnictwo Politechniki Śląskiej, Gliwice, 2009.

[9] Kasperska E., Some remarsks about chosen structural aspect of system dynamics method, 6eme Congres Europeen de *Science des Systemes*, AFSCET, Paris (2005), p. 1-5.

[10] Kasperska E., Kasperski A,. Mateja-Losa E, Simulation and optimization experiments on some model of sd type – aspect of stability and chaos. *Ambient technology and creativity support systems*, Uniwersytet Ekonomiczny w Katowicach, (2014), p. 84 – 96.

[11] Kasperska E., Mateja-Losa E, Bajon T., Marjasz R, Did Napoleon have to lose the Waterloo battle? *Ambient technology and creativity support systems*, Uniwersytet Ekonomiczny w Katowicach, (2014), p. 97 - 118.

[12] Kasperska E., Mateja-Losa E., Simulation embedded in optimization – a key for the effective learning process in (about) complex, dynamical systems, *Computation Science* – ICCS 2005, part III, V. S. Sunderam, G. D. van Albada, P. M. A. Sloot, J. J. Dongarra, eds., LNCS, 3514, Springer, Berlin (2005), p. 1040 – 1043.

[13] Kasperska.E, Kasperski.A, Mateja-Losa E., *Simulation of production-sale decision- ma king with multiobjective optimization by Vensim language*, Organizacja i zarządzanie, Kwartalnik Naukowy, Wydawnictwo Politechniki Śląskiej Gliwice, 2014.

[14] Krupa K., Modelowanie, symulacja i prognozowanie Systemy Ciągłe. WNT, 2008.

[15] Marjasz R, Wspomaganie logistyki produkcji w firmie z użyciem narzędzi symulacyjnych. *Systemy Wspomagania Organizacji*, Katowice, (2014), p. 58-70.

[16] Ruth M., Hannon B. *Modeling Dynamic Economic Systems*. From book series: Modeling Dynamic Systems, Springer Science+Business Media, LLC, 2012.

[17] Sterman J. D., *All models are wrong: reflections on becoming a system scientist*, System Dynamics, Rev. 18, 2002.

[18] Vensim User's Guide Version 6. Ventana Systems, Inc. 2014.

[19] Ventana Systems INC. Vensim version 6.1,(2013) Ventana Simulation Environment.

Elżbieta Kasperska, Ph.D. D.Sc. (Assistant Professor): Silesian University of Technology, Gliwice 44-100, Poland (Elzbieta.Kasperska@polsl.pl).

Andrzej Kasperski, Ph.D.: Silesian University of Technology, Gliwice 44-100, Poland (Andrzej.Kasperski@polsl.pl).

Tomasz Bajon, M.Sc. (Ph.D. student): Silesian University of Technology, Gliwice 44-100, Poland (tomasz.bajon@polsl.pl).

Rafał Marjasz, M.Sc. (Ph.D. student): Silesian University of Technology, Gliwice 44-100, Poland (rafal.marjasz@polsl.pl), The author gave a presentation of this paper during one of the conference sessions.

# Efficient FEA simulation of structure borne sound radiation
## (NUM133-15)

Matthias Klaerner, Mario Wuehrl, Steffen Marburg, Lothar Kroll

*Abstract:* Lightweight and stiff and thin-walled components tend to significant sound radiation. In addition, fibre reinforced plastics offer a wide range of adjusting the material behaviour by manipulating parameters such as fibre and matrix material, fibre volume content or layup. Thus, there is a need of efficient simulation methods in design and optimisation. In contrast, acoustic measures are commonly not implemented in standard FEA software.

Different velocity based measures fill the gap. The equivalent radiated power is based on the sound intensity in normal direction and the sound pressure on the radiating surface. Assuming a unit radiation efficiency all-over the surface and neglecting local effects, this is an upper bound of structure borne noise. The volume velocity includes local anti-phase vibration such as dipole effects and provides good results for the average power in the lower frequency range with a constant frequency dependent radiation efficiency of all interactions. Lumped parameter model predictions are exact for dipole modes. Besides, the accuracy is dependent on the mesh refinement as well as the compliance with the assumptions of the RAYLEIGH-integral but generally appropriate in the low and mid frequency range. In contrast, the kinetic energy is implicitly given from the energy balance in steady state simulations and thus, a very efficient but only qualitative measure.

Possibilities and limits of estimating the emitted sound power by these methods will be shown by numerical studies on composite components.

### 1. Introduction

Lightweight structures usually are stiff and thin-walled and such tend to be sensitive for structure borne sound. The sound radiation behaviour thus is a common optimisation criterion within lightweight design. The optimisation procedure is related to the adjustment of the material properties of fibre reinforced plastics [7]. There, stiffness and damping are contradictory influenced by fibre volume content, fibre orientation as well as stacking sequence resulting in non-linear dependencies [13]. Numerous finite-element simulations are required either for genetic or gradient based optimisations. Thus, efficient numerical measures of structure borne sound radiation are helpful as an effective objective function of such processes.

In this study, the structural vibrations of continuous systems are used to determine the sound radiation behaviour in the surrounding fluid. The presented mathematical approaches

are based on efficient numerical methods of vibration analysis such as mode based steady state dynamic FE analysis. The treated methods and theories are validated by a thin-walled demonstrator part.

In detail, the radiated sound power is used to express the radiation of components and machines and is formulated as the integral of the intensity over the radiating surface. Analytical solutions of the sound power are limited to a few academic cases. Precise numerical approximation methods are used in addition but computationally expensive solving fluid-structure-interaction in one or both directions.

Another very popular approach for large-scale problems is the boundary element method (BEM) including fast-multipole techniques. This is limited for a large frequency range or modified structures within optimisation loops (e. g. [12]).

Common simplification methods are based on some general assumptions. Stiff thin-walled structures with hard reflecting surfaces show identical particle velocity and structure normal velocity. There, the sound pressure is evaluated on the structure's surface.

This paper compares three different approaches of sound power estimation, the equivalent radiated sound power (ERP), the volume velocity (PVV) and the lumped parameter model (LPM). These measures are to be compared to the kinetic energy within harmonic direct FEA analysis.

## 2. Energy and power estimations

### 2.1. Kinetic energy

Using global quantities, e.g. potential and kinetic energy, is suitable to determine the acoustic behaviour [10]. Within steady state finite element analysis the energy balance is estimated implicitly and consists of different elastic and dissipating components. The kinetic energy of the whole part is given by the integral over the volume $V$

$$W_{kin} = \int_V \frac{1}{2} \varrho_s \ \boldsymbol{v}\boldsymbol{v}^T \mathrm{d}V \tag{1}$$

with the arbitrary oriented surface velocity $\boldsymbol{v}$ and the density of the solid surface $\varrho_s$. According to common standards in acoustics the energy level

$$L_W = 10 \ \lg\left(\frac{W_{kin}}{W_0}\right) \ dB \tag{2}$$

is referred to a level of $W_0 = 10^{-12} J$.

In this study we assume only harmonic vibrations and thus point-wise exact solutions of a steady state FEA. The kinetic energy will be further on rated as mechanical (input) power of the total vibrating system therefore is transformed in every frequency step.

$$P_{kin}(f) = W_{kin}(f) \cdot f \tag{3}$$

### 2.2. Equivalent radiated power

In contrast, the radiation of vibrating parts is often estimated by the radiated sound power $P$ representing the integral of sound intensity $I$ in normal direction over the closed surfaces $\Gamma$ circumscribing the radiating object [5].

$$P = \int \vec{I} \cdot \vec{n} \, \mathrm{d}\Gamma \qquad \text{with} \qquad \vec{I} = \frac{1}{2} \Re \left( p \vec{v} \right) \tag{4}$$

The velocity normal to the surface $v_n = \vec{v}\vec{n}$ is imported from dynamic FE-analysis and further on used to analyse acoustic fields by comparing different numerical estimates for the sound power. Therein, the equivalent radiated power includes a simple, popular and efficient approach for the sound pressure in the local relation

$$\boldsymbol{p} \approx \varrho_f \; c_f \boldsymbol{v} \tag{5}$$

with the fluid's density $\varrho_f$ as well as it's speed of sound $c_f$. The relation between particle velocity and sound pressure is reduced to the fluid's characteristic impedance.

$$Z_0 = \varrho_f \; c_f \tag{6}$$

The approximation is typical in far fields and high frequencies and results in the sound power as a surface integral

$$P_{ERP} = \frac{1}{2} \varrho_f \; c_f \int |v(x)|^2 \, \mathrm{d}\Gamma(x) \tag{7}$$

or a discretised formulation for $N_e$ piecewise constant elements with an area $A_\mu$

$$P_{ERP} = \frac{1}{2} \varrho_f \; c_f \sum_{\mu=1}^{N_e} A_\mu v_\mu v_\mu^* \tag{8}$$

This simple formulation is based on the assumption of the same radiation efficiency $\sigma = 1$ for all elemental sources. It neglects effects such as interaction between local sources. Generally overestimating the radiation, it gives a good impression of an upper bound for convex rigid bodies and high frequencies.

### 2.3. Lumped parameter model

More accurate results can be achieved with the lumped parameter model (LPM) as well as the boundary element method (BEM) [5]. The LPM by Koopmann and Fahnline [3, 4, 10] is related on a simplification of the Rayleigh-integral and includes a Taylor series of the

GREEN's function as a multipole expansion. This formulation is given for a source at $x_\mu$ and a receiver at $y_\nu$ .

$$P_{LPM} = -\frac{1}{2} k \ \varrho_f \ c_f \sum_{\mu=1}^{N_e} \sum_{\nu=1}^{N_e} S_\mu S_\nu \Im \{G_{\mu\nu}\} \Re \{v_\mu v_\nu^*\} \tag{9}$$

$$\text{with} \quad \Im \{G_{\mu\nu}\} = -\frac{\sin(k|x-y|)}{2\pi|x-y|} \tag{10}$$

Therein, the imaginary part of the GREEN's function weights the interacting sources. The double summation is computationally more expensive than ERP but much more efficient than fast multipole BEM. LPM predictions are exact for dipole modes. Besides, the accuracy is dependent on the mesh refinement as well as the compliance with the assumptions of the RAYLEIGH-integral but generally gives appropriate results in the low and mid frequency range.

### 2.4. Volume velocity

The radiation estimation by volume velocity $u$ is an integral of the particle velocity on the surface [10].

$$u = \int v \mathrm{d}\Gamma = \sum_{\nu=1}^{N_e} v_\mu S_\mu \tag{11}$$

The derived radiated sound power PVV is understood as a reduction of the LPM.

$$P_{VV} = \frac{k^2 \varrho_f \ c_f}{4\pi} \ u \ u^* = \frac{k^2 \varrho_f \ c_f}{4\pi} \sum_{\mu=1}^{N_e} \sum_{\nu=1}^{N_e} S_\mu S_\nu \Re \{v_\mu v_\nu^*\} \tag{12}$$

It includes local anti-phase vibrations such as dipole effects but only requires a single sum [5] compared to LPM. In this case all interactions have a constant but frequency dependent radiation efficiency. Thus, the PVV is suitable for the average power in the lower frequency range. It shows no convergence to mesh refinements.

### 2.5. Acoustic efficiency

The mechanical power of the whole system is assumed to be much higher than the radiated power losses. Thus, the acoustic efficiency

$$\eta = \frac{P_{radiated}}{P_{kin}} \tag{13}$$

in the range $[0, 1]$ will be used for all sound power estimates.

## 3. FEA implementation

Based on steady state FEA models with harmonic force excitation, all given sound power estimations have been determined in an external post-processing script. All simulations have been done in ABQUS 6.14. Thus, the script is a python-algorithm.

The implementation of all named sound power estimates (section 2) is related to piecewise constant elements and follows [5].

$$P = \sum_{\mu=1}^{N_e} \sum_{\nu=1}^{N_e} P_{\mu\nu} = \sum_{\mu=1}^{N_e} P_{\mu\mu} + 2 \sum_{\mu=1}^{N_e-1} \sum_{\nu=\mu+1}^{N_e} P_{\mu\nu} \tag{14}$$

The sound power portions $P_{\mu\nu}$ are understood as a partial monopole sound power contributions of all $N_e$ constant elements. Therein, $P_{\mu\mu}$ considers the independent source distributions whereas $P_{\mu\nu}$ $(\mu \neq \nu)$ represents the interactions between these sources.

This interaction matrix is symmetric and its elements can be determined by

$$P_{\mu\nu} = P_{\nu\mu} = \frac{1}{2} \varrho_f \; c_f \; S_\mu \; \sigma_{\mu\nu} \; \Re\{v_\mu v_\nu^*\} \tag{15}$$

with a dimensionless radiation efficiency $\sigma_{\mu\nu}$. For the different sound power models, there is a general formulation of $\sigma_{\mu\nu}$ including the distance $R_{\mu\nu}$ between two elements $\mu$ and $\nu$.

$$\sigma_{\mu\nu} = \delta_{\mu\nu} \qquad \text{for ERP,} \tag{16}$$

$$\sigma_{\mu\nu} = \frac{k^2 \; S_\nu}{2 \; \pi} \qquad \text{for PVV,} \tag{17}$$

$$\sigma_{\mu\nu} = \frac{k^2 \; S_\nu}{2 \; \pi} \frac{\sin(k \; R_{\mu\nu})}{k \; R_{\mu\nu}} \qquad \text{for LPM.} \tag{18}$$

As already mentioned, the numerical estimations are of different computational efforts. ERP and PVV sums are of order $N_e$ whereas LPM requires $N_e^2$ steps. For a given model (section 4) with about 3,500 frequency steps, the total post-processing time is about 20 times more computationally expensive than the FEA solution (figure 1). Therein, reading the model data and extracting the distance between each element is insignificant ($< 0.25\%$). Accessing the the normal velocity fields and determining the matrix $\Re\{v_\mu v_\nu^*\}$ each about 50 % of the original solution. According to (16) to (18), the power estimates are of different computational efforts. ERP in total requires 20 % of the FEA solution, PVV 120 % and LPM 520 % at least.

These high efforts are caused either by the incremental data access in the result file or by a single core solution of the matrix operations in contrast to a ten core solution of the previous FEA problem. For a comparable number of CPU in both processes the acoustic post-processing might still be almost as expensive as the FEA solution.

For the kinetic energy, there is no additional processing.

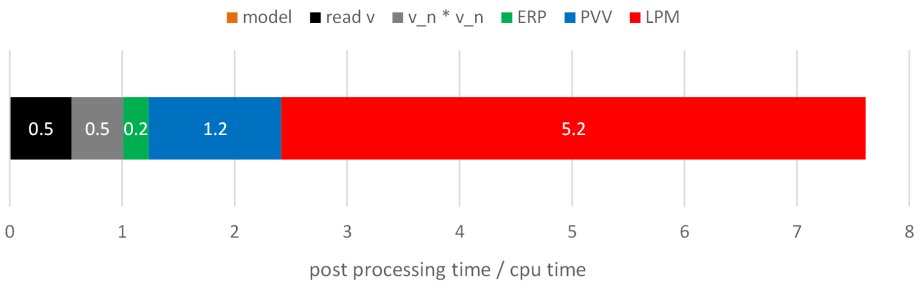


**Figure 1.** Calculation time of the post-processing steps related to the CPU time of the previous FEA solution

## 4. FEA model

For comparative studies of a real thin-walled formed structure with significant sound radiation an oil pan geometry has been chosen for the analysis. The outer dimensions of the shape shown in figure 2 are app. 250 x 210 x 100 mm.

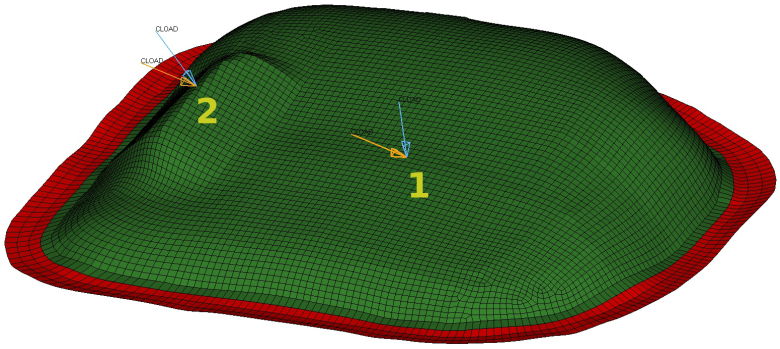


**Figure 2.** FEA model of an oil pan: shell elements, boundary conditions at red elements, normal forces (light blue) and arbitrary directed forces (yellow) at force locations 1 and 2

The mesh has been developed with quadratic shell elements of 2 mm edge length. Thus, the model consists of about 8,500 elements and 25,000 nodes. The frequency range was chosen according to common standards in acoustic analysis from 100 Hz up to 10 kHz.

The composite material consists of ten layers of 4:1 layup with 0° and 90° plies oriented along the largest dimension of the pan. Each layer is 0.2 mm thick and has orthotropic elastic properties as given in table 1. Anisotropic damping referring to a damping model of Adams and Bacon [1,2,11] has been implemented as modal damping including an energetic mapping procedure based on the mode shapes [6,8,9].

**Table 1.** Material properties of unidirectional glass-fibre reinforced polypropylene

| elastic parameters | | | | density | damping | | |
|---|---|---|---|---|---|---|---|
| $E_1/MPa$ | $E_2/MPa$ | $G_{12}/MPa$ | $\nu_{12}$ | $\varrho/g/cm^3$ | $\eta_1/\%$ | $\eta_2/\%$ | $\eta_{12}/\%$ |
| 28,900 | 3,700 | 1,100 | 0.25 | 1.47 | 0.19 | 1.40 | 1.53 |

Related to the figure 2, the part has been excited vertically on the top surface at two different positions. The force direction is arbitrary (along space diagonal) or normal to the surface at the force location with 1 N. The part is fixed with displacement boundary conditions all along the flat face (red elements). Dynamically and acoustically the model behaviour is dominated by 139 modes in the given frequency range starting at 516 Hz. The mode distribution is concentrated within the third octave bands highest in frequency (figure 3).

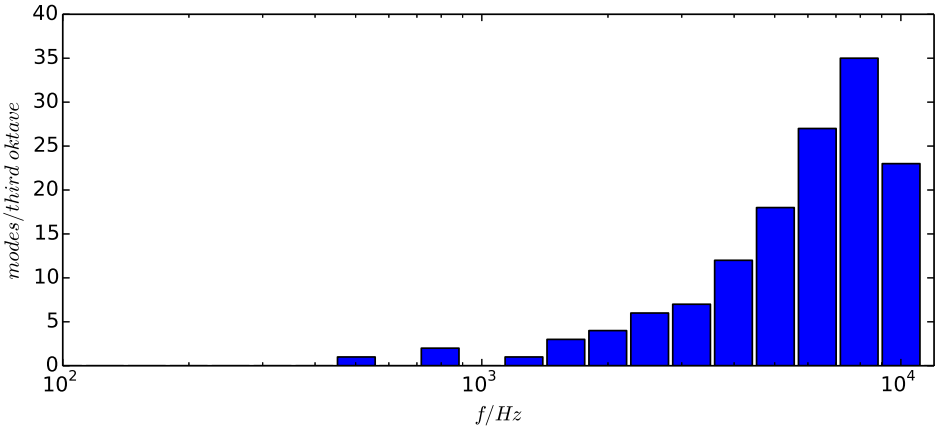


**Figure 3.** Modal density of the gfrp oil pan model

## 5. Numeric results

First comparative studies have been done with a 1 N excitation in arbitrary direction at location one. All further interpretations are based on this loadcase. Figure 4 shows quite similar frequency characteristic of all mechanical and acoustical power estimations. Reasonably, the mechanical power is significantly higher than all acoustic measures. In contrast to the modal density (figure 3), the sound radiation is dominated by the mid frequency range. Therein, the first ten modes contribute most.

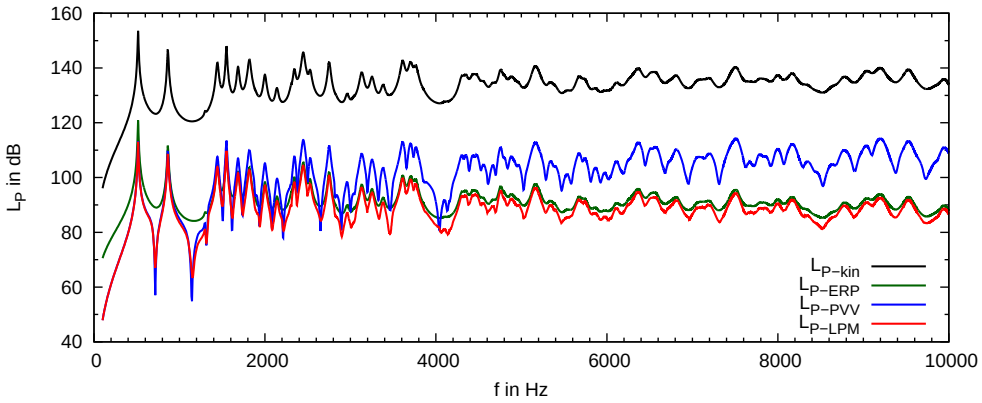


**Figure 4.** Sound power estimates and mechanical power for arbitrary steady state excitation at location 1

Assuming the LPM as the most accurate solution, all other estimated levels have been related to that measure in figure 5. There, the absolute level difference is plotted in absence of an exact physical meaning but for better comparability to figure 4. The comparison shows a parallel deviation of kinetic power and ERP. ERP seems to be not accurate below 1 kHz whereas PVV deviations significantly increase above 1.5 kHz.

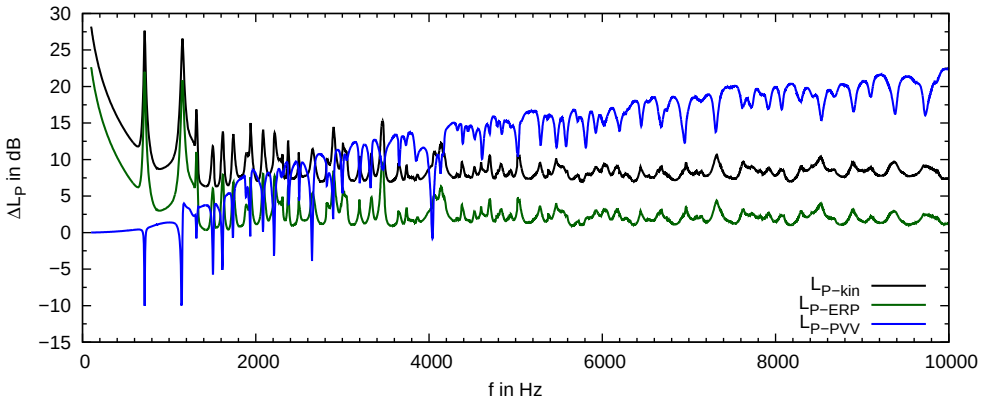


**Figure 5.** Power levels of figure 4 related to the LPM determination

This behaviour is verified by the acoustic efficiency in figure 6. Again, LPM is considered most accurate due to the refined characteristics. In comparison, the overestimation of ERP is represented in a higher acoustic efficiency within the whole frequency range. Last, PVV shows a range of application up to 1.5 kHz but significant high deviations above.

Parametric studies have been done varying force location and direction. Figure 7 com-

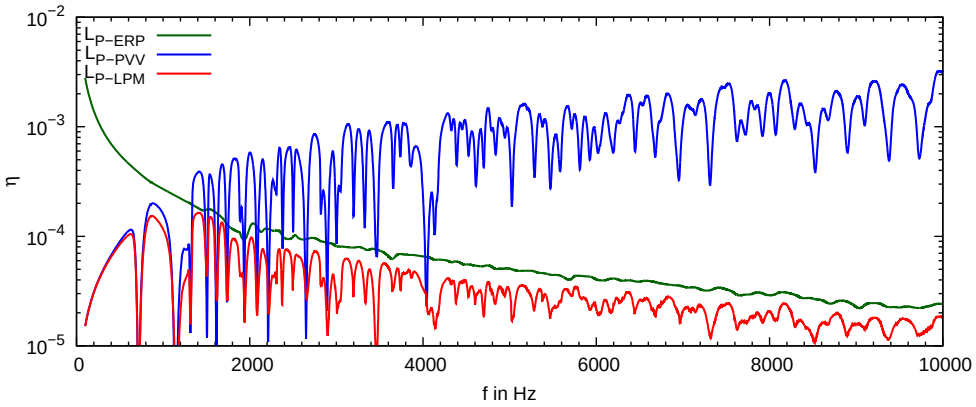


**Figure 6.** Acoustic efficiency of the different sound power estimates

pares mechanical power and LPM for all four different loadcases. In general, forces directed normal to the surface deliver a higher sound emission than arbitrary oriented excitations. Even though, some mode shapes in the mid frequency range are excited more by the arbitrary force in location two.

As expected, the force location influences the sound radiation, too. In this case, location one is located in an area of higher compliance and thus causes higher amplitudes than the stiffer area of excitation at location two.

## 6. Summary and Outlook

In summary, the structural vibrations of continuous systems can be used to determine the sound radiation behaviour in the surrounding fluid. The presented mathematical approaches are based on efficient numerical methods of vibration analysis such as mode based steady state dynamic FE analysis. The treated methods and theories are successfully validated by a thin-walled demonstrator part.

All sound power estimates give reasonable results with similar frequency characteristics. Deviations have been expected due to the different accuracy and efforts of the structural acoustic methods. In detail, LPM is most expensive but most accurate, too. In contrast, PVV is an adequate solution up to 1 kHz. Above, ERP achieves quite good results.

The overall frequency characteristics are well represented by the kinetic energy, too. As sound power estimate, it hardly overestimates the radiation. The acoustic efficiency is less than 1 % all over the frequency range. Thus, the mechanical power is two orders of magnitude greater than the acoustic measures.

But computational time for the acoustic post-processing is significant. Thus, the kinetic

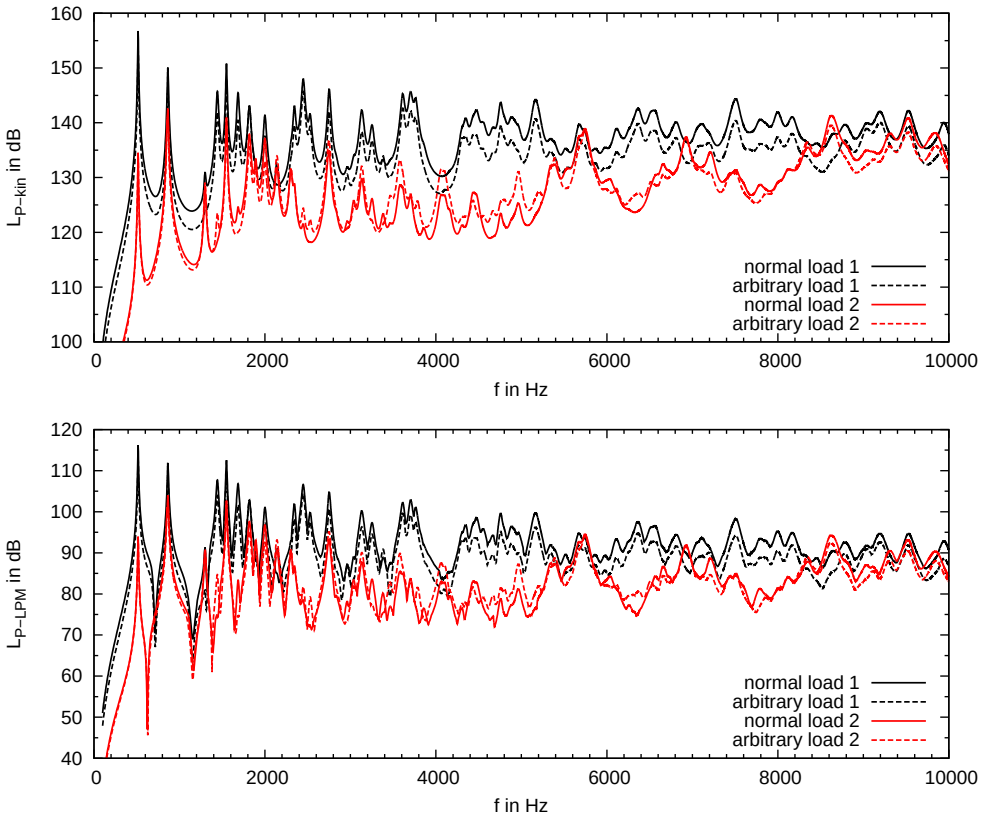


**Figure 7.** Mechanical power and LPM for all different force locations and directions

energy is supposed to be a quite efficient criterion for optimisation routines. One of the next steps e.g. is to predict the best layup or fibre material.

Moreover, other parts with different modal density will be additionally used to investigate especially the lower frequency range.

Last, a more precise validation by measurements, fully coupled fluid-structure FEA or BEM simulations will give a better impression of the accuracy and limits of the chosen measures.

### Acknowledgments

The paper arose in the context of the project DFG-KR 1713/18-1 Schallabstrahlung bei nichtlinearem und lokal variierendem Dämpfungsverhalten von Mehrlagenverbunden funded by the Deutsche Forschungsgemeinschaft (DFG) which is gratefully ackknowledged.

**References**


[1] Adams, R. D., and Bacon, D. G. C. Effect of fibre orientation and laminate geometry on the dynamic properties of cfrp. *Journal of Composite Materials 7* (1973), 402–428.

[2] Adams, R. D., and Maheri, M. R. Dynamic flexural properties of anisotropic fibrous composite beams. *Composites Science and Technology 50*, 4 (1994), 497–514.

[3] Fahnline, J., and Koopmann, G. A lumped parameter model for the acoustic power output from a vibrating structure. *Journal of the Acoustical Society of America 100*, 6 (1996), 3539–3547.

[4] Fahnline, J., and Koopmann, G. Numerical implementation of the lumped parameter model for the acoustic power output of a vibrating structure. *Journal of the Acoustical Society of America 102*, 1 (1997), 179–192.

[5] Fritze, D., Marburg, S., and Hardtke, H.-J. Estimation of Radiated Sound Power: A Case Study on Common Approximation Methods. *Acta Acustica United with Acustica 95* (2009), 833–842.

[6] Jaber, M., Schneeweiss, H., Boes, J., and Melz, T. Vibrational energy flow in carbon composite structures. In *inter.noise 2014: 43rd International Congress on Noise Control Engineering* (2014).

[7] Klaerner, M., Ulke-Winter, L., Marburg, S., and Kroll, L. Damping of Thermoplastic Lightweight Structures - A Sensitivity Analysis and Optimisation Strategy. In *DYNACOMP - 1st International Conference on Composites Dynamics* (2012), B. Troclet, M. Ichchou, and P. Ladevze, Eds.

[8] Klaerner, M., Wuehrl, M., Kroll, L., and Marburg, S. Anisotropic damping of thermoplastic composites. In *Noise and Vibration - Emerging Technologies, NOVEM* (2015).

[9] Klärner, M., Wührl, M., Kroll, L., and Marburg, S. Finite-elemente-modelle für anisotrope dämpfung. In *DAGA 2015 - 41. Jahrestagung fr Akustik* (2015).

[10] Koopmann, G. H., and Fahnline, J. B. *Designing Quiet Structures*. Academic Press, London, 1997.

[11] Maheri, M. R. The effect of layup and boundary conditions on the modal damping of FRP composite panels. *Journal of Composite Materials 45*, 13 (2011), 1411–1422.

[12] Marburg, S., and Nolte, B., Eds. *Computational Acoustics of Noise Propagation in Fluids - Finite and Boundary Element Methods*. Springer-Verlag, Berlin, Heidelberg, 2008.

[13] Ulke-Winter, L., Klaerner, M., and Kroll, L. Determining the damping behavior of fiber reinforced composites. *Composite Structures 100* (2013), 34–39.

Matthias Klaerner, Dipl.-Ing. (Ph.D. student): Technische Universität Chemnitz, Institute for Lightweight Structures, 09107 Chemnitz, Germany (*matthias.klaerner@mb.tu-chemnitz.de*). The author gave a presentation of this paper during one of the conference sessions.

Mario Wuehrl, B.Sc. (M.Sc. student): Technische Universität Chemnitz, Institute for Lightweight Structures, 09107 Chemnitz, Germany (*mario.wuehrl@mb.tu-chemnitz.de*).

Steffen Marburg, Prof. Dr.-Ing.: Technische Universität München, Gerhard Zeidler Endowed Professorship for Vibroacoustics of Vehicles and Machines, 85748 Garching, Germany (*steffen.marburg@tum.de*).

Lothar Kroll, Prof. Dr.-Ing. habil.: Technische Universität Chemnitz, Institute for Lightweight Structures, 09107 Chemnitz, Germany (*lothar.kroll@mb.tu-chemnitz.de*).

# Asymptotic analysis of the model of a wind-powered vehicle moving against the flow (MAT123-15)

Liubov Klimina, Marat Dosaev, Yury Selyutskiy, Shih-Shin Hwang, Kao-Huei Lin

*Abstract:* The model of a wind-powered vehicle is proposed. The mechanism uses the wing to transform the energy of the upcoming wind flow into the energy of the mechanical motion in such a way that the vehicle goes against the wind. The new type of a wind-receiving element is introduced that is based on the principle of a slider-crank mechanism. The corresponding dynamical model is constructed. Asymptotic methods are applied for the parametrical analysis of the dynamical system. The existence of attracting steady regime is shown. Results of the parametrical analysis were used for construction of a prototype of such a vehicle. Experiments with this prototype proved qualitative predictions of the mathematical model.

## 1. Introduction

Novel domains of application of environmentally friendly power systems appear rapidly. This extension of scope arises against the background of modern ecological problems and pushes elaboration of great variety of novel approaches, components, and mechanisms used for design of advanced wind turbines [1-9].

This paper deals with the novel type of wind turbine mechanisms transmitting rotational and translational motion of a wing into the progressive motion of the body of the vehicle against the flow. This system relates to wave turbines – one of new branches of the growing cluster of bionic "green" mechanisms. This project continues the line of bionic wind-powered systems developing in the Institute of Mechanics of LMSU. One of previous mechanism of this line is described in [5]. The next generation of such mechanism with principally different character of motion of the wing is presented in the current paper.

This type of mechanisms has a certain ecological niche: it can be used in an aggressive medium (e.g. water, damp air, or regions with snow) because swinging parts of the construction can be isolated and rotating parts can be placed out of the stream. For example while the wing of the wave-type hydro turbine performs underwater motion the generator can be located over-water.

Practical need causes demand for corresponding scientific research that has to describe preferable modes of exploitation and specify most effective parameters of construction. We started fundamental investigation of wave type wind turbines (WTWT) in response to this challenge: the new few-parametrical model of the WTWT was proposed, theoretical and numerical analysis was performed

for the case of three-linked turbine, results obtained for the model were compared with experimental data and proved to be in good agreement ([6]).

We invented a double-linked (slider-cranked) wave-type wind/hydro turbine (Fig. 1) and constructed the corresponding mathematical model. Note that very similar mathematical modelling was applied before for other types of wind turbines and proved to provide qualitative agreement with experimental results ([6-9]). The system obtained is simple enough, it allows theoretical description of periodical regimes and reveals basic physical principles of WTWT operation.

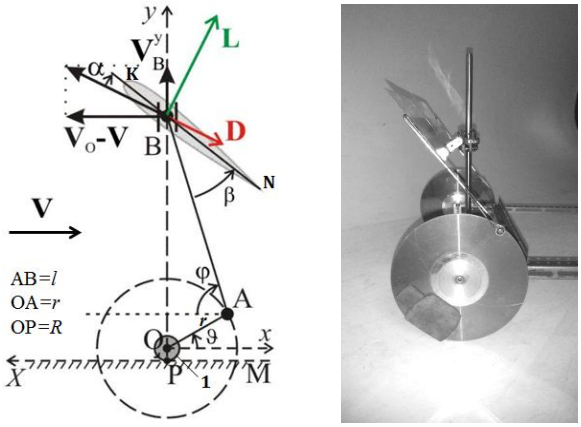


**Figure 1.** The scheme of a slider-crank wave-type wind turbine and the first working prototype.

In this paper we suggest using the slider-cranked wind turbine as an engine of a wind-powered car. We perform detailed investigation of the mathematical model to find operation regimes of this new wind-powered vehicle and to optimize parameters of the construction. Using theoretical results we made the draft of the invented machine and construct the prototype (Fig. 1).

We performed a lot of experiments for checking of different modes of motion and adjusted parameters of the prototype. Our invention proved to maintain all regimes that we expected including the most complicated and amazing one: the car equipped by our slider-crank wind turbine can move against the wind flow via the power of the same wind flow only!

## 2. Description of the mechanism

The mechanism of the slider-cranked wind turbine uses wind energy to induce reciprocating motion of a slider (carrying a wing), and converts this motion into rotation of a crank (carrying a leading gear of wheels). Reduction gears transmit rotation of the crank into rotation of leading wheels of the vehicle. Coefficient of reduction is adjusted to make the work of the drag force less than the work of the lift force. Thus we obtain the vehicle powered via a slider-cranked wind turbine that can move in the wind flow against the flow using only the power produced by this flow.

### 2.1. Geometry and mass

The slider-cranked mechanism consists of two rigid bodies: a first link OA of the length $r$ can rotate around the axis O, a second link AB of the length $l$ is pivotally connected with the first one and carrying a wing with a chord KN rigidly joined to it. Angle between AB and KN equals $\beta$ (Fig. 1). The point B never leaves an axis O$y$ which is orthogonal to the wind speed **V**. The system in fact represents a slider-crank mechanism.

The link OA is rigidly joined to the working element of the machine that is the wheel "1" in the scheme (Fig. 1), $R$ is the radius of the wheel "1". Thus the slider-cranked turbine is mounted at the platform of the vehicle which can move parallel to the axis M$X$ (Fig. 1). We assume that there is no slipping between the wheel "1" and the rail M$X$ (the speed of the point P equals zero). So the whole system has one degree of freedom. Current positions of all points of the mechanism are completely determined by current value of the angle $\vartheta$ between the axis O$x$ and the link OA. Current velocities of all points of the mechanism are determined by the angle $\vartheta$ and its time-derivative $\omega$.

$J_1$, $m_1$ – central moment of inertia and mass of the rigid body "link OA+wheel"; $J_2$, $m_2$ – central moment of inertia and mass of the rigid body "link AB+wing". Assume that the center of mass of the body "link OA+wheel" is located in the point O and center of mass of the body "link AB+wing" coincides with the point A (some counterbalance presents).

Kinetic energy of the mechanism is given by the following expression:

$$K(\vartheta,\omega) = 0.5 J_1 k(\vartheta)\omega^2, \tag{1}$$

$$\text{where } k(\vartheta) = 1 + \frac{m_1 R^2}{J_1} + \frac{m_2}{J_1}\left(R^2 + r^2 + 2rR\sin\vartheta\right) + a^2 \frac{J_2}{J_1}\frac{\sin^2\vartheta}{\sin^2\varphi} \tag{2}$$

$$a = r/l < 1, \ \varphi = \arccos(a\cos\vartheta). \tag{3}$$

### 2.2. Aerodynamic action

Assume that the mechanism is under the action of aerodynamic forces applied to the wing besides the gravity. Neglect the aerodynamic action upon the links of the mechanism and the wheel. Vector **V** is constant and horizontal velocity of wind (or water flow), $\rho$ - density of the medium, $S$ – characteristic area of the wing. The following model (quasi-static) of aerodynamic action is used (similar to [6-9]): the center of aerodynamic pressure always coincides with the point B, aerodynamic force is the sum of a drag force **D** and a lift force **L**, which have the following projections at O$x$ and O$y$ axis:

$$D_x = 0.5\rho S V^2 s\sqrt{s^2 + u^2}\, C_d(\alpha), \tag{4}$$

$$D_y = -0.5\rho SV^2 u\sqrt{s^2+u^2}C_d(\alpha), \tag{5}$$

$$L_x = 0.5\rho SV^2 u\sqrt{s^2+u^2}C_l(\alpha), \tag{6}$$

$$L_y = 0.5\rho SV^2 s\sqrt{s^2+u^2}C_l(\alpha). \tag{7}$$

Here $u = r\omega V^{-1}\sin(\vartheta+\varphi)\sin^{-1}\varphi$ – dimensionless vertical component of the speed of the point B; $s = \left(1+R\omega V^{-1}\right)$ – dimensionless speed of the wind flow with respect to the coordinate system O*xy*; $\alpha = -\arctan\left(us^{-1}\right)+\varphi-\beta$ – instantaneous angle of attack. Aerodynamic coefficients $C_d(\alpha)$, $C_l(\alpha)$ are taken from stationary experiments. Further for numerical calculations coefficients $C_d$ and $C_l$ corresponding to a flat plate with extension 8 are used (Fig. 2).

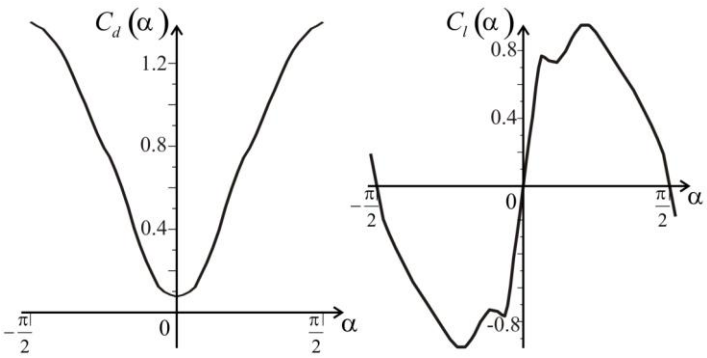


**Figure 2.** Drag and lift force coefficients for a flat plate with extension 8 ($\pi$ –periodical functions).

### 3. Statement of the problem and dynamical equations

For ages people use the power of the wind to perform long distance sailing travels, and it's a normal situation to wait for the favorable wind for a long time. Under-sail traveling up to the wind is as possible as the river carrying something up to the stream. Still the special approach is known in the sailing ship navigation when the ship performs a so-called traverse motion. The mechanism described here provides the new solution of the problem of the up-wind motion. The wing of the mechanism performs traverse-style motion while the main body (the point O) moves directly up-wind along the straight line (Fig. 3). Notice that the projection of the total aerodynamic force **L** upon the axis O*y* during the motion is codirected with the vector $\mathbf{V}_{\mathrm{B}}^{y}$. So lift force supports the desired regime of motion of the mechanism. This is the rough idea of the performance of the vehicle introduced in this paper.

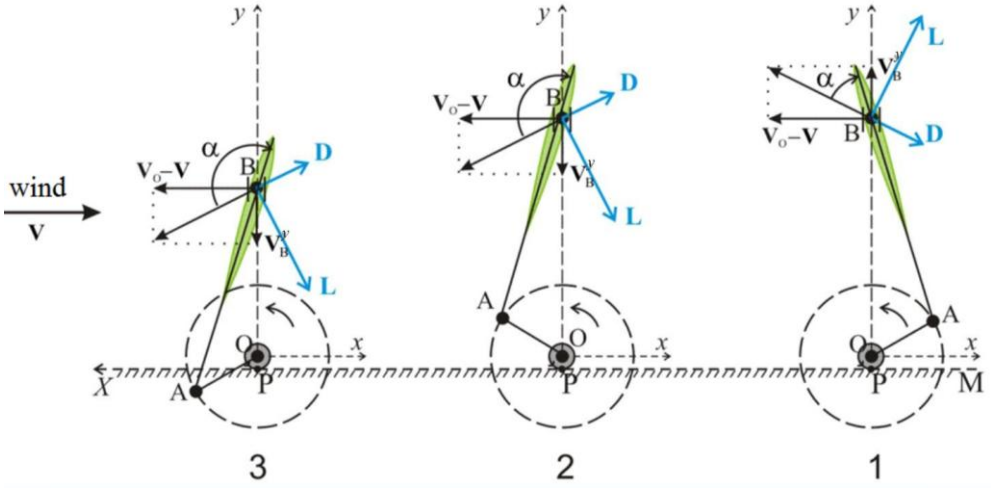


**Figure 3.** The scheme of several stages of motion of the mechanism.

For detailed study of the behavior of the system taking into account both drag and lift force let's prove that dynamical equations of the mechanism possesses a periodical motion in which the speed of the point O is always directed up-wind.

Within the framework of the model described above (see (1-7)), equations of motion of the mechanism can be represented in the following dimensionless form:

$$\begin{cases} \dfrac{d\vartheta}{d\tau} = z; \\ \dfrac{dp}{d\tau} = 0.5k'(\vartheta)k^{-2}(\vartheta)p^2 - 0.5b\cos\vartheta + \varepsilon Q(\vartheta, z). \end{cases} \qquad (8)$$
$$p = k(\vartheta)z.$$

Here $Q(\vartheta, z) = 0.5\dfrac{1}{z}\sqrt{s^2+u^2}\left(u\left(sC_l(\alpha) - uC_d(\alpha)\right) - cz\left(uC_l(\alpha) + sC_d(\alpha)\right)\right)$ – dimensionless generalized force; $\tau = Vt/r$ – dimensionless time, $\varepsilon = \rho S r^3 J_1^{-1}$, $b = 2m_2 g r^3 / J_1 V^2$, $c = R/r$.

The right part of the system (8) is periodic with respect to $\vartheta$, so a phase space of the system is a phase cylinder $(\vartheta \bmod 2\pi, z)$.

An attracting periodic trajectory of the system (8) going around the phase cylinder corresponds to a working regime of the mechanism. The case of an attracting periodical trajectory with always positive $z$ corresponds to the up-wind motion of the vehicle. We would like to find sufficient conditions for existence of attracting periodic solutions of the system (8) and to estimate for which

values of parameters *a* (the relation between lengths of links) and *c* (relation between radius of the wheel and length of the crank) the maximum average speed of the point O can be achieved.

## 4. Sufficient conditions for existence of periodic motions

For $\varepsilon = 0$ the system (8) takes the form of the following conservative system:

$$\begin{cases} \dfrac{d\vartheta}{d\tau} = \dfrac{\partial H}{\partial p}; \\ \dfrac{dp}{d\tau} = -\dfrac{\partial H}{\partial \vartheta}; \end{cases} \qquad (9)$$
$$H(\vartheta, p) = \frac{p^2}{2k(\vartheta)} + \frac{b}{2}\sin\vartheta.$$

Denote $p_h(\vartheta) = k(\vartheta) z_h(\vartheta) = \sqrt{(h - b\sin\vartheta)k(\vartheta)}$ – the trajectory of the system (9) for $H(\vartheta, p) = h/2$ , $h > b$.

Introduce the following notations:

$$Q_h = Q_h(\vartheta) = Q\left(\vartheta, z_h(\vartheta)\right),$$
$$I(h) = \frac{1}{2\pi}\int_0^{2\pi} Q_h(\vartheta)d\vartheta = \langle Q_h \rangle. \qquad (10)$$

For the system (8) all conditions of the Poincare-Pontryagin theorem ([10]) are fulfilled and hence the following holds:

If for some particular value $h_0 > b$ the integral $I(h_0)$ equals zero and its derivative with respect to the parameter $h$ is not equal to zero, then for sufficiently small $\varepsilon$ the system (8) possess a periodic trajectory $\tilde{p}_{h_0}(\vartheta)$ which tends to the trajectory $p_{h_0}(\vartheta)$ of the system (9) when $\varepsilon$ tends to zero. Moreover if $\left.\dfrac{dI(h)}{dh}\right|_{h=h0} < 0$ the trajectory $\tilde{p}_{h_0}(\vartheta)$ is attracting, if $\left.\dfrac{dI(h)}{dh}\right|_{h=h0} > 0$ the trajectory $\tilde{p}_{h_0}(\vartheta)$ is repelling.

So we obtained the sufficient conditions of existence of periodic trajectories of the system (8) for the case when $\varepsilon$ tends to zero as well as the criterion of orbital stability of periodic trajectories originating from trajectories of the Hamiltonian system (9). Practically sufficiently small values of $\varepsilon$ can be obtained by increasing of the moment of inertia $J_1$.

## 5. Bifurcation diagrams of periodic regimes

Average speed of the point O at periodic regimes is of a special interest for practical applications of the mechanism. Let $\left\langle V^*_{O,h_0} \right\rangle$ denote the average speed of the point O corresponding to the periodic trajectory $\tilde{p}_{h_0}(\vartheta)$ of the system (8). This trajectory $\tilde{p}_{h_0}(\vartheta)$ tends to the trajectory $p_{h_0}(\vartheta)$ when $\varepsilon$ tends to zero. Hence for small values of the parameter $\varepsilon$ the value $\left\langle V^*_{O,h_0} \right\rangle$ can be estimated using the average value of the function $z_{h_0}(\vartheta)$:

$$\lambda = \frac{\lim\limits_{\varepsilon \to 0} \left( \left\langle V^*_{O,h_0}(\vartheta) \right\rangle \right)}{V} = c \left\langle z_{h_0}(\vartheta) \right\rangle . \tag{11}$$

The value $\lambda$ is the limit relation between the average speed of the point O (corresponding to the trajectory $\tilde{p}_{h_0}(\vartheta)$) and the wind speed *V*.

Fig. 4 represents limit bifurcation diagrams obtained by the estimation (11) via numerical solution of the equation $I(h) = 0$ for different values of parameters *a* and *c* with fixed values of other parameters: $b = 0.2$, $m_1^2 r^2 J_1^{-1} = 3$, $m_2^2 r^2 J_1^{-1} = 4$, $J_2 J_1^{-1} = 10$, $\beta = 0$. Solid/dashed lines correspond to families of attracting/repelling periodic trajectories.

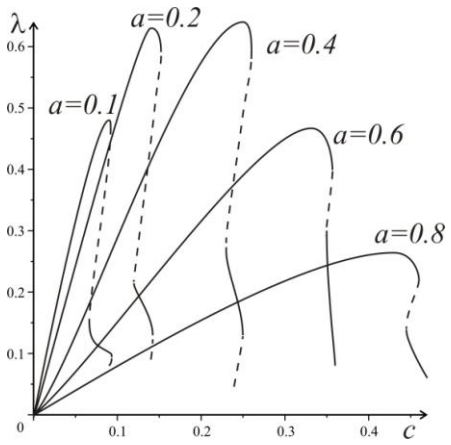


**Figure 4.** Limit bifurcation diagrams.

We obtain (Fig. 4) that maximum values of $\lambda$ are achieved for $a \approx 0.4$. Estimation of $\lambda$ provided here is for sure overvalued because friction is neglected and moreover quasi-static model of aerodynamics may be rather imprecise when the angular speed of the wing is high. Intervals of values

of $c$ where domain of attraction of stable periodical motion is limited by a repelling periodical motion are rather narrow. So for most combinations of parameters even trajectories with zero initial $z$ tend to attracting periodical motion (for certain initial values of $\vartheta$). This corresponds to a self-start of the vehicle for sufficient initial angle between AB and O$x$ axis. Interruption of any curve in the Fig. 4 corresponds to the situation when minimal value of $z$ on a periodic trajectory becomes zero (while average value of $z$ is still far from zero), so the periodic trajectory is destroyed. For each $a$ the value of the parameter $c$ which provides the maximum value of $\lambda$ is close to the upper limit of $c$ for which there exist periodic trajectories originated from trajectories of the system (9).

First prototypes of the mechanism were constructed in the Institute of Mechanics of Lomonosov MSU. During tests in the wind tunnel it was proved that the vehicle is able to move against the wind flow for the wind speed 5-8m/s using only the power produced by the slider-crank wind turbine. So experiments confirm existing of regimes that correspond to attracting periodic solutions of the dynamical system.

## 6. Conclusions

The new type of a wind powered vehicle is introduced. The construction of the mechanism includes the novel slider-crank type wind turbine designed in the Institute of Mechanics of LMSU.

Dynamical model is constructed taking into account the gravity force and the aerodynamic action. In a program operation regime of the mechanism the center of the platform (the point O) moves directly against the horizontal wind flow. This regime corresponds to an attracting periodic trajectory of the dynamical system.

Periodical trajectories of the system are described analytically for small values of the relation $Sr^2/J_1$, where $S$ is the area of the wing, $r$ – radius of the crank, $J_1$ – moment of inertia of the body "crank+wheel". Bifurcation diagrams of periodic trajectories are constructed with respect to the relation between the radius of the wheel and the radius of the crank. Domain of attraction of the stable periodic trajectory is always limited by an unstable one.

The first prototype of the vehicle was constructed and tested in the Institute of Mechanics of LMSU. It does move directly against the wind flow using only the power produced by the slider-crank wind turbine.

Such kind of device can be used in a flow of gas or fluid. The machine takes power from the flow to move up-flow. It can be used to carry loads in regions with stable winds and also inside a river flow: the flow moves this vehicle against the direction of the flow.

**Acknowledgments**

This work was partially supported by the Russian Foundation for Basic Research, projects NN 14-08-01130, and 15-01-06970.

**References**

[1] Leung, D.Y.C., Yang, Y. Wind energy development and its environmental impact: A review. *Renewable and Sustainable Energy Reviews*, V. 16, 2012, pp.1031-1039.

[2] Chinchilla, R., Guccione, S., Tillman, J. Wind Power Technologies: A Need for Research and Development in Improving VAWT's Airfoil Characteristics. *Journal of Industrial Technology*, V. 27, No. 1, 2011, pp.2-6.

[3] Elbahnasy, I., Ellermann, K. An approach for cost and configuration optimization of horizontal axis wind turbine (HAWT). *Renewable Energy and Power Quality Journal*, No. 12, 2014.

[4] Tsai, M.C., Huang C.C., Lin B.J. Kinematic Analysis of Planetary Gear Systems Using the Block Diagram. *Transactions of ASME: Journal of Mechanical Design*, V. 132, 2010, pp. 065001.

[5] Patent RU 2 447 320 C2. (Device for renewable energy conversion) Proprietor: Institute of Mechanics of Lomonosov Moscow State University. 5p. 2012.

[6] Andronov P.R., Dosaev, M.Z., Dynnikova, G.Ya., Selyutskii, Yu.D., Strekalov, S. D. Modeling of oscillating wind turbine. *Journal of Machinery Manufacture and Reliability*, August 2009, V. 38, Issue 4, 2009, pp 383-387.

[7] Klimina, L.A., Lokshin, B.Y., Samsonov, V.A. Parametrical Analysis of the behavior of an Aerodynamic Pendulum with Vertical Axis of Rotation. *Modeling, Simulation and Control of Nonlinear Engineering Dynamical Systems*, 2009, pp. 211-220 2009.

[8] Dosaev, M., Klimina, L., Lokshin, B., Selyutskiy, Yu., Tsai, M.-Ch. On dynamics of a small wind turbine. *11 International Conference "Dynamical systems: theory and applications", Lodz, Poland*, 2011, pp. 277-282.

[9] Dosaev, M.Z., Klimina, L.A., Selyutskiy, Yu.D., Lin, C.H., Lu, W.L., Hwang, S.S., Lin, K.H. Electromechanical Models of Small Wind Turbines. *Proceedings of the 2nd Joint Symposium of Taiwan-Russian Research Cooperation on Advanced Problems of Robotics, Mechatronics and Mechanical Engineering, Taipei*, 2011, pp. 41-46.

[10] Bautin N.N., Leontovich E.A. *Methods and techniques of the qualitative research of the dynamic systems in the plane*. Science, Moscow, 1990. (in Russian).

Liubov Klimina, PhD: Lomonosov Moscow State University, Institute of Mechanics, Michurinsky prosp.,1, 119192, Moscow, Russia (*klimina@imec.msu.ru*).

Marat Dosaev, Associate Professor: Moscow State University, Institute of Mechanics, Michurinsky prosp.,1, 119192, Moscow, Russia (dosayev@imec.msu.ru). The author gave a presentation of this paper during one of the conference sessions.

Yury Selyutskiy, Associate Professor: Moscow State University, Institute of Mechanics, Michurinsky prosp.,1, 119192, Moscow, Russia (seliutski@imec.msu.ru).

Shih-Shin Hwang, Associate Professor: Chien Hsin University of Science and Technology, No.229, Jianxing Rd., Zhongli Dist., Taoyuan City 32097, Taiwan (stanhwang@uch.edu.tw).

Kao-Huei Lin, Associate Professor: Chien Hsin University of Science and Technology, No.229, Jianxing Rd., Zhongli Dist., Taoyuan City 32097, Taiwan (khlin@uch.edu.tw).

# Eighth-order direct numerical method for second-order ordinary differential equations (NUM010-15)

Robert Kostek

*Abstract:* This article presents eighth-order multi-derivative numerical method for solving second-order ordinary differential equations. This method is based on integration Hermite polynomials, which provides an opportunity to avoid numerical effects, for example Runge phenomenon. Moreover, Hermite polynomials interpolate the time history of acceleration with small error, thus this method is more computationally effective, than, for instance, the eighth-order Cooper-Verner method. This method provides an opportunity to use large time steps, which is important for the simulation of multi-degree-of-freedom systems. For easier application and understanding, these method is presented in the form of pseudo-code. The presented approach to integration second-order ordinary equations is a result of the simulation of non-linear mechanical systems with impact and Coulomb friction.

## 1. Introduction.

Newton's laws of motion are the foundation of classical mechanics. One of these laws is the second law of motion, which describes the relationship between acceleration vector of a point mass, vector of the resultant force acting on a point mass, and mass of the point mass:

$$\vec{a} = \vec{F}_r(t)/m \tag{1}$$

where $\vec{a}$ denotes acceleration vector of a point mass, $\vec{F}_r(t)$ represents the vector of the resultant force acting on a point mass, $t$ is time, and $m$ is the mass of the point mass. As is evident, the second low of motion is described by a second-order differential equation. In consequence, the dynamics of discrete mechanical systems can be described by a system of second-order ordinary differential equations. Similarly, continuous media after discretisation can be described (e.g. FEM).

The system of second-order differential equations can be integrated in two ways. The first way, which is the most common approach, is two-step method. First, the system of second-order differential equations is transformed in to a system of first-order differential equations, and then is integrated with a method dedicated to first-order differential equations, for example, the Runge-Kutta method. The transformation of second orders equations to first order equations takes time and human effort. Whereas the second way is the direct integration of the second-order differential equations,

which is a simple and fast method [12, 20]. The basic idea of direct methods is the integration of the time history of acceleration to the time histories of velocity and displacement:

$$v(t_1) = v(t_0) + \int_{t_0}^{t_1} a(t)dt \quad x(t_1) = x(t_0) + \int_{t_0}^{t_1} v(t)dt \tag{2}$$

where $a(t)$ denotes the time history of the acceleration, $a(t)=d^2x/dt^2(t)$; $v(t)$ denotes the time history of velocity, $v(t)=dx/dt(t)$; and $x(t)$ denotes the time history of the displacement $x=f(t)$; whereas $v(t_0)$ and $x(t_0)$ are the initial conditions, and $t_0$ and $t_1$ are the lower and upper limits. This integration is the consequence of kinematics, because velocity and acceleration are time derivatives of displacement.

The time history of acceleration, which is usually unknown, is approximated with Hermite polynomials; and then, Hermite polynomials are integrated to the time histories of velocity and displacement, which is the main idea of the presented methods. It should be mentioned, that Hermite polynomials interpolate the time history of acceleration very near exact solution, and are not sensitise to the Runge phenomenon, which make methods based on Hermite polynomials accurate and fast [12]. These features are particularly important when non-linear vibrations are simulated, because the exact solutions are usually unknown, hence, numerical and perturbation methods are used [15].

Hermite polynomials are calculated from values of a function and their derivatives; thus methods based on Hermite polynomials use higher-order derivatives. Both methods dedicated to first-order differential equations (see, e.g., [4, 5 {p119}, 7, 8, 14, 16, 18]) and second-order differential equations [9, 12, 17, 20] use higher-order derivatives, because higher-order derivatives make numerical errors smaller. Also, some direct methods used in astronomy were inspired by Hermite polynomials (see, e.g., [1, 9, 17]). However, in this paper, the formulae and examples are different from those presented in the afore-mentioned articles.

## 2. Algorithms for the presented methods.

Hermite polynomial used in the presented methods is calculated from values of acceleration and three first derivatives of acceleration, which are calculated for two nodes (time instances). Calculation of three first derivatives is described in literature, moreover derivatives can be approximated with difference quotients, thus calculation derivatives should not lead to difficulties [2, 13, 14]. After calculation coefficients Hermite polynomial is expressed by the following formula:

$$a(t) \approx P_{(7)}(t) = c_0 + c_1 t + c_2 t^2 + c_3 t^3 + c_4 t^4 + c_5 t^5 + c_6 t^6 + c_7 t^7 \tag{3}$$

where $P_{(7)}$ is Hermite polynomial of degree seven, whereas $c_0$ – $c_7$ denote the coefficients of this polynomial. Convergence of polynomials and errors are described in the literature [14, 15, 20].

Methods based on Hermite polynomials can follow the consecutive stages. First, the values of acceleration and derivatives of accelerations are calculated from an equation of motion (8). Next, the coefficients of Hermite polynomial are calculated. And then, Hermite polynomial is integrated two

times, to the time histories of velocity and displacement [12]. This algorithm provides an opportunity to study the time histories between nodes, but is computationally expensive. The simplified algorithm does not calculate the coefficients of Hermite polynomial, thus, it calculates velocity and displacement for consecutive nodes from initial conditions, accelerations and its derivatives. This leads to the linear multi-step multi-derivative predictor-corrector method:

$$x(t_1) = x(t_0) + v(t_0)h + a(t_0)h^2 k_{x1} + a'(t_0)h^3 k_{x2} + a''(t_0)h^4 k_{x3} + a'''(t_0)h^5 k_{x4} + a(t_1)h^2 k_{x5} + a'(t_1)h^3 k_{x6} + a''(t_1)h^4 k_{x7} + a'''(t_1)h^5 k_{x8}, \quad (4)$$

$$v(t_1) = v(t_0) + a(t_0)h\ k_{v1} + a'(t_0)h^2 k_{v2} + a''(t_0)h^3 k_{v3} + a'''(t_0)h^4 k_{v4} + a(t_1)h\ k_{v5} + a'(t_1)h^2 k_{v6} + a''(t_1)h^3 k_{v7} + a'''(t_1)h^4 k_{v8}, \quad (5)$$

$$x(t_2) = x(t_0) + v(t_0)h2 + a(t_0)h^2 p_{x1} + a'(t_0)h^3 p_{x2} + a''(t_0)h^4 p_{x3} + a'''(t_0)h^5 p_{x4} + a(t_1)h^2 p_{x5} + a'(t_1)h^3 p_{x6} + a''(t_1)h^4 p_{x7} + a'''(t_1)h^5 p_{x8}, \quad (6)$$

$$v(t_2) = v(t_0) + a(t_0)h\ p_{v1} + a'(t_0)h^2 p_{v2} + a''(t_0)h^3 p_{v3} + a'''(t_0)h^4 p_{v4} + a(t_1)h\ p_{v5} + a'(t_1)h^2 p_{v6} + a''(t_1)h^3 p_{v7} + a'''(t_1)h^4 p_{v8}, \quad (7)$$

where $k_{x1} - k_{v8}$ denote the coefficients of the corrector, $p_{x1}$ - $p_{v8}$ represent the coefficients of the predictor, and $' = d/dt$. The values of the coefficients are shown in Table 1. It is worth noting that some absolute values of the coefficients are equal; thus, this method can be simplified one more time. Moreover, equation (5) corresponds to an Adams–Moulton method [5 {p119}].

Simulation vibrations of a single degree-of-freedom non-linear system (Fig. 1) is taken as an example, to make understanding of this method easier. These vibrations are described by the following equation of motion:

$$\frac{d^2x}{dt^2} = m^{-1}\left(F_s(x) + F_d(\frac{dx}{dt}) + F_e(t)\right), \quad (8)$$

where $F_s$, denotes the spring force $F_s = f_s(x)$; $F_d$ is force the damping, $F_d = f_d$ (d$x$/d$t$); and $F_e$ is the external force, $F_e = f_e$ ($t$) and $x \in \Re$. This simplified method is presented as a pseudo-code in Fig. 2, thus it is easy to analyse. In the first step, the acceleration and its derivatives are calculated for the time instances $t_0$ and $t_1$. If this method is started, then $x(t_1)$ and $v(t_1)$ can be calculated with a partial sum of the Taylor series or a Runge-Kutta type method from $t_0$, $x(t_0)$ and $v(t_0)$. Next, the displacements $x(t_1)$ and velocity $v(t_1)$ are calculated with a corrector for the time instance $t_1$ (Eqs. 4,5). Iterations provide an opportunity to reduce numerical errors, obtain self-agreement; thus, the number of iterations $n_i$ is a significant factor. Finally, after leaving the iteration loop, the displacements $x(t_2)$ and velocity $v(t_2)$ are extrapolated with the predictor for the time instance $t_2$ (Eqs. 6, 7). The last step is the assignment of new values to variables, which ends one cycle of the procedure. This method uses classical iteration and is called the first method in this article.

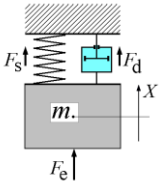


**Figure 1.** Forces acting in a single degree-of-freedom system.

Table 1. Values of the coefficients.

| Coefficients of the corrector. | Values of the coefficients. | Coefficients of the predictor. | Values of the coefficients. |
|---|---|---|---|
| $k_{x1}$ | 131040/9! | $p_{x1}$ | 2016000/9! |
| $k_{x2}$ | 24480/9! | $p_{x2}$ | 852480/9! |
| $k_{x3}$ | 2520/9! | $p_{x3}$ | 149760/9! |
| $k_{x4}$ | 120/9! | $p_{x4}$ | 10752/9! |
| $k_{x5}$ | 50400/9! | $p_{x5}$ | -1290240/9! |
| $k_{x6}$ | -14400/9! | $p_{x6}$ | 921600/9! |
| $k_{x7}$ | 1800/9! | $p_{x7}$ | -184320/9! |
| $k_{x8}$ | -96/9! | $p_{x8}$ | 24576/9! |
| $k_{v1}$ | 181440/9! | $p_{v1}$ | 12337920/9! |
| $k_{v2}$ | 38880/9! | $p_{v2}$ | 5702400/9! |
| $k_{v3}$ | 4320/9! | $p_{v3}$ | 1036800/9! |
| $k_{v4}$ | 216/9! | $p_{v4}$ | 76032/9! |
| $k_{v5}$ | 181440/9! | $p_{v5}$ | -11612160/9! |
| $k_{v6}$ | -38880/9! | $p_{v6}$ | 6635520/9! |
| $k_{v7}$ | 4320/9! | $p_{v7}$ | -1382400/9! |
| $k_{v8}$ | -216/9! | $p_{v8}$ | 165888/9! |

// Calculation of $a(t_0)$, $a'(t_0)$, $a''(t_0)$, and $a'''(t_0)$ for $t_0$, $x(t_0)$, $v(t_0)$

// Calculation of $a(t_1)$, $a'(t_1)$, $a''(t_1)$, and $a'''(t_1)$ for $t_1$, $x(t_1)$, $v(t_1)$

**for (** $n = 0$ ; $n < n_i$ ; $n$++ **) {// The iteration loop** Calculation of $x(t_1)$ and $v(t_1)$ $h = t_1\text{-}t_0 = t_2\text{-}t_1$ **corrector**

$$x(t_1) = x(t_0) + v(t_0)h + a(t_0)h^2k_{x1} + a'(t_0)h^3k_{x2} + a''(t_0)h^4k_{x3} + a'''(t_0)h^5k_{x4} +$$

$$a(t_1)h^2k_{x5} + a'(t_1)h^3k_{x6} + a''(t_1)h^4k_{x7} + a'''(t_1)h^5k_{x8} \ ;$$

$$v(t_1) = v(t_0) + a(t_0)h\ k_{v1} + a'(t_0)h^2k_{v2} + a''(t_0)h^3k_{v3} + a'''(t_0)h^4k_{v4} +$$

$$a(t_1)h\ k_{v5} + a'(t_1)h^2k_{v6} + a''(t_1)h^3k_{v7} + a'''(t_1)h^4k_{v8} \ ;$$

// Calculation of $a(t_1)$, $a'(t_1)$, $a''(t_1)$, and $a'''(t_1)$ for $t_1$, $x(t_1)$, $v(t_1)$

**}**

// Calculation of $x(t_2)$ and $v(t_2)$ extrapolation - **predictor**

$$x(t_2) = x(t_0) + v(t_0)h2 + a(t_0)h^2p_{x1} + a'(t_0)h^3p_{x2} + a''(t_0)h^4p_{x3} + a'''(t_0)h^5p_{x4} +$$

$$a(t_1)h^2p_{x5} + a'(t_1)h^3p_{x6} + a''(t_1)h^4p_{x7} + a'''(t_1)h^5p_{x8};$$

$$v(t_2) = v(t_0) + a(t_0)h\ p_{v1} + a'(t_0)h^2p_{v2} + a''(t_0)h^3p_{v3} + a'''(t_0)h^4p_{v4} +$$

$a(t_1)h\ p_{v5} + a'(t_1)h^2 p_{v6} + a''(t_1)h^3 p_{v7} + a'''(t_1)h^4 p_{v8}$;

$t_0 = t_0 + h$; $x(t_0) = x(t_1)$;...; $a'''(t_0) = a'''(t_1)$; $x(t_1) = x(t_2)$; $v(t_1) = v(t_2)$; // Assignment of new values to variables

**Figure 2.** Pseudo-code of the first method.

## 3. Analysis of the direct method.

### 3.1. Local error and consistency.

The local error $\delta$ represents the departure of the numerical solution from the exact solution after one time step $h$. If the Taylor series converges to the exact solution, then the local errors for the corrector and predictor are described by the following equations:

$$\delta_{kxt1} = \frac{1}{14*10!}\frac{d^{10}x}{dt^{10}}h^{10} + Oh^{11} \tag{9}$$

$$\delta_{kvt1} = \frac{1}{70*9!}\frac{d^{9}x}{dt^{9}}h^{9} + Oh^{10} \tag{10}$$

$$\delta_{pxt2} = \frac{192}{3*10!}\frac{d^{10}x}{dt^{10}}h^{10} + Oh^{11} \tag{11}$$

$$\delta_{pvt2} = \frac{736}{35*9!}\frac{d^{9}x}{dt^{9}}h^{9} + Oh^{10} \tag{12}$$

where $\delta_{\text{kxt1}}$ denotes the local error of the corrector $x(t_1)$, $\delta_{\text{kvt1}}$ is the local error of the corrector $v(t_1)$, $\delta_{\text{pxt2}}$ represents the local error of the predictor $x(t_2)$, and $\delta_{\text{pvt2}}$ is the local error of the predictor $v(t_2)$. As is evident from equations (9-12), this method is consistent, and is of order eight. Order of method and consistency are presented in the same section, because they are related notions [5].

### 3.2. Global error, stability, and convergence.

If the spring and damping forces are described by linear functions (Fig. 1), then numerical errors and stability regions can be easily calculated. Hence, free vibrations of linear single degree-of-freedom system are taken as a test problem:

$$\frac{d^2x}{dt^2} = -m^{-1}\left(kx + c\frac{dx}{dt}\right), \tag{13}$$

where $k$ denotes the stiffness of the spring, and $c$ is the damping coefficient.

The global error $\varepsilon$ represents the departure of the numerical solution from the exact solution after $j$ time steps; thus, the departure is studied for the time instance $jh$. The exact solution $x_e=f(t)$ of the test problem (Eq. 13) is known, thus the global error can be easily calculated:

$$E_1 = X_{n(jh+t_0;h+jh+t_0)} - X_{e(jh+t_0;h+jh+t_0)} = \begin{bmatrix} \varepsilon_{x(jh+t_0)} \\ \varepsilon_{v(jh+t_0)} \\ \varepsilon_{x(h+jh+t_0)} \\ \varepsilon_{v(h+jh+t_0)} \end{bmatrix} = \begin{bmatrix} x_n(jh+t_0) \\ v_n(jh+t_0) \\ x_n(h+jh+t_0) \\ v_n(h+jh+t_0) \end{bmatrix} - \begin{bmatrix} x_e(jh+t_0) \\ v_e(jh+t_0) \\ x_e(h+jh+t_0) \\ v_e(h+jh+t_0) \end{bmatrix}, \quad (14)$$

where $E_1$ denotes the vector of global errors, $X_n$ is the vector of numerical solutions, and $X_e$ is the vector of exact solutions. The vectors of numerical solutions can be calculated with matrix equations:

$$X_{n(jh+t_0;h+jh+t_0)} = (PK^{n_i})^j X_{e(t_0;h+t_0)} = T^j X_{e(t_0;h+t_0)} = (Q\Lambda Q^{-1})^j X_{e(t_0;h+t_0)} = Q\Lambda^j Q^{-1} X_{e(t_0;h+t_0)}, \quad (15)$$

where $X_{e(t_0;h+t_0)}$ denotes the exact initial condition, $P$ is the matrix of the predictor, $K$ is the matrix of the corrector, $T$ is the transformation matrix, $Q$ is the matrix of the eigenvectors, $\Lambda$ is the diagonal matrix of eigenvalues, $j$ is the number of time steps, and $n_i$ is the number of iterations [3, 12].

Based on the diagonal matrix of eigenvalues $\Lambda$, a stability criterion can be formulated. If for a chosen time step $h$ and the test equation (13), the largest absolute value of the eigenvalues is less than or equal to unity, then the numerical solution does not grow to infinity; hence, the numerical solution and the numerical method are stable. This stability criterion is express by the following expression:

$$\max|\Lambda| \le 1. \quad (16)$$

The stability regions obtained for the presented method are depicted in Fig. 3. This figure shows the evolution of the stability regions due to the consecutive iterations. First, the stability region of the predictor is depicted in Fig. 3a for $n_i = 0$. The obtained area is the smallest, but exists; thus this predictor (Eqs. 6, 7) can be used as a numerical method without any corrector. Next, consecutive iterations make the stability regions larger, because the stability region of corrector is larger than the stability region of the predictor (Fig. 3a-d). Finally, after a large number of iterations, the stability region tends to the stability region obtained for the corrector (Fig. 3d). The stability regions are important during simulations as they determine the largest time step which can be used. If roots $r$ of the test equation (13), multiplied by the time step $h$ are inside a stability region, then the numerical solution is stable, otherwise, the numerical solution is unstable (Fig. 3b). If a solution is unstable, then the following effect can be observed: numerical solutions grow exponentially to infinity, amplitude of vibrations grows exponentially to infinity, amplitude of numerical noise grows exponentially to infinity. The stability intervals obtained for $c = 0$ are presented in Table 2.

At this stage, convergency is discussed. A sufficient condition for convergence is when a linear multi-step method is stable and consistent [5]. Next, the global error can be described. If the studied method is convergent, the test equation has a stable exact solution, the test equation has a solution with continuous derivatives up to order $p$+1, the starting values are exact, the rounding errors equal zero, and the time step $h$ tends to zero, then the global error is expressed by the following expression:

$$|\varepsilon| \le \xi h^p, \quad (17)$$

where $\varepsilon$ denotes the global error for the considered time instance $t_0+jh$, $p$ is the order of the method $p = 8$, and $\xi$ depends on the interval of integration $[t_0, t_0+jh]$, the method used, and the test problem. This formula describes convergence of the presented methods (see, e.g., [4, 5, 6, 18, 19]).

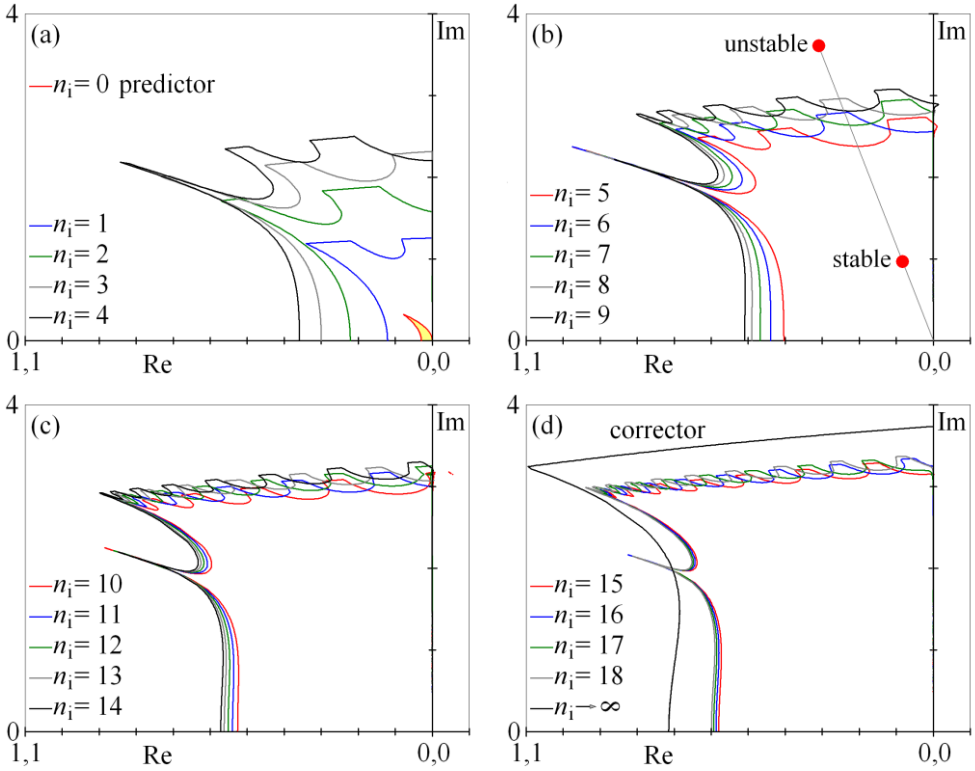


**Figure 3.** Stability regions of the first method obtained for various numbers of iterations $n_i$ (a – d).

Table 2. Stability intervals obtained for $c = 0$.

| Number of iterations $n_i$ | Stability intervals | Number of iterations $n_i$ | Stability intervals |
|---|---|---|---|
| 0 | | 6 | [2.5637 i; 2.4487 i] [0.6746 i; 0 i] |
| 1 | [**1.2558 i**; 0 i] | 7 | [**1.8078 i**; 0 i] |
| 2 | [0.2549 i; 0 i] | 8 | [**2.8091 i**; 0 i] |
| 3 | [2.3166 i; 2.3165 i] [0.7933 i; 0 i] | 9 | [2.9011 i; 1.9694 i] [0.9834 i; 0 i] |
| 4 | [**2.2051 i**; 0 i] | 10 | [3.1693 i; 2.6036 i] [**1.1076 i**; 0 i] |
| 5 | [2.6623 i; 1.5238 i] [0.5883 i; 0 i] | 11 | [3.0009 i; 2.8918 i] [**2.0761 i**; 0 i] |

## 4. An example application.

Two factors are very important in numerical simulations; they are numerical errors and CPU times, by which numerical methods are judged. These two factors are studied in this section for the following methods: the first method, the classical fourth-order Runge-Kutta method, the fifth-order

Dormand-Prince method, the sixth-order Verner method, the seventh-order Runge-Kutta type method [5 {p196}], and the eighth-order Cooper-Verner method.

If the exact solution is known, then the numerical errors can be precisely calculated, hence the linear test equation (13) is solved with the afore-mentioned numerical methods. The following parameters and initial conditions have been used: $m$ = 1[kg], $c$ = 0[Nsm$^{-1}$], $k$ = 1[N/m], $t_0$ = 0[s], $x(t_0)$ = 1[m], and $v(t_0)$ = 0[m/s], which leads to the following solution:

$$x = \cos(t) \quad . \tag{18}$$

Despite the fact that the exact solution is the entire function, some numerical effects can be observed for such simple system. They are the numerical excitation or damping vibrations, the error in the period, and numerical noise growing to infinity. These two first effects are described by equations:

$$\delta_A = \left|1 - \sqrt{x_n^2(T_e) + v_n^2(T_e)}\right| / 1 \ , \tag{19}$$

$$\delta_T = \left|T_n - T_e\right| / T_e \ , \tag{20}$$

where $\delta_{\mathrm{A}}$ is the relative error of the amplitude, $x_n(T_e)$ is the displacement calculated with a numerical method for the time instance $T_{\mathrm{e}}$ =2π, $v_n(T_e)$ is the velocity calculated with a numerical method for the time instance $T_{\mathrm{e}}$, $\delta_{\mathrm{T}}$ is the relative error in the period, $T_{\mathrm{e}}$ represents the exact period of oscillation $T_{\mathrm{e}}$ =2π[s], and $T_{\mathrm{n}}$ is the period of oscillation obtained with a numerical method. For the studied test problem these errors are obvious, but for sophisticated systems they can lead to misinterpretation of results. These numerical errors and effects are associated with matrix of eigenvalues [3, 12]. The exact initials conditions were used for the time instance $t$ = 0, whereas for the time instance $t = h$, the results of extrapolation (Eqs. 6, 7) calculated from the exact solution were used. The remaining methods use the exact initials conditions for the time instance $t$ = 0.

Reference to CPU times should be mentioned, in that calculations performed for the Dormand-Prince method were limited to the fifth-order algorithm, and calculations performed for the Verner method were limited to the sixth-order algorithm. Moreover, source codes of the first method was optimised, and then compiled in C++ version 6.0. The computations were performed on a computer with an Intel Desktop Board D525MW motherboard and an Intel Atom D525 1.8GHz processor running Windows XP Professional, and thus can be compared with previously presented results [12]. Finally, the computation times for one period of vibration $t_{\mathrm{c}}$ were measured.

First, the relative error of amplitude $\delta_{\mathrm{A}}$ was calculated for various numbers of time steps per period, $T_e/h$ (Fig. 4a). Additionally, the first method was studied for various numbers of iterations $n_{\mathrm{i}}$. As is evident from the obtained results, the amplitude error $\delta_{\mathrm{A}}$ obtained for the first method can be reduced both with increasing number of time steps per period $T_e/h$, and increasing number of iterations $n_{\mathrm{i}}$ . However, increasing the number of iterations over twenty-five does not yield a

significant reduction of this error (Eq. 19). A large number of iteration provides an opportunity to reduce significantly the amplitude error below $\delta_A$ < 1e-13 for large time steps being $h = T_e/3$, which is an advantage. The observed reduction of the amplitude error is a result of a better fit of the Hermite polynomial to the interpolated function. The error of amplitude is large for the predictor $n_i = 0$, because the predictor is unstable for this test problem, but after two iterations this error is definitely smaller than obtained for the Cooper-Verner method.

Next, the relative error of amplitude $\delta_A$ is presented versus the CPU time required for calculating one period $t_c$ (Fig. 4b), by which numerical methods are judged. The CPU time indicates the cost of computation. As is evident from the obtained results, the first method is more effective than the Cooper-Verner method, for numbers of iteration from one to twenty-five. To better illustrate this issue, the CPU times $t_c$ , which were obtained for the first method $n_i = 3$, the second method (which is not described) and the Cooper-Verner method are compared for $\delta_A = 10^{-9}$ in Fig. 4b.

Then, the error in the period $\delta_T$ was calculated for various numbers of time steps per period, $T_e/h$ (Fig. 5a). Additionally, the first method was studied for various numbers of iterations $n_i$. As is evident from the obtained results, the error in the period $\delta_T$ obtained for the first method is primarily reduced by increasing the number of time steps per period, $T_e/h$. In contrast to this, only the first two iterations significantly reduce this error, whereas the consecutive iterations reduce this error only for large time steps ($h = T_e/3$). The error in the period $\delta_T$ obtained for predictor $n_i = 0$ is large, because the predictor is unstable for this test problem, but after three iterations it is definitely smaller than the error obtained for the Cooper-Verner method.

Finally, the error in the period $\delta_T$ is presented versus the CPU time required for calculating one period $t_c$ (Fig. 5b), by which numerical methods are judged. As is evident from the obtained results, the first method is the most effective for one or two iterations, depending on the time step. Summarising this, the Cooper-Verner method is less computationally effective than the first method for number of iteration being from $n_i = 1$ to $n_i = 11$.

In summary, if the relative error of the amplitude $\delta_A$ , the relative error in the period $\delta_T$ and the CPU time required for calculating one period $t_c$ are taken as criteria, then the first method for numbers of iterations being from $n_i = 1$ to $n_i = 11$ is more effective than the eighth-order Cooper-Verner method (Fig. 4b, 5b). At the same time, the first method is more effective than the classical fourth-order Runge-Kutta method, the fifth-order Dormand-Prince method, the sixth-order Verner method, and the seventh-order Runge-Kutta type method [5 {p196}]. It should be mentioned that these conclusions are valid for the considered test problem and used computer.

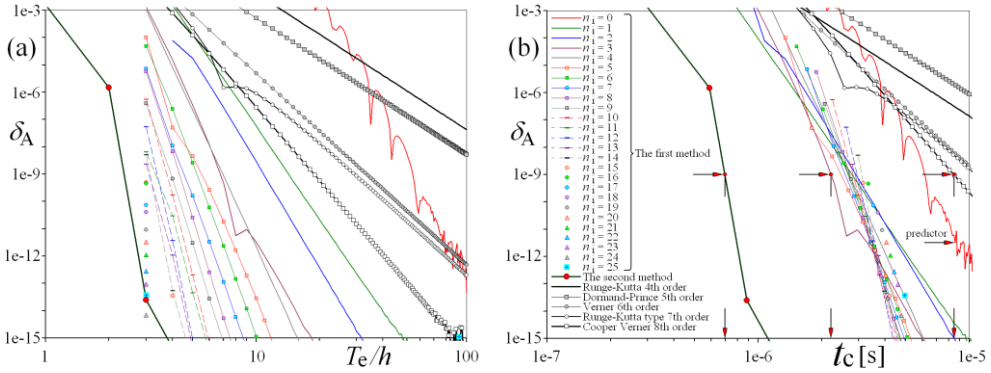


**Figure 4.** Comparison of the first method with the Runge-Kutta type methods. The plots show the relative amplitude error $\delta_A$ calculated for the presented numbers of iterations $n_i$ versus the number of time steps per period $T_e/h$ (a), and the relative amplitude error $\delta_A$ versus the computational time $t_c$ required to calculate one period $T_e$ (b).

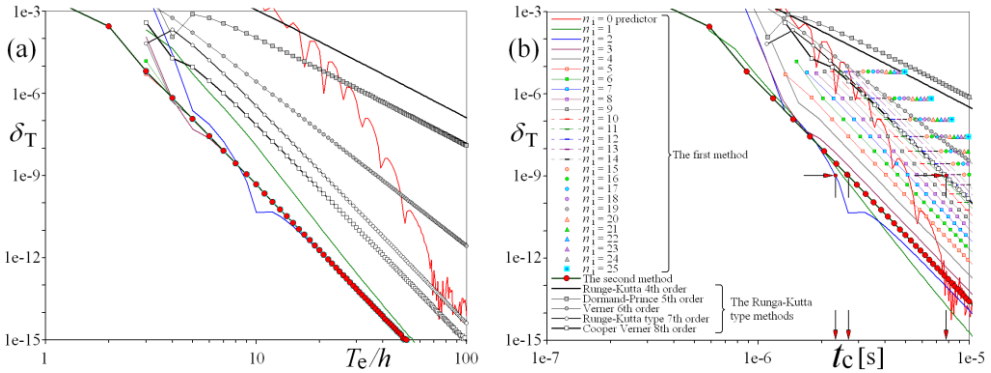


**Figure 5.** Comparison of the first method with the Runge-Kutta type methods. The figures show the relative error in period $\delta_T$ calculated for the presented numbers of iterations $n_i$ versus the number of time steps per period $T_e/h$ (a), and the relative period error $\delta_T$ versus the computational time $t_c$ required to calculate one period $T_e$ (b).

The first method provides an opportunity to use large time step, which is important during simulation of multi-degree-of-freedom systems (finite element method, discrete element method). This is because the highest natural frequency determines the time step and CPU time required. Nevertheless, for the time step being larger than $h > T_n/2$ aliasing is observed, which is a limitation. Moreover, the first method can be used when the parameters of a system are identified using time histories that were sampled with a large sampling period, because these methods can use large time steps, and use only data known for two nodes. Finally, the time step is a taken constant during simulation, because it makes data processing fast and efficient (e.g. Fourier transform). Local

instability problem can be solved with local reduction of the time step $h$, application of larger number of iteration $n_i$, or by an approximation time history of acceleration by non-smooth or discontinuous functions. Numbers of iterations from one to four are reasonable for common simulations. If the number of time steps per period is larger than sixty $T_e/h > 60$, then both the amplitude error $\delta_A$ and the error in the period $\delta_T$ are below 1e-15, for the first method - except the predictor. Thus these errors are a near round-off error offered by double-precision floating-point format, this shows convergence.

## 5. Conclusions.

This article presents direct numerical method based on Hermite polynomials. Hermite polynomials interpolate time history of acceleration with small error, moreover, number of numerical operations was reduced, thus the presented methods are accurate and computationally effective. The basic idea of these methods is the integration of the time history of acceleration to the time histories of velocity and displacement. The most important features of the presented methods are summarised below.

- This method is more computationally effective, than, for instance, the eighth-order Cooper-Verner method, because they use simple formulae.
- In addition, this method can be easily started, because it uses values of the acceleration and its derivatives known only for two nodes.
- Furthermore, the time step can be changed easily during simulation, if necessary.
- Additionally, the presented iteration procedures provide an opportunity to reduce numerical errors for large time steps; which is an advantage.
- Moreover, if the acting forces are described by non-smooth or discontinuous functions, then these methods can be used; because Hermite polynomials are not very sensitive to the Runge phenomenon. But the best solution is to divide time step to sub-steps (sub-intervals). This provides an opportunity to avoid points of discontinuity within integrated interval.
- Finally, the time histories of acceleration, velocity, and displacement can be studied between nodes if the coefficients of Hermite polynomial $P_{(7)}$ were calculated. This is important in non-linear dynamics during the calculation of Poincaré maps.

## References

[1] Aarseth S.J., From NBODY1 to NBODY6: The Growth of an Industry, Publications of The Astronomical Society of The Pacific, 111 (1999) 1333-1346

[2] Barrio R., Blesa F., Lara M., VSVO formulation of the taylor method for the numerical solution of ODEs, Computers & Mathematics with Applications, 50 (2005) 93-111

[3] Bathe K.J., Wilson E.L., Stability and accuracy analysis of direct integration methods, Earthquake Engineering & Structural Dynamics, 1 (1973) 283-291

[4] Brown R.L., Some characteristics of implicit multi-step multi-derivative integration formulas, SIAM Journal on Numerical Analysis, 14 (1977) 982-993

[5] Butcher J.C., Numerical Methods for Ordinary Equations, John Wiley & Sons, Inc. 2008

[6] Dahlquist G., Björck Å., Numerical methods, Prentice-Hall, 1974

[7] Enright W.H., Second derivative multistep methods for stiff ordinary differential equations, SIAM Journal on Numerical Analysis 11 (1974) 321-331

[8] Filippi S., Knecht T., Generalized Hermite multistep methods of high order with a variable step-size, Journal of Computational and Applied Mathematics 59 (1995) 173-180

[9] Kokubo E., Yoshinaga K., Makino J., On a time-symmetric Hermite integrator for planetary N-body simulation, Monthly Notices of the Royal Astronomical Society, 297 (1998) 1067-1072

[10] Kostek R., Influence of an external normal harmonic force on reduction of friction force, Journal of Polish CIMAC, 4 (2009) 67-73

[11] Kostek R., Analysis of the primary and superharmonic contact resonances – Part 1, Journal of Theoretical and Applied Mechanics, 51 (2013) 475-486

[12] Kostek R., Direct numerical methods dedicated to second-order ordinary differential equations, Applied Mathematics and Computation, 219 (2013) 10082-10095

[13] Lara M., Elipe A., Palacios M., Automatic programming of recurrent power series, Mathematics and Computers in Simulation, 49 (1999) 351-362

[14] Mathews J.H., Fink K.D., Numerical Methods Using Matlab, fourth ed., Prentice Hall 2005

[15] Nayfeh A.H., Problems in Perturbation, John Wiley & Sons, Inc. 1985

[16] Nguyen-Ba T., Bozic V., Kengne E., Vaillancourt R.: A one-step 7-stage Hermite–Birkhoff–Taylor ODE solver of order 11. Journal of Computational and Applied Mathematics, 234 (2010) 192-208

[17] Nitadori K., Makino J., Sixth- and eighth-order Hermite integrator for N-body simulations, New Astronomy, 13 (2008) 498–507

[18] Sacks-Davis R., Solution of stiff ordinary differential equations by a second derivative method, SIAM Journal on Numerical Analysis, 14 (1977) 1088-1100

[19] Stoer J., Bulirsch R., Introduction to numerical Analysis, Springer-Verlang, 1983

[20] Wilson E.L., Three-dimensional static and dynamic analysis of structures, SCI third edition 2002

Robert Kostek, Ph.D.: University of Science and Technology, 85-789 Bydgoszcz, Poland (*robertkostek@o2.pl*).

# Tenth-order direct numerical method for second-order ordinary differential equations (NUM011-15)

Robert Kostek

*Abstract:* This article presents direct tenth-order multi-derivative numerical method for solving second-order ordinary differential equations. The basic idea of this method is the integration of Hermite polynomials, which estimate the time history acceleration (second time derivative of displacement). The use of Hermite polynomials provides an opportunity to avoid the Runge phenomenon, and reduce numerical errors; this is because the Hermite polynomials interpolate the time history of acceleration with small errors. Consequently, these methods are more computationally effective, than, for instance, the tenth-order Ono-Stone method. Moreover, if necessary, large time steps can be used, and time steps can be changed during simulation. Finally, these methods can be used, if the acting forces are described by non-smooth or discontinuous functions. It refers, for example, to simulation mechanical systems with impact and dry friction. The presented approach to numerical methods is a result of solving strongly non-linear equations of motion.

## 1. Introduction.

The second law of motion, is the foundation of mechanical systems dynamics. This law is describes by a second order ordinary differential equation, thus many engineering problems are described by sets of second-order ordinary differential equations. These sets are used for example in: the multi-body systems (MBS), the finite element method (FEM), the smoothed finite element method (S-FEM), the discrete element method (DEM), and the molecular dynamics (MD). This shows that second-order ordinary differential equations are used in many methods, which is a result of discretisation continuos media. Continuos media are described by partial differential equations, but after discretisation are described by systems of second-order ordinary differential equations. Usually a system of second-order ordinary differential equations is transformed in to a system of first-order ordinary differential equations, and then is solved with the fourth-order Runge-Kutta method. This is the most common approach to solving second-order ordinary differential equations. Nevertheless, these equations can be solved with direct methods, which are effective, easy to understand, and provide an opportunity to avoid numerical effects [10]. The basic idea of direct methods is direct integration of the time history of acceleration, to the time histories of velocity and displacement.

The key factor for the direct numerical methods is the approximation of the time history of acceleration, which can be done, for example, with linear functions, partial sums of the Taylor series, or polynomials [19]. In the presented method, the time history of acceleration is approximated with the Hermite polynomials. The Hermite polynomials interpolate the time history of acceleration with small errors, are not very sensitive to discontinuous derivatives, and thus are not very sensitive to the Runge phenomenon; moreover, they can easily be calculated and integrated. These advantages make methods based on the Hermite polynomials computationally effective [10], and thus are used by many researchers. The direct methods based on Hermite polynomials are successfully used, for example, in astronomy [1, 9, 14, 18, 21, 22]. The Hermite polynomials are computed from values of an approximated function and their derivatives; thus presented method use higher-order derivatives. The higher-order derivatives increase the order of numerical methods, reduce numerical errors, and thus are used in many methods dedicated both to first-order differential equations (see, e.g., [4, 5 {p119}, 6, 7, 12, 15, 17, 20]) and second-order differential equations [1, 9, 10, 14, 16, 18]. These methods are related to the Hermite polynomials, even if it is not mentioned. As is evident from the literature search, there are many numerical methods based on the Hermite polynomials. However, method presented in this article is different from those presented in the afore-mentioned articles, and are not described in literature known to the author.

## 2. Algorithms for the presented method.

Algorithm of this directed method is presented for the following equation of motion:

$$\frac{d^2x}{dt^2} = m^{-1}\left(F_s(x) + F_d\left(\frac{dx}{dt}\right) + F_e(t)\right) \tag{1}$$

where $F_s$ is the spring force, $F_s = f_s(x)$; $F_d$ denotes the damping force, $F_d = f_d\,(dx/dt)$; and $F_e$ represents the external force, $F_e = f_e\,(t)$. This equation describes, for example, the classical problem in mechanics; it means vibrations of the Single Degree-of-Freedom (SDOF) system (Fig. 1).

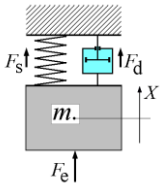


**Figure 1.** Forces acting in a single degree-of-freedom system.

It has been assumed that the time history of acceleration is estimated with the Hermite polynomial of degree nine, which is express by the following expression:

$$a(t) \approx P_{(9)}(t) = c_0 + c_1t + c_2t^2 + c_3t^3 + c_4t^4 + c_5t^5 + c_6t^6 + c_7t^7 + c_8t^8 + c_9t^9 \tag{2}$$

where $P_{(9)}$ denotes the Hermite polynomial of degree nine, and $c_0 - c_9$ are the coefficients of this polynomial. This polynomial is calculated from values of acceleration and four first time derivatives of acceleration computed for two time instances – $t_0$, $t_1$ [2, 12, 13, 15]. Next, for $t_0$ being $t_0$=0, this polynomial can be integrated to thefollowing time histories of velocity and displacement:

$$v(t_2) = v(t_0) + c_0 t_2 + \frac{1}{2}c_1 t_2^2 + \frac{1}{3}c_2 t_2^3 + \frac{1}{4}c_3 t_2^4 + \frac{1}{5}c_4 t_2^5 + \frac{1}{6}c_5 t_2^6 + \frac{1}{7}c_6 t_2^7 + \frac{1}{8}c_7 t_2^8 + \frac{1}{9}c_8 t_2^9 + \frac{1}{10}c_9 t_2^{10} \quad (3)$$

$$x(t_2) = x(t_0) + v(t_0)t_2 + \frac{1}{2}c_0 t_2^2 + \frac{1}{6}c_1 t_2^3 + \frac{1}{12}c_2 t_2^4 + \frac{1}{20}c_3 t_2^5 + \frac{1}{30}c_4 t_2^6 + \frac{1}{42}c_5 t_2^7 + \frac{1}{56}c_6 t_2^8 + \frac{1}{72}c_7 t_2^9 + \frac{1}{90}c_8 t_2^{10} + \frac{1}{110}c_9 t_2^{11} \quad (4)$$

where $t_0$=0, $v(t_0)$ and $x(t_0)$ denote the initial conditions. These equations provide opportunities to study the time histories between nodes ($t_0<t_2<t_1$), change the time step if necessary ($t_2$-$t_1 \neq t_1$-$t_0$), use iterations ($t_2=t_1$) and extrapolation ($t_2>t_1$). If non-linear vibrations are simulated, then these features are important. If Poincaré maps are calculated, then the time histories between nodes can be studied. Moreover, if acceleration or its derivatives are discontinuous functions [11], then the time step should be changed to avoid points of discontinuity within integrated intervals. Furthermore, iterations provide an opportunity to reduce numerical errors. Finally, comparison results obtained with predictor and corrector provides valid information about errors, convergence and points of discontinuity. This algorithm has advantages and application areas, but is computationally expensive, because the coefficients of the polynomial are calculated; thus the simplified algorithm avoids this stage.

The simplified algorithm, which is called the first method in this article, does not calculate the coefficient of the Hermite polynomial and uses constant time step ($h$=$t_1$-$t_0$=$t_2$-$t_1$). These assumptions lead to very simple equations:

$$x(t_1) = x(t_0) + v(t_0)h + a(t_0)h^2 k_{x1} + a'(t_0)h^3 k_{x2} + a''(t_0)h^4 k_{x3} + a'''(t_0)h^5 k_{x4} + a^{(4)}(t_0)h^6 k_{x5} + a(t_1)h^2 k_{x6} + a'(t_1)h^3 k_{x7} + a''(t_1)h^4 k_{x8} + a'''(t_1)h^5 k_{x9} + a^{(4)}(t_1)h^6 k_{x10}, \quad (5)$$

$$v(t_1) = v(t_0) + a(t_0)h\ k_{v1} + a'(t_0)h^2 k_{v2} + a''(t_0)h^3 k_{v3} + a'''(t_0)h^4 k_{v4} + a^{(4)}(t_0)h^5 k_{v5} + a(t_1)h\ k_{v6} + a'(t_1)h^2 k_{v7} + a''(t_1)h^3 k_{v8} + a'''(t_1)h^4 k_{v9} + a^{(4)}(t_1)h^5 k_{v10}, \quad (6)$$

$$x(t_2) = x(t_0) + v(t_0)h2 + a(t_0)h^2 p_{x1} + a'(t_0)h^3 p_{x2} + a''(t_0)h^4 p_{x3} + a'''(t_0)h^5 p_{x4} + a^{(4)}(t_0)h^6 p_{x5} + a(t_1)h^2 p_{x6} + a'(t_1)h^3 p_{x7} + a''(t_1)h^4 p_{x8} + a'''(t_1)h^5 p_{x9} + a^{(4)}(t_1)h^6 p_{x10}, \quad (7)$$

$$v(t_2) = v(t_0) + a(t_0)h\ p_{v1} + a'(t_0)h^2 p_{v2} + a''(t_0)h^3 p_{v3} + a'''(t_0)h^4 p_{v4} + a^{(4)}(t_0)h^5 p_{v5} + a(t_1)h\ p_{v6} + a'(t_1)h^2 p_{v7} + a''(t_1)h^3 p_{v8} + a'''(t_1)h^4 p_{v9} + a^{(4)}(t_1)h^5 p_{v10} \quad (8)$$

where $h$ represents the time step, $k_{x1}$ - $k_{v10}$ are the coefficients of the corrector and $p_{x1}$ - $p_{v10}$ denote the coefficients of the predictor. The values of these coefficients are presented in Table 1. Thus, the equation (6) can be simplified, because some absolute values of its coefficients are equal (see $k_{v1}$-$k_{v10}$). It should be noted, that this method can be classified as a direct linear multi-step, multi-

derivative predictor-corrector method. Furthermore, equations (6) and (8) are similar to the Adams–Moulton and Adams–Bashforth type methods [5 {p119}].

Table 1. Values of the coefficients.

| Coefficients of the corrector. | Values of the coefficients. | Coefficients of the predictor. | Values of the coefficients. |
|---|---|---|---|
| $k_{x1}$ | 120960/332640 | $p_{x1}$ | -7076160/332640 |
| $k_{x2}$ | 23520/332640 | $p_{x2}$ | -3427200/332640 |
| $k_{x3}$ | 2730/332640 | $p_{x3}$ | -692160/332640 |
| $k_{x4}$ | 186/332640 | $p_{x4}$ | -71040/332640 |
| $k_{x5}$ | 6/332640 | $p_{x5}$ | -3200/332640 |
| $k_{x6}$ | 45360/332640 | $p_{x6}$ | 7741440/332640 |
| $k_{x7}$ | -13440/332640 | $p_{x7}$ | -3870720/332640 |
| $k_{x8}$ | 1890/332640 | $p_{x8}$ | 913920/332640 |
| $k_{x9}$ | -144/332640 | $p_{x9}$ | -109056/332640 |
| $k_{x10}$ | 5/332640 | $p_{x10}$ | 7424/332640 |
| $k_{v1}$ | 166320/332640 | $p_{v1}$ | -63201600/332640 |
| $k_{v2}$ | 36960/332640 | $p_{v2}$ | -30085440/332640 |
| $k_{v3}$ | 4620/332640 | $p_{v3}$ | -6061440/332640 |
| $k_{v4}$ | 330/332640 | $p_{v4}$ | -623040/332640 |
| $k_{v5}$ | 11/332640 | $p_{v5}$ | -28160/332640 |
| $k_{v6}$ | 166320/332640 | $p_{v6}$ | 63866880/332640 |
| $k_{v7}$ | -36960/332640 | $p_{v7}$ | -33116160/332640 |
| $k_{v8}$ | 4620/332640 | $p_{v8}$ | 7687680/332640 |
| $k_{v9}$ | -330/332640 | $p_{v9}$ | -929280/332640 |
| $k_{v10}$ | 11/332640 | $p_{v10}$ | 60544/332640 |

The first method is presented as a pseudo-code (Fig. 2), to show clearly the consecutive stages. First, the acceleration and its four first time derivatives are calculated for two time instances, being $t_0$ and $t_1$. If this method is started for known $t_0$, $x(t_0)$ and $v(t_0)$; then $x(t_1)$ and $v(t_1)$ can be calculated, with e.g. the Taylor series method or a Runge-Kutta type method. Then, corrector iterations are used to reduce numerical errors and make the stability region larger. Moreover, classical iterations can lead to self-agreement, but are computationally expensive. Thus, the number of iterations $n_i$ is a significant factor. Next, the predictor is used to calculate $x(t_2)$ and $v(t_2)$. After that, new values are assigned to variables, which finally end one cycle of computation. This clearly shows the first method.

More information about convergence of polynomials should be presented in this section. Numerical and analytical methods are used to solve the studied equation of motion (1). For example, a solution obtained with a perturbation method can be presented as a Furier series, and thus it can be an entire function, because the sine and cosine are the entire functions. If the exact solution is an entire function, then it can be express as a Taylor series. If a Taylor series is convergent to the exact solution within an interval, then a polynomial is convergent to the exact solution within this interval [8]. It means that polynomials can be used to solve the studied equation of motion (1).

Otherwise, if a polynomial is not convergent to the exact solution, or a numerical method is unstable, than numerical effects can be observed e.g.: the Runge phenomenon or a numerical noise. These effects are coupled, for example, with points of discontinuity, and large time steps. The numerical effects make simulation difficult and the obtained results are useless in this case; additional information is presented in literature [8, 15].

// Calculation of $a(t_0)$, $a'(t_0)$, $a''(t_0)$, $a'''(t_0)$, and $a^{(4)}(t_0)$ for $t_0$, $x(t_0)$, $v(t_0)$
// Calculation of $a(t_1)$, $a'(t_1)$, $a''(t_1)$, $a'''(t_1)$, and $a^{(4)}(t_1)$ for $t_1$, $x(t_1)$, $v(t_1)$

**for (** $n = 0$ ; $n <$ $\boldsymbol{n}_i$ ; $n$++ **) { // The iteration loop – corrector**

$$x(t_1) = x(t_0) + v(t_0)h + a(t_0)h^2k_{x1} + a'(t_0)h^3k_{x2} + a''(t_0)h^4k_{x3} + a'''(t_0)h^5k_{x4} + a^{(4)}(t_0)h^6k_{x5} + a(t_1)h^2k_{x6} + a'(t_1)h^3k_{x7} + a''(t_1)h^4k_{x8} + a'''(t_1)h^5k_{x9} + a^{(4)}(t_1)h^6k_{x10} ;$$

$$v(t_1) = v(t_0) + a(t_0)h\ k_{v1} + a'(t_0)h^2k_{v2} + a''(t_0)h^3k_{v3} + a'''(t_0)h^4k_{v4} + a^{(4)}(t_0)h^5k_{v5} + a(t_1)h\ k_{v6} + a'(t_1)h^2k_{v7} + a''(t_1)h^3k_{v8} + a'''(t_1)h^4k_{v9} + a^{(4)}(t_1)h^5k_{v10} ;$$

// Calculation of $a(t_1)$, $a'(t_1)$, $a''(t_1)$, $a'''(t_1)$, and $a^{(4)}(t_1)$ for $t_1$, $x(t_1)$, $v(t_1)$
**}**
// Calculation of $x(t_2)$ and $v(t_2)$ extrapolation - **predictor**

$$x(t_2) = x(t_0) + v(t_0)h2 + a(t_0)h^2p_{x1} + a'(t_0)h^3p_{x2} + a''(t_0)h^4p_{x3} + a'''(t_0)h^5p_{x4} + a^{(4)}(t_0)h^6p_{x5} + a(t_1)h^2p_{x6} + a'(t_1)h^3p_{x7} + a''(t_1)h^4p_{x8} + a'''(t_1)h^5p_{x9} + a^{(4)}(t_1)h^6p_{x10} ;$$

$$v(t_2) = v(t_0) + a(t_0)h\ p_{v1} + a'(t_0)h^2p_{v2} + a''(t_0)h^3p_{v3} + a'''(t_0)h^4p_{v4} + a^{(4)}(t_0)h^5p_{v5} + a(t_1)h\ p_{v6} + a'(t_1)h^2p_{v7} + a''(t_1)h^3p_{v8} + a'''(t_1)h^4p_{v9} + a^{(4)}(t_1)h^5p_{v10} ;$$

// Assignment of new values to variables

**Figure 2.** Pseudo-code of the first method, which is based on the polynomial P(9).

## 3. Analysis of the direct method.

### 3.1. Local error and consistency.

Local error $\delta$ is the error incurred in one time step $h$, thus it represents the departure of the numerical solution from the exact solution after one time step. If the Taylor series converges to the exact solution within an interval, then this error can be easily calculated [8]. In this case, the local errors for the corrector and predictor are described by the following expressions:

$$\delta_{kxt1} = \frac{-1}{42*12!}\frac{d^{12}x}{dt^{12}}h^{12} + Oh^{13} , \tag{9}$$

$$\delta_{kvt1} = \frac{-1}{252*11!}\frac{d^{11}x}{dt^{11}}h^{11} + Oh^{12} , \tag{10}$$

$$\delta_{pxt2} = \frac{384}{7*12!}\frac{d^{12}x}{dt^{12}}h^{12} + Oh^{13} , \tag{11}$$

$$\delta_{pvt2} = \frac{2656}{63*11!}\frac{d^{11}x}{dt^{11}}h^{11} + Oh^{12} , \tag{12}$$

where $\delta_{\text{kxt1}}$ represents the local error of the corrector $x(t_1)$, $\delta_{\text{kvt1}}$ denotes the local error of the corrector $v(t_1)$, $\delta_{\text{pxt2}}$ is the local error of the predictor $x(t_2)$, and $\delta_{\text{pvt2}}$ is the local error of the predictor $v(t_2)$. As is evident from these expressions (9-12), this method (Eqs. 5-8) is consistent, and is a tenth-order method [5, 8]. Moreover, the error of the predictor is larger than the error of the corrector.

### 3.2. Global error, stability, and convergence.

Global error and stability regions are studied for the following linear second-order ordinary differential equation:

$$\frac{d^2x}{dt^2} = -m^{-1}\left(kx + c\frac{dx}{dt}\right) \tag{13}$$

where $k$ represents the stiffness of the spring ($F_s$=-$kx$), and $c$ denotes the damping coefficient ($F_d$=-$c$ $dx/dt$) (Fig. 1). The exact solution of this equation is known, thus numerical errors can be easily calculated. Moreover, the studied method can be written in matrix notation for this equation (13), which is very helpful in stability analysis [3, 10]. So this equation is selected as a test problem.

The global error $\varepsilon$ is the error incurred in $j$ time steps, thus it represents the difference between numerical solution and the exact solution for the time instance being $jh$. The global errors for this method is expressed by the following equations:

$$E_1 = X_{n(jh+t_0;h+jh+t_0)} - X_{e(jh+t_0;h+jh+t_0)} = \begin{bmatrix} \varepsilon_{x(jh+t_0)} \\ \varepsilon_{v(jh+t_0)} \\ \varepsilon_{x(h+jh+t_0)} \\ \varepsilon_{v(h+jh+t_0)} \end{bmatrix} = \begin{bmatrix} x_n(jh+t_0) \\ v_n(jh+t_0) \\ x_n(h+jh+t_0) \\ v_n(h+jh+t_0) \end{bmatrix} - \begin{bmatrix} x_e(jh+t_0) \\ v_e(jh+t_0) \\ x_e(h+jh+t_0) \\ v_e(h+jh+t_0) \end{bmatrix} \tag{14}$$

where $E_1$ represents the vector of global errors $\varepsilon$, $X_n$ represents the vector of numerical solutions, and $X_e$ is the vector of exact solutions. Presented method for the test equation (13) can be written in matrix notation, which leads to the following equation:

$$X_{n(jh+t_0;h+jh+t_0)} = (PK^{n_i})^j X_{e(t_0;h+t_0)} = T^j X_{e(t_0;h+t_0)} = (Q\Lambda Q^{-1})^j X_{e(t_0;h+t_0)} = Q\Lambda^j Q^{-1} X_{e(t_0;h+t_0)} \tag{15}$$

where $X_{e(t_0;h+t_0)}$ represents the exact initial condition, $P$ denotes the matrix of the predictor, $K$ is the matrix of the corrector, $T$ is the transformation matrix, $Q$ is the matrix of the eigenvectors, $\Lambda$ is the diagonal matrix of eigenvalues, $j$ is the number of time steps, and $n_i$ is the number of iterations. This equation provides an opportunity to calculate vectors of the numerical solutions from initial conditions for the time instance being $jh$. In this case, the transformation matrix or the diagonal matrix of eigenvalues is raised to the $j$-th power.

Matrix notation provides an opportunity to study stability regions, in this context the diagonal matrix of eigenvalues $\Lambda$ is very important. If the largest absolute value of the eigenvalues is less than unity, then the numerical solution approaches zero as $j$ tends to infinity, and studied method is stable:

$$\max|\Lambda| \le 1 \cdot \tag{16}$$

This criterion is used to calculate the stability regions. The stability regions are presented in (Fig. 3).

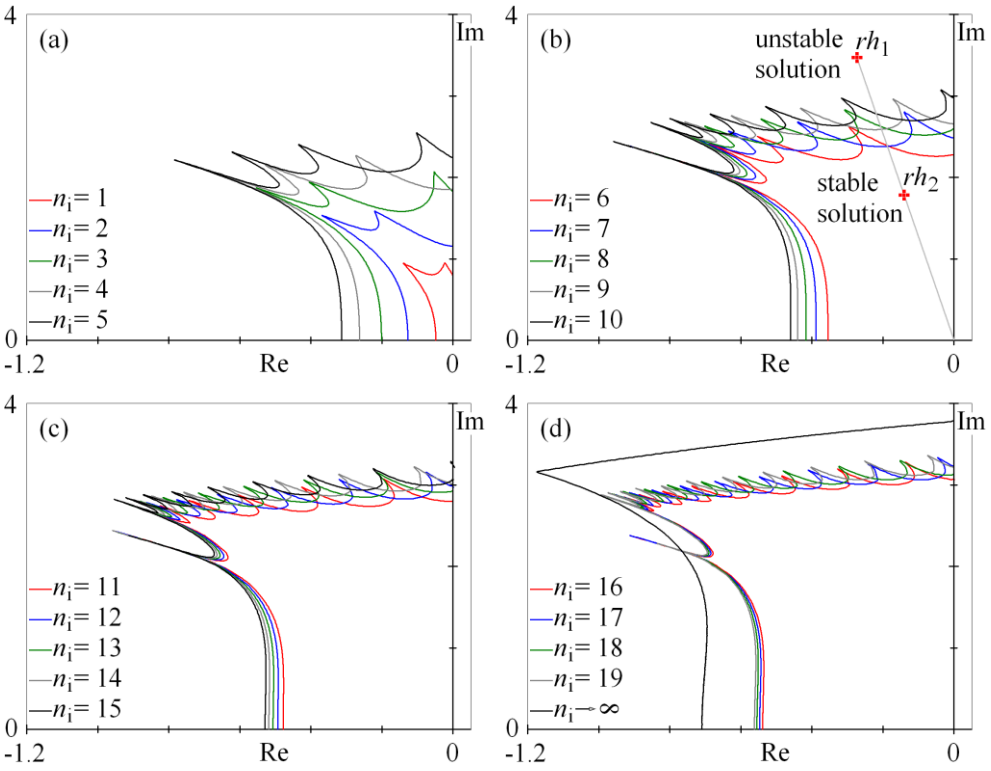


**Figure 3.** Comparison of stability regions obtained for various numbers of iterations $n_i$ (a – d).

An evolution of these regions due to iteration number is observed. The predictor is unstable (Eqs. 7, 8), thus a stability region does not exist ($n_i$ = 0), and thus the predictor can not be used without a stable corrector. After first iteration, the stability region is observed ($n_i$ = 1). Then, the consecutive iterations make the stability regions larger, and shapes of the stability regions tend to the shape of predictor ($n_i \to \infty$). Nevertheless, initially shapes of the stability regions become more sophisticated and some separate stability "island" regions are observed. The stability regions play an important role in simulation. If roots $r$ of the test equation (13) multiplied by the time step $h$ are inside the stability region obtained for a certain number of iteration $n_i$ , then the obtained numerical solution is stable [12]. Otherwise, the obtained numerical solution is unstable and numerical phenomena are observed (Fig. 3b). Therefore, the stability regions determine the largest time step which can be used. The stability intervals obtained for $c$ = 0 are presented in Table 2.

At this stage convergence of this numerical method is discussed, if a linear multistep method is consistent and stable, then it is convergent [5, 12]. Next, the global error can be discussed. If the

studied method is convergent, the exact solution is stable, the exact solution has continuous derivatives up to order $p$+1, the starting values are exact, the rounding errors are zero, and the time step approach zero $h \to 0$; then the global error is expressed by the following formula:

$$|\varepsilon| \leq \xi h^p \tag{17}$$

where $\varepsilon$ represents the global error for the considered time instance $t_0+jh$, and $p$ denotes the order of the method $p$ = 10, and $\xi$ depends on the test problem, the method used, and the interval of integration $[t_0, t_0+jh]$. This inequality shows the relation between $\varepsilon$ and $h$ [4, 5, 8, 12, 20]).

Table 2. Stability intervals obtained for $c$ = 0.

| $n_{i.}$ | Stability intervals. | $n_{i.}$ | Stability intervals. |
|---|---|---|---|
| 0 | | 6 | [**2.2794** i; 0 i] |
| 1 | [0.2941 i; 0 i] | 7 | [2.4790 i; 1.3762 i] [0.9556 i; 0 i] |
| 2 | [**1.1545** i; 0 i] | 8 | [2.5942 i; 2.3548 i] [**1.0312 i**; 0 i] |
| 3 | [**1.8243** i; 0 i] | 9 | [2.6553 i; 2.6416 i] [**1.5765** i; 0 i] |
| 4 | [0.6070 i; 0 i] | 10 | [**2.4306 i**; 0 i] |
| 5 | [0.9874 i; 0 i] | 11 | [2.7966 i; 1.7029 i] [**1.3102 i**; 0 i] |

## 4. An example application.

In this section, the test equation (13) is solved with numerical methods for the following parameters and initial conditions: $m$ = 1[kg], $c$ = 0[Nsm$^{-1}$], $k$ = 1[N/m], $t_0$ = 0[s], $x(t_0)$ = 1[m], and $v(t_0)$ = 0[m/s]. The exact solution is the following entire function:

$$x = \cos(t) \ , \tag{18}$$

which provides an opportunity to study numerical errors. In spite of the fact that the exact solution is an entire function, and can be approximated with a Taylor series and polynomials, some numerical phenomena are observed e.g.: numerical noise (parasite eigenvalues), numerical damping or excitation - error of amplitude, and error in the period. More information about numerical effects is presented in literature [3, 8, 10, 12]. These two errors are described by the following equations:

$$\delta_A = \left|1 - \sqrt{x_n^2(T_e) + v_n^2(T_e)}\right| / 1 \ , \tag{19}$$

$$\delta_T = |T_n - T_e| / T_e \ , \tag{20}$$

where $\delta_{\mathrm{A}}$ denotes the relative error of the amplitude, $x_n(T_e)$ is the displacement calculated with a numerical method for the time instance $T_{\mathrm{e}} = 2\pi$, $v_n(T_e)$ is the velocity calculated with a numerical method for the time instance $T_{\mathrm{e}}$, $\delta_{\mathrm{T}}$ represents the relative error in the period, $T_{\mathrm{e}}$ represents the exact period of oscillation $T_{\mathrm{e}} = 2\pi$[s], and $T_{\mathrm{n}}$ is the period of oscillation obtained with a numerical method. These two numerical errors, which are associated with errors of the eigenvalues, are criteria by which numerical methods are judged. The next criterion is CPU time (time of computation), which shows

the cost of computation. A number of factors influence CPU time, and are thus mentioned. The source codes and algorithms were optimised, and then compiled in C++ version 6.0. A computer with Windows XP Professional and an Intel Desktop Board D525MW motherboard with an Intel Atom D525 1.8GHz processor was used to solve this test problem, and the obtained results can be compared with previously presented results [10]. Finally, the CPU times necessity to compute one period of oscillation $t_c$ were measured.

Numerical errors and CPU times are studied for this numerical method and following the Runge-Kutta type methods: the classical fourth-order Runge-Kutta method, the fifth-order Dormand-Prince method, the sixth-order Verner method, the seventh-order Runge-Kutta type method [5 {p196}], the eighth-order Cooper-Verner method, the ninth-order Tsitouras-Stone method [23], and the tenth-order Ono-Stone method [24]. The Runge-Kutta type methods, with local error estimations, are limited to the highest order algorithm. The first method uses the exact initial conditions for $t = -h$ and $t = 0$, which are extrapolated with predictor to $t = h$, whereas the Runge-Kutta type methods use the exact initial conditions for $t = 0$. The second method is not described in this article.

At this stage results can be presented and discussed. The relative error of amplitude $\delta_A$ obtained for various numbers of time steps per period $T_e/h$ is depicted in (Fig. 4a). As is evident from this figure, the amplitude error $\delta_A$ obtained for the first method can be reduced both by increasing the number of time steps per period $T_e/h$, and increasing the number of iterations $n_i$. The relative error of amplitude is reduced below $\delta_A < 10^{-15}$ for $T_e/h \geq 28$ and $n_i \geq 1$; and for $T_e/h \geq 3$ and $n_i = 26$. This shows convergence of the first method. Depending on the number of iterations $n_i$ and time steps per period $T_e/h$ the relative error of amplitude obtained for direct method can be smaller than the amplitude error obtained for these Runge-Kutta type methods.

Next, the relative error of amplitude $\delta_A$ is presented versus the CPU time required for calculating one oscillation period $t_c$ (Fig. 4b). As is evident from this figure the first method is more effective than these Runge-Kutta type methods.

Then, the error in the period $\delta_T$ obtained for various numbers of time steps per period $T_e/h$ is depicted in Fig. 5a. As is evident from this figure, the error in the period obtained for the first method is reduced both by increasing the number of time steps per period $T_e/h$, and increasing the number of iterations $n_i$. If the number of time steps per period is greater than or equal to $T_e/h \geq 4$, and $n_i \geq 3$, then the error in the period $\delta_T$ obtained for the first method is smaller than the error in the period obtained for these Runge-Kutta type methods.

Finally, the error in the period $\delta_T$ is presented versus the CPU time required for calculating one oscillation period $t_c$ (Fig. 5b). If the number of iterations is from $n_i = 1$ to $n_i = 5$ and the relative error

of amplitude is below $\delta_T < 6.6*10^{-5}$, then the first method is more effective than these Runge-Kutta type methods.

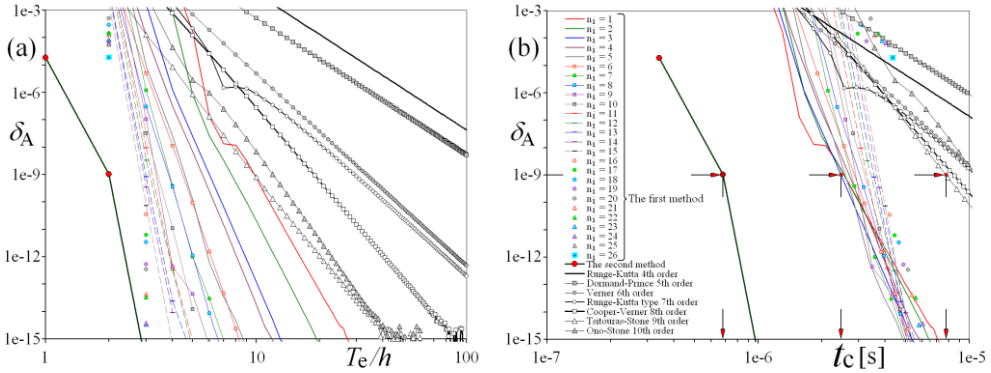


**Figure 4.** Comparison of the first method with the Runge-Kutta type methods. The plots show the relative amplitude error $\delta_A$ calculated for the presented numbers of iterations $n_i$ versus the number of time steps per period $T_e/h$ (a), and the relative amplitude error $\delta_A$ versus the computational time $t_c$ required to calculate one period $T_e$ (b).

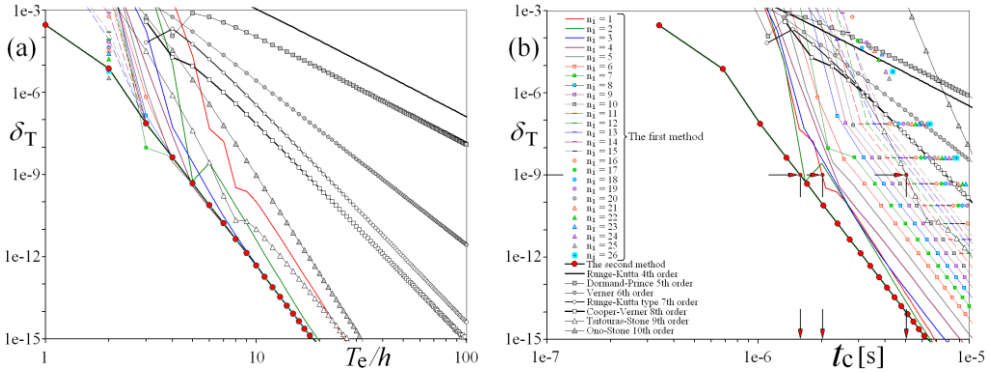


**Figure 5.** Comparison of the first method with the Runge-Kutta type methods. The figures show the relative error in period $\delta_T$ calculated for the presented numbers of iterations $n_i$ versus the number of time steps per period $T_e/h$ (a), and the relative period error $\delta_T$ versus the computational time $t_c$ required to calculate one period $T_e$ (b).

The most important conclusions are presented below. If $\delta_A$, $\delta_T$, and $t_c$ are criteria by which these methods are judged, then the first method is more effective than these Runge-Kutta type methods for the number of common iterations being from $n_i = 1$ to $n_i = 5$ and $\delta_T < 6.6*10^{-5}$. These conclusions are valid for the computer used and this test problem. If the number of time steps per period is greater than $T_e/h > 28$, then these two errors obtained for the first method are below $10^{-15}$. It means that for

the number of time steps per period being greater than $T_e/h > 28$, these two errors are not reduced for the double-precision floating-point numbers, which is a result of the round-off errors. Moreover, this direct method provides an opportunity to use large time steps (Table 1), which is important during the simulation of multi-degree-of-freedom systems and identification.

## 5. Conclusions.

The direct, linear, multi-derivative method, which use Hermite polynomials, is studied in this article. First, the time history of acceleration is estimated with the Hermite polynomial, and then the Hermite polynomial is integrated to the time histories of velocity and displacement, which is the primary idea of this method. Hermite polynomials provide an opportunity to interpolate the time history of acceleration with small errors, thus obtained errors are small. Moreover, this procedure can be simplified, which makes this method computationally effective. Finally, numerical errors can be reduced with iterations. Additionally iterations make the stability region larger. Thus, large time steps can be used to solve second order ordinary differential equations. Finally, this method is more effective than the studied Runge-Kutta type methods for this computer, and the solved test problem, which is the most important conclusion. This method can even be used if acceleration is non-smooth or discontinuous function, because Hermite polynomials are not very sensitive to the Runge phenomenon. Nevertheless, a very elegant solution is to divide a time step to sub-steps, and in this way avoids discontinuity points within an integrated interval. This solution is not a problem, because this method can be easily started, and the time step can be changed, because they use derivatives calculated only for two nodes. Moreover, this method can be used to identify directly parameters of a system from time histories that were sampled with a large sampling period or various sampling periods. Finally, the time histories can be studied between nodes. This feature is important during the calculation of Poincaré maps. This shows potential areas of applications.

## References


[1] Aarseth S.J., From NBODY1 to NBODY6: The Growth of an Industry, Publications of The Astronomical Society of The Pacific, 111 (1999) 1333-1346

[2] Barrio R., Blesa F., Lara M., VSVO formulation of the Taylor method for the numerical solution of ODEs, Computers & Mathematics with Applications, 50 (2005) 93-111

[3] Bathe K.J., Wilson E.L., Stability and accuracy analysis of direct integration methods, Earthquake Engineering & Structural Dynamics, 1 (1973) 283-291

[4] Brown R.L., Some characteristics of implicit multi-step multi-derivative integration formulas, SIAM Journal on Numerical Analysis, 14 (1977) 982-993

[5] Butcher J.C., Numerical Methods for Ordinary Equations, John Wiley & Sons, Inc. 2008

[6] Enright W.H., Second derivative multistep methods for stiff ordinary differential equations, SIAM Journal on Numerical Analysis 11 (1974) 321-331

[7] Filippi S., Knecht T., Generalized Hermite multistep methods of high order with a variable step-size, Journal of Computational and Applied Mathematics 59 (1995) 173-180

[8] Fortuna Z., Macukow B., Wąsowski J., Metody numeryczne, fourth ed., WNT, Warszawa, 1998 (in Polish)

[9] Kokubo E., Yoshinaga K., Makino J., On a time-symmetric Hermite integrator for planetary N-body simulation, Monthly Notices of the Royal Astronomical Society, 297 (1998) 1067-1072

[10] Kostek R., Direct numerical methods dedicated to second-order ordinary differential equations, Applied Mathematics and Computation, 219 (2013) 10082-10095

[11] Kostek R., Analysis of the primary and superharmonic contact resonances – Part 1, Journal of Theoretical and Applied Mechanics, 51 (2013) 475-486

[12] Krupowicz A., Metody numeryczne zagadnień początkowych równań różniczkowych zwyczajnych", PWN, Warszawa, 1986 (in Polish)

[13] Lara M., Elipe A., Palacios M., Automatic programming of recurrent power series, Mathematics and Computers in Simulation, 49 (1999) 351-362

[14] Makino J., Aarseth S.J., On a Hermite integrator with Ahmad–Cohen scheme for gravitational many-body problems, Publications of the Astronomical Society of Japan, 44 (1992) 141-151

[15] Mathews J.H., Fink K.D., Numerical Methods Using Matlab, fourth ed., Prentice Hall 2005

[16] Mikkola S., Aarseth S.J., An efficient integration method for binaries in N-body simulations, New Astronomy, 3 (1998) 309-320

[17] Nguyen-Ba T., Bozic V., Kengne E., Vaillancourt R.: A one-step 7-stage Hermite–Birkhoff–Taylor ODE solver of order 11. Journal of Computational and Applied Mathematics, 234 (2010) 192-208

[18] Nitadori K., Makino J., Sixth- and eighth-order Hermite integrator for N-body simulations, New Astronomy, 13 (2008) 498–507

[19] Rasdi N., Majid Z.A., Ismail F., Senu N., See P.P., Radzi H.M., Solving second order delay differential equations by direct two and three point one-step block method, Applied Mathematical Sciences, 7 (2013), 2647 – 2660

[20] Sacks-Davis R., Solution of stiff ordinary differential equations by a second derivative method, SIAM Journal on Numerical Analysis, 14 (1977) 1088-1100

[21] Tanikawa A., Yoshikawa K., Okamoto T., Nitadori K., N-body simulation for self-gravitating collisional systems with a new SIMD instruction set extension to the x86 architecture, Advanced Vector eXtensions, New Astronomy, 17 (2012) 82-92

[22] Yoshinaga K., Kokubo E., Makino J., The stability of proto-planet systems, Icarus, 139 (1999) 328-335

[23] http://www.peterstone.name/Maplepgs/RKcoeff_9.html – file RKcoeff9a_5.pdf – 2/2014

[24] http://www.peterstone.name/Maplepgs/RKcoeff_10.html – file RKcoeff10f_2.pdf – 2/2014

Robert Kostek, Ph.D.: University of Science and Technology, 85-789 Bydgoszcz, Poland (*robertkostek@o2.pl*).

# Modified strip method utilization for wheel/rail contact stress assessment (NUM040-15)

Tomáš Lack, Juraj Gerlici, Josef Soukup

*Abstract:* The Strip Method is often used for rail /wheel contact area and contact normal stress evaluation. The paper deals with the computational time saving procedure when the computation accuracy is guaranteed. We included the local coordinate system with a presupposed semi-circular course of the normal stress for the purpose of the integral that is needed for deformation in the middle of separate strips evaluation, computation. The integral is solvable analytically. After analytical solution expression the input parameters for separate parts of splines and separate strips could be possible to insert.

## 1. Introduction

An important parameter influencing the power effect of a wheel on the rail is the size and shape of the contact area as well as the normal stress distribution which has the impact on it. Nowadays various methods are used to find out the size of contact areas and stresses. It is necessary to mention the Hertz method as one of the oldest an up to date used methods. It provides acceptable results for a large area in spite of many simplifications. Another computational procedure is the Kalker variation method or the stripe method which is, thanks to its results, close to reality and it is used in the following calculations. Nowadays, another group of calculation program systems (ANSYS, ADINA) is used in certain situations. The systems work on the base of finite elements method theory.

## 2. Strip method

The Strip Method presupposes quasi-static rolling. The principal idea of the theory is to take into consideration slim contact areas in the y-direction. In Fig. 2 there are two bodies in contact. In fact the geometrical parameters (of railway wheel and rail) should be very similar in reality the deformation zones are similar too. In spite of this fact the parameters (the displacements $w_1$ and $w_2$) in the Fig. 1 are rather different for better understanding of the theory.

In fact the contact area should be plane (parallel with the *x*-*y* plane).

The method presupposes the existence of two rotating bodies 1 and 2 with surfaces *S*1 and *S*2. The bodies touch in the point 0, which is at the same time the beginning of their spatial coordinate systems. The axe *x* and *y* determinate the horizontal base. We will mark the horizontal coordinate as

the $z$ – axis. If there is no the influence of a normal force $Q$, then there exclusively exists geometrical binding between the bodies.

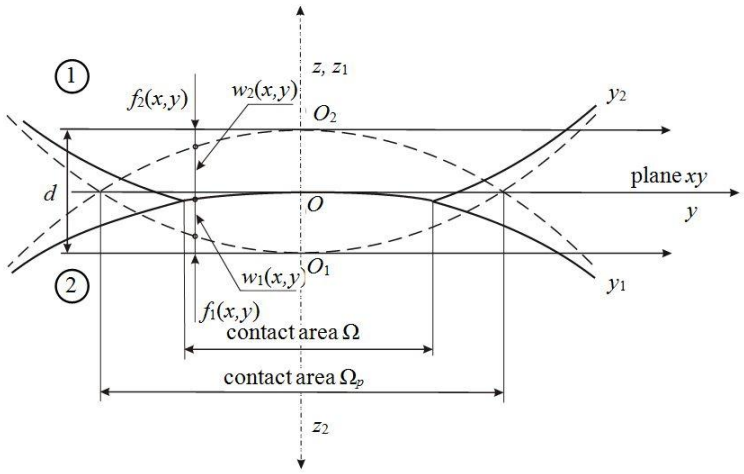


**Figure 1.** Variation Coordinate body system at the contact.

If the bodies are pressed against each other by the normal force $Q$, there is a deformation and a contact area Ω between the bodies appears instead of a contact point

- the geometrical profile shape of the first body surface will be marked $f_1(x, y)$, the geometrical profile shape of the second body surface will be marked $f_2(x,y)$
- the elastic displacement in the z-axis direction caused by the deformation of the first body surface will be marked $w_1(x,y)$, the displacement in the z-axis direction caused by the deformation of the second body surface will be marked $w_2(x,y)$
- the displacement of bodies centers against each other in the axis-z direction will be marked $d$
- the perpendicular distance between the points of the deformed bodies surfaces will be marked $\delta(x,y)$.

## 3. Normal stress approximation over a strip

The stress evaluation over the $k$-th strip is approximated in a standard way

$$p_k(x_k, y_k) = p_{0k}\sqrt{1-\left(\frac{x}{x_{dk}}\right)^2} \tag{1}$$

where $p_k$ $(x,y_k)$ - normal stress in the x position, $p_{0k}$ -maximum normal stress, $x_{dk}$ - half length of the k-th strip.

We aimed our interest in the previous research to semi-elliptic, polynomial approximation and approximation with the cubic spline [4]. The cubic spline approximation method appeared for this purpose as the most effective computational procedure. In this case, we aimed our interest to the computational effort. To obtain the requested results, there are deformation in the middle of strips and them corresponding stresses, we utilized the procedures introduced in the next text.

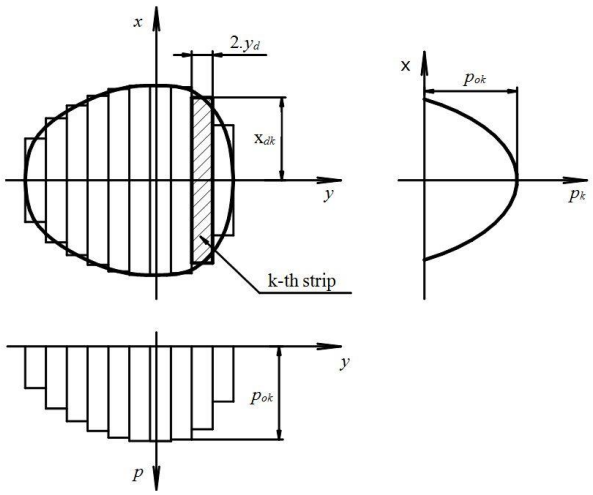


**Figure 2.** Contact patch distribution into the strips, stress distribution over individual strips.

## 4. Time optimized computational procedure for contact stresses assessment

The equation system assembly is necessary for the stress evaluation in the middle of strips:

$$[M]\{p^{(0)}\}=\{w^{(0)}\} \tag{2}$$

Where [$M$] - influence coefficients matrix, $\{p^{(0)}\}$ - normal stresses in the middle of strips vector, $\{w^{(0)}\}$ - in the middle of strips strains vector.

The [$M$] matrix elements are of values

$$M_{k,s} = H.I_{k,s}^{(0)} \qquad \text{where} \qquad H = \frac{1}{\pi}\left(\frac{1-\mu_1^2}{E_1}+\frac{1-\mu_2^2}{E_2}\right) \tag{3}$$

where $\mu_1$ - Poisson's ratio of a first body, $\mu_2$ - Poisson's ratio of a second body, $E_1$ -modulus of stiffness of a first body, $E_2$ - modulus of stiffness of a second body.

The vector elements are of values:

$$w_k^{(0)} = z_{2k} - z_{1k} - D \tag{4}$$

where $w_k^{(0)}$ - deformation in the middle of *k*-th strip, $z_{1k}$ - coordinate of a first body in the middle of *k*-th strip, $z_{2k}$ - coordinate of second body in the middle of *k*-th strip, *D* - mutual bodies approach.

The aim is to compute the value $I_{k,s}^{(0)}$ in accordance to relation below

$$I_{k,s}^{(0)} = 2\int_0^{x_{dk}}\int_{y_{lk}}^{y_{rk}} \sqrt{\frac{1-\left(\frac{x}{x_{dk}}\right)^2}{x^2+(y_s-y)^2}}\,dy\,dx \tag{5}$$

when

$$y_{lk} = y_k - y_d \tag{6}$$

$$y_{rk} = y_k + y_d \tag{7}$$

where $x_{dk}$ - half length of the *k*-th strip, $y_k$ - *y*-coordinate of *k*-th strip, $y_s - y$ - coordinate of *s*-th strip, $y_d$ - half width of strips.

This integral can be modified into one- dimension integral in the shape

$$I_{k,s}^{(0)} = -\frac{2}{|x_{dk}|}\int_0^{x_{dk}} \sqrt{x_{dk}^2 - x^2}\, Ln\{AA\}dx \tag{8}$$

$$AA = \frac{[AB][AC]}{x^2} \tag{9}$$

$$AB = \sqrt{x^2 + (y_s - y_{rk})^2} + y_s - y_{rk} \tag{10}$$

$$AC = \sqrt{x^2 + (y_s - y_{lk})^2} - y_s + y_{lk} \tag{11}$$

There is unavoidable to solve the integral in the relation (9) numerically, because it has not an analytical solution. This computation is for separate strips in the relationship to other strips very time consuming.

This is the reason for the new procedure development that is not dependent on real strip length – unit-length of a strip is assumed.

For the value $I_{k,s}^{(0)}$ is valid the relation

$$I_{k,s}^{(0)} = i_{k,s}^{(0)}\, x_{dk} \tag{12}$$

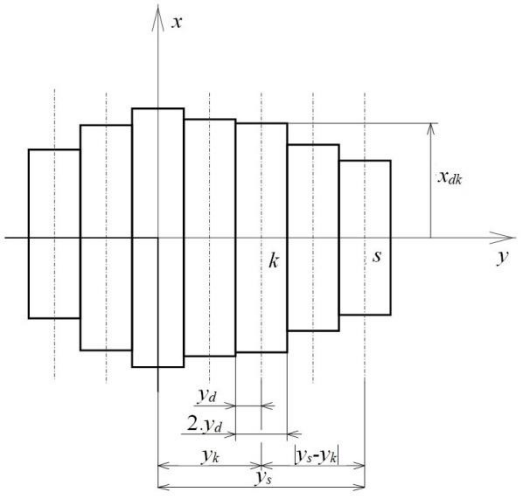


**Figure 3.** Description of individual parameters in the *x*, *y* coordinate system.

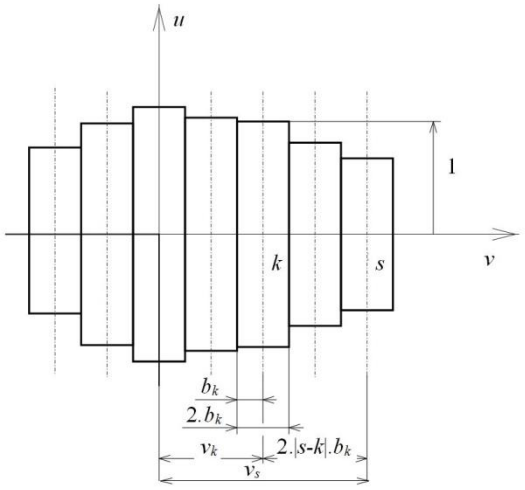


**Figure 4.** Description of individual parameters in the *u*, *v* coordinate system.

Provided that we establish

- the *k*-th strip length in the *u*, *v* system has the value of 1
- the *k*-th strip width in the *u*, *v* system has the value

$$- \quad b_k = \frac{y_d}{x_{dk}} \tag{13}$$

-The relationship for the $I_{k,s}^{(0)}$ computation is valid:

- $$i_{k,s}^{(0)} = 2\int_{0}^{1}\int_{-1}^{1}\sqrt{\frac{1-u^2}{u^2+\left[\left(2|s-k|-v\right)b_k\right]^2}}\,dv\,du \qquad (14)$$

-The value of this integral is possible to show in graphs.

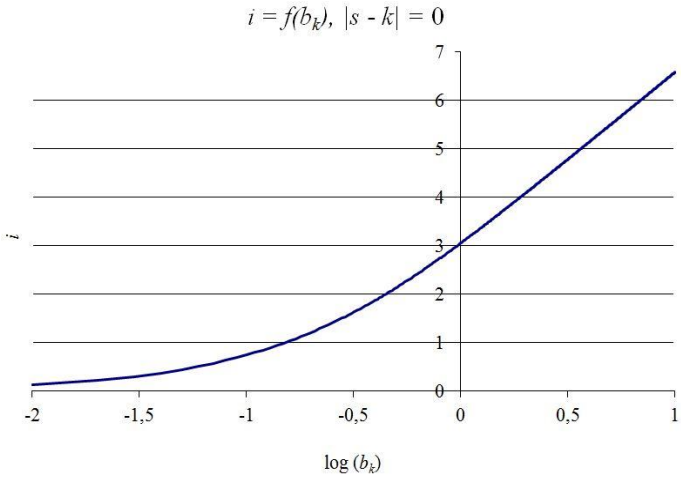


**Figure 5.** $i$ is the integral value in dependence to $\log(b_k)$, when $|s - k| = 0$.

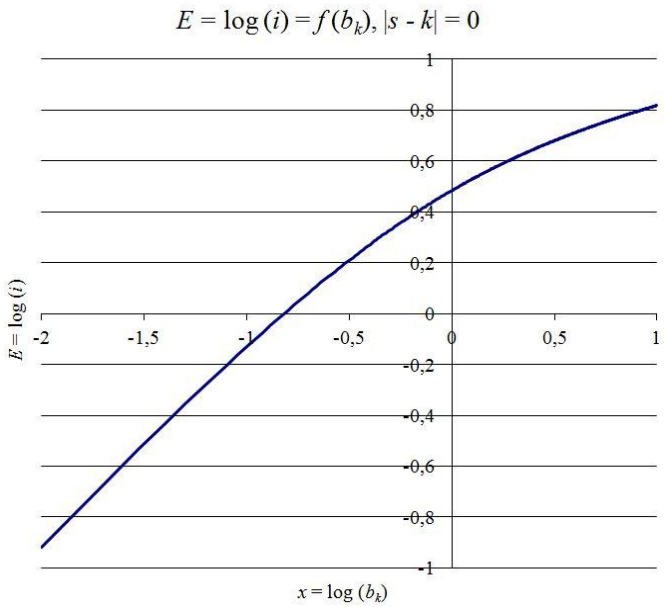


**Figure 6.** $i$ is the $E$ is the value of decimal integral logarithm in dependence to $\log(b_k)$ and $|s - k| = 0$.

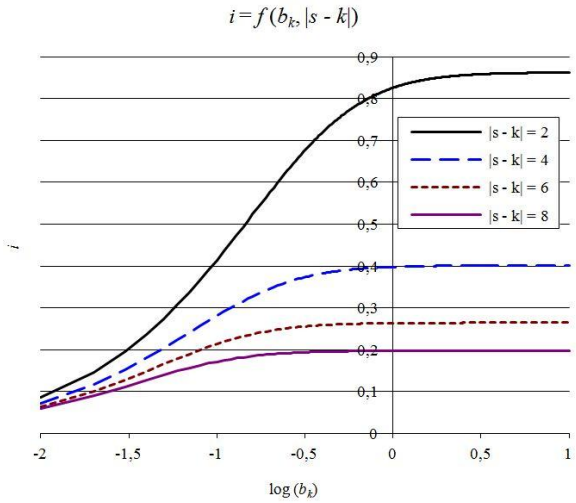


**Figure 7.** $i$ is value of integral in dependence to $\log(b_k)$ and $|s - k| = \langle 2;8 \rangle$.

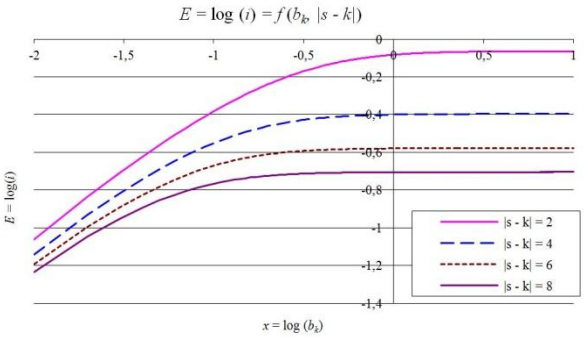


**Figure 8.** $i$ is value of integral in dependence to $\log(b_k)$ and $|s - k| = \langle 2;8 \rangle$.

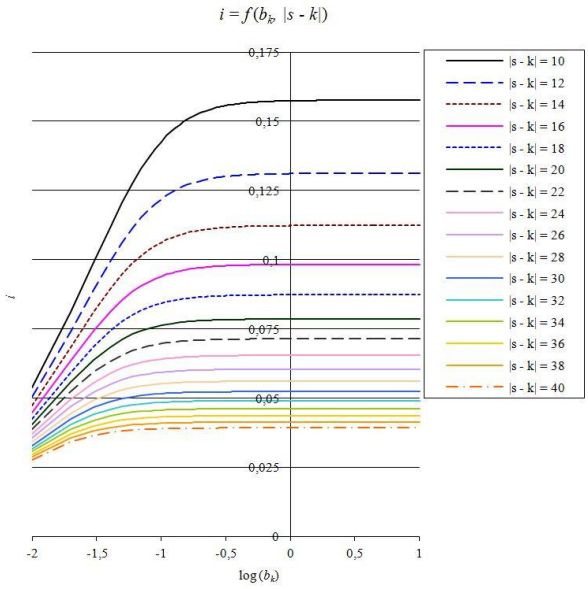


**Figure 9.** *i*- integral in dependence to log($b_k$) and |*s* - *k*| = <10;40>.

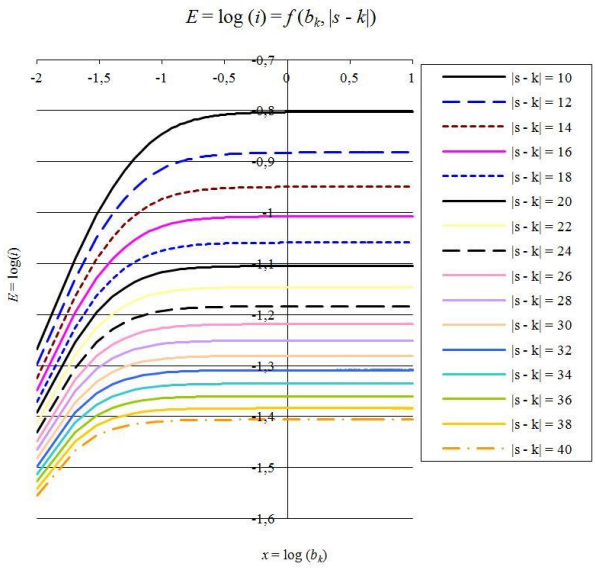


**Figure 10.** *E* is the value of decimal integral logarithm in dependence to log($b_k$) and |*s* - *k*| = <10;40>

The E value is possible to express via the polynomial of 6-th grade

$$E = \{[(((a_6 L + a_5)L + a_4)L + a_3)L + a_2]L + a_1\}L + a_0 \qquad (15)$$

where

$$L = \log(b_k) \tag{16}$$

Polynomial coefficients from $a_6$ to $a_3$ are in Table 1.

Table 1. Polynomial coefficients $a_6$ to $a_3$

| $\|s - k\|$ | $a_6$ | $a_5$ | $a_4$ | $a_3$ |
|---|---|---|---|---|
| 0 | -0.00255 | -0.001497 | 0.022573 | 0.009238 |
| 2 | -0.00756 | -0.026714 | 0.015249 | 0.105083 |
| 4 | 0.003839 | -0.008085 | -0.02931 | 0.068803 |
| 6 | 0.007608 | 0.004252 | -0.03718 | 0.037078 |
| 8 | 0.007902 | 0.009316 | -0.03513 | 0.019712 |
| 10 | 0.007030 | 0.01098 | -0.03057 | 0.010126 |
| 12 | 0.005830 | 0.011066 | -0.02574 | 0.004737 |
| 14 | 0.004628 | 0.010462 | - 0.0213 | 0.001656 |
| 16 | 0.003549 | 0.009613 | -0.01744 | -0.00014 |
| 18 | 0.002611 | 0.008678 | -0.01415 | -0.00115 |
| 20 | 0.001806 | 0.007735 | -0.01138 | -0.00165 |
| 22 | 0.001127 | 0.006837 | -0.00907 | -0.00186 |
| 24 | 0.000534 | 0.005942 | -0.00714 | -0.00182 |
| 26 | 0.000064 | 0.005204 | -0.00551 | -0.00174 |
| 28 | -0.000320 | 0.00455 | -0.00417 | -0.00164 |
| 30 | -0.00063 | 0.003985 | -0.00305 | -0.00152 |
| 32 | -0.00087 | 0.003496 | - 0.0021 | -0.00139 |
| 34 | -0.000102 | 0.003193 | -0.00132 | -0.00141 |
| 36 | -0.00128 | 0.002579 | -0.00064 | -0.00097 |
| 38 | -0.0014 | 0.002248 | -7.3E-05 | -0.00083 |
| 40 | -0.00151 | 0.001912 | 0.000334 | -0.00069 |

Polynomial coefficients from $a_2$ to $a_0$ are in Table 2.

Table 2. Polynomial coefficients $a_2$ to $a_0$

| $\|s - k\|$ | $a_2$ | $a_1$ | $a_0$ |
|---|---|---|---|
| 0 | -0.16037 | 0.467393 | 0.483852 |
| 2 | -0.14821 | 0.079591 | -0.08251 |
| 4 | -0.04814 | 0.015369 | -0.39959 |
| 6 | -0.0153 | 0.005056 | -0.5794 |
| 8 | -0.0027 | 0.00233 | -0.7058 |
| 10 | 0.00236 | 0.001448 | -0.80338 |
| 12 | 0.004248 | 0.001116 | -0.88289 |
| 14 | 0.004707 | 0.000973 | -0.95 |
| 16 | 0.004506 | 0.000906 | -1.00807 |
| 18 | 0.004019 | 0.000859 | -1.05925 |
| 20 | 0.003431 | 0.000813 | -1.10502 |
| 22 | 0.002834 | 0.000765 | -1.1464 |
| 24 | 0.002282 | 0.000698 | -1.18418 |
| 26 | 0.001758 | 0.000651 | -1.21892 |

Table 2. Polynomial coefficients $a_2$ to $a_0$ – continue

| | | | |
|---|---|---|---|
| 28 | 0.001302 | 0.000611 | -1.25109 |
| 30 | 0.0009 | 0.000577 | -1.28104 |
| 32 | 0.000545 | 0.000544 | -1.30905 |
| 34 | 0.000223 | 0.000551 | -1.33537 |
| 36 | -0.00002 | 0.000445 | -1.36018 |
| 38 | -0.00026 | 0.000409 | -1.38364 |
| 40 | -0.0004 | 0.000389 | -1.40591 |

The $i_{k,s}^{0}$ value can be expressed via this relation

$$i_{k,s}^{(0)} \approx 10^{E} \tag{17}$$

For a strip with the coordinate *x* deformation computation is valid the relation

$$w_k(x) = H\sum_{s=1}^{n} p_s^{(0)} I_{k,s}(x) \tag{18}$$

where integral

$$I_{k,s}(x_k) = \int_{-x_{dk}}^{x_{dk}} \int_{y_{lk}}^{y_{rk}} \sqrt{\frac{1-\left(\frac{x}{x_{dk}}\right)^2}{(x_k-x)^2-(y_s-y)^2}}\,dy\,dx \tag{19}$$

This integral can be modified into the one-dimensional integral in shape:

$$I_{k,s}(x_k) = -\frac{1}{|x_{dk}|}\int_{-x_{dk}}^{x_{dk}} \sqrt{x_{dk}^2-x^2}\,Ln\left(\frac{\sqrt{(x-x_k)^2+(y_s-y_{lk})^2}-y_s+y_{lk}}{\sqrt{(x-x_k)^2+(y_s-y_{rk})^2}-y_s-y_{rk}}\right)dx \tag{20}$$

This integral has not the analytical solution, so unavoidable this integral must be computed numerically. Mentioned solution is for strip by strip computation, in the relation to other strips, very time consuming.

Provided that we establish

the *k*-th strip length in the *u*, *v* system has the value of 1

the *k*-th strip width in the *u*, *v* system has the value

$$b_k = \frac{y_d}{x_{dk}} \qquad \text{and} \qquad u_k = \frac{x_k}{x_{dk}} \tag{21}$$

where $x_k$ - coordinate, in the *x*, *y* coordinate system on *k*-th strip, $x_{dk}$ - length of the *k*-th strip, $u_k$ – *u* - coordinate, in the *u*, *v* coordinate system on *k*-th strip.

$$I_{k,s}(x_k) = i_{k,s}(u_k)\,x_{dk} \tag{22}$$

where

$$i_{k,s}(u_k) = i_{k,s}^0 \frac{q_{k,s}(u_k) + q_{k,s}(-u_k)}{q_{k,s}^{(0)}}, \tag{23}$$

$$q_{k,s}^{(0)} = 2\int_0^1 \int_{-1}^1 \frac{1-u^2}{\sqrt{u^2 + \left[2\left(|s-k|-v\right)b_k\right]^2}} dvdu \tag{24}$$

$$q_{k,s}(\chi) = \int_0^1 \int_{-1}^1 \frac{1-u^2}{\sqrt{(\chi-u)^2 + \left[2\left(|s-k|-v\right)b_k\right]^2}} dvdu \tag{25}$$

The $q_{k,s}^{(0)}$ integral values and $q_{k,s}(\chi)$ integral are utterable analytically.

In the next we compare the precise and rapidity results gained by the Kalker's method with the results of other method.

## 5. Computation results obtained by different methods

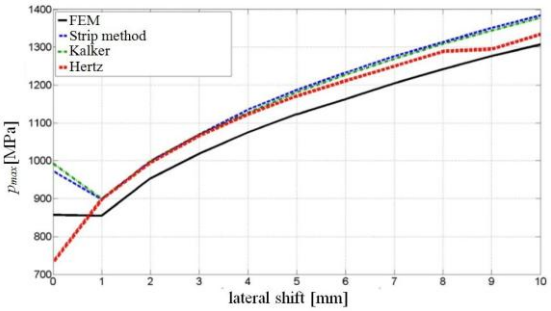


**Figure 11.** Maximum stresses ($p_{max}$) in contact courses against lateral shift of the wheel tread along a rail head movement from a wheel rim, wheel 1.

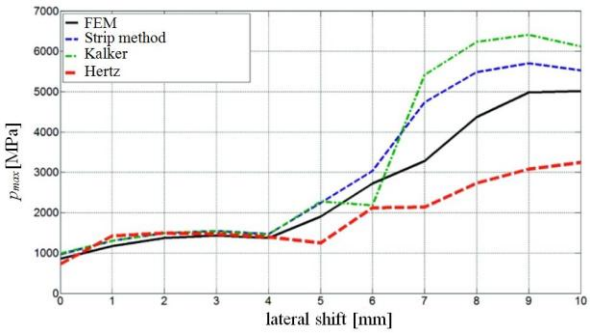


**Figure 12.** Maximum stresses ($p_{max}$) in contact courses against lateral shift of the wheel tread along a rail head movement to a wheel rim, wheel 2.

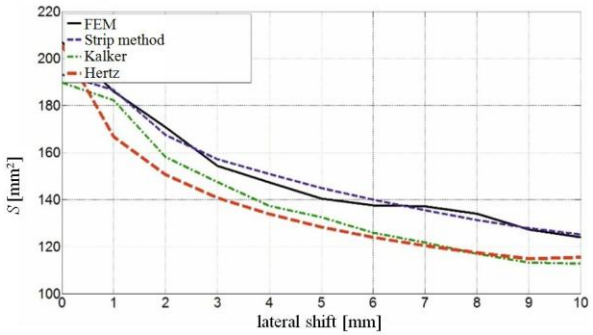


**Figure 13.** Contact patch values (*S1*) courses against lateral shift of the wheel tread along a rail head, movement from a wheel rim.

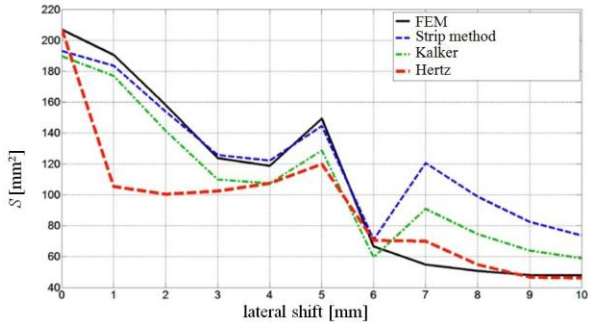


**Figure 14.** Contact patch values (*S2*) courses against lateral shift of the wheel tread along a rail head, movement from a wheel rim.

The computational time consumption reached on the P5 computer, with 2GB RAMM, 3GHz frequency. Utilized methods:

- **Strip method** - level of tenth of second
- **Kalker method with input of strip method results** – level of second
- **Kalker variation method** - level of more ten second.

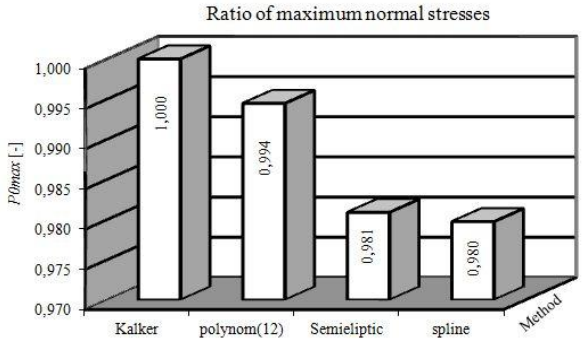


**Figure 15.** Plot of a ratio of maximum normal stresses against the type of computational method

## 6. Conclusions

The Strip Method is often used for rail /wheel contact area and contact normal stress evaluation. It presupposes quasi-static rolling. The principal idea of the theory is to take into consideration slim contact areas in the *y*-direction. The paper deals with the *computational time saving procedure* when the computation accuracy is guaranteed.

The introduced method enables contact patches and contact stresses between railway wheel and rail under decreased computational time consumption condition computation. Rules and procedures characteristic of the Strip method are preserved. The stress computation acceleration is in this case based on the numerical integrals solution algorithm. We included the local coordinate system with a presupposed semi-circular course of the normal stress for the purpose of the integral that is needed for deformation in the middle of separate strips evaluation, computation. The integral is solvable analytically. The input values for the separate spline parts and separate strips computation are possible to insert after analytical solution of the integral. The procedure application may bring the practical benefit for researchers and computation – analysis experts they are interested into this field.

## Acknowledgements

This paper was created during the processing of the project "RAILBCOT - RAIL Vehicles Brake Components Test Stand", ITMS Code 26220220011 based on the support of Research and Development Operational Program financed by European Fund of a Regional Development. The work was also supported by the Scientific Grant Agency of the Ministry of Education of the Slovak Republic and the Slovak Academy of Sciences in project No. 1/0347/12: "Railway wheel tread profile wear research under the rail vehicle in operation conditions simulation on the test bench.", project No. 1/0383/12: "The rail vehicle running properties research with the help of a computer simulation." and the project No. APVV-0842-11: "Equivalent railway operation load simulator on the roller rig."

**References**


[1] Gerlici, J., Lack, T. et al.: Transport Means Properties Analysis. *EDIS Publishing house of University of Žilina*, (2005), 214.

[2] Lack, T. and Gerlici, J.: Contact Area and Normal Stress Determination on Railway Wheel / Rail Contact. *Communications, Scientific Letters of the University of Žilina*, vol.7(2), (2005), 38-45.

[3] Shackleton, P. S. Iwnicky, S.: Comparison of wheel–rail contact codes for railway vehicle simulation: an introduction to the Manchester Contact Benchmark and initial results. *Vehicle System Dynamics*. 46(1–2), (2008), 129–149.

[4] Gerlici, J. and Lack, T.: Strip Method Modification for Stresses in a Wheel / Rail Contact Computation. (In Slovak). *Proceedings of the 7th International Conference Dynamics of Rigid and Deformable Bodies 2009*, (2009).

[5] Lack, T. and Gerlici, J.: Contact Stresses between Railway Wheel and Rail Computation by means of Strip Method Optimized Procedure. (In Slovak). *Proceedings of the 9th International Conference Dynamics of Rigid and Deformable Bodies 2011*, (2011).

[6] Gerlici, J. and Lack, T.. Railway wheel and rail head profiles development based on the geometric characteristics shapes. *Wear* Vol. 271, No. 1-2 Sp. iss. (2011), 246-258.

[7] Gerlici, J. and Lack, T.: Contact geometry influence on the rail / wheel surface stress distribution. *Procedia Engineering*, Vol. 2, iss. 1 (2010), 2249-2257.

[8] Lack, T. and Gerlici, J: Modified Strip Method Utilisation for Wheel /Rail Contact Stress Evaluation. *Proceedings of the 9th International Conference on Contact Mechanics and Wear of Rail/Wheel Systems (CM2012)*, (2012).



Prof. Ing. Dr. Juraj Gerlici, Professor: Univerzity of Žilina, Slovak republic, Faculty of Mechanical Engineering, Department of Transport and Handling Machines, Univerzitná 1, Žilina 010 26, Slovak Republic (juraj.gerlici@fstroj.uniza.sk)

Doc. Ing. Tomáš Lack, ass. professor: Univerzity of Žilina, Slovak republic, Faculty of Mechanical Engineering, Department of Transport and Handling Machines, Univerzitná 1, Žilina 010 26, Slovak Republic (tomas.lack@fstroj.uniza.sk)

Doc. Ing. Josef Soukup, Ass. professor: UJEP in Usti nad Labem, Czech Republic, Faculty of Production Technology and Management, Department of Machines and Mechanics, Na Okraji 1001/7, Usti nad Labem, 400 11, Czech Republic (soukupj@fvtm.ujep.cz). The author gave a presentation of this paper during one of the conference sessions.

# Numerical modelling of wave phenomena in the Zahorski material using ADINA software (NUM159-15)

Maciej Major, Izabela Major

*Abstract:* Paper presents numerical modelling of wave phenomena in simple elastic structures which are rods and shields made of hyperelastic Zahorski material. The difference between the Zahorski material, which is an elastic material in the Green sense and commonly used Mooney-Rivlin material is the nonlinear term including constant $C_3$. As a result, relative to the Mooney-Rivlin material are obtained qualitative and quantitative differences, for example in the values of effective stress. Modelling of Zahorski material in the ADINA software becomes possible by using the author's extension for ADINA software which enables the development of 2D and 3D libraries of program. Under the introduced modification, a comparison of wave phenomena accompanying the propagation of disturbances in Mooney-Rivlin and Zahorski materials was made. It is worth emphasizing that Zahorski material behaves much better at high strains during the analysis of incompressible rubber and rubber-like hyperelastic materials and can be used in various fields of science where the model of Mooney-Rivlin material is successfully applied. The results are shown in the graphical form, and conclusions of numerical analysis are given in the summary of the paper.

## 1. Introduction

Presentation of overall principles that govern continuum mechanics, that govern continuum mechanics, is important for describing the behavior of the body under the influence of external factors. The process of propagation of disturbances modelled as a moving surface that moves in a material continuum remains to be one of the most difficult problems of contemporary continuum mechanics. Wave phenomena are related with the movement of this surface in any of compressible and incompressible material continuum, and the propagating wave is a disturbance strictly limited to the surface. The benefit of this concept is opportunity to analyse wave phenomena within a relatively uniform theory that does not require simplifying assumptions. The scientific investigations which were carried out in the first half of the twentieth century were limited to determination of the principles, which did not take into consideration specific physical properties of the specific type of medium. Introduction in subsequent years new models of bodies and the related elastic potentials has enabled substantial progress in this field of science. Constantly improved methods to determine

elasticity constants for compressible materials enable more accurate analysis of wave phenomena, both based on a new mathematical models as well as through still developing numerical analysis.
The use of finite element method for modelling of wave phenomena in hyperelastic materials becomes a common form of the development of various scientific disciplines, which are based on the description of the material continuum modelled as a hyperelastic material. The data obtained in this way are necessary for the development of modern measurement techniques and modelling of wave processes occurring together with the disturbance propagation. This is an invaluable help in the formulation and adoption of physical principles for determining the mathematical model of the body and is the basis for verifying the correctness of the performed calculations. In turn, presentation of mathematical description of the propagation of disturbances creates the basis for a better understanding of wave phenomena occurring during propagation of disturbances in hyperelastic materials and allows for realization of a new analytical solutions.

## 2. Basic information about hyperelastic materials

Constitutive equations describe the behavior of a particular material under the influence of various external factors. For uniform isotropic elastic bodies, the constitutive equations can be written as:

$$W = W(I_1, I_2, I_3) \tag{1}$$

where $I_1$, $I_2$, $I_3$ - invariants of the deformation tensor.
Considering the elastic body with imposed internal bonds one should remember that it can not be subjected to any deformation, in contrast to an elastic body having no bonds, which may be subjected to any deformation. The basic form of internal bonds of the body is incompressibility, the only acceptable deformations with regard to incompressible bodies are deformations which do not change its volume (isochoric). Then have to meet the following condition for permissible deformation:

$$I_3 = 1 \tag{2}$$

Condition (see Eq. 2) causes the $I_3$ is not used as the argument in the function of the deformation energy, which for the incompressible elastic body is only a function of only two other invariants. This can be re-written in a form which is analogous to the condition (see Eq.1):

$$W = W(I_1, I_2) \tag{3}$$

The above equations (see Eq. 2) and (see Eq. 3) define the constitutive relations for incompressible material. Non-linear theory of elasticity leads to the necessity to defining each time a constitutive relationship, which would correspond to the considered issue. With large deformations, each of the rubber-like materials behaves in a specific manner and one cannot adopt one generalized

constitutive relationship. Therefore, it is necessary to determine, for each individual case by experimental procedure, a constitutive equation for considered model.

In the forties and fifties, the first attempts were also made to determine the constitutive relationships that describe behaviour of rubber and rubber-like materials [1], [2]. A general form of the function of elastic energy was obtained in 1951 by Rivlin and Saunders [3] . Based on the studies above, rubber-like materials are considered as incompressible. The function of deformation energy for these materials depends on two first invariants of the deformation tensor and on two additional constants. The next step in the development of knowledge about hyperelastic materials was introduction in 1959 of the function of deformation energy by Zahorski, for incompressible material described by non-linear dependency on the invariants of deformation tensor [4]. It became possible describing the elastic behaviour of rubber-like materials with substantial deformations.

## 3. Incompressible hyperelastic Zahorski material

The constitutive relationship for hyperelastic Zahorski material (see [4]) is described by the following equation:

$$W(I_1,I_2) = C_1(I_1-3) + C_2(I_2-3) + C_3(I_1^2-9) \tag{4}$$

where $C_1$, $C_2$, $C_3$ are material constants and $I_1$, $I_2$ denote invariants of deformation tensor.

Constitutive equations describe the behaviour of a medium affected by various external factors. Therefore, the choice of the model of material depends on the factors which have the most importance to behaviour of the analysed medium and represent the subjective choice. The relationship (see Eq. 4) shows that elastic energy for the isotropic, incompressible hyperelastic Zahorski material is non-linearly dependent on the invariants of deformation tensor. The above condition was used for analysis of wave phenomena concerning disturbance propagation in e.g. study [5], [6] and [7]. The relationship proposed by Zahorski allows for a more complete analysis of wave phenomena that propagate in hyperelastic incompressible materials compared to Mooney-Rivlin constitutive equation. The non-linear term $C_3(I_1^2-9)$ in the above equation (see Eq. 4) allows for fuller analysis and obtaining individual qualitative components useful in the description of wave processes. If $C_3=0$, Mooney-Rivlin material is obtained, commonly used for modelling rubber and rubber-like materials. It is noticeable that the constitutive Zahorski relation reflects behaviour of rubber for the principal strain, even for $\lambda=3$, whereas for strain greater than $\lambda=2$, Mooney-Rivlin material should not be used (for this material, the satisfactory results are obtained for $\lambda=1.4$ [8]).

The diagrams (see figure 1) of stress-strain function for Zahorski and Mooney – Rivlin material are generated from ADINA software after author's modifications introduced into material libraries [9].

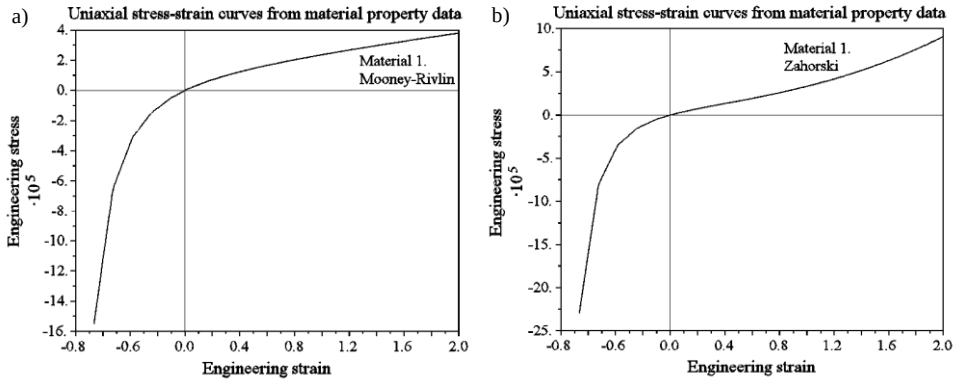


**Figure 1.** Stress - strain diagram for analyzes rubber. a) Mooney - Rivlin material, b) Zahorski material.

The Table 1 presents elastic constants for rubber considered in the work. The values are based on the study [10] and were obtained by computing per SI system.

**Table 1.** Constants $C_1$, $C_2$, $C_3$

| **Constants** | $C_1$ [Pa] | $C_2$ [Pa] | $C_3$ [Pa] |
|---|---|---|---|
| **Rubber** | $6.278 \cdot 10^4$ | $8.829 \cdot 10^3$ | $6.867 \cdot 10^3$ |

The Table 2 presents strength parameters for analyzes rubber (see [10]).

**Table 2.** Strength parameters for analyzes rubber

| | |
|---|---|
| Time of vulcanization in minutes 3at. 143$^o$C | 5 |
| Strength in kN/m$^2$ at 500 mm/min | $\sim 3.01 \cdot 10^4$ |
| Strength in kN/m$^2$ at 5 mm/min | $\sim 1.05 \cdot 10^4$ |
| Elongation in % at 5 mm/min | $\sim 5.81 \cdot 10^4$ |

## 4. Modelling of wave phenomena using FEM programs

Progress in technology have contributed to the development of the research studies on wave phenomena in material continuum, including the continuum modelled as a continuous compressible or incompressible hyperelastic material. Modern numerical software allows to save time during calculations and allows also for a more comprehensive analysis of materials described by more complex constitutive relationships.

FEM is an approximate method of solving partial differential equations. Numerical programs which utilizes finite elements method (FEM) are used to analysis of behaviour of non-linear hyperelastic materials. The most of numerical software that are based on the FEM feature libraries of selected models of materials, including models of hyperelastic material. Choosing one of them allows for more comprehensive numerical analysis of non-linear behaviour of the components designed (see [11]).

There are many programs that are based on commonly known elastic potentials. The most commonly used software for computation of this type include: ANSYS, ABAQUS, MARC, NASTRAN, ALGOR, ADINA. Unfortunately, in this group of programs Zahorski material is not included. This study compares this incompressible hyperelastic Zahorski material, using the author's solution for the ADINA software [9], with the commonly used Mooney-Rivlin material in the range of stress distribution.

## 5. Numerical analysis in hyperelastic incompressible materials

### 5.1. First example - rod

The first of the simple hyperelastic structure analysed is rod with diameter equal 10 centimeters and length equal 1 meter. Rod is fixed on the plane „yz", according to Fig. 2.

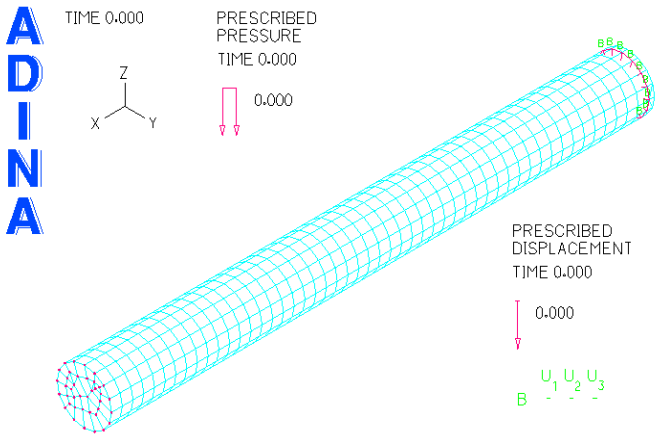


**Figure 2.** 3D model of the rod - grid, load, boundary conditions and the adopted coordinate system for the time t=0.

Discretization of the rod was carried out by elements „3-D Solid" type, dividing rod along its length every 0.02 m. 2155 nodes and 3749 finite elements were obtained. Before the application of load rod has been extended in time t=20s on the direction of the *x* axis for main elongation $\lambda=2$. The load of elongated rod is represented by a pressure pulse with value 10 000 Pa applied to the cross-

section of the rod at a distance of 1cm from the bonds in the time t=0.001 s. Direction of the applied pressure is along the *x* axis (in the direction of frontal area of the rod), Fig. 3.

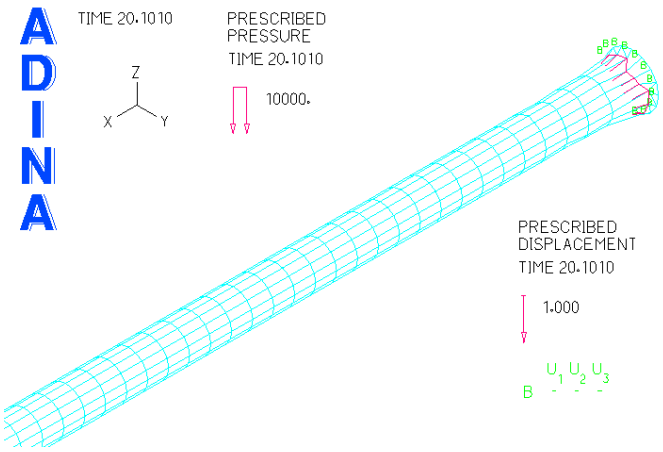


**Figure 3.** Fragment of 3D model of the rod - load, boundary conditions and the adopted coordinate system for the time t=20.1010.

To the numerical calculations "Dynamic - Implicit" type of analysis in an environment of Adina software was used . In Fig. 4. comparison of effective stress, near the supported area of the rod (as a result of its stretching with $\lambda=2$), for analysed in this paper Zahorski and Mooney-Rivlin materials was made.

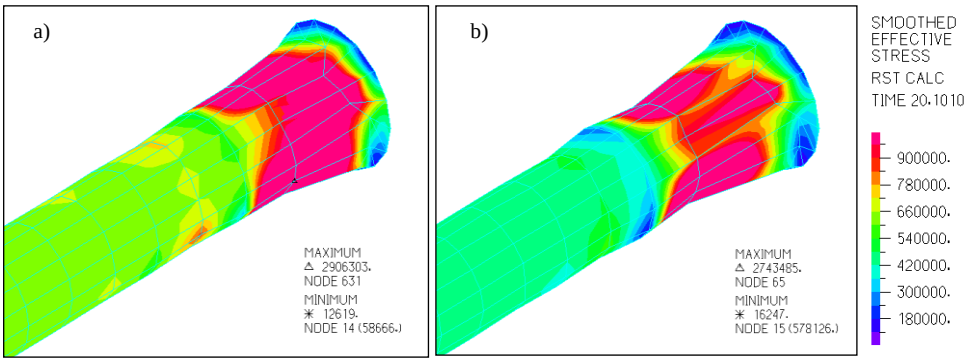


**Figure 4.** Distribution of effective stress [Pa] near the supported area of the rod: a) Zahorski material, b) Mooney-Rivlin material.

The differences in stress distribution and its values are clearly visible in the particular cross-sections of the analyzed rod. Thus not only quantitative but also qualitative differences were obtained. Moreover the maximum stress value in the rod made of Zahorski material was equal 2 906 303 Pa,

whereas for the rod made of Mooney-Rivlin material this value was 2 743 485 Pa, respectively. The difference was 162 818 Pa, which was ~5,6%. In the case where minimum value have been taken into considerations for the rod made of Zahorski material the value was 12 619 Pa, while for Mooney-Rivlin material was 16 247 Pa. The difference was 3628 Pa, which was ~22.3%.

For assumed numerical model, as a result of the applied pressure pulse propagation of disturbances in the analyzed hyperelastic rod made of Zahorski (Fig. 5.) and Mooney-Rivlin (Fig .6.) materials is followed.

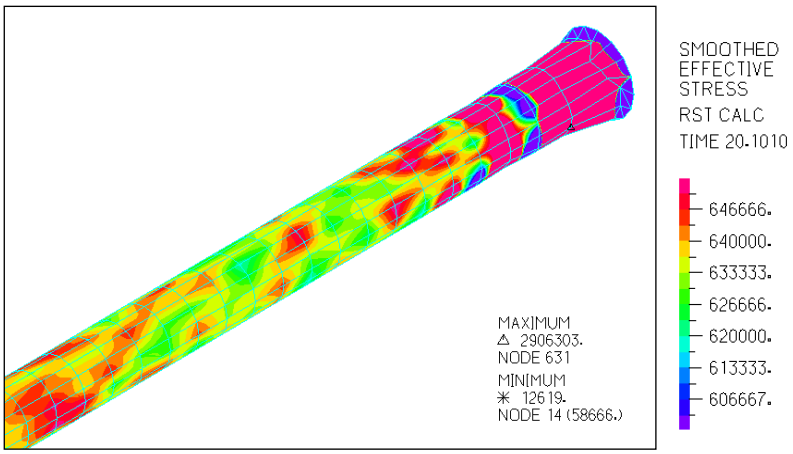


**Figure 5.** The view of propagation of disturbances in rod – distribution of fields of effective stress [Pa] in Zahorski material.

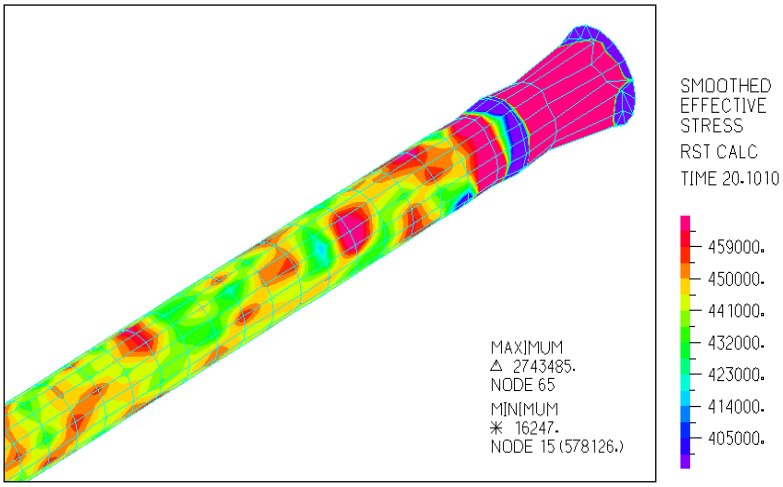


**Figure 6.** The view of propagation of disturbances in rod – distribution of fields of effective stress [Pa] in Mooney-Rivlin material.

In both above numerical analyzes, appropriate scale to the analyzed material was assumed, whereby it can be seen the distribution of the fields of stress in the rod as a result of propagation of the disturbance.

### 5.2. Second example - shield

The second of the simple hyperelastic structure analysed is shield with thickness equal 10 centimeters, its height is 1 meter and length equal 5 meters. Shield is fixed on the plane „yz", according to Fig. 7.

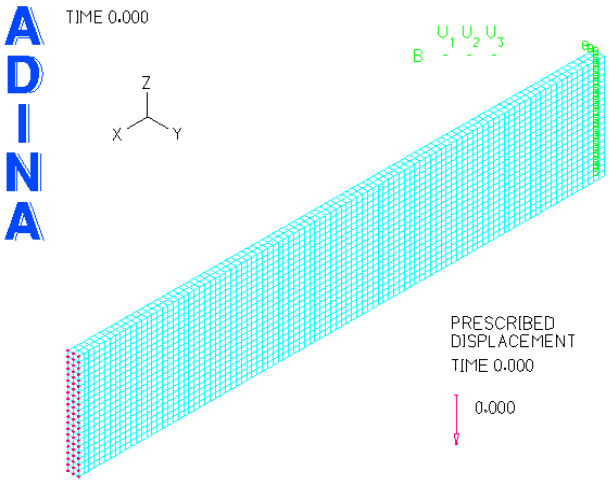


**Figure 7.** 3D model of the shield - grid, load, boundary conditions and the adopted coordinate system for the time t=0..

Discretization of the shield was carried out by elements „3-D Solid" type, dividing shield along its length, width and thickness every 0.05 m. 6363 nodes and 4000 finite elements were obtained. Before the application of load shield has been extended in time t=20s on the direction of the *x* for main elongation $\lambda=2$. The load of elongated shield is represented by a pressure pulse with value 100 000 Pa applied to the cross-section of the shield at a distance of 5cm from the bonds in the time t=0.001 s. Direction of the applied pressure is along the *x* axis (in the direction of frontal area of the shield), see Fig. 8.

To the numerical calculations "Dynamic - Implicit" type of analysis in an environment of Adina software was used (as for above analyzed rod). In Fig. 9. comparison of effective stress, near the supported area of the shield (as a result of its stretching with $\lambda=2$), for analysed in this paper Zahorski and Mooney-Rivlin materials was made.

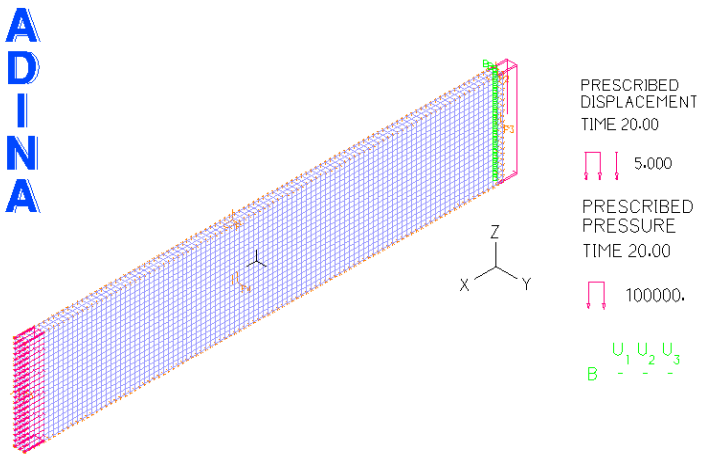


**Figure 8.** Fragment of 3D model of the shield - load, boundary conditions and the adopted coordinate system for the time t=20.1010.

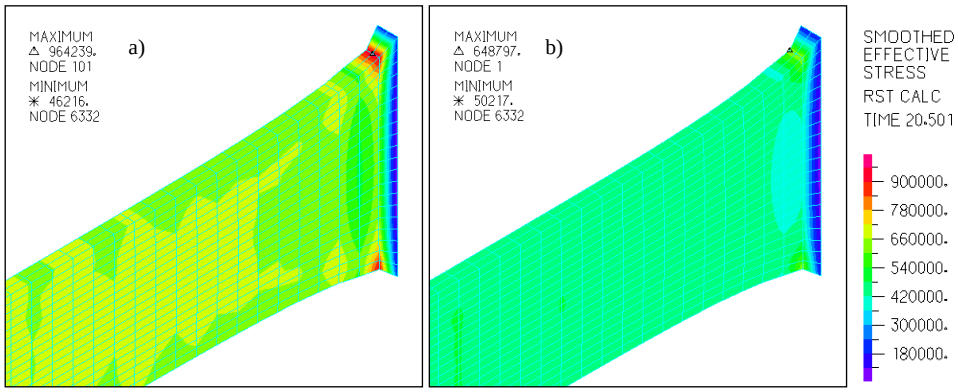


**Figure 9.** Distribution of effective stress [Pa] near the supported area of the shield: a) Zahorski material, b) Mooney-Rivlin material.

The differences in stress distribution and its values are clearly visible in the particular cross-sections of the analyzed rod. Thus not only quantitative but also qualitative differences were obtained. In addition the maximum stress value in shield made of Zahorski material was 964 239 Pa, while for Mooney-Rivlin material maximum stress value was equal 648 797 Pa. Obtained difference was 315 442 Pa, which was about 32.7%. In the case of the minimum value the value for Zahorski material was 46 216 Pa, whereas for Mooney-Rivlin was 50 217 Pa. The difference between those two values was 4001 Pa, which was about 7.9%.

For assumed numerical model, as a result of the applied pressure pulse propagation of disturbances in the analyzed hyperelastic shield made of Zahorski (see figure 10.) and Mooney-Rivlin (see figure 11.) materials is followed.

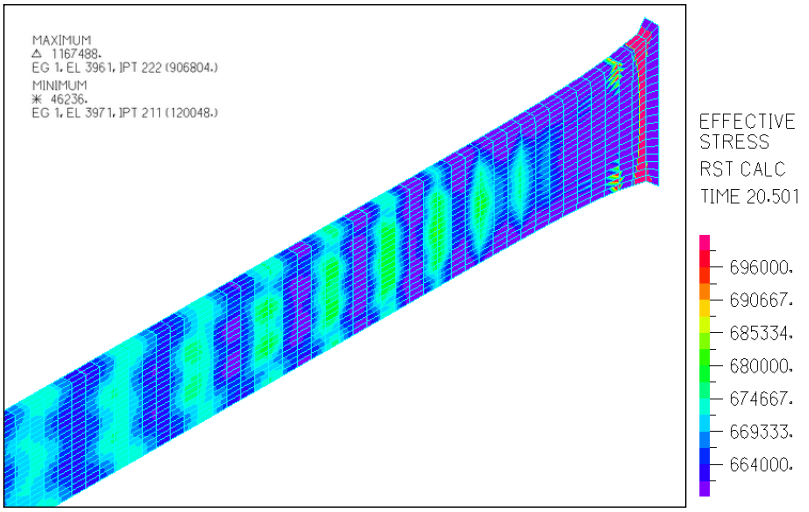


**Figure 10.** The view of propagation of disturbances in shield – distribution of fields of effective stress [Pa] in Zahorski material.

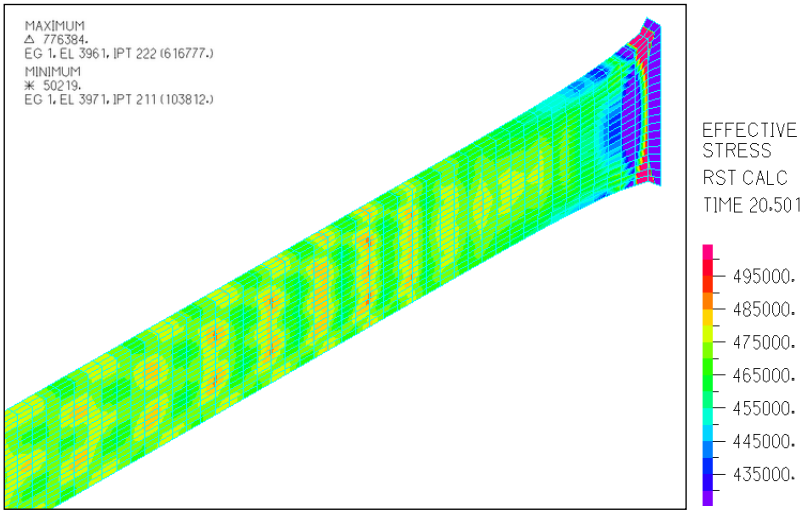


**Figure 11.** The view of propagation of disturbances in shield – distribution of fields of effective stress [Pa] in Mooney-Rivlin material.

In both above numerical analyzes, appropriate scale to the analyzed material was assumed, whereby it can be seen the distribution of the fields of stress in the shield as a result of propagation of the disturbance.

## 6. Conclusions

From the comparison of stress results in rod (Fig. 4) and elastic shield (Fig. 9) one can be stated that for Zahorski material the maximum effective stress is higher and minimum effective stress is lower than the values obtained for Mooney-Rivlin material. For the rod the difference in maximum effective stress was ~5.6%, while for the hyperelastic shield was up to ~32.7%. The difference in minimum effective stress values was ~22.3% for the rod and ~7.9% for the shield, respectively. The quantitative differences in the effective stresses near the support area can be clearly visible for the analyzed Zahorski hyperelastic material and Mooney-Rivlin material for the considered simple elastic structures i.e. rod and shield.

Wave phenomena which accompany the disturbance propagation in the rod for the Zahorski material was shown in Fig. 5 and for Mooney-Rivlin material in Fig. 6, respectively. The view of disturbance propagation was determined by fields of the effective stress distribution where for Zahorski material it can be observed in the range of (600 000; 650 000) Pa, whereas for the Mooney-Rivlin material it was observed in the range of (400 000; 460 000) Pa.

Similarly, propagation accompany wave phenomena in the shield for Zahorski material have been shown in Fig. 10 and for the Mooney-Rivlin material in Fig. 11. Here the disturbance propagation was also determined by the field of distributed effective stress which fits the same range values adopted for the rod. In that case the differences in the distributed effective stress for the analyzed Zahorski and Mooney-Rivlin material can also be clearly visible.

To conclude, it can be clearly visible that performed in that paper numerical modelling of wave phenomena in the simple hyperelastic structures as a result of pressure pulse allowed showing differences in the effective stress distribution fields for Zahorski and Mooney-Rivlin material. The use of numerical methods and computer techniques for modelling the wave phenomena appear to be reasonable for showing the differences which occur under dynamical influence in analyzed materials. Presented here computer simulations provides scientific information that may be useful for research in many science areas, where hyperelastic Mooney-Rivlin is utilized and indicates that utilize of Zahorski material can provide new information even before experimental research, which can significantly contribute to lower the costs of undertaken projects.

## References

[1] Mooney, M. A theory of large deformations. *J. Appl. Phys*. 11 (1940), 582-592.

[2] Rivlin, R.S. Large elastic deformations of isotropic materials. I Fundamental concepts., Phil. Trans. Roy. Soc. Lond. A 240 (1948), 459-490.

[3] Rivlin, R.S., and Saunders D.W., Large elastic deformations of isotropic materials. VII Experiments of the deformation of rubber, Phil. Trans. Roy. Soc. Lond. 243, (1951), 251-288.

[4] Zahorski S. A from of elastic potential for rubber-like materials. *Archives of Mechanics* 5 (1959), 613-617.

[5] Kosiński, S. *Odbicie i ewolucja fali uderzeniowej w wybranych materiałach hipersprężystych*, Wydawnictwo IPPT PAN, Warszawa, 1995.

[6] Major, M. Velocity of Acceleration Wave Propagating in Hyperelastic Zahorski and Mooney-Rivlin Materials. *J. Theoret. Appl. Mech.* 43, 4 (2005), 777-787.

[7] Major, I. and Major, M. Traveling Waves in a Thin Layer Composed of Nonlinear Hyperelastic Zahorski's Material. *J. Theoret. Appl. Mech.* 47, 1 (2009), 109-126.

[8] Kosiński, S., *Fale sprężyste w gumopodobnych kompozytach warstwowych*. Wydawnictwo Politechniki Łódzkiej, Łódź, 2007.

[9] Major, M., *Modelowanie zjawisk falowych w hipersprężystym materiale Zahorskiego*. Wydawnictwo Politechniki Częstochowskiej, Częstochowa 2013.

[10] Zahorski, S. Doświadczalne badania niektórych własności mechanicznych gumy. Rozprawy inżynierskie, tom 10 (1), 1962.

[11] Major, M., and Major, I. Przegląd wybranych materiałów hipersprężystych. *Tendencje rozwoju budownictwa miejskiego i przemysłowego*. Wydawnictwo Politechniki Częstochowskiej, Częstochowa, 2008.

Maciej Major, Eng. Ph.D.: Czestochowa University of Technology/Faculty of Civil Engineering/Department of Technological Mechanics, Akademicka 3, 42-202 Częstochowa, Poland (mmajor@bud.pcz.czest.pl).

Izabela Major, Assoc. Prof. Eng. Ph.D.: Czestochowa University of Technology/Faculty of Civil Engineering/Department of Technological Mechanics, Akademicka 3, 42-202 Częstochowa, Poland (imajor@bud.pcz.czest.pl). The author gave a presentation of this paper during one of the conference sessions.

# Numerical simulation of the vibration control system designed for Continuous Miner machines (NUM173-15)

Arkadiusz Mężyk, Wojciech Klein, Mariusz Pawlak, Jan Kania

*Abstract:* The Continuous Miner machines are exposed on time depended loads during normal operation of rock cutting process. These loads cause vibrations which have negative influence on whole structure of machine. This phenomena can be eliminated by applying passive or active vibration control systems (VCS). Generally these systems are consisted with additional elements which provide dispersion or transfer energy. Acquired in this way energy can also reinforce native process which for mining machines such as roadheaders is rock cutting operation. The goal of this paper is to present application and method of proposed by authors VCS which is designed for Continuous Miner machines. The main function of presented system is to reduce displacement of cutting drum by using elastic element joined to machine chassis and applying appropriate algorithm of control angular velocity of cutting drum. The described method improve efficiency of mining and increase durability of machine. In aim of determine mechanical and control parameters of VCS was used genetic algorithm optimization method conjugate with numerical modal analysis. Finally the transient dynamic analysis was done for full-scale model of Continuous Miner in order to verification of VCS in normal working condition.

## 1. Introduction

The cutting system in the boring or mining machines is responsible for generating forces and dynamic torques, which – on the one hand – enable the crushing of rocks, and – on the other – negatively affect the entire structure of the machine [1]. Therefore, it is extremely important to improve the dynamic parameters of the cutting system, thereby making it possible to minimise the unfavourable vibrations in the selected nodes of the machine, while ensuring proper conditions for the mining process. [2-4] One of the many possibilities presented in literature [5-7] is to optimally control the kinematic parameters of the drive system in order to actively reduce vibrations . The vibration control system, proposed by the authors of the paper, as per the patent application no. P.410713 (see figure 1), contains an additional spring element (5) mounted in the support structure (chassis) of the drive system (6). The vibrations may be minimised through an appropriate change in the rotational speed of the cutting drum (1) during the cutting process. This change should cause a shift in the excitation frequency for which the mode shapes obtained will have nodes in the critical points of the machine's structure, while maintaining an increased influence on the mined wall. This process requires a detailed analysis of the entire system and a selection of natural frequency that guarantees the desired cutting effect, while ensuring low vibration levels of the machine. By controlling the speed of the

drive motor in an appropriate manner, it is possible to force peri-resonance phenomena for the indicated natural frequency.

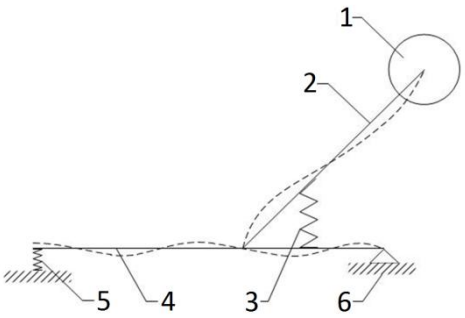


**Figure 1.** A schematic model of the optimised structure.

## 2. Calculation methodology

In the literature can be find many methods of analysis nonlinear vibrating systems [7-9]. The adopted by authors calculation methodology presented in figure 2 is based on the application of genetic algorithms for the optimisation of kinematic parameters of the drive system.

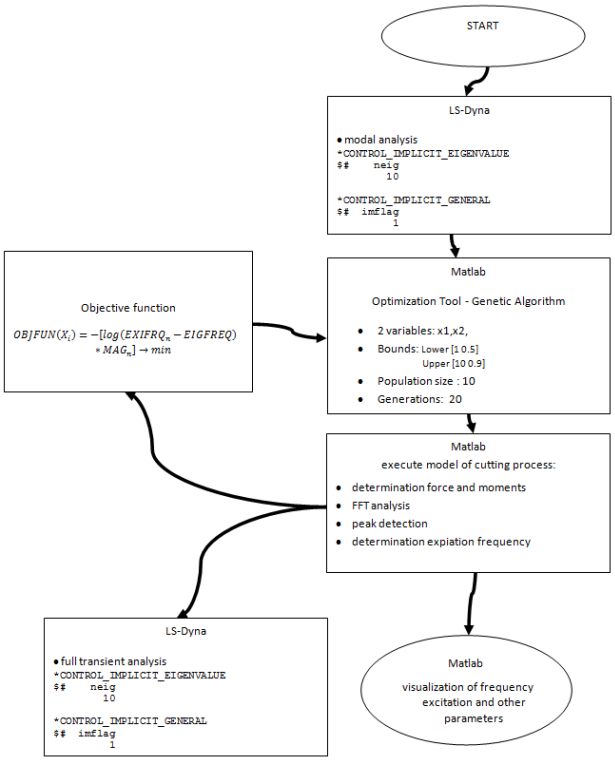


**Figure 2.** The method adopted for the optimisation of cutting parameters.

The first step of this process involves identification of the mode shapes ensuring the reduction of vibrations in appropriate constructional nodes of the machine. This is done through a numerical modal analysis. The eigenvectors and eigenfrequency thus selected are the input values for the objective function developed. The implemented analytical model of the cutting process allows for determining the excitation frequency in the rotational speed function of the cutting drum and the distribution of the individual blades on the perimeter of the cutting drum. On that basis, the optimisation algorithm determines the values of decision variables related with the kinematic parameters of the drive system of the cutting drum. In order to verify the results, the last stage involves a dynamic analysis for complete identification of the dynamic characteristics of the structure and for determination of the benefits of changing the nature of the excitation.

## 3. Modal analysis of an optimised structure

According to the methodology adopted, the first step in tuning the natural frequency to the excitation frequency resulting from the interaction of the cutting drum with the mined area is to perform a modal analysis of the entire structure in boundary conditions corresponding to the actual operational conditions of the machine. Figure 3 presents the first 8 mode shapes of the machine under analysis.

| No | Mode shape | Freq. [Hz] | No | Mode shape | Freq. [Hz] |
|---|---|---|---|---|---|
| 1 | 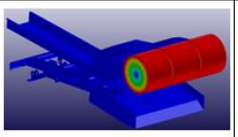 | 0.1 | 2 | 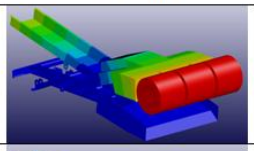 | 0.75 |
| 3 | 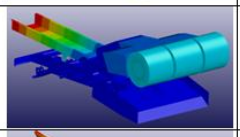 | 0,79 | 4 | 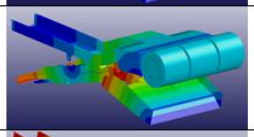 | 5,12 |
| 5 | 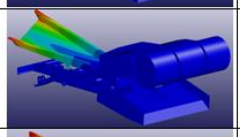 | 5,77 | 6 | 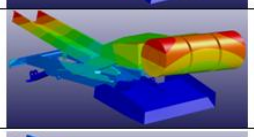 | 7,21 |
| 7 | 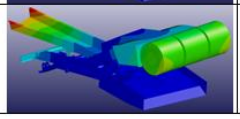 | 9,42 | 8 | 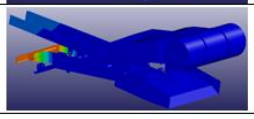 | 11,8 |

**Figure 3.** Modal analysis of the Continuous Miner machine.

The choice of a proper mode shape is dependent on the adopted durability criteria and the criteria related with the cutting process. Based on the obtained vector values of the particular mode shape, it was found that the best having a favourable influence on both the cutting process and the individual components of the machine is the fourth one with the eigenfrequency of 5.12 Hz. This results from the minimum eigenvectors in the cutting drum location and proper deformation of other machine components.

## 4. Optimisation process

In order to identify the character of excitation, test simulations were performed for the three angular velocities of the cutting drum: 2 rad/s, 4 rad/s and 6 rad/s, which has been presented in the figures 4-6.

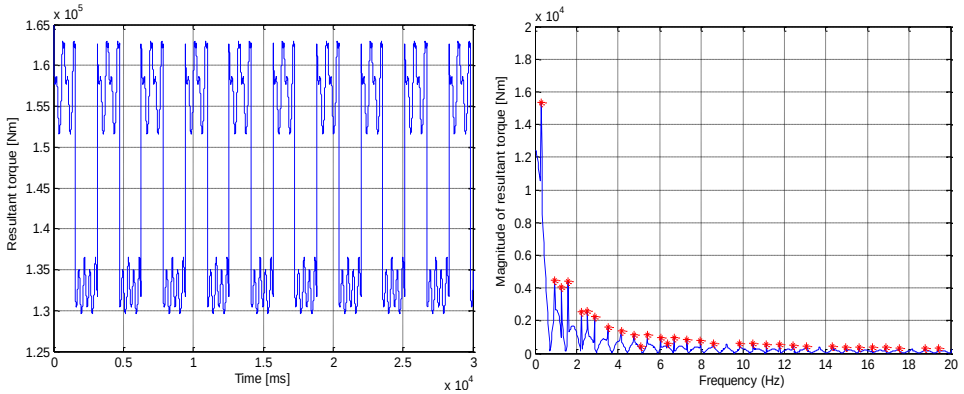


**Figure 4.** The characteristics of the excitation torque and its spectrum for the speed of 2 rad/s.

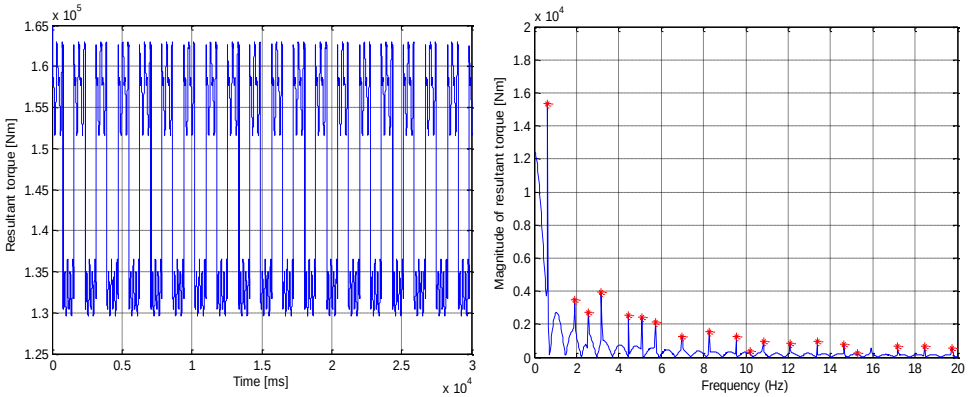


**Figure 5.** The characteristics of the excitation torque and its spectrum for the speed of 4 rad/s.

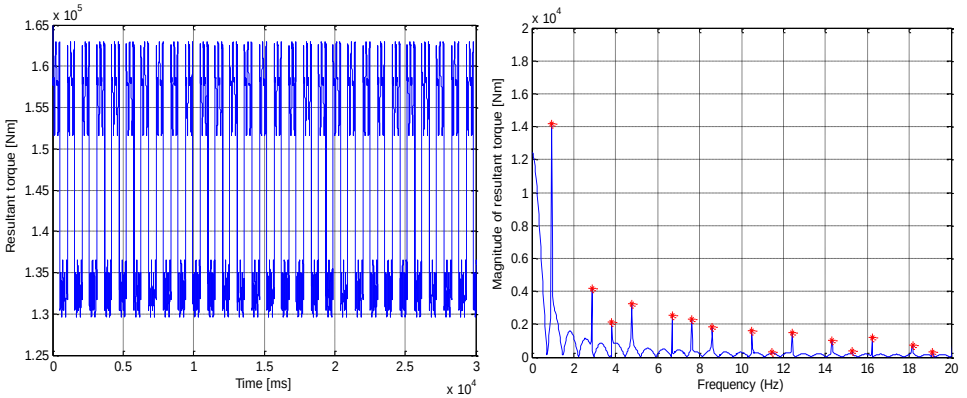


**Figure 6.** The characteristics of the excitation torque and its spectrum for the speed of 6 rad/s.

In order to tune the excitation frequency to the eigenfrequency, the following form of objective function has been developed:

$$OBJFUN(X_i) = -\left[log\left(EXIFRQ_n - EIGFREQ\right) \cdot MAG_n\right] \longrightarrow min \tag{1}$$

where:

$X$ – vector of design variables,

$i$ – index of design variable,

$EXIFRQ$ – vector of the excitation frequency,

$MAG$ – value of the cumulative torque amplitude,

$n$ – index of peaks in the excitation spectrum,

$EIGFREQ$ – value of the tuned eigenfrequency.

The optimisation process helped to obtain the frequency characteristics of an excitation signal consistent with the assumptions adopted. The unit is excited by a frequency that results in reaching the dominant, selected mode shape of the machine (the value of the third peak in the excitation frequency spectrum overlaps the fourth eigenfrequency of the unit), thus ensuring high efficiency in the mining of walls (see figure 7).

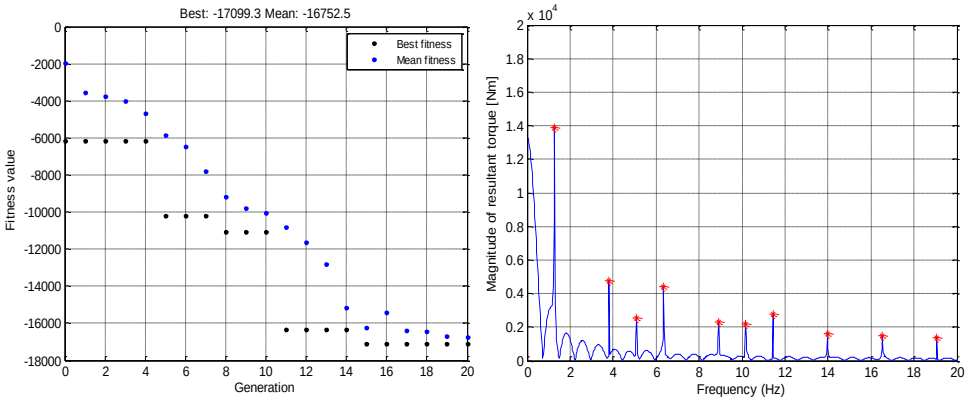


**Figure 7.** The course of the optimisation process and the frequency characteristics of the excitation.

## 5. Transient analysis by explicit method

In order to verify the optimisation results, a dynamic analysis of the optimised structure was performed with the excitation parameters related to the angular velocity of the cutting drum, applied before and after the optimisation process. The model used for conducting the dynamic analysis of a transient state is a modification of the model used in the modal analysis described before. The modification consisted in the introduction of starting and boundary conditions in the form of applying an appropriate excitation in a function of time. The simulation was conducted in the LS-Dyna

environment using the explicit method. The model presented in figure 8 combines both deformable elements and rigid bodies, containing kinematic pairs.

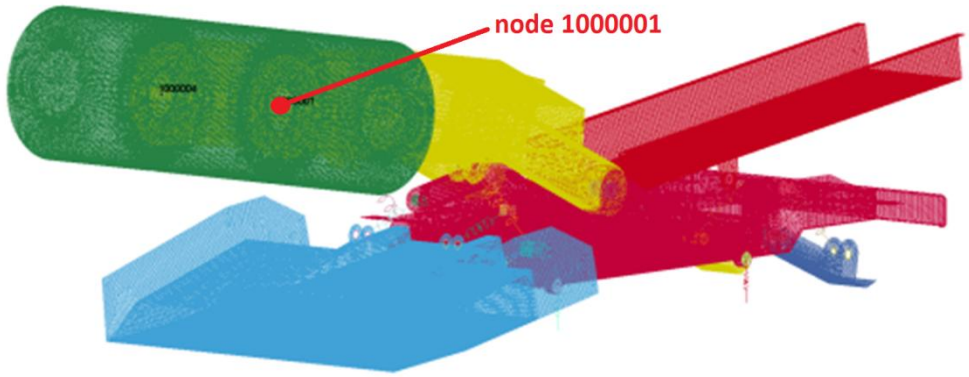


**Figure 8.** Finite element model of Continuous Miner machine.

Simulations were conducted for two variants of excitation: 5.23 rad/s (before optimisation) and 6.44 rad/s (after optimisation). The complexity of the model resulting from the multitude of degrees of freedom and from the application of kinematic joints enforced the limitation of simulation time to 6 seconds at a sampling rate not higher than 10e-4 seconds.

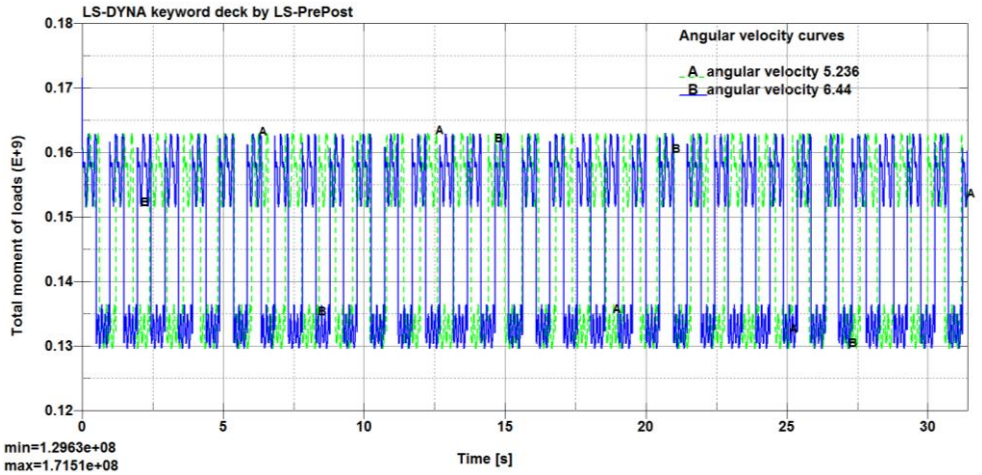


**Figure 9.** Total excitation moment for angular velocities 5.23 rad/s and 6.44 rad/s.

The simulation results are presented in figures 10 and 11. The red colour was used to mark the results for excitation parameters adopted before the optimisation process. As can be seen, the amplitudes of both the displacements and the velocities in the critical node no. 1000001 situated in the axis of the cutting drum are clearly lower for the parameters after the optimisation process (green).

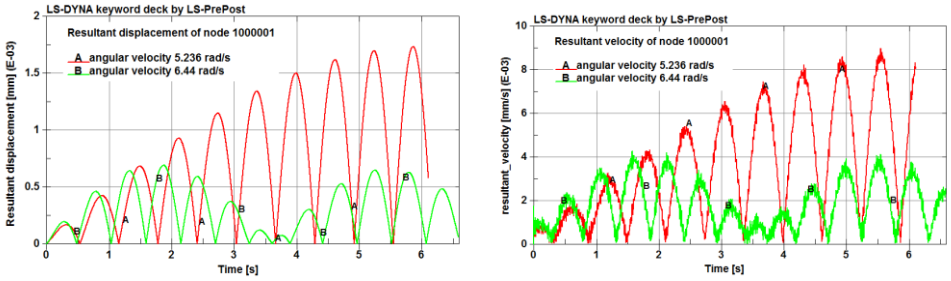


**Figure 10.** Resultant displacement and velocity of node 1000001 in function of time.

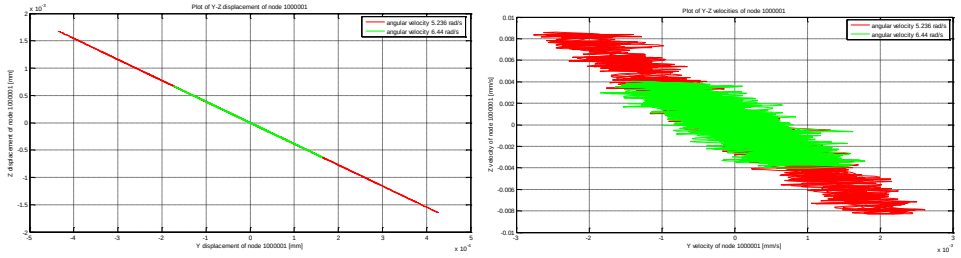


**Figure 11.** Displacement and velocity of node 1000001 in function of Y-Z coordinates.

## 6. Conclusions

The concept and analysis presented in the article, concerning the active vibration control system designed for cutting or boring mining machines, makes it possible to verify the assumptions adopted and the efficiency of its operation. The practical implementation of presented method needs to verify the accuracy of the numerical simulation and their influence on experimental results while normal operation of machine. To obtain such correlation of results may be quite difficult, given the complexity of the mining machines and cutting process. However it is possible to adjust the calculation methodology to practical applications. For this purpose, the physical values reached in a numerical way must be obtained through real-time data acquisition by means of sensors attached to the body of the machine. Taking into consideration the level of contemporary technology in the handling and processing of measurement data, it is possible to develop an algorithm based on the presented methodology using experimental methods such as an operational modal analysis. Selection of the optimum cutting speed could be the result of a real-time genetic algorithm, and its verification would take place in a continuous manner. This, in turn, would make it possible to react to changes occurring in the cutting process.


## Acknowledgments

The authors have been supported by National Science Centre, Poland, under grants 3383/B/T02/2011/40.

**References**

[1] Kępski P., Barszcz T. Condition Monitoring of Machinery in Non-Stationary Operations. *Application of Vibration Monitoring for Mining Machinery in Varying Operational Conditions*, 2012, p. 461-469.

[2] Roxborough F., King P., Pedroncelli E. Tests on the cutting performance of a continuous miner. *Journal of The South African Institute of Mining and Metallurgy*, 1981, p. 9-25.

[3] Khair A. Research and innovations for Continuous Miner's cutting head, for efficient cutting process of rock/coal. *17th International Mining Congress and Exhibition of Turkey - IMCET2001,* 2001, Volumes 308-310, p. 1885-1888.

[4] Cao Y. L., Li X. H., Sha Y. D., Liu H. M. The Effects of Cutting Speed on Continuous Miner Cutting Performance. *Advanced Materials Research,* 2010, Volumes 156-157, p. 1675-1679.

[5] Kaliński K., Galewski M. A modified method of vibration surveillance by using the optimal control at energy performance index. *Mechanical Systems and Signal Processing*, 2015, Volumes 58 p. 41-52

[6] Sibielak M., Raczka W., Konieczny J., Kowal J. Optimal control based on a modified quadratic performance index for systems disturbed by sinusoidal signals. *Mechanical Systems and Signal Processing* 2012, Volumes 64–65, p. 498–519.

[7] Awrejcewicz J., Starosta R., Sypniewska-Kamińska G. Decomposition of governing equations in the analysis of resonant response of a nonlinear and non-ideal vibrating system. *Nonlinear Dynamics* 2015, p. 1-11.

[8] Yong W., Qibai H., Minggang Z., Yongbo Z. A new approach on vibration analysis of locally nonlinear stiffness and damping system. *International Journal of Mechanics and Materials in Design* 2006, Volume 3 p. 1-6.

[9] Rossikhin Y., Shitikova M. Analysis of nonlinear vibrations of a two-degree-of-freedom mechanical system with damping modelled by a fractional derivative. *Journal of Engineering Mathematics*, 2000, Volume 37 p. 343-362.

Arkadiusz Mężyk, Professor: Silesian University of Technology/ Faculty of Mechanical Engineering/ Department of Theoretical and Applied Mechanics, ul. Konarskiego 18a, 44-100 Gliwice, Poland *(arkadiusz.mezyk@polsl.pl*).

Wojciech Klein, Ph.D.: Silesian University of Technology/ Faculty of Mechanical Engineering/ Department of Theoretical and Applied Mechanics, ul. Konarskiego 18a, 44-100 Gliwice, Poland (*wojciech.klein@polsl.pl*).

Mariusz Pawlak, Ph.D.: Silesian University of Technology/ Faculty of Mechanical Engineering/ Department of Theoretical and Applied Mechanics, ul. Konarskiego 18a, 44-100 Gliwice, Poland (*mariusz.pawlak@polsl.pl*).

Jan Kania, Ph.D.: Silesian University of Technology/ Faculty of Mining and Geology/ Institute of Mining Mechanisation, ul. Akademicka 2, 44-100 Gliwice, Poland (*jan.kania@polsl.pl*).

# Influence of position of an anvil beam on vibrations of collecting electrodes (NUM061-15)

Andrzej Nowak, Paweł Nowak, Jan Awrejcewicz

*Abstract:* The paper presents experimentally verified computational model of the collecting electrodes in electrostatic precipitator (ESP). Discretisation of the whole system, both the beams and the electrodes, is carried out by means of the modified rigid finite element method (RFEM). The RFEM allows easy to reflect mass and geometrical features of the considered. Moreover, the method is convenient for the introduction of additional concentrated masses which reflects elements such as the joints that fasten the electrodes to the suspension beam, distance-marking bushes, riveted or screw joints, etc... The system of nine electrodes 16 m long and several various positions of an anvil beam in this system are analyzed. Position of the anvil beam in the system has essential influence on tangent and normal accelerations at different points of the plates, and thus on the effectiveness of the dust removal process. The aim of the simulations is to find optimal position of an anvil beam, which guaranties the maximum amplitudes of vibrations and their proper distribution in the plates.

## 1. Introduction

Particulate matter emitted by power and industrial plants is a polydisperse particulate – it constitutes a group of particles of different size, from submicron particles to particles of a diameter of several tens μm [1]. Particle size distribution is affected by both the pollution generated by the same source and the efficiency of the used dust collector [2]. Modern electrostatic precipitators, thanks to their high total dust extraction efficiency, reaching 99.9%, are used for a thorough purification of gases from dust particles. A scheme of a single-sectional electrostatic precipitator is demonstrated in Fig. 1.

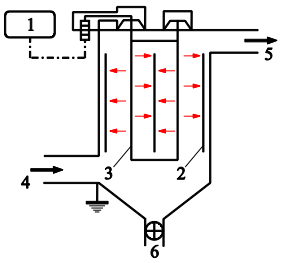


**Figure 1.** Scheme of a single-sectional electrostatic precipitator.

The basic elements of currently built ESP are: a set of emitting electrodes **2**, a set of collecting electrodes **3**, electric power system **1** and housing with supply **4** and discharge **5** conduits for the gas from the dust collector. The dust is discharged using channel **6**.

The interior of a dry ESP is a complex steel structure. It consists of multiple, repetitive subassemblies, called sections of collecting electrodes (Fig. 2a). Sectioning of the ESP is applied in the case of dust extraction of large volumes of gas. A single section is formed by up to several tens of collecting electrodes, separated alternately with sets of discharge electrodes (Fig. 2b).

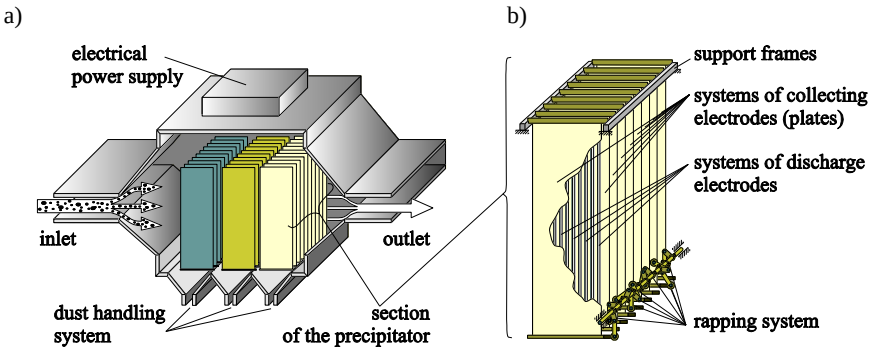


**Figure 2.** Scheme of: a three-sectional dry ESP, b) a section of collecting electrodes.

The effective operation of an ESP is largely dependent on, among others, the structure and proper selection of the profile of collecting electrodes [3]. One of the profiles, often used in domestic structures, is presented in Fig. 9b. The systems of collecting electrodes are connected with the sets of rappers, responsible for the removal of dust accumulated on these electrodes. In the case of ESP with a gravitational system of rappers, each section has its own drive shaft of rappers. The number of rappers corresponds to the number of the systems of collecting electrodes in the section. An important element of a rapping system, in terms of vibrations induced in the system of collecting electrodes, is a beater hanging on the arm rotated by a drive shaft (Fig. 3). The removal of the particulate matter collected on the electrodes occurs as a result of excitation of vibrations of accelerations allowing for the effective removal of particles coagulated on their surfaces. The analysis of the phenomena accompanying the operation of rapping devices, the improvement of reliability of the operation of rapping systems and the achievement of more efficient removal of particulates from collecting electrodes have been under investigation for many years [4, 5]. Initially, the studies were based on physical models. For example [6] presents a physical model of a dry ESP, which served to search for optimal parameters of rapping, expressed by the thickness of the particulate layer, the value of the generated acceleration only in 2 control points of collecting electrodes. However, in the last decade,

instead of building physical models of ESP, specialized, numerically advanced models are created, which serve to perform simulations of a whole device [7] or only its selected subassemblies [8].

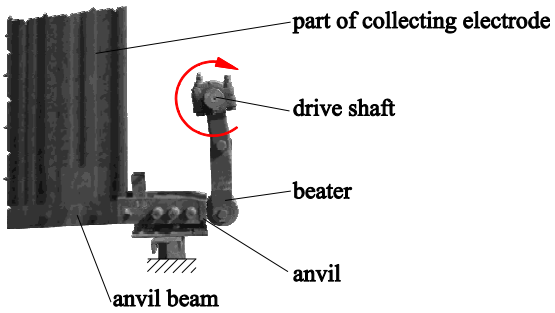


**Figure 3.** Rapping system.

The earlier works of the authors [9-12] present models allowing for a simulation of vibrations of electrodes, induced by an impulse force. The models were obtained using: the finite element method [12], the slab strip method [9] and the rigid finite element method [10, 11]. In the above-mentioned publications much space is devoted to the validation of the models – by comparing the results of measurements and computer simulations. The adopted compatibility criteria demonstrated that practically all the applied methods give a satisfactory consistency of the results in the range of peak values of accelerations. It also applies to the RFEM, used in the current study.

Based on the models verified with the use of measurements, an attempt was made to use the developed computer software to determine the effect of geometric and structural parameters of the electrode-rapper system on the values of accelerations. The results of the conducted analyses may be useful to engineers and designers of ESP.

## 2. SES model of a system of collecting electrodes

The RFEM is an original Polish method, developed since the 70s of the twentieth century [13, 14]. Its essential feature is a simple physical interpretation and numerical effectiveness – particularly in the area of the analysis of vibrations around the position of static equilibrium. In the present study the subject for modeling is a single set of collecting electrodes (Fig. 4) comprising a suspension beam (upper beam), on which $p$ electrodes are hung (usually no more than 10), braced at the bottom by the anvil beam (bottom beam). An anvil is completed with an anvil, hit by the beater.

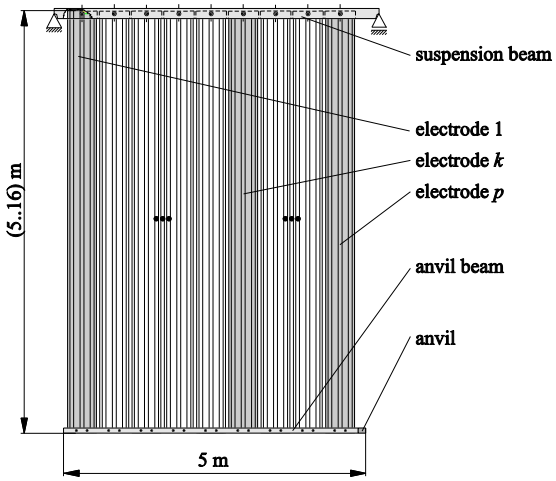


**Figure 4.** The system of collecting electrodes.

Based on the analysis of the shapes of collecting electrodes presented in the introduction, it can be noted that they consist of several long slab strips, connected at certain angles. This implies the way of their division into elements, presented below. The electrode *k* is associated with a coordinate system with axes directed according to Fig. 5.

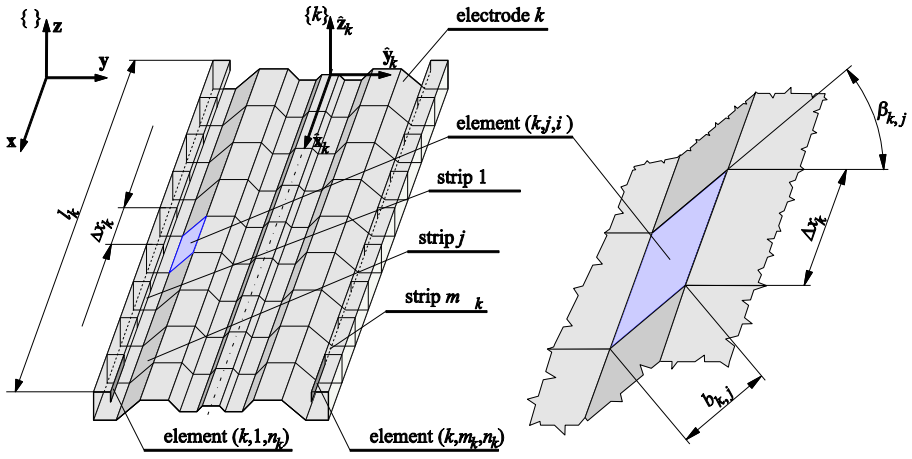


**Figure 5.** Strip *j* with width $b_{k,j}$ and angle of inclination $\beta_{k,j}$ towards axis $\hat{\mathbf{y}}$, {} – global coordinate system, {k} – local coordinate system connected with electrode *k* with axes parallel to those of system {}.

A single strip of an electrode has a constant width and thickness. It is assumed that the strips are numbered from 1 to $m_k$, while the extreme left-hand strip has number 1, and the extreme right-hand one number $m_k$. In the direction **x** the strip is divided into $n_k$ elements of the length:

$$\Delta x_k = \frac{l_k}{n_k}, \tag{1}$$

where $l_k$ –length of the electrode (and thus the length of strips from 1 to $m_k$). Therefore, the whole collecting electrode is divided into

$$n_e^{(k)} = m_k n_k \tag{2}$$

elements. It should be noted that the elements of the strip *j* of the electrode *k* are of the same size. The introduced division will serve to determine the energy of elastic strain of element of the electrode and its kinetic energy, using rectangular shell elements. In the RFEM the presented division is called a primary division. In the secondary division, primary elements are divided into four parts – rigid finite elements (rfe), as shown in Fig. 6 and connected by means of spring-damping elements (sde).

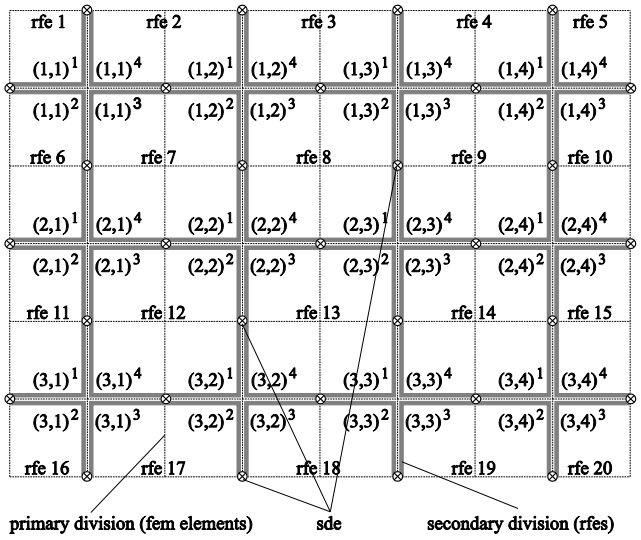


**Figure 6.** Exemplary scheme of discretisation in RFEM : primary (┼) and secondary (╬) divisions.

In the present study spring-damping elements sde are placed similarly as in [16] and in contrast to [15]. This way of sde arrangement provides the opportunity to consider the torsion of discretized plates and eliminates singularities in the model. Upper and lower beams are discretized in a similar way (Fig. 7).

a)

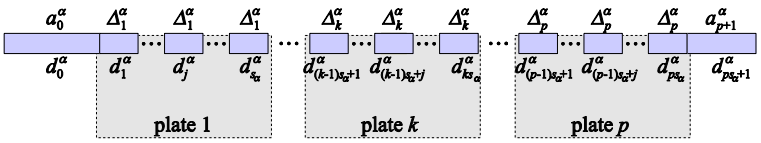


b)

After calculating mass parameters of rfe and stiffness coefficients of sde for plates and beams, the equation of motion can be presented in the general form:

$$\mathbf{M}\ddot{\mathbf{q}} + \mathbf{C}\mathbf{q} = \mathbf{f} \tag{3}$$

where: **M** – mass matrix of constant elements, **C** – stiffness matrix of constant elements, **q** – the vector of generalised coordinates, **f=f(q**, **F)** and $F(t)$ – force applied to the anvil of the bottom beam (Fig. 8).

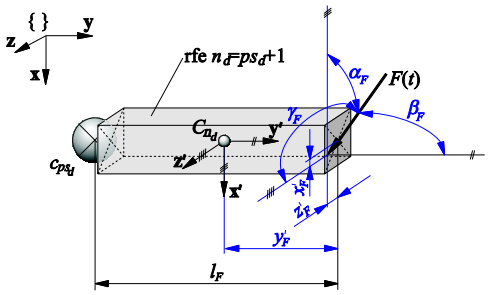


**Figure 7.** Model of an impulse force inducing vibrations in the lower beam.

In equation (3) damping is omitted, as from the engineering point of view, it is important to determine the maximum possible acceleration values. However, these are obtained for systems without damping. It should also be considered that in the structures of real ESP the following factors are higher than material damping: damping of the structure and damping caused by particulates accumulated on the electrodes.

## 3. Test calculations

The model presented in this study was used to simulate vibrations induced by an impulse force, the course of which was demonstrated in Fig. 9a. In the further part the results of exemplary numerical simulations of the vibrations of a set of electrodes of the profile presented in Fig. 9b, were demonstrated. The analysis covered sets of 9 electrodes of a length of 16 m, differing with the

position of an anvil beam in the system (Fig. 9c, variants *H*6..*H*16), made of rolled sheet having a thickness of 1,5 mm. The calculations were made for angles of application of impulse force $\alpha_F = \beta_F = \gamma_F = 0$ applied to a point $(x_F, y_F, z_F) = (0,0,0)$, Fig. 8.

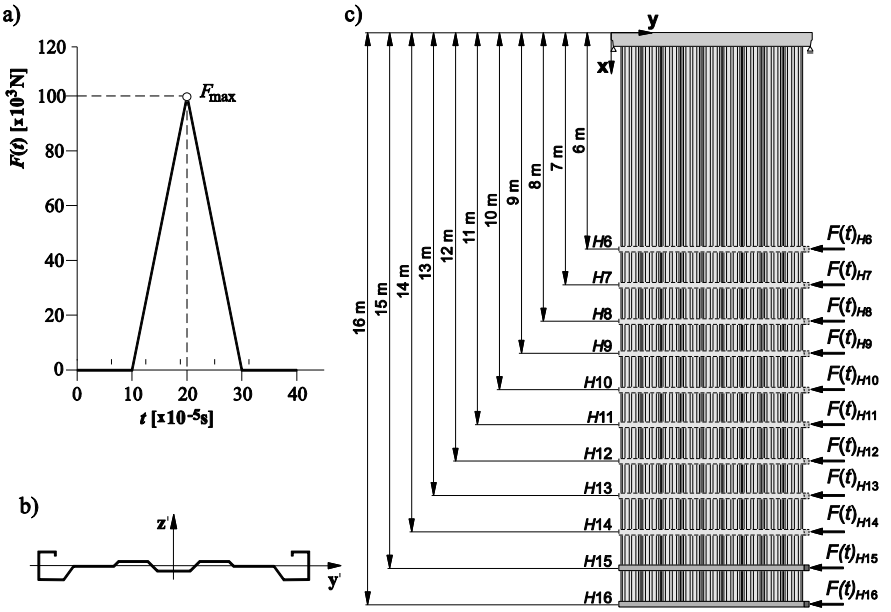


**Figure 8.** Scheme of the system for tests: a) course of the impulse force, b) analyzed profile of electrodes, c) variants with a variable height of anvil beam position (*H*6.. *H*16).

Vibrations of electrodes have a nature of high-frequency processes. However, a direct comparison of such courses is not very effective. For this reason, the present study compares peak values $W_{\max}$ representing indirectly analyzed courses of accelerations in the field of amplitudes, expressed by the following dependencies:

$$W_{max}\left(a_{s,i}\right) = \max_{0 \le t \le T} \left|a_{s,i}\right|, \tag{4}$$

where: *T*- time of the analysis, *i* – number of the control point. In the above equation it was assumed that $a_{s,i}$ can be one of the following values:

$$a_{s,i} = \begin{cases} a_{x,i} & \text{– acceleration in the direction of axis } \mathbf{x}, \\ a_{y,i} & \text{– acceleration in the direction of axis } \mathbf{y}, \\ a_{\tau,i} = \sqrt{a_{x,i}^2 + a_{y,i}^2} & \text{– tangential acceleration in plane } \mathbf{xy}, \\ a_{v,i} = a_{z,i} & \text{– normal acceleration in plane } \mathbf{xy}, \\ a_{c,i} = \sqrt{a_{x,i}^2 + a_{y,i}^2 + a_{z,i}^2} & \text{– total acceleration,} \end{cases}$$

therefore $s = \{x, y, t, n, c\}$ .

Simulations of vibrations for the above-mentioned variants were conducted at the following calculation and material parameters:

- force impulse: the course as shown in Fig. 9a,
- integration step: $h_c = 1 \times 10^{-6}$s,
- density of discretisation of electrode strips: $n_k = 400$,
- simulation time: $T = 1 \times 10^{-2}$s,
- Young's modulus: $E = 2{,}06 \times 10^{11}$ Pa,
- Poisson number: $\nu = 0{,}3$.

Peak values $W_{max}(a_s)$ of the tangential and normal component and total acceleration were compared. 100 control levels, spaced at 0.16 m were assumed. At each level acceleration values were determined in 225 points. No numbers were assigned to the points.

### 3.1. Analysis of the shift of the anvil beam

The study of the impact of the position of the anvil beam on the distribution of accelerations in the system of electrodes was limited to the analysis of 11 cases (Fig.8c). In the first case the beam was located at the bottom edge of electrodes (16 m below the suspension beam), and thus in the position applied most often in the ESP produced in Poland. In successive cases the beam was "raised" 1 meter up as compared to a previous case. For clarity, the presentation of the maps of peak values was limited to total accelerations. Fig. 9 presents a map of peak values $W_{\max}(a_c)$ of total accelerations of control points of the system, obtained during the simulation. Based on the presented results it can be observed that the shift of the anvil beam towards the upper beam allows for a more even distribution of peak values $W_{\max}(a_c)$ throughout the system.

The quantitative assessment of the vibrations in the system was performed by comparing mean peak values $\bar{W}_{\max,H}(a_c)$ of control levels (Fig. 10) and mean peak levels $\bar{W}_{\max}(a_s)$ of the system of electrodes (Fig. 11). The analysis of the values $\bar{W}_{\max,H}(a_s)$ from Fig. 11 helps to observe that the position *H*8 of the anvil beam allows for a more even distribution of peak values of accelerations in the system.

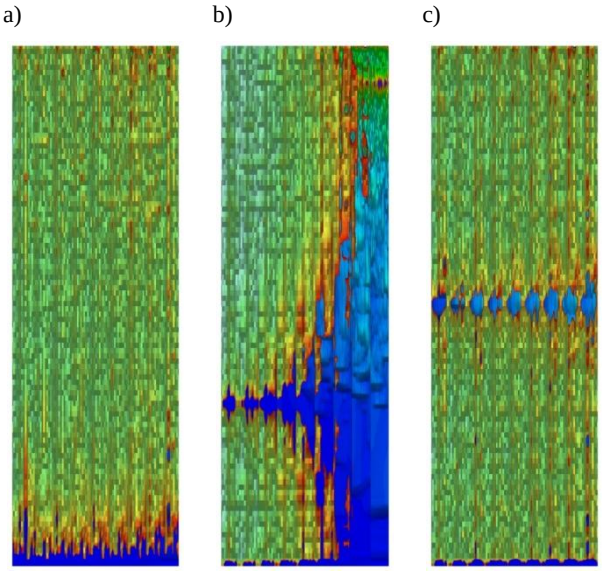


**Figure 9.** Peak values $W_{\max}(a_c)$ of the total acceleration at time $t = 1 \times 10^{-2}$ s after the application of the impulse force; the position of the anvil beam: a) *H*16, b) *H*11, c) *H*8.

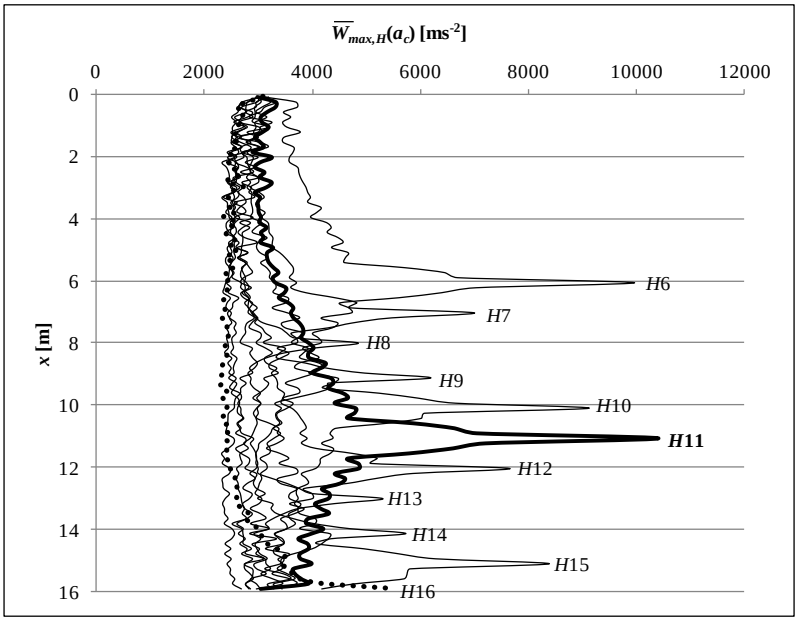


**Figure 10.** Impact of the position of the anvil beam on mean peak values $\overline{W}_{\max,H}(a_c)$ in the following variants: *H*6..*H*16 of the position of the anvil beam.

On the other hand, in the position *H*11 mean peak values of: $\bar{W}_{\max}(a_n)$ - normal component, $\bar{W}_{\max}(a_t)$ - tangential component and $\bar{W}_{\max}(a_c)$ - total acceleration are in this case the highest (Fig. 11).

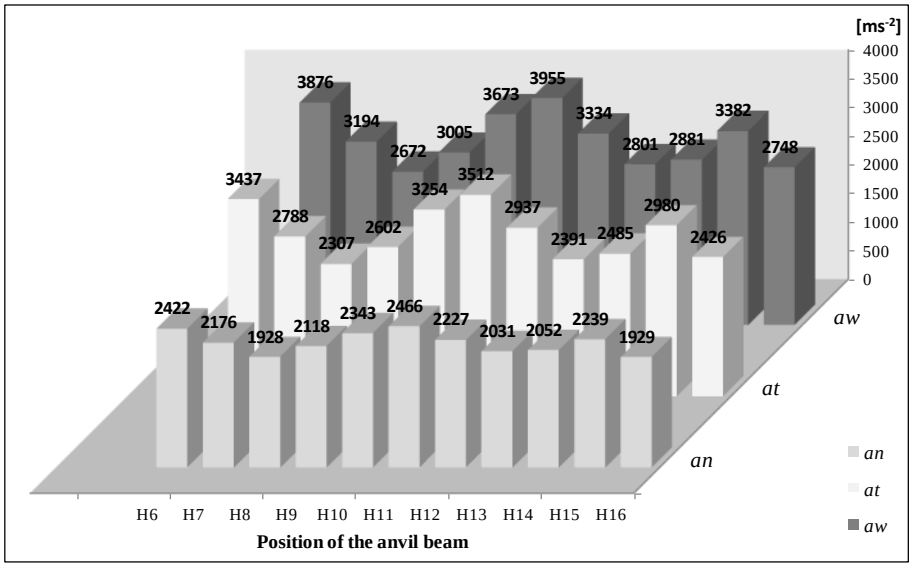


**Figure 11.** Impact of the position of the anvil beam on mean peak values $\bar{W}_{\max}(a_s)$ of the electrode system in the following variants: *H*= 16 m .. *H*=6 m of the position of the beam, where *s* in {*n*, *t*, *c*}.

## 4. Conclusions

In summary, it should be concluded that the process of inducing vibrations and their propagation in the electrode system is a resultant of many factors. It depends not only on the size of impulse force, but also on physical, geometrical and structural parameters of all the components of the system. The experiments presented in the present study imply the following remarks:

1. Treating the normal component of acceleration as the sole criterion for the selection of collecting electrodes and the beater of the rapper is not correct and may lead to incorrect conclusions.

2. The values of total acceleration cannot also determine the selection of a profile of electrodes as the sole factor. Only the combined use of indicators of the assessment of peak values of all the components of acceleration allows for the selection of the optimal variant.

3. The position (height) of anvil beam installation in the system of electrodes may affect the size and distribution of generated vibrations, as well as the time of their propagation. As shown in the study, the "classical" position of the rod in the system is not the most favorable.

4. The shift of rapping rod towards the upper beam does not cause a significant increase in the acceleration values, but it can contribute to their more even distribution.

The results of test calculations demonstrate that intuition of engineers responsible for the design of electrodes was generally correct. The location of the anvil beam in a position other than the "classic" one would require significant changes in current structures, encountering a number of technical difficulties.

**References**


[1] Jaworek, A., Krupa, A., Adamiak, K. Removal of submicrometer dust particles by a charged spherical collector, *Proceedings: 6th International Conference on Electrostatic Precipitation* (ICESP V), June 18–21, 1996, Birmingham, AL., USA,Washington, DC USA, (1996).

[2] Brocilo, D., Podlinski, J., Chang, J. S., Mizeraczyk, J., Findlay, R.D. Electrode geometry effects on the collection efficiency of submicron and ultra–fine dust particles in spikeplate electrostatic precipitators. *Journal of Physics: Conference series* 142, 012032 (2008), pp. 1–6.

[3] Lind, L., Bojsen, E.M. Experience with baffle–free collecting plates in an electrostatic precipitator, *Proceedings: 5th International Conference on Electrostatic Precipitation* (ICESP V), April 5–8, 1993, Washington, DC USA (1993), pp. 36.1–14.

[4] Talaie, M.R. Mathematical modeling of wire–duct single–stage electrostatic precipitators, *Journal of Hazardous Materials* 124, 1–3 (2005), pp. 44–52.

[5] Yang, X.F., Kang, Y.M., Zhong, K. Effects of geometric parameters and electric indexes on the performance of laboratory–scale electrostatic precipitators, *Journal of Hazardous Materials* 169, 1–3 (2009), pp. 941–947.

[6] Lee, J.–K., Ku, J.–H., Lee, J.–E., Kim, S.–C., Ahn, Y.–C., Shin, J.–H., Choung, S.–H. An experimental study of electrostatic precipitator plate rapping and reentrainment, *Proceedings, ICESP VII*, Sep. 20–25, 1998, Kyongju, Korea (1998).

[7] Franci,s S.L., Bäck, A., Johansson, P. Reduction of Rapping Losses to Improve ESP Performance, *Proceedings, ICESP XI*, October 20–25, 2008, Hangzhou, China (2008), pp. 45–49.

[8] [8] Caraman, N., Bacchiega, G., Gallimberti, I., Arrondel, V., Hamlil M. Development of an industrial model of rapping–effect on the collecting efficiency, *Proceedings, ICESP X*, June 25–29, 2006, Cairns, Australia (2006).

[9] Adamiec-Wójcik, I., Nowak, A., Wojciech, S. Comparison of methods for vibration analysis of electrostatic precipitators. *Acta Mech. Sinica* 1, 27 (2011), pp. 72–79.

[10] Adamiec-Wójcik, I. Modelling of Systems of Collecting Electrodes of Electrostatic Precipitators by means of the Rigid Finite Element Method. *Archive of Mechanical Engineering* 58, 1 (2011), pp. 27–47. DOI: 10.2478/v10180-011-0002-x.

[11] Adamiec-Wójcik, I., Awrejcewicz, J., Nowak, A., Wojciech, S. Vibration Analysis of Collecting Electrodes by means of the Hybrid Finite Element Method. *Mathematical Problems in Engineering* 2014, Article ID 832918, 19 pages (2014). doi:10.1155/2014/832918.

[12] Nowak, A. *Modelling and measurements of vibrations of collecting electrodes of dry electrostatic precipitators*, (in Polish *Modelowanie i pomiary drgań elektrod osadczych elektrofiltrów suchych*). Rozprawy Naukowe 35, Wydawnictwo Naukowe Akademii Techniczno-Humanistycznej, Bielsko-Biała, 2011.

[13] Kruszewski, J., Gawroński, W., Wittbrodt, E., Najbar, F., Grabowski, S. *Rigid finite method* (in Polish: *Metoda sztywnych elementów skończonych*), Arkady, Warszawa, 1975.

[14] Gawroński, W., Kruszewski, J., Ostachowicz, W., Tarnowski, J., Wittbrodt, E. *The finie element metod in Dynamics of structures* (in Polish *Metoda elementów skończonych w dynamice konstrukcji*). Arkady, Warszawa, 1984.

[15] Adamiec-Wójcik, I., Wojciech, S. Application of a rigid finite element method in dynamic analysis of plane manipulators. *Mechanism and Machine Theory* 28, 3 (1993), pp 327–334.

[16] Abramowicz, M. *Modelowanie drgań przestrzennych i identyfikacja parametrów dyskretnych modeli stalowo-betonowych belek zespolonych*, Ph.D. thesis, West Pomeranian University of Technology, Szczecin, 2014, Berczyński, S.

Jan Awrejcewicz, Professor: Technical University of Łódź , Department of Automation, Biomechanics and Mechatronics, 1/15 Stefanowskiego Street, 90-924 Łódź, Poland, (jan.awrejcewicz@p.lodz.pl).

Andrzej Nowak, Associate Professor: University of Bielsko-Biala, Department of Transport and Informatics, Willowa 2, 43-300 Bielsko-Biala, Poland (*a.nowak@ath.bielsko.pl*).

Paweł Nowak, M.Sc.: University of Bielsko-Biala, Department of Transport and Informatics, Willowa 2, 43-300 Bielsko-Biala, Poland. The author gave a presentation of this paper during one of the conference sessions (*pnowak@ath.bielsko.pl*).

# 1D model of pulsating flows in pipes dynamics using MOC (ENG038-15)

Tomasz Pałczyński

*Abstract:* This paper presents a model of 1D pulsating flows in partially opened pipes. This is typical of inlet and exhaust pipes of internal combustion engines and piston compressors. The introduction describes the current state of affairs at one dimensional modeling pulsations according to the Method of Characteristics (MOC). Subsequently, the main idea of MOC is presented. In the fourth chapter general guidelines at initial and boundary conditions were presented. The parameters were analyzed at space times domain as 3D diagrams. Next, two crucial resonant frequencies are presented: first and second waveform which can be defined as a quarter and half-length waves. Firstly, partially open end phenomena at space and stage plane were presented. Secondly, the theory of acoustic wave propagation with description of stage waves at analyzed ends of pipe was shown. Finally, existing test rig dedicated to research the pulsating flow in pipes was shortly presented. This test rig was built at Flow Metrology Division of Lodz University of Technology. In the second part of this chapter the main assumption of an elaborated simulation algorithm at Matlab Simulink environment was shown. Lastly, simulation results compared with presented conceptions of modeling those systems with the emphasis into pulsation dynamics according to resonant frequencies were discussed.

## 1. Introduction

The dynamics of pulsating flows in pipes is a very interesting case at various pipelines designs which enables more efficient and silent fluid transport. Sometimes resonance effect is used to improve a significant parameter of chosen process. The method of characteristics is a mathematical technique for solving a hyperbolic type of partial differential equations. This method reduces partial differential equations (PDE) into the family of ordinary equations enabling to integrate a solution from initial data [12]. This is a type of finite difference methods which can be divided into implicit and explicit. A first order of accuracy explicit method was introduced in 1952 by Courant for use with the Characteristics form of the hyperbolic type PDE [12]. In 1952 Hartee proposed schemes with second order accuracy and in 1964 Benson proposed a method based on Courant schemes dedicated for simulating internal combustion engines and reciprocating compressors. The method compares well with other first order of accuracy explicit methods and has advantages over them dealing with boundary conditions.

In 1960 Lax and Wendorff introduced a second order of accuracy explicit method a Two Step version developed later by Richmyer. In the 80's and 90's the development of Total Variation Dimensioning

schemes and Flux Corrected Transport has allowed for the practical use of conservations scheme such as two step Lax Wendorff LW2 or MacCormack methods for intra pipe modeling. The association of TVD and LW2 or MC method is nowadays a recognized solution for efficient 1D manifold modelling, and is embedded into research (GASDYN) or commercial (GT-POWER) codes. Polish authors have also consequently used MOC according to fluid dynamics: Jungowski [2], Wisłocki [3], Prosnak [4], Puzyrewski and Sawicki [5] and at manifold modeling: Jungowski, Kordziński [6] and Sobieszczański [7]. Guderlay constructed general theory of characteristics in which variable specific heat capacities where introduced into Riemann invariants. Those methods were applied graphically by Benson and Winterbone and Pearson.

## 2. Governing equations

Flows are assumed to be one dimensional, ideal compressive gas is assumed to be inviscid.

Continuity equation: the rate of change of mass within the control volume is equal to net mass flow rate through the element:

$$\frac{\partial \rho}{\partial t} + \frac{\partial \rho u}{\partial x} + \frac{\rho u}{F}\frac{dF}{dx} = 0 \tag{1}$$

a) Momentum equation: the rate of change momentum within the control volume is equal to the sum of forces applied to the control volume. This covers friction between the flow and the wall, a shear stress opposed to the flow.

$$\frac{\partial \rho u}{\partial t} + \frac{\partial \rho u^2 + p}{\partial x} + \frac{\rho u^2}{F}\frac{dF}{dx} + \rho G = 0 \tag{2}$$

$$G = \frac{1}{2} u|u| f \frac{4}{D} \tag{3}$$

b) Energy equation is derived from the first law of thermodynamics applied to control volume:

$$\frac{\partial \rho e_0}{\partial t} + \frac{\partial \rho u h_0}{\partial x} + \frac{\rho u h_0}{F}\frac{dF}{dx} - \rho q = 0 \tag{4}$$

The governing equations can be rewritten at vectorial form, where there are particular vectors: state vector of conservative variables (mass, momentum and total energy), flux vector and correction.

## 3. Principles of M.O.C.

Benson's [12] non dimensional notation was used in figure 1. For first step approximation, where heat transfers and friction in pipes are often omitted. Analyzed flow can be defined as a homentropic. Additionally, there is no area section change. According to that condition two non-dimensional Rieman invariants ($\alpha$ and $\beta$) are defined along the characteristics lines $C^+$and $C^-$:

$$\beta = A_i^{n+1} - \frac{\kappa-1}{2} * U_i^{n+1} = A_R^n - \frac{\kappa-1}{2} U_R^n \quad (5)$$

$$\beta = A_i^{n+1} - \frac{\kappa-1}{2} * U_i^{n+1} = A_L^n + \frac{\kappa-1}{2} U_L^n \quad (6)$$

For the homentropic flow contraction of the gas between S and mesh node $(i, n+1)$ can be defined:

$$\frac{p_S^n}{(\rho_S^n)^\kappa} = \frac{p_i^{n+1}}{(\rho_i^{n+1})^\kappa} \quad (7)$$

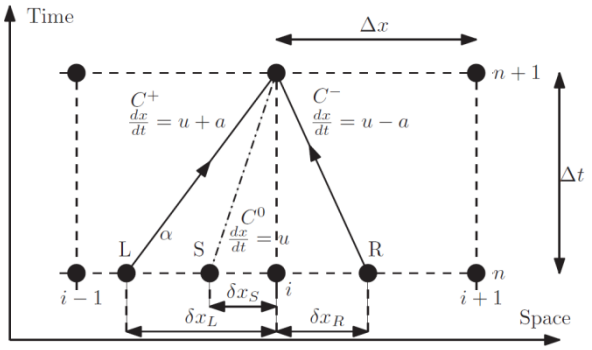


**Figure 1.** Method of characteristics on space time diagram [11]

Having found $\delta x_L$, $\delta x_R$, $\delta x_S$ thermodynamic states can be determined at nodes L, R and S by linear interpolation. After that, there should be calculated: $\rho_i^{n+1}$ , $u_i^{n+1}$, and $p_i^{n+1}$.

Gas parameters are presented at two planes: space $t = f(x)$ and stage $a = f(u)$; where: a – speed of sound [m/s] and u - velocity of flow at x direction [m/s]. In figure 1 we can find, three areas at space plane (1, 2, and 3) which are also represented at stage plane, according to the two basic phases of valve at A section. Upper index ‘ – represents small opening of valve and “ – represents small closing of valve.

For subsonic flows the pressure at pipe should be equal to external one, initially, while and after wave reflection. A nozzle at the end of pipe is added. This nozzle can be described as cross section area change coefficient as a relation: $\varphi = \frac{F_n}{F_p}$, where $F_{n,p}$ –area of nozzle or pipe cross section [$m^2$].

According to boundary conditions and gas state for each value of mentioned coefficient the line is possible at state plane. It can be proven additionally, the $\varphi = const$ curve is straight line for sonic flows and their extension crosses the centre of coordinate systems of state plane. Limiting values of $\varphi$ corresponds to opened end ($\varphi = 1$ from figure 1) or completely closed ($\varphi = 0$). Solution: initial and

reflected state must be on the $\varphi = 0$ curve. It is worth to be mentioned, that abundance wave can be reflected as rarity, abundance or without reflection.

## 4. Boundary conditions for pressure and velocity at opened, closed and partially opened end [3,6]

The acoustic phenomenon is very useful at investigations of pulsating flows in pipes dynamics. Pulsating pipe flow propagates along acoustic wave, it means that the elements move in parallel to wave direction. This way, it can be said that we consider pulsations at plane wave with time-like variable. According to this, the argument of acoustic wave is$(\omega t + kx)$, so called wave phase, where: $\omega$ - wave frequency, $k$ - wave number [1]. Mentioned variables are connected as follows:

$$a = \frac{\omega}{k} = \frac{\lambda}{T} \tag{8}$$

where:

$\lambda$ – wave length [m]

$T$ – wave period [s]

Thanks to this equation, speed of sound is also called phase wave speed. As it was shown in figure 5 there are following rules for pressure and speed values according to the boundary conditions:

a) "*open end*" reflection of pressure wave is within change of sign. Speed and displacement reflect with phase change about $\lambda/2$ . Arising standing wave has characteristic arrows and nodes at boundaries. For speed standing wave, there is an "arrow" and there is node for pressure standing wave.

b) "c*losed end*" reflected pressure wave has the same sign as falling ones. Reflection of speed and displacement waves is within change of sign. Arising standing wave has characteristic arrows and nodes at boundaries. For speed standing wave there is node and there is arrow for pressure standing wave.

### 4. Experimental background and measurement data.

According to the main presented idea of MOC and their boundary conditions a simulation model of pipe with pulsating flow was prepared from test rig at Institute of Turbomachinery (Lodz University of Technology) presented in figure 2. The extensive research on dynamic phenomena in a straight pipe supplied with a pulsating flow of gas, shows, that the character of variation of flow parameters (pressure, temperature, velocity) depends on the nature of the pipe outlet. Based on research of Olczyk [9] experimental data could be implemented into simulation model elaborated at Matlab Simulink. The main idea of this model was presented at [15,16]. Simulation and experiment

parameters of the dynamic states of pulsating flow parameters were compared and results of their synthesis is presented below.

The main parameters of simulated flow [9]:

a) Range of desired values of frequency of pulse generator $f = (20 \div 200)$ [Hz]
b) Pipe diameter $D_p = 42\ 10^{-3}$[m]
c) Pipe length $L_p = 0{,}544$ [m], determined with resonance at 70 Hz and 140 Hz
d) Nozzle diameter $D_n = 10\ 10^{-3}$ [m]. Nozzle is mounted at the end of pipe, at (3) cross section.
e) Desired flow temperature $T = 313{,}15$ [K]
f) Mean Flow speed $u = 20$[m/s] (mean value)
g) Mean Pressure $p = 115000$ [Pa]

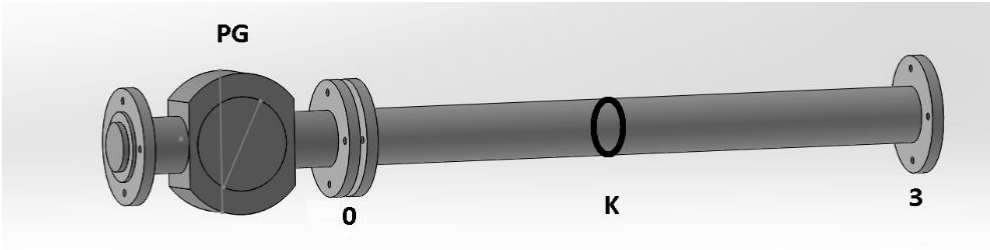


**Figure 2.** The main elements of the test rig with test pipe

Measurement of transient and mean values of pressure, temperature and specific mas flow rate were conducted at control sections (0) and (3) shown in figure 4. Additionally, transient pressure was measured in section (K) placed in the pipe in the mi length.

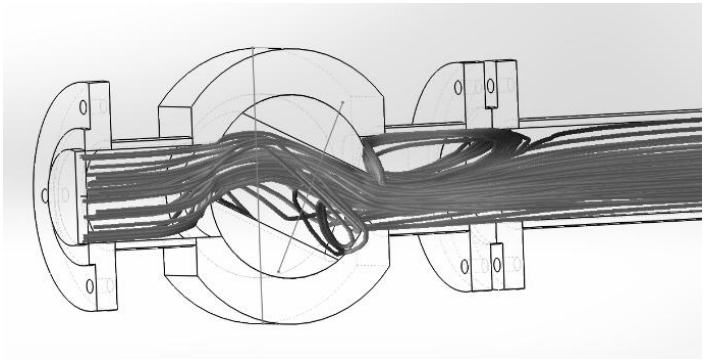

**Figure 3.** Flows visualization at pulse generator

Pulse generator enables measurements of variable reliable and repeatable flow pulsations as it was shown in figure 3. Example stream line was prepared using SOLIDWORKS Flow Simulation. This unit works almost contactless and is driven by electric motor with inverter controlled speed.

As far as measurement devices are concerned, the following equipment was used:

– piesoresistive transducers for pressure measurements: Endevco 8510C-15 and 8510C-50 (Endevco 2003);

– constant current thermometers (CCT) for temperature measurements;

– constant temperature anemometers (CTA) for specific mass flow rate measurements.

Both CCT and CTA probes incorporated a 5 lm tungsten wire.

The simulation algorithm was prepared according to listed assumption:

a) The heat transfer and friction phenomena were not taken into consideration. Adding successive parameters to complete the solution with mentioned phenomena is possible.

b) Two direction iteration process is provided, first at space field (*i* in figure 1), there is fifteenth steps, second at time (*n* in figure 1) 200 iterations. This is enforced by Courant Lewy condition connected with demanded calculation resolution. This is needed because of the angle between space axis and the $u - a$ characteristic line.
When the maximum space iteration "*i*" is reached, the time "n" is switched to next value.

c) Implemented algorithm enables easy switching between boundary conditions presented at paragraph 3. Thanks to that, acquisition of simulation data for clear comparison is possible.

d) The initial conditions were implemented from measurement data, to make calculation more adequate with the experiment, that data were processed by FFT.

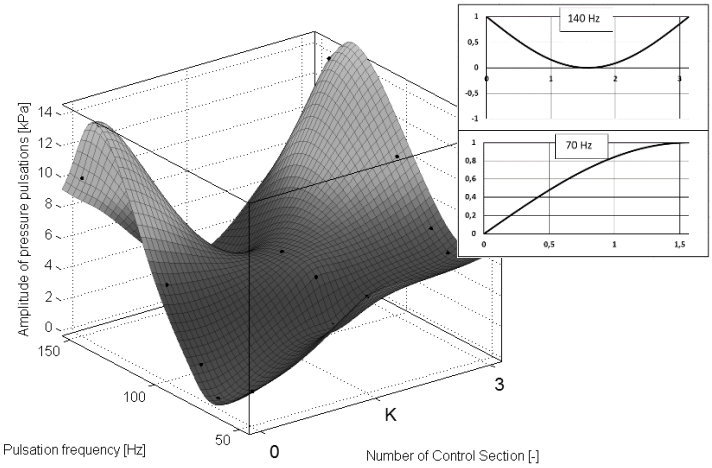


**Figure 4.** Estimation of pressure pulsations amplitude *(on the right side: quarter sinus wave for 70 Hz resonance and the half sinus wave for 140 Hz resonance)*

According to the experiment estimation of amplitude of pressure pulsations was established at the pulsation frequency and control section domain, as it was shown in figure 4. Estimation was based on Curve Fitting tool at Matlab R2015a software, figure 4. This estimation assumes whole spectrum of measured frequencies according to the three defined cross sections. Two forms of resonant wave were identified, for 70 Hz – explicit increase of pulsations amplitude along the pipe length (fig. 5), 140 Hz decrease of pulsations amplitude in the middle of pipe length (fig. 6).

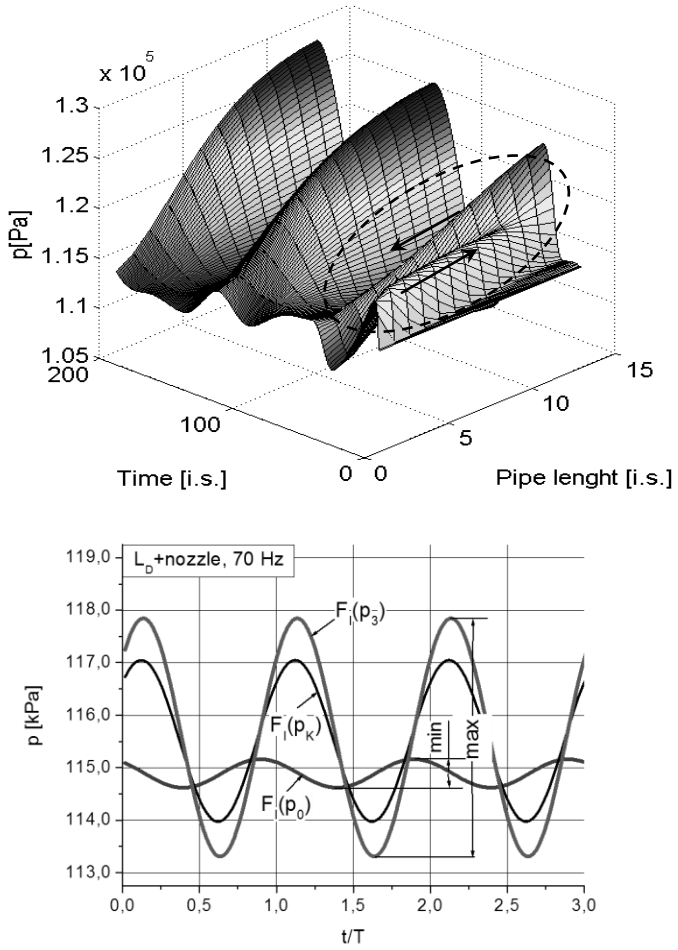


**Figure 5.** Pressure scope for resonant frequency 70Hz *(simulation-upper, measurements – down [10])*

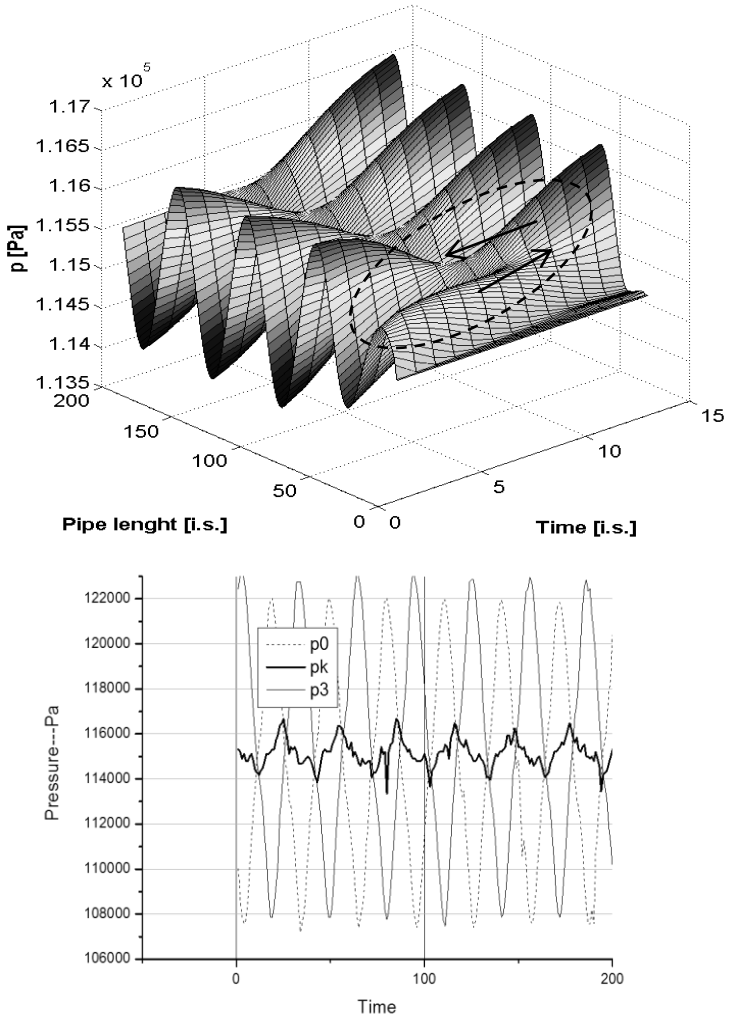


**Figure 6.** Pressure scope for resonant frequency 140Hz *(simulation- top, measurements – bottom [10]).*

Next, numerical simulations of the analysed pipe were provided and results were compared with experimental data. These cases can be also identified as a first and second harmonic figure of oscillations what can be defined as a 1/4 sinusoid and the half sinusoid. Figures 5 and 6 are presented at time-space domain using iteration step unit. It means, that there are 15 steps along pipe length ($L_p = 0{,}544$ [m]) and 200 steps at time domain (0,01 [s]).

Acoustic phenomena of simulation model can be easily found for the initial time steps pointed in figures 5 and 6 by dashed lines. Propagating wave is divided into two parts proportionally to cross section area change coefficient defined at 3. Reflected part of propagating wave will have boundary conditions from closed end type. Rest of the falling wave will propagate outside of the nozzle.
Qualitative comparison results of numerical experiment with measurements can be found quite satisfying. According to the mentioned above similarities, in author's opinion, quite good qualitative compliance between measurements and numerical experiment results was reached.

Similarly, figures 5 and 6, waveforms of instantaneous variations of fluid velocity, temperature and the local speed of sound are calculated.

The proposed numerical model is very simplified as it was presented in previous articles [15, 16], it does not take into consideration the heat transfer and friction phenomena. This simplification causes that the results obtained are mostly qualitative. Thanks to that, the model is simple and needs a little time for solving particular cases (about 15 seconds).

Comparing simulation results from figures 5 and 6 with measurement approximated in figure 4 it can be concluded that the proposed approximation method in figure 4 is acceptable. The proposed method enables to predict results for the length of the analyzed pipe to be estimated on the basis of measurements of only three control sections.

## 5. Conclusions

In this paper a simple and fast model of one dimensional pulsating flow in partially opened pipes was presented. This is a typical case for inlet and exhaust pipes of internal combustion engines and piston compressors. Proposed numerical model enables easy analysis of dynamics for pipes with pulsating flows especially resonances and their influence into crucial parameters such as pressure, temperature along pipe length.

## References


[1] Whitham, G. *Linear and nonlinear Waves*, Willey, p. 127, New York 1974.
[2] Jungowski, W. *Podstawy dynamiki gazów*, WPW, p. 101-105, Warszawa 1972.
[3] Wisłocki K, *Systemy doładowania szybkoobrotowych silników spalinowych*, WKiŁ, Warszawa 1991.
[4] Prosnak W. J. *Mechanika Płynów, Tom II – Dynamika gazów,* PWN Warszawa 1971.
[5] Puzyrewski R, Sawicki J, *Podstawy mechaniki płynów i hydrauliki*, Wydawnictwo Naukowe PWN, Warszawa 1998.
[6] Kordziński C., Środulski T *Układy dolotowe silników spalinowych* WKiŁ, Warszawa 1968.
[7] Sobieszzański M, *Modelowanie procesów zasilania w silnikach spalinowych*, WKiŁ Warszawa 2000.
[8] Mysłowski J, *Doładowanie bezsprężarkowe silników z zapłonem samoczynnym*, WNT Warszawa 1995.

[9] Olczyk A. *Analiza niestacjonarnych zjawisk przepływowych w przewodach zasilanych pulsacyjnie* – Zeszyty Naukowe Politechniki Łódzkiej Nr 1003, seria Rozprawy Naukowe, zeszyt 360 (DSc thesis).
[10] Olczyk A. *Investigation of the specific mass flow rate distribution in pipes supplied with a pulsating flow*, Int. J. Heat Fluid Flow 2009 Vol.30 nr 4 s.637-346,
[11] Brejaud P, Higelin P, Charlet A, Chamailard Y, *Development and experimental valildation of new one-dimensional valve boundary condition based on method of characteristics*, Proceedings of the Institution of Mechanical Engineers, Part D: Journal of Automobile Engineering August 4, 2011 0954407011409653.
[12] Benson S.R. The thermodynamics and Gas Dynamics of Internal Combustion Engine, Vol 1, volume 1, Clarendon Press. Oxford, 1982.
[13] Godlewski E., Raviart P.A., *Numarical Aproximation of Hyperbolic Systems of Conservation Laws*, Sprinder, New York 1996.
[14] Winterbone, Desmond E, *Theory of engine manifold design: wave action methods for IC engines*, Professional Engineering Publishing, 2000
[15] Palczynski T., *A boundary conditions at modeling 1-D pulsating flows in pipes according to the method of characteristics*, J. KONES 2012 Vol.19 nr 2 s.395-402.
[16] Palczynski T., *Symulacje jednowymiarowych przepływów pulsacyjnych w przewodach w oparciu o metodę charakterystyk*, Postepy Nauki Tech. 2012 nr 14 s. 197-207.

Tomasz Palczynski, Ph.D. Eng: Lodz University of Technology//Institute of Turbomachinery, 219/223 Wólczańska Street, 90-924, Poland (*tomasz.palczynski@p.lodz.pl*). The author gave a presentation of this paper during one of the conference sessions.

# Advances in dynamical simulation and analysis of granular flow (ENG118-15)

Anthony Rosato, Denis Blackmore

*Abstract:* After a brief of survey of recent nonlinear dynamics based approaches to granular flows, several advances effected by novel combinations of discrete element simulation and dynamical systems modelling and analysis shall be described in considerable detail. This includes a simplified infinite-dimensional dynamical system model that, informed and confirmed via simulation, is capable of predicting both the motion and density wave behaviour of a wide range of granular flows. In addition, it is shown how simulations inspired and verify the efficacy of approximate reduced models, in the form of low-dimensional discrete dynamical systems, able to predict with surprising accuracy such features as bifurcations, transitions to chaos, strange attractors and perturbation wave properties. Examples for tapping and periodic shaking of granular configurations are presented to illustrate the effectiveness of the combined simulation dynamical systems approach. Finally, open problems and plans for future research are presented.

## 1. Introduction

Unlike fluid dynamics, where the Navier–Stokes equations provide an almost complete description of all fluid phenomena via computational simulation or analysis, granular flow (particulate) dynamics research is in its infancy, relatively speaking. This is largely due to the fact that there seems to be nothing like a ubiquitous mathematical model for a wide range of granular flow dynamics, with the possible exception of the old reliable differential equations of classical mechanics. And since granular flows typically comprise an enormous number of particles, the classical differential equation systems are of extremely high dimension and usually nonlinear, thereby rendering thorough mathematical analysis very difficult at best. This is one of the reasons that the majority of advances (other than from experimental studies) in our knowledge of granular flow dynamics over the last three-score years of rather extensive and intense research activity have come from computational simulation of the classical dynamical systems models, which has offered numerous challenges because of the high dimensions and stiffness of the equations.

Although experimental studies such as those in [9, 26, 27, 52, 53] continue to be an integral part of granular flow research that have provided data and insights that have helped in advancing the state-of-the-art, these studies are now often complemented with simulation

components, such as in [52]. The simulation scheme used in [52] is the discrete element method (DEM) - closely related to standard molecular dynamics codes - initially developed by Walton and Braun [48–51], which has, over the years, been extensively refined and extended by Rosato and his collaborators (see e.g. [24, 25, 36–40]). Rosato's simulation scheme and some of the advances in the granular dynamics knowledge base to which it has contributed shall be described in more detail in the sequel, but there are a host of other simulation approaches, using methods similar to that of Rosato, that have also been rather successful. For example, there is the work of Alexeev et al. [1], which has added significantly to our understanding of liquid and solid state phenomena if vibrated particle columns. There are also the simulations of Brennan, Wassgren and their collaborators, such as in [9], which have revealed interesting dynamical aspects of oscillating granular bed motions. In addition, there are the influential investigations of Luding and his collaborators such as in [26] and Pöschel and Herrmann using combinations of direct simulations and numerical solutions of various mathematical models, exemplified by [34], that have greatly enhanced our knowledge of granular flow dynamics and segregation phenomena.

Another active area of research in particulate dynamics involves the development and application of a variety of mathematical models (or theories), which are solved numerically and sometimes analyzed mathematically to predict the evolution of granular flows. Many different modeling approaches have been taken, and several of these have been quite successful in predicting granular dynamics for special types of flows, where success is measured by the ability of the model predictions to compare favorably with experimental and simulation results. By treating the particles of their conglomerates as cells that move under the action of external and applied forces, Baxter and Behringer [2] were able to use a cellular automata model to predict the evolution of granular flows in a way that compared rather well with experiments and simulations of certain dynamical particle configurations. Caram and Hong [10] exploited the perceived similarities between sparse nearly elastic (identical) particle flows and Brownian motion to formulate a random-walk model that proved to be reasonably effective for certain flows. In somewhat the same stochastic vein, Dybenko et al. [12] employed a Monte Carlo model to predict density relaxation phenomena for tapped particle columns, which agreed well with DEM simulations. Another modeling approach that has proven to be rather successful in predicting the evolution of fairly simple particle configurations has been lattice dynamics such as in the work of Friesecke and Wattis [14], MacKay [28] and Sen and Manciu [44, 45], and the related Langevin-based investigation of Wakou et al. [47]. A particularly nice aspect of these approaches is that they are more amenable to mathematical analysis that others; for example, it is possible to prove the existence of special types of solution such as traveling waves.

Among the more popular formulations used to study granular flows are those that feature continuum models. There have been quite a few of these; some of which have been rather successful - at least in predicting the behavior of some kinds of granular flows, and there are likely to be many more continuum models developed in the future. One of the most popular kinds of continuum models postulated for granular flows are those of the Navier–Stokes type. In such investigations as those of Bougie et al. [8], Goldshtein and Shapiro [15] and Hayakawa and Hong [18], the Navier–Stokes type models have been able to predict shock wave and convection patterns in some vibrating granular bed scenarios with reasonably good accuracy. There also are several hybrid continuum models, such as those of Farrel et al. [13], Henann and Kamrin [19], Jenkins and Savage [21], Jenkins and Richman [22], Nesterenko and Dario and their collaborators [11, 31, 33], Pitman [32], Savage [41] and Schaeffer and his collaborators [42, 43], which have proven to be rather effective for certain types of granular flow. It is worth noting here that some of these models have been analyzed mathematically with respect to existence and stability of solutions [35,42,43]. Of particular note is the soliton connection of the work of Nesterenko [31]: he obtained a long-wave continuum limit (partial differential equation) of a line of particles interacting according to a standard nonlinear perfectly elastic force model, proved that the equation was Hamiltonian and completely integrable (for definitions see also [5]). He also experimentally confirmed the soliton behavior associated with integrability. Lastly, we mention the continuum model of Blackmore et al. [3, 4], which we shall describe in the sequel. This so-called BSR model has been rather successful in predicting the dynamics of several granular flows and appears to have the potential to work well for a wide range of flows.

## 2. Preliminaries

We begin with the classical equations of motion of a system of $N$ particles. In the interest of simplicity, we assume that all of the particles are solid spheres. Let the spheres have masses and radii $(m_1, r_1) \ldots, (m_N, r_N)$ with centers located at the points $x_1, \ldots, x_N \in \mathbb{R}^d, d = 1, 2$ or 3. To further simplify the equations of motion, we also neglect the rotation of the spheres, which is quite reasonable if the particles are all very small, as is often the case. Then, the equations of motion are given by Newton's $2^{\text{nd}}$ law; namely,

$$m_n \ddot{x}_n = E_n + F_n, \tag{1}$$

where $E_n$ represents the external force on each particle, which is usually just gravity, and $F_n$ is the interaction force on $m_n$ resulting from collisions with the remaining spheres and solid portions of the boundary, denoted $\partial_s\Omega$ of the domain $\Omega$ in which contains the granular configuration for all time. Note that the domain $\Omega$ may be a function of time as, for example,

in a granular configuration that starts in a vibrating beaker. The interaction forces are usually represented by nonlinear expressions based on reliable experiments and theory, such as Hertzian, Walton–Braun or Walton–Braun–Mindlin–Deresiewicz models (cf. [16, 30, 48]. We note here that something like the Mindlin–Deresiewicz model is necessary if oblique collisions are to be considered even if the rotational effects are ignored. It should also be noted that the Newton–Euler equations comprise the complete classical equations of motion, which have $6N$ degrees-of- freedom for motion in $\mathbb{R}^3$and that some of the more effective DEM simulation schemes, such as Rosato's, is capable of dealing with the full Newton–Euler equations of motion for a granular flow in a plane or 3-space.

The system (1) is of dimension $2dN$ and has $dN$ degrees-of-freedom. If the interaction forces are perfectly elastic, (1) can be recast in the usual way as a Hamiltonian system of first order equations with $dN$ degrees of freedom. In the ideal perfectly elastic Hamiltonian case, the symplectic structure can be used to effect the usual types of simplifications, but even then the usually enormous number of degrees-of-freedom and the nonlinearity of the Hamiltonian function make complete mathematical analysis extremely difficult and effectively impossible. Therefore, it is clear that one needs to employ computational simulation techniques or find effective simpler mathematical models to analyze the dynamics of the system. In the sections that follow, we shall describe some simulation, continuum modeling and reduced modeling schemes that we have developed to deal with the challenges associated with granular flow analysis and prediction.

## 3. DEM Simulations

Our DEM employs a Verlet leap-frog numerical integrator, which provides global accuracy of $O\left(\Delta t^2\right)$, where $\Delta t$ is the typical time step, which can be varied to increase the efficiency of the code. Of course there are more accurate integrators such as the fourth order Runge-Kutta, but our method is far more effective in dealing with the stiffness of the system and enables accurate numerical studies for systems of many thousands of particles over substantial periods of time.

The discrete element method entails the numerical solution of the equations of motion of a system of particles that interact via approximate collisions models. For macroscopic particles, part of the incident kinetic energy in a collision is converted into plastic work which deforms the surfaces in the contact region. The resulting energy loss is typically modeled via a dashpot (i.e., viscous damping) or through a hysteretic force-displacement law. Our results are based on the soft-sphere hysteretic model developed by Walton and Braun [48–51] , in which the contact interaction is a bilinear function of an allowed overlap a between the spheres. This model has been shown to agree with finite element calculations of

elastic-plastic spheres (i.e., elastic/perfectly plastic constitutive behavior) undergoing quasi-static normal displacement, and also to reproduce experimentally observed behavior in the collision of ductile spheres. In simplified form, the normal force (along the line of centers) between two contacting spheres is given by

$$F := \begin{cases} K_1\alpha, & \text{loading} \\ K_2(\alpha - \alpha_0), & \text{unloading} \end{cases} \tag{2}$$

where $\alpha_0$ is the residual overlap when the unloading force goes to zero. In particular, particles load on linear spring of stiffness $K_1$ and unload on a linear spring of stiffness $K_2$, with $K_2 > K_1$. Unloading continues on the $K_2$ path until the (normal) interaction force is zero, at which time a small residual overlap $\alpha_0$ remains. Further unloading will take place at zero force to $\alpha = 0$; or reloading will follow along a path of slope $K_2$ until it reaches the original the original loading path (of slope $K_1$). It can be shown that this model admits a constant coefficient of restitution given be $e = \sqrt{K_1/K_2}$, which is valid for spheres whose relative normal impact velocity is of the order of 1 meter/sec or less [16]. We note that the typical time step used in our simulations is $\Delta t = (e/2m)\sqrt{3\rho\pi r^3/K_1}$, where $m, r$ and $\rho$ are the average mass, radius and material density of the particles, respectively.

### 3.1. Application to a tapped column of particles

We shall illustrate the effectiveness of our simulation scheme by using it to determine the dynamics of a tapped vertical column of particles under the action of gravity.

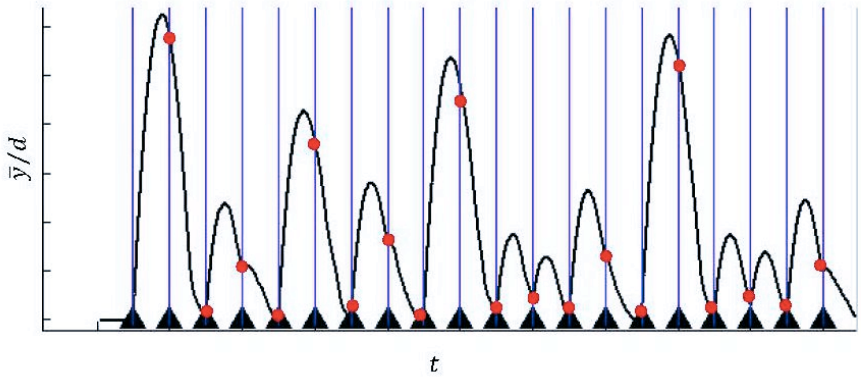


**Figure 1.** Normalized mass center $\bar{y}/d$ versus $t$ for the first 20 taps at $a/d = 1.5$ and $f = 10$ Hz. The vertical blue lines positioned at $t_1 = 0, T, 2T, 3T, \ldots, 99T$ intersect the trajectory at points of the Poincaré map identified by the red dots.

The Poincaré map is constructed by extracting the position of the mass center over $M = 100$ taps at times that are multiples of $T = 1/2f + t_r$, from which the influence of variations in $a/d, f$ and $t_r$ can be visualized. As an example, suppose that $f = 10$ Hz and $t_r = 0.4$ s so that $T = 1/2f + t_r = 0.45$ s. Let $\mathcal{T} := \{t_k\}, k = 1, 2, 3, \ldots, 100$ such that for each $k, t_k := \{(j + 0.01(k-1))T | j = 0, 1, 2, \ldots, 99\}$. The mass center location is thus extracted from the discrete trajectory at $t_k$. The procedure is illustrated in Fig. 1, in which the intersections of the vertical blue lines with the mass center trajectory are the points $y/d$ of the map. Note that the figure shows only a small portion of the mass center trajectory. Studies of an inelastic ball on an oscillating plate have shown that, depending on the tap parameters ($a/d$ and $f$) and $e$, various behaviors are possible, such as periodicity and period doubling cascades leading to chaos. While it is relatively straight forward to identify the amplitude at which period doubling takes place, the process to locate other orbits (period 4, 8, etc.) is not a trivial matter. And the complexity is magnified when considering the mass center of a column represents the average dynamics of the motion of all of the particles in the column. Furthermore, the difficulty is compounded by the sensitivity of the dynamics to initial conditions, coupled with the need to resolve the time domain into sufficiently small intervals.

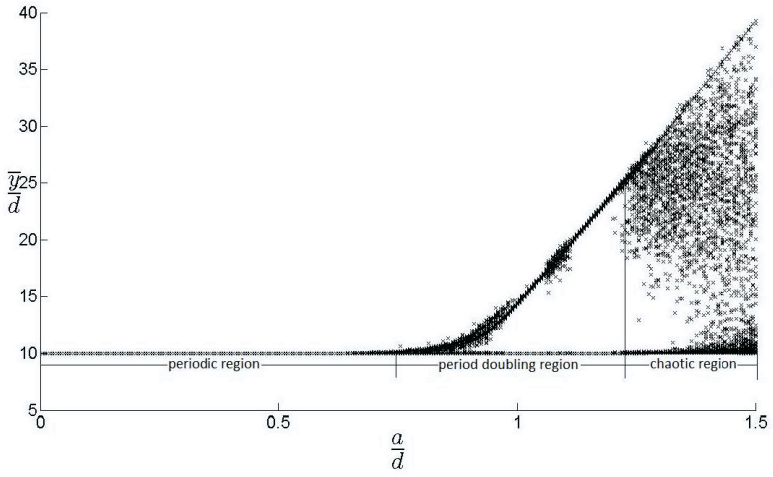


**Figure 2.** Bifurcation diagram of Poincaré map of $\bar{y}/d$ versus $4a/d$ sampled at $t_1 = 0, T, 2T, \ldots, 99T$ ($N = 20, f = 10$ Hz; $t_r = 0.4$ s) reveals periodic, period doubling and chaotic regimes.

The Poincaré map of Fig. 2 ($N = 20, f = 10$ Hz; $t_r = 0.4$ s) shows what appears to be

a single line for $0 < a/d < 0.75$, corresponding to the periodic region. At each value of $ad$ in this region, there are 100 nearly identical values of $\bar{y}/d$ that correspond to the positions of the mass center at $t_1 = 0, T, 2T, , 99T$. As the amplitude is increased, the mass center locations start to disperse until the onset of period doubling, while further increase in $ad$ ultimately produces what appears to be chaotic behavior.

By computing the deviation of the mass center trajectory (denoted by $S_{\bar{y}}$) from its mean path taken over the time span from when the taps begins provides a reasonably accurate means of delineating the dynamical regimes depicted in Fig. 2, which is illustrated in Fig. 3.

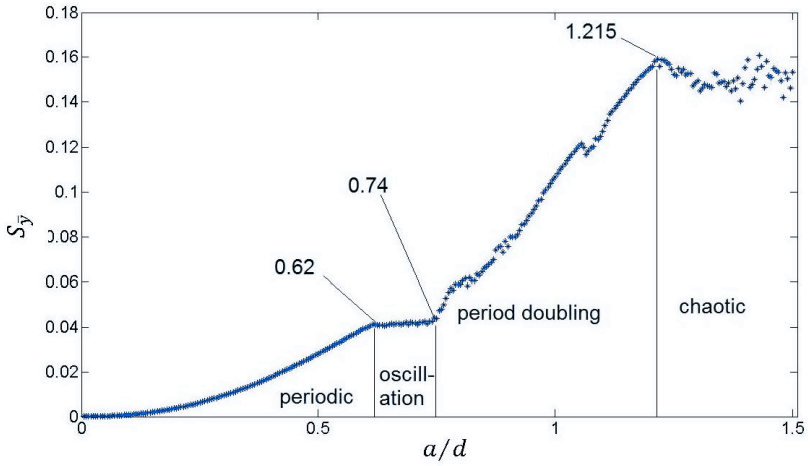


**Figure 3.** Standard deviation of the mass center $S_{\bar{y}}$ trajectory versus $ad$ for $t_r = 0.4$ s, $f = 10$ Hz and $N = 20$.

The result in Fig. 3 for $t_r = 0.4$ s, $f = 10$ Hz and $N = 20$, reveals the amplitudes at which the dynamics transitions from periodic to chaotic.

## 4. The BSR Continuum Model

The BSR continuum model was derived in [3] as a limiting continuum model for granular and other flows. It is a system of integro-partial differential equations of the form

$$\begin{aligned} \boldsymbol{u}_t &= \boldsymbol{\alpha}\left(\boldsymbol{x}, t; \boldsymbol{\mu}\right) - \langle \boldsymbol{u}, \nabla \rangle \boldsymbol{u} + \int_{B_r(\boldsymbol{x})} \rho(\boldsymbol{y}, t) \boldsymbol{\Theta}\left(\boldsymbol{x}, \boldsymbol{y}, \boldsymbol{u}(\boldsymbol{x}, t), \boldsymbol{u}(\boldsymbol{y}, t)\right) d\boldsymbol{y}, \\ \rho_t &= -\left[\langle u, \nabla \rangle \rho + \rho \operatorname{div} \boldsymbol{u}\right], \end{aligned} \tag{3}$$

which is subject to the initial conditions

$$\boldsymbol{u}(\boldsymbol{x},0)=\boldsymbol{u}_0(\boldsymbol{x}),\rho(\boldsymbol{x},0)=\rho_0(\boldsymbol{x}),\ \boldsymbol{x}\in\Omega, \tag{4}$$

where $\Omega$ is a fixed, $C^2$ submanifold of $\mathbb{R}^n$ with boundary $\partial\Omega$ and the system is defined for $\Omega\times[0,\infty)$. Here the function $\boldsymbol{\alpha}$ represents the external and any inertial forces present.

The versatility and effectiveness of the BSR model have been demonstrated in [4,6,7,40]. For example, analogous to the results of Nesterenko [31], it has been shown that the 1-dimensional version of the BSR is completely integrable if the interaction forces are perfectly elastic [4]. The proof is accomplished by showing the system is bi-Hamiltonian, so the result follows from Magri's theorem (see e.g. [5]).

### 4.1. Well-posedness of BSR model

The following theorem, which is apparently somewhat unique for reliable continuum granular flow models (cf. [35]), is proved in [54].

**Theorem.** *If the BSR system and its boundary and initial conditions are $C^2$ and the density $\rho$ is bounded, the system has a unique $C^1$ solution that depends smoothly on the auxiliary conditions and exists for all time.*

### 4.2. Reduced discrete dynamical model for column dynamics

For the vibrating column one can demonstrate, using either the BSR model or the classical Newtonian equations, that the center of mass dynamics can be approximated by a standard map of the Holmes type [20], which shows how the dynamics can transition to chaos with a strange attractor [7]. Thus the dynamics can exhibit all of the exotic behavior of a ball bouncing on an oscillating plate (cf. [17, 20, 23, 29, 46]. The map has the form

$$\begin{aligned}&\Phi:\mathbb{S}^1\times\mathbb{R}\to\mathbb{S}^1\times\mathbb{R},\\ &\Phi\left(\theta,v\right):=\left(\left[\!\left[\theta+v\right]\!\right],ev+\gamma W(\theta+v)\right),\end{aligned} \tag{5}$$

where $[\![\cdot]\!]$ denotes the congruence class mod $\omega T$, generates a discrete dynamical system that closely approximates the times $t_n$ and velocities $V_n$ of successive impacts of the "ball" of (**??**) with the vibrating floor. Here, $\theta:=\omega t$, $v:=2\omega V/g_*$, $\gamma:=(2a\omega^2/N)(1+e)/g_*=2a\omega^2(1+e)/g$ and $W$ is a $\omega T$-periodic function defined on a period interval as

$$W(s):=\begin{cases}\cos s, & 0\le s\le\pi\\ 0, & \pi\le s\le\omega T\end{cases}. \tag{6}$$

## 5. Conclusions

We have shown that advanced DEM simulations coupled with the BSR model and related reduced models is a powerful tool for studying granular flow dynamics. Our future research is aimed at extending and generalizing this combination in an effort to demonstrate how versatile it is.


## Acknowledgments

The authors have been supported by NSF Grant CMMI-1029809.


## References


[1] Alexeev, A., Goldshtein, A. and Shapiro, M., The liquid and solid states of highly dissipative vibrated granular columns: one-dimensional computer simulations. *Powder Technology,* 123 (2002), 83-104.

[2] Baxter, G.W. and Behringer, R.P., Cellular automata models of granular flow. *Phys. Rev. A*, 42 (1990), 1017-1020.

[3] Blackmore, D., Samulyak, R. and Rosato, A., New mathematical models for particle flow dynamics. *J. Nonlin. Math. Phys.*, 6 (1999), 198-221.

[4] Blackmore, D., Urban, K. and Rosato, A., Integrability analysis of regular and fractional Blackmore–Samulyak–Rosato fields. *Condens. Matter Phys.*, 13 (2010), 1-7.

[5] Blackmore, D., Prykarpatsky, A.K. and Samoylenko, V.Hr., *Nonlinear Dynamical Systems of Mathematical Physics.* World Scientific, Singapore, 2011.

[6] Blackmore, D., Rosato, A., Tricoche, X., Urban, K. and Ratnaswamy, V., Tapping dynamics for a column of particles and beyond. *JOMMS,* 6 (2011), 71-86.

[7] Blackmore, D., Rosato, A., Tricoche, X., Urban, K. and Zuo, L., Analysis, simulation and visualization of 1D tapping dynamics via reduced dynamical models. *Physica D*, 273-274 (2014), 14-27.

[8] Bougie, J., Moon, S.J., Swift, J.B. and Swinney, H.L., Shocks in vertically oscillated granular layers. *Phys. Rev. E*, 81 (2010), 061301.

[9] Brennen, C., Ghosh, S. and Wassgren, C., Vertical oscillation of a bed of granular material. *Trans. ASME,* 63 (1996), 156-161.

[10] Caram, H. and Hong, D.C., Random-walk approach to granular flows. Phys. Rev. Lett., 67 (1991), 828-831.

[11] Daraio, C., Nesterenko, V., Herbold, E. and Jin, S., Tunability of solitary wave properties in one dimensional strongly nonlinear phononic crystals. *Phys. Rev. E,* 73 (2006), 026610.

[12] Dybenko, O., Rosato, A. and Horntrop, D., Monte Carlo modeling of density relaxation induced by energetic taps. *Kona Particle and Powder* 25 (2007), 133.

[13] Farrel, M., Lun, C., and Savage, S., A simple kinetic theory for granular flow of binary mixtures of smooth, inelastic spherical particles. *Acta Mech.*, 63 (1986), 45-60.

[14] Friesecke, G. and Wattis, J., Existence theorem for solitary waves on lattices. *Commun. Math. Phys,* 161 (1994), 391-418.

[15] Goldshtein, A. and Shapiro, M., Mechanics of collisional motion of granular materials, Part 1. General hydrodynamic equations. *J. Fluid Mech.*, 282 (1995), 75-114.

[16] Goldsmith, W., *Impact: The Theory and Physical Behavior of Colliding Solids.* Edward Arnold, London, 1960.

[17] J. Guckenheimer and P. Holmes, *Nonlinear Oscillations, Dynamical Systems, and Bifurcations of Vector Fields*, Springer-Verlag, New York, 1983.

[18] Hayakawa, H. and Hong, D., Two hydrodynamical models of granular convection. *Powders and Grains 97*, Behringer, R. and Jenkins, J. (eds), Balkema, Rotterdam, 1997, 417-420.

[19] Henann, D. and Kamrin, K., A predictive, size-dependent continuum model for dense granular flows. *PNAS,* 110 (2) (2013), 6730-6735.

[20] Holmes, P., The dynamics of repeated impacts with a sinusoidally vibrating plate, *J. Sound Vib.* 84 (2) (1982), 173-189.

[21] Jenkins, J. and Savage, S., A theory for rapid flow of identical smooth, nearly elastic particles. J. Fluid Mech., 130 (1983), 187-202.

[22] Jenkins, J. and Richman, M., Grad's 13-moment system for a dense gas of inelastic spheres. Arch. Rat. Mech. An al., 87 (1985), 355-357.

[23] Katok, A. and Hasselblatt, B., *Introduction to the Modern Theory of Dynamical Systems*, Cambridge University Press, Cambridge, 1995.

[24] Lan, Y. and Rosato, A., Macroscopic behavior of a vibrating bed of smooth inelastic particles. *Phys. Fluids*, 7 (1995), 18-18-1831.

[25] Lan, Y. and Rosato, A., Convection related phenomena in vibrating granular beds. *Phys. Fluids*, 9 (1997), 3615-3624.

[26] Luding, S., Clement, E., Blumen, A., Rachenbach, J. and Duran, J., Studies of columns of beads under external vibrations. *Phys. Rev. E*, 49 (1994), 1634.

[27] Lumay, G., Darbolo, S., Gerasymov, O. and Vanderwalle, N., Experimental study of a vertical column of grains submitted to a series of impulses. *Eur. Phys. J. E,* **36** (2013), 13016.

[28] MacKay, R., Solitary waves in a chain of beads under Hertz contact. *Phys. Lett. A,* 251 (1999), 191-192.

[29] Mello, T. and N. Tufillaro, N., Strange attractors of a bouncing ball. *Am. J. Phys.*, 55 (1987), 316-319.

[30] Mindlin, R.D. and Deresiewicz, H., Elastic spheres in contact under varyng oblique forces. *J. Appl. Mech.*, 20 (1953), 327-344.

[31] Nesterenko, V., Propagation of nonlinear compression pulses in granular media, *J. Appl. Mech. Tech. Phys.,* 24 (1984), 733-743.

[32] Pitman, E.B., Gudonov method for localization in elastoplastic granular flow. *Int. J. Num. Anal. Methods*, 17 (1993), 385-400.

[33] Porter, M., Daraio, C., Szelengowicz, I., Herbold, E. and Kevrekidis, P., Highly nonlinear solitary waves in heterogeneous periodic granular media. *Physica D,* 238 (2009), 666-676.

[34] Pöschel, T. and Herrmann, H.J., Size segregation and convection. *Europhys. Lett.*, 29 (1995), 123-128.

[35] Rajagopal, K., Existence of solutions to the equations governing the flow of granular material. *Euro. J. Mech. B/Fluids*, 11 (1992), 265-276.

[36] Ratnaswamy, V., Rosato, A., Blackmore, D., Tricoche, X., Ching, N. and Zuo, L., Evolution of solids fraction surfaces in tapping: Simulation and dynamical systems analysis. *Granular Matte,r* 14 (2012), 169-174.

[37] Rosato, A., Blackmore, D., Zhang, N. and Lan, Y., A perspective on vibration-induced size segregation of granular materials. *Chem. Eng. Sci.*, 57 (2) (2002), 265-275.

[38] Rosato, A., Ratnaswamy, V., Horntrop, D., Dybenko, O. and Kondic, L., Temporal dynamics in density relaxation. Proc. Joint IUTAM-ISIMM Sympos. on Mathematical Modeling and Physical Instances of Granular Flows, Reggio-Cabria, Italy, 14-18 Sept. 2009, *AIP Conference Proceedings* 1227, 89-99.

[39] Rosato, A., Dybenko, O., Ratnaswamy, V., Horntrop, D. and Kondic, L., Microstructure development in tapped granular systems. *Phys. Rev. E,* 81 (2010), 061301.

[40] Rosato, A.D., Zuo, L., Wu, H., Blackmore, D., Horntrop, D., Windows-Yule, C. and D. Parker, Tapped granular columns: simulations, experiments and modeling, *J. Comput. Particle Mech.* (in press)

[41] Savage, S., The mechanics of rapid granular flows, *Adv. Appl. Math.*, 24 (1984), 289-366.

[42] Schaeffer, D., Instability in the evolution equations describing incompressible granular flow. *J. Diff. Eqs.,* 66 (1987), 19-50.

[43] Schaeffer, D., Shearer, M. and Pitman, E., Instability in critical state theories of granular flow. *SIAM J. Appl. Math.*, 50 (1990), 33-47.

[44] Sen, S. and Manciu, M., Discrete Hertzian chains and solitons. *Physica A,* 268 (1999), 644-649.

[45] Sen, S. and Manciu, M., Solitary wave dynamics in generalized Hertz chains: An improved solution of the equation of motion. *Phys. Rev. E,* 64 (2001), 056605-1 - 056605-4.

[46] Vogel, S. and Linz, S., Regular and chaotic dynamics in bouncing ball models. *Int. J. Bifurc. & Chaos,* 21 (2011), 869-884.

[47] Wakou, J., Ochiai, A., and Isobe, M., A Langevin approach to one-dimensional granular media fluidized by vibrations. *J. Phys. Soc. Jpn.*, 77 (2008), 034402.

[48] Walton, O.R. Numerical simulation of inelastic, frictional particle-particle interactions. Roco M.C. (ed), *Particulate Two-Phase Flow*, Butterworths, Boston, 1992, 884-911.

[49] Walton, O.R., Numerical simulation of inclined chute flows of monodisperse, inelastic, frictional spheres. *Mechanics of Materials,* 16 (1993), 239-247.

[50] Walton, O.R. and Braun, R.L., Stress calculations for assemblies of inelastic spheres in uniform shear. *Acta Mechanica,* 63 (1-4) (1986), 73-86.

[51] Walton, O.R. and R.L. Braun, R.L., Simulation of rotary-drum and repose tests for frictional spheres and rigid sphere clusters. *Joint DOE/NSF Workshop on Flow of Particulates and Fluids*, Ithaca, NY, 1993.

[52] Windows-Yule, C.R., Rosato, A.D., Rivas, N. and Parker, D.J., Influence of initial conditions on granular dynamics near the jamming transition. *New J. Phys.*, 16 (2014), 063016.

[53] Windows-Yule, C.R., Weinhart, T., Parker, D.J. and Thornton, A.R., Effects of packing density on the segregative behavior of granular systems. Phys. Rev. Lett., 112 (2014), 098001.

[54] Wu, H., Investigation of infinite-dimensional dynamical system models applicable to granular flows. PhD thesis, New Jersey Institute of Technology, Department of Mathematical Sciences, 2015. Supervised by Prof. D. Blackmore.

Anthony Rosato, Ph.D.: New Jersey Institute of Technology, Department of Mechanical and Industrial Engineering, University Heights, Newark, NJ 07102-1982 USA
(*anthony.rosato@njit.edu*).

The author gave a presentation of this paper during one of the conference sessions.

Denis Blackmore, Ph.D.: New Jersey Institute of Technology, Department of Mathematical Sciences and Center for Applied Mathematics and Statistics, University Heights, Newark, NJ 07102-1982 USA (*deblac@m.njit.edu*). The author gave a presentation of this paper during one of the conference sessions.

# Artifical tactile sensors with pre-curvature for object scanning (ENG053-15)

Anton Sauter, Christoph Will, Joachim Steigenberger, Carsten Behn

*Abstract:* Biological observations have shown that rodents like rats use their vibrissae (tactile hairs in the snout region) to estimate obstacle contact and obstacle shape within a few contacts of the tactile hair. We model a single vibrissa as an elastic bending rod (one-sided clamped) that interacts with a rigid obstacle in the plane. The aim is to determine the obstacle's contour by one quasi-static sweep along the obstacle (describable by a strictly convex function). For this, we firstly have to generate the support reactions (i.e., observables of the process an animal solely relies on, measured by a technical device in experiments), and then, use these observables for a reconstruction algorithm which yields a series of contact points (i.e., the discrete profile contour). To come closer to the biological paradigm, we incorporate the natural pre-curvature of vibrissae to our model. This makes the analytical treatment a bit harder and results in numerical solutions of the process. But, the analysis of the problem results in an extension of a former decision criterion for the reconstruction by the radius of curvature. Further, we get a formula for the contact point of the rod with the profile. This is new in literature. Based only on the reactions (forces and moments) at the support it is possible to reconstruct the profile.

## 1. Introduction

In recent years, the development of vibrissae-inspired tactile sensors gain center stage in the focus of research, especially in the field of (autonomous) robotics, see e.g. [2, 13, 14, 16, 19]. These tactile sensors complement to and/or replace senses like vision, because they provide reliable information (object distance, contour and surface texture) in a dark and noisy environment (e.g. seals detect freshet and turbulence of fish in muddy water [5–7]), and are cheaper in fabrication.

Most mammals exhibit such vibrissae, in a variety of types and located in various areas of the skin/fur. Vibrissae differ from typical body hairs: they are thicker, longer, embedded in an own visco-elastic support (the so-called "follicle-sinus complex" (FSC)). Moreover, they feature a pre-curvature, a conical shape, cylindrical cross-section and are made of different material with hollow parts (like a multi-layer system), [3, 17, 18]. The vibrissa mainly serves as a force transmission (due to an obstacle contact) to its support. Hence, movement and deformation of the vibrissa can only be detected by mechanoreceptors in the FSC, [1, 2]. It

is hypothesized, that changing the blood-pressure in the FSC allows the animal to adjust the stiffness of the tissue to control the movement of the vibrissa, [3, 17]. Furthermore, the surrounding tissue (fibrous band) and muscles (intrinsic and extrinsic musculature) enable the animal to actively move the vibrissa (active mode for surface texture detection) or to passively return the vibrissa to a rest position after deflection (due to a obstacle contact in passive mode), [8].

The pre-curvature is due to a kind of protection role: purely axial forces are prevented and, including the conical shape, the area of the tip of the vibrissa is limp. This results in a tangential contact to an object, [3, 15].

In this paper, the investigations focus the influence of the *pre-curvature* to the static bending behavior of a vibrissa in context of obstacle contour detection and reconstruction. We describe a quasi-static scanning process of obstacles: 1. analytical/numerical generation the observables in the support which an animal solely relies on, 2. reconstruction of the scanned profile contour using only these observables, and 3. verification of the working principle by means of experiments. These steps were done in [19] and [20] for cylindrical vibrissae. Therefore, we extend these results to pre-curved vibrissae in this paper.

## 2. Some State of Art of Precurved Vibrissae

From the biological point of view, there are a lot of works focussing on the determination of vibrissae parameters. E.g., in [17] was pointed out an important fact that the mostly vibrissae are curved in a plane. The deviation of the vibrissa from this plane (referred to the length) is less than 0.1%. In [4, 9–12, 15, 17], the vibrissa is described using a polynomial approximation of 2nd-, 3rd- and 5th-order, which is rather low. In contrast to this references, we present numerical results using one of order 10. In [15] it is stated that approximately 90% of rat vibrissae exhibit a pre-curvature $\kappa_0 \in (0.0065/mm, 0.074/mm)$, and in [4] that extremely curved vibrissa provide $\kappa_0 > 0.25/mm$. References [4, 15, 18] publish the following dimensionless parameters

$$\frac{L}{d} \approx 30\,, \quad \frac{r_0}{d} \approx 90\,,$$

whereas $L$ is the length, $d$ is the base diameter, and $r_0$ is the pre-curvature radius of the vibrissa.

From the technical point of view, pre-curved vibrissae are rarely used in applications. In [9, 12, 15], experimental and theoretical investigations concerning the distance detection to a pole are presented, using a pre-curved artificial vibrissa, also incorporating the conical shape. The pros and cons of a positive (curvature forward, CF) and negative (CB) curved vibrissae are stated in [15] whereas the vibrissa is used for tactile sensing of a pole. The CF-scanning

results in low axial forces, but higher sheer ones; CB the inverse results. Summarized, the pre-curvature influences mainly the support forces instead of the support moment.

## 3. Modeling

This section shall serve as an introduction to the profile scanning procedure.

**Beam Deflection Formula** The deflection of a largely deformed beam with pre-curvature is described in using the so-called *Winkler-Bach-Theory*:

$$\frac{d\varphi(s)}{ds} = \frac{1}{r_0(s)} \cdot \left(1 + \frac{N(s)}{E\,A} + \frac{M_{bs}(s)}{E\,A\,r_0(s)} \cdot \left(1 + \frac{1}{\lambda(s)}\right)\right), \tag{1}$$

with

$$\lambda(s) := \frac{1}{A} \int\limits_A \frac{\eta}{r_0(s) - \eta}\, dA \tag{2}$$

and normal force $N$, Young's modulus $E$, cross-section $A$, bending moment $M_{bs}$, and radius of pre-curvature $r_0$.
Assume, that the radius of curvature is much greater than die cross-section dimension, than (1) can be simplified to

$$\frac{d\varphi(s)}{ds} = \frac{1}{r_0(s)} + \frac{M_{bs}(s)}{E\,I_z}, \text{ with second moment of area } I_z := \int\limits_A \eta^2 dA \tag{3}$$

**Scanning Procedure** Here, we describe the scanning procedure of *strictly convex profile contours* using pre-curved technical vibrissae *in a plane*. This is done in two steps:

Step 1: Because of analytical interest, we firstly generate the observables (support reactions) during the scanning process. Since our intension is from bionics, we simply model the support as a clamping (being aware that this does not match the reality). Hence, the support reactions are the clamping forces and moment $\vec{M}_{Az}$, $\vec{F}_{Ax}$, $\vec{F}_{Ay}$, which an animal solely relies on.

Step 2: Then, we use these observables in an algorithm to reconstruct the profile contour.

Figure 1 sketches the scanning process of a plane, strictly profile. For this scanning process, several assumptions are made:

- The technical vibrissa is moved from *right to the left* (negative $x$-direction), i.e., the base point is moved.

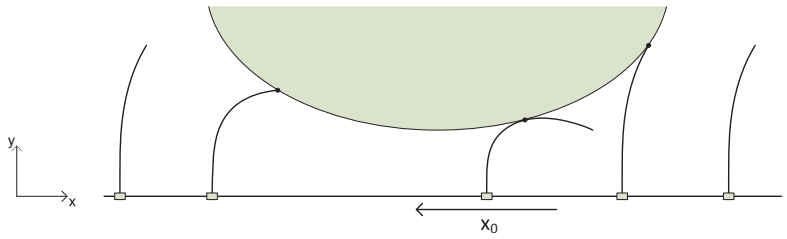


**Figure 1.** Scanning procedure using an artificial vibrissa; adapted from [19].

- The problem is handled *quasi-statically*, i.e., the vibrissa is moved incrementally (and presented in changes of the boundary conditions). Then, the elastically deformed vibrissa is determined.
- Since we do not want to deal with friction at the beginning, we assume an *ideal contact*, i.e., the contact force is *perpendicular* to the contact point tangent of the profile.

The scanned profile is given by a function $g : x \mapsto g(x)$, where $g \in C^1(\mathbb{R};\mathbb{R})$. Since the graph of $g$ is convex by assumption, the graph can be parameterized by means of the slope angle $\alpha$ in the $xy$-plane. Then we have, [19]:

$$\begin{aligned} \frac{dg(x)}{dx} &= g'(x) = \tan(\alpha) \\ \longrightarrow x &= \xi(\alpha) := g'^{-1}\big(\tan(\alpha)\big) \\ y &= \eta(\alpha) := g\big(\xi(\alpha)\big) \end{aligned}$$

Therefore, each point of the profile contour is given by $(\xi(\alpha), \eta(\alpha))$, $\alpha \in (-\frac{\pi}{2}, \frac{\pi}{2})$. For generality, we introduce dimensionless variables, starting with the arc length $s$ with $s = Ls^*$, $s^* \in [0,1]$. Then, all length are measured in $\mathbf{L}$, all moments in $\mathbf{EI_z L^{-1}}$, and all forces in $\mathbf{EI_z L^{-2}}$, whereby we omit the asterisk $*$ for brevity from now on.

**Boundary-value Problem in Step 1** The system of differential equations (ODEs) describing the deformed pre-curved, technical vibrissa in a plane in dimensionless quantities is:

$$\left.\begin{aligned} \frac{dx(s)}{ds} &= \cos(\varphi(s)) \\ \frac{dy(s)}{ds} &= \sin(\varphi(s)) \\ \frac{d\varphi(s)}{ds} &= \frac{1}{r_{0L}(s)} + f\Big(\big(y(s)-\eta(\alpha)\big)\sin(\alpha) + \big(x(s)-\eta(\alpha)\big)\cos(\alpha)\Big) \end{aligned}\right\} \tag{4}$$

Observing figures 1 and 2 gives the hint to distinguish two phases of contact between the vibrissa and the obstacle:

- *Phase A – tip contact:* We have still ODE-system (4) with the boundary conditions (BCs)

$$y(0) = 0\,, \quad \varphi(0) = \frac{\pi}{2}\,, \quad x(1) = \xi(\alpha)\,, \quad y(1) = \eta(\alpha) \tag{5}$$

- *Phase B – tangential contact:* Only the BCs change:

$$y(0) = 0\,, \quad \varphi(0) = \frac{\pi}{2}\,, \quad x(s_1) = \xi(\alpha)\,, \quad y(s_1) = \eta(\alpha)\,, \quad \varphi(s_1) = \alpha \tag{6}$$

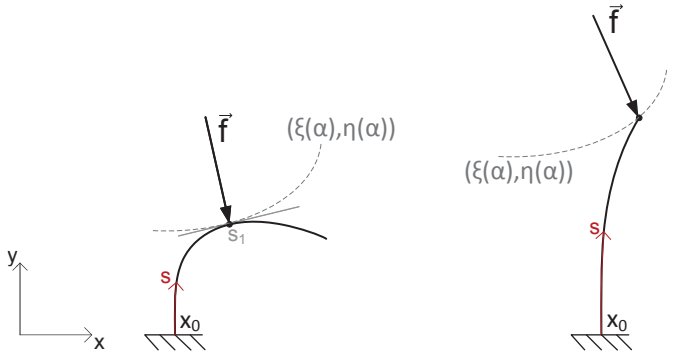


**Figure 2.** Contact of vibrissa and obstacle in *Phase A* (left) and in *Phase B* (right) during scanning process.

A direct inspection of the occurring problems (4) & (5) and (4) & (6) yield the choice of a shooting method to determine the parameters $f$ and $s_1$, and finally with $f$ the clamping reactions $\vec{M}_{Az}$, $\vec{F}_{Ax}$, $\vec{F}_{Ay}$.

**Initial-value Problem in Step 2** Here, we use only the generated observables (measured in experiments) $\vec{M}_{Az}$, $\vec{F}_{Ax}$, $\vec{F}_{Ay}$ and known base of the vibrissa $x_0$ to reconstruct the scanned profile. Due to [16], we determine the bending moment, see figure 3, to formulate the initial-value problem (IVP) in this step:

$$\left.\begin{aligned} \frac{dx(s)}{ds} &= \cos(\varphi(s)) \\ \frac{dy(s)}{ds} &= \sin(\varphi(s)) \\ \frac{d\varphi(s)}{ds} &= \frac{1}{r_{0L}(s)} - M_{Az} - F_{Ax}y(s) + F_{Ay}\big(x(s) - x_0\big) \end{aligned}\right\} \tag{7}$$

with initial conditions (ICs)

$$x(0) = x_0\,, \quad y(0) = 0\,, \quad \varphi(0) = \frac{\pi}{2} \tag{8}$$

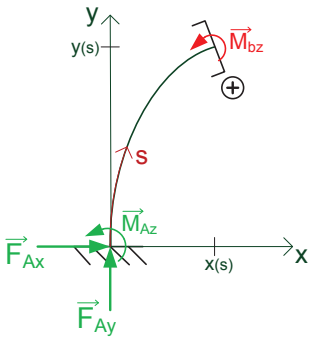


**Figure 3.** Applying method of sections to the vibrissa.

Now, it is necessary – for each input $\{M_{Az}, F_{Ax}, F_{Ay}, x_0\}$ – to determine the contact point $(x(s_1), y(s_1))$ (note, that $s_1$ is known in step 1, but is not an observable). But, it is still unknown in which phase we are. We only have

$$M_{bz}(s_1) = 0$$

In accordance to [19], we determine a decision criterion to distinguish both phase. The vibrissa is in Phase B, iff it holds:

$$\boxed{M_{Az}^2 + \frac{2M_{Az}}{r_{0L}} - 2F_{Ay} = 0} \tag{9}$$

In comparison to the condition in [19], we get one new term $\frac{2M_{Az}}{r_{0L}}$. And, in a limiting case for $r_{0L} \longrightarrow \pm\infty$, condition (9) forms the condition in [19], which serves as a validation.

## 4. Profile Scanning Using a Constant Pre-curvature Radius

Here, we present numerical simulations of the described profile scanning algorithm (based of two steps). At first, we focus on a *constant* pre-curvature radius $r_{0L} \neq r_{0L}(s)$. Referring to [19], we consider a profile described by $g_1 : x \mapsto= \frac{1}{2}x^2 + 0.3$. Exemplarily, two scanning processes are presented in figures 4 and 5. Note, that the vibrissae in Phase B are only plotted to the contact point, just for clarity. One can clearly see, that the smaller the pre-curvature radius is no Phase A occurs, i.e., no tip contact, which might explain the protective role of the pre-curvature of vibrissae.

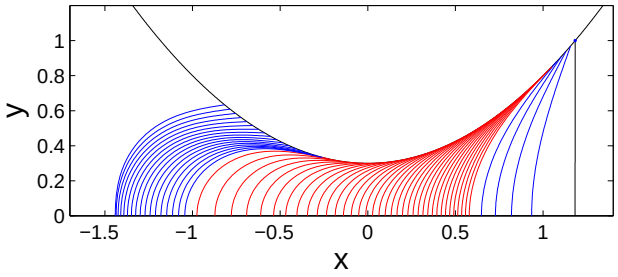


**Figure 4.** Profile scanning using a pre-curved vibrissa with $r_{0L} = -1000$: in blue *Phase A*, in red *Phase B*.

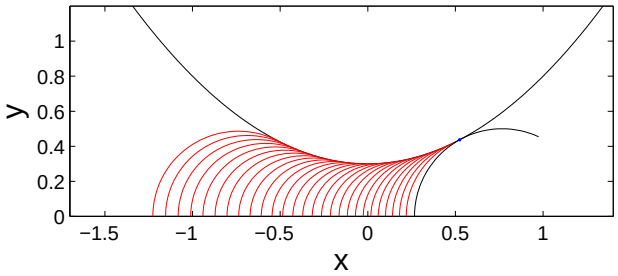


**Figure 5.** Profile scanning using a pre-curved vibrissa with $r_{0L} = -0.5$: in red *Phase B*, no Phase A.

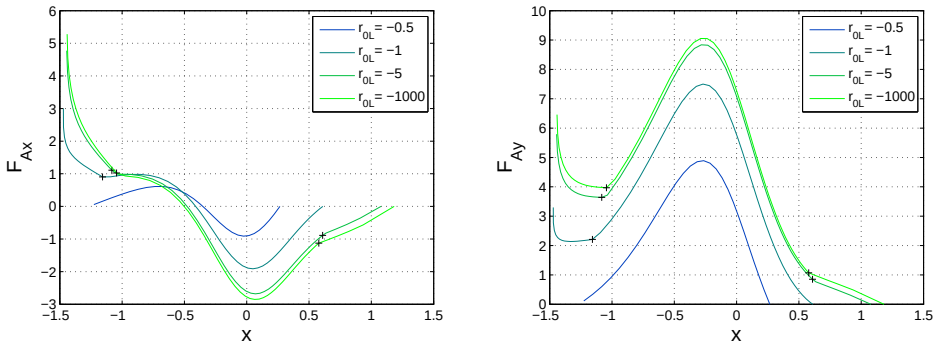


**Figure 6.** Observables clamping forces $F_{Ax}$ (left) and $F_{Ay}$ (right) for varying pre-curvature radius $r_{0L}$.

Figures 6 and 7(left) show the observables during a scanning process in dependence on the pre-curvature radius. The transition between both phases is marked with a "+". It becomes clear: the smaller the pre-curvature radius the smaller the bending behavior of the vibrissa, the smaller the observables, but the smaller the scanning area. Therefore, a small pre-curvature radius results in poor scanning results. Figure 7(right) presents the reconstruction error of magnitude $10^{-6}$.

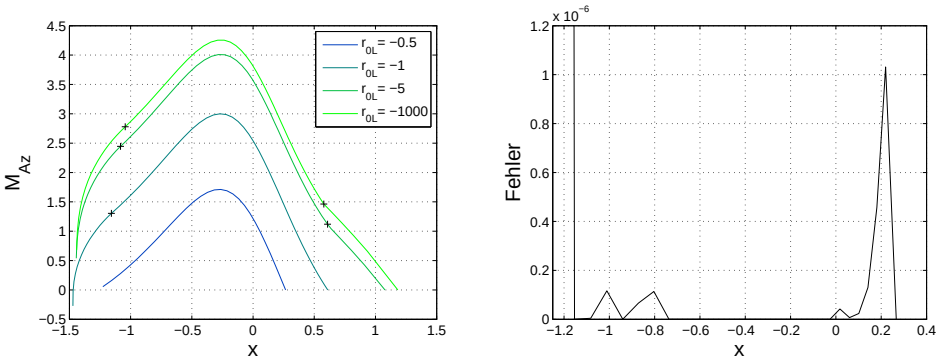


**Figure 7.** Observable clamping moment $M_{Az}$ for varying pre-curvature radius $r_{0L}$ (left); error of given and reconstructed profile for $r_{0L} = -0.5$ (right).

## 5. Experiments in Scanning with Variable Pre-curvature Radius

To verify the algorithms, we present numerical investigations of scanning vibrissae with variable pre-curvature and experimental results, using a parabola profile $g_1(x) = 2x^2 + 0.55$. Three different technical vibrissae with different pre-curvature are used in an experiment. Figure 8 shows that the first vibrissae is straight, the second and the third one have a variable pre-curvature radius.

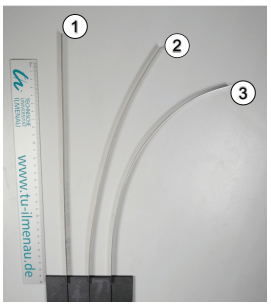


**Figure 8.** Three different pre-curved vibrissae for the experiment.

With the help of a computer-aided evaluation of the graphic representation of the vibrissae in figure 8, their pre-curvature radius $r_{0L}(s)$ is determined in dependence of the arc length $s$ as polynomials of order 10.
The simulated scanning processes (using the vibrissa pre-curvature radii in form of polynomial of order 10) are shown in figure 9 for vibrissa 1 and 3.

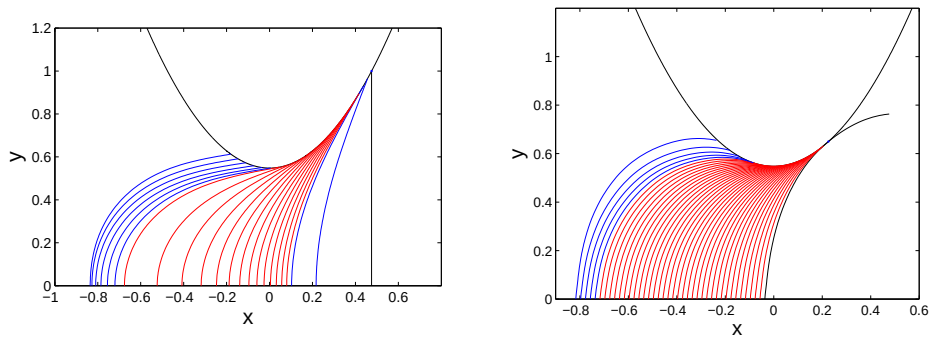


**Figure 9.** Scanning process using vibrissa 1 (left) and vibrissa 3(right); in blue *Phase A*; in red *Phase B*.

Figures 10 and 11(left) show exemplarily the observables (simulation vs. experiment) of the experiment using vibrissa 3. An easy inspection confirms prior results, that the maximal values of $M_{Az}$, $F_{Ax}$ and $F_{Ay}$ decrease the bigger the pre-curvature and the smaller the pre-curvature radius are. The figure show a good coincidence of the simulated and measured curves of the observables.

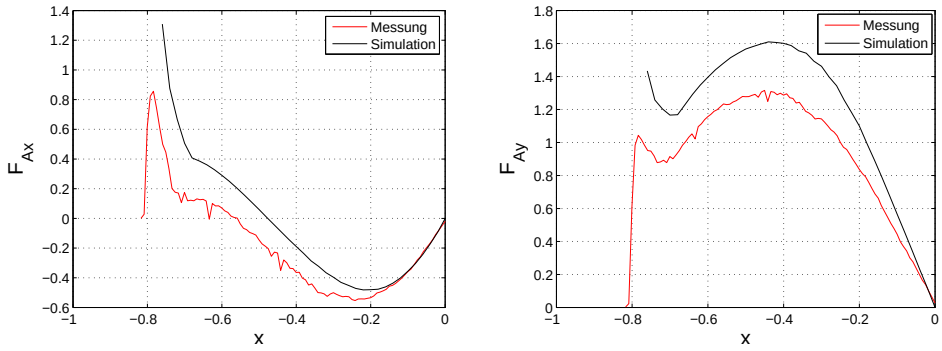


**Figure 10.** Experiment using vibrissa 3: clamping forces $F_{Ax}$ (left) and $F_{Ay}$ (right) of a simulation and the experiment.

Figure 11(right) presents the reconstruction of the profile. Compared to further simu-

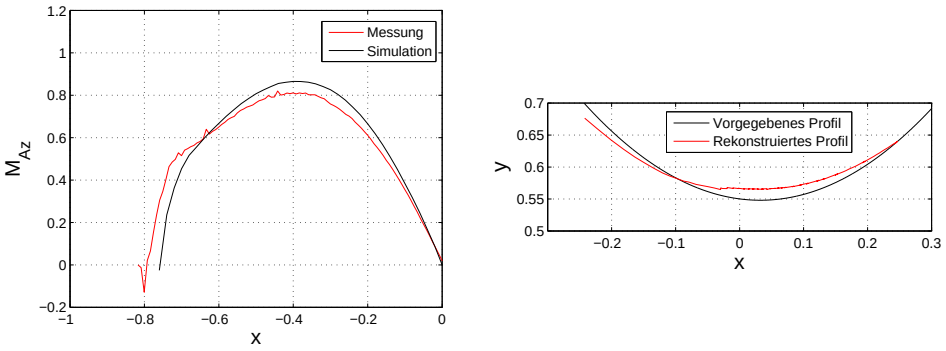


**Figure 11.** Experiment using vibrissa 3: clamping moment $M_{Az}$ (left) and reconstruction error (right) of a simulation and the experiment.

lations, we point out that the smaller the pre-curvature radius is the smaller is the reconstruction error.

Summarizing, we show that it is promising to use pre-curved vibrissae for object contour scanning and reconstruction. The simulated and measured curves of the observables show up a good coincidence. The presented algorithms work effectively.

## 6. Conclusions

It was possible to illustrate the characteristics and influences of pre-curved technical vibrissae in view of profile scanning. Based on the Winkler-Bach-Theory for pre-curved beams we set up the equations for a deformed vibrissa during a scanning process. We presented an algorithm to reconstruct the scanned profile in using the generated observables (which an animal is supposed to solely rely on) via shooting methods. The reconstruction then was based on solving initial-value problems on contrast to the generation procedure where we solved boundary-value problems. The investigations respective the scanning of a strictly convex profile with a pre-curved vibrissae showed noticeable differences to the profile scanning with a straight vibrissa. The extrema of the bending reactions and the size of the scanned profile area depends on the pre-curvature radius of the vibrissa. With a smaller radius tangential contact *phase B* in the scanning process could be extended. Experiments confirmed the numerical results and algorithms in this paper. Moreover, the investigation showed that the profile reconstruction works better with a pre-curved vibrissa.

## References

[1] Ahl, A. The role of vibrissae in behavior: A status review. *Veterinary Reserarch Communications 10* (1986), 245–268.

[2] Berg, R., and Kleinfeld, D. Rhythmic whisking by rat: Retraction as well as protraction of the vibrissae is under active muscular control. *Journal of Neurophysiology 89*, 1 (2002), 104–117.

[3] Carl, K., Hild, W., Mämpel, J., Schilling, C., Uhlig, R., and Witte, H. Characterization of statical properties of rat's whisker system. *IEEE Sensors Journals 12*, 2 (2012), 340–349.

[4] Clack, N. G., O'Connor, D. H., Huber, D., Petreanu, L., Hires, A., Peron, S., Svoboda, K., and Myers, E. W. Automated tracking of whiskers in videos of head fixed rodents. *PLoS Computational Biology 8*, 7 (2012), e1002591.

[5] Dehnhardt, G. Tactile size discrimination by a california sea lion (zalophus californianus) using its mystacial vibrissae. *Journal of Comparative Physiology A 175*, 6 (1994), 791–800.

[6] Dehnhardt, G., and Kaminski, A. Sensitivity of the mystacial vibrissae of harbour seals for size differences of actively touched objects. *The Journal of Experimental Biology 198* (1995), 2317–2323.

[7] Dehnhardt, G., Mauck, B., and Bleckman, H. Seal whiskers detect water movements. *Nature 394* (1998), 235–236.

[8] Dörfl, J. The musculature of the mystacial vobrissae of the white mouse. *Journal of Anatomy 135*, 1 (1982), 147–154.

[9] Hires, S. A., Pammer, L., Svoboda, K., and Golomb, D. Tapered whiskers are required for active tactile sensation. *eLife* (2013), e01350.

[10] Knutsen, M., Biess, A., and Ahissar, E. Vibrissal kinematics in 3d: Tight coupling of azimuth, elevation, and torsion across different whisking modes. *Neuron 59* (2008), 35–42.

[11] Knutsen, M., Derdikman, D., and Ahissar, E. Tracking whisker and head movements in unrestrained behaving rodents. *Journal of Neurophysiology 93* (2004), 2294–2301.

[12] Pammer, L., O'Connor, D. H., Hires, S. A., Clack, N. G., Huber, D., Myers, E. W., and Svoboda, K. The mechanical variables underlying object lokalisation along the axis of the whisker. *The Journal of Neuroscience 33*, 16 (2013), 6726–6741.

[13] Pearson, M. J., Gilhespy, I., Melhuish, C., Mitchinson, B., Nibouche, M., Pipe, A. G., and Prescott, T. J. A biologically inspired haptic sensor array for use in mobile robotic vehicles. *Proceedings of Towards Autonomous Robotic Systems (TAROS)* (2005), 189–196.

[14] Pearson, M. J., Pipe, A. G., Melhuish, C., Mitchinson, B., and Prescott, T. J. Whiskerbot: A robotic active touch system modeled on the rat whisker sensory system. *Adaptive Behavior 15*, 3 (2007), 223–240.

[15] Quist, B. W., and Hartmann, M. J. Z. Mechanical signals at the base of a rat vibrissa: the effect of intrinsic vibrissa curvature and implications for tactile exploration. *Journal of Neorophysiology 107* (2012), 2298–2312.

[16] Scholz, G. R., and Rahn, C. D. Profile sensing with an actuated whisker. *IEEE Transactions on Robotics and Automation 20*, 1 (2004), 124–127.

[17] Towal, R. B., Quist, B. W., Gopal, V., Solomon, J. H., and Hartmann, M. J. Z. The morphology of the rat vibrissal array: A model for quantifying spatiotemporal patterns of whisker-object contact. *PLoS Computational Biology 7*, 4 (2011), e1001120.

[18] Voges, D., Carl, K., Klauer, G. J., Uhlig, R., Schilling, C., Behn, C., and Witte, H. Structural characterization of the whisker system of the rat. *IEEE Sensors Journals 12*, 2 (2012), 332–339.

[19] Will, C., Steigenberger, J., and Behn, C. Object contour reconstruction using bio-inspired sensors. In *Proceedings 11th International Conference on Informatics in Control, Automation and Robotics (ICINCO 2014)* (2014), vol. 1, SciTePress, pp. 459–467.

[20] Will, C., Steigenberger, J., and Behn, C. Quasi-static object scanning using technical vibrissae. In *Proceedings 58. International Colloquium, Ilmenau (Germany)* (2014).

Anton Sauter, B.Sc.: Ilmenau University of Technology, Department of Technical Mechanics, Max-Planck-Ring 12 (Building F), 98693 Ilmenau, Germany (*anton.sauter@tu-ilmenau.de*).

Christoph Will, M.Sc. (Ph.D. student): Ilmenau University of Technology, Department of Technical Mechanics, Max-Planck-Ring 12 (Building F), 98693 Ilmenau, Germany (*christoph.will@tu-ilmenau.de*).

Joachim Steigenberger, Professor: Ilmenau University of Technology, Institute of Mathematics, Weimarer Straße 23, 98693 Ilmenau, Germany (*joachim.steigenberger@tu-ilmenau.de*).

Carsten Behn, Associate Professor: Ilmenau University of Technology, Department of Technical Mechanics, Max-Planck-Ring 12 (Building F), 98693 Ilmenau, Germany (*carsten.behn@tu-ilmenau.de*). The author gave a presentation of this paper during one of the conference sessions.

# Application of analysis of resonance vibration for the diagnostic of a pair of friction of the railway disc brake (NUM136-15)

Wojciech Sawczuk, Grzegorz M. Szymański

*Abstract:* Attempt to raise the train speed involves application of a greater braking power i.e. braking systems rapidly absorbing and dispersing stored heat energy. Work instability arises from the occurrence of vibrations on friction element, which affects the lower efficiency of the braking process. In practice, this means that, during braking the vehicles currently alternative at a time of friction resistance may cause uneven braking process. The effects of these changes can be manifested in the form of vibrations with the high amplitude of the input. The vibrations generated by the assemblies are moved per vehicle, which also adversely affects driving comfort. The purpose of this article is to determine the resonant frequencies of the selected elements of the railway disc brake.

## 1. Introduction

One of the negative factors affecting the deterioration of the environment (especially acoustic one) where people are, is the noise generated by motor vehicles.

Unfortunately, vibro-acoustic phenomena emitted particularly by braking systems are regarded as highly undesirable. The problem of vibration in the brakes of both rail and road vehicles has already been noticed in the 30s of the twentieth century, according to [2, 3, 10]. At the beginning the researchers pointed out that the vibration and noise generated by the brake, stem from the friction characteristics of the tribological pair, subordinate the appearance of this effect to the fact that the coefficient of friction changes its value from rotational speed. It was also claimed that the coefficient of static friction is greater than kinetic friction. The consequence of vibration in the brake, in combination with the propagation of sound is the instability system work, which is manifested by variable course of the instantaneous coefficient of friction.

## 2. Selected models of vibration in the brakes

To the basic components of disc braking system belong a brake disc, which is rigidly connected with wheelset and jaw (holder), with a fixed friction pad in it, as shown in Figure 1. For the calculation of the disc lever system parameters, models with varying degrees of simplification are used. Due to the use o disc brake lever system models, they can be classified as follows:

− models for the kinematic calculation,

− models to calculate the braking parameters,

− models to calculate the natural frequency of the lever mechanism elements.

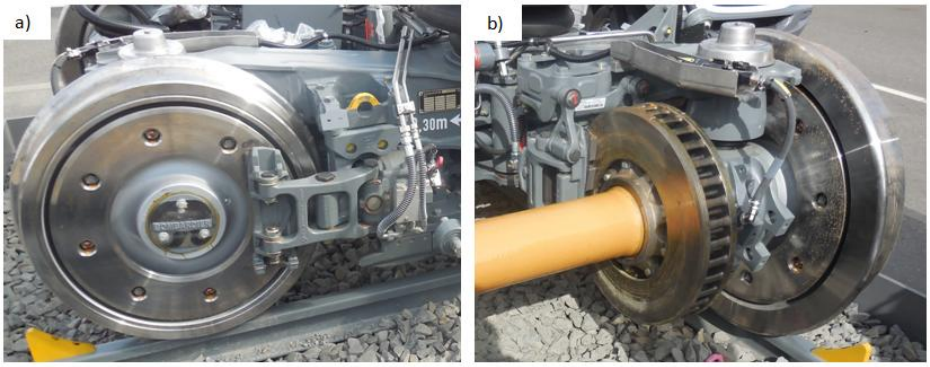


**Figure 1.** A view of the disc brake friction pair cooperating with a disc mounted: a) at the wheel of the wheelset, b) on the axis of the wheelset.

In papers [1, 4] to calculate the kinematic size the displacement of individual elements of the brake lever system, the structural disc brake lever system has been proposed.

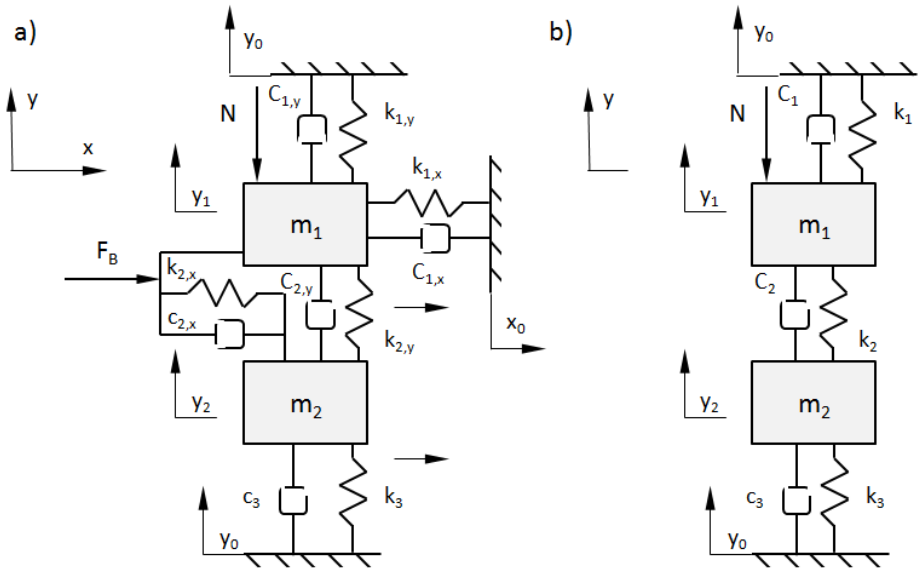


**Figure 2.** A dual mass model with the friction of the resilient friction system: a) $m_1$- friction pad stiffening metal sheet mass, $m_2$ – friction pad mass, $k_{1,\,x,\,y}$ – longitudinal and lateral stiffness of the brake holder, $c_{1,\,x,\,y}$ – longitudinal and lateral damping of the brake holder, $k_{2,\,x,\,y}$ – longitudinal and lateral stiffness of the of the reinforcing sheet, $c_{2,\,x,\,y}$ – longitudinal and lateral damping of the of the

reinforcing sheet, $k_3$ – the stiffness of the friction pad , $c_3$ – the damping of the friction pad, N – pad's pressure force to the brake disc, $F_B$ – the inertial force.

Motion of the system shown in Figure 3a) can be described by a system of differential equations (1).

$$\begin{cases} m_1\ddot{x}_1 + C_{1,x}(\dot{x}_1 - \dot{x}_0) + k_{1,x}(x_1 - x_0) + C_{2,x}(\dot{x}_1 - \dot{x}_2) + k_{2,x}(x_1 - x_2) = F_B \\ m_2\ddot{x}_2 + C_{2,x}(\dot{x}_2 - \dot{x}_1) + k_{2,x}(x_2 - x_1) = 0 \\ m_1\ddot{y}_1 + C_{1,y}(\dot{y}_1 - \dot{y}_0) + k_{1,y}(y_1 - y_0) + C_{2,y}(\dot{y}_1 - \dot{y}_2) + k_{2,y}(y_1 - y_2) = N \\ m_2\ddot{y}_2 + C_{2,y}(\dot{y}_2 - \dot{y}_1) + k_{2,y}(y_2 - y_1) + C_{3,y}(\dot{y}_2 - \dot{y}_0) + k_{3,y}(y_2 - y_0) = 0 \end{cases} \quad (1)$$

The studies have analyzed only the perpendicular motion to the brake disc because the model shown in Fig. 2a) simplified the model schematically shown in Figure 2b). The motion of this system is described by set of equations (2).

$$\begin{cases} m_1\ddot{y}_1 + C_1(\dot{y}_1 - \dot{y}_0) + k_1(y_1 - y_0) + C_2(\dot{y}_1 - \dot{y}_2) + k_2(y_1 - y_2) = N \\ m_2\ddot{y}_2 + C_2(\dot{y}_2 - \dot{y}_1) + k_2(y_2 - y_1) + C_3(\dot{y}_2 - \dot{y}_0) + k_3(y_2 - y_0) = 0 \end{cases} \quad (2)$$

Variables from equations 1 and 2 given in the description for figure 2. In the last period of time, the braking system which is often cited and developed, is the model presented by Rudolph and Popp [6, 7]. In 1972, North [5] has developed a special model of the braking system with eight degrees of freedom Figure 3 shows the dual mass model of the friction pad, pressed with the braking holder to the brake disc with the N force .

First models assumed that the brake self-excited vibrations were associated with a decrease in the coefficient of friction and the increase of the lost motion speed. This is true for many of friction materials however, for a limited range of speed changes. If we assume the brake model with one degree of freedom [9].

## 3. Methodology of research

Studies of a self-vibration frequency of the rail braking system components were based on the active experiment assumptions [11]. The experiment involves active purposeful change or distort of the input parameters and the observation of the effect of these changes on the output parameters. For the input parameter a centrifugal force in the impulse test was adopted, while for the output parameters - the vibration acceleration of selected elements of the disc brake lever mechanism.

Triaxial vibration transducers type 4504 of Brüel&Kjær were used for testing. The linear frequency response of the selected transducers was 18kHz. While testing signals in the band of 0.1Hz - 18kHz were recorded. The sampling rate was set at 36000Hz. It means that the analyzed band, according to the Nyquist relationship, may be up to 18kHz.

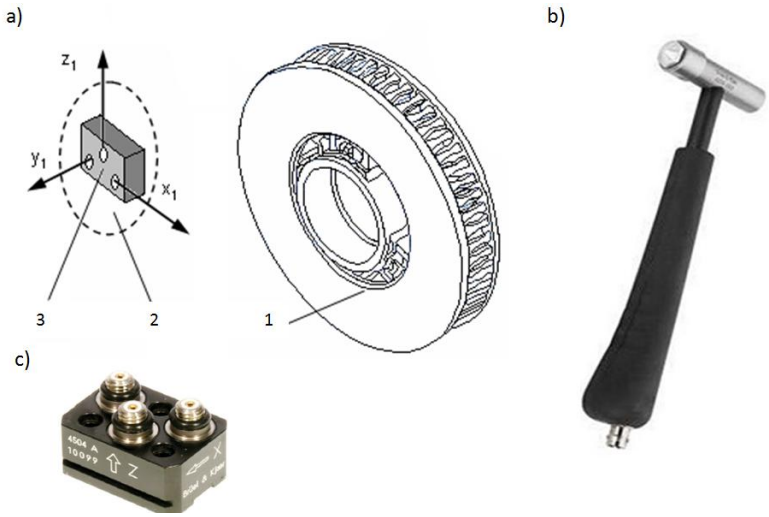


**Figure 3.** An impulsive test: a) the direction orientation of signals recording, b) view of a modal hammer-type 8206-002, c) view of a transducer type 4504, 1 brake disc, 2-transducer mounting element to the disc, 3 - vibration transducer.

The vibration transducers were mounted to a disc brake system by using a beeswax. Such a method of transmitters mounting does not narrow the band of analysis, which results from the characteristics of the transmitter. Directions of the vibration measurement were realized as follows: Direction X parallel to the plane of the tested element (in the direction of the axis of rotation) the Z direction parallel to the plane (direction of rotation) and the Y direction perpendicular to the surface of the tested element (Figure 3)). The impulsive enforcement was performed with a modal hammer type 8206-002 of Brüel&Kjær shown in Figure 3b).

To recorded vibration signals and for the enforcement a multianalyzer PULSE of Brüel&Kjær was used. The device allows to record an electrical fast waveforms parallel to 17 channels with the dynamic of 160dB. A PULSE multianalyzer view on the position in Laboratory of vehicles construction and diagnostics at Poznan University of Technologis is shown in Figure 4a). The tests were conducted for the following elements and units of the rail disc brake: disc brake type 640×110 with ventilation blades, disc brake lever mechanism, brake pad and brake holder with the pads.

A brake disc was underslung by a sling linear to a winch chain in the wheel seat hole. The centrifugal force was applied to the friction ring in its thickness from a vibration transducer mounted on it and on the friction ring behind the ventilation part. The view of a brake disc with mounted vibration transducers during the impulsive tests is shown in Figure 4c).

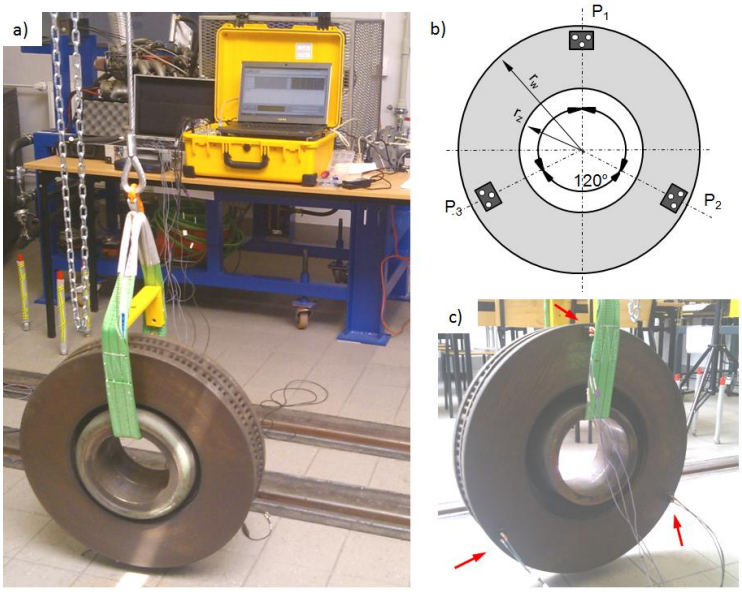


**Figure 4.** An impulsive test on the brake disc: a) view of a PULSE multianalyzer on the position with a slung object of the research, b) fixing scheme of the vibration transducers on the disc, c) view of a brake disc during the impulsive test with the vibration transducers, $r_w$ - inner radius of the disc, $r_z$ - the outer radius of the disc, $P_{1,2,3}$ - vibration transducers.

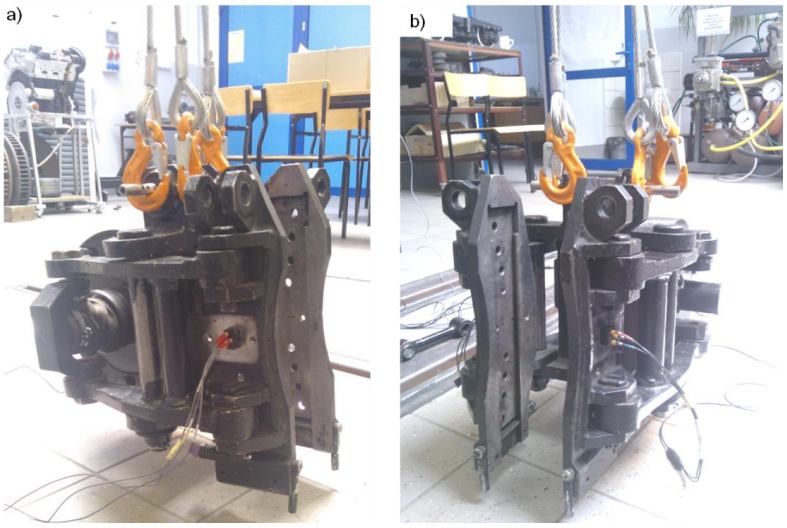


**Figure 5.** A view of the disc brake clamp without the pads: a) from the piston rod side, b) on the brake cylinder housing.

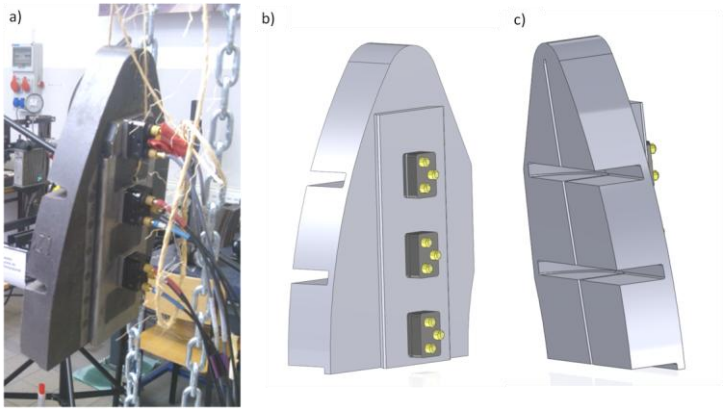


**Figure 6.** A friction pad during the impulsive test: a) view of the pad with vibration transducers, b) a model of the pad with vibration transducers, c) the pad model with visible grooves.

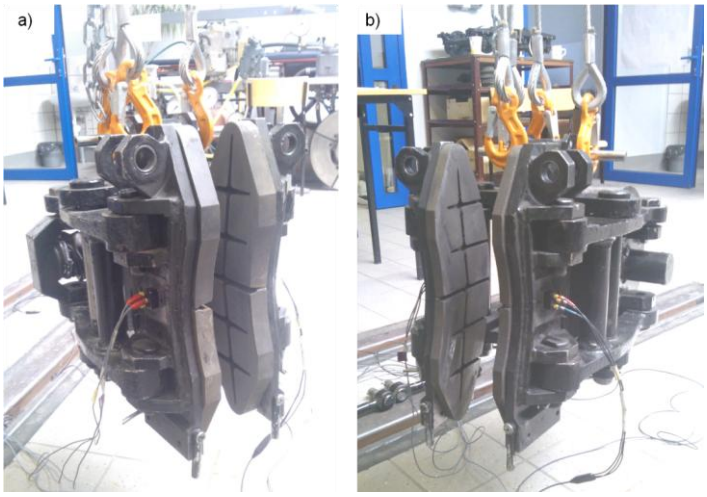


**Figure 7.** A view of the disc brake lever mechanism: a) with a new pads of a thickness of 35mm, b) with the pads worn to 15mm.

The clamp (disc brake lever system) without the pads was mounted to a linear sling ended with hooks. To eliminate the influence of a sling in determining the natural frequency of the clamp self-vibrations, a thin tube was inserted in the middle catch, located on the central lever.

Figure 5 shows a view of the clamping mechanism of the disc brake during the impulsive test. Vibration transducers were mounted in the middle of the brake holders as in position and verification testing. When selecting a measuring point the assumption was made that the transmitter should be placed as close as possible to the place of vibration signal generation and within reach. In the first case, it hits a brake holder  at the installation location of the parallel guides, in the second case the

central site (vibration transducers installation place), while in the third case, in the place of the friction pads block (bottom of the brake holder). The next stage of the study was the measurements of friction pads in varying degree of wear. Figure 6 shows the friction pads view of a rail disc brake while the impulsive test. By contrast, Figure 7 shows a view of the disc brake clamp with the friction pads.

A more accurate method for predicting vibration of the brake system is the finite element method. However, increased complexity of models has not brought a solution in understanding the mechanism of vibration in the brakes. The reason for this is the modeling reduction with the use of the finite elements to the isolated elements than the interconnected systems.

## 4. Resonance frequencies of the tested brake parts

In the suggested method of brakes elements diagnostics it is necessary to estimate the resonance frequencies of the brake elements which are objects of technical condition assessment.

It is known from the vibration theory that the resonance frequency is associated with increase of band amplitude and change of sign of phase in the phase band. That is why for defining the value of resonance frequency of elements of brake system, the impulse tests with the use of external forcing in a form of modal hammer were used. The use of such test enables to define frequency answer function described by equation (1). From the complex form amplitude-frequency characteristics, which is the module of complex spectrum and phase-frequency characteristics, can be defined.

To identify dynamic parameters of structure and resonance frequencies, elements of modal analysis i.e. impulse tests, were used. In case of classic modal analysis, external source of stimulating power in a form of modal hammer or an activator is in use. Such a solution provides parallel measurement of a forcing power as well as an answer of a unit to this power and enables to determine frequency answer function defined by the following equation:

$$H(j\omega) = \frac{X(j\omega)}{F(j\omega)} \tag{3}$$

where $X(j\omega)$ is complex spectrum of an unit answer; $F(j\omega)$ is complex spectrum of a force stimulating the unit vibration; $H(j\omega)$ is complex function of a frequency answer.

In case of objects for which an external source of power forcing vibrations of a unit cannot be applied, there is possibility to use an experimental analysis based on internal forcing powers called operating modal analysis. In order to determine characteristic bands of signal frequencies bound up with resonance vibrations of brake parts, impulse tests were carried out according to assumptions presented in works [88. Sample amplitude-frequency characteristics from impulse test, which was carried out, is presented in Figure 8.

On the basis of obtained characteristics, the frequencies of own vibrations of the brake system element are contained in Table 1.

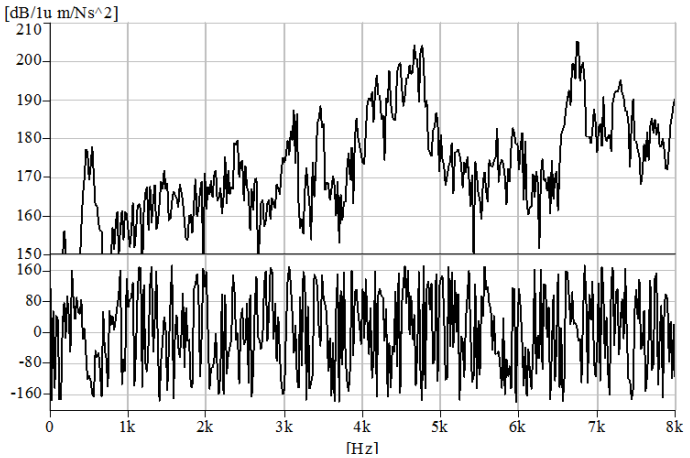


**Figure 8.** Amplitude-frequency characteristics (upper part of the figures) and phase-frequency (bottom part of the figures) from impulse test carried out on the brake system elements (clamp with the pads)

Table 1 Estimated value of the resonant frequency of vibration elements/units of the rail disc brake.

| Element/unit | Frequency [kHz] | | | | | | | | | | | | |
|---|---|---|---|---|---|---|---|---|---|---|---|---|---|
| Disc | 3,0 | | 4,0 | 4,2 | **4,5** | 4,7 | | 5,8 | | 6,2 | | 6,9 | |
| Clamp without pads | | | 4,0 | | **4,5** | | | | 5,9 | 6,2 | | | 7,7 |
| Braking pad | | | | | **4,5** | 4,7 | 5,1 | 5,8 | | | | | |
| Clamp with pads | 3,0 | 3,5 | | 4,2 | **4,5** | 4,7 | | | | | 6,7 | | 7,7 |

The experimentally determined vibration frequencies of described brake system elements will be used to create regressive and structural diagnostic models, which enable an assessment of material consumption in brake system parts using the analysis of vibration signals recorded on the holder brake pads. To create described models, it would be the best to apply those frequencies for that are for each element, in the present case it is a band of 4.4-4.6kHz.

## 5. Algorithm of state assessment of the brake system element

The word “algorithm” comes from Arabic language and designates a recipe, a method of solving a problem. Each algorithm should include the beginning and the end exactly marked objects names (data names) on which the actions would be carried out, descriptions of those actions and the performance order.

The worked out diagnostic model provided the base for projecting an algorithm enabling - on the basis of measured vibration signals - to assess technical condition of elements of the brake system.

Algorithm with binary model is presented in Figure 9. In the presented algorithm the procedure of the band pass filtrating is used. The analysis band is set up individually for each tested brake system – by carrying out impulse tests (resonance band of the brake system parts with the largest energetic participation is applied).

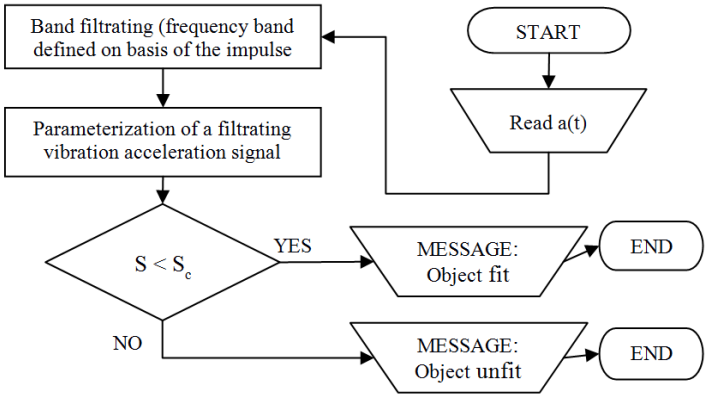


**Figure 9.** Algorithm for diagnosing elements of brake system on the basis of vibration signal parameters with the use of binary model (a(t) – signal of vibration accelerations, tacho – tachometer signal, S – diagnostic symptom, $S_c$ – critical value of diagnostic symptom)

According to presented algorithm, for the two-phase assessment of technical condition of brake system parts, the known characteristics (discriminants) describing vibration signal could be used.

## 6. Application of the proposed method for assessing the thickness of the braking pad

One of the parameters that describe the condition of the rail brake disc friction pair is a wear rate of braking pads demonstrated by the thickness of the friction pad.

In order to assess the suitability of the proposed method for assessing the thickness of the braking pad, an experiment on the inertia positon for testing the friction pair of rail brakes was performed. It was described in the article [12], which consists in determining characteristics of vibration signals for the various pads (new - G1=35mm used and fit - G2=25mm; used and unfit - G3=15mm).

To boost the resonance vibrations, an impulsive force occurring in a lever braking system, during the brake hold-off process (removal of blocks from the brake disc) was used.

The obtained calculations of frequency-amplitude characteristics, are shown in Figure 10**.** On the presented spectra (Fig. 10) a frequency range, determined during the impulsive test was hatched. On the basis of equation (4) the effective value of vibration signals for different variants of the braking pad wear (G1, G2, G3) was determined.

$$a_{\mathrm{RMS}} = \sqrt{\frac{1}{T}\int_0^T [a(t)]^2 \,\mathrm{dt}} \tag{4}$$

where: *a(t)* – instantaneous value of displacement, speed or vibration accelerations, *t* – time, T – average time. The calculation results of measurement point for signals without the use of filtration is shown in Figure 11a), while the effective values of the filtered signals in the band 4.4-4.6kHz in Figure 11b).

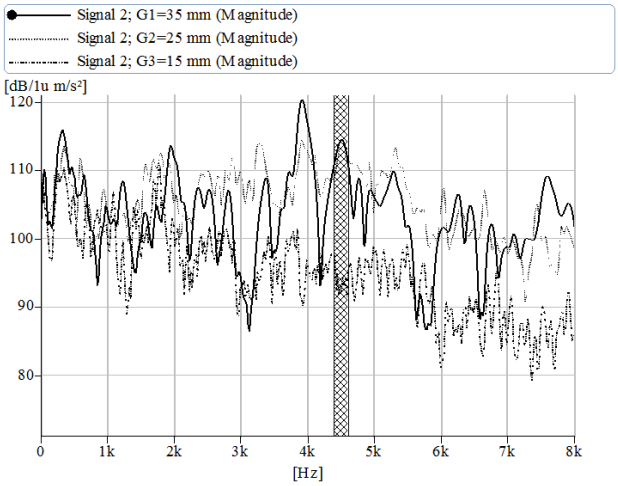


**Figure 10.** Frequency characteristic of acceleration signals recording on a braking clamp with different thicknesses of the friction pads.

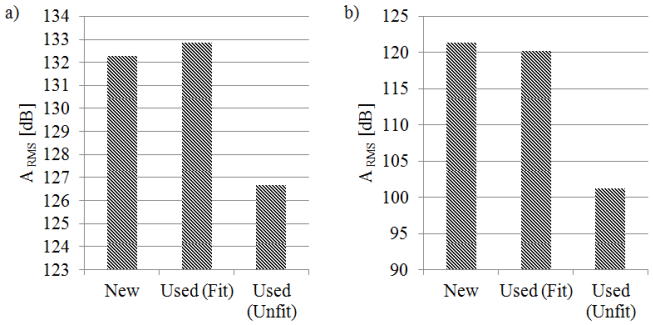


**Figure 11.** The calculated effective values of vibration acceleration signals: a) without filtering, b) with filtering in the resonance band

The dynamics is defined by the relation (5):

$$\mathrm{D} = 20\log\left(\frac{a}{a_0}\right) \tag{5}$$

where: the rate of signal change [dB], $a$- the value of the measured diagnostic parameter for the largest usage of the object, $a_0$ - the value of the measured diagnostic parameter for the new object .

The correlation 5 shows that the dynamics of 6dB means twofold increase of a diagnostic parameter. In the machinery diagnostics, it is assumed that the two-time increase or decrease of the diagnostic parameter indicates a change in the technical state of the object.

During the analysis, the dynamics of the diagnostic parameter with respect to the parameter calculated for new pad was determined. The results of calculations for broadband signals are shown in Figure 12a), while for the filtered signals in the resonance band in Figure 12b).

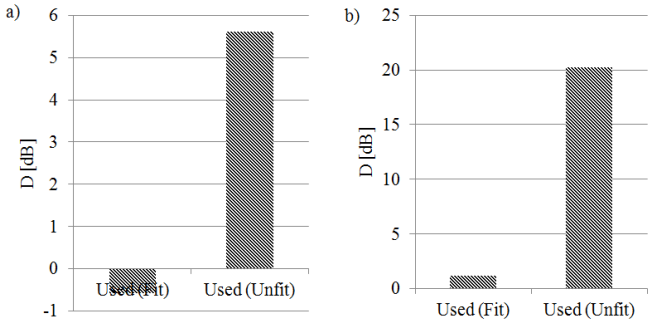


**Figure 12.** The calculated values of dynamic vibration acceleration signals: a) without filtering, b) filtering in the resonance band.

On the basis of the analysis of Figure 10, 11 and 12, it was found that the parameters of the filtered vibration signals in the band 4.4-4.6kHz can be used for assessing the thickness of the braking pad as they meet the conditions required for the diagnostic parameters i.e. they show: monotonicity of waveform in the measurement of operation functions (lack of local extremes), ease of measurement, the rate of signals change is greater than 6dB.

## 7. Conclusions

The article presents a method for evaluating the state of the braking pads by using the resonance vibrations measured on the braking block holder. On the basis of the research, it was found that the vibration signal filtration in the resonance band increases the dynamics of the diagnostic parameter by approximately 14dB (from 5.6dB to 20dB). Taking a criterion, in which it is assumed that the change of the object technical condition is indicated by the increase of diagnostic symptom by 6dB it can be concluded that the diagnostic model without the use of signal filtration does not warrant the distinction of the technical condition of the friction elements in the tested disc brake, while the signal analysis with the filtration in the band 4.4-4.6kHz enables an unequivocal evaluation of the technical condition of the tested elements of a rail braking disc system. The disadvantage of the described

method is that the impulsive test should be performed for each type of the tested brake to determine the resonant frequencies of the tested systems.

*The project is funded by the National Centre for Research and Development, program LIDER V, contract No. LIDER/022/359/L-5/13/NCBR/2014*

**References**

[1] Kędziołka, T, Kowalski. S, Smolarski. D. Paper title Analiza porównawcza wrażliwości dźwigniowych hamulców kolejowych, Pojazdy szynowe nr 1/2011.

[2] Kinkaid N.M., O'Reilly O. M, Papadopoulos P., Automotive disc brake squeal. Journal of sound and vibration 267 (2003) 105-166. Department of Mechanical Engineering, University of California, Berkeley, USA.

[3] Kruse, S. Tiedemann, M. Zeumer, B. Reuss, P. Hetzler, H. Hoffmann, N. Paper title The influence of joints of friction induced vibration in brake squeal, Journal of Sound and Vibration 340 (2015), 239-252.

[4] Nowicki. J. Book title Obliczenia symulacyjne skuteczności hamowania pociągu, XIV Konferencja Naukowa POJAZDY SZYNOWE 2000, Kraków, Arkanów, 9-13 październik 2000, t. 2, s. 139-146.

[5] North M.R, Disc brake squeal—a theoretical model, Technical Report 1972/5, Motor Industry Research Association, Warwickshire, England, 1972

[6] Rudolph M., Popp K., Brake squeal, in: K. Popp (Ed.), Detection, Utilization and Avoidance of Nonlinear Dynamical Effects in Engineering Applications: Final Report of a Joint Research Project Sponsored by the German Federal Ministry of Education and Research, Shaker, Aachen, 2001, pp. 197–225.

[7] Rudolph M., Popp K., Friction induced brake vibrations, in: CD-ROM Proceedings of DETC'01, DETC2001/VIB-21509, ASME, Pittsburgh, PA, 2001, pp. 1–10.

[8] Sawczuk W., Szymański G. Zastosowanie testów impulsowych do oszacowania częstotliwości rezonansowych wybranych elementów kolejowego układu hamulcowego, Logistyka 6/2014.

[9] Ścieszka S.F., Hamulce cierne. Zagadnienia materiałowe, konstrukcyjne i tribologiczne, Wydawnictwo Gliwice-Radom 1998, s.15.

[10] Thompson J. K.,: Brake NVH. Testing and Measurements. SAE International.

[11] Triches Junior M., Samir N. Y. Gerges, Jordan R., Analysys of brake squale noise using finite element method: A parametric study, Federal universyty of Santa.

[12] Szymański, G., Sawczuk, W. (2010). Assessing thickness of friction pad of railway disk brake on the basis of time-frequency analysis of vibration signals. Logistyka, (4), CD-CD. (in Polish).

Wojciech Sawczuk, DEng.: Poznan University of Technology, Institute of Combustion Engines and Transport, Division of Rail Vehicles, 60-965 Poznan, Poland (*wojciech.sawczuk@put.poznan.pl*).

Grzegorz M. Szymański, Ph.D.D.Sc..: Poznan University of Technology, Institute of Combustion Engines and Transport, Division of Rail Vehicles, 60-965 Poznan, Poland (*grzegorz.m.szymanski@put.poznan.pl*).

# On lower- and multi-dimensional pendulum in a nonconservative force fields
## (MAT002-15)

Maxim V. Shamolin

*Abstract:* I showed the integrability of the equations of the plane-parallel motion of a pendulum in a resisting medium, when the first integral, which is the transcendental function of quasi-velocities, was explicitly found for the set of the dynamic equations. In this case, the total interaction of the medium with a rigid body is concentrated on that part of the surface that which has the shape of a one-dimensional plate. Then the problem was generalized to the spatial case, the complete set of transcendental first integrals being found explicitly for the set of dynamic equations. Here already the total interaction of the medium with a rigid body is concentrated on that portion of its surface that has the shape of a flat disk.

### 1. Model assumptions

Let consider the homogeneous flat plate $AB$ symmetrical relative to the plane which perpendicular to the plane of figure and passing through the holder $OD$. The plate is rigidly fixed perpendicular to the tool holder $OD$ located on the cylindrical hinge $O$, and it flows about homogeneous fluid flow (Fig. 1). In this case, the body is a physical pendulum, in which the plate $AB$ and the pivot axis perpendicular to the plane of motion. The medium flow moves from infinity with constant velocity $\mathbf{v} = \mathbf{v}_\infty \neq \mathbf{0}$. Assume that the holder does not create a resistance [1, 2].

I suppose that the total force $\mathbf{S}$ of medium flow interaction is parallel to the holder, and point $N$ of application of this force is determined by at least the angle of attack $\alpha$, which is made by the velocity vector $\mathbf{v}_D$ of the point $D$ with respect to the flow and the holder (Fig. 1, wherein the figure shows the angle of attack equal to $\pi - \alpha$), and also the reduced angular velocity $\omega \cong l\Omega/v_D$, $v_D = |\mathbf{v}_D|$ ($l$ is the length of the holder, $\Omega$ is the algebraic value of a projection of the pendulum angular velocity to the axle hinge). Such conditions arise when one uses the model of streamline flow around plane bodies [5].

The vector $\mathbf{e} = \mathbf{OD}/l$ determines the orientation of the holder. Then $\mathbf{S} = -s(\alpha)v_D^2\mathbf{e}$, where $s(\alpha) = s_1(\alpha)\operatorname{sign}\cos\alpha$, and the resistance coefficient $s_1 \geq 0$ depends only on the angle of attack $\alpha$. By the plate symmetry properties with respect to the point $D$, the function $s(\alpha)$ is even. Let $Dx_1x_2 = Dxy$ be the coordinate system rigidly attached to the body,

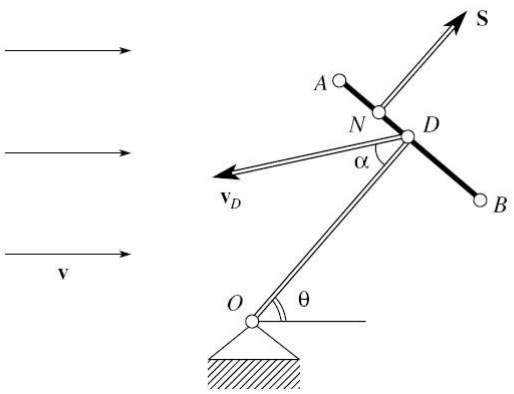


**Figure 1.** Fixed a pendulum on a cylindrical hinge in the stream running medium

herewith, the axis $Dx = Dx_1$ has a direction vector $\mathbf{e}$, and the axis $Dx_2 = Dy$ has the same direction with the vector $\mathbf{DA}$ (Fig. 1). In the same figure it is shown the angle $\theta = \xi$, i.e., the pendulum angle. The space of positions of this physical pendulum is the circle (one-dimensional sphere)

$$\mathbf{S}^1\{\xi \in \mathbf{R}^1 : \ \xi \bmod 2\pi\}, \tag{1}$$

and its phase space is the tangent bundle of a circle

$$T_*\mathbf{S}^1\{(\dot{\xi};\xi) \in \mathbf{R}^2 : \ \xi \bmod 2\pi\}, \tag{2}$$

i.e., two-dimensional cylinder.

To the value $\Omega$, I put in correspondence the skew-symmetric matrix

$$\tilde{\Omega} = \begin{pmatrix} 0 & -\Omega \\ \Omega & 0 \end{pmatrix}, \ \tilde{\Omega} \in \mathrm{so}(2).$$

The distance from the center $D$ of the plate to the center of pressure (the point $N$, Fig. 1) has the form $|\mathbf{r}_N| = r_N = DN\,(\alpha, l\Omega/v_D)$, where $\mathbf{r}_N = \{0, x_{2N}\} = \{0, y_N\}$ in system $Dx_1x_2 = Dxy$.

## 2. Set of dynamical equations in Lie algebra so(2)

If $I$ is a central moment of inertia of a rigid body–pendulum then the general equation of motion has the following form:

$$I\dot{\Omega} = DN\left(\alpha, \frac{l\Omega}{v_D}\right) s(\alpha) v_D^2, \tag{3}$$

where $\{-s(\alpha)v_D^2, 0\}$ is the decomposition of the medium interaction force $\mathbf{S}$ in the coordinate system $Dx_1x_2$.

Since the dimension of the Lie algebra so(2) is equal to 1, the single equation (3) is a group equations on so(2), and, simply speaking, the motion equation.

I can see, that in the right-hand side of Eq. (3), first of all, it includes the angle of attack, therefore, this equation is not closed. In order to obtain a complete system of equations of motion of the pendulum, it is necessary to attach several sets of kinematic equations to the dynamic equation on the Lie algebra so(2).

### 3. First set of kinematic equations

In order to obtain a complete system of equations of motion, it needs the set of kinematic equations which relate the velocities of the point $D$ (i.e., the formal center of the plate $AB$) and the over-running medium flow:

$$\mathbf{v}_D = v_D \cdot \mathbf{i}_v(\alpha) = \tilde{\Omega} \begin{pmatrix} l \\ 0 \end{pmatrix} + (-v_\infty)\mathbf{i}_v(-\xi), \tag{4}$$

$$\mathbf{i}_v(\alpha) = \begin{pmatrix} \cos\alpha \\ \sin\alpha \end{pmatrix}. \tag{5}$$

The equation (4) expresses the theorem of addition of velocities in projections on the related coordinate system $Dx_1x_2$.

Indeed, the left-hand side of Eq. (4) is the velocity of the point $D$ of the pendulum with respect to the flow in the projections on the related with the pendulum coordinate system $Dx_1x_2$. Herewith, the vector $\mathbf{i}_v(\alpha)$ is the unit vector along the axis of the vector $\mathbf{v}_D$. The vector $\mathbf{i}_v(\alpha)$ is the image of the unit vector along the axis $Dx_1$, rotated around the vertical (the axis $Dx_3$) by the angle $\alpha$ and has the decomposition (5).

The right-hand side of the Eq. (4) is the sum of the velocities of the point $D$ when you rotate the pendulum (the first term), and the motion of the flow (the second term). In this case, in the first term, I have the coordinates of the vector $\mathbf{OD} = \{l, 0\}$ in the coordinate system $Dx_1x_2$.

I explain the second term of the right-hand side of Eq. (4) in more detail. I have in it the coordinates of the vector $(-\mathbf{v}_\infty) = \{-v_\infty, 0\}$ in the immovable space. In order to describe it in the projections on the related coordinate system $Dx_1x_2$, I need to make a (reverse) rotation of the pendulum at the angle $(-\xi)$ that is algebraically equivalent to multiplying the value $(-v_\infty)$ on the vector $\mathbf{i}_v(-\xi)$.

Thus, the first set of kinematic equations (4) has the following form in our case:

$$\begin{aligned} v_D \cos\alpha &= -v_\infty \cos\xi, \\ v_D \sin\alpha &= l\Omega + v_\infty \sin\xi. \end{aligned} \tag{6}$$

## 4. Second set of kinematic equations

I also need a set of kinematic equations which relate the angular velocity tensor $\tilde{\Omega}$ and coordinates $\dot{\xi}, \xi$ of the phase space (2) of pendulum studied, i.e., the tangent bundle $T_*\mathbf{S}^1\{\dot{\xi};\xi\}$.

I draw the reasoning style allowing arbitrary dimension. The desired equations are obtained from the following two sets of relations. Since the motion of the body takes place in a Euclidean space $\mathbf{E}^n, n = 2$ formally, at the beginning, I express the tuple consisting of a phase variable $\Omega$, through new variable $z_1$ (from the tuple $z$):

$$\Omega = z_1. \tag{7}$$

Then I substitute the following relationship instead of the variable $z$:

$$z_1 = \dot{\xi}. \tag{8}$$

Thus, two sets of Eqs. (7) and (8) give the second set of kinematic equations:

$$\Omega = \dot{\xi}. \tag{9}$$

I see that three sets of the relations (3), (6), and (9) form the closed system of equations. These three sets of equations include the following two functions: $r_N = DN\,(\alpha, l\Omega/v_D)$, $s(\alpha)$. In this case, the function $s$ is considered to be dependent only on $\alpha$, and the function $r_N = DN$ may depend on, along with the angle $\alpha$, generally speaking, the reduced angular velocity $\omega \cong l\Omega/v_D$.

## 5. Problem on free body motion under assumption of tracing force

Parallel to the present problem of the motion of the fixed body, we study the plane-parallel motion of the free symmetric rigid body with the frontal plane butt-end (one-dimensional plate $AB$) in the resistance force fields under the quasi-stationarity conditions with the same model of medium interaction (Fig. 2).

If $(v, \alpha)$ are the polar coordinates of the velocity vector of the certain characteristic point $D$ of the rigid body ($D$ is the center of the plate $AB$), $\Omega$ is the value of its angular velocity, $I, m$ are characteristics of inertia and mass, then the dynamical part of the equations of motion in which the tangent forces of the interaction of the body with the medium are

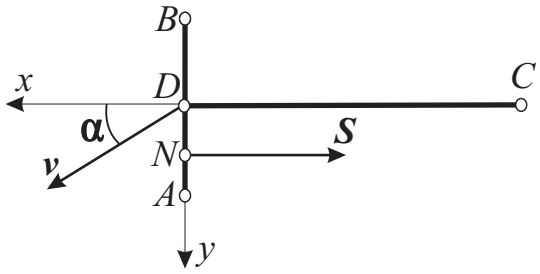


**Figure 2.** Plane-parallel motion of the free symmetric rigid body in a resisting medium

absent, has the form

$$\begin{aligned} \dot{v}\cos\alpha - \dot{\alpha}v\sin\alpha - \Omega v\sin\alpha + \sigma\Omega^2 &= \tfrac{F_x}{m}, \\ \dot{v}\sin\alpha + \dot{\alpha}v\cos\alpha + \Omega v\cos\alpha - \sigma\dot{\Omega} &= 0, \\ I\dot{\Omega} &= y_N\left(\alpha, \tfrac{\Omega}{v}\right) s(\alpha)v^2, \end{aligned} \tag{10}$$

where $F_x = -S,\ S = s(\alpha)v^2,\ \sigma = CD$, in this case $(0, y_N(\alpha, \Omega/v))$ are the coordinates of the point $N$ of application of the force $\mathbf{S}$ in the coordinate system $Dx_1x_2 = Dxy$ related to the body (Fig. 2).

The first two equations of the system (10) describe the motion of the center of a mass in the two-dimensional Euclidean plane $\mathbf{E}^2$ in the projections on the coordinate system $Dx_1x_2$. In this case, $Dx_1 = Dx$ is the perpendicular to the plate passing through the center of mass $C$ of the symmetric body and $Dx_2 = Dy$ is an axis along the plate. The third equation of the system (10) is obtained from the theorem on the change of the angular moment of a rigid body in the projection on the axis perpendicular to the figure.

Thus, the direct product $\mathbf{R}^1 \times \mathbf{S}^1 \times \mathrm{so}(2)$ of the two-dimensional cylinder and the Lie algebra so(2) is the phase space of third-order system (10) of the dynamical equations. Herewith, since the medium influence force dos not depend on the position of the body in a plane, the system (10) of the dynamical equations *is separated from the system of kinematic equations* and may be studied independently (see also [3, 4]).

### 5.1. Nonintegrable constraint

If I consider *a more general problem* on the motion of a body under the action of a certain tracing force $\mathbf{T}$ passing through the center of mass and providing the fulfillment of the equality

$$v \equiv \mathrm{const}, \tag{11}$$

during the motion, then $F_x$ in system (10) must be replaced by $T - s(\alpha)v^2$.

As a result of an appropriate choice of the magnitude $T$ of the tracing force, I can achieve the fulfillment of Eq. (11) during the motion. Indeed, if I formally express the value $T$ by virtue of system (10), I obtain (for $\cos\alpha \neq 0$):

$$T = T_v(\alpha, \Omega) = m\sigma\Omega^2 + s(\alpha)v^2 \left[1 - \frac{m\sigma}{I} y_N\left(\alpha, \frac{\Omega}{v}\right) \frac{\sin\alpha}{\cos\alpha}\right].$$

This procedure can be viewed from two standpoints. First, a transformation of the system has occurred at the presence of the tracing (control) force in the system which provides the corresponding class of motions (11). Second, I can consider this procedure as a procedure that allows one to reduce the order of the system. Indeed, system (10) generates an independent second-order system of the following form:

$$\begin{aligned} &\dot\alpha v\cos\alpha + \Omega v\cos\alpha - \sigma\dot\Omega = 0,\\ &I\dot\Omega = y_N\left(\alpha, \frac{\Omega}{v}\right) s(\alpha)v^2, \end{aligned} \tag{12}$$

where the parameter $v$ is supplemented by the constant parameters specified above.

I can see from (12) that the system cannot be solved uniquely with respect to $\dot\alpha$ on the manifold

$$O = \left\{(\alpha, \Omega) \in \mathbf{R}^2 :\ \alpha = \frac{\pi}{2} + \pi k,\ k \in \mathbf{Z}\right\} \tag{13}$$

Thus, formally speaking, the uniqueness theorem is violated on manifold (13).

This implies that system (12) outside of the manifold (13) (and only outside it) is equivalent to the following system:

$$\begin{aligned} &\dot\alpha = -\Omega + \frac{\sigma v}{I}\frac{y_N\left(\alpha, \frac{\Omega}{v}\right) s(\alpha)}{\cos\alpha},\\ &\dot\Omega = \frac{1}{I} y_N\left(\alpha, \frac{\Omega}{v}\right) s(\alpha)v^2. \end{aligned} \tag{14}$$

The uniqueness theorem is violated for system (12) on the manifold (13) in the following sense: regular phase trajectories of system (12) pass through almost all points of the manifold (13) and intersect the manifold (13) at a right angle, and also there exists a phase trajectory that completely coincides with the specified point at all time instants. However, these trajectories are different since they correspond to different values of the tracing force.

### 5.2. Constant velocity of the center of mass

If I consider *a more general problem* on the motion of a body under the action of a certain tracing force $\mathbf{T}$ passing through the center of mass and providing the fulfillment of the

equality

$$\mathbf{V}_C \equiv \mathbf{const} \tag{15}$$

($\mathbf{V}_C$ is the velocity of the center of mass), then $F_x$ in system (10) must be replaced by zero since the nonconservative couple of the forces acts on the body: $T - s(\alpha)v^2 \equiv 0$.

Obviously, I must choose the value of the tracing force $T$ as follows:

$$T = T_v(\alpha, \Omega) = s(\alpha)v^2, \ \mathbf{T} \equiv -\mathbf{S}. \tag{16}$$

The choice (16) of the magnitude of the tracing force $T$ is a particular case of the possibility of separation of an independent second-order subsystem after a certain transformation of the third-order system (10). Indeed, let the following condition hold for $T$:

$$T = T_v(\alpha, \Omega) = \tau_1\left(\alpha, \frac{\Omega}{v}\right)v^2 + \tau_2\left(\alpha, \frac{\Omega}{v}\right)\Omega v + \tau_3\left(\alpha, \frac{\Omega}{v}\right)\Omega^2 = T_1\left(\alpha, \frac{\Omega}{v}\right)v^2.$$

I can rewrite system (10) as follows:

$$\begin{gathered}
\dot{v} + \sigma\Omega^2\cos\alpha - \sigma\sin\alpha\left[\frac{v^2}{I}y_N\left(\alpha, \frac{\Omega}{v}\right)s(\alpha)\right] = \frac{T_1\left(\alpha, \frac{\Omega}{v}\right)v^2 - s(\alpha)v^2}{m}\cos\alpha, \\
\dot{\alpha}v + \Omega v - \sigma\cos\alpha\left[\frac{v^2}{I}y_N\left(\alpha, \frac{\Omega}{v}\right)s(\alpha)\right] - \sigma\Omega^2\sin\alpha = \frac{s(\alpha)v^2 - T_1\left(\alpha, \frac{\Omega}{v}\right)v^2}{m}\sin\alpha, \\
\dot{\Omega} = \frac{v^2}{I}y_N\left(\alpha, \frac{\Omega}{v}\right)s(\alpha).
\end{gathered} \tag{17}$$

If I introduce the new dimensionless phase variable and the differentiation by the formulas $\Omega = n_1 v\omega, \ < \cdot >= n_1 v <'>, \ n_1 > 0, \ n_1 = \text{const}$, then system (17) is reduced to the following form:

$$v' = v\Psi(\alpha, \omega), \tag{18}$$

$$\begin{gathered}
\alpha' = -\omega + \sigma n_1\omega^2\sin\alpha + \left[\frac{\sigma}{In_1}y_N\left(\alpha, n_1\omega\right)s(\alpha)\right]\cos\alpha - \\
- \frac{T_1\left(\alpha, n_1\omega\right) - s(\alpha)}{mn_1}\sin\alpha, \\
\omega' = \frac{1}{In_1^2}y_N\left(\alpha, n_1\omega\right)s(\alpha) - \omega\left[\frac{\sigma}{In_1}y_N\left(\alpha, n_1\omega\right)s(\alpha)\right]\sin\alpha + \\
+ \sigma n_1\omega^3\cos\alpha - \omega\frac{T_1\left(\alpha, n_1\omega\right) - s(\alpha)}{mn_1}\cos\alpha,
\end{gathered} \tag{19}$$

$$\Psi(\alpha, \omega) = -\sigma n_1\omega^2\cos\alpha + \left[\frac{\sigma}{In_1}y_N\left(\alpha, n_1\omega\right)s(\alpha)\right]\sin\alpha +$$

$$+\frac{T_1\left(\alpha, n_1\omega\right)-s(\alpha)}{mn_1}\cos\alpha.$$

I see that the independent second-order subsystem (19) can be substituted into the third-order system (18), (19) and can be considered separately on its own two-dimensional phase cylinder.

I take the function $\mathbf{r}_N$ as follows (the plate $AB$ is given by the equation $x_{1N}\equiv 0$):

$$\mathbf{r}_N=\begin{pmatrix}0\\ x_{2N}\end{pmatrix}=R(\alpha)\mathbf{i}_N, \tag{20}$$

where $\mathbf{i}_N=\mathbf{i}_v\left(\pi/2\right)$ (see (5)). In our case

$$\mathbf{i}_N=\begin{pmatrix}0\\ 1\end{pmatrix}.$$

Thus, the equality $x_{2N}=R(\alpha)$ holds and shows that for the considered system, the moment of the nonconservative forces is independent of the angular velocity (it depends only on the angle $\alpha$). For the construction of the force field, I use the pair of dynamical functions $R(\alpha), s(\alpha)$; the information about them is of a qualitative nature. Similarly to the choice of the Chaplygin analytical functions (see [5]), I take the dynamical functions $s$ and $R$ as follows:

$$R(\alpha)=A\sin\alpha,\ s(\alpha)=B\cos\alpha,\ A,B>0. \tag{21}$$

### 5.3. Reduced systems

**Theorem 1.** The simultaneous equations (3), (6), (9) under conditions (20), (21) can be reduced to the dynamical system on the tangent bundle (2) of the one-dimensional sphere (1).

Indeed, if I introduce the dimensionless parameter and the differentiation by the formulas

$$b_*=ln_0,\ n_0^2=\frac{AB}{I},\ \ <\cdot>=n_0v_\infty<'>, \tag{22}$$

then the obtained equation has the following form:

$$\xi''+b_*\xi'\cos\xi+\sin\xi\cos\xi=0. \tag{23}$$

After the transition from the variables $z$ (about the variables $z$ see (8)) to the variables $w$ $w_1=-1/n_0v_\infty z_1-b_*\sin\xi$, Eq. (23) is equivalent to the system

$$\begin{aligned}&\xi'=-w_1-b_*\sin\xi,\\ &w_1'=\sin\xi\cos\xi,\end{aligned} \tag{24}$$

on the tangent bundle $T_*\mathbf{S}^1\{(w_1;\xi) \in \mathbf{R}^2 : \ \xi \mod 2\pi\}$ of the one-dimensional sphere $\mathbf{S}^1\{\xi \in \mathbf{R}^1 : \ \xi \mod 2\pi\}$.

The phase pattern of the system (24) ($\alpha \leftrightarrow \xi - \pi, \ \omega \leftrightarrow w_1$) is shown in the Fig. 3.

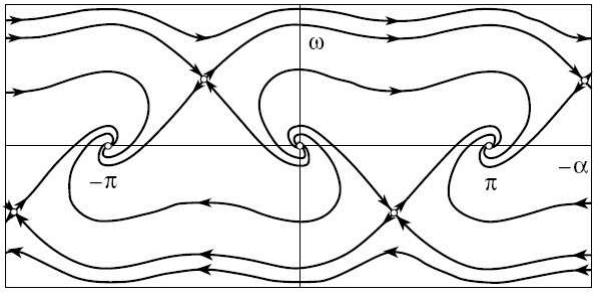


**Figure 3.** Variable dissipation dynamical system

### 5.4. Transcendental first integral

I turn now to the integration of the desired second-order system (24). In the variables $(\xi, w_1)$ the found first integrals have the following forms:

**I.** $b_*^2 - 4 < 0$.

$$[\sin^2\xi + b_* w_1 \sin\xi + w_1^2] \times \exp\left\{\frac{2b_*}{\sqrt{4-b_*^2}}\operatorname{arctg}\frac{2w_1 + b_*\sin\xi}{\sqrt{4-b_*^2}\sin\xi}\right\} = \text{const}. \tag{25}$$

**II.** $b_*^2 - 4 > 0$.

$$[\sin^2\xi + b_* w_1 \sin\xi + w_1^2] \times \left|\frac{2w_1 + b_*\sin\xi + \sqrt{b_*^2-4}\sin\xi}{2w_1 + b_*\sin\xi - \sqrt{b_*^2-4}\sin\xi}\right|^{-b_*/\sqrt{b_*^2-4}} = \text{const}. \tag{26}$$

**III.** $b_*^2 - 4 = 0$.

$$(w_1 - \sin\xi)\exp\left\{\frac{\sin\xi}{w_1 - \sin\xi}\right\} = \text{const}. \tag{27}$$

Therefore, in the considered case the system of dynamical equations (24) has the first integral expressed by relations (25)–(27), which is a transcendental function of its phase variables (in the sense of complex analysis) and is expressed as a finite combination of elementary functions.

**Theorem 2.** Three sets of relations (3), (6), (9) under conditions (20), (21) possess the first integral (the complete set), which is a transcendental function (in the sense of complex analysis) and is expressed as a finite combination of elementary functions.

### 5.5. Topological analogies

Now I present two groups of analogies related to the system (10), which describes the motion of a free body in the presence of a tracking force.

*The first group of analogies* deals with the case of the presence the nonintegrable constraint (11) in the system. In this case the dynamical part of the motion equations under certain conditions is reduced to a system (14).

Under onditions (20), (21) the system (14) has the form

$$\begin{aligned} \alpha' &= -\omega + b\sin\alpha, \\ \omega' &= \sin\alpha\cos\alpha, \end{aligned} \tag{28}$$

if I introduce the dimensionless parameter, the variable, and the differentiation analogously to (22):

$$b = \sigma n_0,\ n_0^2 = \frac{AB}{I},\ \Omega = n_0 v\omega,\ \ < \cdot >= n_0 v <'> . \tag{29}$$

**Theorem 3.** System (28) (for the case of a free body) is equivalent to the system (24) (for the case of a fixed pendulum).

Indeed, it is sufficient to substitute

$$\xi = \alpha,\ w_1 = \omega,\ b_* = -b. \tag{30}$$

**Corollary 1.**

1. The phase pattern of the system (28) is shown in the Fig. 3.

2. The angle of attack $\alpha$ for a free body (Fig. 2) is equivalent to the angle of body deviation $\xi$ of a fixed pendulum (Fig. 1).

3. The distance $\sigma = CD$ for a free body corresponds to the length of a holder $l = OD$ of a fixed pendulum.

4. The first integral of a system (28) can be automatically obtained through the Eqs. (25)–(27) after substitutions (30):

   **I.** $b^2 - 4 < 0$.

   $$[\sin^2\alpha - b\omega\sin\alpha + \omega^2] \times \exp\left\{-\frac{2b}{\sqrt{4-b^2}}\operatorname{arctg}\frac{2\omega - b\sin\alpha}{\sqrt{4-b^2}\sin\alpha}\right\} = \text{const}. \tag{31}$$

   **II.** $b^2 - 4 > 0$.

   $$[\sin^2\alpha - b\omega\sin\alpha + \omega^2] \times \left|\frac{2\omega - b\sin\alpha + \sqrt{b^2-4}\sin\alpha}{2\omega - b\sin\alpha - \sqrt{b^2-4}\sin\alpha}\right|^{b/\sqrt{b^2-4}} = \text{const}. \tag{32}$$

**III.** $b^2 - 4 = 0$.

$$(\omega - \sin\alpha)\exp\left\{\frac{\sin\alpha}{\omega - \sin\alpha}\right\} = \text{const}. \tag{33}$$

*The second group of analogies* deals with the case of a motion with the constant velocity of the center of mass of a body, i.e., when the property (15) holds. In this case the dynamical part of the motion equations under certain conditions is reduced to a system (19).

Then, under conditions (15), (20), (21), and (29), the reduced dynamical part of the motion equations (system (19)) has the form of analytical system

$$\begin{aligned} \alpha' &= -\omega + b\sin\alpha\cos^2\alpha + b\omega^2\sin\alpha, \\ \omega' &= \sin\alpha\cos\alpha - b\omega\sin^2\alpha\cos\alpha + b\omega^3\cos\alpha, \end{aligned} \tag{34}$$

in this case, I choose the constant $n_1$ as follows: $n_1 = n_0$.

If the problem on the first integral of the system (28) is solved using Corollary 1, the same problem for the system (34) can be solved by the following theorem 4.

**Theorem 4.** The first integral of the system (34) is a transcendental function of its own phase variables and is expressed as a finite combination of elementary functions.

Because of cumbersome character of form of the first integral obtained, I represent this form in the case $b = 2$ only:

$$\exp\left\{\frac{\sin\alpha + \omega}{\sin\alpha - \omega}\right\}\frac{1 - 4\omega\sin\alpha + 4\omega^2}{(\omega - \sin\alpha)^2} = C_1 = \text{const}. \tag{35}$$

**Theorem 5.** The first integral of system (28) is constant on the phase trajectories of the system (34).

Thus, I have the following topological and mechanical analogies in the sense explained above.

(1) A motion of a fixed physical pendulum on a cylindrical hinge in a flowing medium (nonconservative force fields).

(2) A plane-parallel free motion of a rigid body in a nonconservative force field under a tracing force (in the presence of a nonintegrable constraint).

(3) A plane-parallel composite motion of a rigid body rotating about its center of mass, which moves rectilinearly and uniformly, in a nonconservative force field.

## 6. Cases of integrability corresponding to the motion of a pendulum in the three-dimensional space

In [4,6,7], the planar problem was generalized to the spatial (three-dimensional) case, where the system of dynamical equations has a complete set of transcendental first integrals. It

was assumed that the interaction of the homogeneous medium flow with the fixed body (the spherical pendulum) is concentrated on a part of the body surface that has the form of a planar (two-dimensional) disk.

**Acknowledgments**

The author has been supported by Russian Foundation for Basic Research, grant No. 12-01-00020-a.

**References**

[1] Chaplygin, S. *Selected Works.* Nauka, Moscow, 1976.

[2] Gurevich, M. *Jet Theory of Ideal Fluid.* Nauka, Moscow, 1979.

[3] Shamolin, M. New integrable cases and families of portraits in the plane and spatial dynamics of a rigid body interacting with a medium. *J. Math. Sci. 114*, 1 (2003), 919–975.

[4] Shamolin, M. Classes of variable dissipation systems with nonzero mean in the dynamics of a rigid body. *J. Math. Sci. 122*, 1 (2004), 2841–2915.

[5] Shamolin, M. *Methods of Analysis of Variable Dissipation Dynamical Systems in Rigid Body Dynamics.* Ekzamen, Moscow, 2007.

[6] Shamolin, M. Dynamical pendulum-like nonconservative systems. *Applied Non-Linear Dynamical Systems, Springer Proceedings in Mathematics and Statistics 93* (2014), 503–525.

[7] Shamolin, M. Classification of integrable cases in the dynamics of a four-dimensional rigid body in a nonconservative field in the presence of a tracking force. *J. Math. Sci. 204*, 6 (2015), 808–870.

Maxim V. Shamolin, D.Sci.: Lomonosov Moscow State University, Institute of Mechanics, 1 Michurinskii Ave., 119192, Moscow, Russian Federation
(*shamolin@rambler.ru, shamolin@imec.msu.ru*).

# Error localization in the finite element modelling of structures (NUM283-15)

Tiago A. N. Silva, Nuno M. M. Maia

*Abstract:* In the present work the authors address the problem of localizing errors in the finite element modelling of structures, subjected to dynamic loading. The objective of this study is to develop a reliable tool that may be used to obtain important information on zones that are not sufficiently well modelled, leading to the improvement of the numerical model or to indicate zones that might be damaged, if one thinks in terms of structural heath monitoring. The procedure is based upon the establishment of an error function focused on the constitutive relations of the material and on the discrepancy between theoretical and experimental results. The latter are introduced in the form of frequency response functions (FRFs), which are supposed to be known at just a few locations along the structure. A numerical example simulating the measured FRFs are given to assess the capability of localizing not sufficiently well modelled regions.

## 1. Introduction

The basic problem in structural model updating is to minimize the discrepancies between the experimental and predicted responses. These discrepancies are driven by a set of modelling assumptions and lack-of-knowledge. Therefore, it is important to localise these ill-modelled regions in order to focus the updating effort, instead of performing a generalized or global updating, where elements of the entire structure are considered. By this, one reduces the number of updating parameters and, ideally, the computational cost of the updating process. Hence, whenever possible, the division of the updating process into two separated stages should be addressed. Thus, the updating process is composed by a localisation stage, where ill-modelled elements or groups of elements are localised, followed by a correction stage (the updating stage itself), which is usually implemented using a gradient-based optimization procedure to locally minimize the modelling errors previously localised. Note that the correction stage may consider any other model updating method, so that it can incorporate any of the methods proposed in this thesis. This localisation-correction process can be implemented as an iterative loop, where, after each correction stage, a new localisation is performed in order to detect regions where the model still does not comply with the real behaviour of the structure. This process ends when the discrepancies between the experimental and predicted responses are below an acceptable threshold.

The objective of the present work is to present a method for localising errors in a structure modelled by the finite element (FE) method, in structural dynamics, using information coming from experimental vibration tests under the form of frequency response functions (FRFs), measured at some of the degrees of freedom (DOF), also considered in the numerical model. Here, only the localisation stage is considered, as this is the fundamental step to take in the first place. As it will be apparent in the follow-up, there are a large number of items to account for before embarking into the updating stage.

The method used for the localisation is based upon the definition of a function which gives a measure of the error in the constitutive relations (ECR). The reason for this is that in solid mechanics both boundary and equilibrium equations can be considered as "reliable" equations, whereas the constitutive relations are less "reliable", as they involve the correct knowledge of the material properties of the structure. Therefore, one has a theoretical model which does not comply exactly with the experimental results; as a consequence, if there are errors in the theoretical model, it makes sense to focus our attention on the constitutive relations. Such a reasoning has led Ladevèze, in 1983, to propose the definition of an error measure based on the notion of error in the constitutive relations [7]. Since then, various works have been produced following that philosophy, evolving from considering experimental results in terms of free vibration tests [9, 11] to taking results from forced vibration tests [2, 8, 12, 14], although in this last case the use of FRFs is not always explicitly mentioned in the formulation of the problem. For instance, in [4], a damping identification method is presented. It is mentioned that the error is only a function of the measured displacement amplitudes in the case of a single excitation force, once the measured displacements are normalized by the excitation force amplitude, which is the definition of an FRF. Although the expression of the error explicitly in terms of the FRFs is not presented, those authors used FRFs obtained by the measurements in 110 points due to 6 force exciters. In [3] the use of FRFs is not referred to either, but only the eigenmodes (first five). In that case, the authors use the eigenmodes of a previously updated model as experimental data [10]. Note that the experimental eigenmodes are obtained by a force appropriation method using five exciters. The usual constitutive relation is Hooke's law. However, as one is dealing with dynamic problems, it is logical to also take into account a second constitutive relation, Newton's second law. Moreover, if one considers viscous damping in the formulation, Hooke's law must be completed with a term comprising the strain rate with respect to time; one may also extend Newton's law including a first order time varying term, i.e, a damping term associated to the mass, but that will not be considered here. Such an error estimate framework can be found in [8, 12].

To consider errors in the constitutive relations implies the assumption that the stiffness,

mass and damping matrices from a finite element discretisation have associated errors and do not reproduce with enough accuracy the real dynamic behaviour of the structure. Note that this approach does not require mode-pairing, which is an advantage when compared to the majority of the available localisation techniques, specially the ones developed in the modal domain. The development that follows aims at formulate an indicator that allows for the localisation of ill-modelled regions or elements in an updating context. It is important to note that this localisation method can also be applied as a damage localisation technique, although this is not the focus of the present work.

## 2. ECR formulation

Consider a study during a time interval $t \in [0, T]$. The structure under study is a solid domain $\Omega$ with boundary $\partial\Omega$. For a dynamic problem, the admissible solution must verify not only the initial and boundary conditions and the dynamic equilibrium equation, but also the constitutive relations [13]. Hence, the triplet $(\underline{\mathbf{u}}, \underline{\underline{\sigma}}, \underline{\mathbf{\Gamma}})$ is an admissible solution to the problem, where $\underline{\mathbf{u}}$ is the displacement field, $\underline{\underline{\sigma}}$ is the stress field and $\underline{\mathbf{\Gamma}}$ is the inertia force density field.

In this context, the constitutive relations are given by:

$$\underline{\underline{\sigma}} = \mathbf{E}\,\underline{\underline{\varepsilon}}(\underline{\mathbf{u}}) \qquad \text{and} \qquad \underline{\mathbf{\Gamma}} = \rho \frac{d^2\underline{\mathbf{u}}}{dt^2} \tag{1}$$

where $\mathbf{E}$ is the Hooke's tensor, $\underline{\underline{\varepsilon}}(\underline{\mathbf{u}})$ is the strain tensor and $\rho$ is the material density.

As $\underline{\mathbf{u}}$ is a "kinematical" quantity and $\underline{\underline{\sigma}}$ and $\underline{\mathbf{\Gamma}}$ are "statical" ones, one can write:

$$\underline{\mathbf{u}}_k = \underline{\mathbf{u}}\,, \qquad \underline{\underline{\sigma}}_s = \underline{\underline{\sigma}} \qquad \text{and} \qquad \underline{\mathbf{\Gamma}}_s = \underline{\mathbf{\Gamma}} \tag{2}$$

Thus, the constitutive relations are, in general, not verified, being:

$$\underline{\underline{\sigma}}_s \neq \mathbf{E}\,\underline{\underline{\varepsilon}}(\underline{\mathbf{u}}) \qquad \text{and} \qquad \underline{\mathbf{\Gamma}}_s \neq \rho \frac{d^2\underline{\mathbf{u}}}{dt^2} \tag{3}$$

However, one can introduce the "kinematical" quantities $\underline{\underline{\sigma}}_k$ and $\underline{\mathbf{\Gamma}}_k$, verifying the "kinematical" constitutive relations:

$$\underline{\underline{\sigma}}_k = \mathbf{E}\,\underline{\underline{\varepsilon}}(\underline{\mathbf{u}}_k) \qquad \text{and} \qquad \underline{\mathbf{\Gamma}}_k = \rho \frac{d^2\underline{\mathbf{u}}_k}{dt^2} \tag{4}$$

as well as, the "statical" quantities $\underline{\mathbf{u}}_\sigma$ and $\underline{\mathbf{u}}_\Gamma$, verifying the "statical" constitutive relations:

$$\underline{\underline{\sigma}}_s = \mathbf{E}\,\underline{\underline{\varepsilon}}(\underline{\mathbf{u}}_\sigma) \qquad \text{and} \qquad \underline{\mathbf{\Gamma}}_s = \rho \frac{d^2\underline{\mathbf{u}}_\Gamma}{dt^2} \tag{5}$$

Summarising, one must find the following displacement fields:

- $\underline{\mathbf{u}}_k$: the kinetically admissible displacement field, verifying $\underline{\underline{\sigma}}_k = \mathbf{E}\,\underline{\underline{\varepsilon}}(\underline{\mathbf{u}}_k)$ and $\underline{\mathbf{\Gamma}}_k = \rho\frac{d^2\underline{\mathbf{u}}_k}{dt^2}$;

- $\underline{\mathbf{u}}_\sigma$: the displacement field associated to the static stress field, verifying $\underline{\underline{\sigma}}_s = \mathbf{E}\,\underline{\underline{\varepsilon}}(\underline{\mathbf{u}}_\sigma)$;

- $\underline{\mathbf{u}}_\Gamma$: the displacement field associated to the static inertia force density field, verifying $\underline{\mathbf{\Gamma}}_s = \rho\frac{d^2\underline{\mathbf{u}}_\Gamma}{dt^2}$.

In this sense, one must find the triplet $(\underline{\mathbf{u}}_k, \underline{\mathbf{u}}_\sigma, \underline{\mathbf{u}}_\Gamma)$ which minimize the ECR.

### 2.1. ECR in a continuous domain

If one consider harmonic data with a given frequency $\omega$, it is possible to find the space of admissible amplitudes $s_\omega$, which minimizes the ECR $\eta^2_\omega(s_\omega)$ for a given frequency range $[\omega_{min}, \omega_{max}]$, given by

$$\begin{aligned}\eta^2_\omega(s_\omega) =& \frac{1-\gamma}{2}\int_\Omega \mathrm{tr}\left[\mathbf{E}\,\left(\underline{\underline{\varepsilon}}(\underline{\mathbf{u}}_k) - \underline{\underline{\varepsilon}}(\underline{\mathbf{u}}_\sigma)\right)\left(\underline{\underline{\varepsilon}}(\underline{\mathbf{u}}_k) - \underline{\underline{\varepsilon}}(\underline{\mathbf{u}}_\sigma)\right)\right]\,\mathrm{d}\Omega \\ &+ \frac{\gamma}{2}\int_\Omega \rho\omega^2\,(\underline{\mathbf{u}}_k - \underline{\mathbf{u}}_\Gamma)\cdot(\underline{\mathbf{u}}_k - \underline{\mathbf{u}}_\Gamma)\,\mathrm{d}\Omega\end{aligned} \tag{6}$$

where $\gamma \in [0,1]$ is a weighting parameter, whose value is assigned to 0 when $\rho$ is completely known, i.e., it only considers error in $\mathbf{E}$. If one has no significant information on the nature of the modelling errors, it is usual to consider $\gamma = 0.5$.

#### 2.1.1. Modified ECR

If one takes into account experimental data, one must increase the ECR by adding an extra term, which quantifies the difference between the experimental data and their corresponding theoretical ones. Denoting the experimental data by $\tilde{\bullet}$, the referred differences are introduced as energy norms, as:

$$\|\underline{\mathbf{u}}_k - \tilde{\underline{\mathbf{u}}}_k\|^2\,, \qquad \|\underline{\mathbf{\Gamma}}_s - \tilde{\underline{\mathbf{\Gamma}}}_k\|^2 \qquad \text{and} \qquad \|\underline{\mathbf{F}}_d - \tilde{\underline{\mathbf{F}}}_d\|^2 \tag{7}$$

where $\underline{\mathbf{F}}_d$ is the force imposed on the boundary.

As the experimental data are only measured at few points along the structure, one needs to evaluate the above norms in a truncated sub-space corresponding to the DOFs where measures were taken. So, the evaluation of the norms is performed after a reduction process and it is denoted as $\big|\|\bullet\|\big|$. Considering $\mathbf{\Pi}$, a projection operator mapping the experimental quantities $\tilde{\underline{\mathbf{u}}}_k$ and $\tilde{\underline{\mathbf{\Gamma}}}_k$ onto the measured coordinates, and $r \in [0,1]$, a weighting parameter which indicates the quality of the experimental data (lower $r$ for noisy data, a common value being 0.5), one can define a modified ECR, as

$$e^2_\omega = \eta^2_\omega + \frac{r}{1-r}\left\{\gamma\big|\|\mathbf{\Pi}\underline{\mathbf{\Gamma}}_s - \tilde{\underline{\mathbf{\Gamma}}}_k\|\big|^2 + (1-\gamma)\,\|\|\mathbf{\Pi}\underline{\mathbf{u}}_k - \tilde{\underline{\mathbf{u}}}_k\|\|^2 + \gamma\|\underline{\mathbf{F}}_d - \tilde{\underline{\mathbf{F}}}_d\|^2\right\} \tag{8}$$

### 2.2. ECR in a discretized domain

Considering the discretized domain, with $N$ DOF, the displacement fields are only known at the FE model nodes, so:

$$\underline{\mathbf{u}}_k \Rightarrow \underline{\mathbf{U}}\ , \qquad \underline{\mathbf{u}}_\sigma \Rightarrow \underline{\mathbf{V}} \qquad \text{and} \qquad \underline{\mathbf{u}}_\Gamma \Rightarrow \underline{\mathbf{W}} \tag{9}$$

note that the displacement fields $\underline{\bullet}$ have dimension $(N \times 1)$.

In terms of displacements at the FE model nodes, one has:

$$\underline{\mathbf{\Gamma}}_s = -\omega^2 \mathbf{M}\underline{\mathbf{W}} \qquad \text{and} \qquad \underline{\tilde{\mathbf{\Gamma}}}_k = -\omega^2 \mathbf{M}_R \underline{\tilde{\mathbf{U}}} \tag{10}$$

So, the expression for the ECR in a discretized domain is

$$\begin{aligned} E_\omega^2 =& \frac{1-\gamma}{2} \left(\underline{\mathbf{U}} - \underline{\mathbf{V}}\right)^T \mathbf{K} \left(\underline{\mathbf{U}} - \underline{\mathbf{V}}\right) + \frac{\gamma}{2}\omega^2 \left(\underline{\mathbf{U}} - \underline{\mathbf{W}}\right)^T \mathbf{M} \left(\underline{\mathbf{U}} - \underline{\mathbf{W}}\right) \\ &+ \frac{r}{1-r} \left\{ \frac{1-\gamma}{2} \left(\mathbf{\Pi}\underline{\mathbf{U}} - \underline{\tilde{\mathbf{U}}}\right)^T \mathbf{K}_R \left(\mathbf{\Pi}\underline{\mathbf{U}} - \underline{\tilde{\mathbf{U}}}\right) \right. \\ &\left. + \frac{\gamma}{2}\omega^2 \left(\mathbf{\Pi}\underline{\mathbf{W}} - \underline{\tilde{\mathbf{U}}}\right)^T \mathbf{M}_R \left(\mathbf{\Pi}\underline{\mathbf{W}} - \underline{\tilde{\mathbf{U}}}\right) + \frac{1}{2} \left(\underline{\mathbf{F}}_d - \mathbf{P}\underline{\tilde{\mathbf{F}}}_d\right)^T \mathbf{K}^{-1} \left(\underline{\mathbf{F}}_d - \mathbf{P}\underline{\tilde{\mathbf{F}}}_d\right) \right\} \end{aligned} \tag{11}$$

where $\mathbf{K}$ and $\mathbf{M}$ are the stiffness and mass matrices, respectively; $\mathbf{K}_R$ and $\mathbf{M}_R$ are reduced stiffness and mass matrices, respectively; and, $\mathbf{P}$ is a projection operator transforming the vector of imposed forces $\underline{\tilde{\mathbf{F}}}_d$ into a vector which is zero except at the coordinate where the force is applied. Note that only the application of a single force at a time is considered.

From the dynamic equilibrium equation, for undamped systems, one has

$$\underline{\mathbf{F}}_d = \mathbf{K}\underline{\mathbf{V}} - \omega^2 \mathbf{M}\underline{\mathbf{W}} \tag{12}$$

and thus eq. (11) can be written only in terms of displacements

$$\begin{aligned} E_\omega^2 =& \frac{1-\gamma}{2} \left(\underline{\mathbf{U}} - \underline{\mathbf{V}}\right)^T \mathbf{K} \left(\underline{\mathbf{U}} - \underline{\mathbf{V}}\right) + \frac{\gamma}{2}\omega^2 \left(\underline{\mathbf{U}} - \underline{\mathbf{W}}\right)^T \mathbf{M} \left(\underline{\mathbf{U}} - \underline{\mathbf{W}}\right) \\ &+ \frac{r}{1-r} \left\{ \frac{1-\gamma}{2} \left(\mathbf{\Pi}\underline{\mathbf{U}} - \underline{\tilde{\mathbf{U}}}\right)^T \mathbf{K}_R \left(\mathbf{\Pi}\underline{\mathbf{U}} - \underline{\tilde{\mathbf{U}}}\right) + \frac{\gamma}{2}\omega^2 \left(\mathbf{\Pi}\underline{\mathbf{W}} - \underline{\tilde{\mathbf{U}}}\right)^T \mathbf{M}_R \left(\mathbf{\Pi}\underline{\mathbf{W}} - \underline{\tilde{\mathbf{U}}}\right) \right. \\ &\left. + \frac{1}{2} \left(\mathbf{K}\underline{\mathbf{V}} - \omega^2 \mathbf{M}\underline{\mathbf{W}} - \mathbf{P}\underline{\tilde{\mathbf{F}}}_d\right)^T \mathbf{K}^{-1} \left(\mathbf{K}\underline{\mathbf{V}} - \omega^2 \mathbf{M}\underline{\mathbf{W}} - \mathbf{P}\underline{\tilde{\mathbf{F}}}_d\right) \right\} \end{aligned} \tag{13}$$

#### 2.2.1. ECR function of the FRFs

In practice, it is common to experimentally obtain frequency response functions (FRF) and thus an extension of the ECR to incorporate results from forced vibration tests can be found in [12, 14]. An FRF for the couple measure/excitation point $i$ and $j$, respectively, is defined as

$$\underline{\tilde{\mathbf{H}}}_{ij} = \frac{\underline{\tilde{\mathbf{U}}}_i}{\tilde{F}_{d_j}} \tag{14}$$

Hence, dividing eq. (13) by the excitation force $\tilde{F}_{d_j}$ for each frequency, it is possible to evaluate the ECR in terms of the FRFs, as follows,

$$\begin{aligned} E_{\omega}^{'2} =& \frac{1-\gamma}{2}\left(\underline{\mathbf{H}}_U - \underline{\mathbf{H}}_V\right)^T \mathbf{K}\left(\underline{\mathbf{H}}_U - \underline{\mathbf{H}}_V\right) + \frac{\gamma}{2}\omega^2\left(\underline{\mathbf{H}}_U - \underline{\mathbf{H}}_W\right)^T \mathbf{M}\left(\underline{\mathbf{H}}_U - \underline{\mathbf{H}}_W\right) \\ &+ \frac{r}{1-r}\left\{\frac{1-\gamma}{2}\left(\mathbf{\Pi}\underline{\mathbf{H}}_U - \underline{\tilde{\mathbf{H}}}\right)^T \mathbf{K}_R\left(\mathbf{\Pi}\underline{\mathbf{H}}_U - \underline{\tilde{\mathbf{H}}}\right) + \frac{\gamma}{2}\omega^2\left(\mathbf{\Pi}\underline{\mathbf{H}}_W - \underline{\tilde{\mathbf{H}}}\right)^T \mathbf{M}_R\left(\mathbf{\Pi}\underline{\mathbf{H}}_W - \underline{\tilde{\mathbf{H}}}\right)\right. \\ &\left. + \frac{1}{2}\left(\mathbf{K}\underline{\mathbf{H}}_V - \omega^2\mathbf{M}\underline{\mathbf{H}}_W - \underline{\mathbf{I}}\right)^T \mathbf{K}^{-1}\left(\mathbf{K}\underline{\mathbf{H}}_V - \omega^2\mathbf{M}\underline{\mathbf{H}}_W - \underline{\mathbf{I}}\right)\right\} \end{aligned} \tag{15}$$

where $\underline{\mathbf{I}}$ is a vector, which is zero except at the coordinate where the force is applied; and $(\underline{\mathbf{H}}_U, \underline{\mathbf{H}}_V, \underline{\mathbf{H}}_W)$ are $(\underline{\mathbf{U}}, \underline{\mathbf{V}}, \underline{\mathbf{W}})$ divided by $\tilde{F}_{d_j}$.

### 2.3. ECR in a discretized domain for damped systems

According to the described in [2, p.31], one can define the constitutive relations given in eq. (1) for damped systems, considering damping proportional to both mass and stiffness [2, p.46]:

$$\underline{\underline{\sigma}} = \mathbf{E}\,\underline{\underline{\varepsilon}}(\underline{\mathbf{u}}) + \mathbf{B}\,\underline{\underline{\dot{\varepsilon}}}(\underline{\mathbf{u}}) \qquad \text{and} \qquad \underline{\mathbf{\Gamma}} = \rho\frac{d^2\underline{\mathbf{u}}}{dt^2} + \mathbf{a}\frac{d\underline{\mathbf{u}}}{dt} \tag{16}$$

where $\mathbf{B}$ and $\mathbf{a}$ are damping operators related to linear damping. Note these operators are real, linear, symmetric and positive-definite. Hence, in terms of the defined displacement fields [2, p.36], one has:

$$\underline{\mathbf{U}}_k = \underline{\mathbf{U}}\ , \qquad \underline{\underline{\sigma}}_s = \mathbf{E}\,\underline{\underline{\varepsilon}}(\underline{\mathbf{V}}) + i\omega\mathbf{B}\,\underline{\underline{\varepsilon}}(\underline{\mathbf{V}}) \qquad \text{and} \qquad \underline{\mathbf{\Gamma}} = -\omega^2\rho\underline{\mathbf{W}} + i\omega\mathbf{a}\underline{\mathbf{W}} \tag{17}$$

However, one considers that the damping is only proportional to the stress field, such as in [3, 4], therefore $\mathbf{a} = \mathbf{0}$ and the admissible solution $(\underline{\mathbf{U}}, \underline{\mathbf{V}}, \underline{\mathbf{W}})$ must verify the dynamic equilibrium equation,

$$\underline{\mathbf{F}}_d = [\mathbf{K} + i\omega\mathbf{B}]\underline{\mathbf{V}} - \omega^2\mathbf{M}\underline{\mathbf{W}} \tag{18}$$

If one considers the error in the dissipated energy along each period $T = \frac{2\pi}{\omega}$, taking into account eq. (15), one can define the following expression for the ECR function of the FRFs of damped structures,

$$\begin{aligned} E_{\omega}^{'2} =& \frac{1-\gamma}{2}\left(\underline{\mathbf{H}}_U - \underline{\mathbf{H}}_V\right)^H [\mathbf{K} + 2\pi\omega\mathbf{B}]\left(\underline{\mathbf{H}}_U - \underline{\mathbf{H}}_V\right) + \frac{\gamma}{2}\omega^2\left(\underline{\mathbf{H}}_U - \underline{\mathbf{H}}_W\right)^H \mathbf{M}\left(\underline{\mathbf{H}}_U - \underline{\mathbf{H}}_W\right) \\ &+ \frac{r}{1-r}\left\{\frac{1-\gamma}{2}\left(\mathbf{\Pi}\underline{\mathbf{H}}_U - \underline{\tilde{\mathbf{H}}}\right)^H [\mathbf{K}_R + 2\pi\omega\mathbf{B}_R]\left(\mathbf{\Pi}\underline{\mathbf{H}}_U - \underline{\tilde{\mathbf{H}}}\right)\right. \\ &+ \frac{\gamma}{2}\omega^2\left(\mathbf{\Pi}\underline{\mathbf{H}}_W - \underline{\tilde{\mathbf{H}}}\right)^H \mathbf{M}_R\left(\mathbf{\Pi}\underline{\mathbf{H}}_W - \underline{\tilde{\mathbf{H}}}\right) \\ &\left. + \frac{1}{2}\left([\mathbf{K} + i\omega\mathbf{B}]\underline{\mathbf{H}}_V - \omega^2\mathbf{M}\underline{\mathbf{H}}_W - \underline{\mathbf{I}}\right)^H \mathbf{K}^{-1}\left([\mathbf{K} + i\omega\mathbf{B}]\underline{\mathbf{H}}_V - \omega^2\mathbf{M}\underline{\mathbf{H}}_W - \underline{\mathbf{I}}\right)\right\} \end{aligned} \tag{19}$$

If one considers Rayleigh's damping, proportional only to the stiffness, one has

$$\mathbf{B} = \alpha \mathbf{K} \tag{20}$$

and eq. (19) is recast as

$$\begin{aligned} E_{\omega}^{'2} =& \frac{1-\gamma}{2}(1+2\pi\omega\alpha)\left(\underline{\mathbf{H}}_U - \underline{\mathbf{H}}_V\right)^H \mathbf{K}\left(\underline{\mathbf{H}}_U - \underline{\mathbf{H}}_V\right) + \frac{\gamma}{2}\omega^2\left(\underline{\mathbf{H}}_U - \underline{\mathbf{H}}_W\right)^H \mathbf{M}\left(\underline{\mathbf{H}}_U - \underline{\mathbf{H}}_W\right) \\ &+ \frac{r}{1-r}\left\{\frac{1-\gamma}{2}(1+2\pi\omega\alpha)\left(\mathbf{\Pi}\underline{\mathbf{H}}_U - \underline{\tilde{\mathbf{H}}}\right)^H \mathbf{K}_R\left(\mathbf{\Pi}\underline{\mathbf{H}}_U - \underline{\tilde{\mathbf{H}}}\right)\right. \\ &+ \frac{\gamma}{2}\omega^2\left(\mathbf{\Pi}\underline{\mathbf{H}}_W - \underline{\tilde{\mathbf{H}}}\right)^H \mathbf{M}_R\left(\mathbf{\Pi}\underline{\mathbf{H}}_W - \underline{\tilde{\mathbf{H}}}\right) \\ &\left.+ \frac{1}{2}\left((1+i\omega\alpha)\mathbf{K}\underline{\mathbf{H}}_V - \omega^2\mathbf{M}\underline{\mathbf{H}}_W - \underline{\mathbf{I}}\right)^H \mathbf{K}^{-1}\left((1+i\omega\alpha)\mathbf{K}\underline{\mathbf{H}}_V - \omega^2\mathbf{M}\underline{\mathbf{H}}_W - \underline{\mathbf{I}}\right)\right\} \end{aligned} \tag{21}$$

### 2.4. Minimization of ECR

The problem one needs to solve is to find the admissible triplet $s_{adm} = (\underline{\mathbf{H}}_U, \underline{\mathbf{H}}_V, \underline{\mathbf{H}}_W)$ which minimizes the modified ECR of eq. (21). Thus, one must compute

$$\frac{\partial E_{\omega}^{'2}}{\partial s_{\mathrm{adm}_i}} = 0 \tag{22}$$

In other terms, minimizing eq. (21) with respect to $s_{adm}$ leads to the following linear system of equations, function of $\omega$,

$$\mathbf{A}(\omega)\left\{\begin{array}{c}\underline{\mathbf{H}}_U \\ \underline{\mathbf{H}}_V \\ \underline{\mathbf{H}}_W\end{array}\right\} = \underline{\mathbf{b}}(\omega) \tag{23}$$

where $\mathbf{A}$ is a hermitian matrix, that can be partitioned given the following sub-matrices:

$$\begin{aligned} \mathbf{A}_{11} =& (1-\gamma)(1+2\pi\omega\alpha)\mathbf{K} + \gamma\omega^2\mathbf{M} + \frac{r}{1-r}(1-\gamma)(1+2\pi\omega\alpha)\mathbf{\Pi}^T\mathbf{K}_R\mathbf{\Pi} \\ \mathbf{A}_{12} =& -(1-\gamma)(1+2\pi\omega\alpha)\mathbf{K} \\ \mathbf{A}_{13} =& -\gamma\omega^2\mathbf{M} \\ \mathbf{A}_{22} =& \left((1-\gamma)(1+2\pi\omega\alpha) + \frac{r}{1-r}(1+\omega^2\alpha^2)\right)\mathbf{K} \\ \mathbf{A}_{23} =& -\frac{r}{1-r}\omega^2\mathbf{M} \\ \mathbf{A}_{33} =& \gamma\omega^2\mathbf{M} + \frac{r}{1-r}\left\{\gamma\omega^2\mathbf{\Pi}^T\mathbf{M}_R\mathbf{\Pi} + \omega^4\mathbf{M}\mathbf{K}^{-1}\mathbf{M}\right\} \end{aligned} \tag{24}$$

and $\underline{\mathbf{b}}$ is a vector partitioned given the following sub-vectors:

$$\begin{aligned} \underline{\mathbf{b}}_1 =& \frac{r}{1-r}(1-\gamma)(1+2\pi\omega\alpha)\mathbf{\Pi}^T\mathbf{K}_R\underline{\tilde{\mathbf{H}}} \\ \underline{\mathbf{b}}_2 =& \frac{r}{1-r}\underline{\mathbf{I}} \\ \underline{\mathbf{b}}_3 =& \frac{r}{1-r}\left\{\gamma\omega^2\mathbf{\Pi}^T\mathbf{M}_R\underline{\tilde{\mathbf{H}}} - \omega^2\mathbf{M}\mathbf{K}^{-1}\underline{\mathbf{I}}\right\} \end{aligned} \tag{25}$$

## 3. Localisation of modelling errors

Within the proposed framework, once eq. (23) is solved for $\underline{\mathbf{H}}_U$, $\underline{\mathbf{H}}_V$ and $\underline{\mathbf{H}}_W$, one can define a relative error at each frequency for each finite element $j$ of the model and for each applied force $k$. Denoting the FRFs at each element as $\underline{\mathbf{H}}_{U_{jk}}$, $\underline{\mathbf{H}}_{V_{jk}}$ and $\underline{\mathbf{H}}_{W_{jk}}$, the local relative error at each frequency may be given by

$$E'^2_{jk\omega} = \frac{(1-\gamma)(1+2\pi\omega\alpha)\left(\underline{\mathbf{H}}_{U_{jk}}-\underline{\mathbf{H}}_{V_{jk}}\right)^H \mathbf{K}_j \left(\underline{\mathbf{H}}_{U_{jk}}-\underline{\mathbf{H}}_{V_{jk}}\right)+\gamma\omega^2\left(\underline{\mathbf{H}}_{U_{jk}}-\underline{\mathbf{H}}_{W_{jk}}\right)^H \mathbf{M}_j \left(\underline{\mathbf{H}}_{U_{jk}}-\underline{\mathbf{H}}_{W_{jk}}\right)}{\frac{(1-\gamma)}{2}(1+2\pi\omega\alpha)\left(\underline{\mathbf{H}}^H_{U_k}\mathbf{K}\underline{\mathbf{H}}_{U_k}+\underline{\mathbf{H}}^H_{V_k}\mathbf{K}\underline{\mathbf{H}}_{V_k}\right)+\frac{\gamma}{2}\omega^2\left(\underline{\mathbf{H}}^H_{U_k}\mathbf{M}\underline{\mathbf{H}}_{U_k}+\underline{\mathbf{H}}^H_{W_k}\mathbf{M}\underline{\mathbf{H}}_{W_k}\right)} \tag{26}$$

with $j = 1, \ldots, N_{el}$, the total number of elements of the model, and $k = 1, \ldots, N_f$, where $N_f$ is the number of force locations.

Note that in $E'^2_{jk\omega}$ the numerator reflects the error, at element level, in the viscoelastic and kinetic energies, weighted by the parameter $\gamma$, and the denominator represents the total viscoelastic and kinetic energies of the whole structure.

It is convenient to normalize this error, so that the results stay between 0 and 1. Therefore, one has to divide the error by the absolute maximum value found out for all the elements, frequencies and force positions:

$$\underline{E}'^2_{jk\omega} = \frac{E'^2_{jk\omega}}{\left\| E'^2_{jk\omega} \right\|_\infty} \tag{27}$$

### 3.1. An error indicator based on the ECR

In order to be capable of detecting small levels of error, which may also be related to structural damage, one shall follow a methodology based on a counting of occurrences, similarly to the proposed by [1]. To do so, it is advisable to change the definition of the error to

$$\eta^2_{jk\omega} = 1 - \underline{E}'^2_{jk\omega} \tag{28}$$

With such a definition, 1 means no error and 0 means total error. Typically, the detection and localisation of modelling errors tend to be difficult for small levels of error, say up to 10%. The main purpose here is to be able of localising modelling errors as small as possible.

Figure 1 illustrates the frequency dependence of $\underline{E}'^2_{jk\omega}$ and allows to conclude that in the cases of small error levels the $\underline{E}'^2_{jk\omega}$ can be close to zero for most of the frequencies. Thus, small values of $\eta^2_{jk\omega}$, indicating the existence of modelling errors, are only apparent for a small percentage of frequency values. This means that a possible indicator based on an average of all the values obtained along the frequency range, can give a result very close to one,

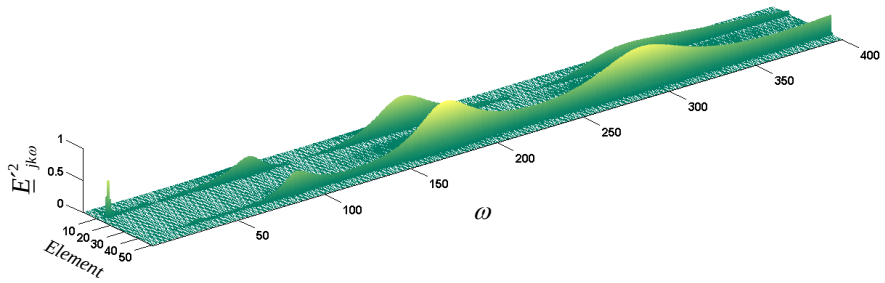


**Figure 1.** Frequency dependence of the normalized local ECR - $\underline{E}'^2_{jk\omega}$ (force at dof 2).

dissimulating the existence of those small values happening at certain frequencies. This can be overcome having into consideration not only the values of $\underline{E}'^2_{jk\omega}$ along the frequency range, but also the number of times that those results happen. Having this into consideration, the values obtained for $\underline{E}'^2_{jk\omega}$ have been classified according to $N_i$ intervals of magnitude of error, for instance, one can consider 10 intervals of 0.1. For each interval $i$, the contribution of the error is given by

$$\left(A_{jk}\right)_i = \frac{\sum_{p=1}^{n_i} \underline{E}'^2_{jk\omega_p}}{N_\omega} \tag{29}$$

where $n_i$ is the number of recorded observations in the interval. In order to evaluate the magnitude of the error as well as the incidence of the number of occurrences $\frac{n_i}{N_\omega}$ in each interval, a possible indicator of error in each interval $i$ could be given by

$$\left(A_{jk}\right)_i = \frac{\sum_{p=1}^{n_i} \underline{E}'^2_{jk\omega_p}}{n_i} \frac{n_i}{N_\omega} \tag{30}$$

As the incidence of the number of occurrences in each interval can be very low for the highest values of $\underline{E}'^2_{jk\omega_p}$, the result of summing up all the $\left(A_{jk}\right)_i$ would dilute those small values of $\underline{E}'^2_{jk\omega_p}$, leading to an erroneous result, indicating no error, which is a false conclusion. It is therefore necessary to give expression to the values of interest, the ones with the highest error. A way to do this is to modify eq. (30) into

$$\left(A_{jk}\right)_i = \left(\frac{\sum_{p=1}^{n_i} \underline{E}'^2_{jk\omega_p}}{n_i}\right)^{\frac{1}{m}} \frac{n_i}{N_\omega} \tag{31}$$

where $m \geq 1$.

Adding for the $N_i$ intervals and for all the applied forces $(N_f)$, one defines the total error at the element $j$ as,

$$\eta_j^2 = 1 - \frac{1}{N_\omega N_f} \sum_{k=1}^{N_f} \sum_{i=1}^{N_i} \left[ n_i \left(\frac{\sum_{p=1}^{n_i} \underline{E}'^2_{jk\omega_p}}{n_i}\right)^{\frac{1}{m}} \right] \tag{32}$$

Note that this the error indicator can be applied as a damage localisation tool, where the FRF data of the structure in its current state or condition should be compared with a baseline signature of the structure in its "healthy" state.

## 4. Numerical Application

As a numerical application, a 2D clamped-free beam with rectangular cross-section is discretised in 50 elements with 3 dofs per node. The material and geometrical constants considered in the present example are: $E = 200$ GPa, $\rho = 7930$ kg/m$^3$, $L = 1.80$ m, $A = 1 \times 10^{-4}$ m$^2$ and $I = 8.333 \times 10^{-10}$ m$^4$, respectively the modulus of elasticity, the material mass density, and the beam length and cross-sectional area and second moment of area.

In order to introduce modelling errors, one imposes a reduction of the second moment of area at the elements located at $x = 0.2L \wedge x = 0.8L$ (elements 12 and 42, in the case of the considered discretization and boundary conditions). Note that this kind of modelling error can be used to simulate open cracks [5, 6]. Moreover, in order to simulate real experimental FRFs, one considers that only translational DOFs, in the out-of-plane direction (y-DOFs), can be measured and forces are applied at only few locations, also in the out-of-plane direction.

## 5. Results

As the simulated modelling error has effect only upon the elastic energy, the following results were obtained considering $\gamma = 0$, so it is considered that the mass matrix is well identified.

Figure 2 illustrates how insignificant is the imposed modelling error in terms of a direct comparison between a particular direct FRF (force and measure in the same FE model DOF) for the experimental data $\underline{\tilde{\mathbf{H}}}$, the approximated FRF of the erroneous FE model $\underline{\mathbf{H}}_V$ and the reconstructed "true" FRF for the correct FE model $\underline{\mathbf{H}}_U$. Regarding the results of Figure 2, one considered a reduction of 50% of the original value of the second moment of area ($I$) of elements 12 and 42 to obtain the erroneous FE model.

Note that the results of Figures 3 to 5 were obtained considering a reduction of 5% of $I$ of elements 12 and 42 (Case 1).

Figure 3 shows the normalized local ECR $\underline{E}'^2_{jl\omega}$ in a front view (2 of the 4 used excitation forces), whereas Figure 1 illustrates the frequency dependence of $\underline{E}'^2_{jl\omega}$, given a single example (force at node 2). From this figures, the ill-modelled elements can be clearly identified. However, one needs to evaluate the error for each excitation force and if one uses noisy data, it can be more difficult to identify ill-modelled locations from a direct analysis of the normalized local ECR, specially if the effect of noise masks the actual modelling errors. Figure 3 also gives the indication that $\underline{E}'^2_{jl\omega}$ varies according to the location of the excitation.

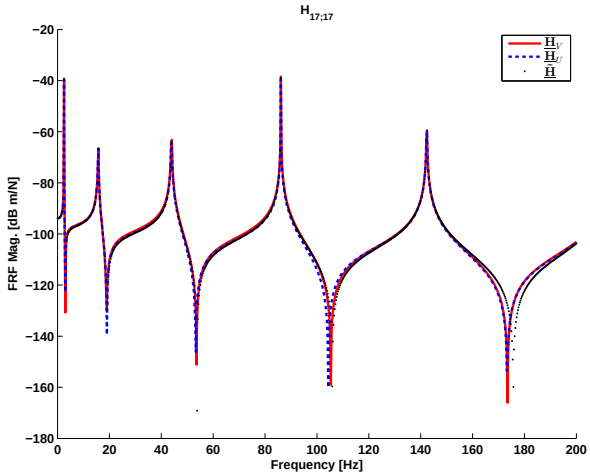


**Figure 2.** Comparison between model FRFs (direct FRF at DOF 17).

Note that one can observe error at elements adjacent to the ones where the modelling errors are imposed. This is due to the fact that adjacent elements share nodes and therefore the quantities at those elements are influenced.

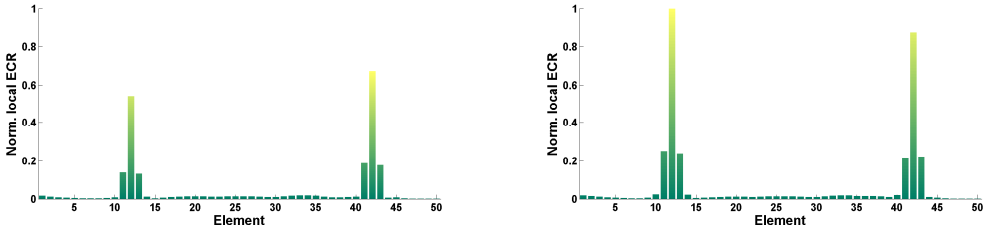


(a) Force at DOF 2 (b) Force at DOF 32

**Figure 3.** Normalized local ECR - $\underline{E}_{jl\omega}^{'2}$ - Case 1.

With the aim of enabling an easier analysis of the described ECR, it is here introduced the total local ECR $\underline{E}_j^{'2}$, the second term at the r.h.s. of eq. (32), which gathers the information of the $\underline{E}_{jl\omega}^{'2}$ for all forced locations frequency lines and the number of observations at a certain error level, considering 10 levels of error between 0 and 1 (being level 1 the most severe). Figure 4 shows the number of occurrences of $\underline{E}_j^{'2}$ at different levels of error, while Figure 5 shows the error indicator computed from $\underline{E}_j^{'2}$, using the information at all levels of error and, from it, the ill-modelled elements are identified.

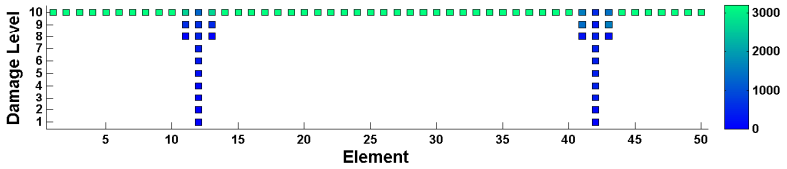


**Figure 4.** Occurrences of $\underline{E}_j^{'2}$ at different levels of error - Case 1.

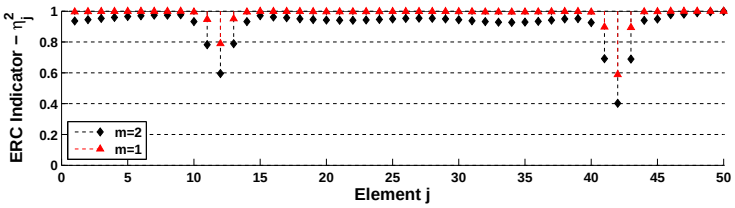


**Figure 5.** Error indicator based on $\underline{E}_j^{'2}$ - Case 1.

If one imposes now a reduction of just 2% of $I$ at the element 12, keeping the reduction of 5% at element 42 (Case 2), one obtains the results of Figures 6 and 7. Note that the ill-modelled elements are identified, specially if one considers the amplification factor $m = 2$. However, the results of Figure 7 suggest that if errors of different amplitudes coexist, one might be able to identify just some of the ill-modelled elements, as the indicator can mask the smaller errors.

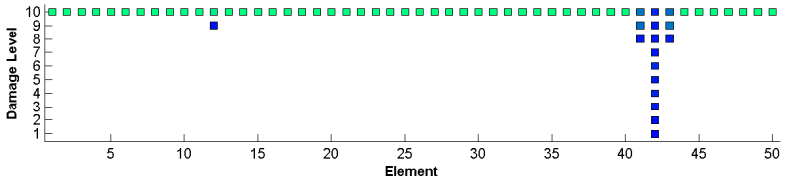


**Figure 6.** Occurrences of $\underline{E}_j^{'2}$ at different levels of error - Case 2.

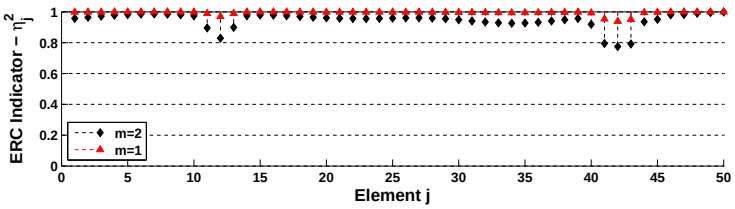


**Figure 7.** Error indicator based on $\underline{E}_j^{'2}$ - Case 2.

The proposed technique to localise modelling errors presents promising results, although

there still issues to deal with in order to establish a robust indicator.

## 6. Conclusions

A modelling errors localisation technique based on existent errors in the materials constitutive relations is presented and details are given on the discretization of the ECR and its modification in order to be defined in terms of FRFs. It is also proposed a error indicator computed from the normalized ECR, which enables both the detection and localisation of ill-modelled regions. Note that the proposed indicator may be used as a damage location tool. A numerical example illustrates the applicability of the proposed technique on the localisation of modelling errors.

Nevertheless, it should be mentioned that the presented localisation technique is a work in progress and it is very sensitive to noise. Therefore, one still needs to cope with the experimental application of it, namely regarding model incompleteness and ill-conditioning issues due to presence of noise in the experimental data.


## Acknowledgments

The authors acknowledge the support of the Portuguese Foundation for Science and Technology, FCT, under the PhD grant SFRH/BD/44696/2008.


## References


[1] Almeida, R. A. B., Urgueira, A. P. V., and Maia, N. M. M. Using transmissibility to detect and quantify structural damage. In *ICEDyn 2011 International Conference on Structural Engineering Dynamics* (Tavira, Portugal, 2011).

[2] Chouaki, A. *Une méthode de recalage de modèles dynamiques de structures avec amortissement*. PhD thesis, Université Paris VI - ENS Cachan, 1997.

[3] Faverjon, B., Ladevèze, P., and Louf, F. Validation of stochastic linear structural dynamics models. *Computers & Structures 87*, 13-14 (2009), 829–837.

[4] Faverjon, B., Ladevèze, P., Néron, D., and Durand, J. F. Damping Identification From Measurements on an Industrial Structure. In *27th International Modal Analysis Conference (IMAC XXVII)* (2009), Society for Experimental Mechanics Inc.

[5] Faverjon, B., and Sinou, J.-J. Robust damage assessment of multiple cracks based on the frequency response function and the Constitutive Relation Error updating method. *Journal of Sound and Vibration 312*, 4-5 (2008), 821–837.

[6] Faverjon, B., and Sinou, J.-J. Identification of an open crack in a beam using an a posteriori error estimator of the frequency response functions with noisy measurements. *European Journal of Mechanics - A/Solids 28*, 1 (2009), 75–85.

[7] Ladevèze, P. Recalage de modélisations des structures complexes (Note technique 33.11.01.4). Tech. rep., Aérospatiale, Les Mureaux, 1983.

[8] Ladevèze, P. Erreur en Relation de Comportement en Dynamique: Théorie et Applications au Modéles de Structures (Rapport interne no.150). Tech. rep., Laboratoire de Mécanique et Technologie de Cachan, 1994.

[9] Ladevèze, P., Nedjar, D., and Reynier, M. Updating of finite element models using vibrations tests. *AIAA Journal 32*, 7 (1994), 1485–1491.

[10] Ladevèze, P., Puel, G., Deraemaeker, A., and Romeuf, T. Validation of structural dynamics models containing uncertainties. *Computer Methods in Applied Mechanics and Engineering 195*, 4-6 (2006), 373–393.

[11] Ladevèze, P., and Reynier, M. A Localization Method of Stiffness Errors for the Adjustment of FE Models. In *12th ASME Mechanical Vibration and Noise Conference* (Montreal, 1989).

[12] Ladevèze, P., Reynier, M., and Maia, N. M. M. Error on the Constitutive Relation in Dynamics: Theory and Application for Model Updating. In *Inverse Problems in Engineering Mechanics*, H. D. Bui and M. Tanaka, Eds. Taylor & Francis, 1994, pp. 251–256.

[13] Ladevèze, P., Rougeot, P., Blanchard, P., and Moreau, J. Local error estimators for finite element linear analysis. *Computer Methods in Applied Mechanics and Engineering 176*, 1 (1999), 231–246.

[14] Maia, N. M. M., Reynier, M., and Ladevèze, P. Error Localisation for Updating Finite Element Models using Frequency-Response-Functions. In *12th International Modal Analysis Conference (IMAC XII)* (Honolulu, Hawaii, USA, 1994), pp. 1299–1308.

Tiago Alexandre Narciso da Silva, Ph.D.: NOVA UNIDEMI, Department of Mechanical and Industrial Engineering, Faculty of Science and Technology, Universidade NOVA de Lisboa, Campus da Caparica, 2829-516 Caparica, Portugal. (*tan.silva@fct.unl.pt*).

Nuno Manuel Mendes Maia, Ph.D.: LAETA, IDMEC, Instituto Superior Técnico, Universidade de Lisboa, Avenida Rovisco Pais, 1, 1049-001 Lisboa, Portugal. (*nmaia@dem.ist.ult.pt*).
The author gave a presentation of this paper during one of the conference sessions.

# Experimental determination of eigen frequency and stiffness of suspension of elastically embedded body – vehicle application (ENG202-15)

Josef Soukup, Jan Skočilas, Blanka Skočilasová

*Abstract:* The essential characteristics of a suspension are represented by the stiffness constants of the equivalent springs and the eigen frequencies of the oscillating movements in reference to the main central inertia axes of a vehicle. The premise of the experimental determination of these characteristic is the knowledge of the gravity center position and the knowledge of the main central inertia moments of the vehicle frame. The vehicle frame performs the general spatial movement when the vehicle moves. An analysis of the frame movement generally arises from Euler's equations which are commonly used for the description of the spherical movement. This solution is difficult and it can be simplified by applying the specific assumptions. The experimental investigation of the railway vehicles is performed in the special stand or by utilizing method "ride on wedges". The eigen frequencies solution and solution of the suspension stiffness are presented in the article. The solutions are applied on the railway and road vehicles with the simplifying conditions. The solution is verified on the twin axle vehicle. A new method which assessed the characteristics is described in the article.

## 1. Introduction

The dynamic analysis of the rail vehicle is an assumption not only for the quality drive assessment. It is necessary to measure or to verify the basic characteristics of the suspension for this analysis. The basic characteristics are the stiffness constant of substitutive equivalent springs and the eigen frequencies of oscillation movements referenced to main central inertia axes of the vehicle [7]. These movements are the rotational movement around longitudinal axis $x$ – roll oscillation $\omega_{xT}$, around transversal axis $y$ - swinging $\omega_{yT}$ and the translational movement in the direction of vertical axis $z$ – wobbling $\omega_{PzT} = f_{PzT}.2\pi$. Also the determination of the damping constants which characterize the energy dissipation is important (e.g. determination of logarithmic decrement, damping coefficient, etc.)

The old method called "Assessment of the characteristics of the eigen oscillation of the suspension from system" has been developed more than 40 years ago. This method is usually used for determination of the frequencies and damping of basic kind of eigen oscillation of the rail vehicle suspension. It assumes the rigidity of the frame, bogie and wheel set, and also assumes symmetrical lay out of the primary and secondary suspension. Moreover it assumes the symmetric vehicles and

therefore their oscillation are not bounded with each other or any other kind of frame oscillation, or bogies etc.

The aim of the methodology is to determine frequencies of the translational or rotational movements with respect to coordinate system with origin in the frame center of gravity. Frequency and damping are obtained from free oscillation of the system mounted into the special stand or by method so called "running over wedges".

The spring-loaded part is deflected from its equilibrium position in the measuring stand. The time course of the frame deflection towards to bogies or fixed point of the stand is measured. The harmonic analysis is applied on the measured time courses to determine the oscillation. Then the frequency and damping are assessed.

The wedges are placed on the straight railroad when the method "running over the wedges" is applied [8]. The length of the railroad is twice of wagon length minimally. The high of the wedge is 30 to 35 mm and it is placed on the surface of rail. The vehicle is running over the wedges. By this method the measuring of the eigen frequencies and damping is performed. The spatial oscillation of the frame and bogie arises from various lay-out of the wedges placed under particular wheels. The separation of the swinging and rolling oscillations from wobbling oscillation is done by connection of the deflectometers into the special schemes of connection.

The number of tests repetition has to be determined with respect to preliminary analysis of the results and in dependence on the value variance. If the difference between tests is less than 10%, the optimal number of measurement is three.

The principle of the method is briefly discussed above. The methodology doesn't content the theoretical motivation of the procedure. The technique is presented in the following text.

## 2. Solution assumptions and frequency determination

Let we assume biaxial vehicle to show the method application, see fig. 1.

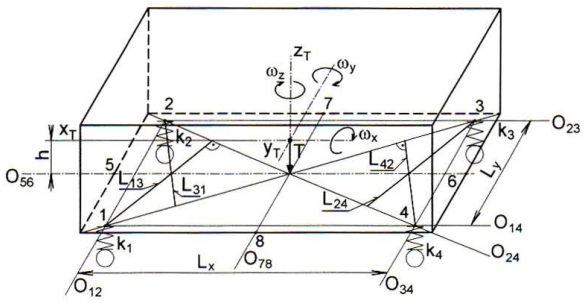


**Figure 1.** Scheme of frame model of biaxial vehicle.

It is important to know the position of the center of gravity and main central moments of inertia of vehicle frame to assess the demanded characteristics [1].

To solve this complicated problem several assumption have to be given: vehicle frame, bogies, and wheel sets are rigid bodies, stiffness characteristics of springs are linear or it can be linearized, angular deflections are very small, damping hysteresis of the springs and damping of the construction are possible to describe by viscous damping.

The vehicle frame does the generally spatial movement during vehicle drive. Therefore the analysis of the general movement of the vehicle frame should arise from solution of Euler's equations for description of the spherical movement of the frame body or bogie, see Šrejtr [2], or Juliš and Brepta [3]. This solution of the general body movement is difficult and it is possible to simplify it respecting several other assumptions: The position of the center of gravity is in the intersection of symmetry axes. These axes are identical with main central inertia axes of frame. The stiffness constant of all springs are small, because of small angular deflections. The spherical movement is possible to neglect, the functions describing movement are linear. Based on the assumptions only vertical movement of one arbitrary point of the vehicle can be observed [5], i.e. resulting vertical movement of point *i* in axis *z* direction is given by superposition of vertical particular displacements, see fig.2.

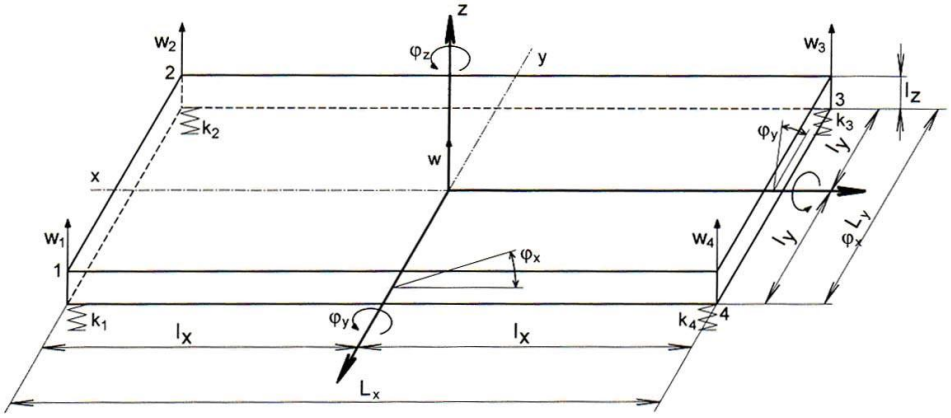


**Figure 2.** Plate support – frame model.

The displacement in the direction of the axis *z*

$$w = w_T + w(x; y; \varphi_x; \varphi_y)\,, \tag{1}$$

Final displacement of the point *i* of the plate

$$w_i = w_T + \varphi_y x_i - \varphi_x y_i \tag{2}$$

where $w_T$ – displacement of the center of gravity of plate – vehicle, plate did only oscillation movement in $z$ direction – wobbling with oscillation frequency, i.e. plate is always parallel with stable position under plate oscillation [6]. All points of the plate have the same vertical displacement, $\varphi_y$ – rotational angle of plate rotation around the $y$ axis passing through the center of gravity. The rotation oscillation movements are generated only around $y$ axis – swinging with angular frequency $\omega_{yT}$, $x_i$ – displacement of the $i$ point from $y$ axis, $\varphi_x$ – rotational angle of plate around $x$ axis passing center of gravity. The rotational movements around $x$ axis are generated – rolling with angular frequency $\omega_{xT}$, $y_i$ – displacement of the $i$ point from $x$ axis.

Distance $x_i$ and $y_i$ point for $i$ = 1, 2, 3, 4

$$x_1 = -l_x \qquad y_1 = +l_y$$

$$x_2 = -l_x \qquad y_2 = -l_y$$

$$x_3 = +l_x \qquad y_3 = -l_y$$

$$x_4 = +l_x \qquad y_4 = +l_y$$

Other movements of the plate – frame are neglected. After that it is possible to obtain motion equations describing oscillation of the plate for $k_i = k$ by Lagrange's equation of second order.

$$m\ddot{z} + 4kz = 0, \qquad J_x\ddot{\varphi}_x + 4kl_y^2\varphi_x = 0, \qquad J_y\ddot{\varphi}_y + 4kl_x^2\varphi_y = 0,$$

Or in matrix form

$$\begin{bmatrix} m & 0 & 0 \\ 0 & J_x & 0 \\ 0 & 0 & J_y \end{bmatrix} \begin{bmatrix} \ddot{z} \\ \ddot{\varphi}_x \\ \ddot{\varphi}_y \end{bmatrix} + 4k \begin{bmatrix} 1 & 0 & 0 \\ 0 & l_y^2 & 0 \\ 0 & 0 & l_x^2 \end{bmatrix} \begin{bmatrix} z \\ \varphi_x \\ \varphi_y \end{bmatrix} = 0$$

Where according to Fig. 1, 2 and 3

$$l_x = \frac{L_x}{2} \qquad l_y = \frac{L_y}{2}$$

It is obvious, that based on these assumptions the particular movement are mutually independent and the frequencies of these three investigated individual movement can be determined by experiment. The system with three degree of freedom is substituted by three systems of one DOF. It can be achieved by the fact that frame movement is allowed always only in one direction, or around one axis.

When the eigen frequencies of translational movement are investigated in direction of *z* axis – wobbling - $f_{PzT}$ the frame movement is excited and limited only in the *z* direction, i.e. the base horizontal plane delimited by four points 1, 2, 3, 4, see Fig. 3 is parallel to static plane at every moment.

The frame is supported in two static supports in the places of unbounded springs when the eigen angular frequency of rolling $\omega_{xT}$ or swinging $\omega_{yT}$ of rotational movement around longitudinal axis $x_T$ or $y_T$ are investigated, see Fig. 3 in points 1 and 4, or 2 and 3, or other couples in points 1 and 2, or 3 and 4 respectively. The connection lines of these couples of point's $o_{14}$, or $o_{23}$ and $o_{12}$ or $o_{34}$ are parallel with *x* axis and *y* axis respectively. In the opposite points 2 and 3 or 1 and 4, or 3 and 4 or 1 and 2 the frame rest supported in the springs.

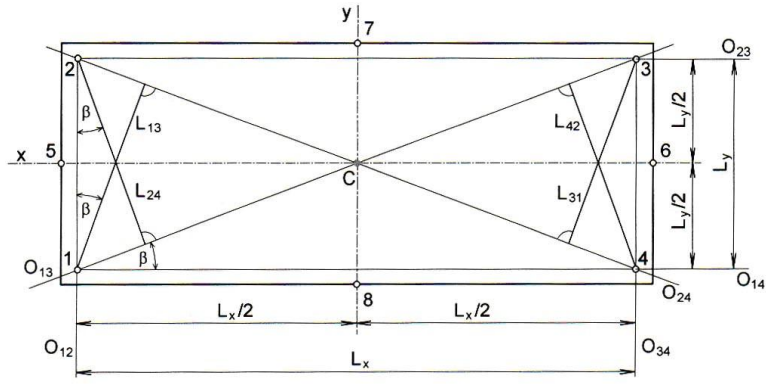


**Figure 3.** The plane model of the body.

The proposed procedure allows aim achievement: eigen frequency determination of the elastically supported frame of vehicle and three basic oscillation movement – wobbling, rolling and swinging in the direction of *z* axis, or around *x* and *y* passing through center of gravity. This method is applicable if the experimental determination of the eigen frequencies of movement related to parallel axes to *x* and *y* will be developed. Necessary condition is also the equation derivation of eigen frequencies of rotational movement of the frame to parallel axes.

### 2.1. Equation of eigen frequencies of rotational movement to parallel axes

Let it is assumed the simplest case of the body supported on two elastic supports with springs characteristics $k_1$, and $k_2$, with distance $l_{x1}$ and $l_{x2}$, from static point 0, which is origin of the coordinate system. Motion equation for rotational movement of the body according to Figure 4.

$$J_0\ddot{\varphi} = -k_1 w_1 l_{x1} - k_2 w_2 l_{x2} + Q\sin\varphi h + Q\cos\varphi x_T \tag{3}$$

where $w_1 = l_{x1}\sin\varphi$ for $\varphi \to 0$ is $\sin\varphi \cong \varphi$ (3a)

$w_2 = l_{x2}\sin\varphi$ for $\varphi \to 0$ is $\cos\varphi \cong 1$

substituting into (3) and after arrangement

$$\ddot{\varphi} + \frac{k_1 l_{x1}^2 + k_2 l_{x2}^2 + Qh}{J_0}\varphi = \frac{Q x_T}{J_0} \tag{4}$$

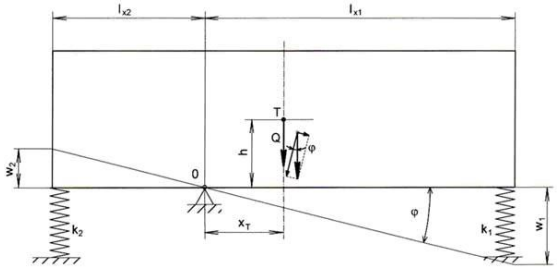


**Figure 4.** Body supported on two springs

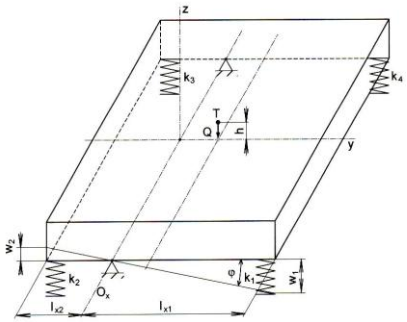


**Figure 5.** Plate (frame) support

Eigen frequency of the system with 1 DOF

$$\omega_0^2 = \frac{k_1 l_{x1}^2 + k_2 l_{x2}^2 - Qh}{J_0} \tag{5}$$

Similarly the equations for calculation for the eigen frequency of rotational movement of the rectangular plate, see Fig. 5, is possible to derive from motion equation

$$J_{0x}\ddot{\varphi} = -k_1 w_1 l_{x1} - k_2 w_2 l_{x2} - k_3 w_3 l_{x3} - k_4 w_4 l_{x4} + Qh\sin\varphi + Q\cos\varphi\, x_T \tag{6}$$

After arrangement (3) using equations (3a) we get

$$\ddot{\varphi} + \frac{k_1 l_{x1}^2 + k_2 l_{x2}^2 + k_3 l_{x3}^2 + k_4 l_{x4}^2 - Qh}{J_{0x}}\varphi = \frac{Q_{xT}}{J_{0x}} \tag{7}$$

Eigen frequency of the system with 1 DOF related to *x* axis

$$\omega_x^2 = \frac{k_1 l_{x1}^2 + k_2 l_{x2}^2 + k_3 l_{x3}^2 + k_4 l_{x4}^2 - Qh}{J_{0x}} \tag{8}$$

Eigen frequencies related to various axes is given by following equations, see figs (1-3)

To axis $o_{12}$ $\omega_{12}^2 = \frac{(k_3 + k_4)L_x^2 - Qh}{J_{12}}$ to axis $o_{34}$ $\omega_{34}^2 = \frac{(k_1 + k_2)L_x^2 - Qh}{J_{34}}$

To axis $o_{78}$ $$\omega_{78}^2 = \frac{(k_1+k_2)\left(\frac{L_x}{2}\right)^2 + (k_3+k_4)\left(\frac{L_x}{2}\right)^2 - Qh}{J_{78}}$$

From these equations it is possible to derive the relation between frequencies related to parallel axes $o_{12}$, $o_{34}$, $o_{78}$ (e.g., see Fig. 3)

$$\omega_{78}^2 = \frac{1}{4J_{78}}\left[\omega_{12}^2 J_{12} + \omega_{34}^2 J_{34} + Qh\right]$$

After that it is possible to derive the equation for calculation of the frequency related to center of gravity using equations for $\omega_{12}$ and $\omega_{34}$

$$\omega_{yT}^2 = \frac{1}{4J_{yT}}\left[\omega_{12}^2 J_{12} + \omega_{34}^2 J_{34} + 2Qh\right] \tag{9}$$

For symmetric case, when $\omega_{12} = \omega_{34}$, $J_{12} = J_{34}$ we get

$$\omega_{yT}^2 = \frac{1}{2J_{yT}}\left[\omega_{12}^2 J_{12} + Qh\right] \tag{10}$$

for $Qh << \omega_{12}^2 J_{12}$ is

$$\frac{\omega_{yT}}{\omega_{12}} = \sqrt{\frac{J_{12}}{2J_{yT}}}$$

It is possible to measure the frequencies related to axes $o_{12}$ and $o_{34}$ from periods of oscillations $\tau_{12}$ and $\tau_{34}$, i.e. from equations

$$\omega_{12} = \frac{2\pi}{\tau_{12}} \qquad \text{and} \qquad \omega_{34} = \frac{2\pi}{\tau_{34}},$$

then the value of the $\omega_{yT}$ is possible to calculate.

Similarly it is possible to determine eigen frequency to any other axis, if the eigen frequencies to two parallel axes are known. From eigen angular frequencies $\omega_{12}$ and $\omega_{34}$ or $\omega_{12}$ and $\omega_{34}$ related to axis $o_{14}$ and $o_{23}$ or $o_{12}$ and $o_{34}$ respectively the eigen frequency of rolling around axis $x_T$ or $y_T$ is possible to evaluate from equations

$$\omega_{xT} = \frac{1}{2}\sqrt{\left(\omega_{14}^2 J_{14} + \omega_{23}^2 J_{23} + 2Qh\right)\frac{1}{J_{xT}}} \tag{11}$$

$$\omega_{yT} = \frac{1}{2}\sqrt{\left(\omega_{12}^2 J_{12} + \omega_{34}^2 J_{34} + 2Qh\right)\frac{1}{J_{yT}}} \tag{12}$$

Where $Q$ – is total mass of the frame [N], $h$ – vertical coordinate of the center of gravity [m], $J_{14}$ – inertia moment of frame related to axis $o_{14}$ [kg.m$^2$], $J_{23}$ – inertia moment of frame related to axis $o_{23}$, [kg.m$^2$], $J_{xT}$ – main central inertia moment of frame related to axis $x_T$, [kg.m$^2$], $J_{12}$ – inertia moment of frame related to axis $o_{12}$ [kg.m$^2$], $J_{34}$ – inertia moment of frame related to axis $o_{34}$ [kg.m$^2$], $J_{yT}$ – main central inertia moment of frame related to axis $y_T$ [kg.m$^2$].

The inertia moments related to particular axes can be evaluated by method presented in [4].

Relations (11) and (12) allow determining angular frequencies to main central axes from known frequencies to parallel axes. They are analogic by theirs signification to Steiner law for evaluation of inertia moments to parallel axes.

### 2.2. Characteristic determination of the equivalent substitution of support

The values of stiffness constant of particular (substituted) springs are possible to evaluate from measured values of oscillation period of free oscillation of the body with 1 DOF. The oscillation is represented by swinging around $O_{ij}$ axis, which is the connection of two points, $i$, $j$ in which the body is supported on the rigid supports. The body is supported on the springs in the other two points.

For particular swinging axis (rotation) the angular frequency is given by equation

$$\omega_{ij} = \sqrt{\frac{\sum_{n=1}^{N} k_n . l_n^2 - Qh}{J_{ij}}} \tag{13}$$

Its value is determined by measured oscillation period of the free oscillation of the body around the axis $o_{ij}$. Its value is possible to determine from oscillation period $\tau_{ij}$

$$\omega_{ij} = \frac{2\pi}{\tau_{ij}}$$

Relation (13) can be transformed to form

$$\sum_{n=1}^{N} k_n l_n^2 = \omega_{ij}^2 J_{ij} + Qh \tag{14}$$

The equation system is obtained by measuring the oscillation period to various axes $o_{ij}$. The system serves to evaluate unknown values of stiffness constant (substituted) springs. There are many of rolling axes. We will consider in the calculation six basic direction (Fig. 3) $o_{14}$, $o_{23}$, $o_{34}$, $o_{12}$, $o_{13}$ and $o_{24}$.

To determine the equivalent substituted support it is necessary to experimentally investigate the eigen angular frequency $\omega_{13}$ or $\omega_{24}$ related to transversal axes $o_{13}$ or $o_{24}$, i.e. the fixed points are 1 and 3, or 2 and 4 respectively in this case, see Fig. 3.

If the values of the eigen angular frequencies $\omega_{14}$, $\omega_{23}$ and $\omega_{12}$, $\omega_{34}$ and $\omega_{13}$, $\omega_{24}$ are known it can be determined the stiffness constant of the substituted equivalent support. According to body support we distinguished following variants:

Variant **A** – fixed supports are in the position of two springs.

Variant **B** – fixed points of support are placed in two positions of the springs, but it is symmetric to geometric axes of symmetry, or to main inertia axes of body.

Variant **C** – fixed supports in the same place as in variant A, plus the effect of the eccentricity of gravity center is investigated.

Variant D – fixed supports in the same place as in variant B, plus the effect of the eccentricity of gravity center is investigated.

*Variant **A***

There are considered three equations for calculation of the springs stiffness

For axis $o_{23}$ $$k_1 + k_4 = \frac{\omega_{23}^2 J_{23} + Qh}{L_y^2} \tag{15}$$

For axis $o_{34}$ $$k_1 + k_2 = \frac{\omega_{34}^2 J_{34} + Qh}{L_x^2} \tag{16}$$

For axis $o_{13}$ $$k_2 + k_4 = \frac{\omega_{13}^2 J_{13} + Qh}{L_{24}^2} \tag{17}$$

By subtraction of (13) from sum of (15) and (16) the final equation is obtained after arrangement

$$k_1 = \frac{1}{2}\left[\frac{\omega_{23}^2 J_{23} + Qh}{L_y^2} + \frac{\omega_{34}^2 J_{34} + Qh}{L_x^2} - \frac{\omega_{13}^2 J_{13} + Qh}{L_{24}^2}\right] \tag{18a}$$

It can be found the following relations by the same way

$$k_2 = \frac{1}{2}\left[\frac{\omega_{34}^2 J_{34} + Qh}{L_X^2} + \frac{\omega_{14}^2 J_{14} + Qh}{L_Y^2} - \frac{\omega_{24}^2 J_{24} + Qh}{L_{24}^2}\right] \tag{18b}$$

$$k_3 = \frac{1}{2}\left[\frac{\omega_{14}^2 J_{14} + Qh}{L_X^2} + \frac{\omega_{12}^2 J_{12} + Qh}{L_Y^2} - \frac{\omega_{13}^2 J_{13} + Qh}{L_{24}^2}\right] \tag{18c}$$

$$k_4 = \frac{1}{2}\left[\frac{\omega_{23}^2 J_{23} + Qh}{L_X^2} + \frac{\omega_{12}^2 J_{12} + Qh}{L_Y^2} - \frac{\omega_{24}^2 J_{24} + Qh}{L_{24}^2}\right] \tag{18d}$$

for $L_{24} = L_{42}$, $L_{13} = L_{31}$ a $L_{24} = L_{13}$ – see Fig. 3 and where $J_{13}$ – inertia moment of the frame to the axis $o_{13}$ [kg.m$^{-2}$], $J_{24}$ – inertia moment of the frame to the axis $o_{24}$ [kg.m$^{-2}$].

The assessment of the constants of the particular springs from dynamical analysis allows validate the assumption correctness about equivalence of stiffness constants of all springs in sense of frame movement (wobbling, rolling, swinging). The process of the calculation of the other variants is similar.

## 3. Eigen frequency of elastically supported frame

The experimental investigation of the eigen angular frequency related to parallel axes is essential for calculation of the eigen frequencies related to main central axes. The values of the eigen frequencies related to these axes are possible to evaluated by two method: from free oscillation of the frame for small damping or from forced oscillation of the frame for high but under critical damping.

### 3.1. Free oscillation

The frame is deflected by static deviation from equilibrium state in the direction of free oscillation. The damped movement is generated for small under critical viscous damping. The free oscillation of the elastically supported frame is measured by acquisition of the acceleration, velocity or displacement (best choice). The oscillation period is read from recorded data and angular frequency $\omega$ or oscillation frequency $f$ is calculated.

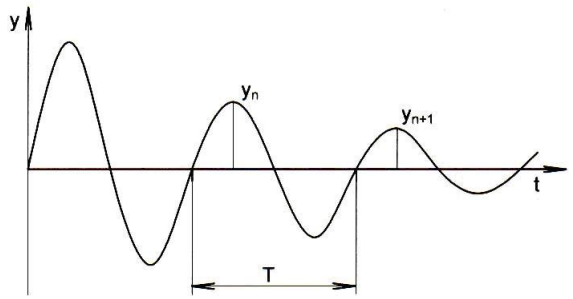


**Figure 6.** Free under critical damped oscillation of the elastically supported frame

$$\omega = \frac{2\pi}{\tau} \quad [s^{-1}] \qquad f = \frac{1}{\tau} \quad [Hz]$$

The damping intensity is then determined from amplitude reduction of two followed cycles of measured quantity, e.g. displacement and logarithmic decrement or damping coefficient $D$.

$$\vartheta = \ln \frac{Y_n}{Y_{n+1}} \qquad D = \frac{1}{\sqrt{1+\left(\frac{2\pi}{\vartheta}\right)^2}} \tag{19}$$

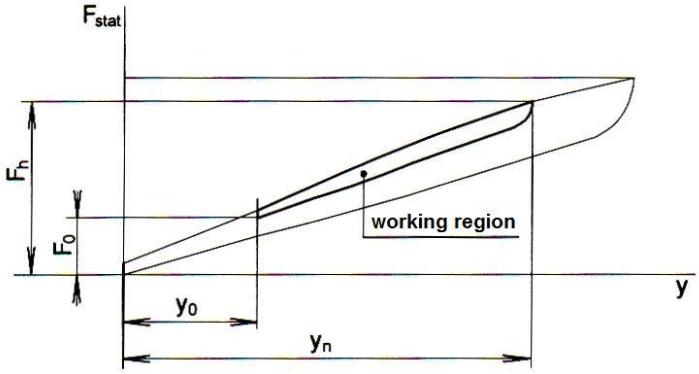


**Figure 7.** Static characteristic of support

### 3.2. Forced oscillation

The frame is supported by the same way like previous case. The oscillation is excited by e.g. hydraulic pistons acting by force in place, where the symmetry to oscillation axis is ensured (in place of fender). All pistons have to be synchronized. The static displacement or support characteristic is determined by static measurement.

The forces of the hydraulic pistons have to be harmonically variable, have to have same amplitude, frequency and phase during dynamic test.

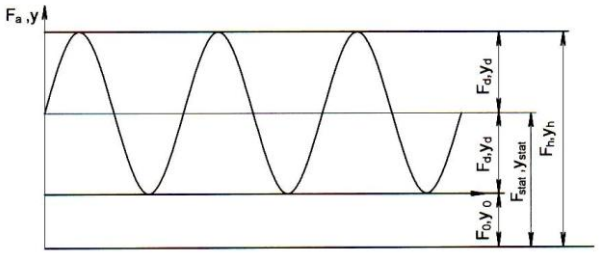


**Figure 8.** Time trend of the excitation force $F_a$ and displacement $y$ under forced oscillation of the vehicle frame

The example of the time trend of excitation force and displacement is presented in the Fig. 8. The dependency of the upper dynamic displacement on the frequency of force under its constant amplitude is presented in the Fig. 9.

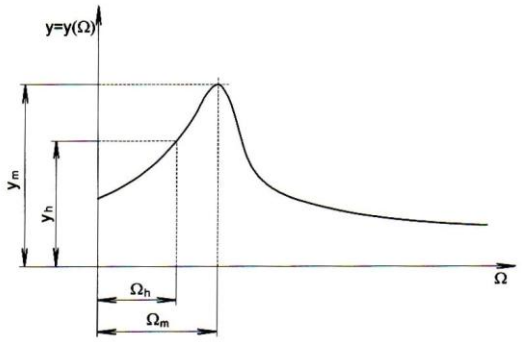


**Figure 9.** Upper dynamic displacement $y_h$ dependency on the oscillation frequency $\Omega$ of excitation force $F$ = const. (const. amplitude)

The testing equipment has to have frequency adjustment of excitation force $\Omega$ under constant amplitude. Then it is possible to determine displacement $y$ with dependency on frequency $\Omega$ of excitation force $y = y(\Omega)$ under constant amplitude, see Fig. 9. It allows us to determine maximal deviation $y_m$ and correspond frequency $\Omega_m$ of excitation force under resonance (Fig. 10).

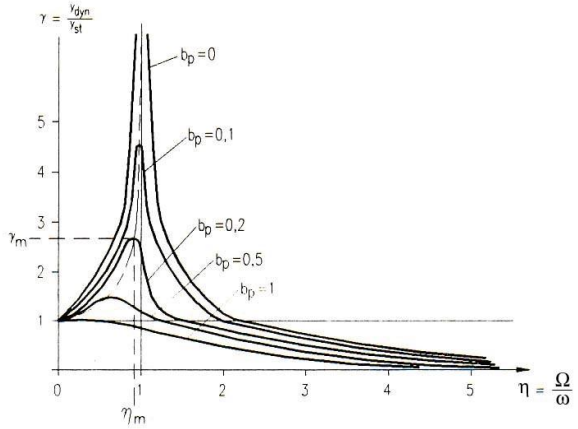


**Figure10.** Resonance characteristic of system with 1 DOF with various damping

From ratio of experimentally determined values $y_{st}$ and $y_m$ ($\gamma_m$) we can obtain coefficient of system tuning $\eta_m$ under resonance.

$$\gamma_m = \frac{y_m}{y_{st}} \qquad\qquad \eta_m = \sqrt[4]{1 - \frac{1}{\gamma_m^2}}$$

The value of eigen frequency $\omega$, or logarithm decrement $\vartheta$, or damping coefficient $D$ (see eq. (19)) can be calculated from:

$$\omega = \frac{\Omega_m}{\eta_m} \qquad \vartheta = 2\pi\sqrt{\frac{1-\eta_m^2}{1+\eta_m^2}} = 2\pi\sqrt{\frac{1-\sqrt{1-1/\gamma_m^2}}{1+\sqrt{1-1/\gamma_m^2}}} \tag{20}$$

From known values $\Omega$, $\omega$, $y$, $y_{st}$ the resonance characteristic (amplitude-frequency) can be obtained. The required characteristic of dynamic analysis of the vehicle can be achieved by described process.

## 4. Conclusion

The described method help to obtain the characteristics of the vehicle dynamic analysis and it was successfully applied in RRI – Railway Research Institute (VUZ, CZ) and it is utilized for drive properties of vehicles, namely railway vehicles. The method is simple and gives relevant results. In the next step of the problem solution the comparison of the proposed method with method ride on wedges will be performed. Also theoretical and experimental analysis of accepted assumption of symmetry arrangement will be implemented. The effect of the different values of the stiffness constant, the effect of eccentricity of gravity center, the effect of support geometry – non equal distance of elastic supports, the effect of main central inertia axis rotation related to symmetry axes etc. will be considered. It allows the generalization of the proposed method.


## Acknowledgments

The work was supported by SGS University J. E. Purkyně in Ústí n. L.


## References


[1] Soukup, J., Volek, J., et all: *Oscillation of mechanical systems. Asymmetry analysis.* Universita J. E. Purkyně v Ústí n. L., 2008

[2] Šrejtr, J.: *Technická mechanika III. Dynamika*. Praha, 1958

[3] Juliš, K., Brepta, R., a kol.: Mechanika II. Dynamika. Technický průvodce 66, SNTL, Praha, 1987

[4] Soukup, J., Skočilas, J., Skočilasová, B.: *Central inertia moments and gravity center of large volume and weight bodies*. International Journal of Dynamics and Control. Springer, Berlin Heidelberg, 2014, ISSN 2195-268X (print), ISSN 2195-2698 (online)

[5] J. Awrejcewicz, L. Kurpa, O. Mazur: *On the parametric vibrations and meshless discretization of orthotropic plates with complex shape*, International Journal of Nonlinear Sciences and Numerical Simulation, 11 (5), 2010, 371-386.

[6] I.V. Andrianov, J. Awrejcewicz, V. Chernetskyy: *Analysis of natural in-plane vibration of rectangular plates using homotopy perturbation approach*, Mathematical Problems in Engineering, 2006, 8 pages (DOI: 10.1155/MPE/ 2006/20598).

[7] S. Iwnicky et. al.: *Hanbook of Railway Vehicle Dynamics*, Taylor and Francis, Boca Raton, USA, 2006, ISBN: 978-0-8493-3321-7.

[8] Z. Cai, G.P. Raymond: *Modelling the dynamic response of railway track to wheel/rail impact loading*, Structural Engineering and Mechanics, 2 (1), 1994, 95-112.

doc. Ing. Josef Soukup, Professor: UJEP in Usti nad Labem, Czech Republic, Faculty of Production Technology and Management, Department of Machines and Mechanics, Na Okraji 1001/7, Usti nad Labem, 400 11, Czech Republic (soukupj@fvtm.ujep.cz).

Ing. Jan Skocilas, Ph.D., Assistant: CTU in Prague, Czech Republic, Faculty of Mechanical Engineering, Department of Process Engineering, Technicka 4, Prague 6, 166 07, Czech Republic (jan.skocilas@fs.cvut.cz).

Ing. Blanka Skocilasova, Assistant: UJEP in Usti nad Labem, Czech Republic, Faculty of Production Technology and Management, Department of Machines and Mechanics, Na Okraji 1001/7, Usti nad Labem, 400 11, Czech Republic (skocilasova@fvtm.ujep.cz).

# Fatigue crack identification by dynamic analysis of elastic wave propagation (NUM025-15)

Adam Stawiarski, Marek Barski, Piotr Pająk

*Abstract:* The safety and reliability of structures mostly depend on the effectiveness of the monitoring methods. In this paper the wave propagation method has been used to detect and identify the fatigue damage in thin walled structure with circular hole. The Structural Health Monitoring (SHM) system based on the propagation of the elastic wave generated by the piezoelectric (PZT) elements has been proposed. The comparison of the intact and defected structures has been used by damage detection algorithm. One part of the SHM system has been responsible for detection of the fatigue crack initiation. The second part observed the evolution of the damage growth and assess the size of the defect. The numerical results of the wave propagation phenomenon has been used to present the effectiveness and accuracy of the proposed method.

## 1. Introduction

In recent years the development of monitoring systems associated with the technological progress have been observed for example in aircraft or space structures. The necessity of permanent monitoring of the structures state and prognosis of the service life is especially important when the direct access for typical non-destructive testing methods is difficult or even impossible. Observation of the structures under fatigue loading is also significant from durability point of view. The great number of the engineering materials and difficulties associated with the accurate estimation of the fatigue strength cause the development of the Structural Health Monitoring (SHM) systems. In most cases the monitoring systems use pre-installed sensors and diagnose the structural health in real life. The Lamb wave propagation phenomenon is one of the most effective method for damage detection and identification in shell structures [1]. The basic assumption of SHM system is the comparison the potentially defected structure with the intact one to detect the change in the dynamic response [2]. SHM can be classified into several levels of analysis. The systems of the first level allow only to confirmation the presence of the damage. The main task of the second level systems is to determine the localization and orientation of the defect. The assessment of the damage size is the aim of the third level systems. The mentioned levels creates the diagnosis part of the SHM. The data from the diagnosis part can be utilized in determining the remaining life of the structures (the forth level) in prognosis part of the SHM [3]. The evolution of the fatigue damage starting from the edge of the hole in structure under different type of loading are considered by many researchers [4,5]. The guided

wave propagation method is mostly considered in shell structures made of isotropic and composite materials [6-10]. The fatigue crack detection near the hole introduces the complications associated with elastic wave reflection from the boundary of the structure [11]. Many researchers are focused only on detection the damage near the hole by analysis of the wave scattering by crack [12,13]. The techniques of the damage identification are the subject of interest for researchers both in time and frequency domain [14-15]. A direct comparison of the signals from defected and intact structures has been utilized by Kessler [16] and Giurgiutiu [17]. The localization of the fatigue damage by wave propagation method has been considered by Hong et al. [18]. In this paper the wave propagation method has been used to detect, localize and assess the size of the fatigue crack in thin walled plate with circular hole. The SHM system consist of two part analysis. The first part is responsible for detection of the fatigue crack initiation. The second part observe and analyze the evolution of the damage growth and assess the size of the defect. The numerical analysis of the problem is implemented in Ansys finite element analysis package.

## 2. Configuration of the SHM system

The proposed multipoint measuring system based on PZT elements is responsible for the elastic wave generation and acquisition of the response data. The comparison of the intact and defected structure is necessary for proper damage detection and identification. In this paper the thin square plate made of PA38 aluminum alloy with circular hole in the middle is considered (figure 1).

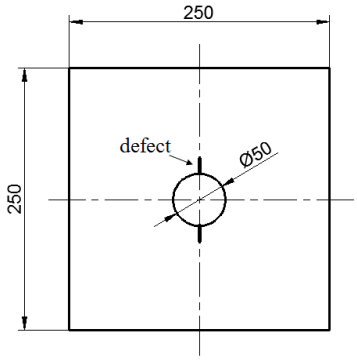


**Figure 1.** Aluminum square plate with a circular hole in the middle.

The basic properties of the considered plate are presented in Table 1:

Table 1. The basic properties of the considered plate.

| Young's modulus ($E$) | Poisson ratio ($\nu$) | Density ($\rho$) | Thickness |
|---|---|---|---|
| 69500 MPa | 0.33 | 2700 kg/m$^3$ | 2 mm |

The configuration schema of the SHM system is presented on figure 2. The basic assumption of the considered case is that localization of the potential fatigue damage is predictable because of the assumed uniaxial fatigue loading applied in the horizontal direction. Many researchers proved that for such a case the fatigue crack starts from the edge of the hole and the orientation is perpendicular to the loading direction. The proposed SHM system is based on comparison the signal received in the intact and defected structures. A presented measurement technique is called a pitch-catch method.

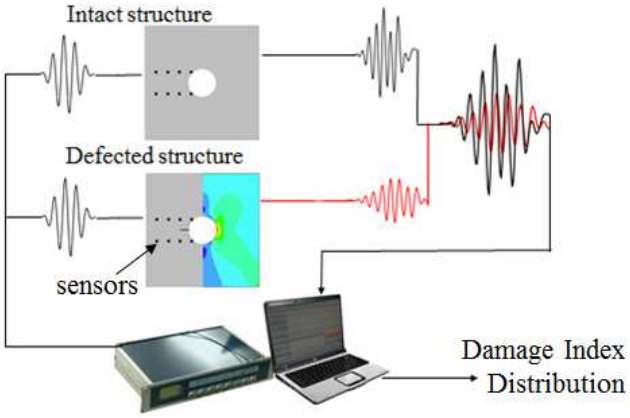


**Figure 2.** The SHM system schema.

The hardware part of the system contain the multichannel elastic waves generation and acquisition system. In numerical FEM investigations the hardware part has been replaced by concentrated force applied to the plate in the compatible with the experiment form. The five cycle of the Hanning windowed tone burst excitation signal was considered (see Eq. 1) with the frequency f=250 kHz.

$$h(t) = \frac{1}{2}\left[1 - \cos\left(\frac{\omega t}{N_c}\right)\right] \qquad 0 \le t \le T_c \tag{1}$$

where $\omega=2\pi f$, $T=1/f$, $T_c=N_c \cdot T$, $N_c$ – number of counts in excitation signal.

The numerical analysis of the transient dynamic problem has been prepared in ANSYS system. The higher order shell elements with a six degrees of freedom at each node was used to define the numerical model of the plate. To obtain the acceptable accuracy of the FE computation, there should be more than 8 nodes per wave length.

According to the assumed material properties and signal frequency the wave speed is equal $v_{wave}=5074$ m/s and the wave length $\lambda=20.3$ mm. Therefore, to fulfill mentioned condition the approximate 2 mm finite element size has been assumed. The total number of the finite elements used

to define numerical model of the considered plate is approximately equal 17000. The configuration of the measuring points on the plate with a defect presents figure 3.

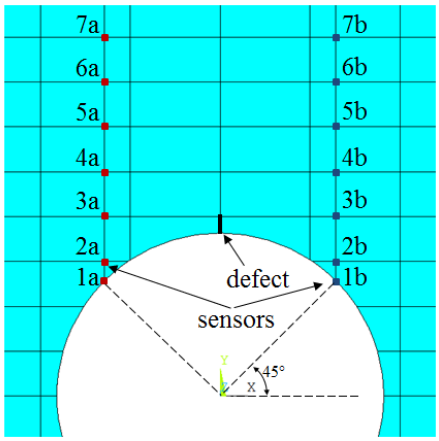


**Figure 3.** Localization of the measuring points in the SHM system.

A considered system contain 14 measuring points classified into two group. If the elastic wave is generated by one of the actuators localized at one side of the hole (1a – 7a), the response signal is detected and collected by all sensors localized at the second side of the hole (1b – 7b). The distance between the sensors at each group is equal 7 mm. The defect has been modelled by duplicate node method as it is shown in figure 4.

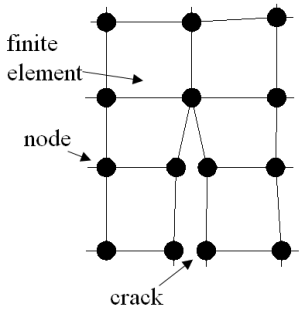


**Figure 4.** The FE damage model introduced by duplicate node method.

An example of the numerical results for intact and defected structure are presented on figure 5.

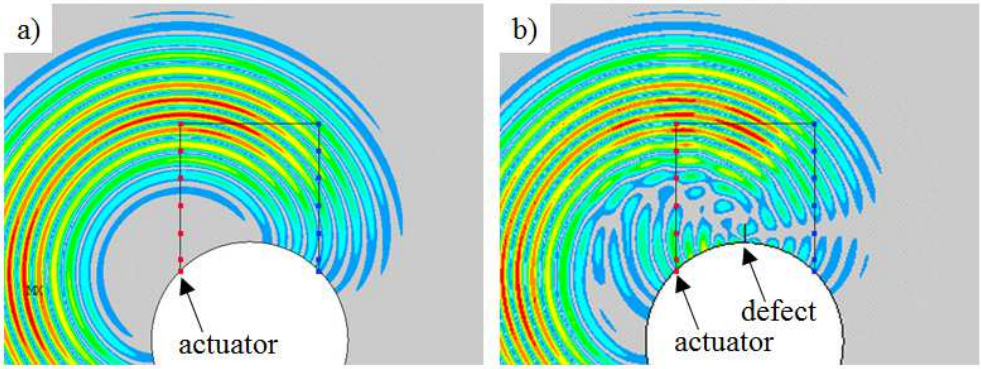


**Figure 5.** Fronts of propagating elastic wave in a) intact structure, b) plate with 5mm defect (time = 2.5e-5 [s]).

Comparison of the elastic wave fronts in intact (figure 5a) and defected (figure 5b) plate demonstrates the effect of the wave disturbance by the crack. It should be emphasized that in practical application of the SHM system the direct view of the wave propagation is inaccessible. The system of the piezoelectric sensors registers the dynamic response of the structure. The configuration of the multipoint measuring system which main aim is to detect the fatigue crack initialization is presented in Figure 6.

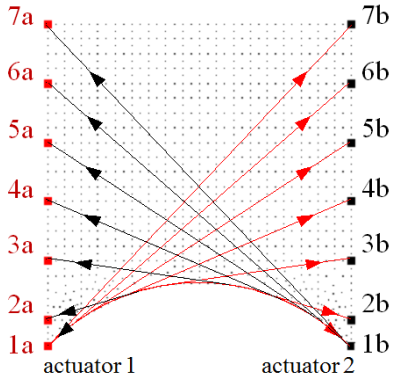


**Figure 6.** The schema of the first part of the SHM system.

The actuator 1a generates the elastic wave which propagates through the structure. The shortest paths between an actuator and the sensors where the response signal is detected are marked by red lines. Subsequently elastic wave is generated by 1b actuator and the response signal is analyzed by sensors 1a to 7a. The comparison of the wave propagation in intact and defected structure in measuring points allow to determine the state of the structure. The appropriate localization of the sensors near the hole allow to the detection of the fatigue crack initiation.

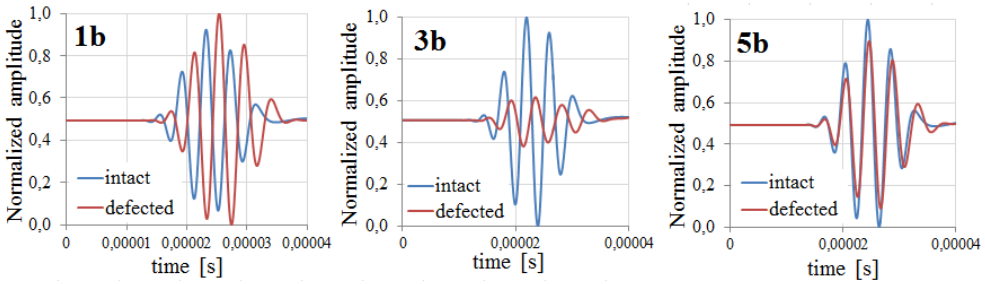


**Figure 7.** A comparison of the response signals from intact and defected plate for three sensor (1b, 3b, 5b).

Figure 7 demonstrates such a comparison for one stage of the analysis where the sensor 1a (see figure 6) is responsible for generation of the elastic wave and sensors 1b to 7b detect and verify the response signals. The significant difference between signals is observed by sensors for which an elastic wave passed through the defected area. It is worth to point out that application of the only one actuator in SHM system and analysis of the response signals from the sensors localized around the hole allow to build of the first level system responsible for damage detection. To determine a detail information about localization and size of the fatigue damage, the multipoint measuring system based on different localization of the actuators have to be considered. Moreover, the measure of the difference between signals from the intact and defected structures should be defined for the automation of the damage detection and identification process.

## 3. Damage Index (DI) definition

The comparison of the response signals from the intact and defected structure is used for damage detection and identification. The determination what changes in signal indicate to the presence of damage is the greatest challenge in signal-based damage identification. The feature extraction associated with the wave propagation phenomenon is therefore crucial for SHM system effectiveness. The software part of the SHM system contain the data acquisition technology and damage identification algorithm which convert the measured data to the information about defect. The most common technique used in SHM system based on the wave propagation phenomenon is the damage index (DI) definition. DI describes the difference between response signal from the intact and defected structure. In this paper the area between the normalized response signals describes the level of the differences caused by the potential damage. The area between two curves is defined as a definite integral of the difference between discrete value of the signals from the intact ($f_{int}(t)$) and defected ($g_{def}(t)$) structures (Eq. 2).

$$NumInt = \int_a^b \left[ f_{\text{int}}(t) - g_{def}(t) \right] dt \tag{2}$$

The area is calculated with the use of numerical integration by the classical form of trapezoidal method (figure 8). The increase of the area (*NumInt*) indicates to the disturbance of the response signal by the structural defect observed on the wave propagation path between an actuator and sensor. The accuracy of the numerical integration depends on the step size in finite element method analysis and sampling frequency in experimental investigation.

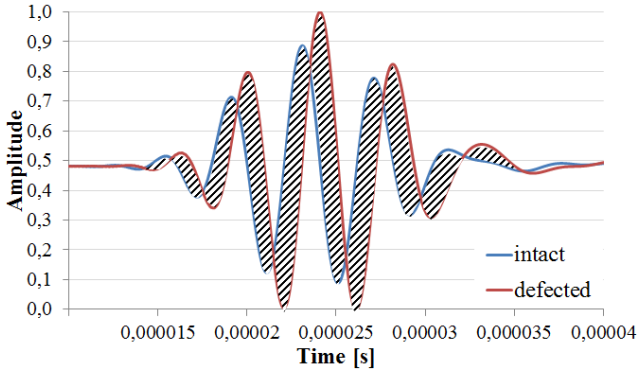


**Figure 8.** Comparison of the normalized response signals from the intact and defected structures.

The Damage Index definition (see Eq. 3) contain two terms from which the first is responsible for the value of the DI and the second describes the geometry of wave propagation path. The width of the elliptic shape of a path is controlled by β parameter.

$$DI(x,y) = \sum_{k=1}^{N} NumInt \cdot \left( \frac{\beta - R(\Omega)}{\beta - 1} \right) \tag{3}$$

where

$$R(\Omega) = \begin{cases} R_c(\Omega), R_c(\Omega) < \beta \\ \beta, R_c(\Omega) \geq \beta \end{cases} \tag{4}$$

$$R_c(\Omega) = \frac{\sqrt{(x - x_{ak})^2 + (y - y_{ak})^2} + \sqrt{(x - x_{sk})^2 + (y - y_{sk})^2}}{\sqrt{(x_{ak} - x_{sk})^2 + (y_{ak} - y_{sk})^2}} \tag{5}$$

$\Omega=[x, y, x_{ak}, y_{ak}, x_{sk}, y_{sk}]$ is a function of the variables connected with the localization of the actuator $(x_{ak}, y_{ak})$ and sensor $(x_{sk}, y_{sk})$.

The Damage Index is calculated for each wave propagation path between an actuator and each sensor. The final form of the Damage Index distribution is determined as a product of the DI obtained for particular wave propagation paths (see Eq. 6.)

$$I(x,y) = \prod_{k=1}^{N_a} DI_k(x,y) \tag{6}$$

where $N_a$ – is a number of actuators.

## 4. Damage detection results

Proposed SHM system is divided into two parts of analysis. The first part detect the initiation of the fatigue crack and the second is responsible for the damage size assessment.

### 4.1. Detection of the fatigue crack initiation

The detection of the fatigue crack initiation is based on two stage analysis in which only two actuators, localized at the edge of the hole, generates an elastic wave (see figure 6). The response signals are detected by sensors placed on the opposite side than actuator. The initiation of the fatigue crack has been modelled as a 2mm crack in the middle between actuators (figure 9a). The comparison of the wave propagation in pattern structure and defected one and analysis of the response signals by damage detection algorithm presented in previous section allow to detect and localize the initiation of the fatigue crack (figure 9b).

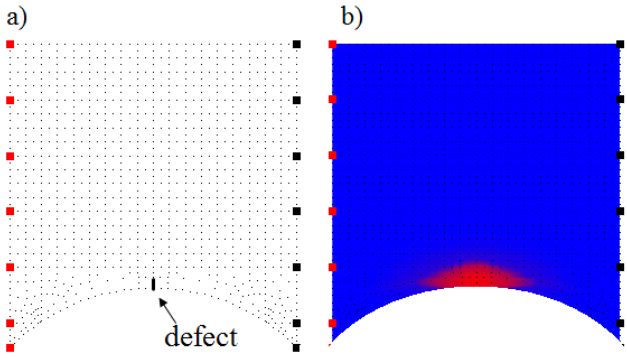


**Figure 9.** a) The view of analyzed area with a schema of 2 mm crack, b) the Damage Index distribution in the analyzed area.

It is worth to point out that even small damage can be detected by proposed SHM system. The wave propagating between an actuator and sensor placed on the edge of the hole is disturbed by small structural change in the material. Therefore the SHM system of the first level which main aim is only

to alarm about the defect occurrence (without information about localization and size assessment) can by designed with the use only two sensors placed near the edge of the hole.

### 4.2. Identification of the fatigue crack

The algorithm of damage identification is applied after detection of the fatigue crack initiation. In this part of the SHM system the detail analysis of the area between the measuring points is investigated. After detection of the potential damage in the structure the multistage measurement is applied (figure 10).

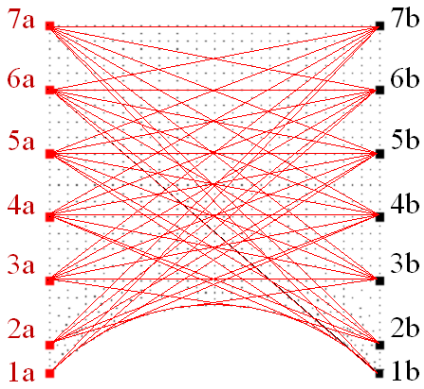


**Figure 10.** The schema of the second part of the SHM system.

At each stage one of the sensors generates an elastic wave and all sensors localized on the opposite side analyze the response signals. After analysis the wave propagation path for each of the 14 actuators the final form of the damage index distribution is calculated with the use of the formula (8).

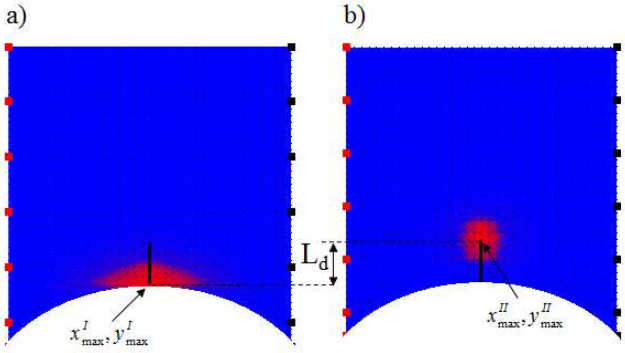


**Figure 11.** The damage detection algorithm results a) detection of the crack initiation, b) analysis of the damage size.

The damage detection algorithm which analyze all of the wave propagation paths allow to detect the peak of the crack (figure 11b). The product of the DI value for particular paths indicates that maximal value of the damage index achieves the greatest value near the damage peak. Connection of the two parts of the analysis allow to determine the size of the detected crack by calculating the length between the points with the DI maximum value from the first and second part (Eq. 7).

$$L_d = \sqrt{(x^{II}_{\max} - x^{I}_{\max})^2 + (y^{II}_{\max} - y^{I}_{\max})^2} \tag{7}$$

$x^{I}_{\max}, y^{I}_{\max}$ - the position of the DI maximum value from the first part of analysis (figure 11a), $x^{II}_{\max}, y^{II}_{\max}$ - the position of the DI maximum value from the second part of analysis (figure 11b).

To verify the accuracy of the proposed damage detection system, the different crack length has been investigated. The numerical model of the three size of the defect (5mm, 10mm and 15mm) was introduced. The results of the second part of the damage detection algorithm are presented on figure 12.

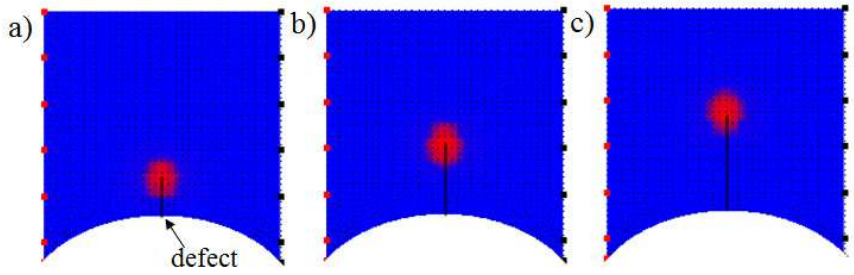


**Figure 12.** The damage detection algorithm results for the different size of the defect a) 5 mm, b) 10mm, c) 15mm.

As it can be seen, the analysis of the wave propagation path based on the described damage index definition allow to observe the evolution of the damage because the DI distribution determined after detection of the defect initiation indicates to the movement of the crack peak. The accuracy of the SHM system can be verified by comparison the modelled and detected damage size (Table 2).

Table 2. Comparison of the modelled damage and detected damage size.

| Modelled damage length | Detected damage length ($L_d$) |
|---|---|
| 5 mm | 5.08 mm |
| 10 mm | 9.38 mm |
| 15 mm | 14.53 mm |

The good agreement between modelled and detected damage size confirm the accuracy of the damage detection algorithm. It is worth to point out that from practical application point of view indication of

the damage peak allow to observe the evolution of the fatigue crack. The periodical verification of the structure state by SHM system allow to observe the growth of the defect by periodical observation of the detected crack peaks. It is especially important in composite materials where the direction of the fatigue damage evolution depends on the configuration of the laminate layers.

## 5. Conclusion

In this research the wave propagation method has been used to design the SHM system for fatigue damage detection and identification localized near the hole in the structure. The proposed damage detection algorithm verified by finite element model calculation can be efficiently and successfully implemented not only to the fatigue crack detection but also for localization and even for the crack size assessment. The modular structure of the system allow to reduce the number of data which have to be analyzed by algorithm. Only two actuators in multipoint measuring system allow to detect and localize the fatigue crack initiation. After that the second module analyze full set of the measured data from each of the sensors to assess the current damage size and to observe the fatigue damage evolution. The efficiency of the proposed method has been verified for different crack size. Presented multipoint measuring system contained 14 sensors. The reasonable and accurate detection analysis requires the careful analysis of the measured data. The detailed analysis of the results demonstrates that the further studies are needed in order to verify proposed system in practical application. From practical point of view it is also interesting to analyze the optimal localization and number of the sensors in multipoint measuring system. The experimental verification of the numerical results will be presented in the feature research.

## Acknowledgments

The research project has been financed by National Science Center Poland pursuant to the decision No. DEC-2013/09/B/ST8/00178.

## References

[1] Staszewski, W., Boller, C., Tomlinson, G.: *Health Monitoring of Aerospace Structures*, John Wiley & Sons, Ltd., Chichester, 2004.

[2] Worden, K., Farrar, C.R., Manson, G., Park, G.: The fundamental axioms of structural health monitoring, *Proc. R. Soc. A* 464 (2007), pp. 1639-1664.

[3] Gopalakrishnan, S., Ruzzene, M., Hanagud S.: *Computational Techniques for Structural Health Monitoring*, Springer, London, 2011.

[4] Fatemi, A., Gates, N., Socie, D.F., Phan, N.: Fatigue crack growth behavior of tubular aluminum specimens with a circular hole under axial and torsion loadings., *Engineering Fracture Mechanics* 123 (2014), pp. 137-147.

[5] Xiangqiao, Y., Baoliang, L.: Fatigue growth modelling of cracks emanating from a circular hole in infinite plate, *Meccanica* 47 (2012), pp. 221-233.

[6] Stawiarski, A., Muc, A., Kędziora, P.: Damage detection, localization and assessment in multilayered composite structure with delaminations, *Key Engineering Materials* 542 (2013), pp. 193-204.

[7] Muc, A., Stawiarski, A.: Identification of damages in composite multilayered cylindrical panels with delaminations, *Composite Structures* 94 (2012), pp. 1871-1879.

[8] Muc, A., Stawiarski, A.: Wave propagation in composite multilayered structures with delaminations, *Mechanics of Composite Materials* 48(1), (2012), pp. 101-106.

[9] Okabe, Y., Nakayama, F.: Damage detection in CFRP laminates by ultrasonic wave propagation using MFC actuator and FBG sensor, *Trans. Jpn. Soc. Aeronaut. Space Sci.*, 7, ists26 (2009), pp. Pc_7-Pc_12.

[10] Muc, A., Stawiarski, A.: Location of delaminations in curved laminated panels, *Composite* Structures 133, (2015), pp. 652-658

[11] Kostson, E., Fromme, P.: Fatigue crack growth monitoring in multi-layered structures using guided ultrasonic waves, *Journal of Physics: Conference Series* 195 (2009).

[12] Chang, Z., Mal, A.: Scattering of Lamb waves from a rivet hole with edge cracks, *Mechanics of Materials* 31 (1999), pp. 197-204.

[13] McKeon, J.C.P., Hinders, M.K.: Lamb wave scattering from a through hole, *Journal of Sound and Vibration* 224 (1999), pp. 843-862.

[14] Carden, P.E., Fanning, P.: Vibration based condition monitoring: a review, *Struct. Health. Monit.* 3 (2004), pp. 355-377.

[15] Adams, D.E.: *Health Monitoring of Structural Materials and Components, Methods and Applications*, John Willey & Sons Ltd., Chichester, 2007.

[16] Kessler, S.S.: *Piezoelectric-based in-situ damage detection of composite materials for structural health monitoring systems*, Ph.D. thesis, Massachusetts Institute of Technology, 2002, S. Mark Spearing.

[17] Giurgiutiu, V.: *Structural Health Monitoring with Piezoelectric Wafer Active Sensors*, Elsevier Inc., 2008.

[18] Hong, M., Zhongqing, S., Lu, S., Sohn, H., Qing, X.: Locating fatigue damage using temporal signal features of nonlinear Lamb waves, *Mechanical Systems and Signal Processing* 60-61 (2015), pp. 182-197.

Adam Stawiarski, Ph.D.: Cracow University of Technology/ Faculty of Mechanical Engineering /Institute of Machine Design, al. Jana Pawła II 37, 31-864 Kraków, Poland (asta@mech.pk.edu.pl) The author gave a presentation of this paper during one of the conference sessions.

Marek Barski, PhD: Cracow University of Technology/ Faculty of Mechanical Engineering/ Institute of Machine Design, al. Jana Pawła II 37, 31-864 Kraków, Poland (*mbar@mech.pk.edu.pl*).

Piotr Pająk M.Sc. (Ph.D. student): Cracow University of Technology/ Faculty of Mechanical Engineering/ Institute of Machine Design, al. Jana Pawła II 37, 31-864 Kraków, Poland (*ppajak@mech.pk.edu.pl*).

# Analysis of critical damping in dynamic relaxation method for reinforced concrete structural elements (NUM113-15)

Anna Szcześniak, Adam Stolarski

*Abstract:* In the paper, we presented an analysis of critical damping to describe the behavior of reinforced concrete structural elements using the dynamic relaxation method with arc-length parameter. In this method, we can reduce the problem to analysis of a pseudo-dynamic process by considering critical damping as an aperiodic motion that approaches the equilibrium state under the acting load. The solution to this problem can be obtained using an iterative process with pseudo-time steps. In the paper we presented an analysis of critical damping for beam and eccentrically loaded column. When analyzing the beam, we considered two types of critical damping that were the results of either bending or shear forces on the structural element. We considered the frequencies of the bending and rotational vibrations. For the damping factor of the transverse displacements, we applied a viscous resistance for bending vibrations, whereas for the damping factor of the rotations (*i.e.* the average rotation angles of the cross-section), we used a viscous resistance for the rotational vibrations. In analysis of critical damping for column, we defined viscous resistance coefficient for the rigidity of the structural system that was determined using the largest stiffness value. To this aim, we analyzed the flexural stiffness of the column, and the longitudinal column stiffness. Analyzing a dynamic process of the beam and column, after applying critical damping, we used the dynamic relaxation method to track the static behavior of the inelastic reinforced concrete structural elements.

## 1. Introduction

In this paper, we present an analysis of critical damping to describe the effort processes of reinforced concrete bent and eccentrically compressed structural elements with use the dynamic relaxation method. This method allows us to analysis of the static behavior of a physically and geometrically nonlinear structural element, which was described by system of dynamic equilibrium equations after applying the critical damping. This damping is a particular value of the damping coefficient related to the displacement velocity in the equation of motion that allows describing the aperiodic motion. To increase the effectiveness of analysis in post-critical range, we included the arc-length parameter built into the solution method in the form of additional constraint equation.

We carried out an analysis of critical damping for reinforced concrete beam that was tested experimentally by Buckhouse [1] and an eccentrically compressed reinforced concrete column that was tested experimentally by Lloyd and Rangan [3]. To verify the accuracy of the proposed solutions,

we compared the results of our numerical studies with the results of experimental, analytical, and theoretical works from the existing literature.

## 2. Method of analysis

For purposes of the analysis, we developed the general computational model of reinforced concrete structural element. We modeled the element using a system of plane bars which is statically loaded with a short-term longitudinal force, bending moment, uniformly distributed load, and concentrated forces acting on the plane perpendicular to the longitudinal axis of the element. Depending on considered case, *i.e.* bent beam or eccentrically compressed column, the computational model was reduced to the less complex models.

This model of structural element considers specific geometrical factors: the variable cross-sectional distribution of concrete and reinforcing steel areas, the initial curvature, and the boundary conditions that result from the support and external load.

The structural element is modeled as a reinforced concrete bar element characterized by the unit mass, the unit mass of inertia, and the unit damping coefficients for the displacements ($c$) and rotations ($c_f$). Moreover, we took into account the linear geometrical relationships that relate to the longitudinal deformation of the central axis, to the change of the average rotation angle in the cross-section, and to the average non-dilatational strain angle. The equilibrium equations of the cross-section we developed under the assumption of layered computational model of the cross-section. The computational cross-section model is dependent on models of the deformation of concrete and steel, and on a kinematic hypothesis of the plane cross-section. For the reinforcing steel we used an elastic–plastic material model with hardening. To describe the behavior of concrete, the elastic–plastic material model was developed by considering the stress softening and degradation of the deformation modulus. In the models of structural materials we considered the reduced plane stress state for compression/tension with shear.

The basic system of equations is presented in differential form, on the basis of the proposed discretization of the computational model. In the proposed model, we divide the element into the inner and the boundary nodes. The internal nodes contain the main nodes (odd), which correspond to the basic division points, and the intermediate nodes (even), which correspond to the line segments that join the basic division points. The system of equations describes the dynamic inelastic behavior of a reinforced concrete element. We solve it using critical damping for displacements $c = \max(c_{i,cr})$ and rotations $c_f = \max(c_{fi,cr})$, which allows us to describe the static problem as the limiting transition. This method is called the dynamic relaxation method.

The basic system of equations of motion presented in matrix form becomes:

$$\Delta\mathbf{q}^n = \Delta\mathbf{q}_G^n + \Delta\lambda^n \Delta\mathbf{q}_P^n \tag{1}$$

where: $\Delta\mathbf{q}^n = \left(\Delta u_i^n, \Delta w_i^n, \Delta\varphi_{i1}^n\right)^T$ - is a vector of searched displacement increments,

$$\Delta\mathbf{q}_P^n = \begin{cases} a_i P_x(s_i) \\ a_i P_z(s_i) \\ a_{fi}[M_{i_{b1}}\delta(x_i - x_{i_{b1}}) + M_{i_{bI}}\delta(x_i - x_{i_{bI}})] \end{cases}$$ - is a vector of components of the displacement increments for the total load, $\delta(x_i - x_{i_{b1}})$, $\delta(x_i - x_{i_{bI}})$ - is the Dirac delta functions,

$$\Delta\mathbf{q}_G^n = \begin{Bmatrix} b_i \Delta u_i^{n-1} + a_i[-N_{i1}\cos\theta_{i1} + N_{i0}\cos\theta_{i0} + Q_{i1}\sin\theta_{i1} - Q_{i0}\sin\theta_{i0}] \\ b_i \Delta w_i^{n-1} + a_i[N_{i1}\sin\theta_{i1} - N_{i0}\sin\theta_{i0} + Q_{i1}\cos\theta_{i1} - Q_{i0}\cos\theta_{i0}] \\ b_{fi}\Delta\varphi_i^{n-1} + a_{fi}(M_{i+2} - M_i - Q_{i1}\Delta s_{i1}) \end{Bmatrix} + \lambda^{n-1}\Delta\mathbf{q}_P^n$$ - is a vector of components of the displacement increments for the load parameter $\lambda^{n-1}$ from the previous time step, $i1 = i+1$ and $i0 = i-1$ represent the segments of the internal spatial division, $N_{i1}$ and $Q_{i1}$ - are the longitudinal and transverse forces in segment division $i1$, $M_i$ - is the bending moment in main node $i$, $m(s_i)$- is lumped mass of main node $i$, $P_x(s_i)$, $P_z(s_i)$ - are components of the load in node $i$, respectively longitudinal and transverse, $u_i, w_i$ - are the linear displacements in node $i$, respectively longitudinal and transverse, $\varphi_{i1}$ - is the rotation of the segment division $i1$, $\Delta s_{i1}$ - is the lenght of the segment division, $\sin\theta_{i0}$, $\cos\theta_{i0}$ - are functions of the rotation angles of the segment division $i0$, $b_i = \dfrac{m_i}{m_i + C_i\Delta t}$, $a_i = \dfrac{\Delta t^2}{m_i + C_i\Delta t}$, $b_{fi} = \dfrac{j_i}{j_i + C_{fi}\Delta t}$, $a_{fi} = \dfrac{\Delta t^2}{j_i + C_{fi}\Delta t}$ - are coefficients of the equilibrium equations, $C(s_i)$- is the damping factor for displacements in main node $i$, $C_f(s_{i1})$- is the damping factor for the rotations of the segment division $i1$.

To increase the effectiveness of this technique for the post-critical analysis we applied the method of solution path tracking for multiple variables [5, 6] to the solution of the system of dynamic nonlinear equilibrium equations (1). The general idea of this method is to incorporate the additional constraints equation (2) that links the load parameter and the vector of displacement increments with the arc length increment on the solution path to the equations of motion (1):

$$f(\mathbf{q}, \lambda) = \Delta\mathbf{q}_m^T \Delta\mathbf{q}_m + \Delta\lambda_m^2 - \Delta l^2 = 0, \tag{2}$$

where: $\Delta l$ - is the increment of the arc length on the solution path, $\mathbf{q} = (u, w, \varphi)^T$ - is a vector of the searched displacements, $\Delta\lambda_m = \lambda^n - \lambda_m$ - is the increment of the current load parameter $\lambda^n$ and $\Delta\mathbf{q}_m = \mathbf{q}^n - \mathbf{q}_m$ - is the increment of the current vector of unknown displacements $\mathbf{q}^n$ in relation to the last convergent values of the load parameter $\lambda_m$ and displacement vector $\mathbf{q}_m$, obtained with the assumed accuracy in the previous load step *m*.

## 3. Analysis of the beam with critical damping

We investigated a C1 type beam that was tested experimentally by Buckhouse, [1, 2]. We analyzed a single-span, simply supported beam with a rectangular cross-section (see Fig. 1). The load on the beam forms two concentrated forces which are applied in 152 cm distance from each edge of the beam. Span of the beam is equal 456 cm, and dimensions of the cross section are equal: width $b = 25.8\,cm$, height $h = 46.4\,cm$.

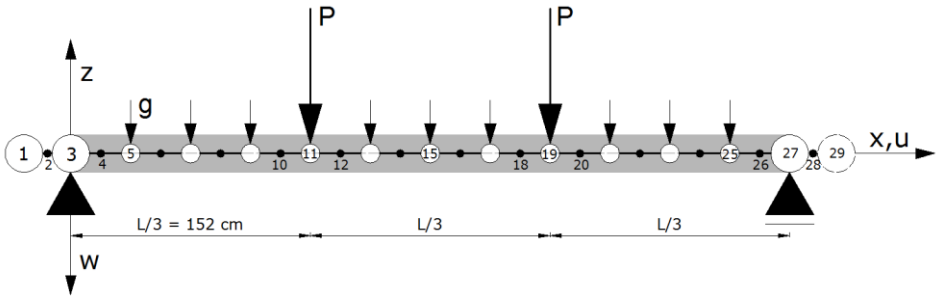


**Figure 1.** Computational model of the beam C1

The beam is reinforced by three $\phi 16$ -mm bars, and the transverse reinforcement is from stirrups made with $\phi 3$ -mm bars. Stirrups are arranged at a spacing equal 19 cm at the edge zone, and 30.4 cm at the mid-span zone. The beam is made from concrete with a compressive strength equal $f_c = 32.9\,MPa$, and reinforced steel with the yield stress for compression and tension equal $f_y = 473.26\,MPa$. In analysis of the beam we omitted the influence of longitudinal forces on displacements of the element.

Figure 2 presents the transversal displacements in the mid-span of the C1 beam in node 15 as the load function. The numerical results for the beam, using the dynamic relaxation method with the arc-length parameter (DRM+AL) after applying a critical damping we compared with Buckhouse's experimental results and theoretical results taken from the literature.

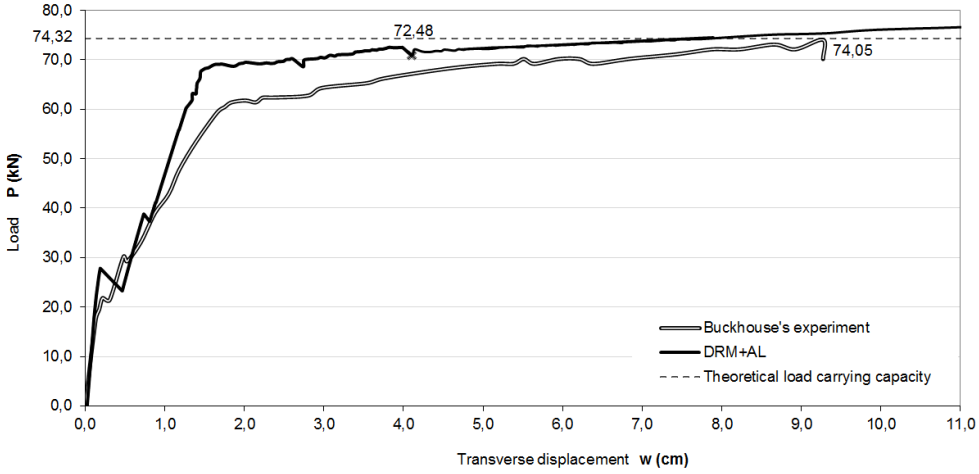


**Figure 2.** The numerical results for node 15 of the C1 beam, compared with experimental and theoretical results

Analyzing a dynamic process of the beam, after applying critical damping, we used the dynamic relaxation method to track the static behavior of the structural element. When analyzing the beam, we considered two types of critical damping that were the results of either bending or shear forces on the structural element. We considered the frequencies of the bending and rotational vibrations [4]. For the damping factor of the transverse displacements, we applied a viscous resistance for bending vibrations of $c_{i,cr}$, whereas for the damping factor of the rotations (*i.e.* the average rotation angles of the cross-section), we used a viscous resistance for the rotational vibrations of $c_{fi,cr}$.

The frequency of bending vibrations was determined using $\omega_o = \sqrt{\frac{K}{m_i}} = \sqrt{\frac{648}{23}\frac{E_c J_{cs}}{m_i l^3}}$, where $K = \frac{648}{23}\frac{EJ}{l^3}$ is the rigidity of the beam in the elastic range, determined using the maximum transverse displacement, which occurs in the mid-span of the beam.

The frequency of the rotational vibrations was determined using [4] $\omega_{of} = \sqrt{\frac{K_f}{J_{m,i}}} = \sqrt{\frac{27E_c J_{cs}}{m_i l^3}}$, where $K_f = \frac{3E_c J_{cs}}{l}$ is the rotational rigidity, determined using the maximum rotation value (which occurs near the support of the beam); and $J_{m,i} = \frac{m_i l^2}{9}$ is the moment of mass inertia.

In the elastic phase, the critical damping value causes displacements that are fixed on the level corresponding to the equilibrium position of the undamped vibrations.

Figure 3 shows the transverse displacement as a function of pseudo-time, for the elastic range of the beam deformation and the load $P = 7.4kN$ (which corresponds to $\sim 10\%$ of the load-carrying capacity) with the pseudo-time step $\Delta t = 4.74 \cdot 10^{-5} s$. We observed the transverse displacement of node 15 (located in the middle of the span of the beam). The beam vibrations without damping are shown by a thin solid line, and the bold solid line represents the vibrations with critical damping. The damped vibrations exactly coincide with the equilibrium position for the undamped vibrations.

Figure 4 displays the maximum rotation observed at node 4 (which was near the edge). The critical damping allows us to determine the rotation value that corresponds to the equilibrium state of the undamped vibrations. In the inelastic range for the structural element, the critical value of the damping can reduce the displacements. In this case, the transverse displacements and the rotations determined for the critical damping are smaller than the displacements that correspond to the equilibrium state of the undamped vibrations.

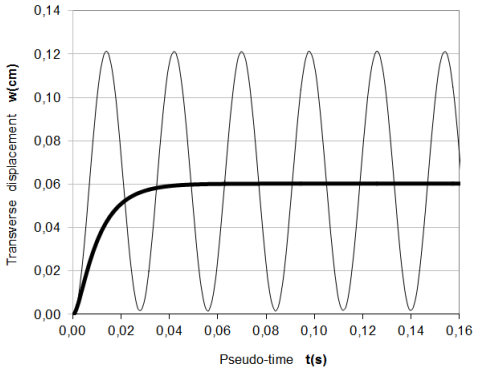


**Figure 3.** Transverse displacement of node 15 vs. pseudo-time, $P = 7.4kN$

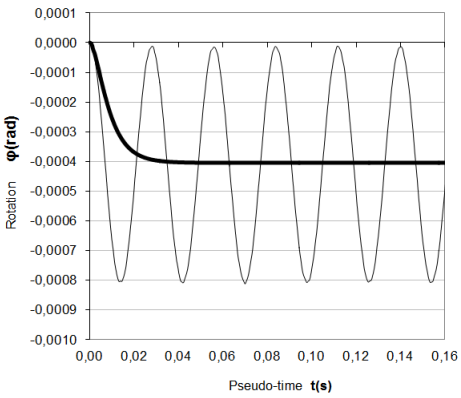


**Figure 4.** Rotations of node 4 vs. pseudo-time, $P = 7.4kN$

Figure 5 shows the transverse displacement as a function of pseudo-time, observed in the mid-span of the beam for load value $P = 38.0kN$. The load is $\sim 50\%$ of the load-carrying capacity of the beam. The damped vibrations are marked by a solid line, and show $38\%$ less displacement than for the equilibrium state of the undamped vibrations.

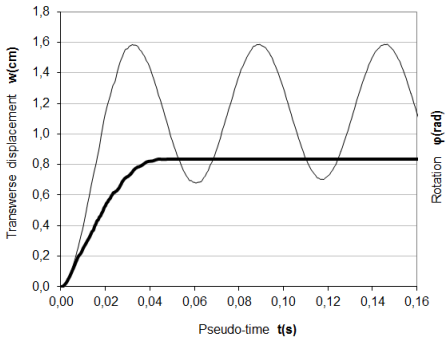


**Figure 5.** Transverse displacement of node 15 vs. pseudo-time, $P = 38.0kN$

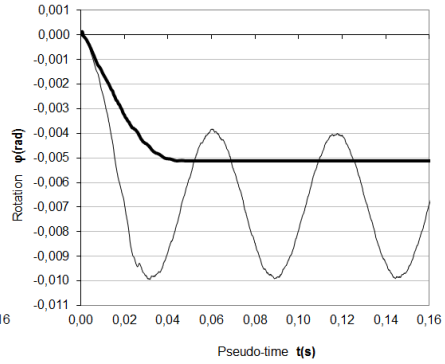


**Figure 6.** Rotations of node 4 vs. pseudo-time, $P = 38.0kN$

Figure 6 show the rotations observed for intermediate node 4. The rotation determined after introducing critical damping is 54% of the rotation value corresponding to the equilibrium state of the undamped vibration. As the inelastic effort range of the structural element increased, we observed an increase in the undamped oscillation period, which is equivalent to decreasing the frequency. This phenomenon is in part dependent on a reduction in the system's stiffness. Because the critical damping factor is determined for the elastic effort range of the beam, it causes overcritical damping of the vibration in the inelastic range.

In [6], the author noted a utility of a reduction in the critical damping in analyses performed using the dynamic relaxation method for the inelastic range of the structure. In this study of a reinforced concrete beam, we introduced a critical damping that is the same in all stages of the deformation process. The critical damping value was represented by the damping factors (*i.e.* the viscous resistance $c_{i,cr}$, $c_{fi,cr}$), which were determined using the elastic stiffness of the beam.

## 4. Analysis of the column with critical damping

We applied our numerical method to the column that was investigated in experimental studies by Lloyd and Rangan [3], which they denoted as IB (see Fig. 7). Length of column is equal 168 cm. It is loaded by two longitudinal forces which were applied at the both ends of column with constant eccentricity The column has constant, square cross-section, which dimensions are equal 17.5 cm.

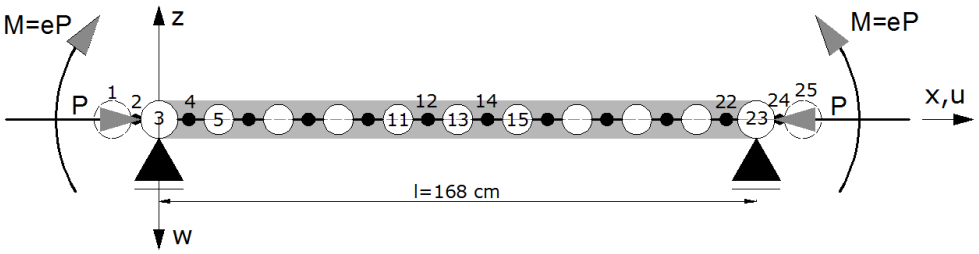


**Figure 7.** Computational model of the column IB

The column is doubly reinforced with three $\phi 12$ -mm bars in each layer. The column is made from concrete with a compressive strength equal $f_c = 44.78\ MPa$, and reinforced steel with the yield stress for compression and tension equal $f_y = 430.0\ MPa$. Analysis of the column IB was conducted on the basis of the reduced form of the computational method described in chapter 2. The reduction involves treating the lateral force as a passive force $Q = \frac{\partial M}{\partial x}$. Consequently, it causes the omitting in the description of geometric relationships, the influence of the average non-dilatational strain angle, which is assumed to be $\gamma = 0$.

Figure 8 presents the transversal displacements in the mid-span of the IB column in node 13 as the load function. The numerical results for the IB column, using the dynamic relaxation method with the arc-length parameter (DRM+AL) after applying a critical damping, we compared with experimental and theoretical results conducted by Loyd - Rangan.

We analyzed the column using the dynamic relaxation method and a critical damping factor (viscous resistance coefficient), defined as $c_{i,cr} = 2\sqrt{m_i \cdot K}$. The rigidity of the structural system was determined using the largest stiffness value. That is, $K = \max\{K_z, K_x\}$, where $K_z = 42\frac{E_c J_{cs}}{l^3}$ is the flexural stiffness of the column, and $K_x = \frac{E_c A_{cs}}{l}$ is the longitudinal column stiffness.

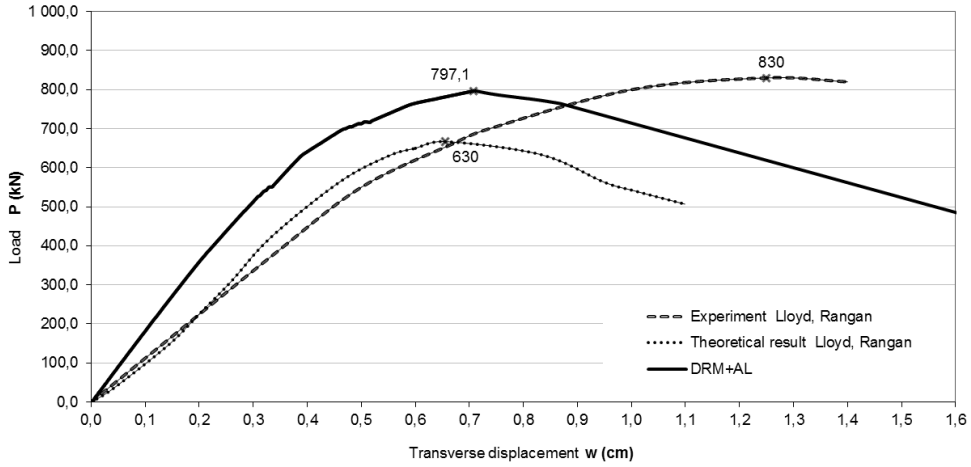


**Figure 8.** The numerical results for node 13 of the IB column, compared with experimental and theoretical results

In the following figures, we illustrated the influence of damping on the vibration of the IB column in the elastic state, for the load value $P = 58.0\,kN$, which corresponds to approximately 7.3% of the load-carrying capacity of the column and with the pseudo-time step of $\Delta t = 3.97 \cdot 10^{-5}\,s$.

Figure 9 shows the results for the transverse displacements of the cross-section located in the mid-span of the column. The thin solid line shows the progress of the undamped vibrations, and the bold solid line shows the displacement after taking into account the critical damping. By introducing the critical damping, we can achieve a limit equilibrium for the damped motion of the transverse displacements in node 13, which corresponds to the equilibrium position of the undamped vibrations of the structural element.

Figure 10 shows the influence of critical damping on the progress function of the longitudinal displacement in node 3. We tested edge node 3, because it had the largest longitudinal displacement. This diagram plots the longitudinal displacement as a function of pseudo-time, after taking into account the critical damping that exactly corresponds to the equilibrium position of the adapted undamped vibrations.

In the inelastic range of the column (as in the case of the beam), we observed smaller displacements for the equilibrium of the aperiodic damped motion, when compared with the equilibrium position for adapted undamped vibrations.

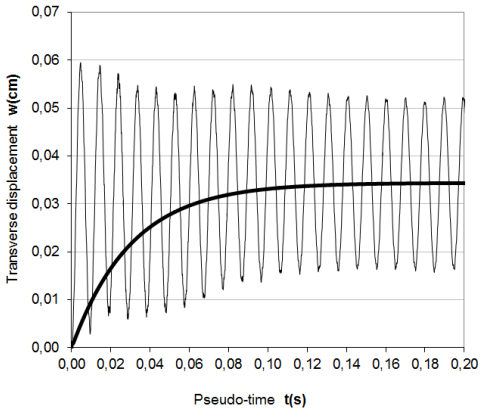


**Figure 9.** Transverse displacement at node 13 vs. pseudo-time, $P = 58.0\,kN$

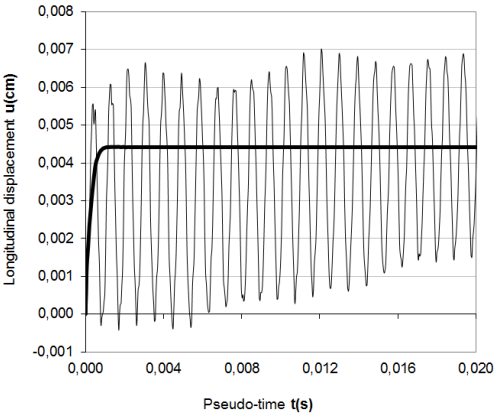


**Figure 10.** Longitudinal displacement at node 3 vs. pseudo-time, $P = 58.0\,kN$

Figure 11 shows the vibration waveform with regard to the critical value of the damping coefficient, compared with the undamped vibrations. We considered the cross-section at node 13 (in the mid-span of the column), for a load of $P = 400.0\,kN$ (which represents approximately 50% of the load-carrying capacity of the column). There was a 33% difference between the transverse displacements that correspond to the equilibrium position of the undamped vibrations and the displacements in aperiodic motion with the critical damping value.

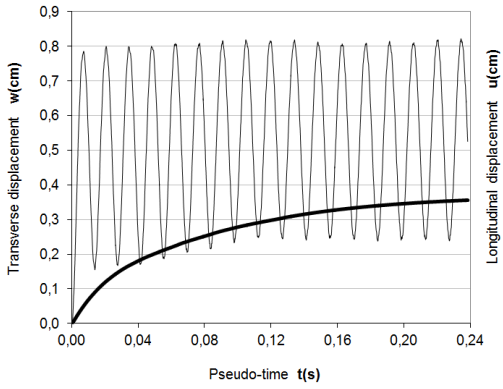


**Figure 11**. Transverse displacement at node 13 vs. pseudo-time, $P = 400.0\,kN$

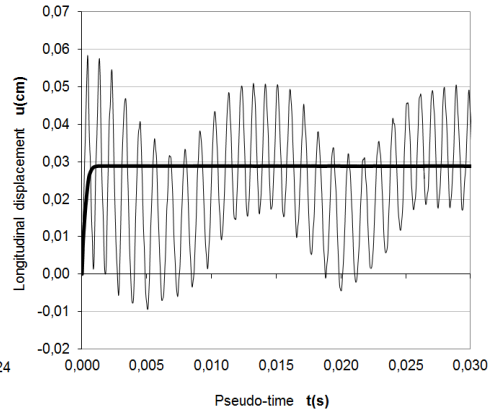


**Figure 12.** Longitudinal displacement at node 3 vs. pseudo-time, $P = 400.0\,kN$

Figure 12 shows a diagram of the longitudinal displacements at node 3 as a function of pseudo-time, for the inelastic range. The longitudinal displacement determined after applying critical damping was 14% larger than the equilibrium position of the undamped vibrations.

## 5. Conclusions

On the basis of our comparison of the results using different methods, we can conclude that the results obtained using critical damping, estimates the lower limit of displacements of the structural element. However, the displacements obtained by analyzing the equilibrium state of the undamped vibrations can be treated as an estimation of the upper limit of displacements of the structural element. Obtained in this way, the estimated limits of the displacements indicate the range of possible solutions.

By introducing the variable factor that reduces the damping value depending on the inelastic effort of the structural element, we can determine a solution that is within the specified range of possible solutions, with even higher accuracy.

The transverse displacements from the damped vibrations reduced when the inelastic effort of the column increased. This is similar to the process observed for the beam. The reduction was slightly smaller for the column, because bending was less prominent process and there was a smaller reduction of the flexural stiffness. We can estimate an acceptable area for the two limiting solutions for the equilibrium position of the undamped vibration and the equilibrium of the damped motion with critical damping. This is smaller for the column than the beam. The damping value can adapt to nonlinear changes of the flexural element stiffness using the reducing factor. For the column, this could increase the transverse displacements in successive phases of the nonlinear effort. However, for the longitudinal displacements, critical damping in the inelastic phase results in a larger observed value for the displacement than from the equilibrium position of the undamped vibrations. This phenomenon is caused by increases to the local stiffness, which are because the structural member becomes shorter. This phenomenon is most pronounced at the edge nodes, which have the greatest longitudinal displacements and associated shortening. The phenomenon declines in the internal nodes. When introduced into analyses of longitudinal displacements, a separate damping factor that considers the specificity of the longitudinal stiffness variations would allow for a slight decrease of the longitudinal displacements, mainly in the edge nodes.

**References**

[1] Buckhouse E. R. External Flexural Reinforcement of Existing Reinforced Concrete Beams Using Bolted Steel Channnels. Marquette University, Milwaukee, Wisconsin. 1997.

[2] Foley C. M., Buckhouse E. R. Strengthening Existing Reinforced Concrete Beams for Flexure Using Bolted External Structural Steel Channels. Structural Engineering Report MUST-98-1, Marquette University, Milwaukee, Wisconsin, 1998.

[3] Lloyd N. A., Rangan B. V. Studies on High-Strength Concrete Columns under Eccentric Compression. ACI Structural Journal, Technical Paper, t. no. 93-S59. November-December 1996, 631-638.

[4] Timoshenko S. P., Young D. H., Weaver W. Jr. Vibration problems in engineering. John Wiley & Sons. New York 1974.

[5] Waszczyszyn Z., Cichoń Cz., Radwańska M. Finite elements method in stability of structure. Arkady, Warsaw, Poland, 1990, in Polish.

[6] Wriggers P. Nonlinear Finite Element Methods. Springer, 2008.

Adam Stolarski, Professor: Military University of Technology, Faculty of Civil Engineering and Geodesy, 2 Kaliskiego Street, 00-908 Warsaw-49, Poland (adam.stolarski@wat.edu.pl).

Anna Szcześniak, Ph. D. Assistant Professor: Military University of Technology, Faculty of Civil Engineering and Geodesy, 2 Kaliskiego Street, 00-908 Warsaw-49, Poland (anna.szczesniak@wat.edu.pl).

# Dynamics simulations of a rigid body lying on a vibrating table with the use of special approximations of the resulting contact forces (MAT203-15)

Michał Szewc, Igor Wojtunik, Grzegorz Kudra, Jan Awrejcewicz

*Abstract:* The work presents simulations and dynamics of a rigid body lying on a vibrating table. An attempt of shaping and control the body dynamical behavior, by the use of manipulation of parameters of the table oscillations, is presented. This work is also an implementation of the specially prepared mathematical models of friction between table and the moving body. Those models are based on the integral model assuming the fully developed sliding on the plane contact area with the foundation of any pressure distribution. In order to simplify the calculations and reduce their computational cost, special approximations of the integral models of friction force and moment are used. They are based on Padé approximants and their generalizations.

## 1. Introduction

The examination of systems with friction forces resulting between contacting bodies is significant part of theoretical and applied mechanics. It has been investigated by scientists for years forming the separate branch of mechanics called tribology. Theoretical foundations analyzed in tribology focus mostly on stationary or periodical parts of motion. However, in mechanics one can encounter many examples, including the motion of bodies with friction, which shows that the transient stages between rolling and sliding can be a crucial part of analysis. The other problem in describing the system consisting of two contacting bodies with the dry friction forces is the normal pressure distribution over the contact area. The above mentioned difficulties can occur in daily life examples like the dynamics of billiard ball moving on the flat table, curling rocks, bowling ball, Celtic stone, rolling bearing and many others issues related to robotics. Many theoretical studies on such dynamical processes have been developed. In most cases they are based on simple static models of the static laws of Coulomb dry friction. Systems with Coulomb dry friction can behave interestingly in the instances of transition from sliding to rolling. However, the shape and size of the contact area may be the most important factor, which influence the global dynamics of the body. With the assumption that the flat base is deformed by the contacting body using the Hooke's law, MacMillan [1] described the normal pressure distribution as a linear function. He used the elliptic integrals to describe the friction forces and torque in the case of the circular contact area. Contensou in 1962 [2] has presented the paper in which he assumes fully developed sliding and the classical Coulomb law of frictions forces with the plane circular contact area. Applying the Hertzian contact distribution, Contensou showed

the integral model of the resultant contact forces. Basing on the Contensou results, Zhuravlev [3] developed his theory and showed exact analytical functions, which defines the frictions forces and torque and he proposed special approximations on the basis of Padé approximations. Those models are much more suitable for the cases in which the relation between the sliding direction and the resultant friction components is considered. The dynamics of the motion of disk on a flat table was analyzed by Borisov et. al [8]. Kireenkov in [9] has proposed the model of rolling resistance, based on Padé approximations of resultant friction force and moment. He used the special contact pressure distribution on a circular contact area. In [4,5] authors presented the generalization of the models based on Padé approximants as the family of approximant models of friction forces. Application of the proposed models was considered in [6,7].

This work is the implementation of the proposed models of friction force and moment in the case of a rigid body lying on the vibrating table. By manipulation of the table oscillations' parameters we shape and control the behavior of the moving body. Proposed models assume the fully developed sliding on the plane contact area with any pressure distribution. To reduce the computational cost of the equations we propose the simplifications of the model as well.

## 2. Modeling of contact forces

This part of the paper is thoroughly described in work [5] and for the purpose of this study we present the most important parts, which are necessary to understand the theoretical foundations of the problem. We consider the dimensionless form of plane, circular contact area F, with the Cartesian coordinate system Axyz., where x and y axes lie in the contact plane. We define the dimensionless length as the quotient of the actual length and the radius of real contact $\hat{a}$. Point situated on the contact area F has the dimensionless coordinates $x = \hat{x}/\hat{a}$ and $y = \hat{y}/\hat{a}$. The following form of the non-dimensional contact pressure distribution is further assumed:

$$\sigma(x,y) = \hat{\sigma}(x,y)\frac{\hat{a}^2}{\hat{N}} = \frac{3}{2\pi}\sqrt{1-x^2-y^2}\left(1+d_c x + d_s y\right), \tag{1}$$

where:

$$d_c = d\cos\gamma = d\frac{v_{rx}}{\sqrt{v_{rx}^2+v_{ry}^2}} \text{ and } d_s = d\sin\gamma = d\frac{v_{ry}}{\sqrt{v_{rx}^2+v_{ry}^2}}. \tag{2}$$

In above expressions (Eq.1-2) $\hat{\sigma}(x,y)$ is the real contact pressure, $\hat{N}$ - normal component of the real resultant force, $d$ – rolling resistance parameter, $\gamma$ - angle describing direction of rolling. The

variables $v_{rx}$ and $v_{ry}$ are the components of the non-dimensional "rolling velocity" $\mathbf{v}_r = \hat{\mathbf{v}}_r / \hat{a} =$ $= v_{rx}\mathbf{e}_x + v_{ry}\mathbf{e}_y$ ( $\hat{\mathbf{v}}_r$ is the corresponding real vector, $\mathbf{e}_i$ is unit vector of i axis). Proposed model of contact pressure distribution (Eq. 1) is the modification of Hertzian stress distribution, with the assumption that the center of pressure distribution does not coincide with the geometrical center A. Due to this assumption, we can implement the non-dimensional rolling resistance:

$$\mathbf{M}_r = \mathbf{f} \times \mathbf{e}_z = y_S \mathbf{e}_x - x_S \mathbf{e}_y = M_{rx}\mathbf{e}_x + M_{ry}\mathbf{e}_y, \tag{3}$$

where:

$$M_{rx} = \frac{1}{5} d_s, \; M_{ry} = -\frac{1}{5} d_c. \tag{4}$$

In above expression (Eq. 3) $\mathbf{f} = \overrightarrow{AS} = x_S \mathbf{e}_x + y_S \mathbf{e}_y$ is a vector denoting the position of center of non-dimensional pressure distribution S. The real counterpart of rolling resistance can be calculated as $\hat{\mathbf{M}}_r = \hat{a}\hat{N}\mathbf{M}_r$. The assumption of fully developed sliding on the contact area F is made. We consider that the deformations of moving bodies are small enough to describe the relative motion as a plane motion of rigid bodies. As the result the motion is described by the following dimensionless linear sliding velocity in centre A: $\mathbf{v}_S = \hat{\mathbf{v}}_S / \hat{a} = v_{sx}\mathbf{e}_x + v_{sy}\mathbf{e}_y$, and the angular sliding velocity: $\mathbf{v}_S = \hat{\mathbf{v}}_S / \hat{a} = v_{sx}\mathbf{e}_x + v_{sy}\mathbf{e}_y$, where $\hat{\mathbf{v}}_S$ and $\hat{\boldsymbol{\omega}}_S$ denote the corresponding real counterparts and $\mathbf{e}_x$, $\mathbf{e}_y$ and $\mathbf{e}_z$ are the unit vectors of the corresponding axes. We apply the Coulomb friction law on each element *dF* of the area F:

$$d\mathbf{T}_S = d\hat{\mathbf{T}}_S / (\mu \hat{N}) = -\sigma(x, y)\, dF\, \mathbf{v}_P / \|\mathbf{v}_P\|, \tag{5}$$

where $d\mathbf{T}_S$ and $d\hat{\mathbf{T}}_S$ are elementary non-dimensional friction force and its real counterpart respectively. $\mathbf{v}_P$ is the local dimensionless velocity of sliding and $\mu$ - dry friction coefficient.

The moment of the friction force $d\mathbf{T}_S$ about the centre *A* of the contact is described as follows:

$$d\mathbf{M}_S = \boldsymbol{\rho} \times d\mathbf{T}_S = d\hat{\mathbf{M}}_S / (\hat{a}\, \mu \hat{N}), \tag{6}$$

where $d\hat{\mathbf{M}}_S$ is the corresponding real moment. Summing up the elementary friction forces $d\mathbf{T}$ and moments $d\mathbf{M}$ we get the total friction force **T** acting in the point *A* and moment **M**. The resulting integral expressions may possess the singularities in the case of lack of the relative motion. Therefore,

we use a small numerical parameter $\varepsilon_t$ to the corresponding integral expressions to avoid above mentioned singularities. Finally we obtain:

$$T_{sx} = \iint\limits_F \sigma(x,y) \frac{\left(v_{sx} - \omega_s\, y\right)}{\sqrt{\left(v_{sx} - \omega_s\, y\right)^2 + \left(v_{sy} + \omega_s x\right)^2 + \varepsilon_t^2}}\, dxdy\,,$$

$$T_{sy} = \iint\limits_F \sigma(x,y) \frac{\left(v_{sy} + \omega_s x\right)}{\sqrt{\left(v_{sx} - \omega_s y\right)^2 + \left(v_{sy} + \omega_s x\right)^2 + \varepsilon_t^2}}\, dxdy\,, \qquad (7)$$

$$M_s = \iint\limits_F \sigma(x,y) \frac{\omega_s\left(x^2 + y^2\right) + v_{sy}x - v_{sx}y}{\sqrt{\left(v_{sx} - \omega_s y\right)^2 + \left(v_{sy} + \omega_s x\right)^2 + \varepsilon_t^2}}\, dxdy\,.$$

The real counterparts of the friction force and moment can be found as $\hat{\mathbf{T}}_s = \mu\hat{N}\,\mathbf{T}_s$ and $\hat{\mathbf{M}}_s = \hat{a}\mu\hat{N}\mathbf{M}_s$ respectively. The above mentioned expressions (Eq. 7) have the integrals over the contact area and for the numerical simulations they are very time consuming and may be inconvenient. Therefore, we propose the corresponding components of the integral model, basing on special modifications of Padé approximants:

$$T_{sx}^{(I)} = \frac{v_{sx} - b_T c_{0,1,1}^{(x,y)} \omega_s}{\sqrt{\left(\left|v_s\right|^{m_T} + b_T^{m_T}\left|\omega_s\right|^{m_T}\right)^{2m_T^{-1}} + \varepsilon_t^2}}\,,$$

$$T_{sy}^{(I)} = \frac{v_{sy} + b_T c_{1,0,1}^{(x,y)} \omega_s}{\sqrt{\left(\left|v_s\right|^{m_T} + b_T^{m_T}\left|\omega_s\right|^{m_T}\right)^{2m_T^{-1}} + \varepsilon_t^2}}\,, \qquad (8)$$

$$M_s^{(I)} = \frac{b_M c_{0,0,-1}^{(x,y)} \omega_s - c_{0,1,0}^{(x,y)} v_{sx} + c_{1,0,0}^{(x,y)} v_{sy}}{\sqrt{\left(b_M^{m_M}\left|\omega_s\right|^{m_M} + \left|v_s\right|^{m_M}\right)^{2m_M^{-1}} + \varepsilon_t^2}}\,,$$

where:

$$c_{i,j,k}^{(x,y)} = \iint_F x^i y^j \left(x^2 + y^2\right)^{-\frac{k}{2}} \sigma\left(x, y\right) dxdy\,. \tag{9}$$

Full set of relations and expressions can be found in the work [5].

Using the proposed model of contact pressure distribution (Eq. 1) we get:

$$c_{0,1,1}^{(x,y)} = \frac{3}{32}\pi d_s\,,\quad c_{1,0,1}^{(x,y)} = \frac{3}{32}\pi d_c\,,\quad c_{0,0,-1}^{(x,y)} = \frac{3}{16}\pi\,,\quad c_{0,1,0}^{(x,y)} = \frac{1}{5}d_s\,,\quad c_{1,0,0}^{(x,y)} = \frac{1}{5}d_c\,. \tag{10}$$

Model presented in (Eq. 8) has the constant parameters: $b_T$, $m_T$, $b_M$ and $m_M$, which can be found by the process of optimization of the approximate model to the integral components. Those parameters may be identified experimentally as well. For this work we propose the following objective functions:

$$F_T\left(b_T, m_T\right) = \int_D \left(\left(T_{sx} - T_{sx}^{(I)}\right)^2 + \left(T_{sy} - T_{sy}^{(I)}\right)^2\right) dD\,,$$

$$F_M\left(b_M, m_M\right) = \int_D \left(M_s - M_s^{(I)}\right)^2 dD\,, \tag{11}$$

where D is the representative area of model's kinematic parameters. Above expressions results in the following set of optimal parameters: $b_T = 0.771$, $m_T = 2.655$, $b_M = 0.419$ and $m_M = 3.073$.

Finally, using expressions (Eq. 10) and the simplified model (Eq.8) adding a small parameter to avoid singularities we get the following form of total friction force and moment:

$$T_{sx\varepsilon}^{(I)} = \frac{v_{sx} - \frac{3}{32}\pi b_T d_{s\varepsilon}\omega_s}{\sqrt{\left(\left|v_s\right|^{m_T} + b_T^{m_T}\left|\omega_s\right|^{m_T}\right)^{2m_T^{-1}} + \varepsilon_t^2}}\,,$$

$$T_{sy\varepsilon}^{(I)} = \frac{v_{sy} + \frac{3}{32}\pi b_T d_{c\varepsilon}\omega_s}{\sqrt{\left(\left|v_s\right|^{m_T} + b_T^{m_T}\left|\omega_s\right|^{m_T}\right)^{2m_T^{-1}} + \varepsilon_t^2}}\,, \tag{12}$$

$$M_{s\varepsilon}^{(I)} = \frac{\frac{3}{16}\pi b_M \omega_s - \frac{1}{5}d_{s\varepsilon}v_{sx} + \frac{1}{5}d_{c\varepsilon}v_{sy}}{\sqrt{\left(b_M^{m_M}\left|\omega_s\right|^{m_M} + \left|v_s\right|^{m_M}\right)^{2m_M^{-1}} + \varepsilon_t^2}}\,.$$

## 3. Modeling the rigid body on the vibration table

In this paper we propose the application of the friction model presented in (Eq.12) as the rigid body lying on the vibration table. Rigid body is assumed to be a ball (for example the billiard ball), situated on the table, which is allowed to make vibrations in x and y direction. Those vibrations have influence on the movement of the ball. We assume that the table can be rotated around x or y axis with angle α, which result in the external force $\mathbf{F}_g$ acting on the body. Model is presented in figure 1, where the following notation is used: $\mathbf{v}$ – velocity of the ball center *O*; $\hat{\mathbf{v}}_\mathbf{r}$ – linear rolling velocity; $\hat{\mathbf{v}}_\mathbf{s}$ - linear sliding velocity at the point *A;* $\hat{\boldsymbol{\omega}}_s$ – angular sliding velocity; $\hat{\mathbf{T}}_{s\varepsilon}$ – the resultant friction force acting at the contact center *A*; $\hat{\mathbf{N}} = \hat{N}\mathbf{e}_z$ - the normal reaction acting on the ball; $\hat{\mathbf{M}}_{s\varepsilon}$ – moment of friction forces; $\hat{\mathbf{M}}_{r\varepsilon}$ – moment of rolling resistance. It is assumed that a rigid ball rolls and slides over the vibration table, then: $\hat{\mathbf{v}}_\mathbf{r} = \mathbf{v}$ .

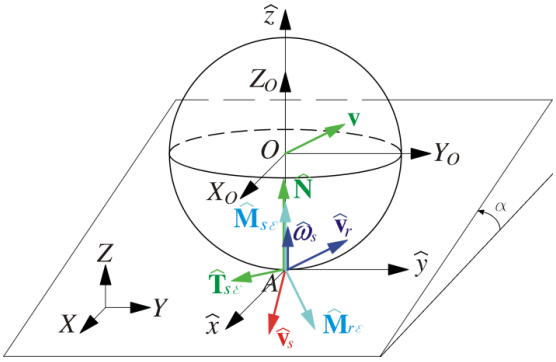


**Figure 1.** Rigid body and the vibration table contact area

The analyzed dynamical system has five degrees of freedom and is governed by the following set of differential equations:

$$m\frac{d\mathbf{v}}{dt} = \hat{\mathbf{T}}_{s\varepsilon} + \mathbf{F}_g\,, \quad \mathbf{B}\frac{d\boldsymbol{\omega}}{dt} = \mathbf{r}\times\hat{\mathbf{T}}_{s\varepsilon} + \hat{\mathbf{M}}_{s\varepsilon} + \hat{\mathbf{M}}_{r\varepsilon}\,, \tag{13}$$

where $\mathbf{r} = \overrightarrow{OA}$, m is the mass of the ball, **B** is a tensor of inertia in the mass center O. The matrix representation of the equation 13 can be presented as:

$$\mathbf{v} = \begin{bmatrix} v_x \\ v_y \\ v_z \end{bmatrix}, \quad \boldsymbol{\omega} = \begin{bmatrix} \omega_x \\ \omega_y \\ \omega_z \end{bmatrix}, \quad \mathbf{r} = \begin{bmatrix} 0 \\ 0 \\ -r \end{bmatrix}, \quad \hat{\mathbf{T}}_{s\varepsilon} = \mu mg\cos(\alpha)\begin{bmatrix} T_{sx\varepsilon} \\ T_{sy\varepsilon} \\ 0 \end{bmatrix}, \mathbf{F}_g = \begin{bmatrix} mg\sin(\alpha) \\ 0 \\ 0 \end{bmatrix},$$

$$\hat{\mathbf{M}}_{s\varepsilon} = \hat{a}\mu mg\cos(\alpha)\begin{bmatrix} 0 \\ 0 \\ M_{s\varepsilon} \end{bmatrix}, \quad \hat{\mathbf{M}}_{r\varepsilon} = \hat{a}mg\cos(\alpha)\begin{bmatrix} M_{rx\varepsilon} \\ M_{rx\varepsilon} \\ 0 \end{bmatrix}, \quad \mathbf{B} = \begin{bmatrix} B & 0 & 0 \\ 0 & B & 0 \\ 0 & 0 & B \end{bmatrix}, \tag{14}$$

with the assumption that ball is homogenous and $B=2/5mr^2$ is the central inertia moment of the body.

The dynamical system in the Cartesian coordinate system *Axyz* is represented by the two scalar differential equations for the linear motion:

$$\frac{dv_x}{dt} = -\mu g\cos(\alpha)T_{sx\varepsilon} + g\sin(\alpha), \ \frac{dv_y}{dt} = -\mu g\cos(\alpha)T_{sy\varepsilon}. \tag{15}$$

Since the permanent contact of the ball with the table is assumed, the third equation is $dv_z/dt = 0$. The angular motion of the billiard ball is governed by the following equations:

$$\frac{d\omega_x}{dt} = -\frac{5}{2}\frac{g\cos(\alpha)}{r}\left(\mu T_{sy\varepsilon} - \frac{1}{r}\hat{a}M_{rx\varepsilon}\right),$$

$$\frac{d\omega_y}{dt} = \frac{5}{2}\frac{g\cos(\alpha)}{r}\left(\mu T_{sx\varepsilon} + \frac{1}{r}\hat{a}M_{ry\varepsilon}\right), \ \frac{d\omega_z}{dt} = -\frac{5}{2}\frac{g\cos(\alpha)}{r^2}\hat{a}\mu M_{s\varepsilon}, \tag{16}$$

where: $r$ – radius of the ball; $v_x$, $v_y$ – the corresponding components of velocity of the ball center $O$; $\omega_x$, $\omega_y$, $\omega_z$ – components of angular velocity. In the global coordinate system XYZ presented in figure 2, $X_O$ and $Y_O$ denote the coordinates of the ball center O. To compute the absolute position of the ball center we use the following expressions:

$$\frac{dX_O}{dt} = v_x, \ \frac{dY_O}{dt} = v_y. \tag{17}$$

The following relations can be used for calculations of the arguments of the above presented models of friction, in the case of no vibrations of the table:

$$v_{sx} = \frac{v_x - r\omega_y}{\hat{a}}, \ v_{sy} = \frac{v_y + r\omega_x}{\hat{a}}, \ v_{rx} = \frac{v_x}{\hat{a}}, \ v_{ry} = \frac{v_y}{\hat{a}}. \tag{18}$$

Since, the rigid body is lying on the vibrating table we apply the vibrations to the dynamical system by changing the expressions (18). We add the vibration parameters to the sliding and rolling velocities of the ball as follows:

$$v_{sx} = \frac{v_x - r\omega_y + A_x\cos(\omega_a t)}{\hat{a}}, \quad v_{sy} = \frac{v_y + r\omega_x + \mathrm{A}_y\cos(\omega_b t + \varphi_y)}{\hat{a}},$$

$$v_{rx} = \frac{v_x + A_x \cos(\omega_a t)}{\hat{a}}, \quad v_{ry} = \frac{v_y + A_y \cos(\omega_b t + \varphi_y)}{\hat{a}}. \tag{19}$$

where $A_x$, $A_y$ are the amplitudes of the vibrations, $\omega_a$, $\omega_b$ are the angular frequencies and $\varphi_y$ is the phase of the oscillations in y direction.

The results of the simulations of the ball's motion are presented in figure 3. We use the model of friction forces (Eq. 12), changing the sliding velocity (Eq. 19) with the following parameters and initial conditions: $\hat{a} = 0.003\text{m}$, $\mu = 0.2$, $d = 1$, $\varepsilon_t = 0.01$, $\varepsilon_r = 0.01$, $g = 9.81\text{m/s}^2$, $r = 0.02m$, $m_T = 2.655$, $m_M = 3.073$, $b_T = 0.771$,, $b_M = 0.419$, $X_O(0) = 0$, $Y_O(0) = 0$, $\alpha_x(0) = 20$, $\alpha_y(0) = 0$, $\alpha_z(0) = 0$, $v_x(0) = 0$, $v_y(0) = 0.4$.For the simulations presented in figure 2 the following other parameters were used for the graph on the left: $A_x = 1$, $A_y = 0.5$, $\omega_a = 1000rad/s$, $\omega_b = 500rad/s$, $\varphi_y = 0$; and for the right graph: $A_x = 1000$, $A_y = 800$, $\omega_a = 1500rad/s$, $\omega_b = 1200rad/s$, $\varphi_y = 1$. Table was rotated around y axis resulting.

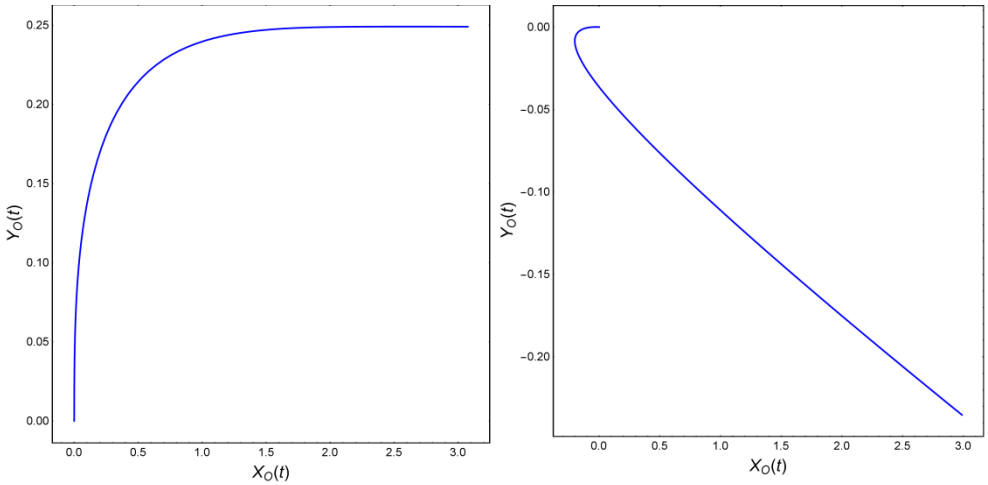


**Figure 2.** Simulations of rigid body's movement

For the simulations presented in figure 3 the following parameters were used for the top left graph: $A_x = 1$, $A_y = 1$, $\omega_a = 1000rad/s$, $\omega_b = 500rad/s$, $\varphi_y = 0$; for the top right graph: $A_x = 1$, $A_y = 3$, $\omega_a = 1200rad/s$, $\omega_b = 1000rad/s$, $\varphi_y = 1$; for the bottom left graph: $A_x = 1$, $A_y = 1$, $\omega_a = 2000rad/s$, $\omega_b = 1000rad/s$, $\varphi_y = 1$; finally for the bottom right

graph: $A_x = 1$, $A_y = 1$, $\omega_a = 800 rad/s$, $\omega_b = 1500 rad/s$, $\varphi_y = 0.5$ and table was rotated around x axis.

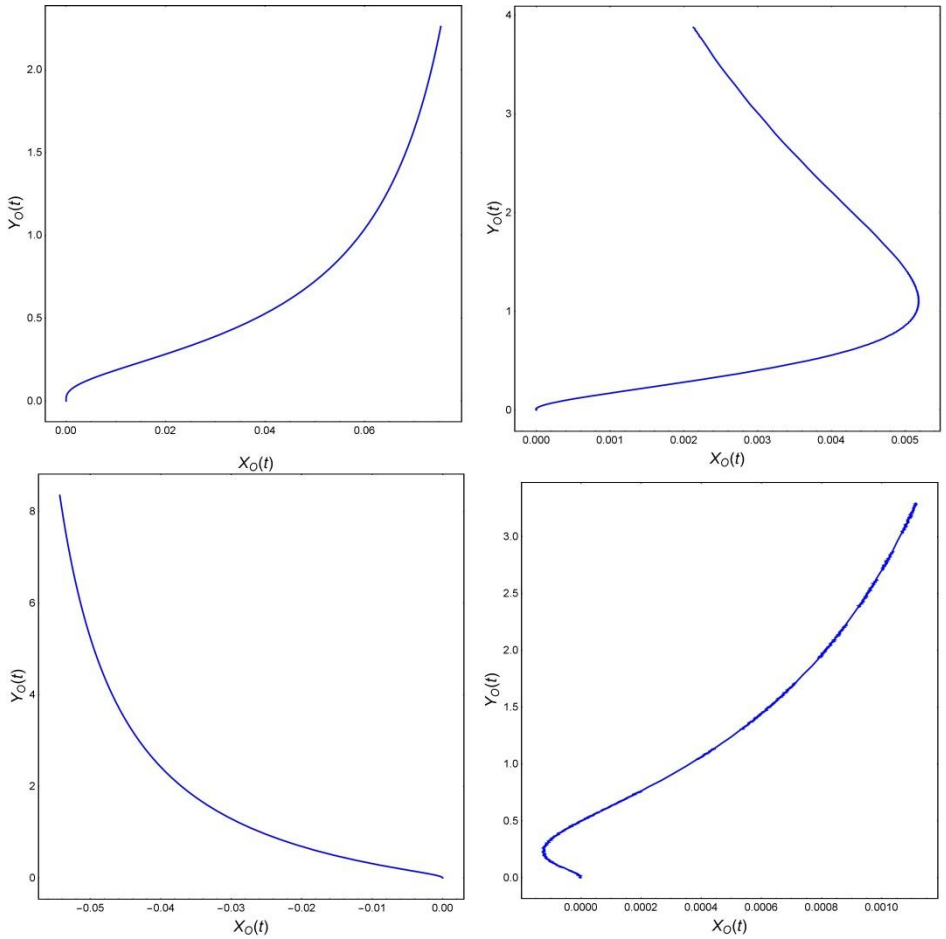


**Figure 3.** Simulations of rigid body's movement

## 4. Conclusions

This work presents the possible implementation of the model of the resultant contact forces. Due to the complexity of computation of the integrals over the contact area, the authors proposed a model for the numerical simulations, which is based on Padè approximant. Possible application of the model is a dynamical system consisting of a rigid body (billiard's ball) lying on a vibrating table. By manipulating the oscillations of the vibrating table, different ball's movements have been achieved. Results presented in this paper may be a good starting point for the verification of the presented

model not only by numerical simulations, but with the real object as well. Developing such a dynamical system and its technical implementation may be the authors' object of interest in future.

**Acknowledgments**

This work has been supported by the Polish National Science Centre, MAESTRO 2, No. 2012/04/A/ST8/00738.

**References**

[1] Macmillan W.D., *Dynamics of Rigid Bodies*. McGraw-Hill, New York, 1936

[2] Contensou, P., *Couplage entre frottement de glissement et de pivotement dans la téorie de la toupe*, In: Ziegler H. (Ed.), Kreiselprobleme Gyrodynamic, IUTAM Symposium Celerina, Springer-Verlag, Berlin, 1962, pp. 201-216.

[3] Zhuravlev, V.P., The model of dry friction in the problem of the rolling of rigid bodies, *Journal of Applied Mathematics and Mechanics*, 62(5), 1998, pp. 705-710.

[4] Kudra, G., Awrejcewicz, J., "Application and experimental validation of new computational models of friction forces and rolling resistance", *Acta Mechanica*, 2015, pp. 2831-2848.

[5] Kudra, G., Awrejcewicz, J., "Approximate modelling of resulting dry friction forces and rolling resistance for elliptic contact shape", *European Journal of Mechanics A/Solids*, 42, 2013, pp. 358-375.

[6] Kudra, G., Szewc, M., Wojtunik, I., Awrejcewicz J. "Shaping the trajectory of the billiard ball with approximations of the resultant contact forces", *3rd Int. Conference on Mechatronics — Ideas for Industrial Applications*, May 11-13, Gdansk, 2015

[7] Kudra, G., Szewc, M., Wojtunik, I., Awrejcewicz J. "On some approximations of the resultant contact forces and their applications in rigid body dynamics", *International Conference on Structural Engineering Dynamics (ICEDyn 2015)*, June 22-24, Portugal, 2015

[8] Borisov A.V., Karavaev Y. L., Mamaev I.S., Erdakova N. N., Ivanova T. B., Tarasov V. V. "Experimental Investigation of the Motion of a Body with an Axisymmetric Base Sliding on a Rough Plane", *Regular and Chaotic Dynamics*, 2015, Vol. 20, No. 5, pp. 518–541.

[9] A. A. Kireenkov, "Combined model of sliding and rolling friction in dynamics of bodies on a rough plane", *Mechanics of Solids*, 43, 3, 2008, pp. 412-425

Awrejcewicz Jan, Professor: Lodz University of Technology, Department of Automation, Biomechanics and Mechatronics, Stefanowskiego 1/15, 90-924 Lodz, Poland (jan.awrejcewicz@p.lodz.pl).

Kudra Grzegorz, Ph.D.: Lodz University of Technology, Department of Automation, Biomechanics and Mechatronics, Stefanowskiego 1/15, 90-924 Lodz, Poland (grzegorz.kudra@p.lodz.pl).

Wojtunik Igor, M.Sc. (Ph.D. student): Lodz University of Technology, Department of Automation, Biomechanics and Mechatronics, Stefanowskiego 1/15, 90-924 Lodz, Poland (*igor.wojtunik@dokt.p.lodz.pl)*.

Szewc Michal, M.Sc. (Ph.D. student): Lodz University of Technology, Department of Automation, Biomechanics and Mechatronics, Stefanowskiego 1/15, 90-924 Lodz, Poland (*michal.szewc@dokt.p.lodz.pl*). The author gave a presentation of this paper during one of the conference sessions.

# Model of the gas journal bearing dynamics with a flexibly supported foil
## (NUM209-15)

Eliza Tkacz, Zbigniew Kozanecki, Dorota Kozanecka, Jakub Łagodziski

*Abstract:* The work is devoted to an analysis of the journal bearing dynamics employing a numerical model which takes into account factors related to motion and friction of non–rotating elements of the sleeve. This model yields the basis for simulations carried out in order to determine correctly dynamic characteristics of an oil–free machine rotating system at the early stage of its design and during its operation. On the basis of those simulations, the thickness of gas film was determined as well as the pressure distribution in the bearing and its lift capacity. Moreover, the numerical program led to an analysis of proper vibrations and forced vibrations of the system under consideration. It was possible to obtain attenuation of the force and to visualize a journal trajectory for the dynamic harmonic input function. The FFT (Fast Fourier Transform) analysis of vibrations was implemented. In the spectrum, only a frequency of the input function was observed, whereas and a lack of subsynchronous frequencies pointed to the stable operation of the bearing.

### 1. Introduction

The development of modern turbomachinery of special reliability requirements resulted in search for new bearing systems solutions. Especially, nominal speeds of 10000–100000 rpm are impossible to reach with the use of conventional rolling element bearings or common oil–lubricated bearings, since their operation in these conditions may lead to instability of the machine rotating system. Furthermore, in ORC turbomachines propelled by a low–viscosity, organic working gas or liquid, an application of bearings lubricated with the working medium makes it possible to maintain the purity of the cycle.

In the present paper the coupling of a gas hydrodynamic model to a model of structure deformation is introduced. Accurate methods for the gas hydrodynamic behavior and the foil structure elastic behaviour are described. Finally, unsteady equations are formulated for the hydrodynamic model in order to predict the dynamic properties of a foil bearing. The equations are solved by means of numerical calculations.

As a result of the work, a parametric model has been created, which allows its universal use for calculations of the journal foil bearings dynamics . It was found that computational methods offer the possibility of deeper understanding of the phenomena occurring in the foil bearing.

## 2. Foil bearing technology

Two types of gas bearings can be distinguished: self–acting, so called aerodynamic bearings and gas powered or aerostatic bearings. The foil bearing is an aerodynamic type support, which is made up of compliant surfaces (a bump and a top foil). As shown in figure 1, during the foil bearing operation the top foil is clenched on the rotating journal by means of the elastic bump foil. The aerodynamic film of a very low thickness, theoretically close to the cylindrical one, is generated by viscosity effects. Since the viscosity of gas is much lower than for liquids, gas bearings have limited load capacity in comparison to oil–lubricated bearings.

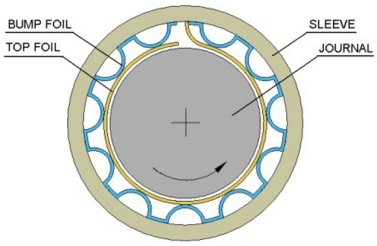


**Figure 1.** Compliant foil bearing

Miazga [7] has shown, that an important problem of the aerodynamic gas bearings application is related to the start–up and the shut–down in contact with the shaft surface. He has noticed a high drive moment during the start-up (disputable from the viewpoint of turbine mechanical characteristics) and so a limited number of start-up/shut-down cycles (wear). From this point, the heat generation was observed due to the friction phenomena, therefore the right choice of coating materials is crucial form the viewpoint of machine reliability.

Furthermore, the analysis of gas foil bearings is difficult due to interactions between the gas film pressure and the complicated deflection of the top foil and the underlying bump strip support structure. On the other hand, Garcia cited numerous benefits from aerodynamic bearing technology [3]:

- high rotational speeds,
- little maintenance,
- compliance thanks to the bump foil structure,
- compactness,
- no impact on the machinery environment thanks to the absence of external lubrication system.

From the application point of view, a great advantage of foil bearings is such that they

require no external pressurization system for the working fluid and so the surrounding gas can be used as the lubricant.

## 3. Numerical model

In order to define a numerical model of the foil bearing, at first, three systems have to be isolated: rotor, gas film and elastic structure, [1]. In table 1 physical hypothesis are presented for each of the systems.

**Table 1.** Hypothesis adopted for foil bearing analysis

| System | Hypothesis |
|---|---|
| Rotor | non-deformable<br>in equilibrium position for given rotational speed |
| Gas film | thin–film<br>compressible, Newtonian fluid<br>isothermal, continue, laminar flow<br>general curvature of the film is negligible<br>non–slip boundary conditions<br>inertial forces and mass forces are negligible<br>viscosity and density do not vary along film thickness |
| Elastic structure | elastic deformation<br>quasi-static |

The mathematical analysis will be therefore applied to each of the systems separately, then, their mutual interactions will be determined. Main parameters values adopted for calculation are listed in tab. 2.

### 3.1. Gas film

The cylindrical geometry of the gas film in the bearing can be found from equation 1, [2].

$$H = 1 - \varepsilon \cos(\theta - \eta_L) \tag{1}$$

The Reynolds Equation formulated for a cylindrical coordinate system (equation 2) is used to describe the pressure distribution in nearly any type of fluid film bearing under hypothesis cited in table 1.

$$-\frac{\partial}{\partial\theta}\left(\mathbf{PH}^3\frac{\partial\mathbf{P}}{\partial\theta}\right) - \frac{\partial}{\partial\xi}\left(\mathbf{PH}^3\frac{\partial\mathbf{P}}{\partial\xi}\right) + \Lambda\frac{\partial}{\partial\theta}(\mathbf{PH}) + \frac{\partial}{\partial\tau}(\mathbf{PH}) = 0 \tag{2}$$

**Table 2.** Parameters values adopted for numerical simulations

| Parameter | value |
|---|---|
| **Bearing** | |
| Bearing diameter, $D_{\mathrm{B}}$ [mm] | 34.0 |
| Bearing length, $L$ [mm] | 40.0 |
| Radial clearance, $C_{\mathrm{B}}$ [mm] | 0.035 |
| **Lubricant** | |
| Ambient pressure, $P_{\mathrm{a}}$ [bar] | 1.01325 |
| Vapour dynamic viscosity, $\mu$ [Pa·s] | $0.185 \cdot 10^{-4}$ |
| **Meshing** | |
| Circumferential number of nodes (gas), $N$ | 96 |
| Axial number of nodes (gas), $M$ | 34 |
| **Foils** | |
| Friction coefficient, $\nu$ | 0.5 |

where $\Lambda = \frac{6\mu\omega R^2}{p_{\mathrm{a}} C^2}$ is the compressibility number, $\mathbf{P}$ – the dimensionless pressure, $\tau$ – time, $\theta$ and $\xi$ are circumferential and axial coordinates respectively.

$$2P\frac{\partial H}{\partial \tau} + \frac{H}{P}\frac{\partial Q}{\partial \tau} + 2\Lambda P\frac{\partial H}{\partial \theta} + \Lambda\frac{H}{P}\frac{\partial Q}{\partial \theta} - H^3\left(\frac{\partial^2 Q}{\partial \xi^2} + \frac{\partial^2 Q}{\partial \theta^2}\right) + \\ -3H^2\left(\frac{\partial H}{\partial \theta}\frac{\partial Q}{\partial \theta} + \frac{\partial H}{\partial \xi}\frac{\partial Q}{\partial \xi}\right) = 0 \tag{3}$$

By replacing $P^2 = Q$, the Reynolds equation can be rewritten (equation 3). According to the finite difference method, derivatives in partial differential equations can be replaced by central differences, [6]. In order to solve the Reynolds equation, the Alternating Direction Implicit (ADI) method was used.

### 3.2. Elastic structure

In order to calculate the deformation of the structure, four hypothesis have been formulated:

H1: The structure deflection in a point depends only on pressure acting in this point.

H2: The rigidity of the structure is linear and the elastic force is given by relation $F_{\mathrm{S}} = k_{\mathrm{f}}\Delta h$, where $k_{\mathrm{f}}$ is the elasticity coefficient and $\Delta h$ – length change of the spring.

H3: There is no axial deformation of the structure.

H4: For given $\theta$ and different $\xi$ the deformation has the same value.

$$fb_i^{t+\mathrm{d}t} - fb_i^t = \frac{h_{ij}^{t+\mathrm{d}t} - h_{ij}^t}{s} + c_\mathrm{f}\left(\left.\frac{\mathrm{d}h}{\mathrm{d}t}\right|_{t\to t+\mathrm{d}t} - \left.\frac{\mathrm{d}h}{\mathrm{d}t}\right|_{t-\mathrm{d}t\to t}\right) \tag{4}$$

Based on these hypothesis the spring–damper model has been programmed and the relationship between the change in punctual force, $fb_i$ and foil deflection, $h$, can be expressed by equation 4, [4], where $s = 1/k_\mathrm{f}$ and $c_\mathrm{f}$ is a damping coefficient.

### 3.3. Rotor

The rotor of mass $2M$ is treated as a rigid structure and it is supported symmetrically in two identical finite lengths bearings (without gyroscopic motion) (see fig. 2).

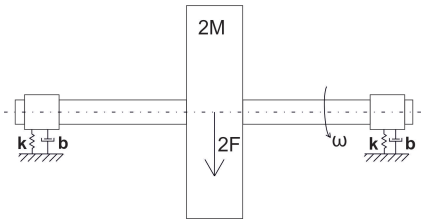


**Figure 2.** Rotating system model

Forces acting on the rotor result from its own weight, the unbalance, any dynamic (changing in time) loads and the pressure field in the gas film, [1]. They depend on the shaft position and the rotational speed. This can be expressed by Newton's second law equations in dimensionless form:

$$\begin{cases} \overline{M}\ddot{\overline{x}} = \overline{W}_0 + \overline{W}_{\mathrm{d}_x}(T) + \overline{M}e_\mathrm{b}\omega^2\cos(T) + \overline{F}_x(T) \\ \overline{M}\ddot{\overline{y}} = \overline{W}_{\mathrm{d}_y}(T) + \overline{M}e_\mathrm{b}\omega^2\sin(T) + \overline{F}_y(T) \end{cases} \tag{5}$$

where $(x, y)$ are rotor centre coordinates. Dimensionless variables are:

- forces $\overline{F} = \frac{F}{P_\mathrm{a}R^2}$,
- displacements $X = \frac{x}{C}$, $Y = \frac{y}{C}$,
- accelerations $\ddot{X} = \frac{\ddot{x}}{C\omega^2}$, $\ddot{Y} = \frac{\ddot{y}}{C\omega^2}$.
- time $T = \omega t$
- mass $\overline{M} = \frac{MC\omega^2}{P_\mathrm{a}R^2}$

with $P_\mathrm{a}$–ambient pressure, and $C = R - R_\mathrm{a}$ – a difference between the bush radius and the shaft radius.

### 3.4. Program for static calculations

In order to find the dynamic properties of the foil bearing, first the equilibrium position needs to be calculated. The equilibrium position is reached when the generated lift force, $\boldsymbol{F}$ balances the applied static load. This position is defined by the eccentricity, $\varepsilon$ and the centres angle, $\varphi$. The algorithm for the equilibrium position calculation is shown in fig. 7.

### 3.5. Program for dynamic calculations

The aim of the nonlinear method is to find the journal trajectory within the bearing caused by external, time varying load. This problem requires to solve equations for elastic deformation of nonrotating parts, motion equations and unsteady equations for pressure distribution in the gas film. The algorithm for dynamic calculation is shown in fig. 3.

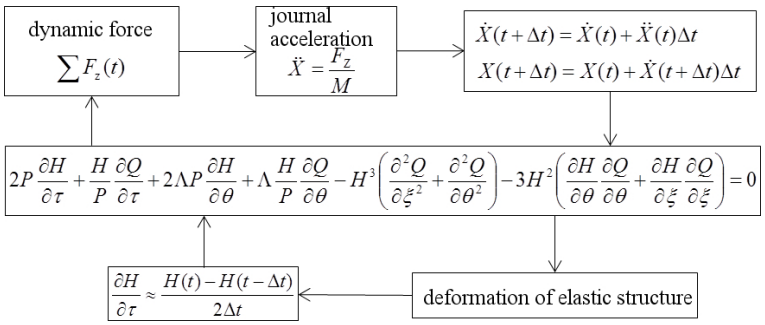


**Figure 3.** Dynamic calculation algorithm

## 4. Numerical results

The purpose of this chapter is to evaluate numerical procedures and verify bearing characteristics. The pressure distribution in the gas film is found so that the calculation of structure deformation is possible. It is also important to evaluate the structure model. The gas film is much more rigid than the foil structure, so it is the structure characteristics, which govern the static behaviour of the bearing.

### 4.1. Static characteristics

The static parameters are defined, when for given static force, the corresponding equilibrium position ($\varepsilon$, $\varphi$) is found. In figure 4 static characteristics curves are traced.

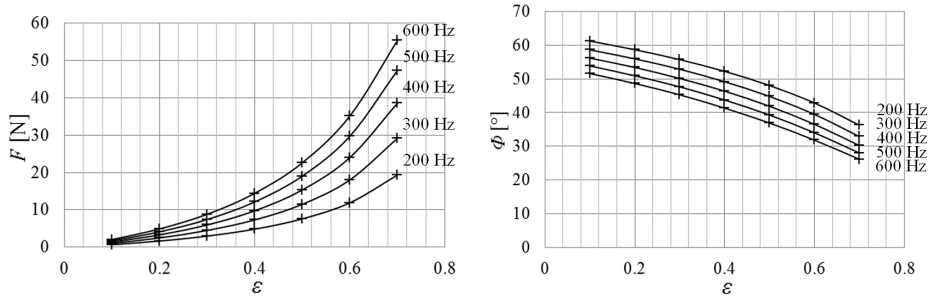


a) b)

**Figure 4.** Flexible structure

### 4.2. Dynamic characteristics according to the non–linear method

First, for given static force, $F_0$, the equilibrium position has been found (see fig. 4). This position is determined by an eccentricity and a centres angle,$(\varepsilon_0, \varphi_0)$. Then the harmonic perturbation has been added. In fig. 5 the rotor trajectory is shown in response to different frequencies of excitation, $\nu$. Comparing those to experimental results, [5], the qualitative resemblance was found. The test rig consisted of a fixed journal, frictionlessly supported sleeve and a modal shaker. The shaker excited the sleeve with a sinusoidal waveform force. It simulated real synchronous excitation caused by rotor unbalance. During the experiment, the excitation force and the sleeve displacement were measured. A few obtained hysteresis loops allowed for identification of the experimental stiffness and damping values of the compliant foil bearings. The conclusion was made that the bearing stiffness increases with the excitation frequency.

Back to numerical simulation results, for the excitation frequency of $\nu = 400$ Hz, the Fast Fourier Transform (FFT) of vibrational response was calculated in order to examine the frequencies spectrum. The dominant frequency of response is of 400 Hz (see fig. 6), so it is equal to the frequency of excitation. This points to the stable work of the bearing.

## 5. Conclusions

In the present paper main algorithms for foil bearing static and dynamic calculations have been described. The analytical equations were programmed by means of numerical modelization and the programme in Fortran has been developed. The ADI numerical method for solving the Reynolds equation has given a good convergence. A choice of the spring–dumper model for the elastic structure deformation is an important simplification, since it requires less computational resources in comparison to finite element method based codes. Rotor tra-

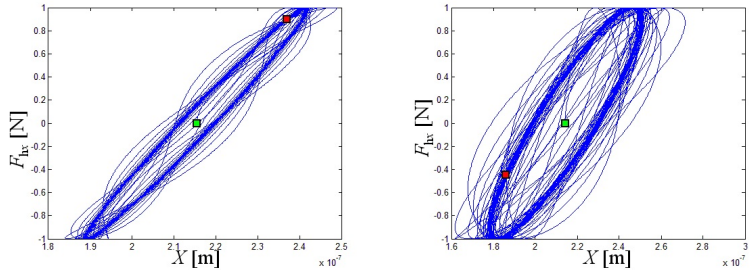


a) for $\nu = 100$ Hz b) for $\nu = 200$ Hz

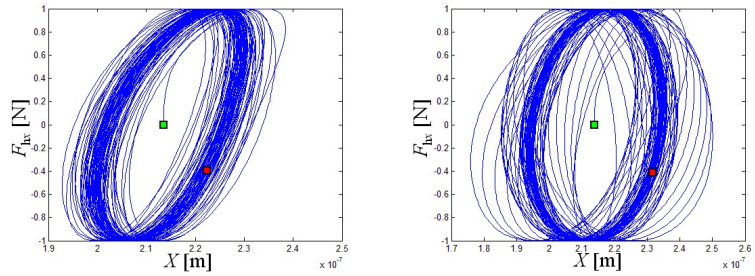


c) for $\nu = 400$ Hz d) for $\nu = 600$ Hz

**Figure 5.** Rotor trajectory

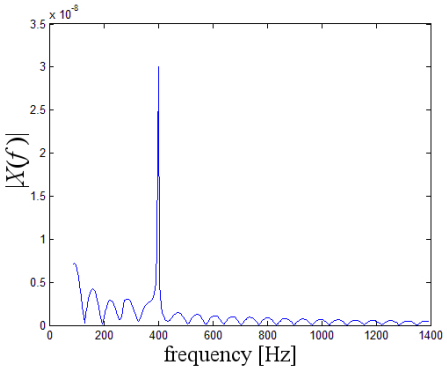


**Figure 6.** FFT of $X$ vibrations for excitation frequency $\nu = 400$ Hz

jectories for harmonic excitations have been shown for different excitation frequencies. The results pointed to the good programme performance and the simulation behaviour shown the qualitative accordance to experimental tests. The vibrational numerical analysis has revealed a good stability of the rotating system.

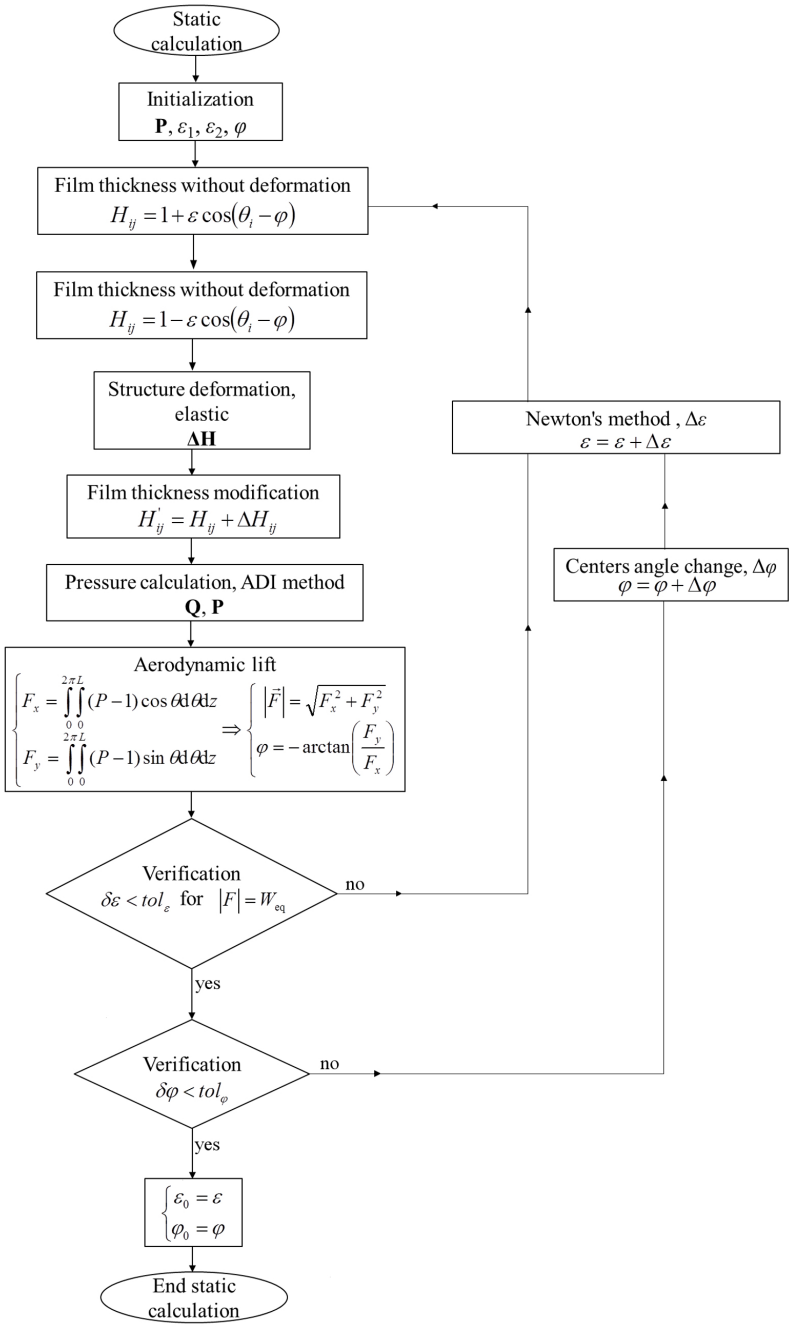


**Figure 7.** The algorithm for static parameters calculation

**References**


[1] Barzem, L. *Analyse théorique et expérimentale de la dynamique du rotor sur paliers à feuilles lubrifié par l'air.* PhD thesis, l'Institut National des Sciences Appliques de Lyon, Lyon, 2012.

[2] Frêne, J., Nicolas, D., Degueurce, B., Berthe, D., and Godet, M. *Lubrification hydrodynamique. Paliers et Butées*, Eyrolles ed. Cellection de la Direction des études et recherches d'électricité de France, Paris, 1990.

[3] Garcia, M. *Refrigerant - Lubricated Gas Foil Bearing - A Thermo-Hydrodynamic Study (Application to Rigid Bearings).* PhD thesis, l'Institut National des Sciences Appliques de Lyon, Lyon, 2012.

[4] Grau, G. *Paliers aérodynamiques radiaux à structure à feuilles: contribution à l'étude statique et comportement dynamique non linéaire.* PhD thesis, l'Institut National des Sciences Appliques de Lyon, Lyon, 2004.

[5] Kozanecki, Z., Tkacz, E., Łagodziński, J., and Miazga, K. Theoretical and experimental investigations of oil-free bearings and their application in diagnostics of high-speed turbomachinery. In *Key Engineering Materials* (2014), vol. 588, Trans Tech Publ, pp. 302–309.

[6] Krysiski, J., and Kazimierski, Z. *Łożyskowanie gazowe i napędy mikroturbinowe.* WNT,, Warszawa :, 1981.

[7] Miazga, K., Tkacz, E., Kozanecki, Z., and Łagodziński, J. Investigations of coating materials for air-foil bearings. *Zeszyty Naukowe. Cieplne Maszyny Przepływowe-Turbomachinery/Politechnika Łódzka* (2011), 149–156.



Eliza Tkacz, M.Sc. (Ph.D. student): Lodz University of Technology Institute of Turbomachinery, 90–924 Lodz, 219/223 Wolczanska Street (*eliza.tkacz@p.lodz.pl*). The author gave a presentation of this paper during one of the conference sessions.

Dorota Kozanecka, Professor: Lodz University of Technology Institute of Turbomachinery, 90–924 Lodz, 219/223 Wolczanska Street (*dorota.kozanecka@p.lodz.pl*).

Zbigniew Kozanecki, Professor: Lodz University of Technology Institute of Turbomachinery, 90–924 Lodz, 219/223 Wolczanska Street (*zkozan@p.lodz.pl*).

Jakub Lagodzinski, Ph.D.: Lodz University of Technology Institute of Turbomachinery, 90–924 Lodz, 219/223 Wolczanska Street (*jakub.lagodzinski@p.lodz.pl*).

# Theoretical analysis of the foil bearings dynamic characteristics (MAT179-15)

Eliza Tkacz, Zbigniew Kozanecki, Dorota Kozanecka, Jakub Łagodziski

*Abstract:* In the theoretical analysis, three systems were identified: a rotor, a gas film and a flexible structure. The mathematical analysis involves formulation of analytical equations for each of these elements and determination of their interactions. It was found that the rotor dynamics was subject to Newton's second law of motion, the gas flow in the bearing could be described by the Reynolds equation, whereas a spring-damper model was selected for the structural analysis. The Reynolds equation is a differential equation the exact solution to which is unknown. The work describes the finite difference method in detail, where the partial derivatives in the Reynolds equation are replaced by a system of algebraic equations. In order to solve the resulting system, the Alternating Direction Implicit method (ADI) was used. Thanks to those calculations, it was possible to determine the bearing dynamic characteristics using both the linear and non-linear method.

## 1. Introduction

The foil bearing is a modern type of oil–free, aerodynamic bearing used in high speed turbomachines such as high temperature compressors and microturbines. The demand for this type of solution is derived from electricity production for micro combined heat and power (CHP) plants, so–called distributed energy resource (DER), where the power of the installation is usually less than 5 kWe. The small power system can be based on the Organic Rankine Cycle (ORC) with a low boiling working medium. In this solution the basic machine is a small turbine driving an electric generator. In order to reach the nominal power in the reduced size machine the generator needs to rotate at a speed of 10000–100000 rpm. Such high speeds are impossible to reach with the use of conventional rolling–element bearings or common oil–lubricated bearings, since their operation in these conditions may lead to instability of the machine rotating system. Furthermore, in order to maintain the purity of the cycle, we are searching for a hermetic solution, where the machine is equipped with bearings lubricated with the working medium.

The presented here concept of a foil journal bearing is related to these assumptions.

## 2. General considerations about gas foil bearings

Because of the method of lift generation two types of gas bearings can be distinguished: self–acting, so called aerodynamic bearings and gas powered or aerostatic bearings. The foil

bearing is an aerodynamic support, which is made up of compliant surfaces (a bump and a top foil) (see figure 1), [1]. The uniqueness of foil bearing operation results from the fact that the top foil is clenched during the bearing operation on the rotating journal by means of an elastic bump foil. The aerodynamic film of a very low thickness, theoretically close to the cylindrical one, is generated by viscosity effects.

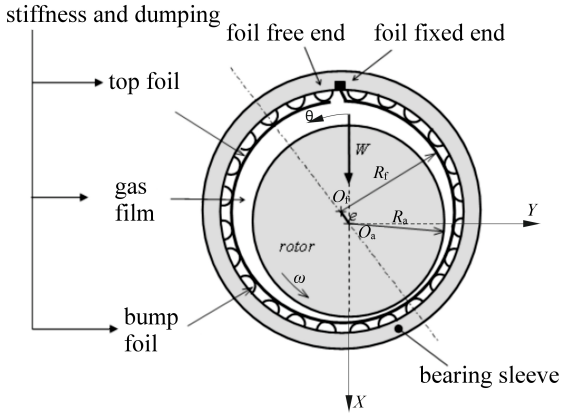


**Figure 1.** Compliant foil bearing

An important problem of the aerodynamic gas bearings application is related to the start–up and the shut–down in contact with the shaft surface, and thus:

- a high drive moment for the start-up (disputable from the viewpoint of turbine mechanical characteristics) is needed,
- there is a limited number of start-up/shut-down cycles (wear),
- in a case of the heat generation, a cooling system is required.

In general gas bearings have a limited load capacity. Furthermore, the analysis of gas foil bearings is difficult due to interactions between the gas film pressure and the complicated deflection of the top foil and the underlying bump strip support structure.

A great advantage of foil bearings is such that they require no external pressurization system for the working fluid and so the surrounding gas can be used as the lubricant. Other benefits are [2]:

- high rotational speeds,
- little maintenance,
- compliance thanks to the bump foil structure,
- compactness,
- no impact on the machinery environment thanks to the absence of external lubrication system.

## 3. Theoretical analysis of the gas foil bearing

In order to define a mathematical model for foil bearings, at first, three systems have to be isolated: rotor, gas film and elastic structure. In table 1 physical hypothesis are presented for each system.

**Table 1.** Hypothesis adopted for foil bearing analysis

| System | Hypothesis |
|---|---|
| Rotor | non-deformable<br>in equilibrium position for given rotational speed |
| Gas film | thin–film<br>compressible, Newtonian fluid<br>isothermal, continue, laminar flow<br>general curvature of the film is negligible<br>non–slip boundary conditions<br>inertial forces and mass forces are negligible<br>viscosity and density do not vary along film thickness |
| Elastic structure | elastic deformation<br>quasi-static |

The mathematical analysis will therefore apply to each system separately and determine their interactions. This section will discuss analytical equations describing the phenomena occurring in the foil bearing.

### 3.1. Foil bearing geometry and coordinate systems

Due to the geometry of the bearing it is convenient to define a cylindrical coordinate system $\theta\eta z$ (fig. 2) where the $z$ axis coincides with the $Z$ axis of the bearing global coordinate system. The $\eta$ axis is the radial coordinate measured from points located on the sleeve surface to shaft surface located points. The angle $\theta$ determines the circumferential coordinate. It is assumed that the parallel displacement of the journal axis is characterized by the relative eccentricity of the bearing $\epsilon$, where $\epsilon = e/C$, $C$ being the bearing clearance. In the local coordinate system the angle $\varphi$ is determined for a given equilibrium position by the centers line, i.e. the axis intersecting points $O_\mathrm{f}, O_\mathrm{a}$ (the angle between the $X$ and $X'$ axis in. fig. 2).

Then the cylindrical geometry of the gas film in the bearing can be found from equation 1.

$$H = 1 - \varepsilon \cos(\theta - \eta_L) \tag{1}$$

where $H$ is the dimensionless film thickness, $\varepsilon$ – the dimensionless eccentricity and $\eta_L$ – the

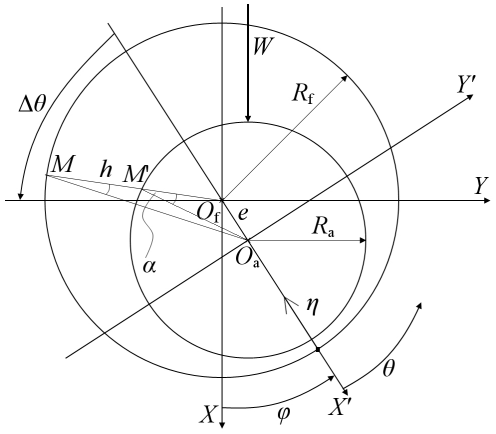


**Figure 2.** Cylindrical coordinate system for gas film calculation

angle determining the position of the foil locket.

### 3.2. Hydrodynamic model for gas foil bearings

The theoretical work of Reynolds, [6], is generally considered to be the hydrodynamic lubrication theory basis since it led to the Reynolds Equation. The Reynolds Equation is a partial differential equation derived from the mass and momentum conservation equations (Navier–Stokes equations) governing the pressure distribution of thin viscous fluid films and the lubricant flow. The Reynolds Equation (2) was used to describe the pressure distribution in nearly any type of fluid film bearings under hypothesis cited in table 1.

$$-\frac{\partial}{\partial\theta}\left(\mathbf{PH}^3\frac{\partial\mathbf{P}}{\partial\theta}\right)-\frac{\partial}{\partial\xi}\left(\mathbf{PH}^3\frac{\partial\mathbf{P}}{\partial\xi}\right)+\Lambda\frac{\partial}{\partial\theta}\left(\mathbf{PH}\right)+\frac{\partial}{\partial\tau}\left(\mathbf{PH}\right)=0 \tag{2}$$

where

$\Lambda=\frac{6\mu\omega R^2}{p_a C^2}$ is the compressibility number,

$\mathbf{P}$ – the dimensionless pressure,

$\tau$ – time.

$$\begin{cases} F_x=-\int_{\xi_1}^{\xi_2}\int_0^{2\pi} P\cos\theta\,\mathrm{d}\xi\,\mathrm{d}\theta \\ F_y=-\int_{\xi_1}^{\xi_2}\int_0^{2\pi} P\sin\theta\,\mathrm{d}\xi\,\mathrm{d}\theta \end{cases} \tag{3}$$

When the pressure distribution is known, the aerodynamic lift force can be calculated according to the equation 3.

### 3.3. Model for the foil structure elastic deformation

The geometry of the flexible structure shown in fig. 3a) is taken into consideration. Its material properties and stresses allow to consider the elastic solid and so the structure can be modelled as series of springs and dampers (see fig. 3b)). Damping properties being originated from friction phenomena.

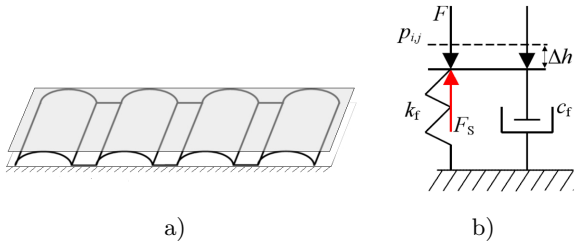


**Figure 3.** Flexible structure

In order to calculate the deformation of the structure, four hypothesis have been formulated:

H1: The structure deflection depends only on pressure.

H2: The rigidity of the structure is linear and the elastic force is given by the relation $F_S = k_f \Delta h$, where $k_f$ is the elasticity coefficient and $\Delta h$ is a length change of the spring.

H3: There is no axial deformation of the structure.

H4: For given $\theta$ and different $\xi$ the deformation has the same value.

Based on these hypothesis the relationship between the change in punctual force, $fb_i$ and foil deflection, $h_{ij}$, can be expressed by equation 4, [3]

$$fb_i^{t+\mathrm{d}t} - fb_i^t = \frac{h_{ij}^{t+\mathrm{d}t} - h_{ij}^t}{s} + c_f \left( \left.\frac{\mathrm{d}h}{\mathrm{d}t}\right|_{t\to t+\mathrm{d}t} - \left.\frac{\mathrm{d}h}{\mathrm{d}t}\right|_{t-\mathrm{d}t\to t} \right) \tag{4}$$

where $s = 1/k_f$ and $c_f$ is a damping coefficient.

### 3.4. Rotor dynamics

The rotor of mass $2M$ is treated as a rigid structure and it is supported symmetrically in two identical finite lengths bearings (without gyroscopic motion) (see fig. 4). This approach allows to evaluate the influence of the bush behaviour on the rotor trajectory. Forces acting on the rotor result from its own weight, the unbalance, any dynamic (changing in time) loads and the pressure field in the gas film. They depend on the shaft position and the rotational speed.

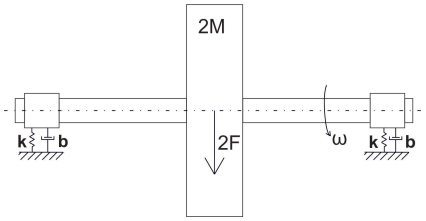


**Figure 4.** Rotating system model

More specifically, when the journal rotates, each bearing supports, [1]:

- the mass $M$,
- the static force $W_0 = F$,
- a dynamic force of harmonic type $W_{\mathrm{d}}(t) = W_{\mathrm{d}} \sin(\gamma t)$, where $\gamma$ is a frequency of pulsation,
- a vibrational synchronous excitation due to the unbalance. This excitation is characterised by its eccentricity $e_{\mathrm{b}}$,
- the aerodynamic forces $F(t)$ calculated from the pressure distribution in the gas film.

This can be expressed by Newton's second law equations:

$$\begin{cases} M\ddot{x} = \sum F_{\mathrm{ext}/x} \\ M\ddot{y} = \sum F_{\mathrm{ext}/y} \end{cases} \tag{5}$$

or with the right–hand side of the equation developed and put in dimensionless form:

$$\begin{cases} \overline{M}\ddot{\overline{x}} = \overline{W}_0 + \overline{W}_{\mathrm{d}/x}(T) + \overline{M} e_{\mathrm{b}} \omega^2 \cos(T) + \overline{F}_x(T) \\ \overline{M}\ddot{\overline{y}} = \overline{W}_{\mathrm{d}/y}(T) + \overline{M} e_{\mathrm{b}} \omega^2 \sin(T) + \overline{F}_y(T) \end{cases} \tag{6}$$

where $(x, y)$ are rotor centre coordinates.

According to the linear theory, dynamic properties of aerodynamic gas bearings are usually represented by a set of eight coupled dynamic coefficients $(k_{ij}, b_{ij})$, linearized around the static equilibrium position of the bearing, [4]. Limited excitation loads allow one to linearize the forces in the bearing film and to determine the equivalent values of coupled bearing stiffness and damping coefficients.

The bearing static equilibrium position determines the initial conditions for an analysis of the bearing dynamics and it is noted by subscript $_{.0}$. Then, we introduce the position perturbation and the velocity perturbation, whence stiffness and damping coefficients are defined as follows

$$\left.\frac{\partial F_x}{\partial x}\right|_0 = K_{xx},\ \left.\frac{\partial F_x}{\partial y}\right|_0 = K_{xy},\ \left.\frac{\partial F_y}{\partial x}\right|_0 = K_{yx},\ \left.\frac{\partial F_y}{\partial y}\right|_0 = K_{yy} \tag{7}$$

$$\left.\frac{\partial F_x}{\partial \dot{x}}\right|_0 = B_{xx},\ \left.\frac{\partial F_x}{\partial \dot{y}}\right|_0 = B_{xy},\ \left.\frac{\partial F_y}{\partial \dot{x}}\right|_0 = B_{yx},\ \left.\frac{\partial F_y}{\partial \dot{y}}\right|_0 = B_{yy} \tag{8}$$

It should be highlighted that the lack of precise criteria, which allows one to determine the applicability range of the linear method, often leads to serious errors in the dynamic analysis of the rotor–bearings system.

## 4. Numerical methods

Due to the non–linear nature of the equations of fluid motion, they can be solved in only a few, very specific situations, hence the need for a numerically approximated solution. In order to make possible the approximation process of solving, partial differential equations need to be discretized. As a result of the discretization, differential equations are replaced by an algebraic equations system. There exists different methods of discretization, the most common are: Finite Difference Method (FDM), Finite Element Method (FEM) and Finite Volume Method (FVM). For the project needs the Finite Difference Method was used to solve equations governing the gas film behaviour. All described methods were solved using the structured programming language, Fortran.

By replacing $P^2 = Q$, the Reynolds equation can be rewritten (equation 9). According to the finite difference method, derivatives in partial differential equations can be replaced by central differences, [5]. For example, first derivatives will be approximated according to equations 10 and second derivatives – according to equations 11.

$$\begin{aligned} 2P\frac{\partial H}{\partial \tau} + \frac{H}{P}\frac{\partial Q}{\partial \tau} + 2\Lambda P\frac{\partial H}{\partial \theta} + \Lambda\frac{H}{P}\frac{\partial Q}{\partial \theta} - H^3\left(\frac{\partial^2 Q}{\partial \xi^2} + \frac{\partial^2 Q}{\partial \theta^2}\right) + \\ -3H^2\left(\frac{\partial H}{\partial \theta}\frac{\partial Q}{\partial \theta} + \frac{\partial H}{\partial \xi}\frac{\partial Q}{\partial \xi}\right) = 0 \end{aligned} \tag{9}$$

$$\begin{aligned} \frac{\partial H}{\partial \theta} &\approx \frac{H^n_{i,j+1} - H^n_{i,j-1}}{2\Delta\theta} \\ \frac{\partial H}{\partial \xi} &\approx \frac{H^n_{i+1,j} - H^n_{i-1,j}}{2\Delta\xi} \end{aligned} \tag{10}$$

$$\begin{aligned} \frac{\partial^2 Q}{\partial \xi^2} &\approx \frac{Q^n_{i+1,j} - 2Q^n_{ij} + Q^n_{i-1,j}}{(\Delta\xi)^2} \\ \frac{\partial^2 Q}{\partial \theta^2} &\approx \frac{Q^n_{i,j+1} - 2Q^n_{ij} + Q^n_{i,j-1}}{(\Delta\theta)^2} \end{aligned} \tag{11}$$

In order to solve the Reynolds equation, the Alternating Direction Implicit (ADI) method can be used. This method is applied to the finite differences and consists on splitting the calculation into two steps. In the first step derivatives with respect to $\theta$ are evaluated while derivatives with respect to $\xi$ are evaluated in the second step. Then, according to the tridiagonal elimination method, the summands are grouped and equations 12 and 14 can be written.

$$A_{ij}^n Q_{i,j-1}^{n+1} + B_{ij}^n Q_{ij}^{n+1} + C_{ij}^n Q_{i,j+1}^{n+1} = f_{ij}^n \tag{12}$$

where

$$\begin{aligned} Q_{ij}^{n+1} &= X_{ij} Q_{i,j+1}^{n+1} + Y_{ij} \\ X_{ij} &= \frac{-C_{ij}^n}{B_{ij}^n + A_{ij}^n X_{i,j-1}} \\ Y_{ij} &= \frac{f_{ij}^n - A_{ij}^n Y_{i,j-1}}{B_{ij}^n + A_{ij}^n X_{i,j-1}} \\ Q_{i,1}^{n+1} &= Q_{i,N+1}^{n+1} = Q_{i,1}^n \end{aligned} \tag{13}$$

$$D_{ij}^n Q_{i-1,j}^{n+2} + E_{ij}^n Q_{ij}^{n+2} + F_{ij}^n Q_{i+1,j}^{n+2} = g_{ij}^{n+1} \tag{14}$$

where

$$\begin{aligned} Q_{ij}^{n+2} &= X_{ij} Q_{i+1,j}^{n+2} + Y_{ij} \\ X_{ij} &= \frac{-F_{ij}^n}{E_{ij}^n + D_{ij}^n X_{i-1,j}} \\ Y_{ij} &= \frac{g_{ij}^n - D_{ij}^n Y_{i-1,j}}{E_{ij}^n + D_{ij}^n X_{i-1,j}} \\ Q_{1,j}^{n+2} &= Q_{M,j}^{n+2} = 1 \end{aligned} \tag{15}$$

The calculation of $Q_{1,j}^{n+2}$ ends an iteration cycle. The statements $Q_{ij}^n = Q_{ij}^{n+2}$ and $P_{ij}^n = \sqrt{Q_{ij}^{n+2}}$ start new iteration process.

## 5. Rotor trajectory in step function test

First, for the given static force, $F_0$, the equilibrium position is found. This position is determined by an eccentricity and a centers angle,$(\varepsilon_0, \varphi_0)$ (see fig. 5, green point). Second, for a static force, $F_1 = F_0 + \Delta F$, another equilibrium position is calculated, $(\varepsilon_1, \varphi_1)$. Then, the dynamic calculation has been carried out for the dynamic force, the step function, defined in equation 16.

$$F_d(t) = \begin{cases} F_0 + \Delta F, \ n_t \geq 60 \\ F_0, \ n_t < 60 \end{cases} \tag{16}$$

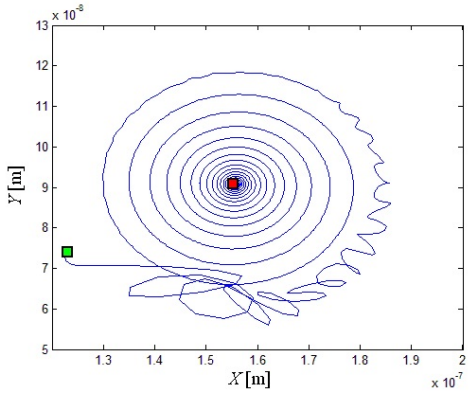


**Figure 5.** Pressure distribution in the gas film

The rotor trajectory can be observed in fig. 5. The final position, $(\varepsilon_d, \varphi_d)$ (red point) is then compared with $(\varepsilon_1, \varphi_1)$ position. The deviation was less than 1% for $\varphi$ and about 1.5% for $\varepsilon$.

## 6. Conclusions

The present paper is a trial to show major equations and methods for the theoretical analysis of a journal foil bearing. The equations were programmed by means of numerical modelization and the model in Fortran have been developed. The ADI numerical method for solving the Reynolds equation has given a good convergence. A choice of the spring–dumper model for the elastic structure deformation is an important simplification, since it requires less computational resources in comparison to finite element method based codes. The rotor trajectory in step function dynamic excitation has been shown. The results pointed to good programme performance. Other numerical tests have revealed a good stability of the foil bearing.

## References

[1] Barzem, L. *Analyse théorique et expérimentale de la dynamique du rotor sur paliers à feuilles lubrifié par l'air*. PhD thesis, l'Institut National des Sciences Appliques de Lyon, Lyon, 2012.

[2] Garcia, M. *Refrigerant - Lubricated Gas Foil Bearing - A Thermo-Hydrodynamic Study (Application to Rigid Bearings)*. PhD thesis, l'Institut National des Sciences Appliques de Lyon, 2012. Supervisor Benyebka Bou–Saïd.

[3] Grau, G. *Paliers aérodynamiques radiaux à structure à feuilles: contribution à l'étude statique et comportement dynamique non linéaire*. PhD thesis, l'Institut National des Sciences Appliques de Lyon, Lyon, 2004.

[4] Kozanecki, Z., Tkacz, E., Łagodziński, J., and Miazga, K. Theoretical and experimental investigations of oil-free bearings and their application in diagnostics of high-speed turbomachinery. In *Key Engineering Materials* (2014), vol. 588, Trans Tech Publ, pp. 302–309.

[5] Krysiski, J., and Kazimierski, Z. *Łożyskowanie gazowe i napędy mikroturbinowe*. WNT,, Warszawa :, 1981.

[6] Reynolds, O. On the theory of lubrication and its application to mr. beauchamp tower's experiments, including an experimental determination of the viscosity of olive oil. *Proceedings of the Royal Society of London 40*, 242-245 (1886), 191–203.

Eliza Tkacz, M.Sc. (Ph.D. student): Lodz University of Technology Institute of Turbomachinery, 90–924 Lodz, 219/223 Wolczanska Street (*eliza.tkacz@p.lodz.pl*). The author gave a presentation of this paper during one of the conference sessions.

Dorota Kozanecka, Professor: Lodz University of Technology Institute of Turbomachinery, 90–924 Lodz, 219/223 Wolczanska Street (*dorota.kozanecka@p.lodz.pl*).

Zbigniew Kozanecki, Professor: Lodz University of Technology Institute of Turbomachinery, 90–924 Lodz, 219/223 Wolczanska Street (*zkozan@p.lodz.pl*).

Jakub Lagodzinski, Ph.D.: Lodz University of Technology Institute of Turbomachinery, 90–924 Lodz, 219/223 Wolczanska Street (*jakub.lagodzinski@p.lodz.pl*).

# Simulating the damped vibrations of a fractional oscillator with fuzzy initial conditions
## (MAT111-15)

Stefania Tomasiello, Jan Awrejcewicz

*Abstract:* A Picard-like scheme using quadrature and differential quadrature rules, formerly introduced to solve integro-differential equations, is herein adapted to solve the problem of an oscillator with damping defined by the Riemann-Liouville fractional derivative and with fuzzy initial conditions. Considering fuzzy initial conditions has the meaning of a fuzzification of the problem via the Zadeh's extension principle. Following Zadeh, fuzziness is a way to take into account an uncertainty which cannot be identified as randomness. In the crisp domain, the proposed approach is able to approximate the reference analytical solutions with high accuracy and a relatively low computational cost. In the linear regime, the technique proposed becomes a non-recursive scheme, providing semi-analytical solutions by means of operational matrices and vectors of known quantities. In this sense, an example of application is given by the free damped vibrations of a linear oscillator in a medium with small viscosity, usually solved by using the method of multiple scales (in the crisp domain).

### 1. Introduction

In this manuscript, we investigate a class of fuzzy differential equations in presence of a Riemann-Liouville fractional derivative

$$L_t^{(2)}\tilde{u}(t) + \delta\, {}^{RL}D^{\beta}(\tilde{u}(t)) = f(\tilde{u}(t)) + \tilde{g}(t), \tag{1}$$

subject to the initial conditions

$$L_t^{(i)}\tilde{u}(0) = \tilde{a}_i, \qquad i = 0, 1 \tag{2}$$

where $L_t^{(i)}$ is the $i$th-order derivative operator with respect to $t$, ${}^{RL}D^{\beta}$ is the Riemann-Liouville fractional derivative of order $\beta$, with $0 < \beta < 1$. Besides, $f(\tilde{u}(t))$ is a functional form in $\tilde{u}$, $\tilde{g}(t)$ a given fuzzy-valued function and $\tilde{a}_i$ a fuzzy number, with $i = 0, 1$. Here, $\tilde{u}(t)$ represents the unknown fuzzy function for $t \in [0, 1]$. Obviously, assuming $[0, 1]$ as the problem domain is not a loss of generalization, because it is possible scaling the independent variable $t$.

It should be pointed out that (1) may be seen as the fuzzification via the Zadeh's extension principle of the same equation but without fuzzy variables and parameters. The introduction of 'fuzziness' in (1) means to take into account an uncertainty in the value of the equation variables which cannot be read as randomness [1]. Considering fuzziness in decision processes [2] and in regression analysis [3, 4] is very important. In the same way, it allows to model adequately realistic problems in science and engineering which traditionally involve ordinary differential equations [5, 6].

The problem corresponding to (1) in the crisp domain has been solved by means of several approaches [7], depending on the presence or not of nonlinearity and forcing term.

In the present work, we extend the approach proposed in [8] to solve (1). More precisely, we discuss a numerical scheme combining differential quadrature rules [9] (which provide high-order finite-difference approximations) and a Picard-like recursion into the fuzzy domain. In spite of its recursive nature, the proposed approach in the linear regime leads to a non-recursive approximate solution by means of operational matrices and vectors of known quantities. Notice that the scheme herein discussed is different from the one presented in [10].

As a first example application, we consider herein the free damped vibrations of a linear oscillator in a medium with small viscosity, which has been solved in the crisp domain by using the method of multiple scales [11].

Numerical simulations show that results obtained through our method are very accurate if compared in the crisp domain with the analytical solutions available in the literature.

## 2. Theoretical background

In this section, some basic notions are provided. Throughout, the set $U$ will represent a nonempty and fixed (though arbitrary) closed interval of $\mathbb{R}$.

**Definition 1.** *A* **fuzzy number** $\tilde{u}$ *is defined by a membership function* $\mu_u(x) : U \to [0, 1]$*, and it satisfies the following properties:*

- $\tilde{u}$ *is* **normal***, that is* $\sup_{x \in U} \mu_u(x) = 1$*,*
- $\tilde{u}$ *is* **convex** *on* $U$*, meaning that* $\mu_u(\alpha x + (1 - \alpha)y) \geq \min(\mu_u(x), \mu_u(y))$ *for each* $x, y \in U$ *and each* $\alpha \in [0, 1]$*,*
- $\tilde{u}$ *is upper semi-continuous and*
- $[\tilde{u}]_0 = cl(\{x \in U : \mu_u(x) > 0\})$ *is compact, where cl denotes closure in the standard topology of* $U$*.*

**Definition 2.** *An* $\alpha$**-cut** *of the fuzzy number* $\tilde{u}$ *is the crisp set defined by*

$$[\tilde{u}]_{\alpha} = \{x \in U : \mu_u(x) \geq \alpha\}, \qquad \alpha > 0. \tag{3}$$

Notice that for $\alpha = 0$, the $\alpha$-cut of a fuzzy number $\tilde{u}$ reduces to $[\tilde{u}]_0$ in Definition 1.

**Definition 3.** *The* **parametric form** *of the fuzzy number* $\tilde{u}$ *is a pair* $[\underline{u}(\alpha), \overline{u}(\alpha)]$ *satisfying the following properties for each* $\alpha \in [0,1]$*:*

1. $\underline{u}(\alpha)$ *is a bounded, left-continuous, monotonic increasing function over* $[0,1]$*,*
2. $\overline{u}(\alpha)$ *is a bounded, left-continuous, monotonic decreasing function over* $[0,1]$ *and*
3. $\underline{u}(\alpha) \leq \overline{u}(\alpha)$*.*

*The notation* $[\tilde{u}]_{\alpha} = [\underline{u}(\alpha), \overline{u}(\alpha)]$ *is employed if such form exists.*

In particular, a fuzzy *triangular* number $\tilde{u}$ is generally identified by an ordered triplet of numbers $(d_C, d_L, d_R)$, where $d_C$ is the center, $d_L$ and $d_R$ are the left and the right spreads, respectively. Using an $\alpha$-cut operation, any triangular fuzzy number may be written as

$$[\tilde{u}]_{\alpha} = [\underline{u}(\alpha), \overline{u}(\alpha)] = [d_C + (\alpha - 1)d_L, d_C + (1 - \alpha)d_R], \tag{4}$$

for each $\alpha \in [0,1]$.

In what follows, $\tilde{f}(x)$ denotes a continuous and Lebesgue-integrable fuzzy-valued function on the bounded interval $[a,b]$ and $\Gamma(.)$ represents the Gamma function.

The concept of strongly generalized $H$-differentiability [12], was extended in [13] to the context of fractional derivatives. In the latter work, the following definition was considered.

**Definition 4.** *Let* $0 < \beta < 1$*. The fuzzy-valued function* $\tilde{f}(x)$ *is a* **Riemann-Liouville fuzzy fractional differentiable function** *of order* $\beta$ *at* $x_0 \in (a,b)$ *if either*

$${}^{RL}D^{\beta}\tilde{f}(x_0) = \lim_{h \to 0^+} \frac{\tilde{\phi}(x_0 + h) \ominus \tilde{\phi}(x_0)}{h} = \lim_{h \to 0^+} \frac{\tilde{\phi}(x_0) \ominus \tilde{\phi}(x_0 - h)}{h} \tag{5}$$

*or*

$${}^{RL}D^{\beta}\tilde{f}(x_0) = \lim_{h \to 0^+} \frac{\tilde{\phi}(x_0) \ominus \tilde{\phi}(x_0 + h)}{-h} = \lim_{h \to 0^+} \frac{\tilde{\phi}(x_0 - h) \ominus \tilde{\phi}(x_0)}{-h}, \tag{6}$$

*where* ${}^{RL}D^{\beta}\tilde{f}(x_0)$ *denotes the Riemann- Liouville fuzzy fractional derivative of* $\tilde{f}$ *at* $x_0$*, and*

$$\tilde{\phi}(x) = \frac{1}{\Gamma(1-\beta)} \int_0^x \tilde{f}(s)(x-s)^{-\beta} ds. \tag{7}$$

Following [13], the $\alpha$-cut representation of the Riemann- Liouville fuzzy fractional derivative is

$$[{}^{RL}D^{\beta}\tilde{f}(x_0)]_{\alpha} = \begin{cases} [{}^{RL}D^{\beta}\underline{f}(x_0,\alpha), {}^{RL}D^{\beta}\overline{f}(x_0,\alpha)], & \text{for (5)}, \\ \\ [{}^{RL}D^{\beta}\overline{f}(x_0,\alpha), {}^{RL}D^{\beta}\underline{f}(x_0,\alpha)], & \text{for (6)}, \end{cases} \tag{8}$$

for each $0 \leq \alpha \leq 1$.

With regard to (1), we assume that sufficient derivatives of the solution exist. There are different notions of fuzzy derivatives [14], but we refer to $H$-differentiability [15], which has the advantage that it always exists and provides fuzzy numbers as the solution of fuzzy differential equations.

In order to obtain numerical solutions of (1), we will use the $\alpha$-cut approach, which allows to replace the computation of a function of a fuzzy number by a sequence of interval computations on successive $\alpha$-cuts. This approach follows the idea that, in many practical applications, it is sufficient to know the solution of the problem in a finite set of points in order to approximate the solution over the entire domain.

Let $[\tilde{u}(t)]_{\alpha}$ be the $\alpha$-cut of a function $\tilde{u}(t)$. In light of [16], we may rewrite $[\tilde{u}(t)]_{\alpha} = [\underline{u}(t,\alpha), \overline{u}(t,\alpha)]$. Assuming that the derivatives exist, we obtain (see [15])

$$\begin{cases} L_t^{(2)}\underline{u}(t) + \delta^{RL}D^{\beta}\underline{u}(t,\alpha) &= \underline{f}(\underline{u}(t,\alpha), \overline{u}(t,\alpha), \alpha) + \underline{g}(t,\alpha), \\ L_t^{(2)}\overline{u}(t) + \delta^{RL}D^{\beta}\overline{u}(t,\alpha) &= \overline{f}(\underline{u}(t,\alpha), \overline{u}(t,\alpha), \alpha) + \overline{g}(t,\alpha), \\ L_t^{(i)}\underline{u}(0,\alpha) &= \underline{a}_i(\alpha), \qquad i = 0,1 \\ L_t^{(i)}\overline{u}(0,\alpha) &= \overline{a}_i(\alpha), \qquad i = 0,1 \end{cases} \tag{9}$$

Alternatively, we can write (9) as

$$\begin{cases} L_t^{(2)}\mathbf{U}(t,\alpha) + \delta^{RL}D^{\beta}\mathbf{U}(t,\alpha) &= \mathbf{F}(\mathbf{U}(t,\alpha),\alpha) + \mathbf{G}(t,\alpha), \\ L_t^{(i)}\mathbf{U}(0,\alpha) &= \mathbf{a}_i(\alpha), \quad i = 0,1 \end{cases} \tag{10}$$

where

$$\mathbf{U}(t,\alpha)^T = (\underline{u}(t,\alpha), \overline{u}(t,\alpha)), \tag{11}$$

$$\mathbf{F}(\mathbf{U}(t,\alpha),\alpha)^T = \big(\underline{f}(\underline{u}(t,\alpha), \overline{u}(t,\alpha), \alpha), \overline{f}(\underline{u}(t,\alpha), \overline{u}(t,\alpha), \alpha)\big), \tag{12}$$

$$\mathbf{G}(t,\alpha)^T = \big(\underline{g}(t,\alpha), \overline{g}(t,\alpha)\big), \tag{13}$$

$$\mathbf{a}_i(\alpha)^T = (\underline{a}_i(\alpha), \overline{a}_i(\alpha)). \tag{14}$$

## 3. Methodology

### 3.1. Integral and differential quadrature

Integral and differential quadrature are very similar in the underlying principle. The term integral in addiction to quadrature was introduced by C. Shu in order to highlight the difference between the two approaches [17]. Integral quadrature consists in replacing the integral of a function $u(t)$ over an interval, e.g. $[0,1]$, by a weighted sum of the functional values $u_1, u_2, \ldots, u_N$ at the discrete points $0 = t_1 < t_2 < \ldots < t_N = 1$, that is

$$\int_0^1 u(t)dt = \sum_{i=1}^{N} C_i u_i. \tag{15}$$

The differential quadrature (DQ) rules provide the approximation of the $r$th-order derivative of the function $u(t)$ at a point $t = t_j$ by a weighted sum [9] as follows

$$\left[\frac{d^r u}{dt^r}\right]_{t=t_j} = \sum_{i=1}^{N} A_{ji}^{(r)} u_i, \qquad i,j = 1,2,\ldots,N \tag{16}$$

where the constants $A_{ji}^{(r)}$ are the weight coefficients computed in $N$ grid points. By letting $u(t) = \sum_{i=1}^{N} l_i(t)u_i$, where $l_i(t)$ is the Lagrange polynomial at the point $t_i$, for each $i = 1,2,\ldots,N$, one gets

$$C_i(t) = \int_0^x l_i(t)dt, \qquad A_i^{(r)}(t) = \frac{d^r l_i}{dt^r}(t). \tag{17}$$

Obviously, it is $A_{ji}^{(r)} = A_i^{(r)}(t_j)$ for every $i,j = 1,2,\ldots,N$.

By using Lagrange's polynomials as test functions, then there is no restriction on the choice of the grid points, which may be equally spaced or not. Usually grid coordinates are obtained through the Gauss-Tchebychev-Lobatto (GCL) distribution. As a result of the fuzzification of the integral and differential quadrature rules, one has respectively:

$$\left[\int_0^1 \tilde{u}(t)dt\right]_\alpha = \left[\int_0^1 \underline{u}(t)dt, \int_0^1 \overline{u}(t)dt\right]_\alpha = \left[\sum_{i=1}^{N} C_i \underline{u}_i, \sum_{i=1}^{N} C_i \overline{u}_i\right], \tag{18}$$

$$\left[\frac{d^r \tilde{u}}{dt^r}\right]_\alpha = \left[\frac{d^r \underline{u}}{dt^r}, \frac{d^r \overline{u}}{dt^r}\right]_\alpha = \left[\sum_{i=1}^{N} A_i^{(r)}(t)\underline{u}_i(\alpha), \sum_{i=1}^{N} A_i^{(r)}(t)\overline{u}_i(\alpha)\right]. \tag{19}$$

### 3.2. The Picard-like approach

In this section we extend the approach discussed in [8] to solve (10). Let us consider then the inverse operator

$$L_t^{-1}(\cdot) = \int_0^t \int_0^t (\cdot)dtdt. \tag{20}$$

In light of Theorems 5–8 in [18] , we may apply (20) on both sides of (10). So by recalling the definition of the Riemann–Liouville fractional derivative, we obtain

$$\mathbf{U}(t,\alpha) = \mathbf{A}(\alpha)\mathbf{w} + L_t^{-1}\Big(\mathbf{F}(\mathbf{U}(t,\alpha),\alpha) + \mathbf{G}(t,\alpha) - \delta^{RL}D^{\beta}\mathbf{U}(t,\alpha)\Big), \tag{21}$$

where

$$\mathbf{w}^T = (1,t)\,, \tag{22}$$

$$\mathbf{A}(\alpha) = \begin{pmatrix} \underline{a}_0(\alpha) & \underline{a}_1(\alpha) \\ \overline{a}_0(\alpha) & \overline{a}_1(\alpha) \end{pmatrix}. \tag{23}$$

Here, for $i = 0, 1$, we convey that $\underline{a}_i(\alpha)$ and $\overline{a}_i(\alpha)$ will represent the $i$th derivative with respect to $t$ of $\underline{u}$ and $\overline{u}$ respectively, at the point $(0,\alpha)$.

Using successive approximations, the solution $\mathbf{U}(t,\alpha)$ can be expressed as

$$\mathbf{U}(t,\alpha) = \sum_{k=0}^{\infty}\mathbf{U}_k(t,\alpha), \tag{24}$$

where $\mathbf{U}_k^T(t,\alpha) = (\underline{u}_k(t,\alpha), \overline{u}_k(t,\alpha))$ has to be determined recursively using the formulas

$$\mathbf{U}_0(t,\alpha) = \mathbf{A}(\alpha)\mathbf{w} + L_t^{-1}(\mathbf{G}(t,\alpha)), \tag{25}$$

$$\mathbf{U}_{k+1}(t,\alpha) = L_t^{-1}\left(-\delta^{RL}D^{\beta}\mathbf{U}_k(t,\alpha) + \mathbf{F}(\mathbf{U}_k(t,\alpha),\alpha)\right). \tag{26}$$

Consider fixed (though arbitrary) partitions $t_1 < t_2 < \ldots < t_{N-1} < t_N$ of the interval $[0,1]$.

Additionally, if we let $\underline{u}_{k,j}(\alpha) = \underline{u}_k(t_j,\alpha)$ and $\overline{u}_{k,j}(\alpha) = \overline{u}_k(t_j,\alpha)$, then

$$\mathbf{U}_k^T(\alpha) = \big(\underline{u}_{k,1}(\alpha),\ldots,\underline{u}_{k,N}(\alpha),\overline{u}_{k,1}(\alpha),\ldots,\overline{u}_{k,N}(\alpha)\big)\,. \tag{27}$$

Using numerical integration and the differential quadrature rules, we obtain that

$$\mathbf{U}_0(t,\alpha) = \mathbf{A}(\alpha)\mathbf{w} + \mathbf{C}(t)\mathbf{Q}(\alpha), \tag{28}$$

$$\mathbf{U}_{k+1}(t,\alpha) = \mathbf{C}(t)\left[-\gamma\mathbf{B}\mathbf{U}_k(\alpha) + \mathbf{F}(\mathbf{U}_k(\alpha),\alpha)\right], \tag{29}$$

where $\gamma = \delta/\Gamma(1-\beta)$ and

$$\mathbf{Q}^T(\alpha) = \big(\underline{g}(t_1,\alpha),\ldots,\underline{g}(t_N,\alpha),\overline{g}(t_1,\alpha),\ldots,\overline{g}(t_N,\alpha)\big)\,, \tag{30}$$

$$\mathbf{C}(t) = \begin{pmatrix} \mathbf{C}_0(t) & \mathbf{0} \\ \mathbf{0} & \mathbf{C}_0(t) \end{pmatrix}, \tag{31}$$

$$\mathbf{B} = \begin{pmatrix} \mathbf{B}_0 & \mathbf{0} \\ \mathbf{0} & \mathbf{B}_0 \end{pmatrix} \tag{32}$$

with $\mathbf{C}_0(t) = (C_1(t), \ldots, C_N(t))$ and $\mathbf{B}_0 = \mathbf{A}^{(1)}\mathbf{C}^{(\beta)}$. Here, $\mathbf{A}^{(1)}$ denotes the matrix of the DQ weighting coefficients and $\mathbf{C}^{(\beta)}$ the matrix of which entries are, for each $i = 1, \ldots, N$,

$$C_i^{\beta}(t) = \int_0^t l_i(s)(t-s)^{-\beta} ds, \tag{33}$$

with $l_i(s)$ being the Lagrange polynomial at the point $x_i$.

For the linear case, i.e. $f(\tilde{u}(t)) = -\omega_0^2 \tilde{u}(t)$, one gets

$$\mathbf{U}_{k+1}(t, \alpha) = \mathbf{H}(t)\mathbf{U}_k(\alpha) \tag{34}$$

where

$$\mathbf{H}(t) = \begin{pmatrix} \mathbf{H}_0 & \mathbf{0} \\ \mathbf{0} & \mathbf{H}_0 \end{pmatrix} \tag{35}$$

with $\mathbf{H}_0(t) = -\mathbf{C}_0(t)\left(\gamma \mathbf{B}_0 + \omega_0^2 \mathbf{I}\right)$, $\mathbf{I}$ being the identity matrix of size $N$.

Let $\mathbf{D}$ be the matrix

$$\mathbf{D} = \begin{pmatrix} \mathbf{D}_0 & \mathbf{0} \\ \mathbf{0} & \mathbf{D}_0 \end{pmatrix} \tag{36}$$

where $\mathbf{D}_0^T = [\mathbf{H}_0(t_1), \ldots, \mathbf{H}_0(t_N)]^T$. Since

$$\mathbf{U}_k(\alpha) = \mathbf{D}\mathbf{U}_{k-1}(\alpha) = \mathbf{D}^k \mathbf{U}_0(\alpha), \tag{37}$$

the truncation of (24) after $p$ terms becomes

$$\mathbf{U}^{[p]}(t, \alpha) = \mathbf{U}_0(t, \alpha) + \mathbf{H}(t) \sum_{k=0}^{p-1} \mathbf{D}^k \mathbf{U}_0(\alpha), \tag{38}$$

where $\mathbf{U}_0^T(\alpha) = \left(\underline{u}_{0,1}(\alpha), \ldots, \underline{u}_{0,N}(\alpha), \overline{u}_{0,1}(\alpha), \ldots, \overline{u}_{0,N}(\alpha)\right)$.

For the remainder of this work, we will represent the spectral radius of the matrix $\mathbf{D_0}$ by $\rho(\mathbf{D_0})$.

**Lemma 5.** *Suppose that $\rho(\mathbf{D}_0) \leq 1$. Then the solution $\mathbf{U}(t, \alpha)$ in (24) is given by*

$$\mathbf{U}(t, \alpha) = \mathbf{U}_0(t, \alpha) + \mathbf{H}(t)(\mathbf{I} - \mathbf{D})^{-1}\mathbf{U}_0(\alpha). \tag{39}$$

*Proof.* The proof follows as that of Theorem 1 in [8], by considering that in (38) there is a geometric series of matrices and that the spectral radius of $\mathbf{D}$ is equal to that of $\mathbf{D}_0$. □

It is the case to point out that an error bound can be derived similarly to the ones presented in [8], [10].

## 4. Simulations

As an example application, we discuss herein the free damped vibrations of a linear oscillator in a medium with small viscosity. The analytical solution of this problem in the crisp domain has been obtained in [11] by means of the method of multiple scales. In reason of the Zadeh's extension principle and in particular the $\alpha$-cut approach, we compared our solution on successive $\alpha$-cuts with the corresponding analytical solution [11] in the crisp domain.

We assumed null initial velocity and a triangular fuzzy number as initial displacement, that is

$$[\tilde{a}_0]_\alpha = [\alpha - 1, 1 - \alpha] \tag{40}$$

Besides, we fixed $\delta = 10^{-4}$ and $\omega_0 = 1$. In our simulations, we assumed $N = 9$ GCL points. We used (39) in view that the condition $\rho(\mathbf{D}_0) \leq 1$ holds. Figure 1 shows the approximate solution for $\beta = 0.75$.

With regard to the same value of $\beta$, the graphs of the approximate and analytical solutions obtained for some values of $\alpha$ are depicted in figure 2. The graphs are referred to the functions $\underline{u}$ (below) and $\overline{u}$ (above).

We obtained similar accurate results also for other values of $\beta$, such as $\beta = 0.5$ and $\beta = 0.995$. In our simulations, we observed that the maximum error, intended as the distance between the approximate and the analytical solution in accordance with the $\alpha$-cut approach, is of the order of $10^{-5}$.

## 5. Conclusions

In this work, a Picard-like numerical scheme which was formerly employed to solve integro–differential equations, has been extended to handle fuzzy initial value problems involving Riemann–Liouville fuzzy fractional derivatives. In the linear regime, the technique proposed here is a non-recursive scheme. As an example application, the problem of free damped vibrations of a linear oscillator in a medium with small viscosity has been considered. Numerical results show the effectiveness of the proposed approach.

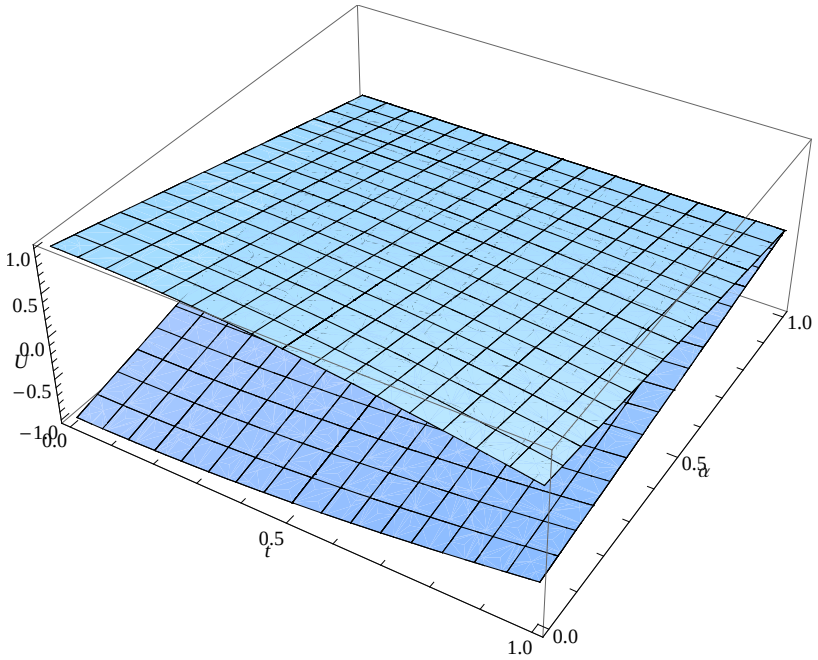


**Figure 1.** Approximate solution for $\beta = 0.75$. The graphs correspond to the functions $\underline{u}$ (below) and $\overline{u}$ (above).

**Acknowledgments**

Dr. Tomasiello wishes to thank Prof. Awrejcewicz for his kind support encouraging this work.

**References**

[1] ZADEH, L. A., Fuzzy sets. *Information and Control*, 8 (3) (1965), 338–353.

[2] BELLMAN R., ZADEH L. A., Decision-making in a fuzzy environment. *Management Science*, 17 (4) (1970), B–141.

[3] PAN, N. F., LIN, T.C., PAN, N.H., Estimating bridge performance based on a matrix-driven fuzzy linear regression model. *Automation in Construction*, 18 (5) (2009), 578–586.

[4] SÁNCHEZ, J. A., Calculating insurance claim reserves with fuzzy regression. *Fuzzy Sets and Systems*, 157 (23) (2006), 3091–3108.

[5] BUCKLEY, J. J., JOWERS, L. J., *Simulating Continuous Fuzzy Systems*, vol. 188 of Studies in Fuzziness and Soft Computing, Springer, 2006.

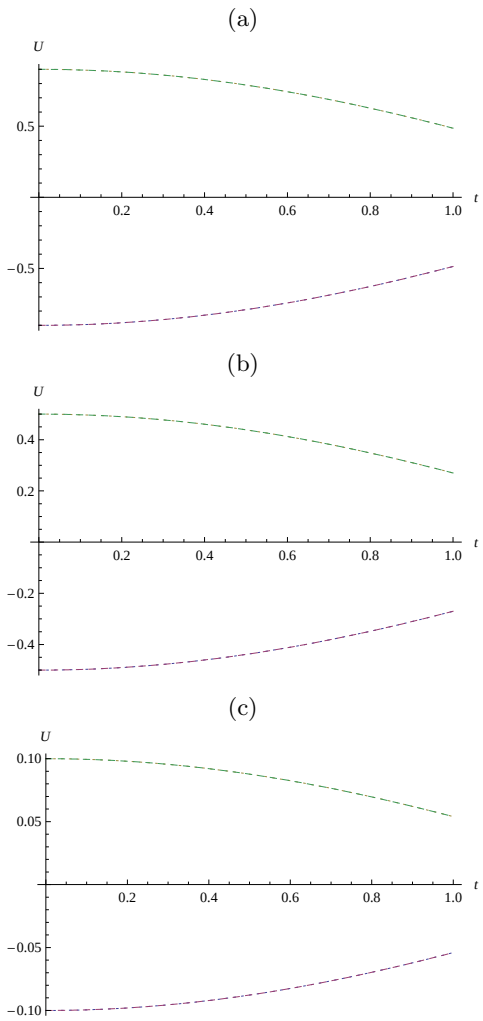


**Figure 2.** Graphs of the numerical (dotted line) and the analytical solutions (dashed line) for $\beta = 0.75$ and (a) $\alpha = 0.1$, (b) $\alpha = 0.5$, (c) $\alpha = 0.9$.

[6] VALLIAPPAN, S., PHAM, T., Fuzzy finite element analysis of a foundation on an elastic soil medium. *International Journal for Numerical and Analytical Methods in Geomechanics*, 17 (11) (1993), 771–789.

[7] ROSSIKHIN, A. YU., SHITIKOVA, M. V., Application of Fractional Calculus for Dynamic Problems of Solid Mechanics: Novel Trends and Recent Results. *Applied Mechanics Reviews*, 63 (2010), 010801-1–52.

[8] TOMASIELLO, S., Some remarks on a new DQ-based method for solving a class of Volterra integro-differential equations. *Applied Mathematics and Computation*, 219 (1) (2012), 399–407.

[9] BELLMAN, R., CASTI, J., Differential quadrature and long-term integration. *Journal of Mathematical Analysis and Applications*, 34 (2) (1971), 235–238.

[10] MACIAS-DIAZ, J.E., TOMASIELLO, S., A differential quadrature-based approach à la Picard for systems of partial differential equations associated with fuzzy differential equations. *Journal of Computational and Applied Mathematics* (2015), http://dx.doi.org/10.1016/j.cam.2015.08.009

[11] ROSSIKHIN, A. YU., SHITIKOVA, M. V., New Approach for the Analysis of Damped Vibrations of Fractional Oscillators. *Shock and Vibration*, 16 (2009), 365-387.

[12] BEDE, B., GAL, S.G., Generalizations of the differentiability of fuzzy-number-valued functions with applications to fuzzy differential equations. *Fuzzy sets and systems*, 151 (3) (2005), 581–599.

[13] ALLAHVIRANLOO, T., SALAHSHOUR, S., ABBASBANDY, S., Explicit solutions of fractional differential equations with uncertainty. *Soft Computing* 16(2) (2012), 297–302.

[14] BUCKLEY, J. J., FEURING, T., Fuzzy differential equations, *Fuzzy Sets and Systems*, 110 (1) (2000), 43–54.

[15] PURI, M. L. Puri, RALESCU, D. A., Differentials of fuzzy function, *Journal of Mathematical Analysis and Applications*, 91 (2) (1983), 552–558.

[16] BUCKLEY, J. J., QU, Y., On using $\alpha$-cuts to evaluate fuzzy functions. *Fuzzy Sets and Systems*, 38 (3) (1990), 309–312.

[17] SHU, C., *Differential quadrature and its application in engineering*, Springer–Verlag, London, 2000.

[18] GOMES, L. T., BARROS, L. C., Fuzzy calculus via extension of the derivative and integral operators and fuzzy differential equations. *Proceedings of the 2012 Annual Meeting of the North American Fuzzy Information Processing Society*, (2012), 1–5.

Stefania Tomasiello, Ph.D.: CORISA and Department of Information Engineering, Electrical Engineering and Applied Mathematics, University of Salerno, Via Giovanni Paolo II 132, 84084 Fisciano (SA), Italy (*stomasiello@unisa.it*). The author gave a presentation of this paper during one of the conference sessions.

Jan Awrejcewicz, Professor: Lodz University of Technology, Department of Automation, Biomechanics and Mechatronics, 1/15 Stefanowskiego Street, 90-924 Lodz, Poland (*jan.awrejcewicz@p.lodz.pl*).

# Application of the rigid finite element method in the dynamics of grab cranes (MAT077-15)

Andrzej Urbaś

*Abstract*: A dynamics analysis of grab cranes in the form of open-loop kinematic chains is presented in the paper. This analysis allows us to take into account these cranes' flexible connections with the ground as well as the flexibility of their links. The rigid finite element method is used to discretise the flexible links. Joint coordinates and homogeneous transformation matrices are used to describe the geometry of the system. Equations of motion are derived using the formalism of Lagrange equations. As an example, a grab crane built of eight links is presented. It is assumed that only one selected link of the crane is flexible. The influence of the flexible supporting system of the grab crane and the flexibility of the link on the movements of load are analysed. The author of this paper believes that the results of the method may have practical significance. The application of effective algorithms, taken from robotics, may be treated as an essential advantage of the method proposed.

## Introduction

The general mathematical model of a grab crane used for statics and dynamics analysis is presented in the paper. The grab crane can be built of any number of links. In order to discretise the flexible links, the rigid finite element method [3] is used in a modified formulation [5]. The selected links of grab crane are driven by means of flexible drives. The model's flexible connection with the ground is taken into account [4]. Joint coordinates and homogeneous transformation matrices are used to describe the motion of the links. Equations of motion of the system are derived by means of the formalism of Lagrange equations [2]. The numerical calculations include statics analysis (determining the initial configuration of the system as a result of taking into consideration the flexibility of the supports, links and drives) and dynamics analysis. The statics equations (nonlinear algebraic equations) were solved using the Newton-Raphson method. The dynamics equations (ordinary differential equations) were integrated by using the classical explicit Runge-Kutta method of the fourth order with a constant step size.

## 2. General model of a grab crane

The general model of a grab crane built of $n_l$ links ( link $p|_{p=1,\ldots,n_l}$ ) is presented in Fig. 1. The crane is supported by means of $n_s$ flexible supports ( sup $i|_{i=1,\ldots,n_s}$ ). The movement of the crane's selected

links is done by means of $n_{dr}$ flexible drives ( dr $p\big|_{p=2,\ldots,n_{dr}}$ ) with torque (force) $\mathbf{t}_{dr}^{(p)}$.

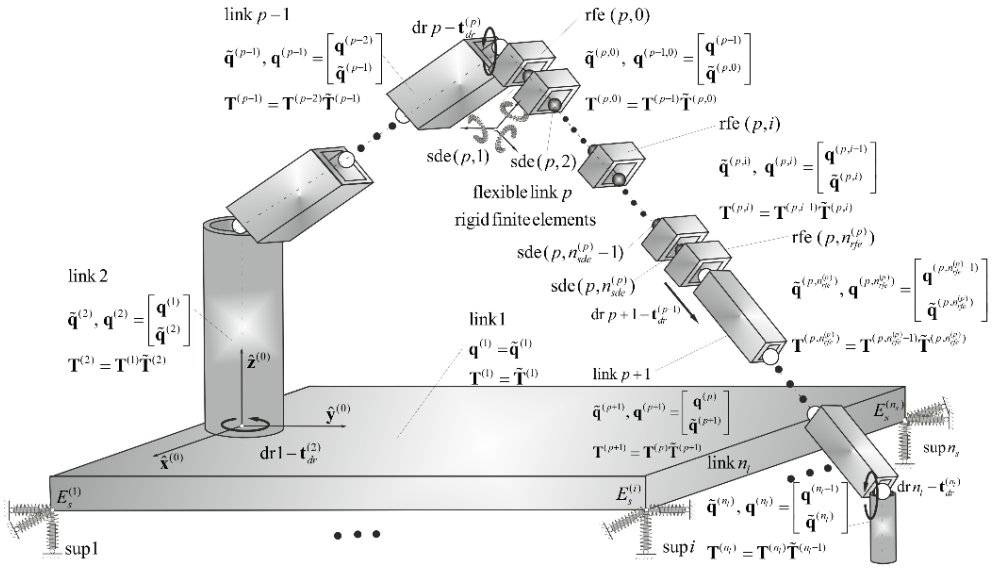


**Figure 1.** General model of a grab crane.

The motion of link $p$ is described by the joint coordinates and defined by vector:

$$\mathbf{q}^{(p)} = q_j^{(p)}\Big|_{\substack{p=1,..,n_l \\ j=1,\ldots,n_{dof}^{(p)}}} = \left[\mathbf{q}^{(p-1)^T} \;\vdots\; \tilde{\mathbf{q}}^{(p)^T}\right]^T, \tag{1}$$

where $\mathbf{q}^{(p-1)}$ – vector of generalised coordinates describing the motion of link $p-1$ with respect to reference system $\{0\}$, $\mathbf{q}^{(0)} = \varnothing$,

$\tilde{\mathbf{q}}^{(p)}$ – vector of generalised coordinates describing the motion of link $p$ with respect to link $p-1$, $\tilde{\mathbf{q}}^{(p)} = \tilde{q}_j^{(p)}\Big|_{\substack{p=1,..,n_l \\ j=1,\ldots,\tilde{n}_{dof}^{(p)}}}$,

$n_{dof}^{(p)}$ – number of generalised coordinates describing the motion of link $p$ with respect to reference system $\{0\}$, $n_{dof}^{(p)} = n_{dof}^{(p-1)} + \tilde{n}_{dof}^{(p)}$, $n_{dof}^{(0)} = 0$,

$\tilde{n}_{dof}^{(p)}$ – number of generalised coordinates describing the motion of link $p$ with respect to link $p-1$, $\tilde{n}_{dof}^{(p)} \le 6$.

The Denavit-Hartenberg notation is used to describe the geometry of particular links [1]. The homogeneous transformation matrices from the local coordinate systems to the reference system $\{0\}$ are determined according to the relationship:

$$\mathbf{T}^{(p)} = \mathbf{T}^{(p-1)}\tilde{\mathbf{T}}^{(p)}, \tag{2}$$

where $\mathbf{T}^{(p-1)}$ – homogeneous transformation matrix from the local coordinate system of link $p-1$ to reference system $\{0\}$, $\mathbf{T}^{(0)} = \mathbf{I}$,

$\tilde{\mathbf{T}}^{(p)}$ – homogeneous transformation matrix from the local coordinate system of link $p$ to the system of link $p-1$.

The equations of motion of the system are derived using the formalism of Lagrange equations. However, this requires determination of the kinetic energy, potential energy (gravity forces, spring deformation), and dissipation of energy.

### 2.1. Kinetic energy and potential energy of gravity forces

The kinetic energy of link $p$ is defined by the following formula:

$$E^{(p)} = \frac{1}{2}\mathrm{tr}\ \dot{\mathbf{T}}^{(p)}\mathbf{H}^{(p)}\dot{\mathbf{T}}^{(p)^T}, \tag{3}$$

where $\mathbf{H}^{(p)}$ – inertia matrix [5],

The Lagrange operators of link $p$ can be written in the following form:

$$\frac{\mathrm{d}}{\mathrm{d}t}\frac{\partial E^{(p)}}{\partial \dot{q}_j^{(p)}} - \frac{\partial E^{(p)}}{\partial q_j^{(p)}} = \begin{bmatrix} \tilde{\mathbf{A}}_{1,1}^{(p)} & \dots & \tilde{\mathbf{A}}_{1,j}^{(p)} & \dots & \tilde{\mathbf{A}}_{1,p}^{(p)} \\ \vdots & & \vdots & & \vdots \\ \tilde{\mathbf{A}}_{i,1}^{(p)} & \dots & \tilde{\mathbf{A}}_{i,j}^{(p)} & \dots & \tilde{\mathbf{A}}_{i,p}^{(p)} \\ \vdots & & \vdots & & \vdots \\ \tilde{\mathbf{A}}_{p,1}^{(p)} & \dots & \tilde{\mathbf{A}}_{p,j}^{(p)} & \dots & \tilde{\mathbf{A}}_{p,p}^{(p)} \end{bmatrix} \begin{bmatrix} \ddot{\tilde{\mathbf{q}}}^{(1)} \\ \vdots \\ \ddot{\tilde{\mathbf{q}}}^{(j)} \\ \vdots \\ \ddot{\tilde{\mathbf{q}}}^{(p)} \end{bmatrix} + \begin{bmatrix} \tilde{\mathbf{h}}_1^{(p)} \\ \vdots \\ \tilde{\mathbf{h}}_i^{(p)} \\ \vdots \\ \tilde{\mathbf{h}}_p^{(p)} \end{bmatrix}, \tag{4}$$

where $\tilde{\mathbf{A}}_{i,j}^{(p)}\Big|_{i,j=1,\dots,p} = \left(\tilde{a}^{(p)}_{n_{dof}^{(i-1)}+k,\,n_{dof}^{(j-1)}+l}\right)_{\substack{k=1,\dots,\tilde{n}_{dof}^{(i)} \\ l=1,\dots,\tilde{n}_{dof}^{(j)}}}$, $\tilde{a}_{i,j}^{(p)} = \mathrm{tr}\ \mathbf{T}_i^{(p)}\mathbf{H}^{(p)}\mathbf{T}_j^{(p)^T}$,

$$\tilde{\mathbf{h}}_i^{(p)}\Big|_{i=1,\dots,p} = \left(\tilde{h}^{(p)}_{n_{dof}^{(i-1)}+k}\right)_{k=1,\dots,\tilde{n}_{dof}^{(p)}}, \quad \tilde{h}_i^{(p)} = \sum_{m=1}^{n_{dof}^{(p)}}\sum_{n=m}^{n_{dof}^{(p)}} \mathrm{tr}\ \mathbf{T}_i^{(p)}\mathbf{H}^{(p)}\mathbf{T}_{m,n}^{(p)^T}\ \dot{q}_m^{(p)}\dot{q}_n^{(p)},$$

$$\mathbf{T}_m^{(p)} = \frac{\partial \mathbf{T}^{(p)}}{\partial q_m^{(p)}}, \quad \mathbf{T}_{m,n}^{(p)} = \frac{\partial^2 \mathbf{T}^{(p)}}{\partial q_m^{(p)}\partial q_n^{(p)}}.$$

The potential energy of gravity forces of link $p$ is defined as:

$$V_g^{(p)} = m^{(p)} g \mathbf{j}_3 \mathbf{T}^{(p)} \tilde{\mathbf{r}}_{C^{(p)}}^{(p)} , \tag{5}$$

where $g$ – acceleration of gravity,

$\tilde{\mathbf{r}}_{C^{(p)}}^{(p)}$ – vector describing the position of the centre of mass of link $p$ in the local coordinate system,

$$\mathbf{j}_3 = \begin{bmatrix} 0 & 0 & 1 & 0 \end{bmatrix}.$$

The derivatives of Eq. 5 take the form:

$$\frac{\partial V_g^{(p)}}{\partial \mathbf{q}^{(p)}} = \begin{bmatrix} \tilde{\mathbf{g}}_1^{(p)} \\ \vdots \\ \tilde{\mathbf{g}}_i^{(p)} \\ \vdots \\ \tilde{\mathbf{g}}_p^{(p)} \end{bmatrix}, \tag{6}$$

where $\tilde{\mathbf{g}}_i^{(p)}\Big|_{i=1,\ldots,p} = \left( \tilde{g}_{n_{dof}^{(i-1)}+k}^{(p)} \right)_{k=1,\ldots,\tilde{n}_{dof}^{(i)}}$, $\tilde{g}_i^{(p)} = m^{(p)} g \mathbf{j}_3 \mathbf{T}_i^{(p)} \tilde{\mathbf{r}}_{C^{(p)}}^{(p)}$.

When considering the system of $n_l$ rigid links, the kinetic energy and potential energy of gravity forces can be written, respectively, as follows:

$$E = \sum_{p=1}^{n_l} E^{(p)}, \quad V_g = \sum_{p=1}^{n_l} V_g^{(p)} , \tag{7}$$

and the equations of motion of $n_l$ links can be written as follows:

$$\mathbf{A}\ddot{\mathbf{q}} = \mathbf{e} , \tag{8}$$

where: $\mathbf{A} = \begin{bmatrix} \mathbf{A}_{1,1} & \cdots & \mathbf{A}_{1,j} & \cdots & \mathbf{A}_{1,n_l} \\ \vdots & & \vdots & & \vdots \\ \mathbf{A}_{i,1} & \cdots & \mathbf{A}_{i,j} & \cdots & \mathbf{A}_{i,n_l} \\ \vdots & & \vdots & & \vdots \\ \mathbf{A}_{n_l,1} & \cdots & \mathbf{A}_{n_l,j} & \cdots & \mathbf{A}_{n_l,n_l} \end{bmatrix}$, $\mathbf{A}_{i,j} = \sum_{l=\max\ i,j}^{n_l} \tilde{\mathbf{A}}_{i,j}^{(l)}$, $\mathbf{e} = \begin{bmatrix} \mathbf{e}_1 \\ \vdots \\ \mathbf{e}_i \\ \vdots \\ \mathbf{e}_{n_l} \end{bmatrix}$, $\mathbf{e}_i = -\sum_{l=i}^{n_l} \tilde{\mathbf{h}}_i^{(l)} + \tilde{\mathbf{g}}_i^{(l)}$

.

## 2.2. Modelling flexibility of the links

As was mentioned before, the rigid finite element method in the modified formulation is used to discretise the flexible links. In this method, flexible link $p$ is replaced by the system of rigid elements (rfe) interconnected by means of spring-damping elements (sde). The procedure of the discretisation is done in two stages. The first stage, called the primary division, consists of dividing the beam of length $l^{(p)}$ into $n_{div}^{(p)}$ sections of equal length $\delta^{(p)}$. The spring-damping features of the link are concentrated in $n_{sde}^{(p)}$ spring-damping elements and placed in the middle of each segment $\delta^{(p)}$ – Fig. 2a. In the second stage, called the secondary division (Fig. 2b), adjacent sections are connected into non-deformable rigid elements of acquiring characteristics inertia link. As a result of this discretisation we obtain a system consisting of $n_{rfe}^{(p)}$ rigid finite elements ($n_{rfe}^{(p)} = n_{div}^{(p)} + 1$) of length

$$l^{(p,i)} = \begin{cases} \delta^{(p)}\big|_{i=1,\ldots,n_{rfe}^{(p)}-2}, \\ 0.5\delta^{(p)}\big|_{i\in\{0,n_{rfe}^{(p)}-1\}}, \end{cases} \tag{9}$$

which are interconnected by means of $n_{sde}^{(p)}$ spring-damping elements ($n_{sde}^{(p)} = n_{div}^{(p)}$).

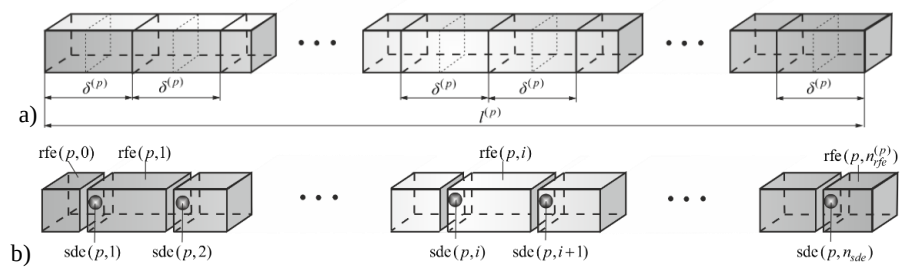


**Figure 2.** Discretisation of flexible link $p$ : a) primary division b) secondary division

The vector of generalised coordinates describing the motion of $\text{rfe}(p,i)\big|_{i=1,\ldots,n_{rfe}^{(p)}}$ with respect to $\text{rfe}(p,i-1)$ has the form:

$$\tilde{\mathbf{q}}^{(p,i)} = \tilde{q}_j^{(p,i)}\ {}^{p=1,\ldots,n_l}_{i=1,\ldots,n_{rfe}^{(p)}}_{j=1,2,3} = \left[\psi^{(p,i)} \quad \theta^{(p,i)} \quad \varphi^{(p,i)}\right]^T, \tag{10}$$

Angles $\psi^{(p,i)}$ and $\theta^{(p,i)}$ correspond to the bending of link $p$ in planes $\hat{\mathbf{x}}^{(p,i)}\hat{\mathbf{y}}^{(p,i)}$ and $\hat{\mathbf{x}}^{(p,i)}\hat{\mathbf{z}}^{(p,i)}$, respectively, whereas $\varphi^{(p,i)}$ is the angle of twist – Fig. 3.

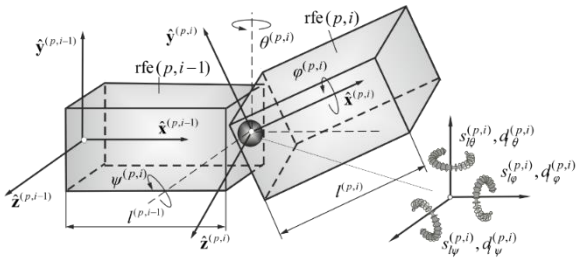


**Figure 3.** Generalised coordinates $\mathrm{rfe}(p,i)$

The vector of generalised coordinates describing the motion of $\mathrm{rfe}(p,i)$ with respect to reference system $\{0\}$ has the following components:

$$\mathbf{q}^{(p,i)} = \left[ \mathbf{q}^{(p-1)^T} \;\vdots\; \tilde{\mathbf{q}}^{(p,0)^T} \quad \tilde{\mathbf{q}}^{(p,i)^T} \right]^T . \tag{11}$$

The homogeneous transformation matrices from the local coordinates system of $\mathrm{rfe}(p,i)$ to reference system $\{0\}$ can be written as follows:

$$\mathbf{T}^{(p,i)} = \mathbf{T}^{(p,i-1)}\tilde{\mathbf{T}}^{(p,i)} . \tag{12}$$

This means that the flexible link is treated as a system of consecutive rigid elements (rfe), each having three-degrees-of-freedom in relative motion. Both the kinetic energy and the potential energy of the gravity forces are calculated according to the formulas that were outlined earlier. However, we need to take into account the potential energy of spring deformation and the dissipation of energy of link $p$, both of which are expressed by the relations:

$$V_l^{(p)} = \frac{1}{2}\sum_{i=1}^{n_{rfe}^{(p)}} \tilde{\mathbf{q}}^{(p,i)^T} \mathbf{S}_l^{(p,i)} \tilde{\mathbf{q}}^{(p,i)} , \; R_l^{(p)} = \frac{1}{2}\sum_{i=1}^{n_{rfe}^{(p)}} \dot{\tilde{\mathbf{q}}}^{(p,i)^T} \mathbf{D}_l^{(p,i)} \dot{\tilde{\mathbf{q}}}^{(p,i)} , \tag{13}$$

where: $\mathbf{S}_l^{(p,i)} = \mathrm{diag}\{s_{l,\psi}^{(p,i)}, s_{l,\theta}^{(p,i)}, s_{l,\varphi}^{(p,i)}\}$ , $\mathbf{D}_l^{(p,i)} = \mathrm{diag}\{d_{l,\psi}^{(p,i)}, d_{l,\theta}^{(p,i)}, d_{l,\varphi}^{(p,i)}\}$ ,

$(s_{l,\alpha}^{(p,i)}, d_{l,\alpha}^{(p,i)}\big|_{\alpha\in\{\psi,\theta,\varphi\}}$ – stiffness and damping coefficients of $\mathrm{rfe}(p,i)$ [3].

The derivatives of Eq. 13 take the form:

$$\frac{\partial V_l^{(p)}}{\partial \tilde{\mathbf{q}}^{(p,i)}} = \mathbf{S}_l^{(p)} \tilde{\mathbf{q}}^{(p,i)} , \; \frac{\partial R_l^{(p)}}{\partial \dot{\tilde{\mathbf{q}}}^{(p,i)}} = \mathbf{D}_l^{(p)} \dot{\tilde{\mathbf{q}}}^{(p,i)} , \tag{14}$$

where: $\mathbf{S}_l^{(p)} = \mathrm{diag}\;\left[\mathbf{S}_l^{(p,1)},\ldots,\mathbf{S}_l^{(p,n_{rfe}^{(p)})}\right]$ , $\mathbf{D}_l^{(p)} = \mathrm{diag}\;\left[\mathbf{D}_l^{(p,1)},\ldots,\mathbf{D}_l^{(p,n_{rfe}^{(p)})}\right]$ .

## 2.3. Modelling of the flexibility of the supports

The grab crane is supported by means of $n_s$ flexible supports ($\sup i\big|_{i=1,..,n_s}$), which are modelled using spring-damping elements – Fig. 4.

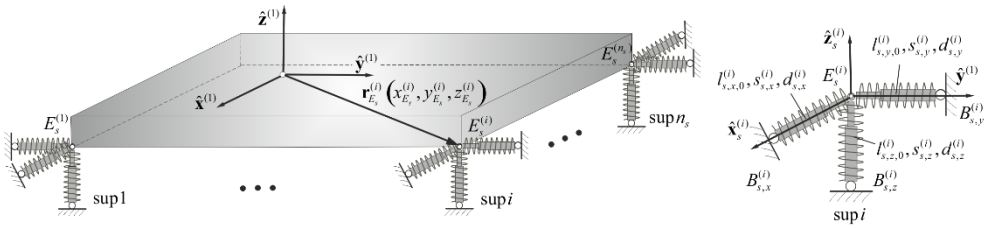


**Figure 4.** Model of flexible supports

The potential energy of spring deformation and the dissipation of energy of $\sup i$ in $\alpha$ direction ($\alpha \in \{x, y, z\}$) can be defined as:

$$V_{s,\alpha}^{(i)} = \frac{1}{2} e_{s,\alpha}^{(i)^T} s_{s,\alpha}^{(i)} e_{s,\alpha}^{(i)}, \; R_{s,\alpha}^{(i)} = \frac{1}{2} \dot{e}_{s,\alpha}^{(i)^T} d_{s,\alpha}^{(i)} \dot{e}_{s,\alpha}^{(i)}, \tag{15}$$

where: $e_{s,\alpha}^{(i)}$ – elongation of spring, $e_{s,\alpha}^{(i)} = l_{s,\alpha}^{(i)} - l_{s,\alpha,0}^{(i)}$,

$l_{s,\alpha}^{(i)}$ – length of the spring tense, $l_{s,\alpha}^{(i)} = \left| \mathbf{U}_{E_s}^{(i)} \tilde{\mathbf{q}}^{(1)} \right|$,

$$\mathbf{U}_{E_s}^{(i)} = \left[\begin{array}{ccc:ccc} 1 & 0 & 0 & 0 & z_{E_s}^{(i)} & -y_{E_s}^{(i)} \\ 0 & 1 & 0 & -z_{E_s}^{(i)} & 0 & x_{E_s}^{(i)} \\ 0 & 0 & 1 & y_{E_s}^{(i)} & -x_{E_s}^{(i)} & 0 \end{array}\right],$$

$l_{s,\alpha,0}^{(i)}$ – initial length of the spring,

$s_{s,\alpha}^{(i)}, d_{s,\alpha}^{(i)}$ – stiffness and damping coefficients.

Generalising, for any number of supports it can be written as:

$$V_s = \sum_{i=1}^{n_s} \sum_{\alpha \in \{x,y,z\}} V_{s,\alpha}^{(i)}, \; R_s = \sum_{i=1}^{n_s} \sum_{\alpha \in \{x,y,z\}} R_{s,\alpha}^{(i)}. \tag{16}$$

The derivatives of Eq. 16 take the form:

$$\frac{\partial V_s}{\partial \tilde{\mathbf{q}}^{(1)}} = \sum_{i=1}^{n_s} \sum_{\alpha \in \{x,y,z\}} s_{s,\alpha}^{(i)} \, l_{s,\alpha}^{(i)} - l_{s,\alpha,0}^{(i)} \, \frac{1}{l_{s,\alpha}^{(i)}} \left[ \mathbf{U}_{E_s}^{(i)^T} \mathbf{U}_{E_s}^{(i)} \tilde{\mathbf{q}}^{(1)} \right], \; \frac{\partial R_s}{\partial \dot{\tilde{\mathbf{q}}}^{(1)}} = \sum_{i=1}^{n_s} \sum_{\alpha \in \{x,y,z\}} d_{s,\alpha}^{(i)} \left[ \mathbf{U}_{E_s}^{(i)^T} \mathbf{U}_{E_s}^{(i)} \dot{\tilde{\mathbf{q}}}^{(1)} \right]. \tag{17}$$

## 2.4. Modelling of flexibility of the drives

The selected links of the grab crane are driven using $n_{dr}$ flexible drives ( $\mathrm{dr}\,p\big|_{p=2,\ldots,n_{dr}}$ ). The models of flexible drives with torque (force) $t_{dr}^{(p)}$ for revolute and prismatic joints are presented in Figs. 5a and 5b. The displacement $q_{dr}^{(p)}$ of the end of the dimensionless spring which models the flexibility of the drive varies according to the assumed function of time (Fig. 5c). Generalised coordinate $q_j^{(p)}$ , which is an unknown quantity, is determined when solving the equations of motion.

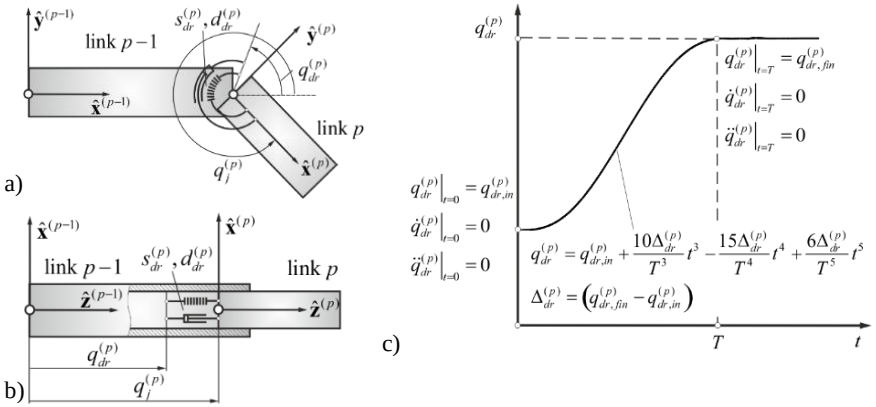


**Figure 5.** Model of the flexible drive

The energy of spring deformation and the dissipation of energy of the drive can be expressed as follows:

$$V_{dr}^{(p)} = \frac{1}{2} s_{dr}^{(p)} \left( q_{dr}^{(p)} - q_j^{(p)} \right)^2, \quad R_{dr}^{(p)} = \frac{1}{2} d_{dr}^{(p)} \left( \dot{q}_{dr}^{(p)} - \dot{q}_j^{(p)} \right)^2. \tag{18}$$

The derivatives of Eq. 18 take the form:

$$\frac{\partial V_{dr}^{(p)}}{\partial \tilde{q}_j^{(p)}} = -s_{dr}^{(p)} \left( q_{dr}^{(p)} - q_j^{(p)} \right), \quad \frac{\partial R_{dr}^{(p)}}{\partial \dot{\tilde{q}}_j^{(p)}} = -d_{dr}^{(p)} \left( \dot{q}_{dr}^{(p)} - \dot{q}_j^{(p)} \right). \tag{19}$$

The driving torque (force) for the flexible drive in a revolute (prismatic) joint can be written in the following form:

$$t_{dr}^{(p)} = -\left( \frac{\partial V_{dr}^{(p)}}{\partial q_j^{(p)}} + \frac{\partial R_{dr}^{(p)}}{\partial \dot{q}_j^{(p)}} \right). \tag{20}$$

An example of the application of the models developed here will be presented based on a grab crane whose kinematic structure consists of eight links.

## 3. Example of analysis

The model of the grab crane analysed here is presented in Fig. 6. It is assumed that only one link is treated as flexible. The crane is supported by means of eight flexible supports.

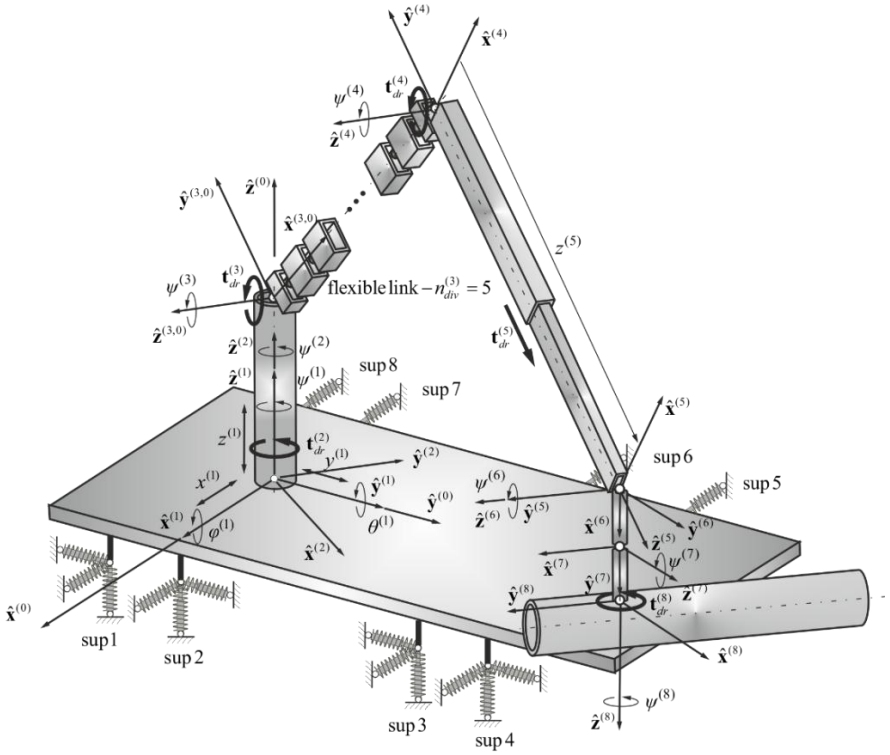


**Figure 6.** Model of the grab crane.

The generalised coordinates are the components of the vector:

$$\mathbf{q} = \left[ \tilde{\mathbf{q}}^{(1)^T} \quad \tilde{\mathbf{q}}^{(2)^T} \quad \tilde{\mathbf{q}}^{(3,0)^T} \quad \tilde{\mathbf{q}}^{(3,i)^T} \quad \tilde{\mathbf{q}}^{(4)^T} \quad \tilde{\mathbf{q}}^{(5)^T} \quad \tilde{\mathbf{q}}^{(6)^T} \quad \tilde{\mathbf{q}}^{(7)^T} \quad \tilde{\mathbf{q}}^{(8)^T} \right]^T, \tag{21}$$

where: $\tilde{\mathbf{q}}^{(1)} = \left[ x^{(1)} \quad y^{(1)} \quad z^{(1)} \quad \psi^{(1)} \quad \theta^{(1)} \quad \varphi^{(1)} \right]^T$, $\tilde{\mathbf{q}}^{(2)} = \left[ \psi^{(2)} \right]$, $\tilde{\mathbf{q}}^{(3,0)} = \left[ \psi^{(3)} \right]$,

$\tilde{\mathbf{q}}^{(3,i)}\Big|_{i=1,\ldots,n_{rfe}^{(3)}} = \left[ \psi^{(3,i)} \quad \theta^{(3,i)} \quad \varphi^{(3,i)} \right]^T$, $\tilde{\mathbf{q}}^{(4)} = \left[ \psi^{(4)} \right]$, $\tilde{\mathbf{q}}^{(5)} = \left[ z^{(5)} \right]$, $\tilde{\mathbf{q}}^{(6)} = \left[ \psi^{(6)} \right]$, $\tilde{\mathbf{q}}^{(7)} = \left[ \psi^{(7)} \right]$,

$\tilde{\mathbf{q}}^{(8)} = \left[ \psi^{(8)} \right]$.

The homogeneous transformation matrices have the following forms:

$$\tilde{\mathbf{T}}^{(1)}=\begin{bmatrix} \mathrm{c}\psi^{(1)}\mathrm{c}\theta^{(1)} & \mathrm{c}\psi^{(1)}\mathrm{s}\theta^{(1)}\mathrm{s}\varphi^{(1)}-\mathrm{s}\psi^{(1)}\mathrm{c}\varphi^{(1)} & \mathrm{c}\psi^{(1)}\mathrm{s}\theta^{(1)}\mathrm{c}\varphi^{(1)}+\mathrm{s}\psi^{(1)}\mathrm{s}\varphi^{(1)} & x^{(1)} \\ \mathrm{s}\psi^{(1)}\mathrm{c}\theta^{(1)} & \mathrm{s}\psi^{(1)}\mathrm{s}\theta^{(1)}\mathrm{s}\varphi^{(1)}+\mathrm{c}\psi^{(1)}\mathrm{c}\varphi^{(1)} & \mathrm{s}\psi^{(1)}\mathrm{s}\theta^{(1)}\mathrm{c}\varphi^{(1)}-\mathrm{c}\psi^{(1)}\mathrm{s}\varphi^{(1)} & y^{(1)} \\ -\mathrm{s}\theta^{(1)} & \mathrm{c}\theta^{(1)}\mathrm{s}\varphi^{(1)} & \mathrm{c}\theta^{(1)}\mathrm{c}\varphi^{(1)} & z^{(1)} \\ 0 & 0 & 0 & 1 \end{bmatrix},$$

$$\tilde{\mathbf{T}}^{(2)}=\begin{bmatrix} \mathrm{c}\psi^{(2)} & -\mathrm{s}\psi^{(2)} & 0 & 0 \\ \mathrm{s}\psi^{(2)} & \mathrm{c}\psi^{(2)} & 0 & 0 \\ 0 & 0 & 1 & 0 \\ 0 & 0 & 0 & 1 \end{bmatrix},\ \tilde{\mathbf{T}}^{(3,0)}=\begin{bmatrix} \mathrm{c}\psi^{(3)} & -\mathrm{s}\psi^{(3)} & 0 & 0 \\ 0 & 0 & -1 & 0 \\ \mathrm{s}\psi^{(3)} & \mathrm{c}\psi^{(3)} & 0 & l^{(2)} \\ 0 & 0 & 0 & 1 \end{bmatrix},$$

$$\tilde{\mathbf{T}}^{(3,i)}\Big|_{i=1,\ldots,n_{rfe}^{(p)}}=\begin{bmatrix} \mathrm{c}\psi^{(3,i)}\mathrm{c}\theta^{(3,i)} & \mathrm{c}\psi^{(3,i)}\mathrm{s}\theta^{(3,i)}\mathrm{s}\varphi^{(3,i)}-\mathrm{s}\psi^{(3,i)}\mathrm{c}\varphi^{(3,i)} & \mathrm{c}\psi^{(3,i)}\mathrm{s}\theta^{(3,i)}\mathrm{c}\varphi^{(3,i)}+\mathrm{s}\psi^{(3,i)}\mathrm{s}\varphi^{(3,i)} & l^{(3,i)} \\ \mathrm{s}\psi^{(3,i)}\mathrm{c}\theta^{(3,i)} & \mathrm{s}\psi^{(3,i)}\mathrm{s}\theta^{(3,i)}\mathrm{s}\varphi^{(3,i)}+\mathrm{c}\psi^{(3,i)}\mathrm{c}\varphi^{(3,i)} & \mathrm{s}\psi^{(3,i)}\mathrm{s}\theta^{(3,i)}\mathrm{c}\varphi^{(3,i)}-\mathrm{c}\psi^{(3,i)}\mathrm{s}\varphi^{(3,i)} & 0 \\ -\mathrm{s}\theta^{(3,i)} & \mathrm{c}\theta^{(3,i)}\mathrm{s}\varphi^{(3,i)} & \mathrm{c}\theta^{(3,i)}\mathrm{c}\varphi^{(3,i)} & 0 \\ 0 & 0 & 0 & 1 \end{bmatrix},$$

$$\tilde{\mathbf{T}}^{(4)}=\begin{bmatrix} \mathrm{c}\psi^{(4)} & -\mathrm{s}\psi^{(4)} & 0 & l^{(3,n_{rfe}^{(3)})} \\ \mathrm{s}\psi^{(4)} & \mathrm{c}\psi^{(4)} & 0 & 0 \\ 0 & 0 & 1 & 0 \\ 0 & 0 & 0 & 1 \end{bmatrix},\quad \tilde{\mathbf{T}}^{(5)}=\begin{bmatrix} 1 & 0 & 0 & 0 \\ 0 & 0 & -1 & -z^{(5)} \\ 0 & 1 & 0 & 0 \\ 0 & 0 & 0 & 1 \end{bmatrix},\quad \tilde{\mathbf{T}}^{(6)}=\begin{bmatrix} \mathrm{c}\psi^{(6)} & -\mathrm{s}\psi^{(6)} & 0 & 0 \\ 0 & 0 & 1 & 0 \\ -\mathrm{s}\psi^{(6)} & -\mathrm{c}\psi^{(6)} & 0 & 0 \\ 0 & 0 & 0 & 1 \end{bmatrix},$$

$$\tilde{\mathbf{T}}^{(7)}=\begin{bmatrix} \mathrm{c}\psi^{(7)} & -\mathrm{s}\psi^{(7)} & 0 & l^{(6)} \\ 0 & 0 & 1 & 0 \\ -\mathrm{s}\psi^{(7)} & -\mathrm{c}\psi^{(7)} & 0 & 0 \\ 0 & 0 & 0 & 1 \end{bmatrix},\ \tilde{\mathbf{T}}^{(8)}=\begin{bmatrix} \mathrm{c}\psi^{(8)} & -\mathrm{s}\psi^{(8)} & 0 & 0 \\ 0 & 0 & 1 & l^{(7)} \\ -\mathrm{s}\psi^{(8)} & -\mathrm{c}\psi^{(8)} & 0 & 0 \\ 0 & 0 & 0 & 1 \end{bmatrix}.$$

The equations of motion of the grab crane can be written as follows:

$$\mathbf{A}\ddot{\mathbf{q}}=\mathbf{e}+\mathbf{f}_{s,l}+\mathbf{t}_{dr}\,, \tag{22}$$

where $\mathbf{A}$ is defined by Eq. 8,

$$\mathbf{f}_{s,l}=\left[-\left(\frac{\partial V_s}{\partial\tilde{\mathbf{q}}^{(1)}}+\frac{\partial R_s}{\partial\dot{\tilde{\mathbf{q}}}^{(1)}}\right)^T\quad 0\quad 0\quad -\left(\frac{\partial V_l^{(3)}}{\partial\tilde{\mathbf{q}}^{(3,\mathrm{i})}}+\frac{\partial R_l^{(3)}}{\partial\dot{\tilde{\mathbf{q}}}^{(3,\mathrm{i})}}\right)^T\quad 0\quad 0\quad 0\quad 0\quad 0\right]^T,$$

$$\mathbf{t}_{dr}=\begin{bmatrix}\mathbf{0} & t_{dr}^{(2)} & t_{dr}^{(3)} & \mathbf{0} & t_{dr}^{(4)} & t_{dr}^{(5)} & 0 & 0 & t_{dr}^{(8)}\end{bmatrix}^T.$$

The equations of motion were integrated by using the classical explicit Runge-Kutta method of the fourth order with a constant step size equal to $10^{-4}\mathrm{s}$.

The geometrical parameters and initial and final configuration of the system analysed here are presented in Fig. 9.

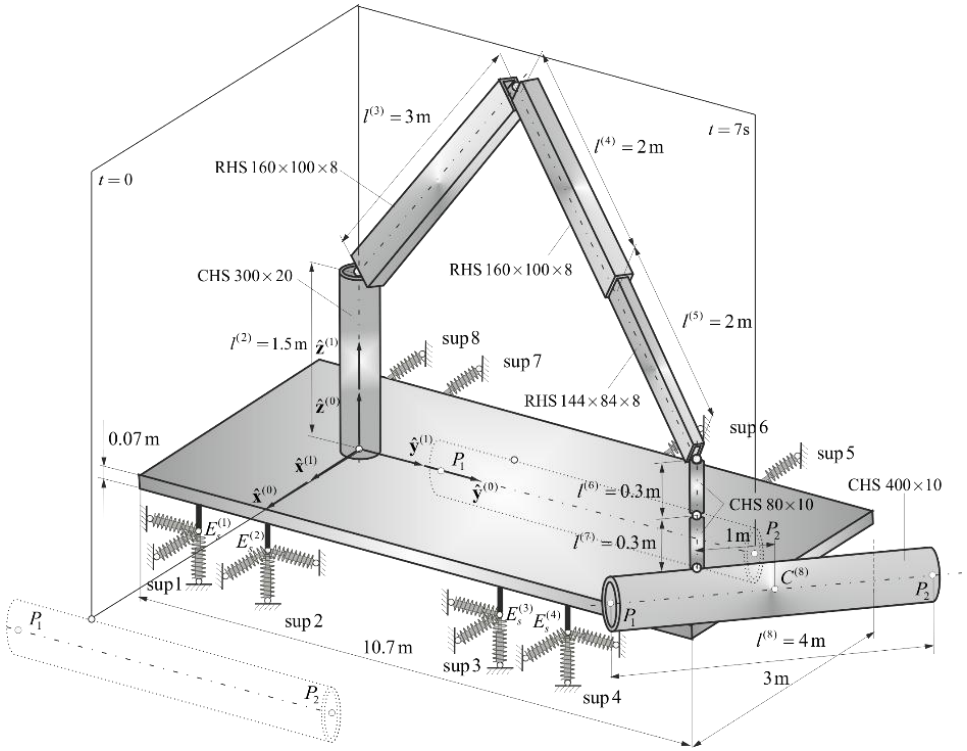


**Figure 7.** Parameters and configuration of the system

The parameters of the supports and drives are presented in Tabs. 1 and 2, respectively.

**Table 1.** Parameters of the supports

| sup $i$ | 1 | 2 | 3 | 4 | 5 | 6 | 7 | 8 |
|---|---|---|---|---|---|---|---|---|
| $x_{E_s}^{(i)}$[m] | 1.5 | 1.5 | 1.5 | 1.5 | −1.5 | −1.5 | −1.5 | −1.5 |
| $y_{E_s}^{(i)}$[m] | 0 | 1.0 | 8.0 | 9.0 | 9.0 | 8.0 | 1.0 | 0 |
| $z_{E_s}^{(i)}$[m] | −0.57 | | | | | | | |
| $l_{s,\alpha,0}^{(i)}\big\|_{\alpha\in\ x,y,z}$ [m] | 0 | | | | | | | |
| $s_{s,\alpha}^{(i)}\big\|_{\alpha\in\ x,y}$ [Nm$^{-1}$] | $3\cdot10^6$ | | | | | | | |
| $s_{s,z}^{(i)}$[Nm$^{-1}$] | $10^7$ | | | | | | | |
| $d_{s,\alpha}^{(i)}\big\|_{\alpha\in\ x,y}$ [Nsm$^{-1}$] | $5\cdot10^4$ | | | | | | | |
| $d_{s,z}^{(i)}$[Nsm$^{-1}$] | $9\cdot10^4$ | | | | | | | |

**Table 2.** Parameters of the drives

| dr $p$ | 2 | 3 | 4 | 5 | 8 |
|---|---|---|---|---|---|
| $q_{dr,in}^{(p)}$[rad],[m] | 0 | 0 | $\frac{1}{2}\pi$ | $-4$ | $\frac{3}{2}\pi$ |
| $q_{dr,fin}^{(p)}$[rad],[m] | $\frac{1}{2}\pi$ | $\frac{7}{18}\pi$ | $\frac{5}{18}\pi$ | $-3$ | $2\pi$ |
| $s_{dr}^{(p)}$[Nmrad$^{-1}$],[N m$^{-1}$] | $10^7$ | $10^7$ | $10^7$ | $10^8$ | $10^7$ |
| $d_{dr}^{(p)}$[Nsmrad$^{-1}$],[Ns m$^{-1}$] | $7\cdot10^3$ | $7\cdot10^3$ | $7\cdot10^3$ | $6\cdot10^4$ | $7\cdot10^3$ |

The trajectories of selected points of load are presented in Fig. 8.

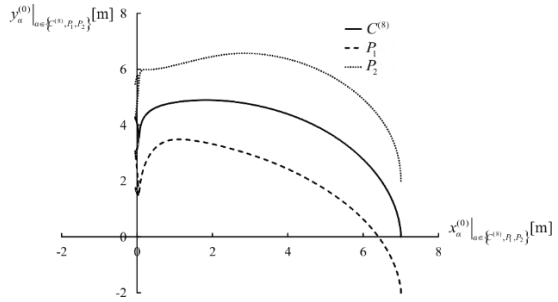


**Figure 8.** Influence of flexibility supports, link and drives on trajectories.

## 4. Conclusions

The mathematical model presented here can be treated as a virtual prototype, and the computer simulations allow us to predict the behaviour of a real object. The calculation results proved the significant influence of flexibility (supports, link and drives) on the dynamics of the grab crane that was analysed here. Thus the results of the work may be of interest to designers of cranes, and in particular when selecting drives in terms of stabilization of the motion of load.

## References


[1] Craig, J. J., *Introduction to robotics. Mechanics and control*, Addison-Wesley Publishing Company, Inc., 1989

[2] Jurevič, E.I. (ed.), *Dynamics of robot control*, Nauka, Moscow, 1984. (in Russian)

[3] Kruszewski, J., Sawiak, S., Wittbrodt, E., *The rigid finite element method in dynamics*. Science and Technical Publishers, Warsaw, 1999. (in Polish)

[4] Urbaś, A., Analysis of flexibility of the support and its influence on dynamics of the grab crane, *Latin American Journal of Solids and Structures* 10, 1 (2013), 109-121.

[5] Wittbrodt, E., Adamiec-Wójcik, I., and Wojciech, S., *Dynamics of flexible multibody systems. Rigid finite element method*. Springer, Berlin-Heidelberg, 2006.



Andrzej Urbaś, Ph.D.: University of Bielsko-Biala, Dept. of Mechanics, Bielsko-Biala, 43-309, Poland, (*aurbas@ath.eu*). The author gave a presentation of this paper during one of the conference sessions.

# Qualitative theory and identification of non-linear dissipative systems (NUM180-15)

Viktorija Volkova

*Abstract:* The article presents the results of experimental and analytic all investigations of an essentially non-linear dynamic system. Non-linearity is a common feature shared by mechanical systems, whereas their linear behaviour is an exception. One of the primary sources of non-linearity in mechanical system dynamics is non-linearity of dissipative characteristics. The author proposes to expand the phase space by taking into account the phase planes, namely, "acceleration -displacement" and "acceleration - speed". An interest taken into accelerations in dynamic systems is conditioned by the fact that these accelerations more sensitive to high-frequency components in oscillating processes. The author has defined behavioural peculiarities of phase trajectories and their mappings in the expanded phase space. It has performed the structural analysis of the phase trajectories obtained in the test records for vibrations of creaked steel reinforced beam in the expanded phase space.

## 1. Introduction

Both the static and dynamic processes in the mechanical systems may possess the non-linear elastic and/or dissipative characteristics, which must not be neglected. It is common knowledge that this is by no means always that a quite extensive and accurate description of the mechanical systems can be grounded merely on the basis of a direct express physical analysis. As a rule, some of the parameters have to be determined on the basis of experiments. In a number of instances even the structure of the mathematical model turns to be obscure [2-4]. Most of the currently available methods of nonparametric identification are based on the polynomial approximation of models. Thus, the targets of research of the majority of the modern methods of nonparametric identification are the time histories (i.e. the time processes), more specifically, studying the recorded changes, which occurred in the displacement of points in the system under investigation, in the time domain. These methods are based on the application of the wavelet transformation, the series of Wiener and Hammerstein. These approaches are cumbersome to implement, they involve the use of the computer technology [3, 5] and generate a need for storing significant amounts of initial information. These methods are also highly restrictive in terms of the types of systems that can be indentified and the modes of external testing excitation.

## 2. Sources of non-linearity

Non-linearity is a common feature shared by mechanical systems, whereas their linear behaviour is an exception. One of the primary sources of non-linearity in mechanical system dynamics is non-linearity of dissipative characteristics. In fact, energy dissipation is the least understood aspect in mechanical systems. Geometric non-linearity takes place when a structure undergoes large displacements and arises from the potential energy. Large deformations of flexible elastic beams, plates and shells are also responsible for geometric non-linearities. Non –linearity may also result due to boundary conditions, for example, free surfaces in fluids, vibro-impacts due to loose joints or contacts with rigid constraints, clearances, or certain external non-linear body forces.

The structural systems involve large number of elements that are connected through the bolts and pins. Joints and fasteners are used to transfer loads from one structural element to another. Structural joints are regarded as major source of non-linear phenomena. The complex behaviour of connecting elements plays an important role in the dynamic characteristics, such as natural frequencies, mode shapes, and non-linear response characteristics to external excitations. The stresses and slip in the vicinity of contact regions determine the static strength, cyclic plasticity, frictional damping, and vibration levels associated with the structure. The need for developing methods for developing models of structures with joints has been discussed in papers [7].

## 3. The phase trajectories and their representations in the nonparametric identification of models of mechanical systems

One of the trends in solving the direct problems of dynamics of structural elements is associated with the investigations into the behavior of the phase trajectories on the plane «displacement - velocity». In spite of the fact that the geometrical approach has been successfully used for quite a long period of time, it is precisely this approach, which forms the basis of nonlinear dynamics and provides possibilities to predict new effects in different fields of knowledge. The qualitative investigations of the dynamic system behaviour are confined to studying the behaviour of trajectories in the phase space. Henri Poincaré laid the foundations of the qualitative theory for studying dynamic processes [1]. The area of application of these techniques is not limited to the problems of autonomous vibrations. There are a number of research works wherein these trajectories were used in solving the inverse problem of mechanics, i.e. identification. The geometric presentation of a single phase trajectory or a set of trajectories enables one to arrive at the important conclusions on the characteristics of vibrations.

## 4. Differential equations of the system oscillations

We consider mechanical systems which can be described by the scalar differential equation

$$m\ \ddot{y}\ +\ h\ \left(y,\ \dot{y}\right)\ +\ r\ \ \left(y\right)=\ 0\,, \tag{1}$$

where $m$ is the mass, $h$ describes the damping force and $r$ is the restoring force.

We suppose that we have some preliminary knowledge about $h$ and $r$, e.g. $h$ has the form $h\left(y,\ \dot{y}\right)=\dot{y}\,g\left(y\right)$. Our goal is to get a more detailed description of $h$ and $r$ by applying some periodic force (excitation) to (see Eq. 1), that means, by studying the system

$$m\,\ddot{y}\ +\ h\left(y,\ \dot{y}\right)\ +\ r\left(y\right)=\ P\left(t\right),P\left(t+\omega\right)=P\left(t\right). \tag{2}$$

The qualitative behaviour of the autonomous system (1.1) can be determined by investigating the singular trajectories (equilibria, limit cycles, separatrices) and their stability in the $\left(y,\ \dot{y}\right)$ - plane, the so called phase plane [1]. The acceleration $\ddot{y}$ is uniquely determined by the state and the velocity $\dot{y}$ according to equation (see Eq. 1). The qualitative study of the $\omega$ - periodic system (see Eq. 2) is based on the investigation of the Poincaré map in the phase plane [3].

As mentioned above, our goal is to improve our knowledge of the functions $h$ and $r$ by applying a periodic force to the equation under consideration.

In practice, we have to do measurements in order to identify unknown parameters and functions. Usually, in this process the method of least squares plays an imported role. The aim of this note is to show that there is another approach in order to get more information about the unknown or only partly known system characteristics, provided we are able to measure not only state and velocity of the mechanical system under periodic excitation but also the acceleration. The role of acceleration in studying mechanical systems (see Eq. 1) has been demonstrated in [2]. In what follows we emphasize its importance also in investigating inverse problems.

## 5. Test of non-linearity

If we do not know the function $h$ and $r$, the first question is the following: Can we conclude from measurements whether the system is linear or non-linear?

We denote by $\left\{\Pi_k\right\}=\left\{\overline{y}_k,\dot{\overline{y}}_k,\ddot{\overline{y}}_k\right\}$ , $k\ =1,\ldots,\ n$, a sequence of points describing the measured state, velocity and acceleration of system (see Eq. 2) at the moment

$t = t_k = t_0 + k\omega$. If we represent this points in the extended phase space $\left(y,\ \dot{y},\ \ddot{y}\right)$ we get a set of points parameterised by the time $t_k$ (see figure 1).

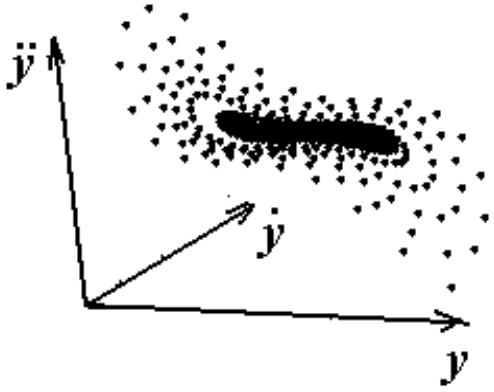


**Figure 1.** Set of measured points $\prod_k$ in the extended phase space.

In the ideal case when we have no measuring error it holds

$$m\ \ddot{\bar{y}}_k + h\left(\bar{y}_k,\ \dot{\bar{y}}_k\right) + r\left(\bar{y}_k\right) = C \text{ for } k = 1,\ldots,\ n, \tag{3}$$

where $C = P\left(t_o\right) = P\left(t_k\right)$ for all $k$. That mean, all points $\prod_k$ are located on the surface defined by $m\,w + h\left(u,\ v\right) + r\left(u\right) = C$ in the $\left(u,\ v,\ w\right)$ - space. If $h$ and $r$ are linear functions, then all points $\prod_k$ must be located in a plane $E$. Therefore, if there are two numbers $\alpha_1$ and $\alpha_2$ such that all points $\prod_k$ satisfy

$$m\,\ddot{\bar{y}}_k + \alpha_1\,\dot{\bar{y}}_k + \alpha_2\,\bar{y}_k = C \text{ for } k = 1,\ldots,\ n, \tag{4}$$

then this is an indicator that (2) represents a linear system. If we replace the force $P\left(t\right)$ by $\beta\ P\left(t\right),\ \beta > 0$, and the corresponding set $\prod_k{}^{(\beta)}$ satisfies $\prod_k{}^{(\beta)} = \beta \prod_k$, then this is another indicator of linearity.

Of course, in practice we have some measure error. If we can find constants $\alpha_1$ and $\alpha_2$ so that all measured points are located near the plane defined by $\alpha_1$, $\alpha_2$ and $C$, then we can conclude that system (see Eq. 2) is linear or weakly non-linear.

If we project the sequence $\{\Pi_k\}$ along the plane $E$ into the planes $(\bar{y},\ \dot{\bar{y}})$, $(\ddot{\bar{y}},\ \bar{y})$ and $(\ddot{\bar{y}},\ \dot{\bar{y}})$, then all points are located in a straight line.

As an example, we consider the linear equation

$$\ddot{y} + 0.1\dot{y} + y = 0.$$

We assume that behaviour of the system until the time $t = 0$ is characterized by the stable equilibrium state $y = 0$. At the moment $t = 0$ we apply the external force $\cos(t)$ and investigate numerically the corresponding initial problem

$$\ddot{y} + 0.1\dot{y} + y = \cos(t),\ y(0) = \dot{y}(0) = 0. \tag{5}$$

As the result we obtain the sequence of points $\{\Pi_k\} = \{\bar{y}_k, \dot{\bar{y}}_k, \ddot{\bar{y}}_k\}$ describing state, velocity and the acceleration at the moment $t = t_k = 2\pi k$, $k = 1, \ldots, n$. It is obvious that all these points satisfy the relationship

$$\ddot{\bar{y}}_k + 0.1\ \dot{\bar{y}}_k + \bar{y}_k = 1.$$

If we introduce the notation $F(k) := \ddot{\bar{y}} + 0.1\dot{\bar{y}} + \bar{y}$, then shows (see figure 2 ) that the points $\{\Pi_k\}$ define a straight line in the $(k,\ F)$ - plane.

Next we investigate a system described by the equation

$$\ddot{y} + 0.1\dot{y} + y + \beta y^3 = 0. \tag{6}$$

To test this system we apply the force $\cos t$ and investigate the initial value problem

$$\ddot{y} + 0.1\dot{y} + y + \beta y^3 = \cos(t),\ y(0) = \dot{y}(0) = 0. \tag{7}$$

and compute the corresponding sequence $\{\Pi^{\beta}{}_k\}$ satisfying

$$\ddot{\bar{y}}_k + 0.1\dot{\bar{y}}_k + \bar{y}_k = 1 - \beta\bar{y}_k^3.$$

Figure 2. shows that in the cases $\beta = 0.2;\ 0.3;\ 0.5$ these points do not define a straight line, and that the deviation from a straight line increases with increasing $\beta$.

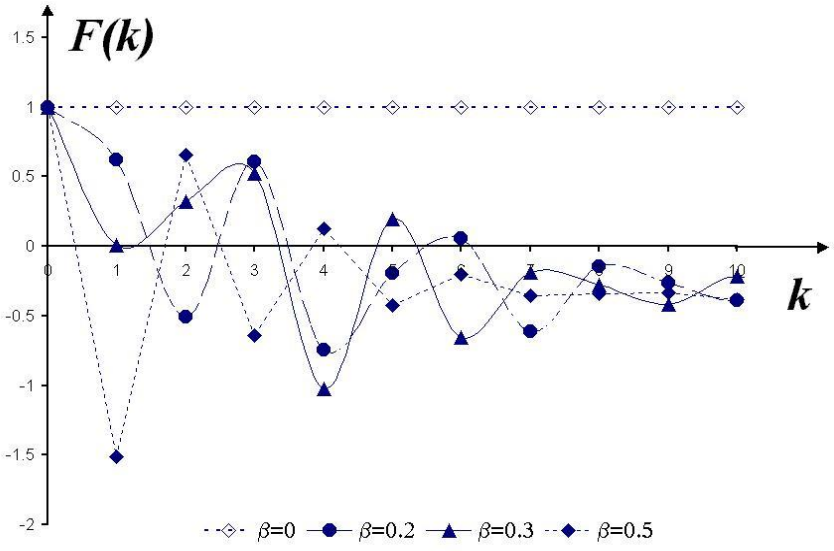


**Figure 2.** Representation of the sequence $\prod_k$ in the $(k,\ F)$ - plane.

As it has been demonstrated by a number of researchers in their works [5, 6], the expansion of the phase space by taking into account the phase planes $(y, \ddot{y})$ and $(\dot{y}, \ddot{y})$ substantially improves the efficiency of the analysis of dynamic system behaviour.

## 6. System with the special damping force

We consider a mechanical system described by the differential equation

$$m\,\ddot{y} \ + \ \dot{y}^2\, g\left(y\right) \ + \ r\left(y\right) = \ 0 \tag{8}$$

with $g\left(0\right) > 0; r\left(0\right) = 0$. We assume that $m$ is given, and that $y = 0$ is a stable equilibrium state of (see Eq. 8). In order to determine $g\left(y\right)$ and $r\left(y\right)$ we apply an $\omega$ - periodic force to (see Eq. 7), that is, we investigate the initial value problem

$$m \ \ddot{y} \ + \ \dot{y} \ \ g \ \ \left(y\right) \ + \ r \ \ \left(y\right) = \ P \ \ \left(t\right) \ , \ \ y \ \ \left(0\right) = 0 \, , \ \dot{y} \ \ \left(0\right) = 0 \, . \tag{9}$$

Using the transformation $t = \omega\tau$ we get from (see Eq. 9)

$$\frac{m}{\omega^2}\tilde{y}'' + \frac{\tilde{y}'^2}{\omega^2} g\ (\tilde{y}) + r(\tilde{y}) = \tilde{P}(\tau)\ ,\ \tilde{y}\ (0) = 0\,,\ \tilde{y}'(0) = 0\,. \tag{10}$$

If we assume that $\omega = m$, then we obtain from (see Eq. 10)

$$\tilde{y}'' + \tilde{y}' g\ (\tilde{y}) + \omega r(\tilde{y}) = \omega \tilde{P}(\tau)\ \ \tilde{y}\ (0) = 0\,,\ \tilde{y}'(0) = 0\,. \tag{11}$$

Now we suppose $\omega << 1$. In that case the initial value problem

$$\tilde{y}'' + \tilde{y}'^2 g\ (\tilde{y}) = 0\ ,\ \tilde{y}(0) = 0\,,\ \tilde{y}'(0) = 0$$

is an approximation of the initial value problem (see Eq. 9). If we suppose that the experimental investigation of (see Eq. 10) yields the sequence of measurements $\{\Pi_k\} = \{\overline{y}_k, \dot{\overline{y}}_k, \ddot{\overline{y}}_k\}$, then we can get a parameterised representation of $g(\tilde{y})$ by mean of the relation

$$g\ (\tilde{y}) = -\ \frac{\tilde{y}_k''}{\tilde{y}_k'},\ k = 0,1,2\ldots n..$$

To obtain more point for parameterised representation of $g(\tilde{y})$ we may proceed as in the section before, also in order to determine $r(y)$.

As an example we consider the dynamical system described by equation

$$m\ \ddot{y} + \dot{y}\ (0.1 + 100\ \ y^2) + y = 0\,.$$

To test this system we apply the force $\alpha \cos \omega t + \beta$ where $\omega = 0.00001;\ 0.00005;\ 0.0001$ and $\alpha = 1\,;\ \beta = -1$. According to our investigation above we arrive at this the initial value problem (see figure 3)

$$\ddot{\tilde{y}} + \dot{\tilde{y}}^2 (0.1 + 100\tilde{y}^2) + \omega\tilde{y} = \alpha \cos\tau + \beta\,,\ \tilde{y}\ (0) = 0\,,\ \tilde{y}'(0) = 0\,, \tag{12}$$

**7. Systems with large mass**

We consider the differential equation

$$m\ddot{y} + h(y, \dot{y}) + r(y) = 0\,, \tag{13}$$

where we assume that $m$ is given and that the damping force $h$ has the form $h(y, \dot{y}) = \dot{y}^k g(y),\ k \geq 1$. We suppose that neither $g$ nor $r$ are known. To determine the unknown function $r$ we consider the initial value problem

$$m\ddot{y} + \dot{y}^k g(y) + r(y) = P(t),\ y(0) = 0,\ \dot{y}(0) = 0, \tag{14}$$

where $P$ is $\omega$ - periodic. Introducing the slow time $\tau$ by $\tau = \omega t$, and using the notation $z(\omega t) = \tilde{z}(\tau)$, we get from (see Eq. 14)

$$\frac{m}{\omega^2}\tilde{y}'' + \frac{\tilde{y}'^k}{\omega^k} g(\tilde{y}) + r(\tilde{y}) = \tilde{P}(\tau),\ \tilde{y}(0) = 0,\ \tilde{y}'(0) = 0. \tag{15}$$

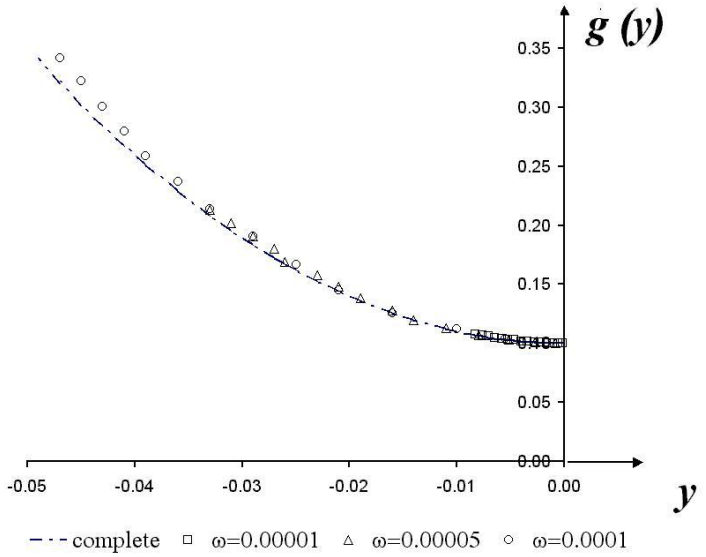


**Figure 3.** . Influence of the parameter $\omega$ to the dependency $g(y)$ for the fixed value of $\beta = -1$ and $\alpha = 1$.

$$\tilde{y}'' + \varepsilon\ \tilde{y}'^k g(\tilde{y}) + r(\tilde{y}) = \tilde{P}(\tau)\ . \tag{16}$$

If we suppose that $\varepsilon$ is small (that is $m$ is large), then we can study the initial value problem

$$\tilde{y}'' + r(\tilde{y}) = \tilde{P}(\tau),\ \tilde{y}(0) = 0,\ \tilde{y}'(0) = 0.$$

We denote the solution of this problem for $t = t_k = k\ \omega$ by $\bar{y}_k$. Thus, we have

$$\bar{y}_k'' + r(\bar{y}_k) = \bar{P}(t_k) = c \text{ for } k = 0, 1, \ldots n,$$

and we can determine $r(y)$ parametrically from the relations

$$r(\bar{y}_k) = c - \bar{y}_k'', \; k = 0, 1, \ldots n. \tag{17}$$

As mentioned above, if we need more points to determine $r(y)$, then we can consider the modified problem

$$\tilde{y}'' + r(\tilde{y}) = \alpha \tilde{P}(\tau) + \beta, \; \tilde{y}(0) = 0, \; \tilde{y}'(0) = 0,$$

where $\alpha$ and $\beta$ are real numbers.

If we have determined $r$, we can use (see Eq. 16) to obtain a parameterised representation of $g(y)$.

As an example, we consider the non-linear equation

$$100 \ddot{y} + 0.015\dot{y} + y + y^3 = 0 /$$

According to our investigation above we arrive at this the initial value problem

$$100 \ddot{\tilde{y}} + 0.015\dot{\tilde{y}} + \tilde{y} + \tilde{y}^3 = \tilde{P}(\tau), \tilde{y}(0) = 0, \; \tilde{y}'(0) = 0 \tag{18}$$

as $P(\tau)$ we choose $\alpha \cos\tau + \beta$.

The investigation of (see Eq. 18) yields the sequence of points $\{\Pi_k\}$. Representing $\{\Pi_k^{\alpha,\beta}\}$ in the $(y, r(\tilde{y}))$ - plane for $\beta = 0$ and $\alpha = 10, 20$ we get the following picture (see figure 4).

This picture shows that the sequence $\{\Pi_k\}$ determined the behaviour of $r$ is only for $-0.45 \le \tilde{y} \le 0$. To obtain more points we apply the force $20 \cos\tau + \beta$.

Figure 5 shows the corresponding parametrical representation of $r$ which sufficiently accurate.

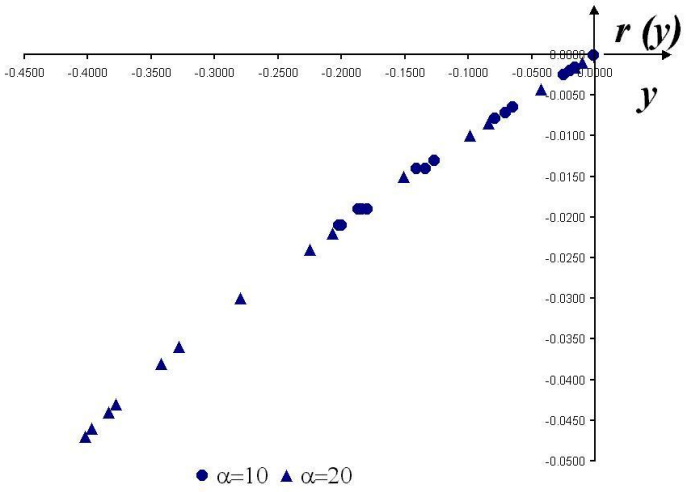


**Figure 4.** Influence of the parameter $\alpha$ to the dependency $r(y)$ for the fixed value of $\beta = 0$.

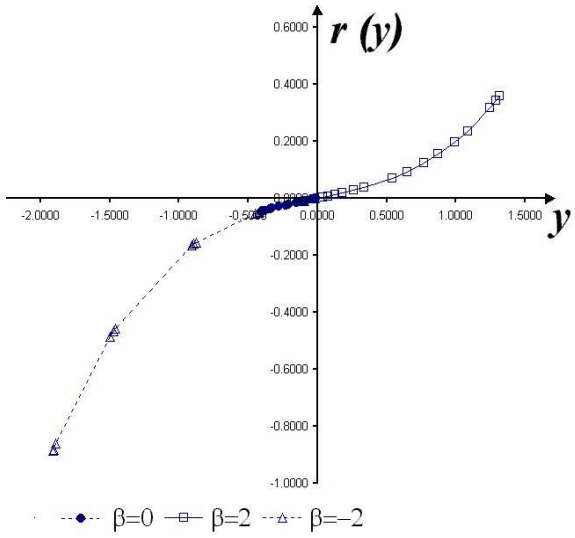


**Figure 5.** Influence of the parameter $\beta$ to the dependency $r(y)$ for the fixed value of $\alpha = 20$.

As it seen from figure 6, the results obtained by the (see Eq. 17) are close to exact soluton. All points lay in aone curve.

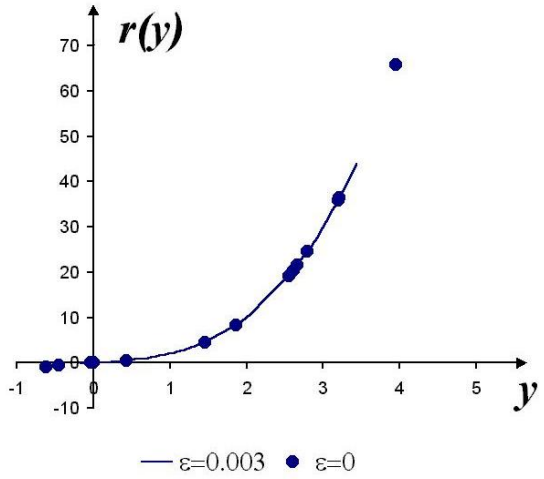


**Figure 6.** . Comparisson of the results obtained by exact formula and dependece (see Eq. 17).

## 8. Conclusions

Most mechanical systems show non-linear features at certain parameters of outer excitement. Various sources of non-linear behavior that may exist in engineering structures, for example, in the structures with bolted and pin joints, reinforced structures, damaged structural elements. Non-linearity is important in many structural dynamic applications that are of interest to engineers.

The identification of a non-linear model of mechanical systems experimental data represents a distinct challenge in view of the absence of superposition principle in non-linear dynamics. The problem discussed in the paper referred to the characterization of non-linearity. The method of nonparametric identification is suggested in the paper. The method is based on the usage of the information about accelerations, displacement, and also outer excitation. It uses the methods of the qualitative theory, and also regression by methods and approximating expressions of the elastic characteristic as functions from generalized co-ordinates. The capabilities of the suggested method are limited only to noise level, measuring error and length of process. The application of the suggested method is of interest and promising for engineering application.

## References

[1] Andronov, A., Leontovich, E., Gordon, I., Mayer, A/ *The Qualitative Theory of Dynamic Systems of the Second Order*: Main publishing house, State publishing house of the physical and mathematical literature, Moscow, 1966.

[2] Grop, D. *Identification of mechanical systems*, Mir, Moscow, 1980.

[3] Plakhtiyenko, M. P. Methods of Identification of Mechanical Oscillating Systems, *International Applied Mechanics*, 36(12), 2000, pp. 38-68 .

[4] Kerschen, G., Worden, K., Vakakis, A.F., Golinval, J.-C., Past, present and future of nonlinear system identification in structural dynamics, *Mechanical Systems. Signal Process*, 20 (3), 2006, pp 505–592.

[5] Volkova, V.E., Kazakevitch M.I., Application of the extended phase trajectories to identification of chaotic systems, *Inverse Problems in Science and Engineering*, 17 (2), 2009, pp.203 - 212..

[6] Volkova, V. E., Schneider, K., Qualitative theory and identification of dynamic system with one degree of freedom, *International Applied Mechanics*, 41(6), 2005, pp. 134 -139.

[7] Ibrahim, R.A., Pettit, C.L. Uncertainties and dynamic problems of bolted joints and other fasteners. *Journal of Sound and Vibration,*.279, 2005,pp. 857–936.

Viktorija Volkova, Professor: SHEI "National Mining University"/ Construction Department, Televizionnaya 12 ap.48, Dnepropetrovsk, UA49005, Ukraine (drvev@mail.ru).

# Experimental and numerical investigations of a pendulum driven by a low-powered DC motor (NUM305-15)

Grzegorz Wasilewski, Grzegorz Kudra, Jan Awrejcewicz, Maciej Kaźmierczak, Mateusz Tyborowski, Marek Kaźmierczak

*Abstract:* The work is a continuation of numerical and experimental investigations of a system consisting of a single pendulum with the joint horizontally driven by the use of a crank-slider mechanism and DC motor. The power supplied to the DC motor is relatively small when compared with our earlier investigations, which results in clear return influence of the pendulum dynamics on the DC motor angular velocity and much more rich bifurcation dynamics of the whole system, including regions of chaotic behaviour. In the experiments, the motor is supplied by the use of different but constant in time voltages. A series of experiments allow for accurate estimation of the model parameters and, in the further step, for prediction of the real system behaviour, also for other functions representing input voltage, including the time-varying ones.

## 1. Introduction

There exist a lot of studies on non-linear dynamics of mechanical systems composed of pendulums in different configurations, including plane or spatial, single or multiple, and sometimes parametrically excited pendulums. Physicians are particularly interested in those kinds of the dynamical systems, since they are relatively simple but can exhibit almost all aspects and phenomena of non-linear dynamics. In some case an experiment is performed in order to confirm analytical or numerical investigations [1-3]. Sometime, in order to achieve a good agreement between the model's predictions and experimental data, one must take into account many details concerning physical modelling of the real process [3].

When considering behavior of the real dynamical systems one can encounter a problem of mutual interactions between the oscillatory system and the energy source of limited power, i.e. non-ideal energy source. Belato et al. [4] investigated numerically the electro-mechanical system composed of a pendulum excited by a crank-shaft-slider mechanism driven by a DC motor considered as a limited power source. A comprehensive numerical analysis of bifurcational dynamics of a similar mechanical system is presented in [5]. An extensive review on the non-ideal vibrating systems one can find in [6].

In the work [7], the authors investigated both numerically and experimentally an electro-mechanical system consisting of a pendulum suspended on the slider of a crank-slider mechanism driven by a DC motor. Since the power of the motor was relatively high, the angular velocity of the

shaft was almost constant. Mathematical modelling of the same system under simplifying assumption of a constant angular velocity of the crank, together with the improved algorithm of the parameters' estimation, is presented in [8].

In the present work, the same structure of the mathematical model as in [7] is used in the analysis of the similar real electro-mechanical system, but in the case of relatively low power supplied to the DC motor, resulting in more variable angular velocity of the crank.

## 2. Experimental rig

Figure 1 presents the experimental setup of mathematical model that will be described in next part of the paper. A voltage generator 1 supplies the low power DC motor 3. Output shaft of the motor is connected with steel shaft 5 by aluminium coupling 4. Shaft 5 is embedded in pair of ball bearings 6 that provides alignment of shafts. Ball bearings are mounted on 'L' bracket 7a with additional two brackets in 'C' 7b and 'L' 7c shape that support first one to be more stable. Two aluminium strips 7d act as rails to set 'L' bracket both with ball bearings and with DC motor to set them in right position.

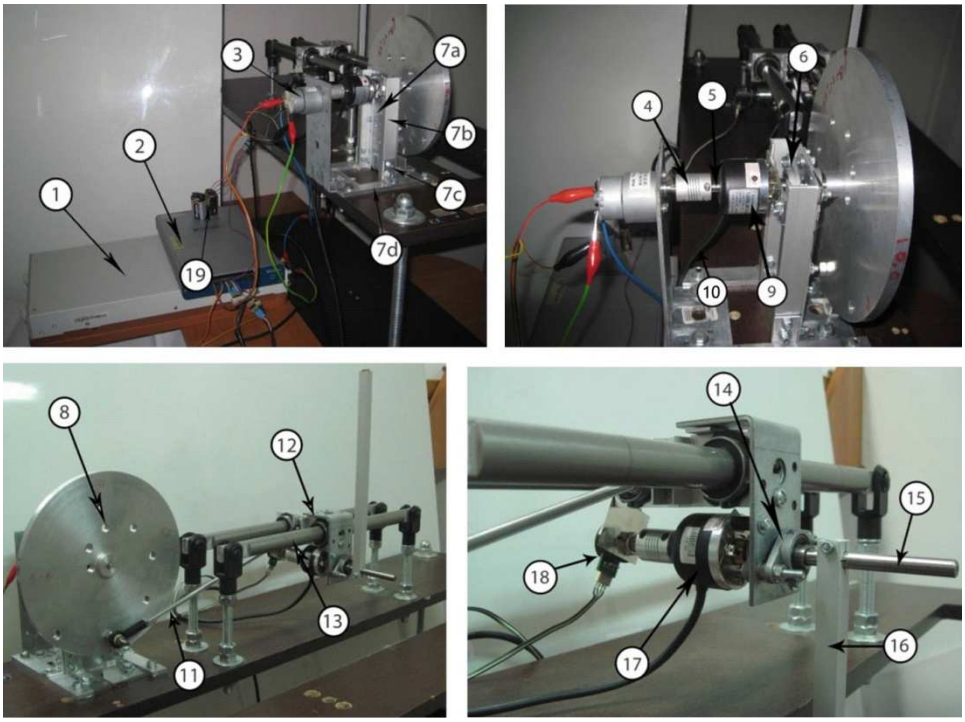


**Figure 1.** Experimental setup

There is also the possibility to change low power DC motor into other one with higher power. On the other end of shaft 5 there is mounted disk 8. Angular position of disk is measured by the use of

encoder 9 (type MHK, 360 steps) supplied by wire 10. Rotational motion of disk is transformed thanks to joint 11 (connecting bar) into linear motion of the slider 12 moving on two horizontal guides 13. To the slider there is mounted bracket with two ball bearings 14 (same type as 5) and shaft 15 inserted into them. On this part there is seated physical pendulum 16. In identical way like disk, angular position of pendulum is measured by two types of encoders. 17 is the same type like in case of measuring position of disk. Encoder 18 (type MAB-analog out, supplied by to batteries 19) is used to perform longer measurement, because encoder 17 (type MHK, 3600 steps) have a high resolution what really quickly fills up available space on PC hard disk. All data from encoders are collected by data acquisition 2.

## 3. Mathematical modelling

In this section there is presented the mathematical model of the experimental rig presented in section 2. It is based on the results published in the work [7]. Figure 2(a) exhibits a block diagram presenting the general structure of the system. It is composed of two main subsystems: i) DC motor (understood as a pure electrical object converting the electrical energy to the mechanical torque; ii) a two-degree-of –freedom mechanical system including all mechanical elements of the system. The input signal (being under control) is the voltage $u(t)$ supplied to the DC motor. The two coordinates $\theta(t)$ and $\varphi(t)$ determining the position of the mechanical system are assumed to be outputs.

For an armature controlled DC motor equipped with a gear transmission and assuming that the armature inductance is negligible, one gets the following equation

$$M = \frac{K_T}{R} i_g u - \frac{K_E K_T}{R} i_g^2 \frac{d\theta}{dt}, \tag{1}$$

where $M$ is the torque on the output shaft of the gear transmission, $u$ – input voltage, $\theta$ – angular position of the output shaft of the gear transmission, $i_g$ – reduction ratio of the gear transmission, $R$ – armature resistance, $K_T$ – the proportionality constant between the torque generated on the output shaft of the DC motor and the armature current, $K_E$ - the proportionality constant between the back electromotive force and the angular velocity of the DC motor.

A sketch of a physical model of the mechanical section of the system is depicted in figure 2(b). This plane two-degree-of-freedom mechanical systems is composed of four rigid bodies (1- disk, 2 – connecting bar, 3 – slider, 4 - pendulum) connected by the use of four rotational joints ($O$, $A$, $B_1$ and $B_2$). Masses of the links 2-4 are denoted as $m_b$, $m_S$ and $m$, respectively. Moments of inertia of the bodies 1, 2 and 4, with respect to their mass centers (located in the points $O$, $C_2$ and $C_4$), are represented by the symbols $I_O$, $I_b$ and $I$, respectively. The corresponding lengths of the mechanical system are denoted as follows: $a=OA$, $b=AB$, $b_1=AC_2$ and $r=BC_4$. The position of the system is determined by two angles: $\theta$ - angular position of the disk (equal to the angular position of the gear

transmission output shaft) and $\varphi$ – angular position of the pendulum. The disk 1 represents all rotating elements of the DC motor, gear transmission and real disk of the experimental rig.

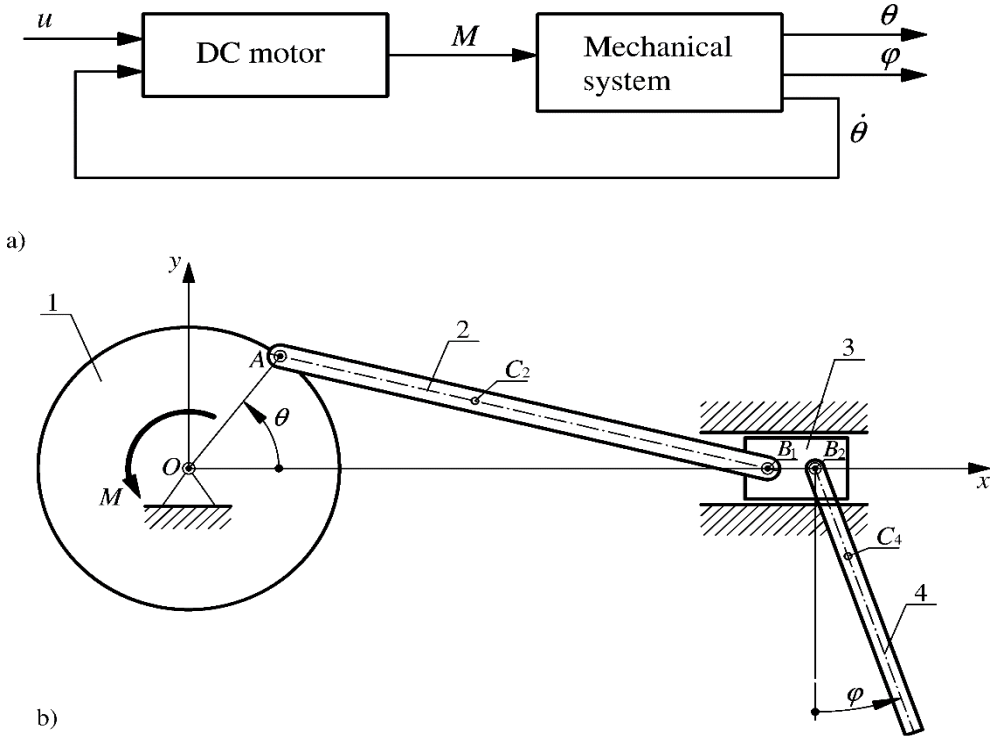


**Figure 2.** Physical model of the system

The governing equations of the investigated system read

$$\mathbf{M}(\mathbf{q})\ddot{\mathbf{q}} + \mathbf{N}(\mathbf{q})\dot{\mathbf{q}}^{\mathbf{2}} + \mathbf{w}(\mathbf{q}) = \mathbf{f}(t) - \mathbf{r}(\mathbf{q}, \dot{\mathbf{q}}), \tag{2}$$

where

$$\mathbf{q} = \begin{Bmatrix} \theta \\ \varphi \end{Bmatrix}, \quad \dot{\mathbf{q}} = \begin{Bmatrix} \dot{\theta} \\ \dot{\varphi} \end{Bmatrix}, \quad \ddot{\mathbf{q}} = \begin{Bmatrix} \ddot{\theta} \\ \ddot{\varphi} \end{Bmatrix}, \quad \dot{\mathbf{q}}^{\mathbf{2}} = \begin{Bmatrix} \dot{\theta}^2 \\ \dot{\varphi}^2 \end{Bmatrix},$$

$$\mathbf{M}(\mathbf{q}) = \begin{bmatrix} I_O + a^2(F^2(m+m_S) + F_1^2 m_b) + \dfrac{a^2}{b^2}\cos^2\theta((b-b_1)^2 m_b + G^2 I_b) & -amrF\cos\varphi \\ -amrF\cos\varphi & I + mr^2 \end{bmatrix},$$

$$\mathbf{N}(\mathbf{q}) =$$

$$= \begin{bmatrix} aFH\left(1+\dfrac{m_S}{m}\right) + aF_1H_1 - \dfrac{a^2}{2b^2}\sin 2\theta\left((b-b_1)^2 m_b + G^2 I_b\left(1 - \dfrac{a^2}{b^2}G^2\cos^2\theta\right)\right) & amrF\sin\varphi \\ -rH\cos\varphi & 0 \end{bmatrix},$$

$$\mathbf{w}(\mathbf{q}) = \begin{Bmatrix} \frac{a}{b}(b-b_1)m_b g\cos\theta \\ mgr\sin\varphi \end{Bmatrix}, \quad \mathbf{f}(t) = \begin{Bmatrix} M(t) \\ 0 \end{Bmatrix}, \quad \mathbf{r}(\mathbf{q}, \dot{\mathbf{q}}) = \begin{Bmatrix} M_{R\theta}(\theta, \dot{\theta}) \\ M_{R\varphi}(\dot{\varphi}) \end{Bmatrix}, \tag{3}$$

and where one has used the following notation

$$G = \frac{1}{\sqrt{1-\frac{a^2}{b^2}\sin^2\theta}}, \quad F = \left(1+\frac{a}{b}G\cos\theta\right)\sin\theta, \quad F_1 = \left(1+\frac{ab_1}{b^2}G\cos\theta\right)\sin\theta,$$

$$H = am\left(\cos\theta + \frac{a}{b}G\cos 2\theta + \frac{1}{4}\frac{a^3}{b^3}G^3\sin^2 2\theta\right),$$

$$H_1 = am_b\left(\cos\theta + \frac{ab_1}{b^2}G\cos 2\theta + \frac{1}{4}\frac{a^3b_1}{b^4}G^3\sin^2 2\theta\right). \tag{4}$$

The vector $\mathbf{r}(\mathbf{q}, \dot{\mathbf{q}})$ contains all resistance forces and their components:

$$M_{R\theta}(\theta, \dot{\theta}) = c_O\dot{\theta} + \frac{2}{\pi}M_O\arctan(\varepsilon\dot{\theta}) + a^2F^2c_S\dot{\theta} - \frac{2}{\pi}aFT_S\arctan(-\varepsilon aF\dot{\theta}),$$

$$M_{R\varphi}(\dot{\varphi}) = c_B\dot{\varphi} + \frac{2}{\pi}M_B\arctan(\varepsilon\dot{\varphi}), \tag{5}$$

The terms $c_O\dot{\theta}$ and $\frac{2}{\pi}M_O\arctan(\varepsilon\dot{\theta})$ represent the viscous damping and dry friction components of the resistance in the joint *O*, where $c_O$ is viscous damping coefficient, $M_O$ - magnitude of dry friction torque, while $\varepsilon$ is large numerical parameter used in the dry friction model regularization. One assumes that $M_O$ is a constant parameter, independent from the loading of the joint *O*. The expressions $a^2F^2c_S\dot{\theta}$ and $-\frac{2}{\pi}aFT_S\arctan(-\varepsilon aF\dot{\theta})$ represents the viscous damping and dry friction components of resistance between the slider and guide, reduced to the coordinate $\theta$, where $c_S$ and $T_S$ are the corresponding constant parameters. Similarly, the terms $c_B\dot{\varphi}$ and $\frac{2}{\pi}M_B\arctan(\varepsilon\dot{\varphi})$ are viscous damping and dry friction components in the joint $B_2$. Resistances in the joints *A* and $B_1$ are not taken into account.

Finally one gathers the right-hand side of Eq. (6) into one vector:

$$\mathbf{f}_r(t, \mathbf{q}, \dot{\mathbf{q}}) = \mathbf{f}(t) - (\mathbf{q}, \dot{\mathbf{q}}) =$$

$$= \begin{Bmatrix} K_M u(t) - C_O\dot{\theta} - \frac{2}{\pi}M_O\arctan(\varepsilon\dot{\theta}) - a^2F^2c_S\dot{\theta} + \frac{2}{\pi}aFT_S\arctan(-\varepsilon aF\dot{\theta}) \\ -c_B\dot{\varphi} - \frac{2}{\pi}M_B\arctan(\varepsilon\dot{\varphi}) \end{Bmatrix}, \tag{6}$$

where

$$K_M = \frac{K_T}{R}i_g, \quad C_O = \frac{K_EK_T}{R}i_g^2 + c_O.$$

Let us note, that the mechanical viscous damping in the joint *O* and the back electromotive force (multiplied by some other constants) have mathematically the same influence on the final torque on the output shaft of the gear transmission. They are mathematically indistinguishable and unidentifiable in the developed model. Their aggregate action is defined by the coefficient $C_O$.

## 4. Parameter estimation

In the process of identification, one has used four experimental solutions, with the input signal $u(t)$ in a form of step function with zero initial value, and constant final value u0, equal to -7, -7.5, -8.0 and -8.5 V, respectively. The initial conditions are the same for all experiments: $\theta(0) = -\frac{\pi}{2}\text{rad},\ \varphi(0) = 0\ \text{rad},\ \dot{\theta}(0) = 0\ \text{rad/s}$ and $\dot{\varphi}(0) = 0\ \text{rad/s}$. The solutions tend to periodic attractors, which allows to avoid problems of identification related to high sensitivity to initial conditions. The angles $\varphi(t)$ and $\theta(t)$ were recorded on the time interval [0, 100] s.

Because of non-ideal behavior of resistances in the system (small random fluctuations of friction), the angular velocity of the disk undergoes some random changes, which cannot be described by the use of deterministic equations. These changes are not big, but after some time they can lead to significant time shift in the angular position of the disk. It may cause problems in fitting of the simulated signals to those obtained experimentally, if we express them in the time domain. This is the reason of the idea to compare the corresponding signals expressed as functions of angular position of the disk $\theta$.

Since we plan to use in the estimation process two different signals (angular position of the pendulum and angular velocity of the disk), we construct the objective function $F_o$ in the form of weighted sum of two different parts:

$$F_O(\boldsymbol{\mu}) = w_\varphi F_{O\varphi}(\boldsymbol{\mu}) + w_\omega F_{O\omega}(\boldsymbol{\mu}), \tag{7}$$

where $\boldsymbol{\mu}$ is vector of the estimated parameters, $w_\varphi$ and $w_\omega$ are the corresponding weights, and where

$$F_{O\varphi}(\boldsymbol{\mu}) = \frac{1}{\sum_{i=1}^{N}\theta_{fi}}\sum_{i=1}^{N}\int_{\theta_0}^{\theta_{fi}}\left(\varphi_{si}(\theta,\boldsymbol{\mu}) - \varphi_{ei}(\theta,\boldsymbol{\mu})\right)^2 d\theta,$$

$$F_{O\omega}(\boldsymbol{\mu}) = \frac{1}{\sum_{i=1}^{N}\theta_{fi}}\sum_{i=1}^{N}\int_{\theta_0}^{\theta_{fi}}\left(\omega_{fsi}(\theta,\boldsymbol{\mu}) - \omega_{fei}(\theta,\boldsymbol{\mu})\right)^2 d\theta. \tag{8}$$

In the expressions (8) $N$ denotes number of the compared pairs of solutions, $\theta_0$ is common initial angle $\theta$, $\theta_{fi}$ ($i$=1, 2, …, $N$) are final angular positions of the disk, $\varphi_{si}$ and $\varphi_{ei}$ are angular positions of the pendulum obtained by the use of $i$-th numerical simulation and experiment, correspondingly. Since we measure the angular position of the disk, we differentiate this signal with respect to time in order to obtain the corresponding angular velocity. We do it numerically, by passing the signal $\theta_{ei}(t)$ (obtained by the linear interpolation of the experimental data) through the filter of the transfer function $G_f(s) = \frac{s}{(T_f s+1)^2}$. As an output we obtain the signal $\omega_{fei}(t)$, which appears in the expressions (8), but as a function of the angle $\theta$. In order to have the proper simulation signal, which

could be compared with the signal $\omega_{fei}$, we also pass through the filter $G_f(s)$ the numerical signal $\theta_{si}(t)$, obtaining $\omega_{fsi}(t)$.

In the estimation process one obtained the following values of the model parameters: $K_M = 3.024 \cdot 10^{-2}$N m/V, $C_O = 2.915 \cdot 10^{-2}$N m s, $M_O = 3.032 \cdot 10^{-2}$N m, $I_O = 5.724 \cdot 10^{-3}$kg m$^2$, $I_b = 5.318 \cdot 10^{-4}$kg m$^2$, $b_1 = 1.026 \cdot 10^{-1}$m, $c_S = 3.597 \cdot 10^{-1}$N s, $T_s = 6.172 \cdot 10^{-1}$N, $I = 1.258 \cdot 10^{-3}$kg m$^2$, $r = 4.689 \cdot 10^{-2}$m, $c_B = 6.830 \cdot 10^{-5}$N m s, $M_B = 2.977 \cdot 10^{-3}$N m. Figure 3 exhibits comparison of four numerical solutions $\varphi(\theta)$ to the model with the corresponding experimental data used during the identification process (only the final parts of the solutions are presented). In figure 4 there are presented comparison of the corresponding solutions $\omega_f(\theta)$.

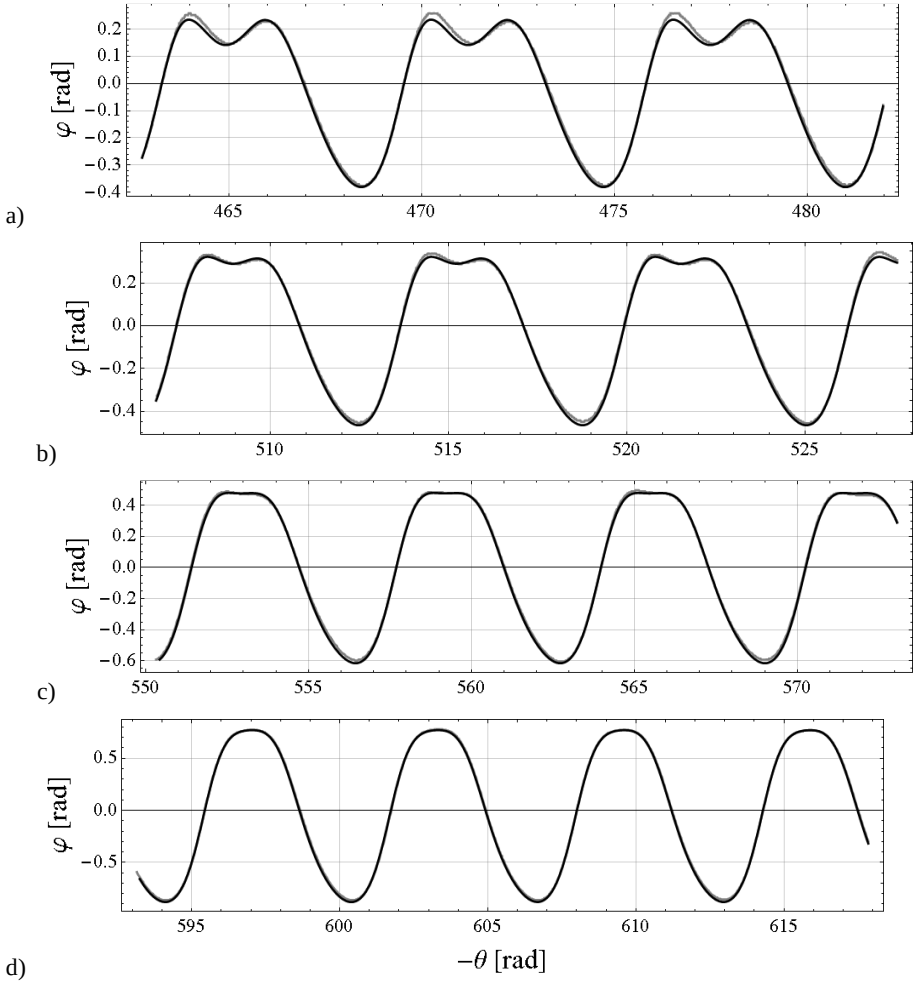


**Figure 3.** Four numerical solutions $\varphi(\theta)$ (black line) compared with the corresponding experimental data (gray line) ($u_0$=-7.0, -7.5, -8.0 and -8.5 V, for subfigures a, b, c and d, respectively).

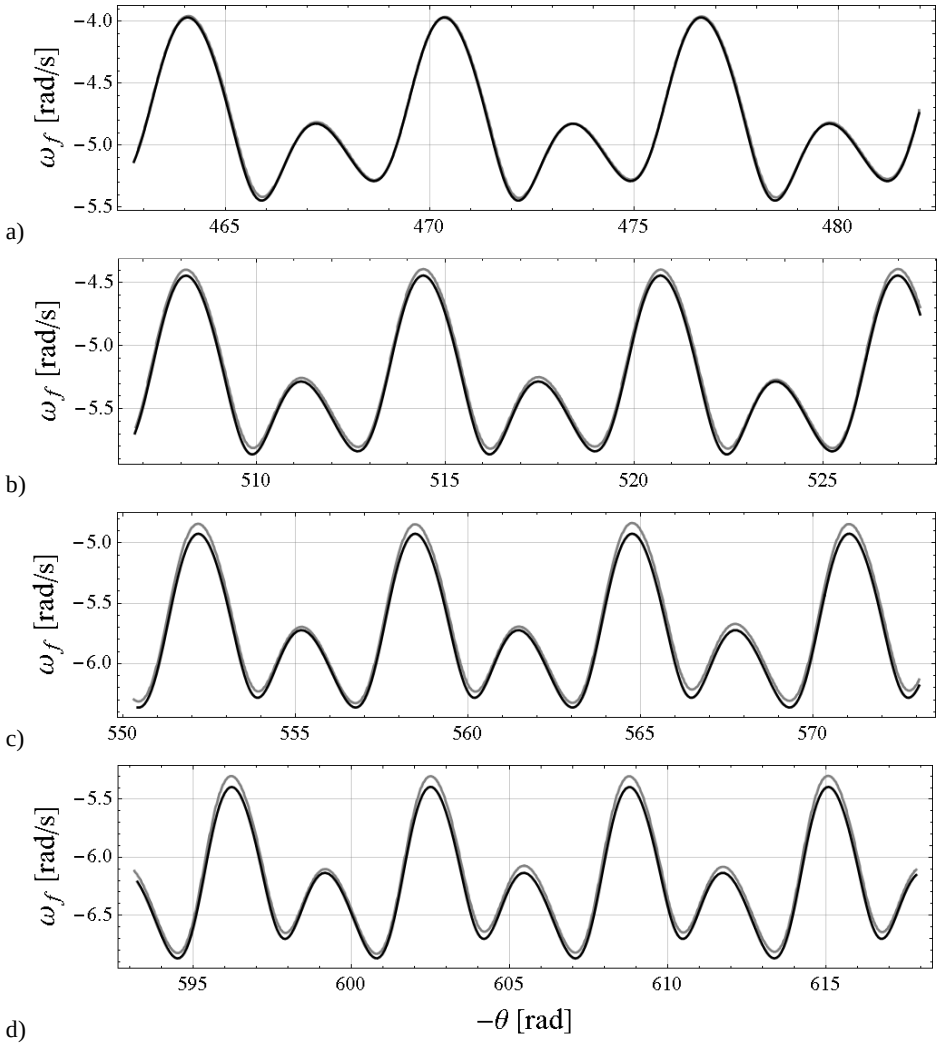


**Figure 4.** Four numerical solutions $\omega_f(\theta)$ (black line) compared with the corresponding experimental data (gray line) ($u_0$=-7.0, -7.5, -8.0 and -8.5 V, for subfigures a, b, c and d, respectively).

Using the functions (8), one assumes that initial conditions and input signals $u(t)$ are known and they are the same for both the experiment and simulation. Moreover, some parameters' values are easy to obtain by the direct measurements of masses and lengths. They are assumed to be constant during the identification process: $m_b = 0.035$ kg, $m_S = 0.777$ kg, $m = 0.226$ kg, $a = 0.080$ m, $b = 0.300$ m. Other parameters assumed to be constant are: $\varepsilon = 10^3$, $g = 9.81\ \mathrm{m \cdot s^{-2}}$. The remaining parameters (as the elements of the vector $\boldsymbol{\mu}$) will be obtained by minimization of the objective function $F_o$, using the Nelder-Mead method [9, 10], also known as downhill simplex

method. This is commonly used optimization algorithm, implemented in Matlab and Scilab functions *fminsearch*. One also assumes the following values of the weights and the time constant of the filter: $w_\varphi = 1\text{rad}^{-2}$, $w_\omega = 1\ \text{s}^2\text{rad}^{-2}$, $T_f = 0.1$ s.

## 5. Bifurcation dynamics

Other experimental investigations of the systems showed that it can also exhibit irregular behavior. For example the constant input voltage of 9 V leads to irregular dynamics, with full rotations of the pendulum, presented in figure 5. This solutions did not be used in the identification process because of potential problems related to high sensitivity to initial conditions. However they are confirmed qualitatively very well by the developed mathematical model and its numerical simulations, as shown in figure 5.

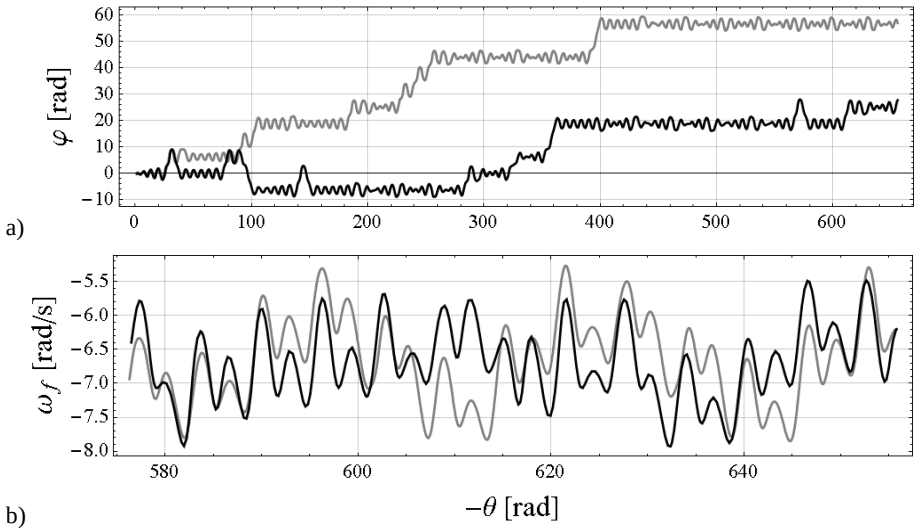


**Figure 5.** The chaotic numerical solutions (black lines) $\varphi(\theta)$ (a) and $\omega_f(\theta)$ (b) compared with the corresponding experimental data (gray lines) for $u_0$=-9 V.

In figure 6 there is presented Poincaré section of the attractor (sampling of the system state at the instances, when the angular position $\theta(t)$ of the disk crosses the zero position) exhibited by mathematical model for $u_0$=-9 V. It indicates the chaotic character of the solution. Figure 7 exhibits the corresponding bifurcation diagram of the mathematical model (for quasi-statically changing the bifurcation parameter $u_0$ from -7 V to -10 V), confirming the chaotic window around the value $u_0$=-9 V and many other zones of interesting bifurcational dynamics.

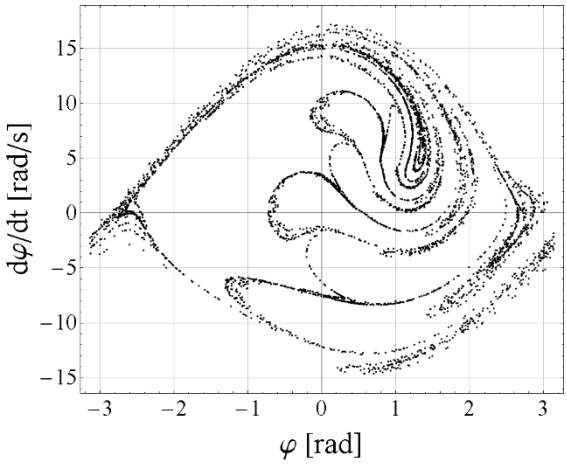


**Figure 6.** Poincaré section of the chaotic attractor obtained numerically for $u_0$=-9.0 V.

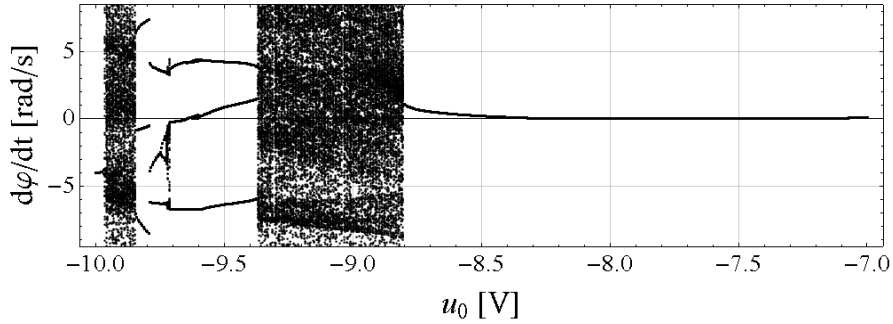


**Figure 7.** Bifurcation diagram with constant in time input voltage $u_0$ as a control parameter.

## 6. Concluding remarks

The paper presents results of the first stage of the larger project, which aim will be numerical and experimental investigation of different configurations of an electro-pendulum system. Here we have developed a simulation model of existing real object consisting of a physical pendulum hung on a horizontal slider, which is driven by a DC motor and a mechanism converting the rotational motion to the rectilinear one. Because of the goal of the project stage, the developed mathematical model is complicated and includes detailed modelling of friction and damping in the system.

Despite a relatively poor a priori knowledge about the system (especially knowledge about the DC motor and the gear transmission), using four time series with different constant values of the input voltage and a few direct measurements of physical quantities (like masses and lengths), we developed the mathematical model, which maps the behavior of the real object very well.

It has been shown in the work, that the built simulation model can be used for both explanation and prediction of nonlinear dynamics phenomena exhibited by the real electro-pendulum. On the other hand, the paper presents only preliminary results of the work being in progress. It is planned, among others, to investigate in more detail the bifurcational dynamics of the system with a constant input voltage, but also in the case of different types of periodic input.

**Acknowledgments**

This work has been supported by the Polish National Science Centre, MAESTRO 2, No. 2012/04/A/ST8/00738.

**References**

[1] Blackburn, J.A., Zhou-Jing, Y., Vik, S., Smith, H.J.T., and Nerenberg, M.A.H. Experimental study of chaos in a driven pendulum. *Physica D* 26, 1-3 (1987), 385-395.

[2] Zhu, Q., and Ishitobi, M. Experimental study of chaos in a driven triple pendulum. *Journal of Sound and Vibration*, 227, 1 (1999), 230-238.

[3] Awrejcewicz, J., Supeł, B., Kudra, G., Wasilewski, G., and Olejnik, P. Numerical and experimental study of regular and chaotic motion of triple physical pendulum. *International Journal of Bifurcation and Chaos* 18, 10 (2008), 2883-2915.

[4] Belato, D., Weber, H.I., Balthazar, J.M., and Mook, D.T. Chaotic vibrations of a nonideal electro-mechanical system. *International Journal of Solids and Structures*, 38 (2001), 1699-1706.

[5] Avanço, R.H., Navarro, H.A., Brasil, R.M.L.R.F., and Balthazar, J.M. Nonlinear Dynamics of a Pendulum Excited by a Crank-Shaft-Slider Mechanism, *ASME 2014 International Mechanical Engineering Congress and Exposition, Volume 4B: Dynamics, Vibration, and Control*, Montreal, Quebec, Canada, 2014.

[6] Cveticanin, L. Dynamics of the non-ideal mechanical systems: A review. *Journal of the Serbian Society for Computational Mechanics* 4, 2 (2010), 75–86.

[7] Kaźmierczak, M., Kudra, G., Awrejcewicz, J., and Wasilewski, G. Numerical and experimental investigation of bifurcational dynamics of an electromechanical system consisting of a physical pendulum and DC motor, in: Awrejcewicz J, Kaźmierczak M, Olejnik P and Mrozowski J (eds.) *Dynamical Systems – Applications.* TU of Lodz Press, Lodz, 2013, 49-58.

[8] Kaźmierczak, M., Kudra, G., Awrejcewicz, J., and Wasilewski, G. Mathematical modelling, numerical simulations and experimental verification of bifurcation dynamics of a pendulum driven by a dc motor. *European Journal of Physics* 36, 5 (2015), 13 pp.

[9] Gershenfeld, N. *The Nature of Mathematical Modelling*. Cambridge University Press, 2011.

[10] Nelder, J.A., and Mead, R. A simplex method for function minimization. *Computer Journal* 7, 4 (1965), 308-313

Grzegorz Wasilewski, Ph.D.: Lodz University of Technology, Department of Automation, Biomechanics and Mechatronics, Stefanowski St. 1/15, 90-924 Lodz, Poland (*grzegorz.wasilewski@p.lodz.pl*).

Grzegorz Kudra, Ph.D., D.Sc.: Lodz University of Technology, Department of Automation, Biomechanics and Mechatronics, Stefanowski St. 1/15, 90-924 Lodz, Poland (*grzegorz.kudra@p.lodz.pl*). The author gave a presentation of this paper during one of the conference sessions.

Jan Awrejcewicz, Professor: Lodz University of Technology, Department of Automation, Biomechanics and Mechatronics, Stefanowski St. 1/15, 90-924 Lodz, Poland (*jan.awrejcewicz@p.lodz.pl*).

Maciej Kaźmierczak (B.Sc. student): Lodz University of Technology, Department of Automation, Biomechanics and Mechatronics, Stefanowski St. 1/15, 90-924 Lodz, Poland (*182720@edu.p.lodz.pl*).

Mateusz Tyborowski (B.Sc. student): Lodz University of Technology, Department of Automation, Biomechanics and Mechatronics, Stefanowski St. 1/15, 90-924 Lodz, Poland (*182777@edu.p.lodz.pl*).

Marek Kaźmierczak, M.Sc.: Lodz University of Technology, Department of Automation, Biomechanics and Mechatronics, Stefanowski St. 1/15, 90-924 Lodz, Poland (*marek.kazmierczak.1@p.lodz.pl*).

# On the clutch dynamics with the approximations of resulting contact forces (MAT140-15)

Igor Wojtunik, Michał Szewc, Grzegorz Kudra, Jan Awrejcewicz

*Abstract:* The aim of the work is to present effectiveness of numerical simulations of clutch with frictional contacts, elaborated by some of the current articles in the last few years. The friction models assumes full developed sliding and the classical Coulomb friction law on each element of the contact with general shape and any pressure distribution. Then special modification of the integral model of friction force and moment are proposed. The approximants based on Padé approximants and their generalizations. In the work the clutch dynamics with contacts forces model is presented. The system was simplified to friction disk on rotating master disk. Two different configurations are investigated: coaxial and non-coaxial arrangement of the two disks. For the appropriate rotations speed, the system of non-coaxial arrangement can exhibit the ability to self-centering. The models based on generalizations of Padé approximants are compared with the simulation results obtained by the use of approximants based on Taylor's expansion and models with exact integral expressions for friction force and torque components.

## 1. Introduction

There are some ways of examination of systems with resultant contact forces. They identify difficulties with correct numerical simulation. Usual integral models are complex. Such situation requires a new method i.e. discretization or approximations.

In 1962, Contensou indicated in his paper [1] the integral model of the resultant friction force. It assumes fully developed sliding and the classical Coulomb friction law on each element of the contact area. In this integral model, circular area and Hertzian contact pressure distribution were applied. Some other authors presented special approximations of expressions for friction force and moment based on Padé approximants [2]. For the purpose of numerical simulations, these models were more convenient and suitable. In the paper [3], the types of generalizations of these approximants were presented. The models were extended with elliptical contact area. Such generalization increased their ability to match experimental data or the integral models. The models were applied in simulation of the Celtic stone [4]. Other example of applications is given in the work [5], where authors attempted to shape the trajectory of billiard ball.

In 2009, Fidlin and Stamm investigated radial dynamics of systems [6], commonly encountered in the clutch and many other applications. Two systems were the objects of their study: pin-on-the-

disk and disk-on-the-disk. To simplify the expressions of friction force and moment, Taylor's expansion was applied. The model was used to study the stability of equilibriums.

Authors of the present work compared three models of resultant contact forces: exact integral expressions for friction force and torque components, approximations based on generalizations of Padé approximants and Taylor's expansions. Then, the system with friction disk on rotating master disk was analyzed and simulated.

## 2. Modeling of contact forces

Let us focused on to the contact pressure distribution. In the Cartesian coordinate system *Axyz*, we consider dimensionless ring contact area *F* (figure 1). Axes *x* and *y* lie in the contact plane. The dimensionless length is obtained by dividing actual length by $\hat{a}$ , which is radius of real contact.

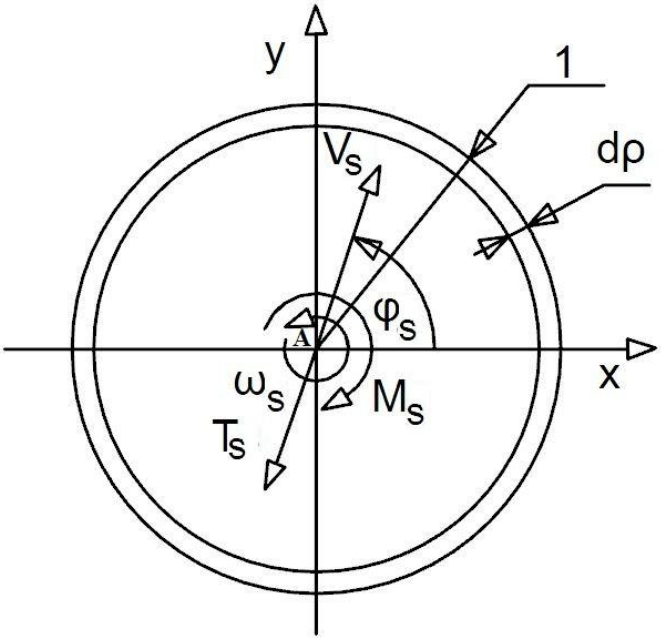


**Figure 1.** The ring contact area

The non-dimensional thickness of the contact ring is elementary small $d\rho \to 0$ and its real value can be presented as follows:

$$d\hat{\rho} = \hat{a}d\rho. \tag{1}$$

The real contact pressure distribution is assumed to be constant and reads [3,4]:

$$\hat{\sigma}(x,y)=\frac{\hat{N}}{\hat{F}}=\frac{\hat{N}}{2\pi\hat{a}^2 d\rho}. \tag{2}$$

In equations (2) there are used the following notations: $\hat{N}$ - normal component of real resultant force loading the contact, $\hat{\sigma}(x,y)$ - real contact pressure, $\hat{F}$ - real contact area. Non-dimensional contact pressure distribution is defined as:

$$\sigma(x,y)=\hat{\sigma}(x,y)\frac{\hat{a}^2}{\hat{N}}=\frac{1}{2\pi d\rho}. \tag{3}$$

We assumed a fully developed sliding. The relative motion of the two bodies is considered as a plane motion of rigid bodies. It is characterised by the non-dimensional angular and linear velocity, respectively: $\boldsymbol{\omega}_S=\hat{\boldsymbol{\omega}}_S=\omega_S\mathbf{e}_Z$ and $\mathbf{v}_S=\hat{\mathbf{v}}_S/\hat{a}=v_{Sx}\mathbf{e}_X+v_{Sy}\mathbf{e}_Y$, where $\hat{\mathbf{v}}_S$ is the real linear sliding velocity in the center *A*, $\hat{\boldsymbol{\omega}}_S$ is the real angular sliding velocity, and $\mathbf{e}_X$, $\mathbf{e}_Y$, $\mathbf{e}_Z$ are the unit vectors of the corresponding axes. Each element *dF* is under action of elementary friction force $d\mathbf{T}=-\sigma(x,y)\,dF\,\mathbf{v}_P/\|\mathbf{v}_P\|$ and moment $d\mathbf{M}=\boldsymbol{\rho}\times d\mathbf{T}=d\hat{\mathbf{M}}/(\hat{a}\,\mu\hat{N})$, where $\mathbf{v}_P$ stands for dimensionless, local velocity of sliding and $\mu$ is dry friction coefficient. Total values of contact forces are equal to: $\mathbf{T}_S=-T_{Sx}\mathbf{e}_X-T_{Sy}\mathbf{e}_Y$ and $\mathbf{M}_S=-M_S\mathbf{e}_Z$, where:

$$\begin{aligned}
T_{Sx}&=\iint_F\sigma(x,y)\frac{(v_{Sx}-\omega_S y)}{\sqrt{(v_{Sx}-\omega_S y)^2+(v_{Sy}+\omega_S x)^2+\varepsilon_t^2}}dxdy,\\
T_{Sy}&=\iint_F\sigma(x,y)\frac{(v_{Sy}+\omega_S x)}{\sqrt{(v_{Sx}-\omega_S y)^2+(v_{Sy}+\omega_S x)^2+\varepsilon_t^2}}dxdy,\\
M_S&=\iint_F\sigma(x,y)\frac{\omega_S(x^2+y^2)+v_{Sy}x-v_{Sx}y}{\sqrt{(v_{Sx}-\omega_S y)^2+(v_{Sy}+\omega_S x)^2+\varepsilon_t^2}}dxdy.
\end{aligned} \tag{4}$$

It is an integral expression with additional, small parameter $\varepsilon_t$ to avoid singularity. It is related to the lack of the relative motion. The real quantities are equal to: $\hat{\mathbf{T}}_S=\mu\hat{N}\,\mathbf{T}_S$ and $\hat{\mathbf{M}}_S=\hat{a}\mu\hat{N}\mathbf{M}_S$. In order to apply (4) in the simulation, the change of coordinate system from Cartesian coordinate system *Axyz* to pole coordinate system was essential. It is presented in Figure 2. The following

relation was implemented: $x = \rho\cos\alpha$, $y = \rho\sin\alpha$ and $dF = dxdy = \rho d\alpha d\rho$, leading to the following form of integrals:

$$T_{sx} = \frac{1}{2\pi}\int_0^{2\pi} \frac{\left(v_{sx} - \omega_s \rho\sin\alpha\right)}{\sqrt{\left(v_{sx} - \omega_s \rho\sin\alpha\right)^2 + \left(v_{sy} + \omega_s \rho\cos\alpha\right)^2 + \varepsilon_t^2}} d\alpha,$$

$$T_{sy} = \frac{1}{2\pi}\int_0^{2\pi} \frac{\left(v_{sy} + \omega_s \rho\cos\alpha\right)}{\sqrt{\left(v_{sx} - \omega_s \rho\sin\alpha\right)^2 + \left(v_{sy} + \omega_s \rho\cos\alpha\right)^2 + \varepsilon_t^2}} d\alpha, \tag{5}$$

$$M_s = \frac{1}{2\pi}\int_0^{2\pi} \frac{\omega_s\left(\rho^2\cos^2\alpha + \rho^2\sin^2\alpha\right) + v_{sy}\rho\cos\alpha - v_{sx}\rho\sin\alpha}{\sqrt{\left(v_{sx} - \omega_s \rho\sin\alpha\right)^2 + \left(v_{sy} + \omega_s \rho\cos\alpha\right)^2 + \varepsilon_t^2}} d\alpha.$$

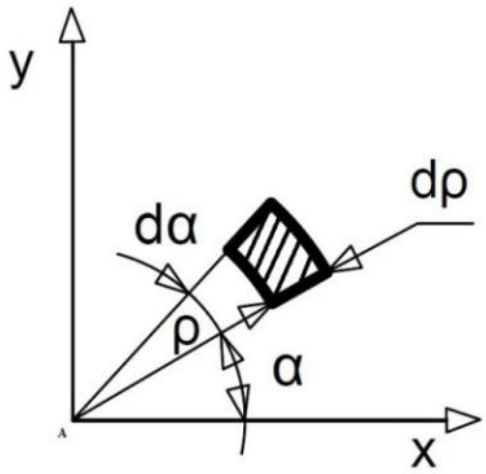


**Figure 2.** The ring contact area

For a fact this expression (3) has a complex integral form where the simulation and the numerical solutions are time consuming. It is inconvenient, and can be avoided by implementing approximate form of resultant contact forces. Based on special modifications of Padé approximants [3] we get:

$$T_{sx}^{(I)} = \frac{v_{sx} - b_T c_{0,1,1}^{(x,y)} \omega_s}{\sqrt{\left(|v_s|^{m_T} + b_T^{m_T}|\omega_s|^{m_T}\right)^{2m_T^{-1}} + \varepsilon_t^2}},$$

$$T_{sy}^{(I)} = \frac{v_{sy} + b_T c_{1,0,1}^{(x,y)} \omega_s}{\sqrt{\left( |v_s|^{m_T} + b_T^{m_T} |\omega_s|^{m_T} \right)^{2m_T^{-1}} + \varepsilon_t^2}}, \tag{6}$$

$$M_s^{(I)} = \frac{b_M c_{0,0,-1}^{(x,y)} \omega_s - c_{0,1,0}^{(x,y)} v_{sx} + c_{1,0,0}^{(x,y)} v_{sy}}{\sqrt{\left( b_M^{m_M} |\omega_s|^{m_M} + |v_s|^{m_M} \right)^{2m_M^{-1}} + \varepsilon_t^2}}.$$

where

$$c_{i,j,k}^{(x,y)} = \iint_F x^i y^j \left( x^2 + y^2 \right)^{-\frac{k}{2}} \sigma(x,y)\, dxdy\,. \tag{7}$$

The integral (6) are equal to the corresponding integral ones for $\varepsilon_t = 0$ and $v_s = \sqrt{v_{sx}^2 + v_{sy}^2} = 0$ or $\omega_s = 0$. Optimization process, with the approximate model being adjusted to the integral components or real experimental data, is based on finding appropriate, constant parameters $b_T$, $m_T$, $b_M$ and $m_M$. For the ringed contact area and the contact pressure distribution (2), the integrals occurring in equations (6) read:

$$c_{0,1,1}^{(x,y)} = c_{1,0,1}^{(x,y)} = c_{0,1,0}^{(x,y)} = c_{1,0,0}^{(x,y)} = 0, \quad c_{0,0,-1}^{(x,y)} = 1. \tag{8}$$

### 3. Determination of the parameters of the model of the resultant contact forces

The proposed approximation based on modification of Padè approximants was adjusted to the corresponding integral components and Taylor's expansion from the work [6]. The following change variables was introduced in order to reduce the number of variables and simplify the optimization process:

$$v_s = \lambda_s \cos\theta_s, \quad \omega_s = \lambda_s \sin\theta_s, \quad v_{sx} = v_s \cos\varphi_s, \quad v_{sy} = v_s \sin\varphi_s, \tag{9}$$

where

$$\lambda_s = \sqrt{v_s^2 + \omega_s^2}\,.$$

Relations (9) were applied to expressions (4), (6) and Taylor's expansion, and the optimal parameters of $b_T$, $m_T$, $b_M$, $m_M$ were found, fitting the corresponding functions on the representative integral $-\pi/2 < \theta_S < \pi/2$.

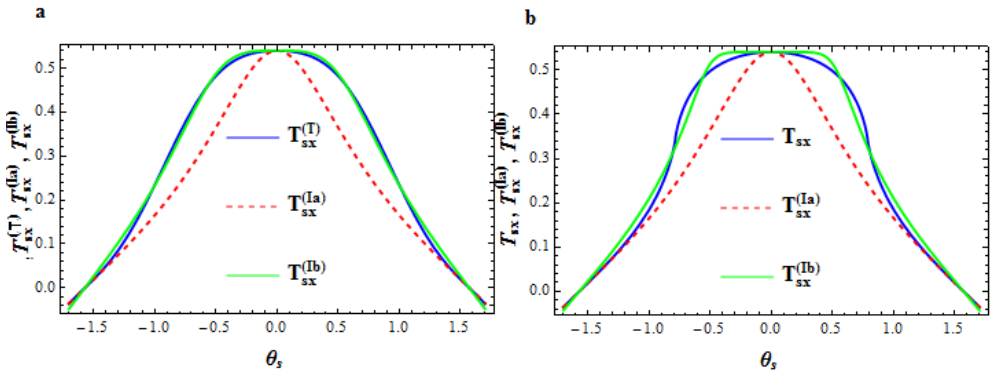


**Figure 3.** Friction force $T_S$ in direction *x*

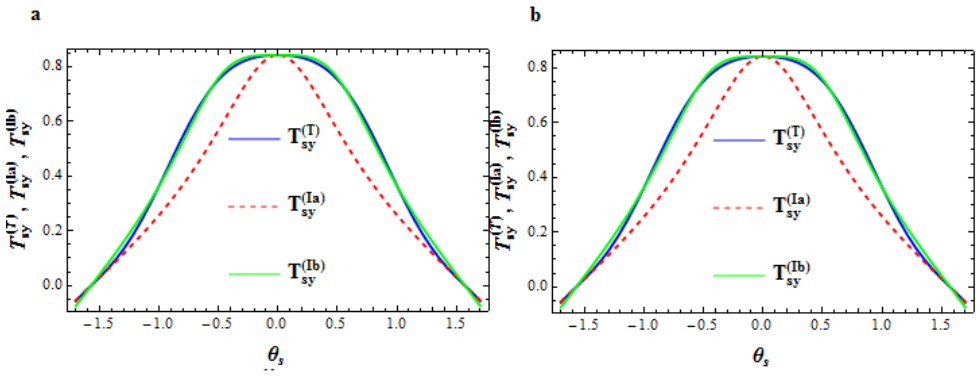


**Figure 4.** Friction force $T_S$ in direct**io**n *y*

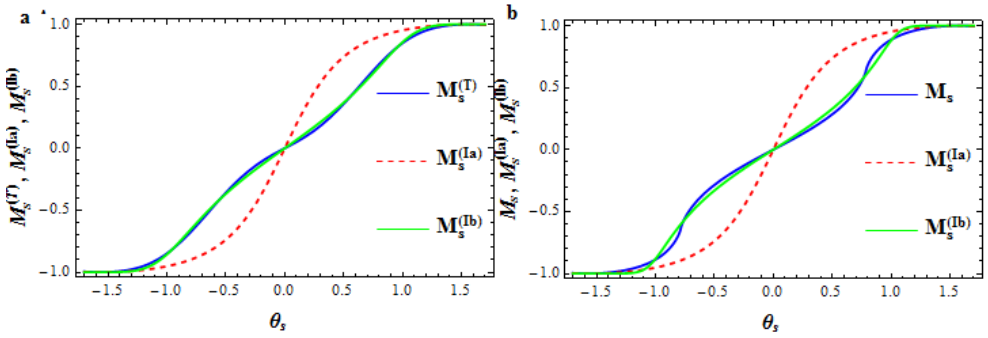


**Figure 5.** Moment $M_S$

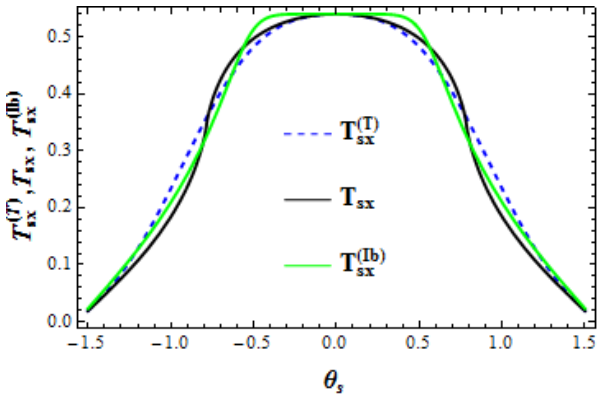


**Figure 6.** Comparison of friction force $T_{SX}$

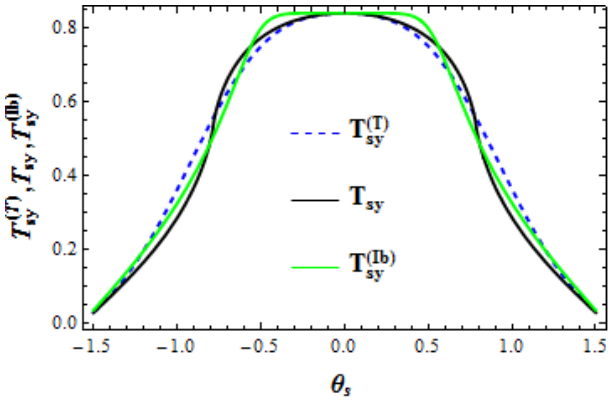


**Figure 7.** Comparison of friction force $T_{Sy}$

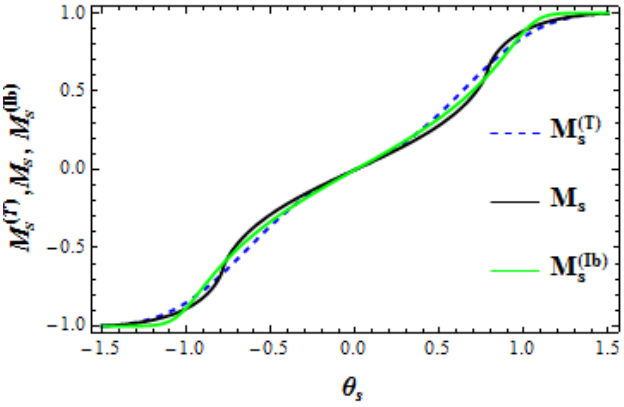


**Figure 8.** Comparison of moment $M_S$

Figures 3, 4 and 5 present resultant contact forces with parameters $b_T$=$m_T$=$b_M$=$m_M$=2 (Ia) and optimal parameters (Ib) to fit to Taylor's expansion (a): $b_T$=1.47, $m_T$=3.6, $b_M$=0.68, $m_M$=3.86 and integral model (b): $b_T$=1.66, $m_T$=7.57, $b_M$=0.61, $m_M$=7.59. The simulation was performed for $\varphi_S$ = 1 rad. Figures 6, 7 and 8 present comparison of all resultant contact forces with (Ib) fitted to the integral model .

## 4. Simulation of disk-on-the-disk system

Presented clutch was simplified to disk-on-the-disk system, which can be seen in figure 6. This is a friction disk laying on the rotating master disk. The two bodies were coupling on the ring area.

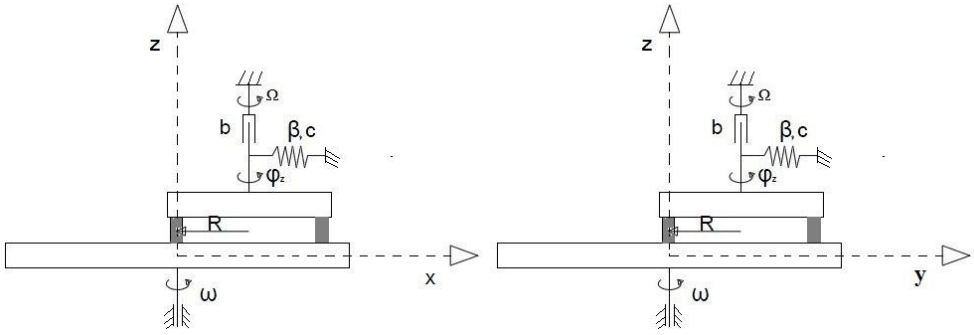


**Figure 9.** Disk-on-the-disk system from paper [6]

The following notation was used: $\hat{\mathbf{T}}_S$ – the resultant friction force acting at the contact center *A*; $\hat{\mathbf{N}}$ - the normal reaction acting on the disk; $\hat{\boldsymbol{\omega}}_S$ – angular sliding velocity; $\hat{\mathbf{M}}_S$ – moment of friction forces; $\hat{\mathbf{v}}_\mathbf{S}$ - linear sliding velocity at the point *A*; $R=\hat{a}$ – radius of contact ring; *m* – mass of the friction disk; *J* – moment of inertia of friction disk; $\omega$ - angular velocity of master disk; $\Omega$ – constant angular velocity of infinity mass connected to the friction disk by element with damping coefficient *b*; $\beta$, *c* – damping coefficient and stiffness of elasto-damping elements supporting friction disk in directions *x* and *y*; $x_0$ – position of spring relaxation in the direction *x*.

The analyzed system has three degree of freedom and the governing equations reads:

$$\begin{aligned}
\frac{d^2x}{dt^2} &= -\frac{\hat{T}_{sx}}{m} - \frac{\beta}{m}\frac{dx}{dt} - \frac{c}{m}(x - x_0), \\
\frac{d^2y}{dt^2} &= -\frac{\hat{T}_{sy}}{m} - \frac{\beta}{m}\frac{dy}{dt} - \frac{c}{m}y, \\
\frac{d^2\varphi_z}{dt^2} &= \frac{\hat{M}_S}{J} - \frac{b}{J}\left(\frac{d\varphi_z}{dt} - \Omega\right).
\end{aligned} \tag{10}$$

The relations between the corresponding kinematic variables occurring in (10) and models (4) and (6) are as follows:

$$\begin{aligned}
\hat{v}_{sx} &= \dot{x} + \omega y, \quad v_{sx} = \frac{\hat{v}_{sx}}{R}, \\
\hat{v}_{sy} &= \dot{y} - \omega x, \quad v_{sy} = \frac{\hat{v}_{sy}}{R}, \\
\hat{v}_s &= \sqrt{\hat{v}_{sx}^{\,2} + \hat{v}_{sy}^{\,2}}, \\
v_s &= \sqrt{v_{sx}^{\,2} + v_{sy}^{\,2}}, \\
\hat{\omega}_s &= \omega_s = \omega - \dot{\varphi}_z.
\end{aligned} \tag{11}$$

Then one can use the integral model (4), taking to account the following relations between real and non-dimensional quantities: $\hat{\mathrm{T}}_{sx} = \mu N \mathrm{T}_{sx}$, $\hat{\mathrm{T}}_{sy} = \mu N \mathrm{T}_{sy}$, and $\hat{\mathrm{M}}_S = R\mu N \mathrm{M}_\mathrm{S}$. The integral

components $T_{sx}$, $T_{sy}$ and $M_s$ can be replaced by the corresponding approximants $T_{sx}^{(I)}$, $T_{sy}^{(I)}$ and $M_s^{(I)}$ (6), or Taylor's expansions proposed in the work [6]:

$$T_{sx}^{(T)} = \frac{1}{\bar{v}_r}\frac{v_{sx}}{R}(1-\frac{R^2\omega_s^2}{2\bar{v}_r^2}+\frac{3}{4}\phi),$$

$$T_{sy}^{(T)} = \frac{1}{\bar{v}_r}\frac{v_{sy}}{R}(1-\frac{R^2\omega_s^2}{2\bar{v}_r^2}+\frac{3}{4}\phi), \qquad (12)$$

$$M_s^{(T)} = \frac{1}{\bar{v}_r R}\omega_s(1-\frac{\left(\frac{v_s}{R}\right)^2}{2\bar{v}_r^2}+\frac{3}{4}\phi),$$

where

$$\bar{v}_r = \sqrt{\left(\frac{v_{sx}}{R}\right)^2+\left(\frac{v_{sy}}{R}\right)^2+R^2\omega_s^2},$$

$$\phi = \frac{R^2(\omega-\dot{\varphi})^2}{\bar{v}_r^2}\frac{\left(\frac{v_s}{R}\right)^2}{\bar{v}_r^2}.$$

To simulate the system, the following parameters and initial conditions were used: $t$ = 20 s; $R$ = 1 m; $\mu N$ = 0.225 N; $J$ = 1 kg/m$^3$; m = 1 kg; $\Omega$ = 1.25 rad/s; $\beta$ = 0.5 s*N/m; $c$ = 1 N/m; $b$ = 0.015 s*N/m; $\varepsilon_t$ = 0.1; $x_0$ = 0.1 m; $x(0) = y(0) = \varphi_Z(0) = \dot{x}(0) = \dot{y}(0) = \dot{\varphi}_Z(0) = 0$. Figure 7 a-b presents three diagrams with simulations performed with the use of integral components of resultant contact forces and their two approximations: 7 a – approximant (I) fitted to Taylor's expansions (T) with the parameter $\omega$ = 2.5 rad/s, 7 b – approximant (I) fitted to integral model with the parameter $\omega$ = 0.8 rad/s. Figure 7 c-f shows trajectory of friction disk with approximants $T_{sx}^{(Ib)}$, $T_{sy}^{(Ib)}$, $M_s^{(Ib)}$ and $x(0)$ = 0.0001 m. Figure 7 c-d presents coaxial arrangement of disk ($x_0$ = 0 m) for $\omega$ = 0.8 rad/s (see figure 7 c) and ω = 2.5 rad/s, (see figure 7 d). Figure 7 e-f presents non-coaxial arrangement of disk ($x_0$=0.1m) for $\omega$= 0.8 rad/s (see figure 7 e) and ω = 2.5 rad/s, (see figure 7 f). The simulation time was 700 seconds.

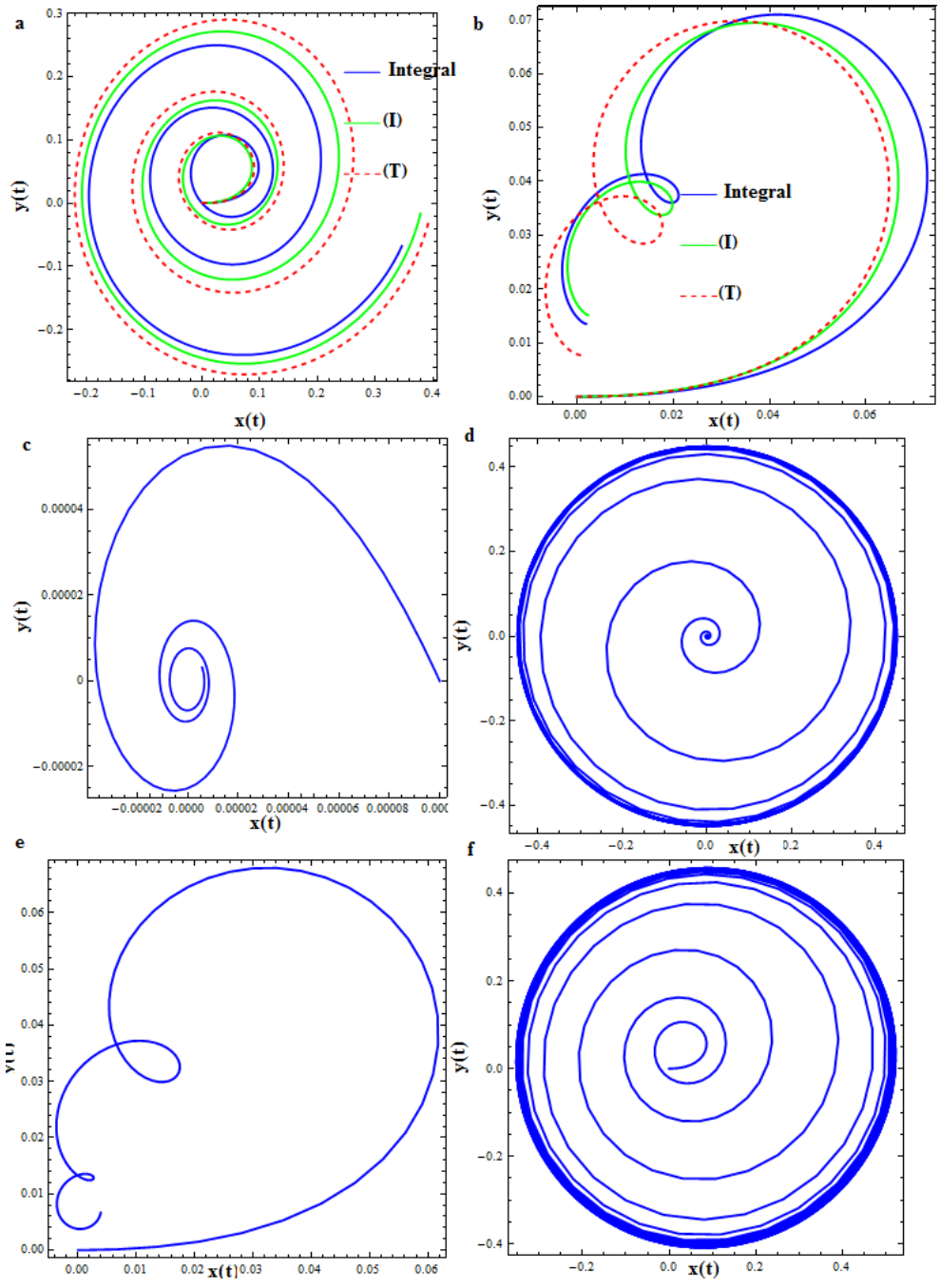


**Figure 10.** Simulation of disk-on-the-disk system.

## 5. Conclusions

The work present flexibility of the proposed model of resultant contact forces based on modifications of Padè approximant. It can be used to simulate disk-on-the-disk system and to study the stability of equilibriums. Such form of the model is more convenient and less time consuming. It gives the possibility of longer simulation. The paper presents simulations of disk-on-the-disk system. Its dynamics maps the clutch behavior in some aspects. It confirms typical behavior of self-centering of the system for low rotation speeds.


## Acknowledgments

This work has been supported by the Polish National Science Centre, MAESTRO 2, No. 2012/04/A/ST8/00738.


## References


[1] Contensou, P., *Couplage entre frottement de glissement et de pivotement dans la téorie de la toupe*, In: Ziegler H. (Ed.), Kreiselprobleme Gyrodynamic, IUTAM Symposium Celerina, Springer-Verlag, Berlin, 1962, pp. 201-216.

[2] Zhuravlev, V.P., The model of dry friction in the problem of the rolling of rigid bodies, *Journal of Applied Mathematics and Mechanics*, 62(5), 1998, pp. 705-710.

[3] Kudra, G., Awrejcewicz, J., "Application and experimental validation of new computational models of friction forces and rolling resistance", *Acta Mechanica*, 2015, pp. 2831-2848.

[4] Kudra, G., Awrejcewicz, J., "Approximate modelling of resulting dry friction forces and rolling resistance for elliptic contact shape", *European Journal of Mechanics A/Solids*, 42, 2013, pp. 358-375.

[5] Kudra, G., Szewc, M., Wojtunik, I., Awrejcewicz J. Shaping the trajectory of the billiard ball with approximations of the resultant contact forces., *3rd Int. Conference on Mechatronics — Ideas for Industrial Applications*, May 11-13, Gdansk, 2015

[6] Fidlin , W. Stamm, On the radial dynamics of friction disks, *European Journal of Mechanics A/Solids*, 2009



Wojtunik Igor, M.Sc. (Ph.D. student): Lodz University of Technology, Department of Automation, Biomechanics and Mechatronics, Stefanowskiego 1/15, 90-924 Lodz, Poland (igor.wojtunik@dokt.p.lodz.pl). The author gave a presentation of this paper during one of the conference sessions.

Szewc Michal, M.Sc. (Ph.D. student): Lodz University of Technology, Department of Automation, Biomechanics and Mechatronics, Stefanowskiego 1/15, 90-924 Lodz, Poland (michal.szewc@dokt.p.lodz.pl).

Kudra Grzegorz, Ph.D.: Lodz University of Technology, Department of Automation, Biomechanics and Mechatronics, Stefanowskiego 1/15, 90-924 Lodz, Poland (grzegorz.kudra@p.lodz.pl).

Awrejcewicz Jan, Professor: Lodz University of Technology, Department of Automation, Biomechanics and Mechatronics, Stefanowskiego 1/15, 90-924 Lodz, Poland (jan.awrejcewicz@p.lodz.pl).

# Numerical analysis of reflection and transmission phenomena of nonlinear ultrasound wave
## (NUM072-15)

Janusz Wójcik, Barbara Gambin

*Abstract:* Numerical analysis of the reflection/transmission problem for a nonlinear acoustic wave is studied. The wave is assumed to be plane and normally incident on the plane discontinuity surface between two lossy media. Numerical calculations are proceeded with the help of self written software (in Fortran). The influence of different propagation parameters (properties of two different media) on the reflected and transmitted wave fields are discussed. Particularly, it is shown that although two media have the same impedance, the effect of the wave nonlinearities is still existing in the reflected and transmitted fields. The performed analysis qualitatively confirmed theoretical predictions quite well.

### 1. Introduction

The wave reflection and transmission phenomena are the effect of the existence of the material interface between two media with different physical properties. In the case of acoustic waves the physical properties which determines the wave propagation are the density and the elasticity of the medium. Discontinuities in the material parameters cause peaks in the backscattered echoes coming from the irradiated objects. In particular, variations of the acoustic impedance of the tissues inside the human body allowed the visualization of organs boundaries in the USG images. These images are created from the collected backscattered RF (RF-Radio Frequency) signals during exposition to the irradiation. Linear models of sound propagation in inhomogeneous media, cf. [2] are sufficient for explanation the reflection and transmission phenomena used in classical USG imaging. However, the searching for new tissue typing features in backscattered row RF signals received by more and more sensitive ultrasound transducers is today a challenge for the development of non-invasive diagnostic methods such as Quantitative Ultrasound Imaging or Parametric Imaging, cf. [4]. It is well known that the high-intensity focused ultrasound cause the appearance of some non-classical effects on the ultrasound wave propagation. One of this effect is a non-classical absorption, other a nonlinear elastic behavior. To take into account both of this effects Wójcik in [6] proposed the special non-local, non-linear equation of the acoustic wave propagation. Let us underline that not only the modelling of the non-classical absorption is still updated problem cf. [5] but the nonlinearity in elastic behaviour as well, e.g. [3], currently valid in the context

of the sono-photoacoustic imaging, [1] and references therein. Reflection and transmission of waves modeling on the base of the non-local and non-linear equation proposed by Wojcik in [6] was first studied by the same author in [7]. The main result of the paper were the general formulae for generalized reflection and transmission coefficients having the form of reflection and transmission operators. The aim of this contribution is to demonstrate by special examples of numerical calculations based on the above mentioned results that the numerical experiments can clarify and enrich our knowledge about reflection and transmission on the boundary between two nonlinear media. The paper is organized as follows. At first the theoretical results of [7] are summarized. Then the numerical experiments are described and at the end conlusions are stated.

## 2. Modeling of reflection and transmission

### 2.1. Basic relations

For simplicity of considerations the following assumptions are stated. The problem of a nonlinear acoustic wave propagation, i.e. the small perturbations imposed on the equilibrium dynamics, is assumed to be a one-dimensional if the plane wave is normally incident to the plane boundary of two media. Than the plane between two different media is reduced to the point, denoted by $x_{RT}$. The dimensionless space-time Cartesian coordinates are denoted by $x$-$t$. In the fixed Cartesian system it is assumed that $x_{RT} = 0$ and for $x < 0$ the all material characteristics are denoted by index $m = 1$ whereas for $x > 0$ by $m = 2$, cf. (see figure 1). In what follows dimensionless system of material parameters is used. The dimensionless equilibrium density and the sound speed of the medium, for $m = 1, 2$, are given by the relations

$$x \equiv x' ko, \qquad t \equiv t' \Omega o, \qquad g_{0m} \equiv \rho_{0m}/\rho_0, \qquad c_{0m} \equiv c_{m0}/c_0, \qquad \Omega o = koc_0, \tag{1}$$

where $\rho_{0m}$, $c_{m0}$ are the equilibrium density and the speed of sound of $m^{th}$ medium, respectively, $\rho_0$, $c_0$ are density and speed of sound of fixed reference medium, respectively. Particularly, one can choose $\rho_0 = \rho_{01}$, $c_0 = c_{10}$.

In general for the solid isotropic medium third order material parameter $\beta_m$ (normalized by $\rho_0 c_0^2$) describes material and geometrical nonlinearities of the $m^{th}$ medium. For fluids $\beta_m \equiv (\gamma_m + 1)/2$, where $\gamma$ is an exponent of the adiabate or $\beta_m \equiv (1 + (B/2A)_m)$, where $(B/A)_m$ is the nonlinearity parameter. In what follows the acoustic Mach number is introduced $q \equiv P_b/\rho_0 c_0^2$ $(= v_b/c_0)$, where $P_b$, $v_b$ are the pressure or velocity ($P_b \equiv \max_t |P_b(t)|$.

It is assumed that the velocity potential $\Phi$ in the media, both nonlinear and lossy, for $x < 0$ have the form of two waves, the incident wave propagating in the forward direction denoted by superscript $+$ and the reflected wave propagating in the backward direction

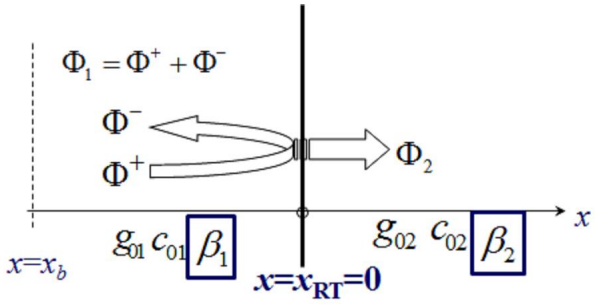


**Figure 1.** The potential fields in the first and the second media.

denoted by superscript $-$. The $\Phi$ for $x < 1$ contains the one transmitted wave propagating in the forward direction denoted here by the subscript 2:

$$\Phi_1(x,t) = \Phi^+\left(t - \frac{x}{c_{01}}, x\right) + \Phi^-\left(t + \frac{x}{c_{01}}, -x\right), \qquad x \le x_{RT} = 0, \quad m = 1, \tag{2}$$

$$\Phi_2(x,t) = \Phi_2\left(t - \frac{x}{c_{02}}, x\right), \quad x \ge x_{RT} = 0, \quad m = 2. \tag{3}$$

From the definition $\mathbf{v} \equiv \nabla\Phi$ it means that the velocity field is linear in respect to the potential. Therefore, the following decompositions of the velocity, corresponding to (2), (3), are valid

$$v_1(x,t) = v^+\left(t - \frac{x}{c_{01}}, x\right) + v^-\left(t + \frac{x}{c_{01}}, -x\right), \tag{4}$$

$$v_2(x,t) = v_2\left(t - \frac{x}{c_{02}}, x\right). \tag{5}$$

The relation between acoustical pressure and potential follows from the definition $\mathbf{v} \equiv \nabla\Phi$, here $v = \frac{\partial}{\partial x}\Phi$, and from the general equations of motion of the continuous non-linear medium, so an operator which maps the potential field to the pressure field is in general a non-linear and non-local operator. Here, we assume that this operator is linear and has the form $P_m \cong -g_{0m}\partial_t$. In [7] it is proved that it is a satisfactory approximation in the range of considered physical scales of the problem. Under such approximations the following decompositions of the acoustical pressure field are obtained

$$P_1(x,t) = P^+\left(t - \frac{x}{c_{01}}, x\right) + P^-\left(t + \frac{x}{c_{01}}, -x\right), \tag{6}$$

$$P_2(x,t) = P_2\left(t - \frac{x}{c_{02}}, x\right). \tag{7}$$

To describe the reflection and transmission at the interface we must determine the relations between $v^+$, $v^-$, $v_2$ and $P^+$, $P^-$, $P_2$ at the interface at $x = x_{RT} = 0$. Then we will search the boundary conditions for $v^-$, $v_2$ and $P^-$, $P_2$ on the plane between two different nonlinear and lossy media. This problem will be solved if we find the functions $R$, $T$ (operators) such that,

$$v^- = \mathsf{R}'_v\left[\{m\}; v^+\right] = \mathsf{R}_v\left[\{m\}; v^+\right] \circ v^+, \tag{8}$$

$$v_2 = \mathsf{T}'_v\left[\{m\}; v^+\right] = \mathsf{T}_v\left[\{m\}; v^+\right] \circ v^+, \tag{9}$$

where $\mathsf{R}_v[\cdot;\cdot]$, $\mathsf{T}_v[\cdot;\cdot]$ are the reflection and transmission operators; in general case $\circ$ – denote operation characteristics for the operator. Generally in almost all considered cases $\circ \equiv \otimes$ is convolution (in time or Fourier frequency domain), but sometimes in special cases $\circ \equiv \cdot$ is the ordinary multiplication; $\{m\}$ denotes a set of the material parameters which characterizes the media. In linear case we have a "classical" problem of reflection and transmission of the plane wave. For no absorbing media $v^- = \widehat{\mathsf{R}}_v[\{m\}] \circ v^+ = R_v[\{m\}] \cdot v^+$, $\hat{v}_2 = \widehat{\mathsf{T}}_v[\{m\}] \circ v^+ = \widehat{T}_v[\{m\}] \cdot \hat{v}^+$. $R$, $T$ are reflection and transmission coefficients.

As a base of our theoretical description we assume equation (24) referred in [7]. It describes finite amplitude potential disturbances in lossy media. For the m-th homogenous phase of the medium it takes the form

$$\partial_{tt}\Phi_m - c_m^2\partial_{xx}\Phi_m + 2\mathcal{A}_m\partial_t\Phi_m + q_m\partial_t(\partial_t\Phi_m)^2 = 0 + o^2, \quad q_m \equiv q\beta_m/c_{0m}^2, \ m = 1, 2. \tag{10}$$

Generally $\mathcal{A}_m$ is the convolution type operator of absorption $\mathcal{A}_m\Phi \equiv A_m(t) \otimes \Phi(x,t)$. For classical absorption $\mathcal{A}_m = -\alpha_2^m\partial_{xx} \simeq -\alpha_2^m\partial_{tt} + o^2$, $\alpha_2^m$ is the dimensionless hybrid viscosity. $o^l$ is a small quantity of the order $l$ respect $q$ or $\alpha = \|A\|$, $o^l = o(q+\alpha)^l$.

Secondly, we would like compare theoretical with numerical calculations results. In numerical calculations we will use unitary description of the nonlinear disturbances in the heterogeneous stationary media. It heave the form

$$\partial_{tt}P - c^2 g\partial_x\frac{1}{g}\partial_x P + 2\mathcal{A}\partial_t P - \overline{q}\partial_{tt}(P)^2 = 0 + o^2, \quad \overline{q} \equiv q\beta/gc^2, \tag{11}$$

In our case $g(x) \equiv g_{0m}$; $c(x) \equiv c_{0m}$; $\overline{q}(x) \equiv q\beta_m/g_{0m}c_{0m}^2$; $P(x,t) \equiv P_m(x,t) = -g_{0m}\partial_t\Phi_m$ for $x \in m$-th phase of the medium. Then (11) reduces to (10) for $x \in (m$-th phase of the medium).

For assumed shapes $\Phi^+$, $\Phi^-$, $\Phi_2$, acoustical pressures and velocities take the form,

$$P^+ = -g_{01}\partial_t\Phi^+ = -g_{01}\partial_{\tau^+}\Phi^+, \tag{12}$$

$$P^- = -g_{01}\partial_t\Phi^- = -g_{01}\partial_{\tau^-}\Phi^-, \tag{13}$$

$$P_2 = -g_{02}\partial_t\Phi_2 = -g_{02}\partial_{\tau_2}\Phi_2, \tag{14}$$

$$v^+ = \partial_x\Phi^+ = -\frac{1}{c_{01}}\partial_t\Phi^+ + \partial_x\Phi^+ = -\frac{1}{c_{01}}\partial_{\tau^+}\Phi^+ + \partial_x\Phi^+ = \frac{P^+}{z_{01}} + \partial_x\Phi^+, \tag{15}$$

$$v^- = \partial_x\Phi^- = \frac{1}{c_{01}}\partial_t\Phi^- + \partial_x\Phi^- = \frac{1}{c_{01}}\partial_{\tau^-}\Phi^- + \partial_x\Phi^- = -\frac{P^-}{z_{01}} + \partial_x\Phi^-, \tag{16}$$

$$v_2 = \partial_x\Phi_2 = -\frac{1}{c_{02}}\partial_t\Phi_2 + \partial_x\Phi_2 = -\frac{1}{c_{02}}\partial_{\tau_2}\Phi_2 + \partial_x\Phi_2 = \frac{P_2}{z_{02}} + \partial_x\Phi_2, \tag{17}$$

where: $z_{0m} \equiv g_{0m}c_{m0}$, are equilibrium impedances. From (15)- (17) we obtain

$$P^+ = z_{01}(v^+ - \partial_x\Phi^+), \tag{18}$$

$$P^- = -z_{01}(v^- - \partial_x\Phi^-), \tag{19}$$

$$P_2 = z_{02}(v_2 - \partial_x\Phi_2). \tag{20}$$

The functions $\partial_x\Phi^+$, $\partial_x\Phi^-$, $\partial_x\Phi_2$ show substantial differences between impedance relations for an ideal linear medium, and for lossy or nonlinear one.

### 2.2. Continuity Conditions. Reflection-Transmission Operators

At $x = x_{RT} = 0$ all functions and relations depend only on time $t$. We assume continuity conditions in the conventional form

$$P_1 \equiv P^+ + P^- = P_2, \tag{21}$$

$$v_1 \equiv v^+ + v^- = v_2. \tag{22}$$

Apply (18)-(20) to reduce $P^+$, $P^-$, $P_2$ from (21) we obtain

$$z_{01}\left((v^+ - v^-) - \partial_x(\Phi^+ - \Phi^-)\right) = z_{02}(v_2 - \partial_x\Phi_2), \tag{23}$$

$$v^+ + v^- = v_2. \tag{24}$$

The terms $\partial_x(\Phi^+ - \Phi^-)$, $\partial_x\Phi_2$ were obtained from approximation discussed in [7]. Using (12)-(14) and (18)-(20)

$$(\partial_x\Phi^+ - \partial_x\Phi^-) = \overline{\mathcal{A}}_1(v^+ - v^-) - \frac{q_1c_{01}}{2}(v^+ - v^-)^2 + o^2, \tag{25}$$

$$\partial_x\Phi_2 = \overline{\mathcal{A}}_2v_2 - \frac{q_2c_{02}}{2}v_2^2 + o^2. \tag{26}$$

Substituting (25)and (26) into (23) with using (24) we obtain

$$[\mathsf{z}_1 + \mathsf{z}_2 + w\cdot v^+]v^- = \left[\mathsf{z}_1 - \mathsf{z}_2 + \frac{1}{2}u\cdot v^+\right]v^+ + \frac{1}{2}u\cdot(v^-)^2, \tag{27}$$

where: $\mathsf{z}_1$, $\mathsf{z}_2$ are the operators of the linear impedance $\mathsf{z}_m \equiv z_{0m}(1 - \overline{\mathcal{A}}_m)$, $m = 1, 2$. $w \equiv z_{01}c_{01}q_1 + z_{02}c_{02}q_2$, $u \equiv z_{01}c_{01}q_1 - z_{02}c_{02}q_2$. Absorption operator may be an integral-differential nonlinear equation in the time domain, or nonlinear convolution equation in the

Fourier frequency domain. We obtain the simplest case when assuming classical absorption $\overline{\mathcal{A}}_m = -\alpha_2^m \partial_t$ for both media (Riccati equation).

The abstract (operational) solution of equation (27) can be presented as follows

$$v^- = \mathsf{R}'_v \left[\{m\}; v^+\right] \equiv \frac{1}{2\mathsf{w}} \left[1 - \sqrt{1 - 4\mathsf{w}\mathsf{R}_0 v^+}\right] = \mathsf{R}_v \left[\{m\}; v^+\right] \circ v^+, \tag{28}$$

$$\mathsf{R}_v \left[\{m\}; v^+\right] \equiv \frac{1}{2\mathsf{w} \circ \mathsf{R}_0 v^+} \left[1 - \sqrt{1 - 4\mathsf{w} \circ \mathsf{R}_0 v^+}\right] \mathsf{R}_0, \tag{29}$$

$$\mathsf{T}_v \left[\{m\}; v^+\right] = 1 + \mathsf{R}_v \left[\{m\}; v^+\right], \tag{30}$$

$$\mathsf{R}_0 \equiv \frac{\mathsf{z}_1 - \mathsf{z}_2 + \frac{1}{2} u v^+}{\mathsf{z}_1 + \mathsf{z}_2 + w v^+}, \qquad \mathsf{w} \equiv \frac{\frac{1}{2} u \cdot}{\mathsf{z}_1 + \mathsf{z}_2 + w \cdot v^+}. \tag{31}$$

The factorizations of $\mathsf{w}$ and $\mathsf{R}_0$ operators was presented in [6], [7]. If absorption is neglect $\mathsf{z}_m = z_{0m}$ (or negligible) $\mathsf{w}[\cdot]$ and $\mathsf{R}_0[\cdot]$ factorize themselves in ordinary functions, and the generalized solutions (28)-(31) simplify to the factorized (algebraic) solutions, i.e. $\circ = \cdot$. Expanding the above formulas in respect to $q$ and keeping the terms of and $o^1$ only, we obtain

$$v^-(t) = \left(\frac{z_{01} - z_{02}}{z_{01} + z_{02}} + \frac{2 z_{01}^2 z_{02}^2 q}{(z_{01} + z_{02})^3} \left(\frac{\beta_1}{z_{01} c_{01}} - \frac{\beta_2}{z_{02} c_{02}}\right) v^+(t)\right) v^+(t), \tag{32}$$

$$v_2(t) = \left(\frac{2 z_{01}}{z_{01} + z_{02}} + \frac{2 z_{01}^2 z_{02}^2 q}{(z_{01} + z_{02})^3} \left(\frac{\beta_1}{z_{01} c_{01}} - \frac{\beta_2}{z_{02} c_{02}}\right) v^+(t)\right) v^+(t). \tag{33}$$

We rewrite the above formulas in the form

$$v^- = \mathsf{R}_v v^+ = (R_v + r_v v^+) v^+, \tag{34}$$

$$R_v \equiv \frac{z_{01} - z_{02}}{z_{01} + z_{02}}, \qquad r_v \equiv \frac{q 2 z_{01}^2 z_{02}^2}{(z_{01} + z_{02})^3} \left(\frac{\beta_1}{z_{01} c_{01}} - \frac{\beta_2}{z_{02} c_{02}}\right), \tag{35}$$

$$v_2 = \mathsf{T}_v v^+ = (T_v + r_v v^+) v^+, \qquad \mathsf{T}_v = 1 + \mathsf{R}_v, \qquad T_v = 1 + R_v = \frac{2 z_{01}}{z_{01} + z_{02}}. \tag{36}$$

In similar way, using the Eqs. (18)-(20) to reduce $v^+$, $v^-$, $v_2$ from (22) we obtain reflection $\mathsf{R}_p$ and transmission $\mathsf{T}_p = 1 + \mathsf{R}_p$ operators for the preasure $P^+$,however this procedure is more complicated, for details see [7],

$$P^-(t) = \left(\frac{z_{02} - z_{01}}{z_{01} + z_{02}} + \frac{2 z_{01} z_{02}^2 q}{(z_{01} + z_{02})^3} \left(\frac{\beta_2}{z_{02} c_{02}} - \frac{\beta_1}{z_{01} c_{01}}\right) P^+(t)\right) P^+(t), \tag{37}$$

$$P_2(t) = \left(\frac{2 z_{02}}{z_{01} + z_{02}} + \frac{2 z_{01} z_{02}^2 q}{(z_{01} + z_{02})^3} \left(\frac{\beta_2}{z_{02} c_{02}} - \frac{\beta_1}{z_{01} c_{01}}\right) P^+(t)\right) P^+(t), \tag{38}$$

$$P^- = \mathsf{R}_p P^+ = (R_p + r_p P^+) P^+, \quad P_2 = \mathsf{T}_p P^+ = (T_p + r_p P^+) P^+, \quad \mathsf{T}_p = 1 + \mathsf{R}_p, \tag{39}$$

$$R_p = \frac{z_{02} - z_{01}}{z_{01} + z_{02}} = -R_v, \quad r_p \equiv \frac{2 z_{01} z_{02}^2 q}{(z_{01} + z_{02})^3} \left(\frac{\beta_2}{z_{02} c_{02}} - \frac{\beta_1}{z_{01} c_{01}}\right) = -r_v \frac{1}{z_{01}} + o^2. \tag{40}$$

The properties of nonlinear part of the boundary conditions for reflected-transmitted waves are described by $r_p$ – the nonlinear reflection-transmission coefficient. Let us notice that the lack of differences of nonlinear parameters in both media ($\beta_1 = \beta_2$) is not a sufficient condition for vanishing of the nonlinear component of the reflection – $\mathsf{R}_p$ and transmission – $\mathsf{T}_p$ operators. This condition have the form

$$r_p = 0 \quad \rightarrow \quad \frac{\beta_2}{z_{02}c_{02}} = \frac{\beta_1}{z_{01}c_{01}}. \tag{41}$$

However, in this case $R_p = R_p$ where,

$$R_p = \frac{z_{02} - z_{01}}{z_{02} + z_{01}} = \frac{\beta_2 c_{01} - \beta_1 c_{02}}{\beta_1 c_{02} + \beta_2 c_{01}}. \tag{42}$$

It means in the case $\beta_1 \neq \beta_2$ that, in spite of a linear dependence between the reflected and incident disturbances on the interface $x = x_{RT}$, the phenomenon of the interaction with the interface preserves its nonlinear character as before.

If one from interconnected media is linear (either $\beta_1 = 0$ or $\beta_2 = 0$), nonlinear reflection ($r_p \neq 0$) also occurs. Let medium $m = 1$ be linear and no dissipative. Pulses propagating in this medium preserves their shapes given by the boundary pulse time shape, denoted as $P_b(t)$. The solution of (10) $m = 1$ for incident waves has the form

$$P^+(t,x) = P_b\left(t - \frac{x - x_b}{c_{01}}\right), \qquad x_b \leq x \leq x_{RT} = 0. \tag{43}$$

Moving left (reflected) solution of (10) have the form $P^-(t,x) = P^-\left(t + \frac{x}{c_{01}}\right)$. Where $P^-(t) \equiv P^-(t, x = 0)$ is the boundary condition. Accordingly Eqs. (41), (43) the boundary condition for reflected in $x = x_{RT} = 0$ wave have the form

$$\begin{aligned} P^-(t) &= \mathsf{R}_p P^+(t) = (R_p + r_p P^+(t))P^+(t) \\ &= \left(R_p + r_p P_b\left(t - \frac{-x_b}{c_{01}}\right)\right) P_b\left(t - \frac{-x_b}{c_{01}}\right). \end{aligned} \tag{44}$$

The solution for reflected wave takes the shape,

$$P^-(t,x) = P^-\left(t + \frac{x}{c_{01}}\right) = R_p P_b\left(t + \frac{x + x_b}{c_{01}}\right) + r_p P_b\left(t + \frac{x + x_b}{c_{01}}\right)^2, \quad x < 0. \tag{45}$$

In the case of nonlinear or absorbing media the shapes of reflecting (transmitting) and propagating pulses still changes. Nevertheless this changes are small on distances $|\delta x| \ll \lambda_{\alpha,q}$. Then propagating near the surface ($x = x_{RT} = 0$) the reflecting-transmitting short pulses almost preserves the shape given by boundary conditions (Reflection-transmission operators).

$$\begin{aligned} &P^-(t,x) = P^-\left(t + \frac{x}{c_{01}}, -x\right) \cong R_p P^+\left(t + \frac{x}{c_{01}}\right) + r_p P^+\left(t + \frac{x}{c_{01}}\right)^2, \\ &|x - x_{RT}| \sim \text{(pulse length)} \ll \lambda_{\alpha,q}. \end{aligned} \tag{46}$$

Because the Mach number $q$ is a small quantity even for relatively strong acoustical disturbances ($q = 0.001$ for water and $P_b = 2.25$ MPa) then effects of the nonlinear reflection may by observed separately if $z_{02} = z_{01}$, $R_p = 0$ ($z_{02} \cong z_{01} | R_p | < |r_p|$). In this cases

$$\begin{aligned} P^-(t,x) &= P^-\left(t + \frac{x}{c_{01}}\right) = r_p \cdot P^+\left(t + \frac{x}{c_{01}}\right)^2, \\ r_p &= \frac{q}{4}\left(\frac{\beta_2}{c_{02}} - \frac{\beta_1}{c_{01}}\right). \end{aligned} \tag{47}$$

If $\beta_1 \neq 0$ equality sign = should be replaced by approximation sign $\cong$ in (47). In the next section we compare results of the numerical solution of (11) with theoretical one expressed by the formulae (47).

## 3. Numerical Calculations

The numerical solutions of (11) are obtained by a solving kernel which does not contain any theoretically received on the basis of (10) information about continuity conditions and the shapes of the reflectition-transmission operators.

Incident pulses $P^+(t,x)$ was excited by the pulse $P^+(t, x = x_b) \equiv P_b(t)$ in the fixed point $x_b$. We assumed that $P_b(t) = P_{0b} \cdot Env(t - t_{en}) \cdot \sin(2\pi\nu_c \cdot (t - t_c))$, $t_c = 0$, $t_{en} = 2/\nu_c$ is four cycles length sine wave with triangle envelope $Env()$, carrier frequency $\nu_c = 5$ MHz ($\lambda_c = 0.3$ mm in water) and maximal amplitude $P_{0b} = 1.125$ MPa. The numerical calculations were performed for three layers of finite dimensions with 27 mm, 3 mm and 21 mm thickness, respectively¿ Total thickness was 51 [mm] $= 170\lambda_c$. The equilibrium material parameters of the first layer were used for normalization, then $g_{01} = 1$, $c_{01} = 1$. We introduced third layer which copy properties of the first one. This is additional test for numerical algorithm. In normalized system the Mach number $q \equiv P_{0b}/\rho_0 c_0^2 = P_{0b}/\rho_{01} c_{01}^2 = 0.0005$ and $\max\limits_t |P_b(t)| = 1$. Normalized carrier frequency and wavelength was equal $\nu = 170$ and $\lambda = 2\pi/170$. Because the pulse length is calculated as $= 4\lambda = 8\pi/170 \ll \lambda_{\alpha,q} = 1/q\nu = 1/q \cdot 170$ it permits on applying (46) and (47) for interpretations that the space shapes of numerical solutions preserve the time shapes of the boundary conditions (37), (38) for reflecting-transmiting pulses. Amplitude level of the incident pulses in $x = x_{RT} = 0$ were $\max\limits_t |P^+(t)| = 1$.

### 3.1. Reflection and transmission by the differences in the non-linear material properties

In (see figure 2) the behaviour of the medium 1 is assumed to be linear. The properties of the nonlinear medium 2 are assumed to be such that the linear part of the reflection coefficient is equal 0, what means that the impedances (equlibrum properties) of both media are equal one to another, $z_{01} = z_{02}$. The reflection is caused by the nonlinear part of the reflection

operator only, with coefficient $r = 0.0005$). In this case like above $z_{01} = z_{02}$, $c_{01} = c_{02} = 1$, but $\beta_1 = 3$, $\beta_2 = 7$, $R_p = 0$, $r_{p12} = (1/4)q(\beta_2 - \beta_1) = q = 0.0005$. Notice, that in reflected waves the effects of the "nonlinear" reflection should occur only. However reflected waves propagates nonlinearly but near (R-T) planes should preserves, predicted by (47), its shape with very good approximation. It means that the shape should be proportional to the "square" of the incident wave shape. The numerically calculated shape and amplitude level of the reflecting pulse are in full accordance with theoretical predictions.

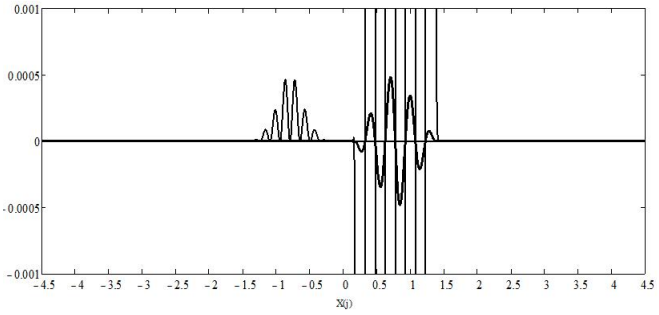


**Figure 2.** Linear-Nonlinear media. Nonlinear reflection.

### 3.2. Reflection and transmission by the differences in the linear as well as nonlinear material properties

In (see figure 3) the medium 1 is assumed to be linear as in the previous case. The properties of the nonlinear medium 2 are such that the value of linear part of the reflection coefficient is equal to the nonlinear part of the reflection coefficient, $R12 = r12 = 0.0005$. The reflection is caused now by the nonlinear part of the reflection operator together with the linear part of the reflection, i.e. reflection coefficient.

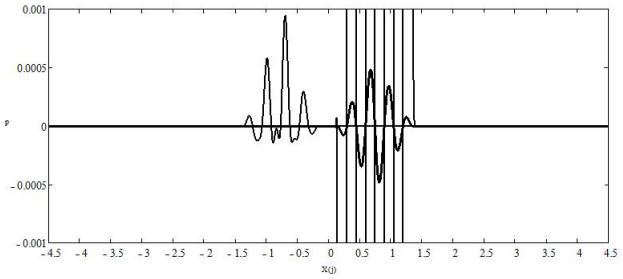


**Figure 3.** Linear-Nonlinear propagation. Linear and nonlinear reflection

### 3.3. Reflection and transmission by the specially selected material properties - differences in impedances

In (see figure 4) the properties of both media are nonlinear, so the pulse propagates with changing its form from the smooth sine form to the saw function form in the medium 1 and in the medium 2, but with the opposite direction of the slope. The properties of both media are assumed to be such that the reflection is caused only by impedance differences meanwhile the nonlinear coefficient $r = 0$.

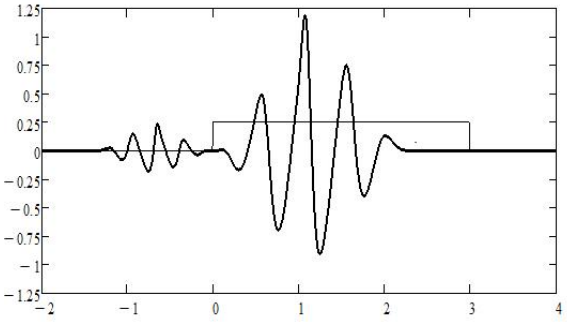


**Figure 4.** Nonlinear-Nonlinear propagation. Linear reflection.

### 3.4. Nonlinear-Nonlinear propagation. Non-linear reflection

In (see figure 5) the properties of both media are nonlinear, so the pulse propagates with changing its shape from the smooth sine form to the saw function form in the medium 1 and in the medium 2, but with the opposite direction of the slope. The properties of both media are assumed to be such that the reflection is caused only by differences in the nonlinear coefficient, so it is fully non-linear reflection and transmission. $r = 0$.

## 4. Conclusions

The selections and applications in the numerical calculations of the characteristics relations (resulting from the theory) between material parameters permits on reciprocal verification theory and numerical algorithm (positive for both if results are conformable).The numerically calculated and theoretically obtained results mutually confirmed themselves. The two features of the nonlinear reflection-transmission phenomenon should be underlined: firstly nonlinear reflection and transmission (R-T) occurring if only one from both media is nonlinear and secondly nonlinear operators of reflection and transmission are nonlocal in the Fourier frequency domain. The reflection and transmission coefficients of every Fourier component

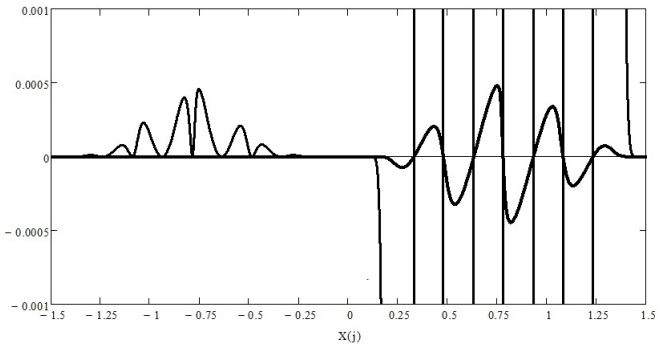


**Figure 5.** Nonlinear-Nonlinear propagation. Non-linear reflection.

of the incident wave depends on the all remaining components. Some comments about the examples of numerical calculations. From (see figure 2) It is clear that the reflected pulse has always positive value. This evident difference between the incident wave with the mean value 0 and the reflected wave having twice greater frequency is the promising parameter to measurable the nonlinearity of medium properties. The (see figure 3) shows that the shape of reflected wave is different than previously, the reflected wave is no longer always positive and loss regular shape of its envelope. Summing up the result of results depicted in figure 4 and figure 5: even if the reflection phenomena is linear itself, the wave propagation in the both media has a nonlinear character, because of the media nonlinearities. They generates saw type pulse form. Directions of slopes in the saw forms are in agreement with the directions of propagation. Besides, due to the speed of sound assumed to be greater in the medium 2 than in the medium 1 the pulse duration in medim 2 is two times greater.

The problem considered in this paper is fundamental for many technologies. As it was discussed in Introduction the detection of reflections from boundaries between different tissues is the base of USG imaging. Often equilibrium parameters (impedances) of tissues differ from each other by a very small amount. It is very important not only for medical diagnostics but for other application of ultrasound, Still there are questions are without answers. How the nonlinear effects impact on general picture of reflection and transmission phenomenon? The nonlinearity parameter B/A for different soft tissues can vary from 5.8 (cardiac muscle) to 11 (fatty tissue). Can the media which differ in this parameter only (or generally by third order material parameters) be differentiated from each other due to different reflections? What is the qualitative and quantitative effect of this phenomenon? The aim of this paper is a small contribution to finding answers to such questions. The calculations are done in the simplest one-dimensional geometrical configuration without taking

into consideration any transverse disturbances, which may occur in relation to the acoustic beam axis.

**Acknowledgements**

This work has been partially supported by the National Science Centre
(grant no. 2011/03/B/ST7/03347).

**References**

[1] Arnal, B., Perez, C., Wei, C.-W., Xia, J., Lombardo, M., Pelivanov, I., Matula, T. J., Pozzo, L. D., and ODonnell, M. Sono-photoacoustic imaging of gold nanoemulsions: Part i. exposure thresholds. *Photoacoustics 3*, 1 (2015), 3 – 10. Special Issue: Contrast Agents for optoacoustic imaging and sensing: Design and biomedical applications.

[2] Brekhovskikh, L.M., G. O. *Acoustics of layered media.* Springer-Verlag, Berlin-Heilderberg, 1990.

[3] Jaros, J., Rendell, A. P., and Treeby, B. E. Full-wave nonlinear ultrasound simulation on distributed clusters with applications in high-intensity focused ultrasound. *International Journal of High Performance Computing Applications* (2015).

[4] Mamou, J., and Oelze, M. L. *Quantitative Ultrasound in Soft Tissues.* Springer Publishing Company, Incorporated, 2013.

[5] Treeby, B. E., Jaros, J., Rendell, A. P., and Cox, B. Modeling nonlinear ultrasound propagation in heterogeneous media with power law absorption using a k-space pseudospectral method. *The Journal of the Acoustical Society of America 131*, 6 (2012), 4324–4336.

[6] Wójcik, J. Conservation of energy and absorption in acoustic fields for linear and nonlinear propagation. *The Journal of the Acoustical Society of America 104*, 5 (1998).

[7] Wójcik, J. Nonlinear reflection and transmission of plane acoustic waves. *Archives of Acoustics 29*, 4 (2004), 607632.

Wójcik Janusz, D.Sc.: Institute of Fundamental Technological Research of the Polish Academy of Sciences, Pawińskiego 5B, 02-106 Warszawa, Poland, (*jwojcik@ippt.pan.pl*). The author gave a presentation of this paper during one of the conference sessions.

Gambin Barbara, D.SC.: Institute of Fundamental Technological Research of the Polish Academy of Sciences, Pawińskiego 5B, 02-106 Warszawa, Poland, (*bgambin@ippt.pan.pl*).

# INDEX OF AUTHORS

**Adamiec-Wójcik Iwona** ..... 11, 21
**Alisverisci Fusun** ..... 31
**Andrianov Igor V.** ..... 41
**Awrejcewicz Jan** ..... 11, 41, 57, 391, 513, 543, 579, 591
**Bajon Tomasz** ..... 267
**Barbanti Luciano** ..... 171
**Barski Marek** ..... 69, 489
**Bayıroğlu Hüseyin** ..... 81
**Behn Carsten** ..... 91, 425
**Bergman Lawrence A.** ..... 245
**Blackmore Denis** ..... 413
**Bolotnik Nikolai** ..... 91
**Bowles Stephen** ..... 177
**Böhm Valter** ..... 105
**Buchacz Andrzej** ..... 117
**Burdzik Rafał** ..... 127, 139
**Burghardt Andrzej** ..... 211
**Cao Dengqing** ..... 149
**Chen Huatao** ..... 149
**Chmielewski Adrian** ..... 159
**Cioch Witold** ..... 139
**Damasceno Berenice** ..... 171
**Diskovsky Alexander A.** ..... 41
**Dosaev Marat** ..... 291
**Drąg Łukasz** ..... 21
**Gallacher Barry** ..... 177
**Gałęzia Adam** ..... 189, 199
**Gambin Barbara** ..... 603
**Gerlici Juraj** ..... 325
**Gierlak Piotr** ..... 211
**Gontarz Szymon** ..... 223
**Górski Grzegorz** ..... 235
**Grzegożek Witold** ..... 11
**Gumiński Robert** ..... 159, 189, 223

**Haris Ahmed** ..... 245
**Harlecki Andrzej** ..... 255
**Hu Zhongxu** ..... 177
**Hwang Shih-Shin** ..... 291
**Jasiński Marcin** ..... 189
**Jiang Jingfei** ..... 149
**Kania Jan** ..... 363
**Kasperska Elżbieta** ..... 267
**Kasperski Andrzej** ..... 267
**Kaufhold Tobias** ..... 105
**Kaźmierczak Maciej** ..... 579
**Kaźmierczak Marek** ..... 579
**Klaerner Matthias** ..... 279
**Klein Wojciech** ..... 363
**Klimina Liubov** ..... 291
**Konieczny Łukasz** ..... 139
**Kostek Robert** ..... 301, 313
**Kozanecka Dorota** ..... 523, 533
**Kozanecki Zbigniew** ..... 523, 533
**Kroll Lothar** ..... 279
**Kudra Grzegorz** ..... 513, 579, 591
**Kurpa Lidiya** ..... 59
**Lack Tomáš** ..... 325
**Lin Kao-Huei** ..... 291
**Litak Grzegorz** ..... 235
**Łagodziński Jakub** ..... 523, 533
**Maia Nuno** ..... 461
**Major Izabela** ..... 339
**Major Maciej** ..... 339
**Marburg Steffen** ..... 279
**Marjasz Rafał** ..... 267
**Mazur Damian** ..... 351
**Mączak Jędrzej** ..... 159, 189
**McFarland Donald M.** ..... 245

**Mężyk Arkadiusz** ..... 363
**Mikulski Maciej** ..... 371, 383
**Mosdorf Romuald** ..... 235
**Motato Eliot** ..... 245
**Muszyńska Magdalena** ..... 211
**Nowak Andrzej** ..... 391
**Nowak Paweł** ..... 391
**Pająk Piotr** ..... 69, 489
**Pałczyński Tomasz** ..... 403
**Pawlak Mariusz** ..... 363
**Piętak Andrzej** ..... 383
**Radkowski Stanisław** ..... 199
**Rosato Anthony** ..... 413
**Rudy Marek** ..... 351
**Rysak Andrzej** ..... 235
**Sauter Anton** ..... 425
**Sawczuk Wojciech** ..... 437
**Selyutskiy Yury** ..... 291
**Shamolin Maxim V.** ..... 449
**Shmatko Tatiana** ..... 59
**Silva Tiago** ..... 461
**Skočilas Jan** ..... 475
**Skočilasová Blanka** ..... 475
**Soukup Josef** ..... 325, 475
**Stawiarski Adam** ..... 69, 489
**Steigenberger Joachim** ..... 425
**Stolarski Adam** ..... 501
**Struvé Ben** ..... 245
**Szcześniak Anna** ..... 501
**Szewc Michał** ..... 513, 591
**Szuster Marcin** ..... 211
**Szybicki Dariusz** ..... 211
**Szymański Grzegorz M.** ..... 437
**Theodossiades Stephanos** ..... 245

**Tkacz Eliza** ..... 523, 533
**Tomasiello Stefania** ..... 543
**Tyborowski Mateusz** ..... 579
**Urbaś Andrzej** ..... 255, 555
**Vakakis Alex** ..... 245
**Volkova Viktorija** ..... 567
**Warczek Jan** ..... 139
**Wasilewski Grzegorz** ..... 579
**Wierzbicki Sławomir** ..... 371, 383
**Will Christoph** ..... 425
**Wojtunik Igor** ..... 513, 591
**Wójcik Janusz** ..... 603
**Wuehrl Mario** ..... 279
**Wojciech Stanisław** ..... 11, 21
**Zeidis Igor** ..... 91, 105
**Zimmermann Klaus** ..... 91, 105

ISBN 978-83-7283-706-6